STATE OF CALIFORNIA • DEPARTMENT OF TRANSPORTATION

TECHNICAL REPORT DOCUMENTATION PAGE

DRISI-2011 (REV 10/1998)

1. REPORT NUMBER	2. GOVERNMENT ASSOCIATION NUMBER	3. RECIPIENT'S CATALOG NUMBER
CA20-2757-2		

4. TITLE AND SUBTITLE	5. REPORT DATE
Experimental and Analytical Studies of a Two-Span Bridge System with Precast Elements Incorporating Rebar Hinge and Socket Connection	July, 2020
	6. PERFORMING ORGANIZATION CODE UNR
7. AUTHOR Jared Jones, M. 'Saiid' Saiidi, Ahmad Itani	8. PERFORMING ORGANIZATION REPORT NO. UNR / CCEER 20-05
9. PERFORMING ORGANIZATION NAME AND ADDRESS Department of Civil and Environmental Engineering University of Nevada, Reno 1664 North Virginia Street Reno, Nevada 89557	10. WORK UNIT NUMBER
	11. CONTRACT OR GRANT NUMBER 65A0589
12. SPONSORING AGENCY AND ADDRESS California Department of Transportation Division of Research, Innovation and System Information P.O. Box 942873 Sacramento, CA 94273-0001	13. TYPE OF REPORT AND PERIOD COVERED Final 08/01/2016-7/31/2020
	14. SPONSORING AGENCY CODE 913

15. SUPPLEMENTARY NOTES

Prepared in cooperation with the State of California Department of Transportation.

16. ABSTRACT

Accelerated bridge construction (ABC) has become an increasingly appealing alternative to conventional cast-in-place construction (CIP) because of the benefits it offers in reducing onsite construction time and traffic impact. Maintaining joint integrity between precast components during seismic events has been a design challenge faced by engineers. Several ABC connections have been developed and shown promise in providing joint behavior emblematic of CIP bridges. However, these projects have been limited to component tests subjected to uniaxial ground motions, leaving questions regarding the seismic performance of ABC connections when subjected to biaxial forces and system interaction as part of a bridge system.

Six ABC connections were implemented in a 0.35 scaled bridge model including: (1) a rebar hinge precast with the footing connected to the column via a pocket for the column-to-footing connection, (2) a fully precast pocket connection for the column-to-cap beam connection. (3) extended strands and headed bars enclosed in the cast-in-place portion of the cap beam for the girder-to-cap beam connection, (4) lap spliced straight bars embedded in ultra-high performance concrete (UHPC) for the deck connection over the pier, (5) precast deck panels to girder connection using deck pockets and projected steel studs from precast concrete girders, and (6) short embedment length lap spliced straight bars for female-to-female deck panel-to-panel connection.

Experimental and analytical studies were conducted to: (1) assess the performance of the ABC connections and bridge system when subjected to multiple bi-directional ground motions of varying acceleration level, (2) review the current design procedure for each connection type and revise the procedure based on findings from the experimental results to account for interaction within the bridge system or for bi-axial ground motions, (3) determine if the behavior of the bridge system under biaxial seismic loading can be captured using existing analytical modeling methods, (4) evaluate parameters for the scaled bridge model that were not tested during the shake table tests, and (5) assess the relative seismic performance of ABC connections in three bridge models and make recommendations based on relative connection performance.

17. KEYWORDS	18. DISTRIBUTION STATEMENT
Seismic, Accelerated Bridge Construction (ABC), Rebar Hinge Base Connection, Socket Connection, Shake Table Tests, Bridge System Tests, Opensees	No restrictions. This document is available to the public through the National Technical Information Service, Springfield, VA 2216

19. SECURITY CLASSIFICATION (*of this report*)	20. NUMBER OF PAGES	21. COST OF REPORT CHARGED
Unclassified	514	

Reproduction of completed page authorized.

ADA Notice For individuals with sensory disabilities, this document is available in alternate formats. For alternate format information, contact the Forms Management Unit at (916) 445-1233, TTY 711, or write to Records and Forms Management, 1120 N Street, MS-89, Sacramento, CA 95814.

Report No. CCEER 20-05

EXPERIMENTAL AND ANALYTICAL STUDIES OF A TWO-SPAN BRIDGE SYSTEM WITH PRECAST ELEMENTS INCORPORATING REBAR HINGE AND SOCKET CONNECTIONS

Jared Jones
M. “Saiid” Saiidi
and
Ahmad Itani

A report sponsored by California Department of Transportation (Caltrans)
under Contract Number 65A0589

Center for Civil Engineering Earthquake Research

University of Nevada, Reno
Department of Civil and Environmental Engineering, MS 258
1664 N. Virginia St.
Reno, NV 89557

July 2020

DISCLAIMER STATEMENT

This document is disseminated in the interest of information exchange. The contents of this report reflect the views of the authors who are responsible for the facts and accuracy of the data presented herein. The contents do not necessarily reflect the official views or policies of the State of California or the Federal Highway Administration. This publication does not constitute a standard, specification or regulation. This report does not constitute an endorsement by the Department of any product described herein.

For individuals with sensory disabilities, this document is available in Braille, large print, audiocassette, or compact disk. To obtain a copy of this document in one of these alternate formats, please contact: the Division of Research and Innovation, MS-83, California Department of Transportation, P.O. Box 942873, Sacramento, CA 94273-0001.

Abstract

Accelerated bridge construction (ABC) has become an increasingly appealing alternative to conventional cast-in-place construction (CIP) because of the benefits it offers in reducing onsite construction time and traffic impact. Maintaining joint integrity between precast components during seismic events has been a design challenge faced by engineers. Several ABC connections have been developed and shown promise in providing joint behavior emblematic of CIP bridges. However, these projects have been limited to component tests subjected to uniaxial ground motions, leaving questions regarding the seismic performance of ABC connections when subjected to biaxial forces and system interaction as part of a bridge system.

This gap in research was addressed by testing a 0.35 scale two-span ABC bridge model, Calt-Bridge 2, on the shake tables at the Earthquake Engineering Laboratory at the University of Nevada, Reno. Experimental and analytical studies were conducted to: (1) assess the performance of the ABC connections and bridge system when subjected to multiple bi-directional ground motions of varying acceleration level, (2) review the current design procedure for each connection type and revise the procedure based on findings from the experimental results to account for interaction within the bridge system or for bi-axial ground motions, (3) determine if the behavior of the bridge system under biaxial seismic loading can be captured using existing analytical modeling methods, (4) evaluate parameters for the scaled bridge model that were not tested during the shake table tests, and (5) assess the relative seismic performance of ABC connections in three bridge models (Calt-Bridge 2 and two other previously tested ABC bridges, Calt-Bridge 1 and ABC-UTC) and make recommendations based on relative connection performance.

The following six ABC connections were implemented in Calt-Bridge 2: (1) a rebar hinge precast with the footing connected to the column via a pocket for the column-to-footing connection, (2) a fully precast pocket connection for the column-to-cap beam connection. (3) extended strands and headed bars enclosed in the cast-in-place portion of the cap beam for the girder-to-cap beam connection, (4) lap spliced straight bars embedded in ultra-high performance concrete (UHPC) for the deck connection over the pier, (5) precast deck panels to girder connection using deck pockets and projected steel studs from precast concrete girders, and (6) short embedment length lap spliced straight bars for female-to-female deck panel-to-panel connection.

Eight bi-directional ground motions were applied to the bridge model ranging from 30% to 225% of the design level earthquake. The 1994 Northridge earthquake measured at Sylmar station was simulated as the input motion for the shake table tests. The seismic performance of the bridge model was emblematic of the behavior expected from conventional CIP bridges with ductile plastic hinges forming in the columns and capacity protected elements remaining essentially elastic. Joint integrity was maintained in the ABC connections during all earthquake runs providing satisfactory load path between joined elements. Large in-plane rotations of the superstructure were observed, which were attributed to unbalanced friction forces at the abutments. The performance of the ABC connections in Calt-Bridge 2 was compared against the connections from two other scaled ABC bridge models, Calt-Bridge 1 and ABC-UTC. Some deterioration of the grout in the rebar hinge pocket connections was observed, therefore it was recommended that socket connections be used for rebar hinge connections at the column base.

Analytical studies were conducted using Opensees to evaluate ability of the model to capture the response of ABC bridge systems and connections. The calculated results were compared against the measured shake table test results to evaluate model accuracy. Base shear

and column displacement histories were captured reasonably well in the longitudinal and transverse directions. In-plane rotation of the superstructure was not captured with roller supports at the abutments. Therefore, friction effects were incorporated at the abutments through a parametric study, which produced similar in-plane rotation response to the measured results when friction was modeled at one abutment.

Overall, this study demonstrated that newly evolved ABC seismic design procedures may be utilized to expand application of ABC in moderate and high seismic regions with confidence.

Acknowledgements

This study was funded by the California Department of Transportation (Caltrans) through grant No. 65A0589. The statements and findings presented in this document are those of the author and do not necessarily represent the views of Caltrans. Caltrans research program manager, Mr. Peter Lee, and Caltrans Bridge engineers, Mr. Tom Ostrom, Dr. Mark Mahan, and Mr. Ron Bromenschenkel, are thanked for their input and support.

Dr. “Saiid” Saiidi is thanked for his guidance and mentorship during this project. His encouragement to critically think through all aspects of the research and keep perspective of the “big picture” has led to development as a researcher, engineer, and individual. This project would not have been what it was without his expertise and input. Dr. Ahmad Itani is thanked for serving as co-advisor for this project and providing his technical advice. And the other committee members, Dr. Mohammed Moustafa, Dr. Gokhan Pekcan, and the graduate school representative, Dr. Javad Sattarvand, are thanked for their feedback for this project.

There are many students and colleagues that aided with this project, but Dr. Jose Benjumea is specifically thanked for his construction assistance, and technical support throughout. He initiated much of the foundation for this project and was an inspiration through his strong work ethic and thorough review and critical evaluation of the bridge projects. Dr. Elmira Shoushtari is also thanked for helping with construction of the bridge and providing data from her bridge study for the comparison of ABC connections. Also, Taylor Schwartz and Christian Camarena are thanked for their help with specimen instrumentation.

This project and many others that have been tested at the Earthquake Engineering Laboratory would not be possible without the assistance of the laboratory staff: Dr. Patrick Lalace, Mr. Chad Lyttle, and Mr. Todd Lyttle. Their sense of constructability, and instrumentation knowledge added depth to the constructability portion of this project that would not be present without their input. The lab technician, Mr. Mark Lattin is thanked for assisting with material testing.

This report is based on a Ph.D. dissertation by the first author supervised by the co-authors.

Executive Summary

1. Introduction

The use of prefabricated bridge elements and systems (PBES) is an essential part of accelerated bridge construction (ABC) that has led to decreased construction time and improved project delivery time (FHWA, 2019b). PBES, structural components of a bridge that are generally constructed offsite and then transported and assembled on site, include features that reduce the onsite construction time and the mobility impact time relative to conventional construction methods. While there are many benefits associated with the PBES, maintaining integrity of connections between precast components (referred to as ABC connections) under seismic loads has led to design challenges in locations with moderate and high seismic activity. Currently, there are no codified guidelines for seismic design of ABC connections. As a result, existing design codes and standards for seismic design of bridges constructed with conventional methods are used to evaluate the performance of ABC connections even though these codes may not be applicable. Bridges constructed conventionally in seismic regions are designed based on the strong beam – weak column principle; meaning that plastic hinging should be directed towards seismic critical members, which in most bridge applications is the columns (Caltrans, 2019). This means that connections in bridges built with ABC should be able to transfer forces between members, form plastic hinges in the columns, and keep capacity protected elements essentially elastic during the design earthquake similar to their cast-in-place counterparts.

Many connections for ABC bridges have been developed and studied over the past decade at the University of Nevada, Reno and elsewhere [Cheng et al, (2009), Haraldsson, et al., (2013), Larosche, et al., (2014), Mehrain & Saiidi (2016), Mehrsoroush & Saiidi (2014), Mohebbi, et al. (2018a), Restrepo, et al., (2011), Tazarv and Saiidi (2015), Vander Werf, et al., 2015]. The majority of these connections have performed well under seismic load testing, having equal or superior performance when compared to their cast-in-place counterparts. While this type of testing is useful for determining local connection behavior and developing preliminary design procedures, a significant limitation in these studies was that testing was limited to the component or subassembly level. Furthermore, the loading in these studies was typically uniaxial and did not expose any shortcoming of the connections under biaxial earthquake loading. Therefore, the effect of biaxial forces and the interaction among connections at the system level as would be observed in practice, was not determined in these studies. Additional confidence in the integrity and resilience of ABC connections can be gained by incorporating these connections in a bridge system subjected to biaxial earthquake loading, prior to recommending these connections for engineering practice.

2. Research Objectives

The primary objectives of this study were to investigate the seismic response of bridges that integrated several precast components and connections at the system level, possibly help facilitate the adoption of accelerated bridge construction (ABC) in the field and identify necessary refinements in emerging connection seismic design guidelines for ABC bridges. This project was a part of a group of ABC bridge system seismic studies that involved three bridge models. Another objective of the study was to compare the performance of all three bridges at the connection and overall bridge system performance. The performance of the various components and connections in each bridge, and interaction among them was assessed. The first bridge was labeled Calt-Bridge 1 (Benjumea et al., 2019) and the second bridge was labeled ABC-UTC (Shoushtari et al., 2019). The focus of the current project was on Calt-Bridge 2, which differed from Calt-Bridge 1 in the column connections to the cap beam and footing. The study presented in this document consisted of experimental and analytical studies of Calt-Bridge 2 and an overall assessment of the seismic performance of the three bridge models.

Experimental and analytical studies were performed to assess six ABC connections viability in seismic regions as part of a bridge system in Calt-Bridge 2. These connections were incorporated at: (1) the column-to-footing connection, (2) column-to-cap beam connection, (3) girder-to-cap beam connection, (4) deck panel connection over the pier, (5) deck-to-girder connection, and (6) deck panel-to-panel connection.

The objectives of the experimental investigation were to: (1) select and evaluate six ABC connections in a scaled bridge model to determine their effectiveness in limiting plastic hinging to the columns and keeping the capacity protected elements essentially elastic during biaxial ground motions, (2) assess the performance of the connections under multiple bi-directional horizontal ground motions of varying acceleration levels, (3) evaluate constructability and interaction among the ABC connections, and (4) review the current design procedure for each connection type and determine any necessary revisions in the said procedure.

The objectives of the analytical studies were: (1) to determine if the behavior of the bridge system under biaxial seismic loading can be captured using existing modeling methods, (2) propose refinement to the analytical model based on measured results, and (3) using parametric studies, evaluate some of the critical parameters for the scaled bridge model that were not tested during the shake table studies.

The purpose of comparing the performance of the three bridges was to: (1) compare local behavior for different connections and make recommendations for implementation based on connection performance, (2) determine if any differences in bridge system performance were present as a result of the ABC connections behavior, (3) assess constructability of like connections and make recommendations.

3. Experimental Studies

A 0.35 scale, two span bridge model (Calt-Bridge 2) incorporating precast components and ABC connections was designed, constructed, and tested at the Earthquake Engineering Laboratory at the University of Nevada, Reno. The bridge system and connection performance were assessed during eight shake table tests, each with increasing acceleration amplitude. This section reviews the bridge model characteristics, construction and instrumentation of the bridge model, and the shake table test results.

3.1 Bridge Model

Calt-Bridge 2 was a scaled bridge model designed and constructed using ABC techniques. Geometric properties of Calt-Bridge 2 are shown in figure 1. Six ABC connections were incorporated in the design of Calt-Bridge 2 to assess their seismic performance when incorporated in a bridge system. Some of the components and ABC connections incorporated in Calt-Bridge 2 are shown in figure 2. A prototype bridge with geometric properties representative of a standard two-span highway bridge was created to establish a baseline design that could be scaled for implementation in a shake table test environment. The largest possible scale factor was used that would allow for testing of the bridge model, while allowing for transportation of bridge components and not exceeding the geometric and force capacities of the shake tables.

Bridge components were designed at the prototype level utilizing the Caltrans Seismic Design Criteria (SDC) (2019), even though SDC is for cast-in-place construction, and then scaled down for implementation in the scaled bridge model. Additional ABC seismic design resources from the literature were used despite the preliminary nature of the recommendations. Six ABC connections were designed for Calt-Bridge 2: (1) the column-to-footing connection, (2) column-to-cap beam connection, (3) girder-to-cap beam connection, (4) deck panel connection over the pier, (5) deck-to-girder connection, and (6) deck panel-to-panel connection. The design intent was for bridge performance to meet or exceed that of a cast-in-place bridge with similar dimensions.

The following six ABC connections were implemented in Calt-Bridge 2: (1) a rebar hinge precast with the footing connected to the column via a pocket for the column-to-footing connection, (2) a fully precast socket connection for the column-to-cap beam connection. (3) extended strands and headed bars enclosed in the cast-in-place portion of the cap beam for the girder-to-cap beam connection, (4) lap spliced straight bars embedded in ultra-high performance concrete (UHPC) for the deck connection over the pier, (5) precast deck panels to girder connection using deck pockets and projected steel studs from precast concrete girders, and (6) short embedment length lap spliced straight bars for female-to-female deck panel-to-panel connection. These connections were selected based on their field implementation readiness and feedback from Caltrans.

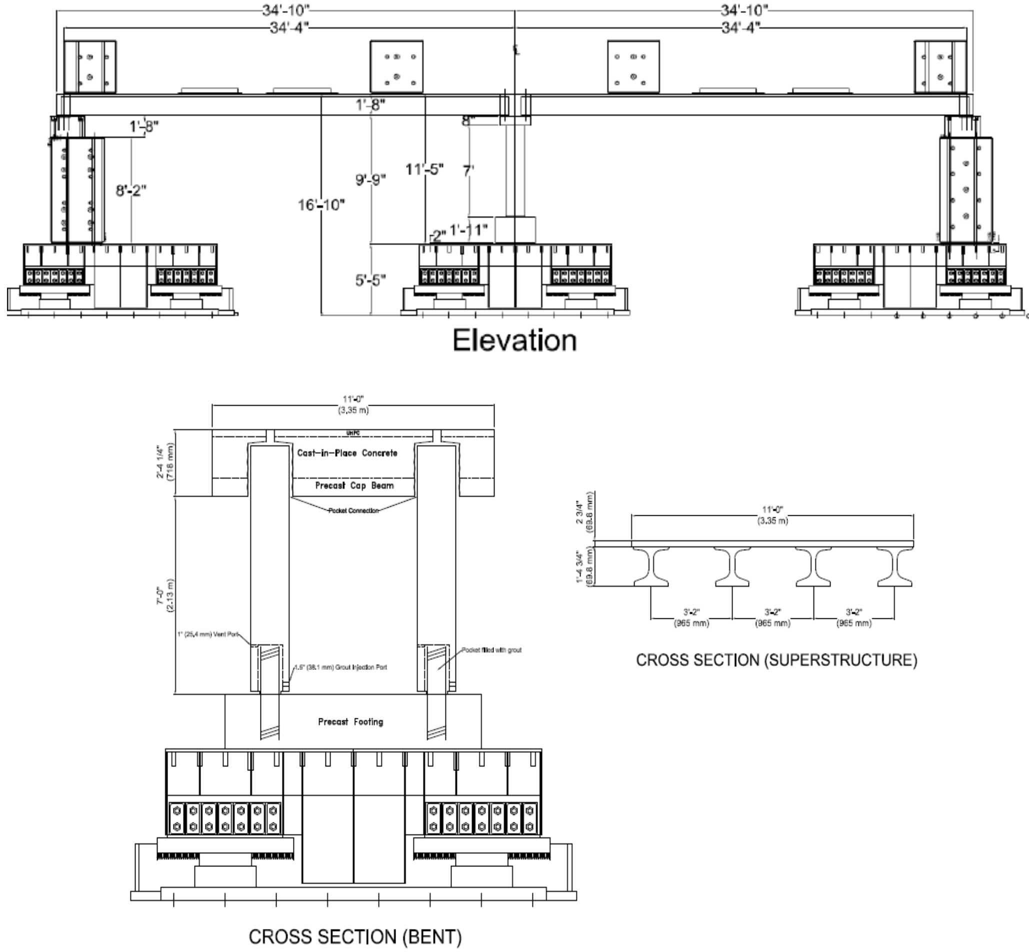

Figure 1: Elevation view of Calt-Bridge 2

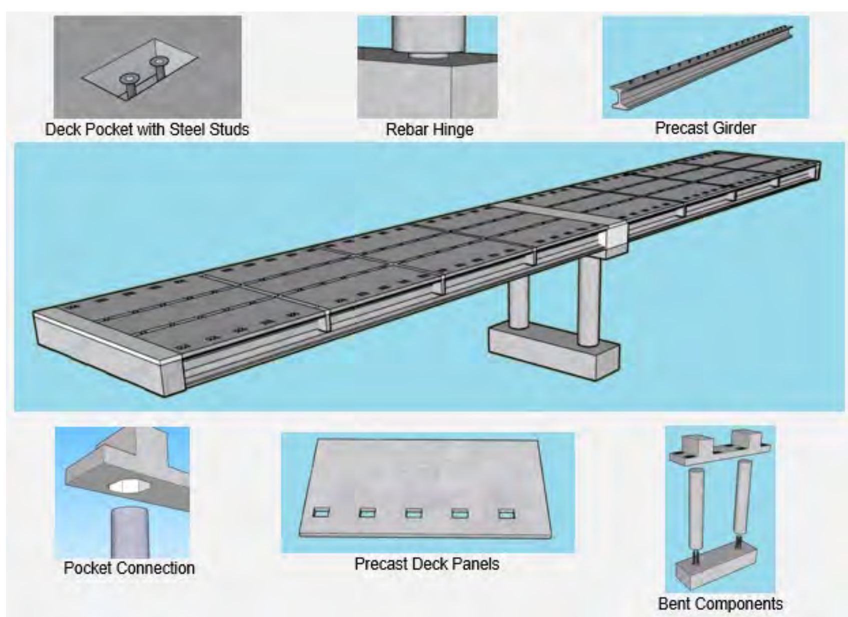

Figure 2: Components and ABC connections in Calt-Bridge 2

3.2 Construction and Instrumentation

Calt-Bridge 2 was constructed using prefabricated elements and systems (PBES) as shown in figure 3. The bent consisted of three components: the footing, columns, and cap beam. Each of these components were precast as individual elements and assembled after 28 days of cure time to ensure adequate concrete strength prior to transportation of the elements. The superstructure included two spans built using two types of precast components, precast deck panels and precast prestressed concrete girders. The spans were assembled in the structures yard simultaneously and were moved into the lab once completed. The construction was sequenced to impose simple for dead load – continuous for live load conditions in the superstructure. Extra weight was added to the superstructure to account to ensure that stresses were at full scale because real concrete and steel were used in the bridge model. The construction procedure is discussed in chapter 3.

Figure 3: Construction of bent and spans for Calt-Bridge 2

The bridge response during the shake table tests was monitored using several instrument types including strain gauges, Novotechnik displacement transducers, accelerometers, and video cameras and the data was recorded over 303 channels and sampled at a rate of 256 Hz. An additional 59 channels were dedicated to monitoring shake table feedback such as force, acceleration, velocity, and displacement. Further detail regarding instrumentation is presented in chapter 4.

3.3 Loading Protocol

The 1994 Northridge earthquake recorded at Sylmar station was used as the input ground motion for this study. The same record had been simulated for Calt-Bridge 1 and ABC-UTC. Dynamic analyses in Opensees were used to predict the response of Calt-Bridge 2 under bi-directional ground motions. The displacement response of the analytical model was used to create the target loading protocol for the shake table tests by adjusting the acceleration scale such that the peak calculated resultant displacement response was equivalent to the displacement demand of Calt-Bridge 2. A loading protocol was developed by scaling the design level earthquake to capture different limit states and the entire displacement range in the pushover curves. The loading protocol is presented in table 1. Eight earthquake runs were conducted, starting at 30% of the design level earthquake and increasing to 225%. The design earthquake was planned for run 3. White noise motions were initialized before each run in the longitudinal and transverse direction to determine the natural frequency of the bridge as damage progressed.

Table 1: Target loading protocol and PGAs for Calt-Bridge 2

Run #	% Design Earthquake	Scale Factor	PGA	
			Transverse (g)	Longitudinal (g)
WN1-L	-			
WN1-T				
1	30%	0.137	0.085	0.125
WN2-L	-			
WN2-T				
2	65%	0.296	0.183	0.271
WN3-L	-			
WN3-T				
3	100%	0.455	0.281	0.417
WN4-L	-			
WN4-T				
4	125%	0.569	0.351	0.521
WN5-L	-			
WN5-T				
5	150%	0.683	0.421	0.626
WN6-L	-			
WN6-T				
6	175%	0.796	0.491	0.729
WN7-L	-			
WN7-T				
7	200%	0.91	0.561	0.833
WN8-L	-			
WN8-T				
8	225%	1.02	0.632	0.938
WN9-L	-			
WN9-T				

3.4 Shake Table Test Results

The global behavior of Calt-Bridge 2 and local behavior of the bridge components and ABC connections was assessed using the measured data and visual evaluation. The connection performance is summarized below and in more detail in chapters 6 and 7.

3.4.1 Bridge Response

The global system level performance of Calt-Bridge 2 during shake table testing was satisfactory. The model did not collapse, and stability was maintained even after extensive yielding of the column bars as evident by the wide hysteretic loops in the force-displacement response (figure 4). Yielding of longitudinal bars occurred exclusively in the plastic hinge regions of seismic critical members (i.e. columns and base hinges), and all capacity protected members remained essentially elastic, even under ground motions substantially stronger than the design level earthquake. Calt-Bridge 2 exhibited ductile behavior undergoing a maximum displacement ductility of 4.6 (table 7.2). Note that this ductility was not the ultimate displacement ductility capacity because the columns did not fail, and the termination of bridge model testing was not due to column failure but because of concerns for unseating at the abutments. Minor in-plane rotation of the superstructure was observed during small earthquake runs. However, rotations became large during strong ground motions as shown in figure 5. Stable plastic hinging was observed in the column tops and base hinges with no abrupt drops in base shear. Spalling of the column cover concrete and large strains in the column longitudinal reinforcement were observed, but bar rupture did not take place. Biaxial response of components was observed indicating the bridge system was subjected to biaxial or coupled forces, meeting one of the primary goals of this study. Substantial in-plane rotation likely caused by asymmetric distribution of friction at the bearing pads induced large transverse displacements at the abutments, ultimately leading to the termination of the test to avoid potential unseating of the superstructure. Due to these displacement limits, the ultimate limit state of the bridge columns was not reached, although near unseating could be considered as the ultimate limit state of the bridge system itself. Nonetheless, because base shear had begun to decrease in both directions, it appeared that column failure could be imminent.

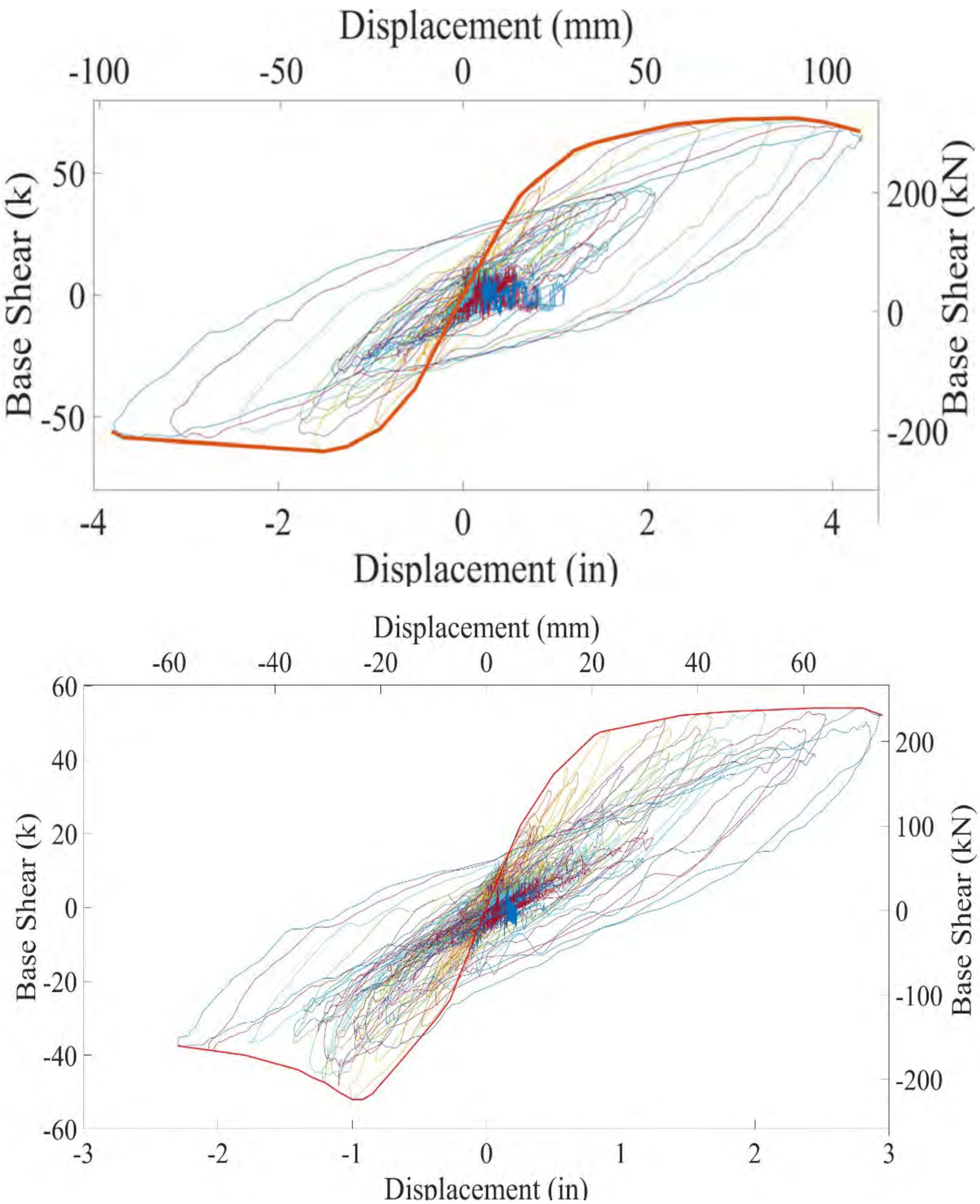

Figure 4: Longitudinal and transverse force displacement relationship, all runs

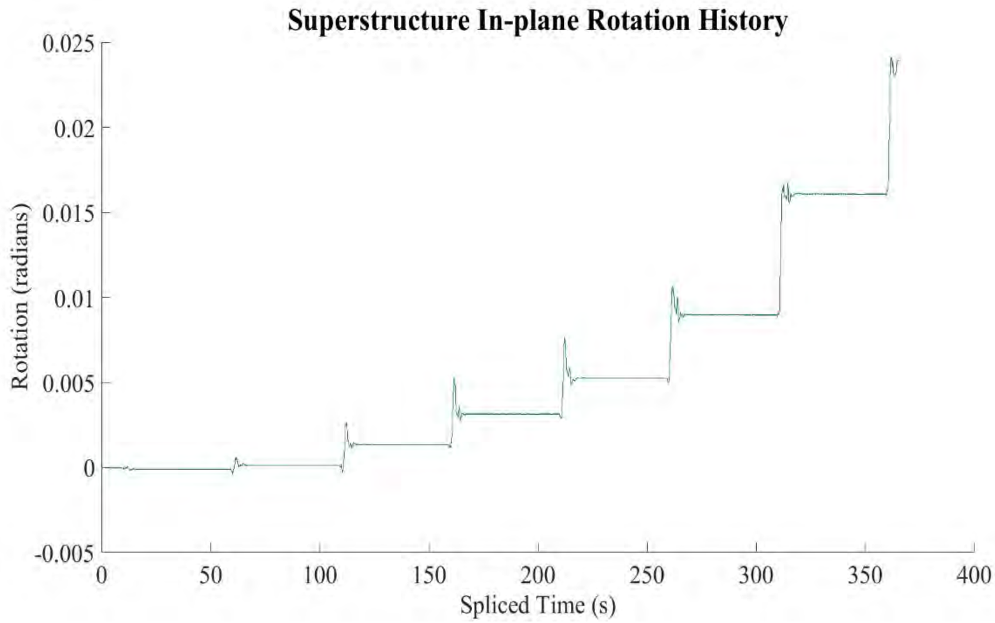

Figure 5: In-plane rotation of superstructure, all runs

3.4.2 ABC Connection Performance

3.4.2.1 Rebar Hinge

The column-to-footing connections consisted of hinge reinforcement cages that were precast with the footing and connected to the columns via an opening left in the precast columns. The observed condition of the rebar hinges under different levels of seismic simulation indicated the hinges performed satisfactorily with no rupture of longitudinal bars even under 225% of the design level earthquake. The pocket connections maintained integrity during all earthquake runs. Spalling occurred in the cover grout at the hinge throat due to the rotation experienced in this zone during lateral translation of the superstructure. No shear failure or excessive shear deformation at the hinge was observed.

3.4.2.2 Socket Connection

The column-to-cap beam connections consisted of two precast columns fitted into an opening within the cap beam via a socket connection, which is labeled as such per definition of the AASHTO LRFD Guide Specifications for ABC (2018) because the columns were fully precast with no exposed column bars protruding into the cap beam "socket." The socket connection provided good anchorage and allowed for formation of plastic hinges in the columns directly adjacent to the cap beam interface, while the cap beam remained capacity protected. Some minor spalling was observed in the grout between the column and cap beam under larger excitations, but no cracking or extensive spalling were seen in the connection. Large strains in the column longitudinal reinforcement were observed at the cap beam interface but dissipated when moving into the capacity protected element. Slippage in the connection was not observed. The column and cap beam performed as would be expected in cast-in-place components subjected to earthquakes, which suggests the socket connections fulfilled their purpose as a fixed connection between prefabricated elements for ABC applications in seismic regions.

3.4.2.3 Cap Beam Connections to Superstructure

The superstructure-to-cap beam connection consisted of projected girder strands with couplers and headed bars with crossties. The deck panel connection over the pier incorporated relatively long lap-spliced deck bars that were embedded in UHPC. These connections remained elastic for all earthquake runs and resisted the applied seismic moments. No separation was observed between the deck panels and UHPC or the superstructure and cap beam. There were no cracks at the joint interfaces and the components and connections remained capacity protected as designed. The measured rotations between the superstructure and cap beam were insignificant, which indicated full connectivity within the superstructure connections.

3.4.2.4 Joints in the Deck

The deck joints incorporated short lap spliced deck bars filled with UHPC. The panel-to-girder connection consisted of projected steel studs from the girders that were fit into pockets in the deck panels and connected via grout. No damage was observed in either connection type. Cracking of the deck panels or joints, or separation of the deck panels did not occur. The superstructure appeared to have performed as a capacity protected member as indicated by the absence of damage. Relative displacements between the deck panels and girders implied good connectivity between the components and suggested that composite action was provided.

4. Analytical Studies

Analytical studies were conducted in Opensees to calculate the response of Calt-Bridge 2 and validate the assumptions and procedures used to formulate the models. A post-test model was created to determine whether the response of a bridge constructed with ABC methods could be accurately captured using analytical methods. In addition, parametric studies of friction effects at the abutments on the in-plane rotational response of the superstructure were performed to investigate reasons for the large in-plane rotations observed during shake table testing. Development of the post-test model is discussed in more detail in chapter 8, and the parametric study of friction effects is presented in chapter 9.

4.1 Posttest Analyses

The response of Calt-Bridge 2 during seismic excitation was predicted using a preliminary analytical model in Opensees prior to finalizing the bridge model design and the shake table testing protocol. After the shake table testing, the measured data was first compared to the predicted response from the pretest analytical model to assess the analytical model accuracy. Various assumptions were made in the pretest analytical model, including the use of target acceleration records and expected material properties. The assumed records and material properties differed from the achieved shake table accelerations and measured material properties from the shake table tests. The differences resulted in significant differences between the measured and predicted data. Several modifications were made to the input data and the pretest model to determine if the response of Calt-Bridge 2 could be reasonably captured using dynamic analysis: changing the input motions to the achieved shake table accelerations, incorporating measured material properties, and refining the modeling of the ABC connections by including bond-slip rotation at the column joints.

The measured and calculated displacement and base shear histories were compared to assess the capability of the posttest analytical model in capturing the global seismic behavior of Calt-Bridge 2. The force-displacement relationship from the post-test analytical model is shown in figure 6. The measured and calculated hysteretic responses are closely matched in the longitudinal directions, particularly for later runs. The elastic stiffness of the bent was overestimated as exhibited in the difference of the measured and calculated force-displacement slopes in runs 1 and 2. This was likely caused by relative deformations in connections among elements, resulting in the system being more flexible in reality compared to the idealized condition of perfectly rigid connections assumed in the posttest model. Once plastic hinges formed in the columns and hinges (run 3 and on), the model more accurately captured the measured response of Calt-Bridge 2, because the post-yield properties of the columns and hinges were accounted for through the material constitutive relationship. The calculated response exhibited nearly symmetric behavior as was observed in the measured results, which contrasts with the behavior of the pretest model where longitudinal displacement was dominant in one direction. The hysteresis curves exhibited comparable energy dissipation between the two methods as demonstrated by the overlapping curves. The correlation is not as strong in the transverse direction with the peak displacements still being overestimated by the analytical model. However, the hysteresis curves are of similar width and shape, showing a stronger fit between the measured and calculated results for the transverse direction than that observed in the pretest analysis. The calculated elastic stiffness was also overestimated in the transverse direction, again attributed to small slippage between elements. The peak displacements were overestimated by the analytical model in the transverse direction in all runs, which was likely caused by the absence of friction forces at the abutments that resisted superstructure translation during the shake table tests. This phenomenon was evaluated further using parametric studies of the effect of friction at the abutment-superstructure interface.

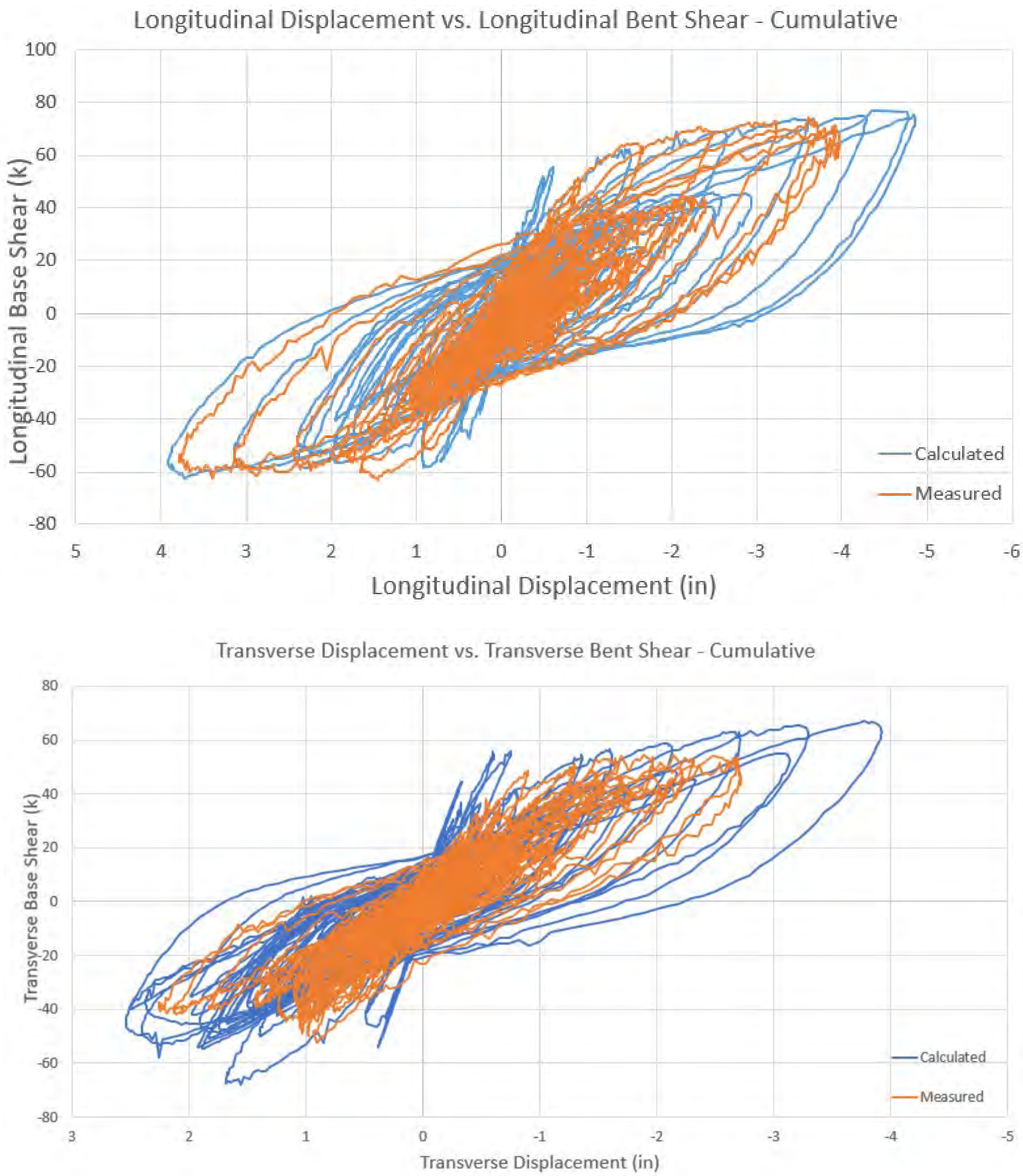

Figure 6: Measured and calculated force-displacement response, all runs

4.2 Parametric Study of Abutment Friction Effects

Relatively large in-plane rotation was observed in the response of Calt-Bridge 2, ultimately leading to termination of testing due to potential superstructure unseating at the abutments. The closeness of the calculated in-plane rotation and translation vibration periods was, in part, responsible. Differential reactions at the abutments due to framing effects in the longitudinal direction combined with uneven friction forces were thought to have imposed these large rotations. To assess this condition, the friction effects on superstructure in-plane rotation were modeled at the abutments in three different configurations (figure 9.1). These models included friction at both abutments (FM-1), friction at the east abutment (FM-2), and friction at the west abutment (FM-3). Results from the post-test model with no friction effects included (NF) were used as a benchmark. These three friction configurations were selected to investigate which of two factors were the primary cause of the in-plane rotation: (1) differences between the vertical reactions at the abutments (caused by the frame action of the bridge under longitudinal displacements), or (2) differences between the friction coefficients between the two abutments. The latter could be a result of slight variation in construction of the bearings and damage in the PTFE bearing pads. The cumulative superstructure in-plane rotation was calculated in each model and is shown in figure 7.

Friction at the west abutment had a clear impact on the rotational response of the superstructure. The good correlation between FM-3 and the measured response implies that the frictional behavior at the stainless steel on PTFE interface was not the same at the two abutments during shake table testing, particularly during later runs. Incorporation of a high friction coefficient at the west abutment with no friction at the east abutment resulted in good estimation of in-plane rotation in runs 1 through 6, which infers the bearing interface at the west abutment may have had variations in the bearing contact surface causing large friction forces. Additionally, the measured residual in-plane rotation was much closer to the peak rotation for runs 7 and 8, which may have resulted from damage in the bearings causing the system to not rebound to the same extent as earlier runs. Some possibilities that may have caused additional friction include: uneven contact of the stainless steel plate with the PTFE pad, which could cause the corners of the steel plate to bear into the PTFE pad rather than slide across it; or the girder bases could have been at slightly different elevations resulting in one or more girders not fully bearing on the PTFE pad. These factors explain the initiation of in-plane rotation in lower runs, but it was likely that the damage to one or more of the PTFE pads in run 6 or 7 that caused the in-plane rotation to greatly increase. This explains why the model captured the in-plane rotation behavior of Calt-Bridge 2 for early runs but poorly estimated the in-plane rotation in runs 7 and 8.

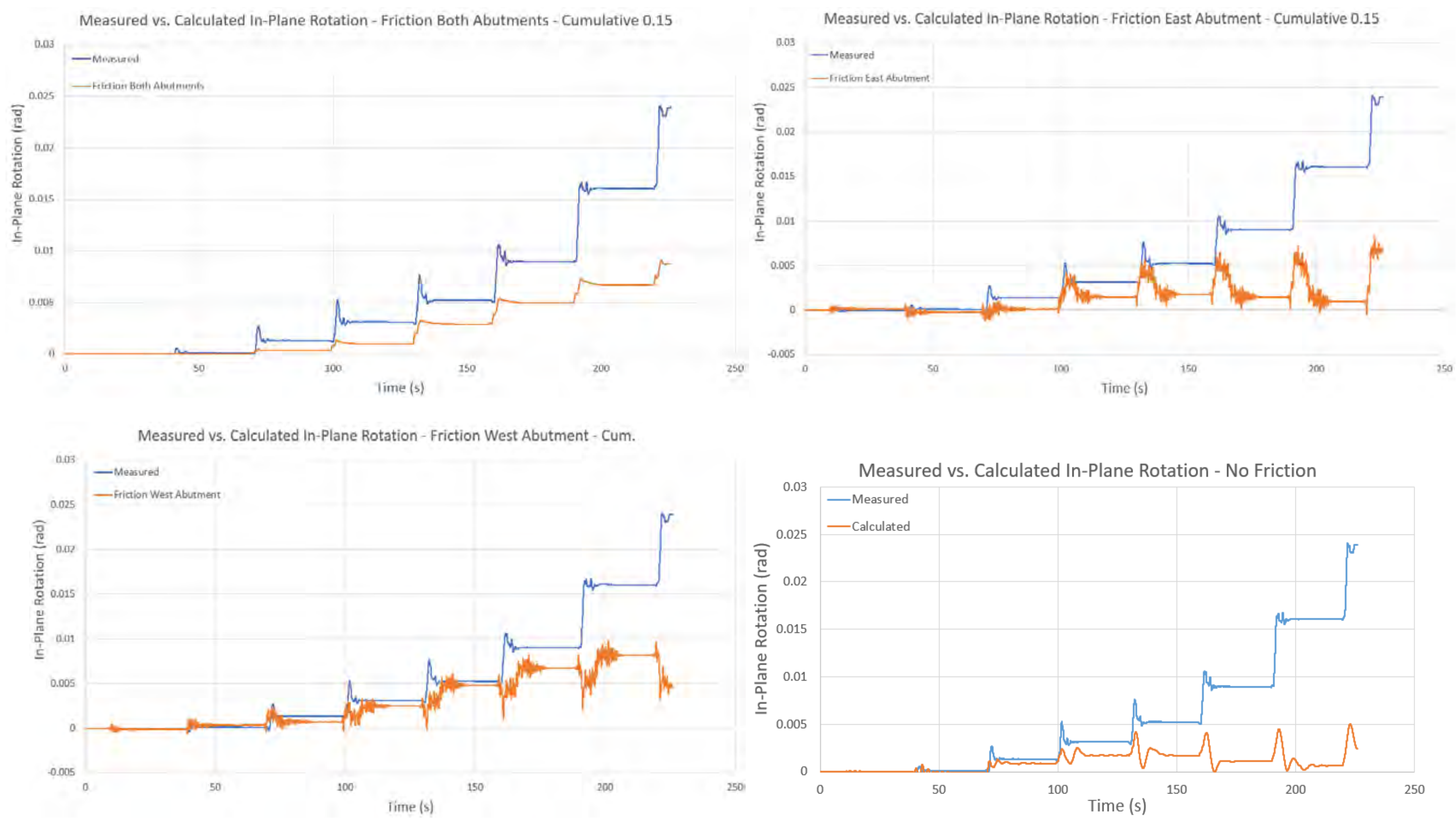

Figure 7: Measured and calculated in-plane rotational response for FM-1 (top left), FM-2 (top right), FM-3 (bottom left), and NF (bottom right)

5. Design Implications

Calt-Bridge 2 and the six ABC connections were designed using a combination of existing guidelines for cast-in-place construction and other documents for ABC from the literature. These connections had not been incorporated in a bridge system utilizing ABC methods. The Calt-Bridge 2 shake table test data provided an opportunity to assess the seismic performance of these connections relative to the design criteria to possibly identify any necessary refinement in the methods. The following design implications were made based on the findings from the shake table tests and analytical studies.

5.1 Column Base Connection

- Pocket connections with pockets in the columns provided complete connectivity for rebar hinges in the column bases. Relative horizontal displacement was observed at the hinges between the bottom of the full column section and the top of the footing during strong ground motions, a part of which was attributed to degradation of the hinge pocket grout under cyclic loading. The other part was due to degradation of the hinge throat itself that is expected. Utilizing a precast concrete hinge stem with socket connection between the footing and column is recommended to alleviate the pocket grout degradation problem.
- The design procedure for rebar hinges developed by Cheng et al. (2009) based on uniaxial loading of cast-in-place hinges led to satisfactory performance for precast ABC hinges subjected to biaxial ground motions with no modifications required.
- Shear design for the rebar hinge provided sufficient capacity to resist the applied biaxial shear for multiple ground motions. Shear failure was not observed in the hinges even when extensive yielding had occurred in the hinge throat.
- The embedment length for the hinge reinforcement in the pocket connection and footing provided sufficient development of the longitudinal reinforcement, which allowed for formation of plastic hinges and large sustained reinforcement strains within the hinge throat.
- The hinge throat thickness was sufficiently large to allow rotation of the rebar hinges without contact between the column edges and footing. This prevented large moments from developing in the foundation due to bearing of the column on the footing during hinge gap closure, which could damage the foundation and increase the column plastic shear.
- Joint integrity was maintained at the column bases under all ground motions even after the hinge longitudinal bar strains and hinge rotations were large. No damage was observed in the pocket connection or footing except for some degradation of the grout in the lower part of the pocket.

5.2 Column-to-Cap Beam Connection

- Socket connections in the column-to-cap beam connection provided sufficient anchorage for the columns. Slippage between the columns and cap beam was insignificant.
- The socket connection guidelines developed by Tazarv & Saiidi (2015) were successfully incorporated for bridge systems implementing ABC methodologies. The design procedure for the socket connections and cap beam dimensions resulted in satisfactory joint behavior for both in-plane and out-of-plane

superstructure translation. The performance of the precast cap beam, columns, and socket connections was emulative of conventional bridge behavior.

- Embedment depths of 1.25 times the column diameter allowed for full transfer of biaxial forces between the superstructure and columns. Whether this depth can be reduced to 1.0 times the column diameter as suggested by a recent proposed AASHTO guideline (Saiidi, et al. 2020) could not be assessed in the present study.
- Cap beam widths equal to the column diameter plus 15 inches (381 mm) on each side of the column at the prototype level as recommended by Tazarv & Saiidi (2015) allowed for insertion of the precast columns into the socket connections with sufficient clearance. The recently released proposed AASHTO guideline (Saiidi, et al. 2020) calls for a minimum of 12 inches (254 mm) on each side of the column for cap beam width. The cap beam width in Calt-Bridge 2 was sufficiently large to allow for large column displacements in the bent out-of-plane and in-plane directions while keeping the cap beam capacity protected.
- Joint integrity was maintained for all ground motions. No damage was observed in the cap beam or socket connections, which implies that the socket connection transferred the loads to the columns, allowed plastic hinges to develop in the column tops, and kept the capacity protected members essentially elastic even under strong ground motions.

5.3 Girder-to-Cap Beam Connection

- The extended strand bent with free end detail developed by Vander Werff et al. (2015) was successfully implemented in a bridge system and provided full positive moment transfer between the spans and cap beam.
- Tension in the cap beam from positive superstructure moment was resisted by two mechanisms: the girder strands, and shear friction between the cast-in-place portion of the cap beam and girders. The strands were utilized more in the exterior girders than the interior girders with 45% and 20% of the tension resisted by the exterior and interior girder prestress strands, respectively. During design, it was assumed that 80% of tension was resisted by the girder strands with the remaining 20% resisted by shear friction. The measured data in Calt-Bridge 2 revealed that shear friction contributed 49% to the tensile resistance in the cap beam with contributions as high as 80% observed in the interior girders, which implies that the number of girder strands anchored in the connection may be reduced.
- No slippage was observed between the spans and the cap beam. This demonstrates that the girder-to-cap beam connection and embedment length for the spans provided sufficient anchorage for the superstructure within the cap beam.

5.4 Deck Connection over Pier

- The projected deck reinforcement over the bent encased in UHPC remained elastic even under strong ground motions. The design procedure for the deck reinforcement in this region was satisfactory in resisting the tension from negative superstructure moment.

- Long lap spliced joints embedded in UHPC demonstrated strong bond between the spliced reinforcement and provided full connectivity. Lap sliced deck bars with UHPC placed over the entire width of the cap beam simplify construction and are recommended for ABC even though current design guidelines do not allow lap splices over the cap beam.
- Part of the tension in the upper region of the cap beam was resisted by UHPC as exhibited by the lower deck bar strains relative to the girder strand strains. Despite the UHPC having significant tensile resistance, it is recommended that the longitudinal deck reinforcement be designed to resist all negative moment, while neglecting any contribution from the UHPC. This results in conservative tensile capacity in the upper region of the cap beam and helps ensure that the connection remains capacity protected.

5.5 Deck-to-Girder Connection

- No damage was observed in the deck-to-girder connections, including the deck panel pockets, pocket grout, and UHPC.
- Slippage did not occur between the deck panel and girders, even at locations with the peak interface shear. No differences were observed in the measured slippage between the deck and the exterior or interior girders. This indicated that both the steel studs in precast deck pockets (exterior girders) and the steel studs along a longitudinal deck joint cast in UHPC (interior girders) provided good shear resistance between the connected elements.
- The design procedure for the size and spacing for the projected steel studs in the girders developed by Shrestha et al. (2017) resulted in composite action between the deck panels and girders for a bridge system.

5.6 Deck Panel-to-Panel Joints

- The deck panel-to-panel joints remained free of cracking and debonding under all ground motions. The joints transferred all longitudinal and transverse deck forces, while remaining capacity protected even under strong ground motions.
- Short lap-spliced joints cast with UHPC were found to adequately transfer deck forces . The development lengths for short lap-splices cast in UHPC proposed by Yuan & Graybeal (2014) were found to be sufficient for ABC bridge system applications.

6. Comparison of Seismic Performance of Three ABC Bridge Models

Three 0.35 scale, two-span bridge models were tested in succession on the shake tables in the Earthquake Engineering Laboratory (EEL) at the University of Nevada, Reno. All bridges were constructed using ABC methods, specifically utilized prefabricated elements and systems (PBES), and incorporated ABC connections between elements. Because the bridges had the same overall geometry and target ground motion histories, there was an opportunity to assess the performance of bridges and connections relative to each other.

6.1 Summary Description of Three ABC Bridge Models

The following three bridge models were tested: (1) the first bridge was tested by Benjumea et al. (2019) and was labeled Calt-Bridge 1, which consisted of concrete components including prestressed precast girders, (2) the second bridge model was labeled ABC-UTC and was tested by Shoushtari et al. (2019), which was a steel girder bridge with reinforced concrete bent and precast deck panels, (3) and the third bridge model was labeled Calt-Bridge 2 and is the subject of this report. This bridge model was similar to Calt-Bridge 1, but the column connections were different between the two. It incorporated prestressed concrete girder bridge, reinforced concrete bent, and precast deck panels.

Calt-Bridge 1 incorporated the following ABC connections: (1) base pipe-pins to attach the columns to the footing, (2) column to cap beam connection formed by grouted duct connections between the column and a precast segment of the cap beam with the column bars extended into the CIP part of the cap beam, (3) extended strands and headed bars enclosed in the cast-in-place portion of the cap beam for the girder-to-cap beam connection, (4) lap spliced straight bars embedded in ultra-high performance concrete (UHPC) for the deck connection over the pier, (5) precast deck panels to girder connection using deck pockets and projected steel studs from precast concrete girders, and (6) short embedment length lap spliced straight bars for female-to-female deck panel-to-panel connection.

The following ABC connections were utilized in ABC-UTC: (1) rebar hinge with socket connection in the footing, (2) grouted duct connection for the column-to-cap beam connection, (3) seismic simple for dead continuous for live (SDCL) girder-to-cap beam connection, (4) lap spliced straight bars embedded in ultra-high performance concrete (UHPC) for the deck connection over the pier, (5) precast deck panels to girder connection using deck pockets and projected steel studs from steel girders, and (6) short embedment length lap spliced straight bars for female-to-female deck panel-to-panel connection.

Six ABC connections were incorporated in each bridge model. The following connections were utilized in Calt-Bridge 2: (1) a rebar hinge precast with the footing connected to the column via a pocket for the column-to-footing connection, (2) a fully precast socket connection for the column-to-cap beam connection. (3) extended strands and headed bars enclosed in the cast-in-place (CIP) portion of the cap beam for the girder-to-cap beam connection, (4) lap spliced straight bars embedded in ultra-high performance concrete (UHPC) for the deck connection over the pier, (5) precast deck panels to girder connection using deck pockets and projected steel studs from precast concrete girders, and (6) short embedment length lap spliced straight bars for female-to-female deck panel-to-panel connection.

6.2 Comparison of Overall Performance of ABC Bridge Systems

Eight earthquake runs were applied to each bridge (table 10.3). Shake table testing of Calt-Bridge 1 and Calt-Bridge 2 was terminated during run 8 after the peak input acceleration had been applied due to concerns about unseating of the superstructure at the abutments that resulted from in-plane rotation. However, because the peak accelerations of the ground motions in run 8 had been applied, the results from that run were still deemed indicative of the effect of the 200% and 225% design level earthquake for Calt-Bridge 1 and Calt-Bridge 2, respectively. Bridge system ultimate state was caused by excessive superstructure displacements at the abutments and not by failure of the columns. Therefore, the ultimate displacement capacity of the bents was not determined. However, reduction in peak base shear during the last runs suggests that failure was imminent in both bridge models. In contrast to Calt-Bridge 1 and 2, the bent in ABC-UTC did reach its near failure state during run 8 due to buckling of column longitudinal bars and extensive column core damage. The in-plane rotations in ABC-UTC were substantially smaller than those in the other two bridges.

Calt-Bridge 2 was the stiffest of the three bridges as exhibited by the relatively low drift ratios in both directions as well as relatively high base shears, particularly in later runs. This behavior was expected due to the larger column sections than those in ABC-UTC and larger column base moment capacity than Calt-Bridge 1. ABC-UTC experienced constant increases in peak displacements in runs 1 through 6 but the peak longitudinal displacements decreased in runs 7 and 8. However, the peak resultant displacement still increased in the last two runs because the peak transverse displacement increased. Calt-Bridge 1 displayed stable increases in displacement and base shear as runs progressed. In all three bridges ductile column plastic hinges were formed with no strength degradation as exhibited by the sustained plastic base shear in the hysteresis curves. Wide hysteresis loops showed that energy dissipation was maintained in all runs, which implied that progressive yielding occurred in the bridge systems while the force and displacement demands were resisted by the bridge components and connections during the shake table tests.

6.3 Comparison of Performance of ABC Connections

There were many differences in the ABC connection details incorporated at the column tops and bases among the three bridges. Therefore, comparisons in connection performance at these locations provided the most insight and are summarized below. The deck and superstructure connections exhibited similar performance among the three bridges and met the respective design criteria and are not discussed further in this section. Section 10.3 contains more detail on the relative performance of each connection.

6.3.1 Rebar Hinge Connections

The rebar hinge connection location in ABC-UTC was a socket connection with opening in the footing, and a pocket connection with opening in the column in Calt-Bridge 2. Most hinge performance parameters including measured strains, and hinge deformation were unaffected by the connection type in the two bridges. Two primary differences were observed between the pocket connections and socket connections: (1) some damage extended into the grout in the pocket connections in Calt-Bridge 2, while the socket connections in ABC-UTC remained essentially damage free, and (2) larger relative horizontal displacements were observed between the hinge base and footing in the pocket connections in Calt-Bridge 2. The rebar hinge connection used in Calt-Bridge 2 consisted of a pocket connection with the opening inside the column that was filled with grout. The larger relative horizontal displacement for the pocket connection was attributed to spalling of the grout around the hinge extending into the opening inside the column. As the hinges and the pocket connections were composed of grout, the cyclic loading applied to the hinge led to deterioration of the grout around the steel reinforcement and into the pocket. This led to reductions in the horizontal stiffness of the hinges that in turn led to larger relative displacements between the hinge column base and the footing. One potential solution to mitigate this loss of stiffness would be to cast concrete rather than grout around the hinge bars and create a precast concrete stem. The stem would then be inserted into the column opening and the space between the stem and column would be filled with grout in much the same way the connection with a footing socket was constructed in ABC-UTC. This adjustment would change the "pocket" connection in to a "socket" connection Calt-Bridge 2. Because of the larger relative horizontal displacements in the pocket connection, only socket connections are recommended for base hinge connections to avoid excessive deterioration in the grout at the hinge throat and the opening.

6.3.2 Recommendations for Pipe-Pin and Rebar Hinge Connections

The pipe-pin connection used in Calt-Bridge 1 provided many advantages over the rebar hinge connection used in the other two bridges. The pipe-pin connection remained essentially elastic even under strong earthquakes, meaning the connection does not need to be repaired or replaced after an earthquake. Flexural capacity was significantly reduced from that of the rebar hinge, thus reducing demand on the footing. Consequently, near pin-like behavior was achieved using the pipe-pin connection, whereas the rebar hinge had significant column base moment, which caused Calt-Bridge 2 to be much stiffer. Relatively low plastic shear was observed in Calt-Bridge 1 as a result of the implementation of the pipe-pin connection, which would result in lower column transverse reinforcement than was used in Calt-Bridge 2.

There are many benefits to the use of pipe-pins in column base connections, however, some drawbacks exist. The pipe-pin has reduced fixity compared to rebar hinges, which is ideal for reducing base shear and the seismic demand on the footing, but this results in larger displacements that must be accounted for in design (e.g. increasing hinge throat thickness to prevent bearing of the column base on the footing, providing sufficient seat lengths at the abutments, etc.). Additionally, the construction of the pipe-pin connection is more complicated than that of a rebar hinge. Changing the column base connection from a rebar hinge to pipe-pin resulted in an additional connection between the precast pedestal and the footing as well as tight tolerances during placement of the upper and lower pipes. Rebar hinges are relatively simple connection details that reduce moment at the column end without requiring additional components and design steps.

Based on the aforementioned discussions, pipe-pins are recommended for cases where relatively small column base moment is of importance. Rebar hinges provide satisfactory performance for ABC applications in seismic regions but may require repairs after strong earthquakes due to yielding in the hinge longitudinal bars. The relative simplicity of the rebar hinge makes it a desirable option if the contractor or designer experience is limited.

6.3.3 Recommendations for Grouted Duct and Socket Connections

The grouted duct connection and socket connections both provided effective moment transfer between the columns and cap beam, while maintaining joint integrity. Extensive plastic hinging was observed in the columns in both connection types. No significant differences in connection behavior were observed and both connection types are recommended for incorporation in ABC bridge systems, although the socket connection might be preferred because of its relative ease of construction due to its better tolerance and the fact that aligning column bars with grouted ducts may present construction challenges.

7. Conclusions

The following conclusions were drawn from the experimental and analytical studies of Calt-Bridge 2 and assessment of the relative performance of Calt-Bridge 1, ABC-UTC bridge, and Calt-Bridge 2:

1) Bridge systems utilizing prefabricated elements and the six ABC connections utilized in this study meet the seismic requirements for CIP bridges in current design codes and can be implemented in the field with confidence.
2) The ABC connection details used in all three bridges and design guidelines resulted in satisfactory seismic performance even under strong earthquakes. Many of these methods have been incorporated in the newly released proposed AASHTO seismic guidelines for seismic design of ABC connections providing tools to implement the results of the present study in practice.
3) The behavior of rebar hinges precast with the footing and connected via column pocket connections resembles that of CIP hinges, providing reduction in the moment transferred to the footing in addition to reducing column plastic shear forces. Pocket connections cast with grout for the hinge material experience limited damage and relative horizontal displacements between joined elements when subjected to cyclic loading. Socket connections are recommended as an alternative to mitigate these issues.
4) Socket connections provide a full moment connection between prefabricated elements and allow plastic hinges to form in connected seismic critical members.
5) Extended strand bent with free end anchorage in the girder-to-cap beam connections are practical and provide sufficient positive superstructure moment resistance. The superstructure behaves as a continuous element over the supports after casting of the integral cap beam, and results in a fixed connection between the bent and superstructure.
6) UHPC provides good continuity for lap spliced bars between precast elements due to its large bond strength and intrinsic tensile capacity even in capacity-protected connections where lap splices are disallowed.
7) Steel studs projected from girders into precast deck panels provide composite action between the deck and girders and maintain their integrity during seismic events.
8) Nonlinear analytical models implemented in OpenSEES can reasonably capture the macroscopic seismic response of bridges constructed with precast elements and ABC connections.
9) Accounting for friction effects at the abutments can lead to better correlation between measured and calculated system response.
10) Pipe-pins provide pin-like behavior when incorporated at the column base and are recommended over rebar hinges because of relatively low column base moment and essentially elastic response during strong earthquakes.
11) No significant differences were observed between the seismic response of socket and grouted duct connections in joining columns to cap beams. Both are recommended for implementation in moment connections.

Table of Contents

List of Tables

List of Figures

Chapter 1. Introduction

1.1 Problem Description

Of the 600,000 bridges in the United States, approximately 25% require rehabilitation, repair, or total replacement (FHWA, 2019a). Many of these bridges are located in high traffic areas, where closing a bridge can have a significant social and economic impact on the surrounding regions. In addition, the direct and indirect costs of detours from partial or full-lane closures can exceed the cost of the structure itself. These concerns have placed an increased interest on bridge construction techniques that can save time and cost. Minimizing traffic reductions by reducing construction time can mitigate the economic and safety impacts stemming from bridge construction. One technique that has been developed to decrease construction time is accelerated bridge construction (ABC). According to the Federal Highway Administration, ABC is bridge construction that uses innovative planning, design, materials and construction methods in a safe and cost-effective manner to reduce the onsite construction time that occurs when building new bridges or replacing and rehabilitating existing bridges. Benefits associated with ABC include improved constructability, improved project delivery time, and improved work-zone safety for the traveling public, all while also reducing traffic impact and onsite construction time (FHWA, 2019a).

The use of prefabricated bridge elements and systems (PBES) is one methodology within ABC (FHWA, 2019b). PBES, structural components of a bridge that are generally constructed offsite and then transported and assembled on site, include features that reduce the onsite construction time and the mobility impact time relative to conventional construction methods. While there are many benefits associated with the use of PBES, maintaining integrity of connections between precast components (referred to as ABC connections) under seismic loads has led to design challenges in locations with seismic activity. Currently, there are no adopted guidelines for seismic design of ABC connections. As a result, existing design codes and standards for seismic design of bridges constructed with conventional methods are used to evaluate the performance of ABC connections even though these codes may not be applicable. Bridges constructed conventionally in seismic regions are designed based on the strong beam – weak column principle; meaning that plastic hinging should be directed towards seismic critical members, which in most bridge applications is the columns (Caltrans, 2019). This means that connections in bridges built with ABC should be able to transfer forces between members, form plastic hinges in the columns, and keep capacity protected elements essentially elastic during the design earthquake like their cast-in-place counterparts.

Several connections for ABC bridges have been developed and studied over the past decade at the University of Nevada, Reno and elsewhere [Cheng et al, (2009), Haraldsson, et al., (2013), Larosche, et al., (2014), Mehrain & Saiidi (2016), Mehrsoroush & Saiidi (2014), Mohebbi, et al. (2018a), Restrepo, et al., (2011), Tazarv and Saiidi (2015), Vander Werf, et al., 2015]. Many of these connections have performed well under seismic load testing, having equal or superior performance when compared to their cast-in-place counterparts. While this type of testing is useful for determining local connection behavior and developing preliminary design procedures, a significant limitation in these studies was that testing was limited to the component or subassembly level under uniaxial loading. Therefore, the effect of biaxial forces and the interaction between connections at the system level as would be observed in practice, was not determined in these studies. Additional confidence in the integrity and resilience of developed ABC connections can be gained by incorporating these connections in a bridge system subjected to biaxial earthquake loading, prior to recommending these connections for engineering practice.

1.2 Literature Review

Six ABC connections were selected for incorporation in Calt-Bridge 2. Four of these connections, which were likely to be less critical under seismic loading, were selected based on a viability study that reflected recent research for these connections (Benjumea et al., 2019). The two most critical connections that were unique to Calt-Bridge 2 were: (1) a rebar hinge precast with the footing connected to the column via a pocket for the column-to-footing connection, and (2) a fully precast socket connection for the column-to-cap beam connection. The other four were: (1) extended strands and headed bars enclosed in the cast-in-place portion of the cap beam for the girder-to-cap beam connection, (2) lap spliced straight bars embedded in ultra-high performance concrete (UHPC) for the deck connection over the pier, (3) precast deck panels to girder connection using deck pockets and projected steel studs from precast concrete girders, and (4) short embedment length lap spliced straight bars for female-to-female deck panel-to-panel connection. This section summarizes the literature review for each connection.

1.2.1 Column-to-Footing Rebar Hinge Connection

A rebar hinge is a reduced column section designed to decrease the moment transfer to an adjacent member. Hinges have been used in many reinforced concrete bridges because they reduce the moment demand on the footing when incorporated at the column base; thereby reducing the size and cost of the substructure. Hinges may also be utilized at the column top to reduce the moment demand in the cap beam, which can reduce the cap beam dimensions and the amount of steel reinforcement. A hinge consists of concrete or grout with longitudinal and transverse reinforcement. A gap is provided between the column and adjacent member to allow for rotation of the column with no contact between components. The hinge maintains some moment capacity that can be significant and therefore the connection cannot be regarded as a pure pin.

Two types of rebar hinge have been developed: one-way and two-way hinges. One-way hinges resist rotation in the strong direction but allow rotation in the weak direction and are used in single column bents and pier walls. Two-way hinges allow rotation in any direction and are generally used for multi-column bents. Due to a multi-column bent being implemented in this study, the two-way rebar hinge was investigated in detail.

Lim et al. (1991) tested several small-scale (1/20 scale) and large-scale (1/5 scale) single column members with two-way rebar hinges at the base subjected to constant axial load and lateral cyclic loading. One detail provided a vertical gap between the column and footing, while a second provided a vertical and horizontal gap between the hinge and the column and footing interfaces. The load carrying capacity of the hinge was found to be stable even under large displacements and the hinging mechanism was found to be similar to that of a conventional column. The failure mechanism was dominated by flexure for all column configurations. The authors concluded that the proposed two-way rebar hinge was stable even under large lateral displacements, and a design procedure was proposed that considered the failure mechanism to be either flexure or shear friction.

Haroun et al. (1994) evaluated the shear capacity of two-way rebar hinges incorporated in six 0.4 scale columns subjected to reverse cyclic lateral loading. The plastic moment capacity of the hinge was developed by inducing lateral displacements on the column under constant axial load. The column was then tested under pure shear to determine the shear capacity of the rebar hinge after formation of the plastic hinge. The effect of the hinge spiral pitch on the shear capacity was studied by reducing the spiral spacing in a separate model and repeating the test. The ultimate shear strength of the pinned column was found to be controlled by the column section and diagonal tension failure of the column was the failure mechanism. Modifications to reinforced concrete beam shear design specified in design codes were recommended.

Cheng et al. (2009) tested five one-third scale reinforced concrete columns with two-way rebar hinges incorporated at the column top in shake table tests under unidirectional loading (figure 1.1). Several parameters were evaluated including, column aspect ratio, axial load magnitude, column longitudinal reinforcement ratio, hinge longitudinal reinforcement ratio, ratio of hinge diameter to column diameter, and the level of confinement in the hinge. The hinges were found to exhibit stable plastic hinging and ductile behavior under dynamic loading. The authors state that the conventional design procedure for the hinge used the shear friction method across the full hinge section, which could lead to unconservative designs. Shear in the hinge was found to be resisted only within the compression region of the hinge section, which is formed under bending rather than shear sliding that is normally assumed in the shear friction theory. The friction coefficient was determined to be 0.45, which was lower than the value specified in design codes due to friction reduction from cyclic action in the hinge. Shear resistance under large displacements was provided by dowel action of the hinge longitudinal bars. Adjustments to the design procedure were recommended based on the findings from the experimental and analytical results.

Mehraein and Saiidi (2016) tested two, two-column bents on a shake table; one of which incorporated rebar hinges at the base (figure 1.2). The design procedure recommended by Cheng et al. (2009) was used. Performance of the hinge when subjected to tension from overturning effects was a new parameter that was studied. The hinge was found to perform as expected with plastic hinges being limited to the rebar hinge zone. The authors recommended that the moment capacity of the hinge be included in estimating the plastic shear, otherwise the column shear design would be unconservative. Also, they recommended the development length of the rebar hinge longitudinal reinforcement be considered, in addition to adequate concrete confinement being provided. Slippage at the hinge-pedestal interface was found to occur when horizontal cracks extended across the entire hinge section. This behavior was more significant in the column with smaller axial load.

Mehrsoroush et al. (2017) evaluated a two-column bent subjected to shake table testing that incorporated a rebar hinge at the top of one column and a one-piece pipe pin at the top of the second column. The cap beam remained damage free during the shake table tests, and the plastic hinges were limited to the pin mechanisms at the column tops. The rebar hinge performed as designed in this application.

Mohebbi et al. (2018a) performed a shake table test on a two-column bent using precast square columns with circular two-way rebar hinges. The rebar hinges were connected to the footing via footing socket connections and were made integral using grout between the hinge and footing interfaces. The rebar hinge performed as designed, and the damage was limited to the hinge. The socket connection remained damage free. The longitudinal hinge reinforcement was debonded over two times the bar diameter above and below the hinge-footing interface to reduce stress concentrations in this zone. The authors note that the debonding was successful in distributing yielding over a larger portion of the reinforcement and prevented bar rupture at the interface.

Shoushtari et al. (2019) incorporated rebar hinges at the column bases for a two-column bent that was part of a two-span steel girder bridge constructed using ABC methods. The purpose of this study was to test the rebar hinge, in addition to other ABC connections, in a scaled bridge subjected to bidirectional shake table testing to determine connection behavior when incorporated in a bridge system and the effect of biaxial forces on the connections. The rebar hinges were precast with the columns and fit into the footing using a socket connection similar to those used in Mohebbi et al (2018a). The hinges were placed in the opening, and grout was cast to form the connection. The hinges were designed using the procedure presented by Cheng et al. (2009). This configuration of rebar hinge provided adequate moment reduction at the column base and footing. The hinge gap was sufficient in preventing contact between the column edge and footing interface under biaxial earthquake loading. Integrity of the connection between the footing and rebar hinge was maintained even under large column displacements. Strains in the longitudinal hinge reinforcement were significantly above the yield strain, meaning adequate bar anchorage was provided in the footing connection and in the portion of the hinge embedded in the column. The proposed design procedure by Cheng et al. was validated for incorporation of rebar hinges in bridge systems.

1.2.2 Column-to-Cap Beam Socket Connection

Socket or pocket connections are used to form a rigid connection between precast elements. The following definitions for socket connections and pocket connections are from Saiidi et al. (2020). A socket connection is composed of a fully precast element fit into an opening in another element and connected via grout. Pocket connections consist of projected reinforcement from one element being fit into a pocket within another element and the full void is cast with concrete or grout. The following projects investigated socket or pocket connection behavior under in-plane loading of bents. No testing of these connections seismic performance under out-of-plane loading or biaxial loading has been reported as of this writing.

Matsumoto et al. (2008) developed multiple precast concrete bent cap connections that could be used with ABC. Four connections were proposed including grouted duct, bolted connection, and two forms of grout-pocket connections. Bar size and embedment depth was adjusted to determine recommendations for reinforcement properties in these connections. Pull out tests were conducted to investigate the anchorage behavior of the proposed connections (straight bar and headed bar). The straight reinforcing bar in grout pocket configuration failed by pullout. A reinforcement anchorage equation was developed based on the pullout test results. The required development length was 50% longer than that required for the grouted duct configuration due to splitting cracks in the top half of the connection reducing bond between the concrete and reinforcing steel. However, the proposed development length was similar to the required development length for reinforcement embedded in concrete by ACI 318-05, meaning reinforcement embedded in a pocket connection provided similar bond compared to rebar placed in cast-in-place concrete. It was found that incorporating confining reinforcement around the pocket connection helped resist crack growth and limit crack widths. The confined connections achieved 50% greater pullout capacity than the unconfined specimen. Additionally, the peak axial load in the confined specimens was sustained under larger displacements when compared to the unconfined specimen. Spiral reinforcement was found to be the most effective confining mechanism for the pocket connection.

Restrepo et al. (2011) tested multiple 0.42 scale column-to-cap beam components including a socket connection (CPFD). The performance of the ABC connections was compared to a cast-in-place control specimen. The bent that incorporated a socket connection was able to withstand extensive drift while maintaining strength. Extensive plastic hinging in the columns was observed, while damage to the joint was limited; meaning the socket connection successfully transferred moment between the column and cap beam while maintaining joint integrity.

Motaref et al. (2013) tested a 0.3 scale two-column bent incorporating socket connections at the base. The columns, footing, and cap beam were precast and assembled to form the bent. Each column was designed using a different method. One column consisted of conventional reinforced concrete that incorporated engineered cementitious composite (ECC) in the plastic hinge region (RC-ECC column). The second column was a glass fiber reinforced polymer (GFRP) tube filled with concrete (FRP column). The columns were connected to the footing using a socket connection with embedment length equal to 1.5 times the column diameter. The bent failed due to fracture of the longitudinal bars in the ECC column and rupture of the GFRP fibers in the FRP column, both at the top of the footing. The provided embedment length was found to be satisfactory in developing the plastic moment in both columns. A second study by Kavianipour and Saiidi (2013) implemented a socket connection using the proposed column embedment length by Motaref et al (2013) on a one-fourth scale 4-span bridge model. GFRP columns were incorporated in one cast-in-place and one precast bent. The embedment length in the sockets were relatively long to compensate for the relatively low bond between the reinforcement and the surface of GFRP. Socket connections were incorporated with a socket depth of 1.5 times the column diameter to accommodate the precast components. In both studies, the socket connection provided good connectivity between the footing and columns and allowed formation of plastic hinges in the column sections. The anchorage length was found to be satisfactory for these applications. Minor spalling was observed in the footing surrounding the columns but did not affect the socket connection behavior.

Mehrsoroush and Saiidi (2016), and Mehraein and Saiidi (2016) incorporated socket connections for the full moment joints between the column and cap beam in two-column bent shake table tests with a socket depth of 1.2 times and one times the column diameter, respectively. These embedment depths were shallower than previous projects because the authors wanted to determine if the column plastic moment could fully develop with shorter column embedment lengths. Both applications performed satisfactorily, with plastic hinges forming in the columns near the connection interface and the cap beams remaining capacity protected.

Mohebbi et al. (2018a, 2018b) tested a single column and a two-column bent on a shake table using precast columns connected to the footing via socket connections. In the single column specimen, the column was connected to the footing via a square socket. UHPC was used in the bottom of the column at a length equal to two times the column width, and in the gap between the footing and column. Two CFRP post-tensioning tendons were placed in the columns to provide re-centering under seismic loads. The longitudinal column bars were debonded at a length of four times the column width above and below the footing interface to prevent strain concentration at the interface due to the high bond strength of UHPC. Minor concrete spalling was observed in the socket connection from the single column specimen due to rocking of the column at the interface.

The two-column bent consisted of two square columns with circular rebar hinges connected to the footing via circular socket connections. The embedment length of the rebar hinges in the footing sockets was equal to 1.35 times the column width. The rebar hinges were precast with the columns using conventional concrete, and the gap between the rebar hinges and footing was cast with non-shrink grout. Square openings were precast in the cap beam and the columns were embedded in the openings and grouted in place to form moment connections between the elements. The embedment length of the columns in the cap beam was one times the column width. Both columns incorporated advanced materials in the column plastic hinge region beginning at the cap beam interface and extending into the column at a depth of 1.5 times the column width. One column used UHPC in the column plastic hinge region, while the second used ECC. The purpose of using these materials was to reduce plastic hinge damage adjacent to the moment connections. Damage in the column-to-footing connections was limited to minor spalling of the hinges, with no damage observed in the socket connection or column base. Damage in the ECC column at the column-to-cap beam connection was limited to the column plastic hinge, which initiated at the column-cap beam interface and extended down into the column as damage progressed The final damage state of the ECC column included significant concrete spalling and longitudinal bar rupture in the column but no damage occurred in the socket connection. One flexural crack was observed in the UHPC column after run 2 but damage progressed into the cap beam as ground motion intensity increased; the column did not experience significant damage below the column-cap beam interface even for the final damage state. The authors suggest the high strength of UHPC shifted the damage from the column to the cap beam under strong earthquakes. This behavior was not exhibited in the ECC column, where damage was limited to the column. The provided embedment length of one times the column width in the column-to-cap beam connection was sufficient to develop plastic hinges in the columns.

1.2.3 Girder-to-Cap Beam Connection

A recently developed girder-to-cap beam connection detail was implemented for this project to create continuity between the spans and bent and to provide a load path for the positive moment in the superstructure to transfer to the cap beam. The support conditions for the spans were designated as simple for dead load and continuous for live load (SDCL), which can cause the negative moment in the bridge due to gravity loads to be small; therefore, positive moment can become significant due to seismic forces. The girder-to-cap beam connection was designed to resist the applied positive moment at the cap beam-superstructure interface.

Vander Werff et al. (2015) evaluated six girder-to-cap beam connections developed using ABC methodologies (figure 1.3). The connections were labeled: (1) Grouted Unstressed Strand Connection (GUSC), (2) Looped Unstressed Strand Connection (LUSC), (3) Extended Strand Bent with Free End (ESBF), (4) Extended Strand with Splice and End Plate (ESSP), (5) Extended Strand with a Mechanical Splice (ESMS), and (6) Extended Strand with a Lap Splice (ESLS). Two of the details (GUSC, LUSC) were designed for connections between dapped-end I-shaped girders with precast inverted-tee cap beams; while the other four were designed for connections between bulb tee girders with rectangular cast-in-place cap beams. The specimens were subjected to forces designed to simulate the shear and moment the girder-to-cap beam connection would experience due to horizontal and vertical seismic forces. The connections needed to resist vertical shear and positive and negative moments. The primary positive moment resisting mechanism was the projected girder reinforcement and shear friction between the cap beam and girder. The connections provided essentially elastic superstructure behavior significantly beyond the overstrength moment in the column due to horizontal seismic forces. Adequate resistance to forces from vertical excitation was also observed. Design recommendations for each connection type were made based on the findings of this study.

1.2.4 Deck Connection over Bent

The deck reinforcement that passes over the bent from one span to the next must be connected to transfer deck forces over the bent. In addition, the deck reinforcement over the bent also serves as the primary negative moment resistance for longitudinal forces resulting from gravity and seismic loads (Vander Werff et al., 2015). In conventional CIP bridges, splices are avoided over the bent and the reinforcement is continuous. When precast deck panels are used in ABC, the longitudinal deck reinforcement over the bent must be hooked or spliced due to reinforcement projecting from deck panels on each side of the bent. Hooked reinforcement has been incorporated on a project by Sadeghnejad and Azizinamini (2017) that evaluated the performance of SDCL for high seismic regions under push-up, push-down, inverse and axial loading. Aktan and Attanayake (2013) implemented mechanical splices in an ABC project but reported that aligning the bars extending from each side of the cap beam was time consuming and difficult.

One alternative for the deck connection over the bent that had not been studied prior to the current UNR research project is to cast UHPC over the projected reinforcement to form a lap splice. UHPC offers high bond strength which can provide a reliable splice in connections and can simplify construction due to the simplicity of lap splices. Lap splices are prohibited in critical connections. However, the deck region above the bent is a capacity protected zone, therefore strains are generally expected to remain below yielding for all members. Yuan and Graybeal (2015) demonstrated, using direct tension pullout tests with UHPC and rebar, that the tensile capacity of UHPC can greatly enhance the bond strength and decrease the development length required for steel reinforcement. Even short splice lengths were capable of developing stresses up to 80 ksi (552 MPa) in the reinforcement.

1.2.5 Deck Panel-to-Girder Connection

Connections between full depth precast deck panels and prestressed concrete or steel girders normally consist of projected steel studs in the top flange of the girder fitting into a deck pocket and being made integral with grout (figure 1.4) (PCI, 2011a). There are no adopted guidelines for the design of full depth deck panels, but the LRFD Guide Specification for Accelerated Bridge Construction (AASHTO, 2018) specifies that deck panels can be designed using the same procedure as what is used for a cast-in-place deck.

Jones et al. (2016) assembled guidelines for the adoption of full-depth precast concrete deck panels based on current practices. A deck that is composite with the girder is considered an essential component for a functional precast deck system. Without composite action, joint leakage occurs commonly (Badie and Tadros, 2008). Section 3.11 of the Full Depth Deck Panel Guidelines for Accelerated Bridge Deck Replacement or Construction (PCI, 2011a) recommends that deck panels should be made composite with the supporting members. Composite action can be achieved by placing steel shear studs or channels into prefabricated pockets, welding the studs/channels to the girder, and filling the pocket with grout (Badie and Tadros, 2008). Non-shrink, flowable, moderate strength (5 ksi, 34.5 MPa), and low permeability grout should be used for the shear connector pockets (PCI, 2011a). Research has shown that spacing of up to 4 ft between deck pockets may be used to attain full composite action between the deck and girder (Badie and Tadros, 2008). Studs should be spaced a minimum of 2.5 in (63.5 mm) from the edge of the shear pocket and welded at least 1.5 in (38.1 mm) away from the edge of the girder (PCI, 2011b).

Shrestha et al. (2017) evaluated different grout types, connector configurations, and number of connectors per pocket for deck panel-to-girder connections that were subjected to earthquake loading. The connections were experimentally assessed by performing pull-out tensile and push-off shear tests on deck-girder connection specimens. Grout type, stud head area, and connection group effect had little effect on the connection shear strength. The connections were further evaluated using analytical studies. Dynamic analyses using horizontal bi-axial ground motions were performed on a prototype bridge with different stud sizes and pocket spacings. Calculated results showed that the degree of composite action was approximately 70% and the connectors remained elastic when subjected to the design level earthquake and 150% maximum credible earthquake.

1.2.6 Deck Panel-to-Panel Connection

Deck panels are placed in sections with the spacing between the panels connected via a panel-to-panel joint. These joints must transfer forces between panels occurring from dead load, live load, and seismic loads. The joints can run in the longitudinal or transverse direction of the bridge, and the location depends on the panel layout. According to Jones et al. (2016), the female-to-female shear key is the most commonly used joint type for full-depth deck panels (figure 1.5). The joints are often filled with UHPC or concrete. If concrete is used, it is common to post-tension the deck by passing strands through ducts in the panels. This is done to mitigate cracking in the deck from tension due to negative moment. UHPC has relatively high tensile capacity, therefore it also performs well in reducing separation of the panels or cracking in the joints due to tension.

Graybeal (2010, 2014) evaluated cast-in-place UHPC deck panel joints subjected to static and cyclic loading. Four transverse and two longitudinal deck joints were tested. The joints were 6 in (152 mm) wide and consisted of headed bars, straight bars and hairpin bars. No debonding of the reinforcement was observed. The strength of each of the deck joints was equal to or exceeded the strength of a deck built with conventional methods.

Lee et al. (2014) studied the behavior of full depth deck panel joints under seismic loading. The experiment consisted of testing two full-scale prestressed deck bulb-tee girders with a 6 in (152 mm) wide deck joint filled with UHPC. The deck panels and connection remained elastic during all shake table runs. No cracking was observed, and no relative displacement was measured between the girders and deck panels.

1.2.7 Bridge System Testing

System level testing of bridge models has been focused on assessing the combined effect and interaction of various connections and components. Specifically, testing scaled bridge models on shake tables allows the effects of earthquakes on global bridge response and local component and connection behavior to be studied. Several scaled bridge models have been tested at the University of Nevada, Reno (UNR), where the effect of various parameters on the seismic performance of bridges has been investigated. This section summarizes multiple system level tests that have been conducted at UNR.

Johnson et al. (2008) performed shake table tests on a quarter-scale two-span bridge frame that was part of a multi-span reinforced concrete bridge model. High amplitude ground motions were limited to the transverse direction relative to the bridge model. Several performance criteria for the bridge were evaluated including, in-plane rotation, load path within the bridge system, and interaction among bridge components. Multiple shake table runs were completed with the final run having a peak ground acceleration (PGA) of 2.0g. Multiple column longitudinal bars fractured or buckled during the final run, but there was no collapse. An additional run was subsequently completed with a PGA of 1.4g under which the bridge model integrity was still maintained. The measured results were compared to results calculated using conventional analytical modeling. The analytical model was found to accurately estimate the bridge response, and the detailing of column transverse reinforcement using NCHRP 12-49 was found to provide sufficient column ductility under large earthquake events.

Saiidi et al. (2013) evaluated the performance of a conventionally designed, four-span reinforced concrete bridge with asymmetric support conditions under shake table testing. This was the first bridge tested in a series of three multi-span bridges subjected to biaxial shake table testing; the remaining two are described subsequently. The goal of the study was to assess the performance of a multi-span bridge under increasing biaxial earthquake loading. The intermediate supports were two-column bents with varying column heights. The different column heights were incorporated to induce in-plane rotation due to eccentricity of the center of stiffness relative to the center of mass. Six individual ground motions of varying amplitude of the 1994 Northridge earthquake were conducted with the final run having a PGA of 1.0g in the longitudinal direction and 1.2g in the transverse direction. After run 6, some columns showed signs of imminent failure. The run was repeated to assess the system performance after the columns had experienced significant damage. Bent failure was observed in a single bent, but collapse was prevented due to redundancy in the system provided by the other two bents. Failure in the columns was attributed to flexure and only minimal shear cracking was observed. The authors concluded that the bridge performed according to the assumed design methodology and that incorporating provisions for seismic design according to NCHRP 12-49 led to adequate seismic performance in a bridge system.

Cruz-Noguez et al. (2010) designed and constructed the second four-span bridge model, which incorporated innovative materials and designs in the piers that would decrease column damage and reduce residual lateral displacement in the bents resulting from earthquakes. The bent configuration was the same as those used in Johnson et al. and Saiidi et al., except that all six column heights were the same and that innovative materials and details were incorporated in the columns. The first bent used Nickel-Titanium bars, a type of shape memory alloy (SMA), in the plastic hinge region of the column. This material was selected because of its capability to undergo large strains and its intrinsic shape recovery properties from stress removal, also known as the superelastic effect. The SMA was intended to provide self-centering capabilities for the columns reducing residual displacements. Engineered cementitious composite (ECC) was used in the SMA region to enhance ductility by mitigating cracking and damage normally observed in the plastic hinge region. The second bent incorporated a post-tensioning rod in the center of the columns to reduce residual lateral displacement. The third bent incorporated an elastomeric bearing pad in the bottom plastic hinge zones of each column, which was constructed integral with the column, in addition to a post-tensioned rod to provide re-centering capability. Seven earthquake runs were conducted. During the final run PGAs of 1.32g and 1.77g were measured in the transverse and longitudinal directions, respectively. The authors state that incorporating SMA and ECC in the bent was found to significantly reduce residual displacement in the system, while also keeping the bridge serviceable after strong earthquake motions. Post-tensioned columns, which were used in the second and third bents were found to reduce residual displacements but could not keep bent 2 serviceable after strong earthquakes due to spalling of the concrete and fracture of the steel reinforcement.

Kavianipour and Saiidi (2013) designed and tested the third quarter-scale bridge model, which incorporated fiber-reinforced polymer (FRP) tubes and fabrics in the piers and implemented two ABC column connections. Parameters evaluated in this study included: the use of glass FRP and carbon FRP wrapping for confinement and shear resistance, the influence of abutment-superstructure interaction on the bridge response, segmental construction with precast columns, socket connections, and a pipe-pin connection incorporating ABC principles. Two of the bents incorporated precast elements that were assembled on-site according to ABC methodologies. Precast concrete-filled glass FRP tubes were used in the first bent, segmental reinforced concrete columns with post-tensioning rods and FRP wrapping were used in the second bent, and a cast-in-place configuration of the first bent was used for the third bent. Socket connections were used to connect the columns and footings in the precast bent. The FRP columns reached a peak drift ratio of 9.3% with little to no apparent damage in the columns in the GFRP shells. The authors concluded that the incorporation of ABC methods and details saved significant time in construction and assembly, while ABC connections led to satisfactory seismic performance. The use of FRP jacketing and tubes was effective in reducing apparent damage. The post-tensioning rod was effective in reducing residual column displacements. The pipe-pin connection in this study was determined to be promising for incorporation in ABC bridges in high-seismic regions.

In another group of studies, three one-third scale two-span bridge models were constructed using ABC methods and tested on shake tables at the University of Nevada, Reno. The purpose of these bridge projects was to evaluate the holistic performance of several ABC connections under biaxial seismic loading when incorporated as part of a bridge system. Overviews of the first two bridge projects are presented subsequently, and the third bridge project is the subject of this document.

Benjumea et al. (2019) conducted the study of the first bridge, labeled Calt-Bridge 1. Precast concrete elements were incorporated for all bridge components. Six ABC connections were incorporated in Calt-Bridge 1 including: (1) two-piece pipe-pin connection at the column-footing connection, (2) grouted duct connection between projected column longitudinal reinforcement and a precast drop cap beam at the column-cap beam connection, (3) extended strands and dowel bars enclosed in the cast-in-place portion of the cap beam for the superstructure-cap beam connection, (4) lap spliced straight bars embedded in UHPC for the deck connection over the pier, (5) precast deck panels and girders connected via deck pocket and shear connectors for the deck-to-girder connection, and (6) lap spliced bars with short embedment lengths for the longitudinal and transverse joints between deck panels for deck continuity. Each of these connections were instrumented and evaluated during eight earthquake runs of varying scale factor for the 1994 Northridge earthquake measured at Sylmar station. The final run was 200% of the design level earthquake but did not complete due to the safety mechanism at the abutments activating to prevent unseating of the superstructure due to transverse displacements caused by large in-plane rotation of the superstructure. All six connections performed as designed; providing comparable performance to that expected from a cast-in-place counterpart. The authors recommended the connections for incorporation in ABC bridges in seismic regions.

Shoushtari et al (2019) summarized the findings from the second bridge, labeled ABC-UTC, which incorporated six connections with precast concrete elements and prefabricated steel girders. The same construction procedure as the first bridge was used in this study. The six connections incorporated in the steel girder bridge were: (1) rebar hinge connection with socket connection in the footing for the column-footing connection, (2) grouted duct connection between projected column longitudinal reinforcement and a precast drop cap beam at the column-cap beam connection, (3) simple for dead load continuous for live load (SDCL) girder-to-cap beam connection, girder-to-deck grouted pocket connection, (4) lap spliced straight bars embedded in UHPC for the deck connection over the pier, (5) precast deck panels and girders connected via deck pocket and shear connectors for the deck-to-girder connection, and (6) lap spliced bars with short embedment lengths for the longitudinal and transverse joints between deck panels for deck continuity. The bridge model was subjected to eight earthquake runs up to 225% of the design level earthquake. At the conclusion of run 8, longitudinal bar buckling was observed at the column plastic hinges in addition to significant concrete core damage directly under the cap beam. All connections performed as designed with the damage state being equal to or better than what would be expected from a cast-in-place counterpart. The authors recommended the connections for incorporation in ABC bridges with steel girder superstructures.

1.3 Objectives and Scope

The primary objectives of this study were to investigate the seismic response of bridges that integrated several precast components and connections at the system level, help facilitate the adoption of accelerated bridge construction (ABC) in the field and identify necessary refinements in emerging connection seismic design guidelines for ABC bridges. This project was a part of a group of ABC bridge system seismic studies that involved three bridge models. Another objective of the study was to compare the performance of all three bridges at the connection and overall bridge system performance. The performance of the various components and connections in each bridge, and interaction among them was assessed. The first bridge was labeled Calt-Bridge 1 (Benjumea et al., 2019) and the second bridge was labeled ABC-UTC (Shoushtari et al., 2019). The focus of the current project was on Calt-Bridge 2, which differed from Calt-Bridge 1 in the column connections to the cap beam and footing. The study presented in this document consisted of experimental and analytical studies of Calt-Bridge 2 and an overall assessment of the seismic performance of the three bridge models.

Experimental and analytical work were performed to assess six ABC connections viability in seismic regions as part of a bridge system in Calt-Bridge 2. These connections were incorporated at: (1) the column-to-footing connection, (2) column-to-cap beam connection, (3) girder-to-cap beam connection, (4) deck panel connection over the pier, (5) deck-to-girder connection, and (6) deck panel-to-panel connection.

The objective of the experimental investigation was to: (1) select and evaluate six ABC connections in a scaled bridge model to determine their effectiveness in limiting yielding to the columns and keeping the capacity protected elements essentially elastic during biaxial ground motions, (2) assess the performance of the connections under multiple bi-directional ground motions of varying acceleration levels, (3) evaluate constructability and interaction between the ABC connections, and (4) review the current design procedure for each connection type and revise said procedure based on findings from the experimental results to account for interaction within the bridge system or for bi-axial ground motions.

The objective of the analytical studies were: (1) to determine if the behavior of the bridge system under biaxial seismic loading can be captured using existing modeling methods, (2) propose refinement to the analytical model based on measured results, and (3) using parametric studies, evaluate various parameters for the scaled bridge model that were not tested during the shake table tests.

The purpose of comparing the performance of the three bridges was to: (1) compare local connection behavior and make recommendations for implementation based on connection performance, (2) determine if any differences in bridge system performance were present as a result of the ABC connections behavior, (3) assess constructability of like connections and recommend based on simplicity and effectiveness.

1.4 Dissertation Overview

This report contains twelve chapters divided by topic. Chapter 1 presents the problem statement, objectives and scope of the project, and a literature review of the ABC connections selected for this study. Chapter 2 describes the design procedure for Calt-Bridge 2. The construction procedure for Calt-Bridge 2 is presented in chapter 3. Chapter 4 describes the development of the instrumentation plan. Pretest analytical modeling and the development of the loading protocol is described in chapter 5. A summary of the shake table test results is presented in chapter 6. Analysis of the shake table test results and the measured connection performance is discussed in chapter 7. Chapter 8 describes the adjustments made to the pretest analytical model and compares the measured and calculated results. The parametric studies are presented in chapter 9. A comparison of the seismic response of the three bridge models (Calt-Bridge 1, ABC-UTC, Calt-Bridge 2) is presented in chapter 10. Chapter 11 presents the ABC connection design recommendations and implications from the measured and analytical studies. Lastly, chapter 12 presents a summary of the study and summarizes the conclusions and findings from this study.

Chapter 2. Design of Bridge Model

2.1 Introduction

Calt-Bridge 2 was a scaled bridge model designed and constructed using ABC techniques. Six ABC connections were incorporated in the design of Calt-Bridge 2 to assess their seismic performance when incorporated in a bridge system. A preliminary prototype bridge with geometric properties representative of a standard two-span highway bridge was created to establish a baseline design that could be scaled for implementation in a shake table test environment. The largest possible scale factor was used which would allow for testing of the bridge model, while allowing for transportation of bridge components and not exceeding the geometric and force capacities of the shake tables in the Earthquake Engineering Laboratory at University of Nevada, Reno. Bridge components were designed at the prototype level utilizing the Caltrans Seismic Design Criteria (SDC) (2019), even though SDC is for cast-in-place construction, and then scaled down for implementation in the scaled bridge model. Additional ABC seismic design resources from the literature were used despite the preliminary nature of the recommendations from these resources. Six ABC connections were designed for the scaled bridge in the following locations: (1) the column-to-footing connection, (2) column-to-cap beam connection, (3) girder-to-cap beam connection, (4) deck panel connection over the pier, (5) deck-to-girder connection, and (6) deck panel-to-panel connection. The design intent was for bridge performance to meet or exceed that of a cast-in-place bridge with similar dimensions.

2.2 Prototype Bridge

A prototype bridge was developed to establish a baseline for design representative of a typical two-span highway bridge. The bridge was assumed to be in a seismically active region, specifically in Lakewood, Southern California. This prototype bridge was developed by Benjumea et. al (2019) for Calt-Bridge 1 and was adopted for this project. A summary of the design and properties for the prototype bridge is presented in this section.

The prototype was designed as a two-span, prestressed concrete girder bridge with a composite deck. The general dimensions for the prototype bridge are shown in figures 2.1 and 2.2. The span lengths were 100 ft (30.5 m) for a total structure length of 200 ft (61.0 m). Two concrete columns with a center-to-center spacing of 18 ft (5.49 m) and clear height of 20 feet (6.10 m) were incorporated at the bent. The bridge was assumed to have seat type abutments. The cap beam was designed to be integral with the superstructure with dimensions of 31 ft (9.45 m) wide (transverse dimension) and 6'-10" (2.08 m) deep. Typically, a two-lane bridge of this configuration would be approximately 40 ft (12.2 m) wide to accommodate two 12 ft (3.66 m) traffic lanes and two 8 ft (2.44 m) shoulders. However, the structure width was the controlling parameter for the test environment, and the width was decreased to allow for a larger scale factor for the test specimen. The superstructure consisted of four prestressed California Wide Flange concrete girders (CA-WF 48) with a center-to-center spacing of 9 ft (2.74 m), and an 8 in (203 mm) concrete deck. Type 732 barriers were assumed to run along each side of the superstructure. Concrete diaphragms were assumed in the superstructure over each abutment and at midspan.

The spans for the prototype bridge were designed to be simple for dead load and continuous for live load (SDCL). This procedure involves placing the spans on the supports and casting the cap beam(s) to create continuity between the spans. In a typical continuous span configuration, all superstructure loads apply negative moment above the intermediate supports. The SDCL method causes all loads applied to the bridge prior to casting of the cap beams to not induce negative moment at the supports due to the spans being simply supported during this construction stage. This is a desirable behavior in seismic regions as the total superstructure moment over the supports is reduced to only moment caused by live load, barrier and wearing surface loads, in addition to seismic moment inducing negative moment in the superstructure. This can reduce the size of the structural components in addition to decreasing the demand on cap beam connections that resist negative moment.

2.2.1 Gravity and Live Load Analysis

The total weight of the superstructure was estimated using hand calculations based on the bridge geometry. The unit weight of concrete was assumed to be 0.15 kcf (24 kN/m^3). A 3 in (76.2 mm) wearing surface with weight of 0.035 ksf (1.68 kN/mm^2) was applied to the superstructure. The weight of the individual components and total self-weight of the superstructure is listed in table 2.1. The dead load of the prototype bridge was validated using a gravity load analysis of the bridge in CSiBridge (table 2.2). The percent difference between the two methods was 2%, which validated the hand calculated gravity loads.

A modal analysis was also performed using the CSiBridge model. Four mode shapes were calculated, which included: symmetric vertical translation, longitudinal translation, transverse translation, and in-plane rotation of the superstructure. The modal periods and associated mode types are listed in table 2.3. According to the criteria detailed in section 1.2.1 of the Caltrans SDC (2019), Calt-Bridge 2 was classified as an ordinary standard bridge.

2.2.2 Bent Design

The column properties including diameter and longitudinal and transverse reinforcement ratios were designed using an iterative process where different configurations were modeled in Opensees and checked against the design criteria from the SDC (Caltrans, 2019). Several configurations were analyzed by Benjumea et. al (2019). Table 2.4 presents a summary of the column designs. The final design (case F) resulted in a column diameter of 4 ft (101.6 mm) with 18-#14 longitudinal bars and a #8 spiral with 3 in (76.2 mm) pitch. This design provided optimal displacement ductility and displacement demand ductility, while minimizing the required steel for the columns.

The cap beam width was assumed to be equal to the column diameter plus 2 ft (610 mm), which is the minimum width required for adequate joint force transfer according to section 7.4.3 of the SDC for cast-in-place conventional bridges (Caltrans, 2019). The prototype was assumed to be constructed using ABC methods, therefore, the cap beam was designed in two components: (1) a precast cap beam that would be placed above the columns and provide an interface for the spans to sit, and (2) a cast-in-place portion of the cap beam that would allow installation of the superstructure connection reinforcement in the bent after placement of the spans. The precast portion of the cap beam was designed to be as shallow as possible to make placement of the precast cap beam simple and optimize the total cap beam depth. The width and depth of the precast portion of the cap beam were 2 ft (610 mm) and 4'-10" (1.47 m), respectively. An embedment length for the girders of 2 ft (610 mm) into the cap beam was provided, which was greater than the minimum embedment length of 22.5 in (572 mm) recommended by Vander Werff et al. (2015) for this connection type.

2.2.3 Superstructure Design

Four California wide-flange girders were incorporated for the prototype bridge. This girder type can be used in spans of up to 200 ft (61.0 m) with a minimum superstructure depth-to-span ratio of 0.04 for continuous spans. The girders were designed to resist the applied loads from Strength I and II and Service I and III load combinations (AASHTO, 2017). The girder concrete strength was assumed to be 5.5 ksi (38.5 MPa) at application of the prestressing force and 8 ksi (56.0 MPa) 28 days after casting of the concrete. Thirty-four 0.6 in (15.2 mm) diameter grade 270 prestressing strands were assumed in the bottom flange of the girder. The shear reinforcement was #5 double-leg stirrups spaced at 2.5 in (63.5 mm). The girders were 4 ft (1.22 m) deep with a top flange width of 4 ft (1.22 m). Assuming a haunch thickness of 2 in (50.8 mm), the total superstructure depth was 4'-10" (1.47 m), which resulted in a superstructure depth-to span ratio of 0.048.

The required deck thickness for a girder spacing of 9 ft (2.74 m) was 8 in (203 mm) according to Caltrans MTD 10-20 Attachment 2 (Caltrans, 2008). The standard deck reinforcement detailing from this attachment was also used. Additional longitudinal reinforcement was included above the bent to meet the negative moment demands in this region.

2.3 Model Scale Factor

The prototype bridge was designed to represent a standard highway bridge. While it would be desirable to test this bridge at full-scale, limitations from the testing facility imposed geometric and weight limits that made full-scale testing impossible. Therefore, the prototype bridge was scaled to allow for shake table testing of a bridge model where the original properties of the bridge would be factored but still be representative of a standard highway bridge. Multiple parameters were scaled to keep the scaled bridge performance and seismic response representative of the prototype.

A geometric scale factor of 0.35 (λ_L=2.86) was selected, which allowed for construction, transportation, assembly, and shake table testing of the bridge model. Time dependent properties are scaled according to the square root of the geometric scale factor. This factor was λ_T=1.69 for Calt-Bridge 2. The time coordinate of the input acceleration was hence divided by this factor. Material properties such as the modulus of elasticity and compressive strength, as well as acceleration scale one-to-one, which allow for testing of a scaled specimen without requiring adjustments to component size or earthquake acceleration magnitude. Because material properties were not scaled, real concrete, steel, etc. of the type that is used in actual bridge construction were used in the bridge model.

2.4 Selection of ABC Connections

The purpose of this bridge project was to assess the seismic performance of different ABC connections when incorporated in a bridge system. Six ABC connections were selected based on the assessed readiness of the connection from existing research and feedback from Caltrans. The connections were applied at the following locations: (1) the column-to-footing connection, (2) column-to-cap beam connection, (3) girder-to-cap beam connection, (4) deck panel connection over the pier, (5) deck-to-girder connection, and (6) deck panel-to-panel connection.

The bent was designed with columns that had pinned bases and fixed tops. Available connections that provide pin-like behavior and had been previously tested included the pipe-pin connection and the rebar hinge connection. Both connections exhibited satisfactory seismic behavior in component tests [Mehraein and Saiidi (2016), Cheng et. al (2009), Mehrsoroush et al. (2017), Mohebbi et al. (2018)], therefore both connections were selected for use in scaled bridge models with the pipe-pin being implemented in Calt-Bridge 1 (Benjumea et al., 2019) and the rebar hinge being implemented in Calt-Bridge 2.

Two options were considered for the moment connection at the column top including grouted ducts and socket connections with precast column. Socket connections had previously been studied in several research projects (see section 1.2.2) and exhibited satisfactory behavior with stable formation of plastic hinges in the column during seismic events, while maintaining connection integrity. Grouted ducts had already been implemented in Calt-Bridge 1 and therefore, socket connections were selected as the column-to-cap beam connection in Calt-Bridge 2.

Six girder-to-cap beam connections were tested by Vander Werff et al. (2015) which could be potentially implemented in ABC applications. Four of these accommodate bulb-tee style girders with rectangular cap beams, which was the configuration used for Calt-Bridge 2. The extended strand bent with free end (ESBF) is preferred by Caltrans because of its relative ease of constructability and low cost. The ESBF girder-to-cap beam connection was selected for the girder-to-cap beam connection because of its positive reviews and applicability to the bridge properties that were incorporated in this study.

The longitudinal deck reinforcement projecting over the bent is connected using a variety of options including hooked reinforcement, mechanical couplers, or lap splices. Hooked reinforcement and mechanical couplers were not desired options because of the steel congestion in the top of the cap beam. Lap splicing of the reinforcement is not permitted because the girder-cap beam connection is considered critical. However, it was decided to embed lap splices in ultra-high-performance concrete (UHPC) to provide high bond strength and to simplify construction. Therefore UHPC-embedded lap spliced longitudinal deck bars were used to provide continuity in the deck reinforcement and serve as the primary resistance to tension stemming from negative moment in the superstructure.

Several options were available for the deck panel-to-girder connection which have previously been implemented in practice. Of the available connections for prestressed girders to deck panels, the projected steel stud into a deck panel pocket was the most commonly used. This connection was implemented in Calt-Bridge 2 with two variations, (1) studs projecting from the girder into deck panel pockets for the exterior girder and cast with grout, and (2) studs projecting from the girder into the longitudinal deck joint between panels and cast with UHPC.

A similar detail to the deck connection over the bent was incorporated for the panel-to-panel connection. Geometric limitations between the panels limited reinforcement connection options. The strong bond provided by UHPC allowed for adequate development of lap splices between deck panels and provided continuity across the deck.

2.5 Design of Scaled Bridge Model

General dimensions for the scaled bridge model (Calt-Bridge 2) were determined by applying the geometric scale factor to the prototype bridge. Limits for the size of Calt-Bridge 2 were controlled by the size of the Earthquake Engineering Laboratory (EEL), the ability to transport components, and the capacities of the shake tables. Calt-Bridge 2 components were designed independently from the prototype bridge counterparts; however, the components were designed to be representative of the prototype bridge behavior under gravity and seismic loading. The general bridge design was completed using provisions from the Caltrans SDC and other documents from the literature. ABC design philosophies were applied to the design of Calt-Bridge 2 using prefabricated elements and systems (PBES). Each component was designed as a precast element and assembled using a variety of ABC connections, which were presented in section 2.4. The ABC connections were designed according to guidelines developed from past research because no codes and formal guidelines for seismic design of ABC connections were available. This section summarizes the designs for the bridge components. The construction drawings for Calt-Bridge 2 are presented in Appendix A.

2.5.1 Scaled Bridge Geometry and Set-up

Calt-Bridge 2 was a two-span bridge with the abutments situated on shake tables 1 and 3, and the bent on the center shake table (shake table 2). The span lengths were 34'-10" (10.6 m), which resulted in a total structure length of 69'-8" (21.2 m). The column clear height was 7 ft (2.13 m) and the superstructure width was 11 ft (3.35 m). Safety frames were installed approximately at mid-span for both spans to prevent damage to the shake tables if the structure were to collapse. Superimposed weight was placed on the superstructure to induce an axial load index in the columns equivalent to that in the prototype bridge. The superimposed weight is discussed in detail in section 2.7.

2.5.2 Bent Design

The bent consisted of three types of precast elements: the columns, the cap beam, and the footing. Each component was precast and then assembled utilizing the ABC connections between the components. The rebar hinge was precast with the footing and projected from the top of the footing. The columns were precast with openings in the base and were connected to the footing by fitting the hinge bars into the column pocket and casting non-shrink grout in the pocket. The cap beam had two components, a precast portion with openings for connection of the columns and a cast-in-place portion, which would be completed after assembly of the bent and placement of the spans. An exploded view of the bent showing placement of the bent components is shown in figure 2.3.

2.5.2.1 Columns

The columns were designed according to the guidelines for seismic critical members presented in section 5.3 of the SDC (Caltrans, 2019). As seismic critical members, the columns were expected to undergo significant yielding during seismic events. Plastic hinges were expected to form at the column tops adjacent to the moment connection provided by the socket connection between the columns and cap beam and at the two-way hinges at the base. The details for the columns are shown in figure 2.5.

The column diameter was 18 in (457 mm) and the clear height was 84 in (2.13 m). However, the total length of the precast columns was 105 in (2.67 m) to allow for placement of the column in the socket connection in the cap beam. Steel reinforcement consisted of 10-#6 longitudinal bars confined with a #3 spiral spaced at 1.75 in (44.4 mm), which provided a reinforcement ratio of 1.73% and 1.65% for the longitudinal and transverse steel, respectively. These reinforcement ratios were designed to match those for the prototype bridge columns. The axial load index for the columns was 4.6% which was less than 6.2% for the prototype bridge. The gravity load could not be increased further for Calt-Bridge 2 due to limitations in the pay load capacity of the shake tables. The column plastic moment capacity was calculated utilizing expected material properties by performing a moment-curvature analysis in Xtract (Chadwell and Imbsen, 2002), a section analysis software package. Three loading conditions were considered for the moment curvature analysis including, gravity load only, gravity load plus tension in one column and compression in the other column from overturning in the transverse direction. The overturning forces were determined from a transverse pushover analysis for the bent which is presented in section 5.3. The plastic moment capacities for the column section were 2291 k-in (258 kN-m), 2132 k-in (241 kN-m), and 2871 k-in (324 kN-m), under gravity, gravity plus tension, and gravity plus compression, respectively. The moment-curvature relationships for each loading condition is presented in figure 2.4. The shear demand for the columns was calculated for the three loading conditions mentioned previously by summing the plastic moment capacity of the column and rebar hinge and dividing by the column clear height. The shear capacity was calculated according to section 5.3.7 of the SDC (Caltrans, 2019). Shear resistance from concrete and steel was included for the dead load, and dead load plus compression conditions. Only the shear resistance from steel was included for the dead load plus tension condition because concrete shear capacity in tension is negligible. The plastic moment capacities, shear demands, and shear capacities for the columns are presented in table 2.5. The shear capacities were much larger than the shear demand for each load case by a minimum factor of 1.5. This large margin for shear was deliberately designed to prevent shear failure in the column prior to full development of the plastic hinges in the column sections. A primary objective of this study was to test the ABC connections under large seismic loads. If shear failure occurred prior to full yielding of the columns, the ability of the joints to transfer forces during large displacements would be unknown. By overdesigning the shear reinforcement, the failure mechanism in the columns would most likely be longitudinal bar buckling or concrete core failure in the plastic hinge, and the ABC connections would be exercised to a greater degree.

2.5.2.2 Cap Beam

Cap beams are designated as a capacity protected element, meaning it should remain essentially elastic for all design loading conditions. Two loading stages were considered in the cap beam design; the first stage included only the precast portion of the cap beam, which was designed to resist the phase 1 gravity loads, the second stage included the combined precast and CIP portion of the cap beam and was designed to resist all gravity and seismic loads. The cap beam was designed according to the guidelines in section 5.4 of the SDC (Caltrans, 2019). Details for the cap beam are presented in figure 2.6. An isometric view of the cap beam is shown in figure 2.7.

The depth of the precast portion of the cap beam was 8 in (203 mm). The scaled width of the cap beam derived from the prototype dimensions was 27.5 in (688 mm); however, this dimension was increased to 32.5 in (826 mm) to accommodate the opening for the precast columns. Nominal material properties for the concrete, f'_c =4 ksi (27.6 MPa), and steel, f_y =60 ksi (414 MPa) were used in the cap beam design. Eight #6 bars were placed longitudinally in the precast cap beam to resist the bending moment from gravity loads. The cap beam was precast with two openings for the socket connections. Consequently, the reinforcement was bundled along the edges to allow the bars to run continuously along the full length of the precast cap beam without interfering with the openings. Shear reinforcement for the full cap beam section was included in the precast cap beam and projected from the top face. Two raised areas were precast around the openings to provide an interface between the precast columns and cap beam. A 4 in (102 mm) duct was precast above the opening to allow for placement of grout in the socket connection during bent assembly. The dimensions of the raised zones were such that no interference would take place between the precast cap beam and spans during bridge assembly. The shear friction capacity between the grout in the cap beam opening and the columns was checked to ensure that the bond between the elements could resist the gravity loads from the superstructure.

The shear and moment demand in the cap beam were calculated using a transverse pushover analysis (section 5.3). The moment demands from the column plastic moments were amplified by 1.2 to account for the overstrength factor. Additional reinforcement was placed to the cap beam after placement of the spans. In the initial design, two #3 bars were supposed to pass through ducts in the girders for the girder-to-cap beam connection. However, the ducts in the girders were not precast in the correct location and it was not possible to create new holes without damaging the girders. The design was adjusted to use headed bars with a screw on head that could be passed through the existing ducts and used to fasten the cross ties. Headed bars were selected to ensure the bars could be adequately developed in the limited available area. Ten #6 longitudinal bars were installed at the top of the cap beam in the UHPC layer to resist tension from negative moment due to transverse translation of the superstructure during seismic events.

2.5.2.3 Footing

The primary function of the footing in the test model was to provide support for the bent and be fixed to the shake table. While the connection zone to the columns was reinforced to represent real footings, the rest of the reinforcement in the footing was designed for the loading condition of the specimen included the tie down forces that are not normally present in real bridge footings. As result, the footing was over-designed to remain essentially elastic and damage free for all applied design loads. The rebar hinge reinforcement was precast in the footing and projected out of the top face of the footing for connection to the columns via pocket connections (figure 2.8). The footing was 10 ft (3.0 m) long, 3 ft (914 mm) wide, and 23 in (584 mm) deep. Longitudinal reinforcement was designed to resist the applied moment from overturning and the moment transfer from the rebar hinges. The transverse reinforcement was designed to resist shear transferred from the columns and punching shear for the rebar hinges. Steel rods connected to the shake table were passed through precast ducts in the footing and anchored using steel nuts tightened against steel plates. The steel rods resistance against uplift and sliding was checked for the longitudinal and transverse directions of the bridge to ensure the footing remained fixed during seismic events. The elevation and plan views of the footing are shown in figure 2.8.

2.5.3 Superstructure Design

The superstructure consisted of two spans each with four prestressed concrete girders, twelve precast deck panels, three intermediate diaphragms, and one end diaphragm in each span. The girders and deck panels were precast separately and assembled prior to placement on the bridge supports. The diaphragms were cast-in-place after the girders were situated. The precast deck panels were placed after the diaphragms were cast and connected to the girders via the deck-to-girder connection. The spans were transported into the laboratory and lowered on the supports, each as a single element. All components in the superstructure were designed to remain essentially elastic for seismic loading. The superstructure design from Calt-Bridge 1 (Benjumea et al., 2019) was adopted for Calt-Bridge 2.

2.5.3.1 Prestressed Concrete Girders

Four prestressed concrete girders were incorporated in each span for Calt-Bridge 2, resulting in eight girders total. Details for the girders are shown in figure 2.9. The girders were scaled versions of the California wide flange girders utilized in the prototype bridge. The girders were 34 ft (10.4 m) long and 16.75 in (425 mm) deep. Eleven 3/8" (9.5 mm) diameter, seven wire, low-relaxation, grade 270 strands were applied in the bottom flange for application of the prestressing force. The shear reinforcement consisted of two #3 stirrups with variable spacing. Shear connectors were precast with the girders, which would be used to form a composite section between the deck and girders. Two #4 headed bars were spaced every 18 in (457 mm). The specified concrete strength was 5.5 ksi (37.9 MPa) at prestress transfer, and 8 ksi (55.2 MPa) for the 28-day strength.

2.5.3.2 Precast Deck Panels

Twelve precast deck panels were designed for each span. The panel configuration is shown in figure 2.9. The panels were designed to be longer in the longitudinal direction with the girders serving as supports. Each panel was 2.75 in (69.9 mm) thick and 7'-11" (2.41 m) long. The exterior panels were wider than the interior panels because of the deck overhang. The exterior panels were precast with pockets to connect with the steel studs in the girders. The pockets were not required for the interior panels because the girder studs ran in the joints between the panels that were later filled with UHPC. The deck panels utilized 5 ksi (34.5 MPa) concrete. The longitudinal reinforcement consisted of #3 bars with a spacing of 6 in (152 mm) and 6.25 in (159 mm) for the exterior and interior panels, respectively. Additional #4 bars were applied in the deck panels adjacent to the bent due to Strength II load demands. The transverse reinforcement consisted of #3 bars spaced at 2.5 in (63.5 mm).

The deck panels were thin sections, which caused concerns for cracking during transportation and superstructure assembly. The tensile stress in the sections was checked according to the procedure specified in section 5.3.3 of the PCI Design Handbook (PCI, 2004). Four anchors were precast in the panels and were used as the lifting points in the analysis. The modulus of rupture was calculated and used as the maximum allowable stress in the deck section. Stresses from the self-weight of the deck panel when transported via the lifting anchors were under the allowable stress for the section, meaning the panels could be safely lifted from the anchor points without cracking.

2.5.3.3 Diaphragms

Three intermediate diaphragms were placed in each span to increase the superstructure stiffness. The intermediate diaphragm dimensions and reinforcement details are presented in figure 2.10. An intermediate diaphragm was provided at each transverse deck panel joint as suggested by Caltrans (figure 2.10). The diaphragm properties were scaled down from typical details that would be present in the prototype bridge as specified in the Caltrans Design Standard Sheet XS1-123 (Caltrans, 2016). The scaled width for the intermediate diaphragms was 3 in (76.2 mm) but this dimension was increased to 4 in (102 mm) to allow the intermediate diaphragm to serve as a form for the UHPC joint between the deck panels. Twelve #3 hooked bars were projected out of each intermediate diaphragm into the UHPC deck panel joint to provide continuity between the diaphragm and deck.

The end diaphragm reinforcement and dimensions were scaled versions of an end diaphragm from a bridge plan set provided by Caltrans (figure 2.11). The diaphragm was 12.5 in (318 mm) wide which was equivalent to the geometric scale factor applied to the recommended minimum width for end diaphragms in Caltrans BDD-14 (Caltrans, 2004).

2.5.3.4 Abutments

The abutment supports consisted of two concrete mass blocks standing upright capped with an abutment seat, all anchored to the shake tables. Shear keys and a back wall were not included in Calt-Bridge 2 because these components are designed to provide resistance for small to moderate earthquakes but to be sacrificial under strong earthquakes. Calt-Bridge 2 was expected to be subjected to a range of earthquakes and tested to failure; therefore, shear keys and a back wall would not be expected to have a significant impact on the displacement response of the structure under strong earthquakes.

The bearing interface at the abutments consisted of stainless-steel on Teflon. The stainless-steel on Teflon interface provides a low friction contact surface, which allows the superstructure to move freely at the ends. The stainless-steel plate was welded to a steel plate that was embedded in the base of the girders. A large Teflon sheet was provided under each girder to allow for large displacements in the superstructure without risking unseating at the bearing.

2.6 Design of ABC Connections

Six ABC connections were implemented in Calt-Bridge 2 including: (1) a rebar hinge precast with the footing connected to the column via a pocket for the column-to-footing connection, (2) a fully precast socket connection for the column-to-cap beam connection. (3) extended strands and headed bars enclosed in the cast-in-place portion of the cap beam for the girder-to-cap beam connection, (4) lap spliced straight bars embedded in ultra-high performance concrete (UHPC) for the deck connection over the pier, (5) precast deck panels to girder connection using deck pockets and projected steel studs from precast concrete girders, and (6) short embedment length lap spliced straight bars for female-to-female deck panel-to-panel connection. The design of each connection including effects on the design of connected members are addressed in this section.

2.6.1 Column Base Connection

A rebar two-way hinge precast with the footing and connected to the column via a pocket connection was used for the column base connection. The hinge is designed to reduce the section moment capacity at the base about both principal axes, which reduces the moment transferred to the footing. This connection was designed according to the design procedure developed by Cheng et al. (2009). No adjustments were required to accommodate the design procedure for ABC applications. The column pocket depth was designed based on the required development length for the longitudinal hinge reinforcement. The rebar hinge properties can be seen in figure 2.5 and 2.7. The step-by-step procedure for the design of a rebar hinge is as follows:

Step 1: Determine the hinge section and the required longitudinal steel:

- Hinge area:

$$A_g \geq \frac{P_u}{0.2f_c'}$$

Where:

A_g: gross area of hinge section;
P_u: design axial load;
f'_c: concrete compressive strength.

- Use minimum longitudinal reinforcement permitted by AASHTO provision for columns:

$$A_s \geq 0.01A_g$$

Where:

A_s: hinge longitudinal reinforcement steel area.

Step 2: Hinge transverse reinforcement design, using Mortensen and Saiidi's (2002) performance-based design method, for a minimum curvature ductility of 10.

Step 3: Find hinge confined concrete properties. Hinges experience "double confinement" from the hinge spiral and the confinement provide by surrounding column above and the footing below. Determine the effective confined lateral pressure and spiral steel ratio for use in Mander's method for the confined compressive strength, f'_{cc}, strain at instance of maximum compressive strength, ε_{cc}, and the ultimate strain, ε_{cu}, (Mander et al., 1988).

- $f_l = \left(\frac{2f_y A_{sh}}{D' s_h}\right)_{hinge} + \left(\frac{2f_y A_{sh}}{D' s_h}\right)_{column}$
- $\rho_s = \left(\frac{4A_{sh}}{D' s_h}\right)_{hinge} + \left(\frac{4A_{sh}}{D' s_h}\right)_{column}$

Where:

f_l: effective hinge confined lateral pressure;
ρ_s: hinge effective volumetric ratio of confining steel;
f_y: yield strength of the reinforcement;
A_{sh}: spiral bar area;
D': diameter of the confined core;
s_h: spiral pitch.

Step 4: Determine the flexural capacity of the hinge using the confined concrete properties. Make sure the hinge moment can be resisted by the footing. Adjust the hinge size, the longitudinal bar ratio, or both as necessary.

Step 5: Calculate hinge shear capacity:
- Run moment curvature analysis; find section compression force (axial load change due to overturning moment needs to be included in the analysis):

$$\mathrm{C} = \mathrm{C_c} + \mathrm{C_s} = \mathrm{P} + \mathrm{T_s}$$

Where:

C: result compression force;
C_c: compression force in concrete;
C_s: compression force in reinforcement;
P_u: design axial load;
T_s: tension force in rebar.

- $\Phi \mathrm{V_n} = \Phi \mu \mathrm{C} = \Phi \mu(\mathrm{C_c} + \mathrm{C_s})$

Where:

Φ: strength reduction factor, 0.85:
μ: friction coefficient, 0.45

Step 6: Calculate hinge plastic shear demand:
- $\mathrm{V_u} = \frac{\mathrm{M_c} + \mathrm{M_h}}{\mathrm{L}}$

Where:

M_c: column section plastic moment;

M_h: hinge section plastic moment;
L: column height.

Step 7: Check to see if $\Phi V_n > V_u$, if not adjust the hinge longitudinal bars, the size of the hinge section, or both, and repeat steps 1 to 7 until the shear capacity is sufficient.

Step 8: Check for hinge gap closure. Determine if $\theta_n < \theta_{close}$, determine hinge gap thickness.

- Assume a hinge gap g = 100 mm (4 in).
- Nominal two-way hinge ultimate rotation:

$$L_p = g + 0.022 f_y d_b \qquad (f_y \text{ in MPa})$$
$$L_p = g + 0.15 f_y d_b \qquad (f_y \text{ in ksi})$$
$$\theta_n = \theta_e + \theta_p$$
$$\theta_e = g * \Phi_y$$
$$\theta_p = L_p(\Phi_u - \Phi_y)$$

Where:

L_p: plastic hinge length;
g: hinge gap thickness;
d_b: diameter of hinge longitudinal rebar
Φ_y: hinge section effective yield curvature;
Φ_u: hinge section ultimate curvature;
θ_n: hinge ultimate rotation;
θ_e: hinge elastic rotation;
θ_p: hinge plastic rotation.

- Two-way hinge rotation for hinge closure:

$$\theta_{close} = sin^{-1}\left(\frac{g}{0.5D}\right)$$

Where:

D: column diameter;

- Check to see if $\theta_n < \theta_{close}$, if not then increase hinge gap thickness until sufficient gap is provided to prevent gap closure.

Step 9: Detailing of the two-way hinge section:

- Distribute the hinge longitudinal reinforcement around the section.
- Provide spiral for the hinge section and extend into column and footing at least a distance of 1.25Ld (Ld = longitudinal bar tension development length).

2.6.2 Column-to-Cap Beam Connection

Socket connections were used between the columns and the cap beam to provide a full moment transfer at the joint and allow formation of plastic hinges in the columns. The socket connection can be viewed in figure 2.5 and section D-D of figure 2.6. The design procedure for cap beam pocket and socket connections is summarized by Tazarv & Saiidi (2015). The Alt-5 detail of precast opening with fully precast column was utilized in Calt-Bridge 2. This guideline recommends the opening depth be greater than or equal to 1.25 times the column diameter. Other research projects [(Mehraein and Saiidi, 2016)

(Mohebbi et al., 2018b)] have reported successful connection performance when column embedment lengths in the socket of one times the column diameter. However, a more conservative value of 1.25 times the column diameter was used in Calt-Bridge 2 because of the lack of research for socket connections in bridge systems and unknown connection performance for out-of-plane loading. The guidelines developed by Tazarv & Saiidi (2015) were utilized to design the socket connection for the column-to-cap beam connection for this study and are presented in appendix B.

2.6.3 Girder-to-Cap Beam Connection

Extended strand bent with free end detail was used for the girder-to-cap beam connections. This connection was designed to resist the positive moment demand at the cap beam-superstructure interface resulting from longitudinal translation of the bridge superstructure. Two primary mechanisms are assumed to resist tension at the base of the cap beam stemming from positive moment: (a) the projected girder prestress strands with welded coupler and (b) shear friction between the CIP cap beam concrete and the girders. However, due to the unpredictability of the shear friction contribution against tension, the girder prestress strands were assumed to resist all tension. The girder-to-cap beam connection details are shown in figure 2.12. The moment demand resisted by the steel strands was calculated using the following equations developed by Vander Werff et al. (2015):

$$M_{cg-super} = M_o + V_o(D_{s1} + D_{CGsuper}) \quad \text{(Eq. 2-1)}$$

$$M_{gir-cap} = \frac{L_{span} - \frac{B_{cap}}{2}}{L_{span}} * DF_{gir} * \left(\frac{M_{cg-super}}{2}\right) \quad \text{(Eq. 2-2)}$$

Where,

$D_{CGsuper}$: distance between centroid of superstructure and top surface of precast cap beam, in (mm).

DF_{gir}: distribution factors for interior and exterior girders, respectively, taken as 0.5.

D_{s1}: precast cap beam depth, in (mm)

L_{span}: span length, in (mm)

$M_{cg-super}$: moment at the CG of the superstructure, kip-in (kN-mm)

2.6.4 Deck Connection over Pier

The connection of the deck reinforcement over the bent consisted of long lap-spliced rebar encased in UHPC. The reinforcement was embedded with a 24 in (610 mm) lap splice in the UHPC, which resulted in an embedment length equal to $64d_b$ and $48d_b$ for the #3 and #4 bars, respectively. This long lap was used because the width of the cap beam made this length available and was longer than those tested successfully by Yuan and Graybeal (2015). The capacity of the section was checked using moment curvature analysis of the superstructure section assuming full composite behavior between the deck and girders. The reinforcement at the top of the cap beam was required to resist the tension from negative superstructure moment. The total moment demand was calculated using the columns plastic moment capacity and the negative moment from the phase 2 superimposed mass. The reinforcement provided sufficient resistance against the negative moment demand with a demand to capacity ratio of 0.6.

2.6.5 Deck-to-Girder Connection

The deck-to-girder connection was comprised of projected steel studs precast with the prestressed concrete girders, which were fit into deck panel pockets and the longitudinal deck joints. The spacing was designed based on full-scale component tests conducted by Shrestha et al. (2016). The final design for Calt-Bridge 2 was two #4 studs spaced every 18 in (457 mm). The shear studs were cast in non-shrink high strength grout for the exterior girders and UHPC for the interior girders. The plans for the girder-to-deck panel connection details are shown in figure 2.13. The design equations were as follows:

$$V_{hi} = \frac{V_u}{d_v} \quad \text{(Eq. 2-3)}$$

$$\Phi V_n = 0.5 A_{sc}\sqrt{f_c' E_c} \leq A_{sc} F_u \quad \text{(Eq. 2-4)}$$

$$\Phi V_{ni} = \frac{\Phi V_n}{s} \quad \text{(Eq. 2-3)}$$

Where,

A_{sc}: cross sectional area of connectors, in^2 (mm^2).

d_v: distance between the centroid of tension steel and the mid-thickness of the deck slab, in (mm).

F_u: specified tensile stress of shear connectors, ksi (MPa).

V_{hi}: factored interface shear per unit length, kip/in (kN/mm).

V_n: nominal shear strength of cluster of connectors, kip (kN).

V_{ni}: nominal shear strength of connectors per unit length, kip/in (kN/mm).

V_u: factored vertical shear at the location of interest, kip (kN).

Φ: resistance factor for shear, 0.9

2.6.6 Deck Panel-to-Panel Joints

The deck panels were connected to adjacent panels via short lap-splices encased in UHPC. The panel-to-panel joints consisted of #3 bars projected from the deck panels towards adjacent panels. The panels were spaced 4 in (102 mm) apart. Yuan and Graybeal (2014, 2015) recommended using embedment lengths of $10d_b$ for bars with cover between $2d_b$ and $3d_b$. This is equivalent to 3.75 in (95.2 mm) for #3 bars. The largest possible splice length of 3.9 in (98.4 mm) was incorporated in the deck panel-to-panel connection to ensure all rebar splices met the required length.

2.7 Superimposed Weight

The weight of the scaled bridge model was reduced from that of the prototype by the cube of the geometric scale factor because the weight is a function of volume when common concrete is used. In scaled bridge models, component cross sectional area is reduced by the square of the geometric scale rather than cube. Recall that real concrete and steel are used in the model, and target model stresses are intended to match those of the prototype. In other words, the scale factor for stresses is 1. For this to happen, additional weight needed to be superimposed to make the total weight correspond to the square of the scale factor. The superimposed weights were placed in two phases; phase 1 weight consisted of dead load from structural components, and phase 2 weight was placed after the cap beam had been cast to represent the barrier and wearing surface weight. The weights were installed in sequence to mimic SDCL construction. The locations and weights of the superimposed loads are shown in figure 2.14.

Phase 1 weight consisted of concrete blocks placed above the abutments, and two sets of lead pallets, and two sets of steel plates applied at midspan for each span. Phase 2 weight was applied by placing a concrete block near the bent on each span to induce negative moment in the superstructure above the bent representative of that applied from barriers and the wearing surface.

Chapter 3. Construction and Assembly of Bridge Model

3.1 Introduction

Calt-Bridge 2 was constructed using accelerated bridge construction (ABC) techniques by incorporating prefabricated elements. The bridge model falls in the category of prefabricated bridge elements and systems (PBES) (FHWA, 2019). Most of the bridge components were cast in the structures yard outside of the Earthquake Engineering Laboratory (EEL) at the University of Nevada, Reno. Strain gauges were attached to the rebar prior to casting of the concrete according to the instrumentation layout discussed in chapter 4. The bent components were cast first, followed by the precast deck panels. The bent and spans were assembled outside the EEL and transported inside and assembled in place on the shake tables. This chapter describes the construction procedure used for the bent and superstructure. An overview of the assembly of the bridge model is also presented. This is followed by a summary of the material testing data for the concrete, grout, UHPC, and steel used for the project.

3.2 Bent Construction

The bent consisted of three components: the footing, columns, and cap beam. Each of these components were precast as individual elements and assembled for the bent after 28 days of cure time to ensure adequate concrete strength had been met prior to transportation of the elements. During casting, there was insufficient concrete in the first mixing truck to finish one of the columns, therefore an additional batch was used to complete that column. Six inch (152 mm) diameter by 12 inch (305 mm) tall test cylinders were cast using concrete from each batch. The concrete slump was measured prior to casting and was 3.25 inches (82.6 mm) as shown in figure 3.1.

3.2.1 Footing

The footing formwork was assembled on a casting slab in the structures yard outside of the EEL. The longitudinal and transverse reinforcement was tied together within the formwork (figure 3.2). An opening was left in two locations along the top reinforcement to allow for placement of the rebar hinge. Four P52 Swift-Lift anchors from Dayton Superior were embedded within the footing and screwed to the formwork to allow for transportation of the footing and bent via cranes. PVC pipes were tied to the footing reinforcement to place ducts through the footing that would allow steel rods to pass through for anchorage of the bent to the shake table. Longitudinal rebar hinge reinforcement was tied to the hinge spiral to form the reinforcement cage for the rebar hinge (figure 3.3). This was followed by installing the hinge cage through the footing reinforcement (figure 3.4). Wooden beams were placed on each side of the rebar hinges to anchor the reinforcement in the correct location. The top of the rebar hinge was tied to the outside edges of the formwork to ensure that the hinge cage remained plumb during concrete casting. Concrete was placed directly in the form using a chute from the mixing truck. The concrete was vibrated during placement around the outside edges of the formwork and near the rebar hinge reinforcement to remove voids in areas with high concentrations of steel. Concrete at the top face of the footing was leveled using a 2x4 and further smoothed using trowels (figure 3.5 and 3.6). The top of the footing was sprayed with a curing agent and covered to retain moisture during the curing process.

The formwork was removed after four days of curing. The footing was moved into the EEL using a forklift which carried it using the Swift-Lift anchors embedded in the footing (figure 3.7).

3.2.2 Columns

Reinforcement cages for the columns were constructed by tying the spiral reinforcement to the longitudinal bars. A Sonotube was capped and attached to the base of the column formwork to provide a pocket within the column for connection to the rebar hinge. The column reinforcement cages were placed over the pocket form and supported with wood bracing (figure 3.8). A Sonotube was placed over each column cage to provide the form for the column concrete. A 1.5 inch (38.1 mm) and 1 inch (25.4 mm) PVC pipe was installed through the Sonotube to provide an access port and vent port for grout placement, respectively. The concrete was cast by pouring it into a large metal bucket and hoisting the bucket over the column forms to place it (figure 3.9). The concrete was internally vibrated after each concrete load was placed. The columns were cast from two batches of concrete from two trucks. The columns were vibrated throughout to ensure that no cold joint formed between the castings. A P52 Swift-Lift anchor was placed at the top of each column to allow for transportation using a forklift or crane. The columns were moved into the EEL and placed on their side twelve days after casting. At this point, it was realized that the column pocket formwork in both columns partially collapsed during casting and therefore, the pocket was partially filled with concrete. The collapse occurred due to the Sonotube having inadequate strength to resist the hydrostatic pressure from the fresh concrete placed in the column. The excess concrete was cut out using a saw to form a pocket large enough for the rebar hinge to be placed inside (figure 3.10). Multiple strain gages at the base of the column were damaged during this process. These gauges were installed on the column (not the hinge) reinforcement near the bottom of the column and were not expected to measure large strains because of reduced moment at the base. The tops of the columns were roughened using a grinder to provide better bond between the column and grout used in the pocket connection (figure 3.11).

3.2.3 Cap Beam

The cap beam reinforcement cage was built by tying the bottom longitudinal bars to the transverse hoops (figure 3.12). A space was left on each side for the column socket connection. The remaining rebar stirrups were installed, and two top longitudinal bars were threaded through the stirrups to provide stiffness during transportation of the cage (figure 3.13). A steel spiral was provided along the bottom quarter of the socket to provide confinement for the socket connection. Originally, circular openings were planned to be formed in the cap beam. However, due to difficulty in constructing a circular form in the cap beam, the opening shape was changed to octagonal. The socket form was built by screwing eight pieces of plywood together and using steel bands around the outside to keep the form confined. Corrugated plastic was fixed to the plywood on each face to increase roughness along the opening and therefore increase grout bond. These openings were placed within the formwork for the lower portion of the cap beam. The cap beam reinforcement was placed inside of the form (figure 3.14), and then additional formwork was installed to form the cap beam opening (figure 3.15). A PVC pipe was installed at the top of each opening to allow grout to be poured into the socket connection during bent assembly. Concrete was poured into the form at the base and into the region surrounding each opening (figure 3.16). The concrete was vibrated within each portion of the form to ensure no voids were present. The formwork and corrugated plastic were removed after four days of cure time and moved into the EEL for assembly. The inside of the cap beam opening after removal of the corrugated plastic sheets is shown in figure 3.17

3.2.4 Bent Assembly

The footing was prepared for column installation by placing a 2 in. (50.8-mm) thick foam pad at the base around each rebar hinge (figure 3.18). Four cutouts were placed in the foam to leave room for leveling bolts. The columns were lifted with a crane and placed over the rebar hinge so that the outside face of the column pocket rested on the leveling bolts and compressed the foam pad which formed a seal (figure 3.19). The bolts were adjusted to plumb the column and create a 1.5 in (38.1-mm) thick gap between the column and footing (indicated by white arrow in figure 3.19). Wood bracing was fixed to the top of the column using Tapcon screws to keep the column in place (figure 3.20). A grout pump was installed in the lower column duct and grout was pumped into the column pocket connection until it bled from the vent port at the top of the pocket (figure 3.21). This process was repeated for the second column. Grout cubes were collected from each grout batch. The rebar hinge is shown in figure 3.22 after removal of the foam form.

Because part of the openings in the cap beam were not covered by concrete at this stage, temporary forms were installed to cover these openings prior to placing the cap beam on the columns (fig. 3.23). The forms were screwed into the cap beam side and restrained with a steel band to prevent the forms from breaking lose during placement of grout in the socket connection. Silicone caulking was applied around the form to prevent grout from leaking. The cap beam was lifted using a crane with straps along the inside edge of each opening (figure 3.24). The cap beam was lowered onto the columns and restrained above the cap beam so that there was 7 feet (2.13 m) of column clear height. Figure 3.25 shows the column inside of the socket connection before placement of grout. Plywood was installed on the underside of the cap beam using Tapcon screws and braced wood beams to keep the grout within the socket connection during casting. Grout was poured into the connection via the ducts that had been placed at the top of each opening (figure 3.26). Sealtight HP1428 grout was initially used for the socket connection. However, upon casting, the grout set off too quickly and did not flow into the connection. The cap beam had to be removed and all grout was scraped off the components. The cap beam was reinstalled, and the procedure was repeated using a SpecChem grout. The second grout was more flowable and filled the connection properly. The sides of the cap beam openings after removal of the formwork are shown in figure 3.27. Figure 3.28 shows the column-to-cap beam connection after grout placement and removal of formwork.

3.3 Superstructure Construction

The superstructure included two spans built using two types of precast components, precast deck panels and precast prestressed concrete girders. The spans were assembled in the structures yard outside EEL simultaneously and were moved into the lab once completed. The main ABC method used for the construction was prefabricated bridge elements and systems (PBES) as discussed in section 3.1. Typically for this method, the deck panels are installed on the bridge once the girders have already been placed. However, the construction technique was adjusted so that minimal construction took place inside EEL. This was done to minimize dust inside the laboratory, which could enter the hydraulics of the shake tables, and to prevent damage to the tables caused by possible falling objects during construction. The construction procedure for the spans and the span assembly is summarized in the following sections.

3.3.1 Girders

The same girder design from Calt-Bridge 1 (Benjumea et al., 2019), was used for this study. The girders for Calt-Bridge 1 and Calt-Bridge 2 were ordered and fabricated concurrently, by KIE-CON Inc. located in Antioch, California. The girders for Calt-Bridge 2 were stored in the structures yard until the spans were ready to be assembled (figure 3.29).

3.3.2 Deck Panels

The deck panels were precast on casting slabs in the structures yard outside of the EEL. The panel forms were built using wood beams for the panel sides. Angled wood forms were placed in the panels to form the deck pockets for the steel studs to pass through for the deck-to-girder connection. PVC pipes were fixed to the forms in locations where superimposed mass would be placed on the deck to allow for anchorage of the mass. Reinforcement projected from the deck panels sides to provide lap splices for the deck joints. Holes were placed in the forms so that the reinforcement could project outside of the precast zone of the deck panel. Female-ended steel lifting eyes were placed in the panel so that lifting bolts could be threaded into the deck panels for transportation. The panels were cast by directly pouring the concrete from the mix truck into the deck panel form. The deck surface was leveled using a wood beam and trowels. Six inch (152 mm) diameter concrete test cylinders were taken from the deck concrete for testing, and the slump was measured at 3.75 inches (95.2 mm) (figure 3.30). The deck panels after casting are shown in figure 3.31. The deck panels were sprayed with a curing agent and covered with tarps to retain moisture in the concrete during curing.

3.3.3 Superstructure Assembly

The spans were assembled individually in the structures yard. Four inch (102 mm) by 4 inch (102 mm) wood posts were placed on the ground 33 feet (10.1 m) apart so that the girders would be raised off the ground and could be lifted using a spreader beam. The girders were transported and placed with two forklifts, one lifting from each side (figure 3.32). Wood spacers were placed between the girder flanges to create the proper spacing between the girders. Once all four girders were placed for each span, the diagonals between the corners of the exterior girders were measured to ensure the girders were not skewed. The final placement of the girders for a span is shown in figure 3.33.

Once the girders were situated, the formwork for the intermediate and end diaphragms was assembled. The diaphragms were constructed using cast-in-place concrete. The diaphragm reinforcement was passed through ducts precast into the girders. Wood forms were cut to match the outline of the girders and braced from the top of the girders using plywood and wood beams (figure 3.34). Plywood was installed on the bottom to complete the form (figure 3.35). Forms were also installed on the outside edge of each girder along the diaphragms to provide anchorage for the longitudinal diaphragm reinforcement (figure 3.36). The process was repeated for the formwork on the interior face of the end diaphragm. Steel plates with rebar welded to one face and a stainless-steel plate welded to the other were epoxied to the bottom of the girders at the end abutment to provide the stainless steel on Teflon interface for the abutments (figure 3.37). The end diaphragm form was completed by installing plywood on the sides and tying the formwork using metal braces to prevent collapse of the form during casting (figure 3.38). Two Swift-Lift anchors were incorporated in each end diaphragm to allow for lifting of the span. The concrete was placed in the diaphragm forms directly using a mixing truck. Concrete cylinders were collected, and the slump was measured at 3.75 inches (95.2 mm).

The deck panels were placed on the girders 2 months after they were cast. The deck panels were transported using lifting bolts and straps connected to a forklift (figure 3.39). The panels were situated so that the projected reinforcement was close to each other. Some of the projected rebar had to be bent during panel placement to allow for proper alignment of the panel. A view of the deck panel-to-panel connection is shown in figure 3.40. The span after the deck panels were placed is shown in figure 3.41.

The deck panel pockets were filled with Sealtight HP1428 grout to complete the girder-to-deck connections. The gaps between the girders and bottom of the deck panels were filled using foam backer rod and silicone caulking. This was done to prevent leakage of ultra-high performance concrete (UHPC) during casting of the closure pours for the deck joints. The deck joints and region over the end diaphragm were cast with UHPC because of the short rebar splice length in these regions (figure 3.42). UHPC enables the lap splice to be fully developed between panels as discussed in section 2.6.6 (Yuan and Graybeal, 2015). The UHPC was prepared based on a mix design from Lafarge using a high-shear mixer. The entire batch of UHPC could not be mixed simultaneously because of the limited volume of the mixer. Several batches were required for both spans. The constituents for the UHPC were measured according to the proper ratio, mixed, and then placed while a new batch of UHPC was mixed. The joints were sprayed with water prior to UHPC placement to assist with bond between the materials. Three inch (76.2 mm) diameter test cylinders were collected from each UHPC batch for material strength testing. During casting, leaks were noted between the deck panels and the girders at small gaps. Backer rod with silicone was applied at the gaps and the leakage ceased. The spans with the UHPC cured are shown in figures 3.43 and 3.44. Upon conclusion of the UHPC casting, the spans were ready for transport.

3.4 Bridge Assembly

The bridge was assembled in four phases. First, the bent was placed on the shake table and anchored using steel rods. Next, the spans including the phase 1 mass were placed on the cap beam and the respective abutment. Afterwards, the cap beam closure pour was completed to create an integral connection between the bent and spans. Lastly, the phase 2 superimposed masses were placed on the bridge. The following sections summarize each step. Note that the abutment seats on shake tables 1 and 3 were already in place prior to assembling Calt-Bridge 2.

3.4.1 Bent Placement

Shake table 2 was prepared for bent placement by removing the caps in the table where the steel anchor rods were placed. The steel rods were threaded into the table and foam pads were glued to the table around each rod to prevent grout from leaking into the shake table holes. The bent was lifted using the Swift-lift anchors in the footing and placed so that the steel rods threaded through the ducts in the footing. A grout pad was cast between the table and the footing to distribute the load. Steel plates and nuts were used to secure the table to the footing with each nut being torqued to the maximum amount allowed for the table connection to produce a tie down force of 570 kips (2.54 MN); which was sufficient to prevent overturning of the bent and slippage at the bent-shake table interface during bridge movement (figure 3.45).

3.4.2 Span Transportation and Placement

The spans were transported into the lab using a crane and a forklift. The lifting plan was designed so the crane would lift the end of the span with the end diaphragm because of the extra diaphragm weight (figure 3.46), and the forklift would lift the lighter end and rotate the span to line up with the laboratory door (figure 3.47). Once the crane had moved the span near the laboratory door, the span was placed on a cart and pushed into the lab (figure 3.48). The span was lifted using the EEL crane and maneuvered so the entire span was inside the lab (figure 3.49). The first span was set on two spreader beams and the transportation process was repeated for the second span. The second span was placed on top of the first span with two spreader beams between them (figure 3.50).

The spans were placed on the superstructure using the EEL cranes and lifted using the Swift-lift anchors in the end diaphragm and the spreader beam. The east span was placed first. The span was lifted and situated above the abutment and cap beam (figure 3.51). When the span was placed near the final location, there was some interference between the precast deck panel and the stirrups in the cap beam. The edge of the deck panel was ground down to allow proper seating of the span. The removal of the deck panel edge was determined to be acceptable because the region would be filled with UHPC from the cap beam closure pour and would not result in voids in the structure. The end diaphragm was set down on the abutment seat, and jacks were placed under each girder near the cap beam so that the span rested near the cap beam but not bearing on it. The bearing surface at the abutments consisted of 12 inch (305 mm) by 19 inch (483 mm) Teflon pads that were 3/8 inch (9.52 mm) thick. The embedded stainless-steel plates in the bottom girder flanges were placed on the Teflon pads to minimize friction and mimic a roller support at the abutments. The spans were placed on the cap beam simultaneously to keep loading in the bent symmetrical as to not create large bending moments in the columns or torque in the cap beam. The west span was lifted in the same manner and placed on the abutment and jacks (figure 3.52). During placement of the spans, the projected prestress strands were bent upwards and rested on the cap beam stirrups to avoid interference between the strands and cap beam reinforcement.

3.4.3 Placement of Phase I Superimposed Mass

Once the spans had been placed on the jacks and abutments, the phase I masses were placed on the superstructure using the EEL crane. The superimposed mass was designed so the mass of the scaled bridge was proportional to the mass of the prototype. The phase

1 mass contributed to the dead load of the bridge and was applied prior to casting of the closure pour over the cap beam to impose positive moment over the bent. This was done to meet the design assumption that the spans were simply supported for dead load and continuous over the bent for live load (SDCL). The weight of each mass component is discussed in section 2.7. The phase 1 mass blocks were placed near the abutment on each span. Threaded rods were passed through the blocks and deck using the holes that had been incorporated in the panels. The threaded rods were anchored to the deck to restrain the mass blocks (figure 3.53). The steel plates and lead baskets were placed in the same manner in the layout shown in figure 2.14. Once the phase 1 mass was placed and anchored, the spans were lowered onto the cap beam. Hydraulic jacks were placed at each side of spreader beams (figure 3.54) and the jacks were connected to the same hydraulic pump. The bridge was lifted off the screw jacks and the jacks were removed. One inch (25.4 mm) thick elastomeric rubber bearing pads were placed under each girder flange to distribute the load on the cap beam. The pressure in the hydraulic jacks was then relieved causing the spans to be lowered at the same rate. Figure 3.55 shows the spans above the cap beam after the bent has been loaded.

3.4.4 Cap Beam Closure Pour

After both spans were placed, the remaining cap beam reinforcement was installed. Headed bars with threaded ends were used for the girder-to-girder connection so that the bars could develop. Headed Reinforcement Corp donated the headed bars for this project. The original design called for the bars to be threaded through the girder slots and the head to be threaded on the bar afterward. However, the bars were longer than needed, and the headed bars projected past the exterior edge of the cap beam for the exterior girders. To remedy this, the bar ends were bent by 90 degrees to fit in the required area (figure 3.56). The crossties and top longitudinal reinforcement were also installed in the bent. The view from the interior girders when looking towards the cap beam is shown in figure 3.57, and the top cap beam reinforcement is shown in figure 3.58. Formwork was installed between each girder and around the exterior face of the cap beam for the cap beam closure pour. Subsequently, concrete was cast in the cap beam up to the top face of the girder top flanges (figure 3.59). The concrete cured for one day and then UHPC was cast in the top region of the cap beam around the projected deck bars (figure 3.60). The UHPC was mixed in the same manner as for that for the deck joints. UHPC was transported to the top of the bridge using plastic tubs and the EEL crane (figure 3.61). Upon removal of the formwork, voids were found in two locations under top girder flanges (figure 3.62). These were caused by the concrete having relatively low slump by the time it was cast due to the transportation time associated with getting the material from the mixing truck to the casting zone. The contractor dry packed the voids to address the issue (figure 3.63)

3.4.5 Placement of Phase 2 Superimposed Mass

14 days after casting of the cap beam closure pour, the phase 2 masses were placed. These masses were designed to induce the negative moment that would stem from barriers and wearing surface which were not implicitly incorporated in the scaled bridge. The phase 2 mass blocks were placed using the EEL crane and anchored to the deck in the same manner as the phase 1 mass blocks had been anchored (figure 3.64). Upon installation of the phase 2 mass blocks, the construction of the scaled bridge was

complete. The shake table test took place 28 days after casting of the UHPC closure pour above the bent.

3.5 Material Test Results

Material properties were measured using test samples of the various construction materials. These properties were measured to determine whether the material strength was representative of the specified design strength for the material and to use these in post-test analytical studies of Calt-Bridge 2. Large differences between the measured material properties and specified properties would indicate that the bridge was not a realistic representation of the design. Another reason for interest in the material strengths was for correlation between the measured and calculated results. Using the actual material properties from the scaled bridge in an analytical model allows for direct comparison between the measured and calculated bridge response and assessment of the modeling methods. Test specimens were tested at 7 days, 28 days, and on the day of testing for all cementitious materials because of their time-dependent material properties.

3.5.1 Concrete

The 6 inch (152 mm) diameter concrete cylinders were all tested in the materials laboratory at UNR. A standard cylinder compression testing device was used with a loading rate of approximately 1000 lb/s (4.45 kN/s). The cylinders were tested to failure and the maximum compressive load was divided by the cylinder area to calculate the compressive strength of the concrete. Three cylinders were tested for each batch and the average was taken to represent the compressive strength of the concrete. The average compressive strengths at 7-days and 28 days after casting and on the test day are listed in table 3.1. The test day strength for each component exceeded the expected strength except for the cast-in-place portion of the cap beam; meaning adequate strength was achieved for each of these components. The measured test-day strength of the cast-in-place concrete part of the cap beam met the nominal specified strength of 4 ksi (27.6 MPa) and was considered acceptable for use in the shake test. Note that because the test took place 28 days after casting of the cap beam, the 28 day strength was equivalent to the test day strength for the cast-in-place part of the cap beam concrete and UHPC. Also, because the prestressed girders were ordered and shipped at the same time as those used in Calt-Bridge 1, the cylinders provided for concrete strength at test day had been tested already for Calt-Bridge 1 and were not available for Calt-Bridge 2. Therefore, the test day strength for the girders for Calt-Bridge was not evaluated.

3.5.2 Grout

Two inch by 2 inch (50.8 mm) grout cubes were cast for each grout pour for the bridge. The same grout was used in the pocket connections for the rebar hinges and the socket connections for the cap beam. Therefore, one set of samples was used to represent the strength of the grout in both regions. The grout cubes were tested using the same compression testing machine that was used for the concrete cylinders. The average compressive strength at 7 and 28 days and test day are listed in table 3.2. Test day strengths of the grout exceeded the target grout strength of 6000 psi (41.4 MPa).

3.5.3 UHPC

Three inch (76.2 mm) diameter by 6 inch (152.4 mm) tall test cylinders were collected from the UHPC casting for the deck panel joints and the closure pour over the cap beam. The cylinders were cut using a wet saw and then ground on both ends to achieve a level surface. This was important because uneven stress distribution in UHPC cylinders can lead to significant differences in the measured compressive strength. The average compressive strengths at 7 and 28 days and test day are listed in table 3.3. The UHPC strengths were lower than those seen in Calt-Bridge 1, (Benjumea et al., 2019), but were still above the minimum required strength of 13.5 ksi (94.5 MPa) for short lap splices recommended by Yuan and Graybeal (2014).

3.5.4 Steel

Test bars were provided with each batch of reinforcing bars during the construction of Calt-Bridge 2. The measured steel data is used to establish the yield strain for comparison to the shake test data, and for input of the material properties into the post-test analytical model. The #3 bar samples were tested on the Instron testing machine in the EEL basement. #4, #5, and #6 bars were tested on the MTS testing machine in the Large Scale Structures Laboratory at UNR because the Instron device had insufficient capacity to test #4 and larger Grade 60 bars. Strain readings were recorded during testing by placing reflective strips of tape at two ends of the rebar specimen and measuring the displacement between the tape under loading using an extensometer. The yield stress, ultimate stress, yield strain and ultimate strain for the rebar are listed in table 3.4 organized by bar size. Note that the yield strains listed in table 3.4 were calculated by dividing the measured yield stress by the modulus of elasticity for steel [29000 ksi (200 GPa)]. The ultimate strain was not recorded for two #3 bars and one #4 bar because the reflective tape fell off the samples prior to the conclusion of the test. All the recorded values were within acceptable range of the expected steel material properties used in design.

Chapter 4. Instrumentation of Bridge Model

4.1 Introduction

The bridge response during the shake table test was monitored using several instrument types including strain gauges, Novotechnik displacement transducers, accelerometers, and video cameras. The instruments were connected to data acquisition systems via cables for recording and monitoring of data. An additional 59 channels were dedicated to monitoring shake table feedback such as force, acceleration, velocity, and displacement. Readings from these instruments were measured and recorded over 303 channels and sampled at a rate of 256 Hz. This chapter presents a description of the methods used to develop the instrumentation plan. The plan is shown in figures 4.1-4.14.

4.2 Strain Gauges

Strain gauges were used to monitor the strains within members of the bridge that were critical for the evaluation of the performance of the ABC connections and the bridge system performance. The measured strains were used to monitor and evaluate the internal behavior of the incorporated connections in Calt-Bridge 2. All strain gauges type was YFLA-2-5LJC manufactured by Texas Measurements. The strain gauges measured strain uniaxially in steel reinforcement. Each gauge location was prepared by grinding the rebar surface until the ribs were removed. The surface was roughened with sandpaper and cleaned with denatured alcohol to improve bond between the gauge and rebar. All strain gauges were fixed to the rebar using an adhesive. Each gauge was wrapped with three layers of electrical tape to prevent shorting of the gauge wire caused by contact between the rebar and exposed copper wire. The initial 4 inches (102 mm) of wire stemming from the gauge was bundled and wrapped in mastic tape to prevent the gauge from being pulled off the rebar from tension on the lead and to protect the instrument during casting and construction. Shrink tubing was applied over the gauge wire to protect the wires during casting.

4.2.1 Column Strain Gauges

The columns were instrumented with strain gauges at five different levels along the longitudinal reinforcement (figure 4.1). The instrumentation levels were labeled with a “C” to indicate a column instrument and a “N” or “S” to indicate whether it was a north or south column. Gauges were attached to rebars along the north, south, east, and west column faces to capture strains due to biaxial bending in the column section. Instrumentation levels CN-1 and CS-1 were placed 4.5 inches (114 mm) above the column-footing interface to monitor the distribution of forces from the rebar hinge into the column base. Because the rebar hinge is designed to have a smaller moment capacity than the column capacity, the column longitudinal bar strains near the base were expected to be small. Four strain gauge layers were installed at the column top at 1 inch (25.4 mm) (CN-4, CS-4), 8 inches (203 mm) (CN-3, CS-3), and 15 inches (381 mm) (CN-2, CS-2) below the cap beam-column interface and 4 inches (127 mm) above the interface embedded in the cap beam (CN-5, CS-5). These locations were chosen to monitor the spread of yielding through the column top and into the embedded longitudinal reinforcement within the cap beam. The longitudinal bar strains were expected to be highest at the cap beam-column interface (CN-4, CS-4) and to dissipate away from the interface if the cap beam socket connections were to behave as cast-in-place connections. The measured data were expected to determine if this were the case. Bending moments are expected to be highest at the column top when full fixity is achieved in the socket connection. Because the cap beam was designed to be capacity protected, longitudinal bar strains within the cap beam were expected to be significantly smaller than those seen at the interface. The cap beam bar strain data were collected to determine if the design objective was met. The spiral reinforcement was also instrumented at each of the column instrumentation elevations to capture the confining and shear stresses (figure 4.2).

4.2.2 Rebar Hinge Strain Gauges

The hinge reinforcement was instrumented at three elevations (figure 4.3). The longitudinal reinforcement along the north, south, east, and west faces of the hinges were instrumented to capture biaxial effects. Gauges were applied at the hinge-footing interface (FN-2, FS-2) and 6 inches (152 mm) above (FN-3, FS-3) and below the interface (FN-1, FS-1). Because the hinge is part of the energy dissipation mechanism in the bridge system, large strains were expected in the reinforcement, particularly at the interface due to the expected rotations in this region. Instrumentation levels F-1 and F-3 above and below the interface were provided to monitor the strains within the column pocket connection and the footing to validate that proper rebar anchorage was provided and to monitor the spread of yielding. The spiral reinforcement was instrumented at the interface and 6 inches (152 mm) into the column pocket (figure 4.4) to monitor confining and shear stresses. Because F-1 was located in the footing, spiral stresses in this region were not expected to be significant and, hence, the spirals were not instrumented at this elevation.

4.2.3 Cap Beam Strain Gauges

Reinforcement within the cap beam was instrumented with strain gauges to monitor strain levels in the cap beam that could be used to assess whether the cap beam performed as a capacity protected member. Because the cap beam was designed to be capacity protected, strains were expected to be below yielding for all earthquake runs if the design and construction were successful. Both the longitudinal and transverse reinforcement was instrumented at select locations to determine stress distribution within the cap beam (figure 4.5). These locations included shear stirrups, and longitudinal bars at the top and bottom of the cap beam section. The confining spirals around the lower half of the socket connections were instrumented at mid-height of the spiral at the north, south, east, and west edges to monitor the confining stresses around the socket connection. The girder-to-cap beam connection in the cap beam was instrumented to monitor force development in the prestress strands, headed bars, and crossties. These components were instrumented on both sides of the girder web to evaluate the positive moment resistance of the connection during shake table testing (figure 4.6 and 4.7).

4.2.4 Deck Strain Gauges

Strain gauges were installed to the projected deck panel reinforcement over the cap beam to monitor the strains in the deck connection over the bent (figure 4.8). The deck is designed as a capacity protected member. Therefore, strains in the connection were expected to remain below yielding in all earthquake runs. Strain gauges were applied to each of the three precast deck panels on both sides of the bent. Two #4 bars and two #3 bars were instrumented in the west and east spans. For each bar, one gauge was embedded 8 inches (203 mm) within the precast portion of the deck panel and one was installed 8 inches (203 mm) from the precast deck panel interface within the UHPC. These two locations were selected to capture differences in the strain distribution in the longitudinal reinforcement within the precast deck panel and the deck connection over the pier.

4.3 Displacement Transducers and String Potentiometers

Displacements during the shake tests were measured using displacement transducers and string potentiometers. String potentiometers were used to measure global displacements of the bridge system, while displacement transducers were used to measure local displacements within components. The displacement transducers used were a combination of Novotechnik TR-50, TR-75, and TR-100, with the number indicating the stroke of the instrument in millimeters. The string potentiometers were UniMeasure PA series linear position transducers with a stroke of 60 inches (1.52 m). Because the distance between the bridge and instrument often exceeded 60 inches (1.52 m), copper wires were tied to the instrument end and connected to the structure via a glued metal bracket. It was desirable for the distance between the sample point on the structure and the instrument to be large because a greater gage length decreases the effect of displacements caused by bridge movement perpendicular to the displacements measured by each instrument.

4.3.1 Column Displacement Transducers

Displacement transducers were installed on the columns to measure local displacements, rotations, curvatures, and angle of twist within and along the column. The displacement transducers were connected to the column with steel rods that were embedded within the column cover concrete. Vertically oriented displacement transducers were installed along three levels at the column top on the north, south, west, and east side of each column (figure 4.9). These displacement transducers measured the rotation of the column relative to the cap beam interface in addition to the curvature within the top 8 inches (203 mm) and 15 inches (381 mm) of each column. This data was important to monitor the condition of the socket connection during the shake tests. Two instrumentation layers were placed at the bottom of the column to measure local displacement and rotation within the hinge. The first layer consisted of four vertically oriented displacement transducers placed 4.75 inches (121 mm) from the footing interface. These measured the rotation of the hinge relative to the footing interface in the longitudinal and transverse directions of the bridge. Four horizontally oriented displacement transducers were placed 2.75 inches (69.8 mm) from the footing interface and were used to calculate the angle of twist and horizontal displacement of the hinge relative to the footing.

4.3.2 Superstructure Displacement Transducers

Local horizontal displacements between the superstructure and cap beam were measured using displacement transducers fixed to the bottom and top of an exterior and interior girder on each span (figure 4.10). These transducers were used to determine if any slippage took place in the girder-to-cap beam connection and to calculate the rotation of the superstructure relative to the cap beam.

A set of displacement transducers was mounted on the top girder flanges to measure any relative movement between the deck panels and girders (figure 4.11). The purpose of these displacement transducers was to capture any slippage between the girder and deck panels. Two displacement transducers were used at each location; one measuring relative longitudinal displacement and the other measuring relative transverse displacement. The girders were instrumented at two locations; the first was located 8 inches (203 mm) away from the cap beam interface, and the second was located 54 inches (1.37 m) away from the interface. These points were chosen because analytical results from Calt-Bridge 1 studies [Benjumea, et al. (2019)] indicated that the maximum interface shear between the deck panel and girder would take place 54 inches from the cap beam interface for a flexible girder-to-cap beam connection. Note that this location was not instrumented in Calt-Bridge 1, and assessment of the girder-to-cap beam connection using this method could not be performed. If the girder-to-cap beam connection were rigid, the maximum slippage was expected to occur at the superstructure-cap beam interface.

4.3.3 String Potentiometers

String potentiometers were installed on the bridge superstructure to monitor global displacements at the abutments, mid-span, and bent in the longitudinal, transverse, and vertical directions (figure 4.12). These data were collected relative to a fixed stationary reference. Therefore, the data were absolute displacements of the superstructure, meaning that table displacement was included in the measured data. Displacement of the superstructure relative to the shake table could be calculated by subtracting the measured table displacements from the measured displacements. String potentiometers were connected to the abutment seats to determine if there were any movements in the seats during the tests. The transverse bent displacement was monitored at two locations, the center of the precast portion of the cap beam, and the center of the cast-in-place portion of the cap beam. This was implemented to capture any possible differences between the precast and cast-in-place concrete and to provide redundancy in the collected data.

4.4 Accelerometers

ADXL326 accelerometers were used to measure the accelerations of the bridge. Triaxial accelerometers were placed at five locations on the bridge deck to measure superstructure acceleration in the longitudinal, transverse, and vertical directions (figure 4.13). Accelerometer 3 was placed above the center of the bent. Accelerometers 1 and 5 were placed above the west and east abutments, respectively. Accelerometers 2 and 4 were installed at midspan of the west and east spans, respectively. An additional accelerometer was placed at the center of the top of the footing to measure table acceleration. Superstructure accelerations were used to calculate bent forces using the inertia mass of the structure.

4.5 Video Cameras

GoPro video cameras were installed to visually monitor the bridge response during the shake table tests. A description of the camera number, type of camera used, and camera viewing location is listed in table 4.1. GoPro Hero5 cameras were used to monitor the longitudinal and transverse bent response and superstructure response at the abutments. GoPro Hero2 cameras were used to record the damage progression of the plastic hinges at the top of each column and at the hinge base. GoPro Hero1 cameras were mounted to the underside of the deck panels facing the cap beam to visualize any relative displacements at the cap beam-girder interface. Two video cameras were used to monitor the overall bridge system response during the tests from the northeast and southwest.

Chapter 5. Pretest Analysis of Bridge Model

5.1 Introduction

Three-dimensional pretest modeling of Calt-Bridge 2 was performed using Opensees to calculate the non-linear response of the bridge under seismic loading. Non-linear static (pushover) analyses along the longitudinal and transverse directions of the bridge were performed independently to estimate the seismic displacement demand for the bridge and the bent displacement capacity in the respective direction. The seismic displacement demands for each direction were combined to calculate the resultant design displacement. Next, a non-linear dynamic analysis was performed using bi-directional ground motions from the 1994 Northridge Earthquake recorded at Sylmar station. The acceleration histories were scaled so that the peak resultant displacement of the non-linear dynamic analysis matched the calculated design displacement. This scaled ground motion was established as the design level earthquake. Different acceleration scale factors were used to plan the loading protocol for the shake test. Forces and displacements during different test runs were estimated using dynamic analysis with ground motion records that included the previous runs. A description of the formulation of the analytical model, the results from each analysis, and the loading protocol are discussed in this chapter.

5.2 Development of Pretest Analytical Model

The pretest analytical modeling was performed in Opensees, an open source structural analysis software package capable of analyzing structural systems subjected to earthquakes (Opensees, 2006). Opensees has been used on several bridge system projects and led to analytical results that correlated well with measured results (Cruz-Noguez and Saiidi, 2010; Varela and Saiidi, 2016; Benjumea, et al., 2019; Shoushtari et al., 2019). A three-dimensional model of the bridge was developed using Opensees to capture the non-linear behavior of elements. Several element and material models have been developed by other researchers for use in non-linear analysis and were used in this study. This section describes the development of the analytical model and the element and material properties selected for each bridge component.

5.2.1 Model Overview

The bridge geometry was defined in the model using a series of nodes and elements. Nodes were defined to represent the bridge geometry along the bent and superstructure and were placed at the centroid of the respective component sections. Elements were defined between nodes and assigned properties based on the component type. The formulation of each component is discussed in the following sections. The node and element layout of the bent is shown in figure 5.1. The node and element layout in the deck along the west and east spans are shown in figures 5.2 and 5.3, respectively. An overview of the analytical model as portrayed by the DisplayModel3D script from the Opensees library is shown in figure 5.4.

5.2.2 Modeling of Columns

The column geometry was defined by placing nodes at the bottom of the columns and bottom of the cap beam where the column and cap beam frame together via the socket connection (defined as nodes 3 and 5 for the south column and 4 and 6 for the north column as shown in figure 5.1). Each column was discretized using five Gauss-Lobato integration points. The columns were defined as forceBeamColumn elements using fiber sections with non-linear material properties, which allowed for distributed plasticity along the length of the element. The concrete in the column was defined using the Concrete04 material model. This model constructs a uniaxial Popovics concrete material object with degraded linear unloading/reloading stiffness (Opensees, 2009). The compressive stress-strain envelope of this concrete model is identical to Mander's model when the modulus of elasticity is defined as 57000 times the square root of the concrete compressive strength in psi. ReinforcingSteel was used to model the longitudinal rebar in the elements. The column transverse steel was not explicitly modeled but the confinement provided by the spirals was accounted for by adjusting the column concrete core strength based on the confinement stresses. The column section was defined using a fiber section discretized into three patch areas, confined core concrete, unconfined cover concrete, and reinforcing steel. Expected material properties were used for all components to create a realistic model of Calt-Bridge 2 that would relate to measured test results. The nominal concrete strength was adjusted to the expected strength using the factor of 1.3 given in the Caltrans Seismic Design Criteria (SDC) (Caltrans, 2019). The cover concrete compressive strength was defined as 5.2 ksi (35.8 MPa) with a strain of 0.002 at the maximum compressive strength. Mander's model for confined concrete (Mander et. al, 1988) was used to calculate the column concrete core properties. The confined concrete compressive strength was 8.35 ksi (57.6 MPa), the concrete strain at maximum compressive strength was 0.008, the failure strain was 0.0178 and the modulus of elasticity was 5208 ksi (35.9 GPa). The concrete was assumed to have no tensile capacity. The expected yield strength for grade 60 reinforcing steel was 68 ksi (469 MPa) and the ultimate strength was 95 ksi (655 MPa) (Caltrans, 2019). The ReinforcingSteel material model was defined with initial strain hardening of 0.015, and a peak strain of 0.12. Because the columns were expected to experience large deformations, a P-delta geometric transformation was applied to the column elements. The socket connection at the top was assumed to be a rigid connection. No bond-slip rotation was defined for the end of the columns at the pretest analytical studies stage. However, bond slip rotation was included at both ends of the columns in the post-test analyses. One-half of the mass of the column was applied at the top column node.

5.2.3 Modeling of Rebar Hinges

In Calt-Bridge 2, there was a 1.5 inch (38.1 mm) gap for the rebar hinges between the top face of the footing and the base of the full columns. This gap was modeled by including a node at the top of the footing where the rebar hinges framed into the footing (nodes 1 and 2, figure 5.1), and a node at the full column base where the rebar hinges fit into the column pocket (nodes 3 and 4, figure 5.1). The rebar hinge elements were defined between nodes 1 and 3, and nodes 2 and 4. The footing was not incorporated in this model due to its designed fixity to the shake table. All degrees of freedom at the bottom of the rebar hinge were fixed with no relative displacement between the rebar hinge and the footing modeled. The rebar hinge elements were modeled in the same manner as discussed in section 5.2.2 using forceBeamColumn elements with fiber sections to capture the distribution of plasticity along the element. Concrete04 and ReinforcingSteel were again used for the grout and steel material models, respectively. The expected grout properties were used for the Concrete04 material model due to the rebar hinge being made from grout from the closure pour between the column and footing. Cover grout was defined as having a compressive strength of 8 ksi (55.2 MPa) and a strain at maximum compressive strength of 0.002. Mander's model for confined concrete was again used to calculate the hinge core material properties. However, because the rebar hinge spiral is contained within the column spiral, confinement was provided by both the hinge spiral and the column spiral, resulting in the grout core being doubly confined. The confined grout compressive strength was defined as 15.3 ksi, the grout strain at maximum compressive strength was 0.0112 and the failure strain of the grout was 0.0136.

5.2.4 Modeling of Superstructure and Cap Beam

The superstructure was modeled using a grillage with the enhanced beam-stick method proposed by Amirihormozaki et. al (2015). Nodes were placed along the centerline of each girder at the centroid elevation of the girder section. A node was placed at the top of each girder to model the location where the steel studs for the deck connections project from the girder. A rigid element was provided between the girder node (nodes 8, 10, 12, and 14, figure 5.1) and the node on the girder top face (nodes 500, 600, 700, and 800, figure 5.1) to force uniformity across the girder cross-section. Nodes were placed along the center of the deck above each girder (nodes 900, 1100, 1200, and 1400, figure 5.1). An extra deck element was added adjacent to each exterior girder to cause the centroid of each deck element to be above the center of the girders (elements 1001 to 1045, 1301 to 1345, figure 5.2 and 5.3). This was done so that a rigid element could be provided between the deck and girder to represent the deck-to-girder connection. Multiple deck-to-girder connections were investigated by Benjumea et. al (2019) using analytical models, and rigid elements were found to be adequate to represent the connection between the deck and girder. Figure 5.5 shows the cross-section of the superstructure as modeled. This cross section was modeled every 18 inches (457 mm) along the superstructure to account for the spacing of the deck-to-girder connection.

All elements within the superstructure were assumed to remain elastic and were modeled with elasticBeamColumn elements. The area of the girder and modulus of elasticity of the girder concrete were assigned to the girder elements. Because the girders were prestressed, gross section properties were used. The deck was modeled using longitudinal and transverse beams that spanned along the deck nodes to represent the stiffness of the deck in each direction (figure 5.2 and 5.3). The tributary area and concrete modulus of elasticity were assigned to the beams for each direction. The deck was assumed to be a cracked section, therefore the effective (cracked) moment of inertia was used, which was 0.4 times the gross moment of inertia. The Poisson's ratio was set to 0 for the deck beams to remove interaction between the axial and bending forces in the longitudinal and transverse directions of the grillage. The torsional constant of the deck beams was factored by 0.5 (Amirihormozaki et. al, 2015). The tributary mass of each element was lumped at the respective node to represent the mass of the superstructure. Only the mass of the longitudinal deck beams was included so that the mass of the deck was not doubly counted.

The intermediate and end diaphragms were modeled using elasticBeamColumn elements at the abutments, quarter-points, and midpoints of each span (figure 5.5). The diaphragm nodes were placed along the centroid of the diaphragm and were connected to the girders and deck with rigid elements. The effective (cracked) moment of inertia was assigned to the diaphragm elements which was 0.4 times the gross moment of inertia.

The cap beam was assumed to remain elastic and was modeled as an elasticBeamColumn element. The cap beam nodes were placed along the center of the cap beam and connected to the column with rigid elements. The modulus of elasticity of the cap beam was set as 3605 ksi (24.9 GPa). Deck nodes were placed above the cap beam and connected with rigid links to allow for connectivity of the spans to the bent. The spans were connected to the bent using girder and deck elements. Full rigidity in the girder-cap beam connection was assumed.

Nodes were added above the superstructure to account for the superimposed mass that was applied to the bridge (figure 5.1). The nodes were placed at the center of elevation of the mass blocks, lead pallets, and steel plates to account for the eccentricity of the mass relative to the superstructure. The mass was distributed to each node based on the tributary weight for that respective node.

5.2.5 Gravity Analysis

Once the analytical model was developed, a gravity analysis was performed to verify the analytical results. Two procedures were compared; the first was the results from a gravity analysis for the Opensees model, the second was hand calculation of the bridge reactions using static equilibrium. The hand calculations were performed by assuming the spans were simply supported for the self-weight and additional mass minus the stage 2 mass blocks. The stage 2 mass blocks were assumed to be applied with the spans fixed at the bent and roller supports at the abutments. The mass was distributed to the interior and exterior girders based on tributary area. Table 5.1 shows the calculated reactions at the abutments and column bases. The results from the Opensees model were close to the hand calculation results. The Opensees model showed a higher proportion of the load being transferred through the bent rather than the columns. This was most likely because staged construction was not modeled in Opensees, but was taken into account in hand calculations. Therefore, all dead load and superimposed mass were placed on the spans under fixed-roller end conditions in Opensees, rather than simply supported conditions according to which the bridge was constructed and hand calculations were done. The distribution of forces to the interior and exterior girders was the same for both methods. This comparison validated that the Opensees model determined the response under gravity loads correctly and could be used for further analysis.

5.2.6 Modal Analysis

A modal analysis was performed after gravity loads had been applied to the bridge. The first four fundamental periods of the structure were calculated from an eigen value analysis using Opensees. The fundamental periods were calculated for the model using the lumped mass method and a distributed mass method. These two methods were compared to determine if using lumped mass would significantly alter the dynamic response of the bridge compared to the more realistic modeling of distributed mass. Performing dynamic analysis with distributed mass requires longer execution time. Therefore, it is desirable to use lumped mass if appropriate. The first four fundamental periods of the bridge model are shown in table 5.2. The first mode was associated with in-plane rotation of the superstructure and was excited at 1.42 seconds for the distributed mass method and 1.40 seconds for the lumped mass model. The next two modes were associated with the longitudinal and transverse translation of the superstructure and were 0.29 and 0.28 second for the longitudinal and transverse directions, respectively. These two translational modes depended on the rebar hinge and column properties but the periods in the two directions were slightly different due to the overturning effect associated with transverse translation. The last mode was associated with vertical movement of the superstructure with the maximum vertical displacement of the fundamental mode shape taking place at mid-span. Because the comparison between the two mass modeling methods showed little difference between the results, the lumped mass model was used for the pushover analysis and the dynamic analyses.

5.3 Pushover Analysis

Pushover analyses were performed in the longitudinal and transverse directions, independently. The purpose of these analyses was to calculate the bent displacement and force capacity and the effective properties of the bent. These effective properties were used to calculate the displacement demand for the bridge. A unit load was applied at the center cap beam node located halfway between the columns (node 11, figure 5.1) in both the transverse and longitudinal pushover analysis and oriented in the direction of interest. The pushover analyses were performed by incrementally increasing the reference load and solving for the bent forces and displacement for each time step. The pushover analyses were continued until 8% drift ratio was achieved.

5.3.1 Idealized Bilinear Capacity Curve

Once the pushover curve was formed, a bilinear idealized curve was generated to determine the bent effective properties. The first yield point was determined by finding the time step where yielding first occurred in the column reinforcement. The effective stiffness was then calculated by dividing the base shear at first yield by the displacement at first yield. The plastic base shear was calculated by equating the area under the calculated curve with the area under the idealized curve. The calculated pushover curves and idealized curves for the transverse and longitudinal directions are shown in figures 5.6 and 5.7, respectively. The analysis succeeded in calculating the bent response up to 8 percent drift. The bent was considered to not have failed during the analysis because only a small amount of base shear degradation took place at 8 percent drift level.

The effective properties of the bent for each analysis are shown in table 5.3. The bent response was nearly identical for both directions, with only small differences in the peak base shear. Each pushover curve had a high initial stiffness but experienced slight softening in the linear region prior to the first yield point. This was caused by yielding in the rebar hinge. The rebar hinge reinforcement strain was not considered for estimation of the first yield point due to the displacements and forces being dominated by the column response. The base shear in the system developed from formation of plastic hinges in the rebar hinge at the base and in the column top. Once the plastic moment capacity had been reached at the top and bottom of the column, a decrease in force was observed. The plastic shear in the longitudinal direction was 72.7 kips (323 kN) and it was 71.8 kips (319 kN) in the transverse direction. Again, the difference between the two directions is caused by the overturning effects associated with transverse displacement. Because the axial forces are not equal in the two columns for the transverse pushover analysis, the plastic moment capacity is not the same between the two columns, which causes the plastic base shear capacity to differ. The maximum displacement (associated with the 8 percent drift ratio, which was the limit set in the analysis) was 6.72 inches (92.9 mm) and the effective yield displacement was 0.56 inches (14.5 mm) in each direction. Because the bent did not fail in the pushover analysis, the displacement capacity was not calculated. However, it was clear that the displacement capacity is at least 6.72 inches (92.9 mm). The estimated displacement ductility capacity for each direction was at least 12, which was greater than the minimum requirement of 3 required by Caltrans SDC section 3.1.3. The effective stiffness of the idealized curve was used to calculate the effective period of the bent, which was 0.38 second and 0.39 second in the longitudinal and transverse directions, respectively.

5.3.2 Displacement Demand

The data from the pushover curves was used to determine the displacement demand on the bridge for the design response spectrum. The Caltrans ARS Online tool (Caltrans, 2017) was used to find the acceleration response spectrum curve for a general area in Lakewood, CA with site class D assumed. The period axis was scaled by 0.592 to account for the geometric scale factor of the bridge model. The effective period was used to determine the spectral acceleration from the curve which was 1.18 g for both the longitudinal and transverse directions. The scaled ARS demand curve is shown in figure 5.8 with the period of interest indicated. The displacement demand was calculated for the longitudinal and transverse directions using Caltrans SDC equation 7.3.1.1-1 (Caltrans, 2019) which is:

$$\Delta_d = \frac{m * S_a}{k_{eff}} \tag{5-1}$$

Where,

m: Seismic mass of the structure, lbm (kg)

S_a: Spectral acceleration from ARS Online tool, in/s^2 (m/s^2)

k_{eff} : Effective stiffness of the bent calculated using the idealized curve, lb/in, (N/m)

The displacement demand was 1.82 inches (46.2 mm) in the transverse direction and 1.79 inches (45.5 mm) in the longitudinal direction. Because the bridge was going to be subjected to bi-directional shaking, the displacements had to be combined to determine the resultant displacement demand. The resultant displacement demand was calculated by taking the larger of equation 5-2 and 5-3, which was 2.36 inches (59.9 mm). The displacement ductility demand was 2.47, which was less than the maximum of 5 allowed by the Caltrans SDC for multi-column bents.

$$\Delta_{d,resultant} = 1 * \Delta_{d,transverse} + 0.3 * \Delta_{d,longitudinal} \tag{5-2}$$

$$\Delta_{d,resultant} = 1 * \Delta_{d,longitudinal} + 0.3 * \Delta_{d,transverse} \tag{5-3}$$

Where,

$\Delta_{d,longitudinal}$: Displacement demand in the longitudinal direction of the bridge, in (mm)

$\Delta_{d,transverse}$: Displacement demand in the transverse direction of the bridge, in (mm)

5.4 Non-linear Dynamic Analysis

A non-linear dynamic analysis was performed to determine the bridge model response to bi-directional earthquakes and to determine the design level earthquake. The Northridge earthquake recorded at Sylmar station was used as the input motion. This ground motion was selected because of its strong peak ground acceleration in each horizontal component, which was important for evaluation of the ABC connections behavior in a bridge system subjected to bi-axial ground motions. Also, the Northridge earthquake recorded at Sylmar station consists of nearly symmetric acceleration records for each component; meaning the record contains accelerations that cause the bridge response to be cyclic, rather than dominant in only one direction. This response type was chosen to evaluate connection behavior under reverse loading. For these reasons, the record was selected in the 2-span bridge system studies in Calt-Bridge 1 (Benjumea et. al, 2019) and ABC-UTC (Shoushtari et. al, 2019). One goal of the study of Calt-Bridge 2 was to compare the behavior of the various connections used on all three bridge models, which is discussed in chapter 11. Using the same ground motion as that of the other two bridges allowed for comparison of the bridge connections.

The horizontal components SCS052 and SCS142 were assigned to the transverse and longitudinal directions, respectively. The stronger ground motion component was simulated in the longitudinal direction of the bridge model to extensively test the socket connection for out-of-plane forces. Previous studies of socket connections [Mehrsoroush & Saiidi (2014), Mohebbi, et al. (2017), Tazarv & Saiidi (2015)] were limited to in-plane ground motions. Because socket connections under in-plane loading have been tested thoroughly, the stronger ground motion was applied to the out-of-plane component of the bent to determine out-of-plane socket connection behavior under strong earthquakes.

The ground motion time record was scaled by 0.592 to account for the geometric scale factor of the bridge. The ground motion was applied using the UniformExcitation load pattern from Opensees. This load pattern applies the ground motions from the acceleration record at nodes constrained against the degree of freedom associated with the acceleration component. Because the abutments were only constrained against vertical movement, the ground motions were only applied at the rebar hinge bases [nodes 1 and 2, (figure 5.1)].

The bridge was assigned a damping ratio of 2% for the first and fifth modes. An RCM numberer which renumbers the nodes and elements automatically for computational efficiency was used to decrease the analysis time. The dynamic analysis was performed using the Newmark integrator and modified Newton-Raphson algorithm. An energy increment test was used with a tolerance of 10^{-14} and a maximum number of iterations per time step of 50. If the solver did not converge within the maximum iteration limit, different solvers and algorithms were incorporated. If adjusting the solver type did still not cause convergence, the time step size was decreased by 25%.

5.4.1 Design Earthquake

The same approach to designate the design level earthquake used by Benjumea et. al (2019) was used in this study. Usually the spectral acceleration of the ground motion and response spectrum are matched and that is designated as the design level earthquake. Caltrans seismic design approach for bents in ordinary bridges is based on the capacity of the system to withstand the imposed displacements by the design level earthquake. Because the bridge performance is determined by displacement capacity and demands, displacement demand was used for this bridge to designate the design level earthquake. The amplitude of the Northridge earthquake record was varied until the resultant displacement from the Opensees model of Calt-Bridge 2 was close to 2.36 inches, the displacement demand calculated in section 5.3.2. The adjustment factors were the same for both earthquake components. The acceleration scale factor that resulted in a resultant displacement close to 2.36 inches (59.9 mm) was 0.455. Even though the spectral acceleration of the design earthquake was not specifically matched to the ARS response spectrum, the combined square root sum of the squares of the response spectrum for the two directions happened to be nearly equal to the ARS spectral acceleration for the period of interest as indicated in figure 5.9.

5.4.2 Development of Loading Protocol

The target loading protocol was developed by scaling the design level earthquake for several earthquake runs to capture different limit states and the entire displacement range in the pushover curves. In all, seven ground motions were selected, starting at 30% of the design level earthquake and increasing to 200%. The design earthquake was planned for run 3. This was done so that the predicted bridge capacity curve could be tracked, with smaller runs being completed first, prior to the onset of significant yielding with subsequent runs causing increased damage. The target loading protocol is listed in table 5.4. White noise motions were planned before each run in each direction of the bridge model so that the natural frequency of the bridge could be tracked throughout the shake table tests.

5.4.3 Pretest Response of Bridge for Target Loading Protocol

The Opensees model was subjected to the target loading protocol with a spliced acceleration record scaled according to the loading protocol. The white noise motions were excluded because they were of very small amplitudes (PGA of 0.07g or less) with insignificant effect on Calt-Bridge 2. The ground motions were trimmed to include the acceleration history for the interval of 0 to 25 seconds because the main portion of the ground motion took place during this time interval. The motions were trimmed to save computation time. Five seconds of zero acceleration input motion was added between each earthquake run to ensure that the system was fully at rest prior to beginning the next run. The displacement response history for the longitudinal and transverse directions is shown in figure 5.10 and the peak displacements for the longitudinal, transverse, and resultant directions are presented in tables 5.5, 5.6, and 5.7, respectively. The peak resultant displacement in run 3, the design earthquake, was 2.18 inches (55.4 mm), which was considered sufficiently close to the resultant displacement demand of 2.36 inches (59.9 mm) to be considered the design earthquake run. A maximum resultant displacement of 4.91 inches (124.6 mm) was expected in run 7 at 200% of the design earthquake, which is a drift ratio of 5.8%. The peak base shear for different runs for the longitudinal and transverse directions are presented in table 5.8 and 5.9, respectively. The peak base shear of 69.1 kips (307.5 kN) in the longitudinal direction was close to the idealized peak plastic shear capacity calculated for the bent in section 5.3.1 of 72.7 kips (323 kN). However, the peak transverse base shear achieved in the non-linear dynamic analysis was 62.3 kips (277.1 kN), which was below what was expected for the transverse direction of 71.8 kips (304 kN). Because the bridge is subjected to bi-axial forces, a higher degree of strength degradation is expected than what would occur in a uniaxial test. It is not expected that the bridge would achieve the peak base shear in each direction, but rather that the resultant base shear would be comparable to the peak base shear capacity predicted by the pushover analyses. The force-displacement relationships are presented in figure 5.11 and 5.12 for the longitudinal and transverse directions, respectively. The hysteresis curves show good energy dissipation in both directions with the longitudinal direction being the more dominant of the two. The transverse force-displacement relationship was symmetrical, while the longitudinal displacement was dominant towards one side. These calculated properties were compared to the measured results at the conclusion of the shake test to determine the accuracy of the pretest analytical model. The predicted results from the dynamic analysis and the measured results from the shake test are compared in chapter 8. Adjustments made to the pretest analytical model to better represent the actual response of the bridge are also discussed in chapter 8.

Chapter 6. Experimental Results of Two-span Shake Test

6.1 Introduction

Eight ground motions ranging from 30% to 225% of the design level earthquake were applied to the bridge during the shake table tests. This chapter describes the results and general behavior of the bridge during these ground motions. Shake table motions and structure accelerations for each run are discussed. A summary of the visual assessments of the bridge that were made at the conclusion of each run is also provided. Next, various displacements of the superstructure and within the bent are summarized. This is followed by a summary of the methods used to calculate bent base shear and the corresponding force-displacement plots for each run. Strain data is analyzed to determine internal component behavior. Finally, an assessment of connection behavior using the measured data is made.

6.2 Measured Shake Table Motions

Input ground motions for the shake table were set according to the load protocol presented in section 5.4.2. These ground motions were the target motions for simulation by the shake tables. Due to tolerances of the shake table controls, some variance is expected between the target ground motions and the achieved (measured) ground motions. Because of the importance of the design level earthquake in relation to evaluation of bridge performance, it was important to determine if the measured shake table motions resembled the target motions. Peak ground acceleration and spectral acceleration were the parameters used to assess and compare ground motion characteristics in this study.

Prior to application of the acceleration data from the test, a band-pass filter was applied for frequencies between 0.1 and 25 Hz to eliminate high-frequency noise in the data. Shake table acceleration data for runs 1 and 2 contained large amounts of noise even after the filter was applied. The fast-Fourier transform amplitude was high for frequencies of 16 Hz in the longitudinal and transverse directions, and 81.9 Hz in the transverse direction. Therefore, a bandstop filter was applied at those frequencies to further reduce noise. A comparison of unfiltered and filtered acceleration histories from the first two runs in the longitudinal and transverse direction are shown in figure 6.1 to 6.4.

6.2.1 Peak Ground Acceleration

Target peak ground accelerations (PGA) were set by multiplying the design level PGA by a scale factor for each run to adjust the earthquake intensity to capture different limit states. Individual targets for each acceleration component were set for the longitudinal and transverse directions of the bridge. The maximum measured PGA for both directions were calculated for all runs and compared to the target values using a ratio of measured to target PGA. An average ratio of PGA for both directions was also calculated to determine how well the measured PGA met the target values for bi-axial acceleration. The PGA values are listed in table 6.1. The measured PGA in the longitudinal direction was higher than the target values for the first two runs but was approximately 70% of the target values for the remaining six runs. The measured PGA in the transverse direction was on target for the first run, averaged 86.4% for runs 2-6, and was on target for runs 7 and 8. Overall, the measured transverse PGA was closer to target values than in the longitudinal direction. The average ratio of measured-to-target PGA was above 100% for the first run and averaged 83% for runs 2-8.

In addition to PGA, the acceleration histories were examined to determine how well the shake table reproduced the input ground motion. This was done through a visual assessment of the acceleration histories. Measured and target acceleration histories for both directions for run 3 (the design run) are shown in figure 6.5. Note that the time axis has been trimmed to only show data between 5 to 25 seconds. This was because the highest accelerations in the ground motion took place during this time interval. This interval is used for all response history plots presented in this chapter. It can be seen in figure 6.5 that the measured and target table accelerations have peaks that match and are synchronous. The correlation between the measured and target acceleration histories for the design level run combined with the comparable measured and target PGAs for all runs, as discussed previously, imply that the shake table adequately replicated the ground motion PGA for each run during the test.

6.2.2 Spectral Acceleration

Spectral accelerations were also compared to determine how closely the frequency content of the achieved shake table accelerations matched the target values. These values are important for comparison because a design level spectral acceleration was used as a design parameter for the bridge specimen; meaning, for the bridge to be appropriately tested the measured spectral accelerations should be close to the target values. The target spectral acceleration was originally selected using the Caltrans ARS tool as described in section 5.3.2. The vector summation of the spectral acceleration components for the design level earthquake were scaled to match the ARS demand acceleration as described in section 5.4.1.

Response spectra were used to calculate the spectral acceleration for the period of interest in this study. The assumed period of the structure was calculated using the effective stiffness from the pushover analyses in each direction, equivalent to 0.39 seconds in the transverse direction and 0.38 seconds in the longitudinal direction. The procedure for determining effective period was discussed in section 5.3.1. A response spectrum was generated for each run and for both the longitudinal and transverse directions. The scaled response spectra from the ground motion record was compared to the measured response spectrum for each run and direction at the period of interest. The response spectra for the measured and target acceleration records are presented in figures 6.6 to 6.13 and the spectral accelerations at the periods of interest are summarized in table 6.2. The measured spectral accelerations in the longitudinal direction were close to the target values for all runs with an average measured/target ratio of 95%. All measured spectral accelerations were within 14% of the target value. The measured transverse spectral acceleration was under the target value for all runs with an average measured/target ratio of 84%. The average measured/target ratio for the final four runs was 94%. Overall, the measured spectral acceleration for both directions were close to the target values. This indicated that the shake table test adequately recreated the spectral acceleration for the period of interest for this study.

6.3 Superstructure Accelerations

Acceleration along the superstructure was monitored in the transverse, longitudinal, and vertical directions during all runs using the accelerometer layout discussed in section 4.4. Several of the acceleration histories were offset from the origin due to precision issues with the accelerometers at low acceleration levels. The largest applied offset occurred at an abutment and was equal to 0.16 g. The bridge is known to be stationary at the beginning of each test run, therefore the acceleration histories were adjusted to begin at 0 g at the start of each run.

6.3.1 Horizontal Acceleration

Acceleration histories in the longitudinal and transverse direction were recorded for each run. The measured acceleration histories for run 3 are shown in figure 6.14 and the corrected histories are shown in figure 6.15. These were the acceleration histories for the design level run and are representative of all other runs. The maximum and minimum accelerations along the superstructure are shown in tables 6.3 and 6.4 for the longitudinal and transverse directions, respectively. The transverse acceleration varied along the length of the bridge due to in-plane rotation of the superstructure. The peak transverse accelerations occurred at the abutments (AT1, AT5) for all runs. The peak acceleration was on average 20% higher at the abutments (AT1, AT5) than it was at midspan (AT3). Longitudinal accelerations were constant along the superstructure because of the high axial rigidity of the superstructure.

Acceleration along the superstructure was compared to the table acceleration (AL6, AT6). A comparison of the maximum table acceleration to the peak superstructure acceleration is shown in figure 6.16 for the longitudinal and transverse directions. The superstructure accelerations were higher than the table accelerations in early runs. In later runs, peak accelerations did not increase with increasing table acceleration. Once the columns in the bent had experienced significant yielding, the lateral force capacity in the bent stabilized and could no longer increase. Hence the accelerations associated with the forces became nearly constant.

6.3.2 Vertical Acceleration

The shake table did not move vertically but there was variation in the superstructure vertical acceleration along the length of the bridge. The vertical acceleration in the superstructure was due to excitation of the fourth vibration mode associated with vertical translation. Vertical acceleration history for run 3 is shown in figure 6.15. The peak vertical accelerations at each instrument location are shown in table 6.5. Accelerations at the abutments and bent were low because of the vertical support provided at these locations.

The largest vertical accelerations occurred at midspan of the west span with a maximum of 0.23 g. This was much larger than the peak of 0.058g and 0.08g in the abutments and bent, respectively. Acceleration is expected to be smaller at the abutments and the bent due to the stiffness provided by the supports. Vertical translation at the bent is constrained by the column axial stiffness, which is much larger than the vertical stiffness of the superstructure at midspans. Most peak accelerations in the east and west midspans were close to each other in all the runs. The small differences in some of the runs may have been caused by the fact that the input longitudinal acceleration was not symmetric causing different midspan vertical displacements with different signs (and accelerations).

6.4 Visual Assessment of Damage

A visual assessment of the bridge was completed at the conclusion of each earthquake run. Observing the damage after each run allowed the progression of damage to be tracked as earthquake intensity increased. In addition to a visual inspection, several key areas were video monitored during the earthquake runs using GoPro cameras as discussed in section 4.5. Key areas that were monitored included: plastic hinges at the top of the columns, rebar hinge at column base, footing, cap beam, girders at girder-to-cap beam connection, deck panels, deck joints, and the superstructure at abutment ends.

After assembly of the bridge but prior to the shake test, all cracks were marked to indicate they resulted from construction or shrinkage as opposed to dynamic action. These were referred to as Run 0 cracks and were marked using a black crayon. At the conclusion of an earthquake run, new cracks were marked with a crayon with each run being marked with a different color. Maximum crack width was recorded for each run. Any concrete that had spalled was removed. This process was completed for runs 1-8.

6.4.1 Column Damage

Pictures of each column were taken from four angles (NW, NE, SW, and SE) at the base and at the top. These pictures are shown in figures 6.17 – 6.28. Some small shrinkage cracks sparsely distributed along the column length can be observed prior to run 1 for both columns. There were also some small voids in the cover concrete that were present immediately following casting of the columns. Some small horizontal cracks began to propagate during run 2 towards the top of the columns. Small vertical cracks at the column bases also appeared during run 2. During the design level run (run 3), some helical cracking propagated between the existing horizontal cracks on the southwest side of the north column. This indicated that the columns were experiencing a combination of shear and torsion. A horizontal crack also opened along most of the circumference in the north and south columns near the cap beam interface indicating stress concentration at this location. There was also minor spalling at the top of the south column on the northwest side. Additional vertical cracks formed in the north column and existing cracks propagated further during run 4. The cracks at the top of the columns began to widen during run 5. During run 6, smaller cracks began to form in the column further from the cap beam interface, due to expansion of the plastic hinge as forces increased. Spalling began to spread around the tops of the columns and some of the spiral reinforcement became visible. At the conclusion of run 7, both columns experienced spalling around the entire circumference at the column tops. Existing cracks had expanded, encompassing the circumference of the column. No reinforcement buckling or column concrete core damage was observed.

6.4.2 Cap Beam Damage

The cap beam was visually inspected on the bottom face between the columns, and on the north and south ends. Recall that the cap beam was designed as a capacity protected member, therefore cracking was expected to be limited. The pictures for these inspections are shown in figures 6.29 – 6.32. There were some small cracks prior to run 1 that formed during construction. During the shake test, small cracks in multiple areas with none being wider than 0.005 in (0.127 mm) were seen. Some flexural cracks formed under the girders. No cracks propagated from the column region and no crack formed at the joint between the precast and cast-in-place portion of the cap beam. Some cracking is expected even in capacity protected members due to shrinkage and minor yielding of longitudinal reinforcement. Because the cracks that had formed prior to the test did not propagate or expand, it was concluded that the cap beam performed as a capacity protected member. A discussion of steel bar strains is presented in subsequent sections.

6.4.3 Superstructure Damage

The superstructure was visually inspected from the top of the bridge at the conclusion of each run. All the connections were carefully inspected for any cracks and damage. The deck panel joint conditions are shown in figure 6.33 – 6.35. Photos from runs 1 through 7 were not included due to no differences being observed between those runs and run 8. Some cracking was observed prior to run one propagating from the deck pocket corners. These cracks did not expand during the tests. No further cracking was observed in the deck panels. No cracking was observed in the girders during any of the runs. The superstructure was a capacity protected member as the cap beam was, therefore no damage was expected in the girders. Because damage was limited to the columns, the design assumption of linear-elastic behavior in the superstructure and non-linear behavior being limited to the columns was upheld.

As each earthquake run became more intensive, increasing residual displacement was observed at the abutment ends. The inspection photos of the superstructure displacement at the abutments are shown in figure 6.36 and 6.37. The superstructure experienced in-plane rotation with the superstructure at the east abutment transversely displacing north and the west end displacing south. This rotation became more severe in later runs causing the superstructure transverse displacement limit of 12 inches at the abutments to be reached in run 8. This limit was imposed to prevent unseating of the superstructure at the abutment ends. Because the limit was reached, run 8 had to be aborted prior to completion of the ground motion, but the peak acceleration in the input record had already been applied meaning the bridge underwent the peak force associated with the eighth earthquake run.

6.4.4 Connection Damage

A primary focus of this study was to determine how different connections would maintain their integrity in seismic events and to monitor apparent damage, deformations, and internal stresses at these connections. Each of the six connections integrated in the bridge was visually inspected at the conclusion of each run. Special attention was given to the areas around the connection and any cracking in or around the connection was noted.

6.4.4.1 Socket Connections

The socket connections can be seen in the photos showing the tops of the column in figures 6.17 to 6.24. Some of the grout used in the socket connection was uneven at the conclusion of construction due to the grout leaking between the form and the cap beam. During the shake table test, some of this excess grout at the interface spalled away. A crack was formed in the grout portion of the south socket connection during run 3 (figure 6.23). In later runs, a crack was formed around the perimeter of the socket connection where the excess grout had been in contact with the cap beam (figure 6.21-6.24). The grout on the inside interface between the column and the cap beam remained damage free for all runs in both connections. The distribution of damage seen in the column tops as discussed in section 6.4.1 as well as the conservation of joint integrity indicated that the column-cap beam socket connection detail and construction method utilized in the test led to a satisfactory, full moment connection.

6.4.4.2 Rebar Hinge

Because the gap between the column and the footing was small, clear pictures of the rebar hinge could not be captured. However, figures 6.25 to 6.28 show that there was no excessive rotation at the base of the columns, suggesting that the pocket connection provided sufficient integrity between the columns and the footing. The rebar hinge throat was visually inspected at the conclusion of run 8. There was significant spalling of the cover grout around the hinge throat. The hinge reinforcement was exposed. This damage was anticipated because the rebar hinge was designed to undergo damage to assist in energy dissipation of the system. Because the gap did not close during testing and the hinge had not experienced any visual rebar failure, it was understood that the rebar hinge maintained structural integrity during the tests.

Due to the placement of the pocket connection within the column, damage could not be assessed of the grout within the column pocket. Hence the performance of the column-footing pocket connection was assessed only based on the measured rotations between the columns and the footing, and the strains in the longitudinal and transverse bars in the hinge region.

6.4.4.3 Superstructure to Cap Beam Connection

The concrete at the interface of the girders and the cap beam was visually inspected after each run for cracking in the girders or cap beam around the connection. The photos showing the girder-to-cap beam interface are presented in figure 6.38 and 6.39. Some small voids under the top flange of the girders and between the deck and cap beam were present prior to run 1 due to inability to pack concrete directly under the flange (figure 6.38). These voids did not lead to crack propagation in any run, and the girder-to-cap beam interface remained crack free for all runs. The superstructure joint was designed to transfer moment via shear friction and tensile forces in the projected prestress strands from the girder. With the cap beam remaining crack-free around the girders, it can be implied that good concrete shear friction was maintained for all runs. No rotation or deformation was observed in the superstructure. These are quantified in subsequent sections. The absence of damage and excessive deformations in the superstructure suggest that the superstructure to cap beam connection maintained joint integrity during the entire test and that the connection behaved as expected.

6.4.4.4 Deck Pockets and Joints

Three connections were incorporated into the deck region including: the deck panel to girder connection, deck panel-to-panel connection, and deck connection over the cap beam. Each of these joints were examined at the end of each run. The state of these connections at the conclusion of run 8 can be seen in figures 6.33 to 6.35. Due to the absence of damage in these components, only the photos from run 8 are presented.

Figure 6.33 shows the deck panel connection over the bent. Figures 6.34 and 6.35 show the same connection but show the joint directly over the exterior and interior girders, respectively. This connection consisted of long lap spliced bars projected from each precast deck panel with UHPC. Due to the limited development length available over this connection, UHPC had been used to increase bond between the bars in the lap splice. No cracking was observed in the UHPC, and no separation was observed between the precast deck panels and the UHPC indicating that the joint had maintained force transfer during all tests.

The deck panel pockets consisted of projected steel studs into a precast deck pocket filled with grout. This connection was used for transfer of shear between the deck and girders to form a composite section. No damage was expected in these joints. Some of the deck panel pockets had shrinkage cracking immediately following grout placement. However, no crack propagation or widening was observed at the conclusion of the shake test. This implied that the deck pocket connection provided good continuity between the deck and girders.

Short lap spliced bars with UHPC were used between the deck panels both longitudinally and transversely to transfer deck forces between the precast panels. The UHPC implemented between the deck panels and over the cap beam remained virtually crack free minus some shrinkage cracking that occurred following casting. No separation was observed at the cold joint between the deck panels and the UHPC. The lack of damage suggests that the superstructure behaved integrally between the deck panels, bent and girder; implying that the connections performed as designed and maintained force transfer and remained elastic for the entire test.

6.5 Abutment Seat Displacement

The abutments at each end of the bridge consisted of a precast concrete seat anchored to two concrete mass blocks as discussed in section 3.4. The abutments resided on shake tables 1 and 3 for the test. No motions were applied to these two tables during any of the test runs, therefore the abutment seats were intended to remain stationary. However, some displacement in the seat could occur as a result from friction between the stainless-steel plates embedded at the bottom of the girders and the Teflon pads. The absolute longitudinal displacements at each abutment seat were measured using string pots, DL2, DL4, DL6, and DL7 and the absolute transverse seat displacements were recorded with string pots, DT2 and DT8. The layout for these string pots is shown in figure 4.12. These instruments were connected to safety frames not excited by shake table 2, therefore the displacements were measured relative to the lab floor to determine if any relative displacement took place between the abutment seat and the table it was anchored to. Each of these displacements were sampled at mid height of the abutment seat. The maximum displacements recorded in these instruments are shown in table 6.6. The largest longitudinal displacement during any run was 0.09 inches. The largest transverse displacement measured was 0.05 inches.

The small displacements during the duration of the test implied that the provided abutment interface was satisfactory in providing a roller support. Also, because there were no large spikes in the seat displacements at any point, it can be assumed that the spans did not abruptly snag on the seat, and that proper seat anchorage was provided. Because the displacements were small, the abutments were assumed to be fixed and seat displacements were not included in other displacement calculations.

6.6 Superstructure Displacement

Displacement along the superstructure was measured using string pots as discussed in section 4.3.3. All string pot labels are referenced in figure 4.12. The string pots were attached to fixed safety and reference frames mounted separately from the bridge. Because the string pots did not move with the shake table, they measured absolute displacement. Relative displacement between the structure and the activated shake table was calculated by subtracting the table displacement from the absolute displacement (measured). Because relative displacement is more useful when looking at bridge response, it will be used in subsequent sections. Displacements of interest included transverse displacement of the superstructure at the abutments and bent, longitudinal displacement, and vertical displacement at mid-span, the abutments, and the bent.

6.6.1 Transverse Displacement

Transverse displacement was measured at five points: the west abutment, the east abutment, midspan on both spans, and the bent. DT1 was used to measure the superstructure displacement at the west abutment, DT7 was used for the east abutment, DT3 was used for midspan on the west span, DT6 was used for midspan on the east span, and DT5 was used for the bent (figure 4.12). The relative transverse displacement histories at the bent and abutments for all runs are shown in figure 6.40 and 6.41. The peak transverse displacements in each direction are shown in table 6.7.

The peak transverse displacements and the residual displacements at the abutments and bent were nearly the same in runs 1 and 2. However, beginning with run 3 and continuing for all subsequent runs, the peak transverse displacements at the abutments became larger in opposite directions, incurring counter-clockwise in-plane superstructure rotation. The difference in transverse residual displacement between the two ends at the conclusion of run 8 was 20.3 in (516 mm). The peak transverse displacement of the superstructure over the bent at the design level earthquake was 1.29 in (32.7 mm). The peak transverse displacement at the bent in run 8 was 2.73 in (69.3 mm).

The in-plane rotation was calculated by dividing the difference in transverse displacement at both abutments by the length of the superstructure. The spliced in-plane rotation of the superstructure for all runs is shown in figure 6.42. The peak rotation and residual rotation after each run are shown in table 6.8. The rotation progressively became larger as earthquake intensity increased, with each subsequent run resulting in a larger increase in in-plane rotation. The displacement at the abutments became large enough that run 8 was terminated prior to completion to prevent unseating of the superstructure at the abutments.

6.6.2 Longitudinal Displacement

The longitudinal displacement of the superstructure was measured at the west and east abutments using string pots, DL1, DL3, DL5, and DL8 (figure 4.12). The average longitudinal displacement at each abutment was calculated by averaging the displacements measured at each string pot. This displacement is representative of the longitudinal displacement at the midpoint of the superstructure cross-section. The average relative longitudinal displacement history for runs 3, 7 and 8 are shown in figure 6.43. These three runs were chosen to illustrate the behavior of the bridge because they represent the design level earthquake, last complete run, and final run of the shake test. The maximum and minimum displacements at each instrumentation location for each run are shown in table 6.9. Because the string pots at the west and east abutments are oriented in opposite directions, the sign of the displacements at each end are opposite. Positive displacement in DL1 and DL3 is in the same direction as negative displacement for DL5 and DL8 and vice versa. The superstructure had an average peak longitudinal displacement of 4.05 in (102.9 mm). The peak longitudinal displacement during the design level earthquake was 1.64 in (41.6 mm). Differences in the peak values between DL1 and DL3, and DL5 and DL8 were a result of in-plane rotation. Because the bridge rotated, one exterior girder would move westward while the other exterior girder moved eastward, causing the peaks to act in opposite directions.

6.6.3 Vertical Displacement

Vertical displacements were monitored at the abutments to determine if any uplift occurred and at midspan to check vertical excitation of the bridge during the shake test. String pots DV1, DV2, DV9, and DV10 measured the vertical displacement at the abutments, DV5 and DV6 measured vertical displacement of the cap beam relative to the footing, and DV3, DV4, DV7, and DV8 measured the vertical displacement of the west and east midspans. Because the bridge moved both longitudinally and transversely, error is introduced due to the string becoming angled relative to the reference point and extending due to the change in angle. The vertical displacement was adjusted with the following equation:

$$\Delta_{adj} = \Delta_{as,meas} - \left(\sqrt{{L_{sp}}^2 + {\Delta_L}^2 + {\Delta_T}^2} - L_{sp}\right) \qquad (6\text{-}1)$$

Where:

Δ_{adj} : Adjusted displacement in string pot, in (mm)

$\Delta_{as,meas}$: Displacement as measured directly by string pot, in (mm)

L_{sp} : Length from instrument to point of measurement on bridge, in (mm)

Δ_L : Longitudinal displacement at point of measurement, in (mm)

Δ_T : Transverse displacement at point of measurement, in (mm)

The vertical displacements along the northernmost and southernmost girder-line are listed in table 6.10 and 6.11, respectively. The maximum vertical displacement at the abutments was 0.52 in (13.2 mm) at the east abutment and 0.30 in (7.6 mm) at the west abutment. This indicates that there could have been a small amount of uplift or the Teflon pad may have become uneven during later runs causing the superstructure to rise as it moved over the pad. The vertical displacements at midspan were consistent for runs 2-8. The maximum displacement at mid-span was 0.61 in (15.5 mm) downward. These displacements at mid-span were caused by flexural deformation of the spans due to frame action of the entire bridge as it underwent longitudinal displacements.

Vertical displacement at the bent increased as earthquake intensity increased. The maximum vertical displacement in the bent was 0.38 in (9.6 mm) upwards. This displacement was most likely a result of the bent extending axially within the columns due to frame overturning effects.

6.7 Column and Bent Horizontal Displacement

6.7.1 Total Relative Column Displacement

The displacements at the top of the north and south columns were calculated at midspan of the precast cap beam using the superstructure displacements discussed in section 6.6. String pots DL1, DL3, DL5, and DL8 (figure 4.12) measured the absolute longitudinal displacement of the superstructure along the exterior girder in each direction. These displacements were assumed to be the longitudinal displacement of the bent at the center of each exterior girder due to the superstructure being essentially rigid longitudinally. The average of the measured longitudinal displacements along each girder was calculated and reduced by subtracting the table displacement to determine the longitudinal displacement of the superstructure relative to the table (equations 6-2 and 6-3). The longitudinal displacement at the tops of the columns was calculated by geometrically adjusting the displacement using similar triangles to account for the columns being 18 in (457 mm) closer to the center of the bent relative to the edge of the cap beam. The longitudinal displacement in each column had to be corrected further to account for longitudinal displacement due to in-plane rotation as shown in equations 6-4 and 6-5. These corrected displacements were assumed to be the total relative longitudinal displacement of each column. Absolute transverse displacement was measured directly using string pot, DT5 (figure 4.12). The table displacement was subtracted from the measured displacement at DT5 to calculate the total relative transverse displacements of the columns.

$$\Delta_{L,\ N.\ ext\ girder} = \frac{\Delta_{DL1}+\Delta_{DL5}}{2} - \Delta_{table,L} \tag{6-2}$$

$$\Delta_{L,\ S.\ ext\ girder} = \frac{\Delta_{DL3}+\Delta_{DL8}}{2} - \Delta_{table,L} \tag{6-3}$$

$$\Delta_{L,\ N-Col} = \Delta_{L,\ N.\ ext\ girder} + 18 * \cos(\theta_{ss}) * \tan(\theta_{ss}) \tag{6-4}$$

$$\Delta_{L,\ S-Col} = \Delta_{L,\ S.\ ext\ girder} + 18 * \cos(\theta_{ss}) * \tan(\theta_{ss}) \tag{6-5}$$

$$\Delta_{T,\ N-Col} = \{\Delta_{DT5} - 27 * [1 - \cos(\theta_{ss})]\} - \Delta_{table,T} \tag{6-6}$$

$$\Delta_{T,\ S-Col} = \{\Delta_{DT5} - 105 * [1 - \cos(\theta_{ss})]\} - \Delta_{table,T} \tag{6-7}$$

Where:

$\Delta_{L,\ N.\ ext\ girder}$: Average relative longitudinal displacement at north exterior girder-line as measured by string pots, DL1 and DL5, in (mm)

$\Delta_{L,\ S.\ ext\ girder}$: Average relative longitudinal displacement at south exterior girder-line as measured by string pots, DL3 and DL8

$\Delta_{DL1}, \Delta_{DL5}$: Displacement from string pots DL1 and DL5, in (mm)

$\Delta_{DL3}, \Delta_{DL8}$: Displacement from string pots DL3 and DL8, in (mm)

$\Delta_{table,L}$: Longitudinal displacement of shake table, in (mm)

$\Delta_{L,\ N-Col}$: Relative longitudinal displacement of north column, in (mm)

$\Delta_{L,\ S-Col}$: Relative longitudinal displacement of south column, in (mm)

$\Delta_{table,T}$: Transverse displacement of shake table, in (mm)

θ_{ss} : In-plane rotation of superstructure, in (mm)

The displacement history for both columns and the bent are shown in figures 6.44 to 6.47. The peak displacements and the corresponding drift ratios for the longitudinal and transverse direction are listed in table 6.12 and 6.13, respectively. In figure 6.44, the longitudinal displacements in the columns and the bent were almost identical for the first two runs. However, from run 3 and on, in-plane rotation became significant which caused there to be differences between the peak displacements in each column. These differences became more pronounced as earthquake runs progressed and in-plane rotation became more substantial (figure 6.45). In run 8, there was a difference of 3.16 in (80.3 mm) and 3.54 in (89.9 mm) in the peak longitudinal displacements between the two columns in each direction. Meaning that the in-plane rotation caused the column maximum displacements to occur in opposite directions. Even though the column peak longitudinal displacements occurred in opposite directions, they still underwent comparable displacements demand as the absolute peak displacements during run 8 were different by only 0.39 in (9.91 mm). The maximum longitudinal displacement during run 3 was 1.78 in (45.2 mm) in the north column and 1.84 in (46.7 mm) in the south column. This was equivalent to a 2.1% drift ratio for the north column and 2.2% drift ratio for the south column; which were calculated by dividing the longitudinal displacement by the clear column height. The maximum longitudinal displacement achieved in both columns occurred during run 8 and was 5.75 in (146 mm) in the north column and 5.36 in (136.1 mm) in the south column. This was equal to a 6.8% drift ratio in the north column and 6.4% drift ratio in the south column and occurred in opposite directions. The maximum transverse column displacement during run 3 was 1.29 in (32.8 mm) in both columns. This is equal to a 1.5% drift ratio. The maximum measured transverse column displacement was recorded in run 8 as 2.73 in (69.3 mm) corresponding to a drift ratio of 3.3%. The peak transverse displacements in both directions were almost the same due to the limited effect of in-plane rotation on transverse displacement of the bent. The maximum longitudinal displacements were higher than the maximum transverse displacements in all runs. This was by design as the stronger ground motion component was oriented in the longitudinal direction of the bridge to place relatively high moment demand on the girder-to-cap beam connection.

Resultant horizontal column displacement histories were calculated. The maximum resultant displacement for each run is presented in table 6.14. Because the maximum transverse and maximum longitudinal displacement may not take place at the same time step, the maximum resultant displacement is not necessarily the same as the resultant maximum transverse and maximum longitudinal displacements. The maximum resultant displacement during run 3 was 1.89 in (48.0 mm) in the north column and 1.99 in (50.6 mm) in the south column, corresponding to a drift ratio of 2.3% and 2.4%, respectively. The maximum resultant displacement during run 8 was 5.78 in (147 mm) in the north column and 5.36 in (136 mm) in the south column, corresponding to drift ratios of 6.9% and 6.4%, respectively. The maximum resultant displacements are close to the maximum longitudinal displacement in each column. This is due to the maximum longitudinal displacement being more than twice as large as the peak transverse displacement and thus dominating the vectoral sum of the components. A more detailed analysis of displacement coupling is discussed in chapter 7.

6.7.2 Net Column Displacement

The displacements discussed in section 6.7.1 are the total column displacements calculated at the mid-depth of the precast portion of the cap beam. This displacement includes the column displacement in addition to shear slippage that occurs at the column base. To calculate the net displacement of the column itself, the slippage at the base needs to be subtracted from the total column displacement. This value will be referred to hereafter as net column displacement. The slippage at the base was measured using Novotechnik displacement transducers (figure 4.9). Equations 6-8 – 6-17 were used to calculate the slippage, uplift and rotation at the base. Each of the parameters listed in the following equations are related to deformations at the column base. However, only shear slippage is pertinent to calculating the net column displacements. The remaining parameters will be discussed further in the rebar hinge connection section.

$$\theta_{base,N-L} = \frac{\delta_{NT18}-\delta_{NT17}}{DVT} \tag{6-8}$$

$$\theta_{base,N-T} = \frac{\delta_{NT28}-\delta_{NT27}}{DVL} \tag{6-9}$$

$$\theta_{base,S-L} = \frac{\delta_{NT08}-\delta_{NT07}}{DVT} \tag{6-10}$$

$$\theta_{base,S-T} = \frac{\delta_{NT38}-\delta_{NT37}}{DVL} \tag{6-11}$$

$$\phi_{base,N} = \left(\frac{\delta_{NT30}-\delta_{NT29}}{DHT} + \frac{\delta_{NT20}-\delta_{NT19}}{DHL}\right) * \frac{1}{2} \tag{6-12}$$

$$\phi_{base,S} = \left(\frac{\delta_{NT10}-\delta_{NT09}}{DHT} + \frac{\delta_{NT40}-\delta_{NT39}}{DHL}\right) * \frac{1}{2} \tag{6-13}$$

$$S_{A,x-y} = -\phi_{base,x}\left(\frac{d_{col}}{2} + d_{NT} - \frac{\delta_{NTxx}}{\phi_{base}}\right) \tag{6-14}$$

$$S_{base,x-y} = S_{A,x-y} * \cos\left(\theta_{base,x-y}\right) - d_a * \theta_{base,x-y} \tag{6-15}$$

$$Z_{A,x-y} = -\theta_{base,x-y}\left(\frac{d_{col}}{2} + d_{NT} - \frac{2}{\theta_{base,x-y}}\right) \tag{6-16}$$

$$Z_{base,x-y} = Z_{A,x-y} * \cos\left(\theta_{base,x-y}\right) - S_{base} * \sin\left(\theta_{base,x-y}\right) \tag{6-17}$$

Where:

$\theta_{base,x-y}$: Rotation at the column base for the north or south column in the transverse or longitudinal direction, radians

δ_{NT} : Novotechnik displacement at the specified instrument, in (see section 4.3 for labels)

DVT, DHT : Distance between vertically or horizontally oriented Novotechniks along the transverse axis, in (mm)

DVL, DHL : Distance between vertically or horizontally oriented Novotechniks along the longitudinal axis, in (mm)

$\phi_{base,x}$: Column base angle of twist in the north or south column, (radians)

$S_{A,x-y}$: Slippage at the level of instrumentation in the north or south column in the longitudinal or transverse direction, in (mm)

d_{col} : Diameter of the column, in (mm)

d_{NT} : Distance from edge of the column to the Novatechnik of interest, in (mm)

δ_{NTxx} : Novatechnik displacement in the direction of interest, in (mm)

$S_{base,x-y}$: Slippage at the column base in the north or south column in the longitudinal or transverse direction, in (mm)

d_a : Distance from elevation of instrumentation to column base elevation, in (mm)

$Z_{A,x-y}$: Vertical displacement in the north or south column in the transverse or longitudinal axis at the instrumented elevation, in (mm)

$Z_{base,x-y}$: Vertical displacement in the north or south column in the transverse or longitudinal axis at the column base, in (mm)

The net column displacement is compared with the total column displacement for runs 3, 7 and 8 in figure 6.48 and 6.49. These runs were selected to represent the response for the design level run, last complete run, and the final run. Net bent displacement was also calculated by taking the average of the net column displacements. Peak net column and bent displacements for each direction are presented in tables 6.15 and 6.16. The net and total column displacements during the smaller runs were nearly the same meaning shear slippage at the base had little impact on column displacement during low amplitude ground motions. During larger runs, hinge shear slippage began to increase causing larger differences between the total and net column displacements. In some runs, the peak net column displacement is larger than the total column displacement because of the residual slippage that occurred with a maximum difference of 0.17 in (4.91 mm) in run 8.

The maximum slippage along the transverse and longitudinal axis for each column during each run are presented in table 6.17. The slippage at the base was small for most runs reaching a maximum of 0.54 in (13.7 mm) in the north column in the transverse direction. The maximum slippage in the longitudinal direction occurred during run 8 in the north column and was 0.46 in (11.7 mm). Slippage was larger in the north column and was larger in the transverse direction in both columns. This may have occurred due to uneven damage in the rebar hinges resulting in increased slippage in the north column.

6.8 Bent Base Shear

Because load cells could not be used to measure force in the bent, the bent base shear was not directly measured. Two methods were used to calculate the bent base shear. The first method used the measured force in the shake table actuator to estimate the bent base shear. The second method used the superstructure acceleration over the bent (accelerometer 3, figure 4.13) and the superstructure mass.

The first method was first proposed by Johnson et al. (2006). For this method, the recorded table actuator force history was used. The forces in both directions are assumed to pass from the superstructure down into the footing and ultimately into the table through the steel rods used for anchorage, with no horizontal force transferred to the abutments. The table actuator measures the force in the system but friction in the actuators must be subtracted to attain the base forces. The friction in each direction was estimated using the actuator force history collected during warm up motions when inertial forces were low. Figure 6.50 shows the force history during the first warmup motion in both the longitudinal and transverse directions. The estimated force in the actuator during this warmup motion was 4.5 kips (20.0 kN) in the longitudinal direction and 4 kips (17.8 kN) in the transverse direction, all of which was attributed to friction. This friction force was applied opposing the direction of motion for all earthquake runs. In addition to friction, the inertial forces of the non-structural components fixed to the tables had to be subtracted from the actuator force to account for forces due to movement of the bridge. The extra weight contributing to the measured inertial forces in the table included the shake table itself, the safety frames anchored to the shake table, and the bent footing. The effective table mass was different in the transverse and longitudinal directions. This is because the rails that control longitudinal displacement are supported on the transverse rails, adding extra weight in the transverse direction. The table weight was 53 kips (236 kN) in the longitudinal direction and 59 kips (262 kN) in the transverse direction. The footing weighed 9 kips (40.0 kN) and the two safety frames together weighed 8.6 kips (38.2 kN). The total inertial weight contributing to the actuator force was 70.6 kips (314 kN) in the longitudinal direction and 76.6 kips (341 kN) in the transverse direction. Again, the inertial force was applied opposing the direction of motion.

The second method used was an acceleration-based method. The acceleration histories from Accelerometer 3 discussed in section 6.3 were used to calculate the acceleration of the seismic mass. The total force exerted upon the bent was assumed to be equal to the seismic mass multiplied by the acceleration measured with AL3 and AT3. The mass included in the seismic mass included the bridge weight minus the weight of the footing.

The bent base shear histories for runs 3, 7, and 8 using both approaches are compared in figures 6.51 and 6.52. Overall, the peaks are in phase, and of similar magnitude in most runs. The abrupt jumps in the force-based method at the start and end of the motion are caused by the friction force and inertial force changing directions. Every time the direction of motion changes, the sign on the inertial forces and friction forces reverses resulting in a force immediately in the opposite direction. At low accelerations during the first few seconds at the start and a few seconds prior to the end of the ground motion, the extra forces are more significant compared to the applied force causing significant jumps every time a change in direction occurs. Visually, the force histories are consistent for both procedures, validating the methods used to calculate the base shear.

The peak base shears for both methods are compared in tables 6.18 and 6.19. The peak shears from the force-based method were higher than the acceleration method for most runs. The average difference between the maximum peaks for all runs was 10.1% for the longitudinal direction and 14.1% for the transverse direction. The differences between the two methods could be attributed to the sensitivity of the accelerometers as well as to uncertainty in the exact amount of friction in the actuator. The force-based method had been used as the primary force calculation in ABC-UTC (Shoushtari et al., 2019) and Calt-Bridge 1 (Benjumea et al., 2019), and was therefore used in this study to allow for direct comparison of the calculated bent forces in chapter 11.

6.9 Bent Force-Displacement Relationship

The hysteretic response of the bent was evaluated using force-displacement relationships in the bent. The net bent displacement was used for displacement as calculated in section 6.7.2 and the bent force from the force-based method was used for the base shear (section 6.8). A band-pass filter was applied for frequencies between 0.1 and 25 Hz to smooth the hysteresis loops. Force-displacement relationships for both directions with the envelope of the cumulative curves are shown in figure 6.53. The maximum longitudinal displacement was larger than the maximum transverse displacement, which caused the cumulative longitudinal hysteresis curves to be wider, meaning more energy was dissipated due to displacement in this direction. This was expected because of the longitudinal direction being subjected to the stronger component of the ground motion, while the longitudinal and transverse stiffness and strength of the bridge model were nearly the same. Little force decay was observed in translation of the bridge in any direction except for movement in the north in the transverse direction. The hysteresis curves in the transverse direction continued to grow and expand with every earthquake run in the south direction but were not excited as heavily in the north. In addition to decreased force, the bent also did not experience as high of displacements in the south direction. The difference in symmetry between the two directions is due to the ground motion components being different and the bidirectional effect of the earthquake. The peak accelerations in the transverse direction was slightly stronger in one direction and may have caused the hysteretic response in the transverse direction to be more dominant towards the south.

The hysteresis loops for the longitudinal direction for each run are presented in figure 6.54 and 6.55. In runs 1 and 2, the hysteresis loops are narrow, implying the system had not yielded. As the bridge system experienced larger earthquake runs, the hysteresis loops expanded. This shows that the system maintained good energy dissipation in high intensity earthquakes. The peak bent shear in later runs did not change significantly, meaning the peak base shear was sustained under increasing ground accelerations. The system ability to maintain the peak bent shear did not decay as accelerations increased. In other words, there was no strength degradation. Displacement demand was nearly equal in both directions, longitudinally. However, higher bent shear was generated in movement of the bridge towards the west, 74 kips (329 kN), compared to an ultimate bent shear of 63 kips (280 kN) in movement towards the east. The difference in peak base shears could have been a result of unsymmetrical distribution of damage in the columns and/or rebar hinges, resulting in additional force capacity associated with movement towards the west.

Force displacement relationships for the transverse direction were plotted for each run in figure 6.56 and 6.57. In later runs, the peak minimum bent shear dropped as input earthquake intensity increased. The maximum peak bent shear increased in each successive run up to run 7. The hysteretic loops in the transverse direction were narrower than in the longitudinal direction, implying less energy dissipation.

The resultant transverse and longitudinal bent base forces and displacements were calculated to determine the combined effect of the transverse and longitudinal motions. Resultant forces and displacements have no sign; therefore, all values are greater than zero. The cumulative resultant force-displacement relationship for all the runs are shown in figure 6.58. The peak base shear increased in runs 1 to 6, with a maximum base shear of 74.9 kips (333 kN). A small amount of force decay was observed in runs 7 and 8 with a maximum base shear of 71.7 kips (319 kN) and 70.7 kips (314 kN), respectively.

6.10 Bridge Model Vibration Periods

Prior to each shake table run and at the conclusion of testing, two white noise motions were generated, one in the transverse direction and one in the longitudinal direction. The purpose of these motions was to determine the bridge modal properties as the bridge response changed due to damage.

A fast Fourier transform of the superstructure accelerations was used to determine which frequencies of the structure were excited during the white noise motions. A Hamming window type was used with 50% overlap. Accelerations from Acc. 4 (figure 4.13) were used for the longitudinal and vertical direction and Acc. 3 (figure 4.13) was used for the transverse direction. The amplitude for the longitudinal and vertical fast Fourier transformation is shown in figure 6.59 and 6.60, respectively. Two distinct peaks in frequencies of interest were found for most runs. Because the peaks were more substantial and decreased in frequency as runs progressed between 5.5 and 6.3 Hz, this range of frequencies were selected as the fundamental frequencies of the structure. Peak frequencies and their corresponding periods for the longitudinal and vertical directions are recorded in table 6.20. Only one frequency was excited in the vertical direction for each run. The fundamental periods in the vertical direction were equal to those in the longitudinal for all runs. The bridge began with a fundamental period of 0.16 seconds which increased to 0.18 seconds at the conclusion of the shake test. The spectra from the transverse acceleration are shown in figure 6.61. The fundamental frequencies and corresponding periods for the transverse direction are shown in table 6.21. The periods associated with the transverse direction were smaller than the other two directions; starting at 0.13 seconds prior to the first run and finishing at 0.16 seconds at the conclusion of the test. The increase in period is expected during repeated dynamic testing due to damage in the bridge model. As the system has more components exceed yielding, the response is softer resulting in lower stiffness, and therefore longer periods.

6.11 Measured Strains

Rebar strain was measured in several key areas of the bridge, specifically in and around the bent, including the columns, the rebar hinge, the cap beam, the girder-to-girder connection, and the deck. The strain gages were installed as discussed in section 4.2 and shown in figures 4.1 to 4.8. Strains were measured and recorded during all shake table runs. Positive strains indicate compression, while negative strains indicate tension. Multiple strain gages were damaged prior to the start of the test or during the test. A dash in the strain gage tables indicates that the strain gage was not functional for that run. The naming convention used for the strain gage layout was as follows: CSGN – north column strain gage, CSGS – south column strain gage, HSGN – north hinge strain gage, HSGS, south hinge strain gage, BSG – cap beam strain gage, DSG – deck strain gage. Strains were compared to their respective measured yield strain as determined by rebar testing described in section 3.5.4. Any strains listed in tables that are above their respective yield strain are shaded. A table summarizing the maximum strains in each element and the corresponding yield ratio is presented in table 6.22.

6.11.1 Column Reinforcement

Longitudinal column bars in all quadrants of each column were instrumented at five levels; four at the column top and one at the column base (figure 4.1). Three levels were used below the cap beam interface to determine the spread of plasticity in the column top. One level was 4 in (101.6 mm) into the cap beam socket connection to determine the spread of plasticity within the socket connection. Because the rebar hinge is designed to have a smaller plastic moment capacity than the column capacity and to behave as a pin, the strain gages on the column (not the hinge) longitudinal bars at the bottom of the column were not expected to see significant action. The strain maxima for each run in the longitudinal column bars is shown in table 6.23 and 6.24. Yielding first occurred in one bar during run 2 directly under the cap beam interface in the north column and in two bars at three levels under the cap beam in the south column. As forces increased in run 3, yielding spread into all four instrumented bars in both columns and spread further down the column and above the cap beam interface. Peak strains of 17000 and 18500 tensile $\mu\varepsilon$ were achieved in the north and south column during the design level run, respectively.

Strains increased as the runs progressed eventually reaching a peak of 26800 $\mu\varepsilon$ in the north column and 37900 $\mu\varepsilon$ in the south column. These are equal to 10.3 and 14.5 times the yield strain of the longitudinal reinforcement. The peak strain in each column for different runs is shown in figure 6.62. The peak strains in the north and south columns were nearly the same during runs 1 through 6, which implied that the column underwent similar damage during these runs. After run 6 the peak south column strain was significantly larger than that in the north column. However, multiple gages at the instrumentation level directly below the cap beam interface broke after run 6, leaving only one gage active at that level for the last two runs. This is the level where most peak strains occurred. It is possible that the maximum strain in the north column was not captured for the last two runs because of the absence of recorded data and may have still been comparable to the peak strains in the south column. Strains in the column longitudinal bars near the base were significantly below yielding in all the runs with a maximum of 172 $\mu\varepsilon$ measured. The low strains in the column bars near the base mean that the rebar hinge was experiencing most of the action and was acting as a pin at the base.

Strains were also recorded at each instrumentation level in the column spiral. The peak spiral strains are presented in table 6.25 and 6.26. No spiral underwent yielding in any run, and the maximum strain recorded was 1680 tensile $\mu\varepsilon$ ($0.69\varepsilon_y$) in the north column and 1080 tensile $\mu\varepsilon$ ($0.44\varepsilon_y$) in the south column.

Strain profiles along the top column plastic hinges were generated for all runs for both the longitudinal and spiral reinforcement (figure 6.63 to 6.66). The strain profiles for the south longitudinal bars show that the highest strains occurred at the instrumentation level 1 in (25.4 mm) below the cap beam interface. The longitudinal bars in the north column had comparable strains at both 1 in (25.4 mm) and 8 in (203 mm) below the cap beam interface during the last two runs. Strains continued to increase significantly at the lower instrumentation levels for the last runs but strains at the cap beam interface only increased slightly. This supports that the maximum longitudinal strain in the north column was probably not captured for later runs due to absence of data. Strain dissipation was observed in the instrumentation level in the cap beam. In later runs, there was as much as 45% drop between the peak strain at the cap beam interface to 4 in (102 mm) within the cap beam. Significant strain reduction while moving into the cap beam is indicative of good longitudinal bar anchorage and good connectivity in the socket connection.

6.11.2 Rebar Hinge Reinforcement

The longitudinal bars in the rebar hinge were instrumented at three levels; 6 in (152.4 mm) above and below the footing interface and directly at the interface. The maximum strains in the north and south rebar hinge are presented in table 6.27 and 6.28. Strain profiles within the rebar hinge are shown in figure 6.67 and 6.68. Most strains were concentrated at the footing interface, and the embedded hinge reinforcement underwent much lower strains, although some minor yielding did occur within the footing in later runs. Significant tensile yielding began during run 2 at the hinge interface and increased in each successive run. Some compressive yielding was observed in earlier runs, but as the tensile yielding increased and residual strains became larger in tension, peak compressive strains decreased. The maximum strains recorded in the north and south rebar hinges were 45600 $\mu\varepsilon$ (17.5ε_y) and 43600 $\mu\varepsilon$ (16.7ε_y), respectively. These were the highest strains recorded at any location. Rebar hinge strains are expected to be high because of the relatively large rotations under lateral loading.

The hinge spiral was instrumented at the footing interface and 6 in (152 mm) above the interface within the cap beam opening. The maximum strains in both hinge spirals are recorded in table 6.29 and 6.30 and the strain profiles for the spiral are presented in figure 6.69 and 6.70. All peak strains were below yielding for runs 1-7. One spiral gage indicated yielding in run 8 at the footing interface.

6.11.3 Cap Beam Reinforcement

The cap beam was instrumented in multiple locations including the transverse bars, top and bottom longitudinal bars, and the socket spiral provided for socket connection confinement. Because the cap beam is designed as a capacity-protected member, no yielding was anticipated in this component if the ABC connections performed as intended. The peak strains during different runs for all reinforcement types are recorded in table 6.31. The peak transverse bars in the cap beam was 1690 $\mu\varepsilon$, which was 0.69ε_y. The peak strains in the top and bottom longitudinal bars were 386 $\mu\varepsilon$ (0.15ε_y) and 1000 $\mu\varepsilon$ (0.38ε_y), respectively. Within the socket connection, the measured peak spiral strain was 1620 $\mu\varepsilon$ (0.66ε_y). The strain in all the reinforcement remained well below yielding, indicating that the cap beam did perform as a capacity-protected member.

6.11.4 Girder-to-Cap Beam Connection

The girder-to-cap beam connection instrumented elements included the longitudinal headed bars, crossties, and extended girder strands. No yielding was expected in these elements as they were all within a capacity protected cap beam member. The peak strains in these elements are presented in table 6.32 and 6.33. The peak strain in the headed bars was 615 $\mu\varepsilon$ and was under tension. No test bar samples were tested, but considering they were Gr. 60 rebar, the peak strain was approximately one-third of the estimated yield strain. The crossties peak strains were minimal at 111 $\mu\varepsilon$, which was five percent of the yield strain.

Some girder strands were mobilized more than others as there was some spread associated with the strains in the strands. The maximum tensile stresses in the prestress strands for each run are shown in figure 6.71. The peak prestress strand strains increased significantly in runs 6 and 7 (table 6.33). The measured peak strain in the strands was 2320 tensile $\mu\varepsilon$ (0.25ε_y). No yielding was observed in any element during any shake table run meaning the girder-to-cap beam connection remained capacity protected. The strains remaining below yield and increasing at higher runs indicate that the connection performed as designed; the strands were mobilized during higher intensity earthquake runs and withstood the applied seismic moment.

6.11.5 Deck Reinforcement

Strains in the deck reinforcement were measured in multiple locations, which could be placed in two categories: within precast deck panels and within the cast-in-place UHPC pour above the bent. Eight bars were instrumented on each span for a total of sixteen strain gages. As the top of the cap beam and deck are considered capacity protected elements, no yielding was expected for the duration of the test if the connections performed well. The peak strains in the deck panels are presented in table 6.34. The peak strain of 975 $\mu\varepsilon$ ($0.40\varepsilon_y$) occurred in run 8. Therefore, none of the deck bars approached yielding. It is clear that the deck panel and deck joint over the cap beam performed as capacity-protected members. This demonstrates that the deck connection over the bent behaved as designed and provided sufficient continuity through the lap splice that was embedded in UHPC.

6.12 Strain Rate

Material properties such as yield strength, ultimate strength, and the corresponding strains depend upon loading or strain rate. When testing material properties for concrete or steel, a slow loading rate is applied to cause the properties to be pseudo-static. The strain rates experienced within the column in this shake test are much higher than those that are used in material testing causing potential discrepancy between the two.

Amplification in yield and ultimate stress based on the strain rate has been proposed to adjust the material properties to account for dynamic loading effect (Kulkarni and Shah, 1998). Considering that the strain rate is variable during earthquakes, a study by Zadeh and Saiidi, 2007, proposed to determine the strain rate effect based on the tensile loading rate between $0.5\varepsilon_y$ to $1.0\varepsilon_y$ during shake table testing.

Tensile strain rate was calculated for strain loading between half to one times the measured yield strain for all longitudinal bars in the plastic hinge region in both columns. Table 6.35 and 6.36 list the results. The average tensile strain rates in the north and south columns were 12618 $\mu\varepsilon$/s and 11528 $\mu\varepsilon$/s, respectively.

The compressive strain rate of concrete was estimated using the compressive strain data for the longitudinal column bars as they underwent compression. Implied in this approach is the assumption that perfect bond existed between the bars and concrete under compression. Limited data was available for the compressive strain rate as only two longitudinal bars yielded under compressive loading. The strain rate for each of these bars is listed in table 6.37. The average compressive strain rate of the two bars was 10997 $\mu\varepsilon$/s. One additional strain gage experienced compressive yielding but the data for this bar was erratic. This data was deemed an outlier and excluded in the analysis.

6.13 Column Plastic Hinge Rotation and Curvature

Rotation in the column sections was measured using the vertical Novotechniks at the top of the columns. Displacement was measured at three elevations along the column top as shown in figure 4.9. Rotation was measured by taking the difference of displacements on opposite sides of the columns and dividing by the horizontal distance between the instruments. The peak rotations in the columns for both directions in all the runs are listed in table 6.38 and 6.39. The peak longitudinal rotations in the columns occurred in the opposite direction due to the in-plane rotation of the bridge. The north column underwent higher rotations associated with longitudinal movement of the bridge than the south column during all runs. Rotations due to movement in the transverse direction were smaller than those associated with longitudinal movement, which is logical due to the peak displacements also being lower in the transverse direction. Peak rotations within the south column were higher in the transverse direction than those in the north column. Because the north column experienced increased longitudinal rotations, and the south column experienced higher transverse rotations; this may have meant that the bridge center of rotation may have been closer to the south column, causing the south column to be pulled transversely while the north column rotated longitudinally due to the in-plane rotation.

The column curvature was calculated by dividing the difference in rotations between two levels of instrumentation by the vertical distance between the levels. This average curvature was assumed to take place halfway between both Novotechnics. The curvature profiles are shown in figures 6.72 to 6.75. The peak curvatures in the transverse direction were mostly symmetric in the south column. The curvature of the north column was more biased towards the south direction. Curvatures were largest directly below the cap beam indicating that the largest amount of yielding occurred at that location. Also, the maximum curvature occurring directly below the cap beam implies fixity between the column and cap beam via the socket connection.

6.14 Rebar Hinge Deformations

The rebar hinges at the column bases were expected to experience significant rotations during the shake table testing, but there could also be slippage and vertical deformation due to the relatively small cross section of the hinges. Novotechnik transducers at the column base were used to monitor the column base and rebar hinge displacement. Vertical displacement, hinge rotation, angle of twist, and shear slippage were all monitored. Some of these measurements were used to calculate the net column displacement in section 6.7.2. Equations for calculating these deformations were also discussed in section 6.7.2.

6.14.1 Rebar Hinge Rotation

Rotation of each rebar hinge about the longitudinal and transverse axes of the bridge was calculated using equations 6-8 through 6-11. A 1.5 in (38.1 mm) gap was incorporated between the column and the footing to allow for rotation without contact between the two interfaces. The rotation limit that the hinge could experience without the gap closure was 0.0833 radians. The displacement history for the most extreme run is shown in figure 6.76 for each direction with the rotation limit indicated. The maximum and minimum measured rotations in each direction for both hinges are listed in table 6.40 and 6.41. The peak hinge rotations associated with transverse displacement of the bridge were comparable. The peak rotation in the north rebar was associated with translation towards the west for run 4 and after; while the south column rotated more with translation towards the east. This is because of the in-plane rotation of the superstructure. Overall, the north rebar hinge experienced more rotation than the south column with maximum rotations of 0.0515 radians compared to 0.0436 radians, both occurring in the longitudinal direction. The maximum rotation in the rebar hinges was 62% of the rotation limit; meaning an adequate gap was provided between the column base and the footing. The maximum rotation in the transverse direction was 0.0291 radians and 0.0293 radians for the north and south rebar hinges, respectively. The rotation in the longitudinal direction was larger than the transverse direction because of the stronger ground motion in the longitudinal direction in addition to the effects of superstructure in-plane rotation on the columns.

Because the rotation limit was not exceeded, the provided gap between the column and footing was deemed adequate.

6.14.2 Rebar Hinge Angle of Twist

The angle of twist history was calculated using equations 6-12 and 6-13 for each hinge and compared to the superstructure in-plane rotation in figure 6.77. The maximum angle of twist in each rebar hinge as well as the in-plane rotation of the superstructure are shown in table 6.42. Correlation between angle of twist in the hinges and the superstructure in-plane rotation was high for runs 1-6. After run 6, angle of twist in the south hinge was higher than that of the north hinge. This again supports the idea that the center of rotation may have been closer to the south column than the north, causing the torsion to be higher in the south hinge and the translation to be higher in the north hinge.

6.14.3 Vertical Displacement in the Rebar Hinge

Vertical displacement in the rebar hinge was calculated for runs 3, 7, and 8 using equations 6-16 and 6-17 (figure 6.78). The peak vertical displacements are listed in table 6.43. The maximum vertical displacement in the hinges was 0.095 in (2.41 mm) in the north hinge and 0.122 in (3.10 mm) in the south hinge. These maxima took place in run 6. Vertical displacement in the last two runs may have been smaller than those in run 6 because damage in the column caused component elongation to occur in the column top rather than in the hinge. The relatively small peak vertical displacement during all the runs shows that the hinge pocket connection was effective in providing good connectivity between the rebar hinge and the column.

6.15 Relative Displacement between Deck Panels and Girders

Relative displacement between the deck panels was measured to evaluate the performance of the deck panel to girder connection. Longitudinally and transversely oriented Novotechnik transducers were mounted to the underside of the deck to measure displacement relative to the top girder flange as shown in figure 4.11. One interior and exterior girder in each span were monitored at two locations: at 8 in (203 mm) from the cap beam interface and at 54 in (1.37 m) from the face of the cap beam. The latter included only longitudinal Novotechiks and was incorporated based on results from testing of Calt-Bridge 1 that suggested that the location of maximum shear between the components would take place 54 in (1.37 m) from the cap beam if the superstructure connection was non-rigid (Benjumea et al., 2019). Therefore, these two locations were monitored to determine the location of the maximum relative displacement. The peak relative displacements between the deck and girders are listed in tables 6.44 to 6.46. Novotechnik - NT49 (figure 4.11) was offline for the test and no data was recorded for that instrument. The relative displacements were all small with a maximum of 0.0119 in (0.302 mm) in the longitudinal direction and 0.0087 in (0.22 mm) in the transverse direction. Displacement was always higher at 8 in (203 mm) from the cap beam interface, which based on the analytical work from Calt-Bridge 1, suggests that the superstructure connection is rigid. All displacements were low, implying that there was good continuity between the deck panels and the precast girders via the grouted pocket connection with steel studs.

6.16 Relative Displacement at Superstructure and Cap Beam Interface

The relative displacement histories between the spans and the cap beam interface was measured to evaluate the continuity of the spans within the cast-in-place portion of the cap beam. Novotechniks were placed at the top of the deck and bottom of the girder for both one interior and one exterior girder in each span near both columns (figure 4.10). The maximum displacements are listed in table 6.47 and 6.48. It can be seen that the displacements were small with the maximum being 0.0105 in (0.267 mm) and 0.00689 in (0.175 mm) at the bottom and top of the span, respectively. The small displacements in this region indicate good integrity at the superstructure-cap beam connection and demonstrates that the connection was capacity protected at all earthquake levels.

The fixity at the superstructure-cap beam interface was evaluated by calculating the rotation at each girder at the connection to the cap beam. The rotation at the interface was measured by dividing the difference between the top and bottom displacements by the vertical distance between them, which was 20 in (508 mm). This was completed for each instrumented girder, and the results are listed in table 6.49. No large jumps in rotation were observed, meaning the spans never slipped relative to the cap beam. The maximum measured rotation was 0.0007 radians. These small rotations imply that the rotational stiffness of the connection was high and can be classified as rigid. It also suggests that good moment transfer from superstructure to cap beam was maintained and that the connection performed as designed.

6.17 Relative Vertical Displacement between Column and Cap Beam Socket Connection

Relative displacement between the column and the bottom face of the cap beam was measured using four Novotechnik transducers on each column (figure 4.9). The average displacement of the four Novotechniks was used to determine the relative vertical displacement in the connection. The displacement history for runs 3, 7, and 8 is presented in figures 6.79 – 6.80. The maximum and minimum slippage in the connection are listed in table 6.50. Slippage of the column towards the cap beam was not observed in either column. The data was nearly symmetric response during all runs with some residual displacement being recorded after run 3. The peak relative displacement in the connection was 0.268 in (6.81 mm) and 0.206 in (5.23 mm) in the north and south column, respectively. These displacements occurred due to degradation of concrete and the loss of axial stiffness in the column plastic hinges. Socket connection integrity is necessary for limiting these displacements. Any large jump in relative displacement between the column and cap beam would indicate that the column was slipping from the connection. Because the connection was able to transfer load to the columns while plastic hinges were formed at the column tops (section 6.11.1) and the relative displacement in the connection was very small in all the runs, socket connection performance for column tops was deemed satisfactory for high intensity seismic events.

Chapter 7. Analysis of Experimental Results

7.1 Introduction

The response of Calt-Bridge 2 during eight shake tables tests was measured using multiple instrument types (chapter 4). These measurements were used to assess the bridge system and ABC connection performance under seismic loading. This chapter summarizes the analysis results from the shake table tests. Bridge system performance parameters including the bent coupling index, displacement ductility, and system energy dissipation were evaluated. Reinforcement strains and relative displacements between the connected elements were used to assess the performance of the ABC connections.

7.2 Bent Particle Displacement and Coupling Index

The particle displacements at the center of the cap beam were used to determine whether the bridge model had indeed undergone biaxial response during the shake table tests. The shake table tests consisted of biaxial input ground motions with significant ground accelerations in both directions of the bridge. However, applying biaxial ground accelerations does not guarantee that coupled movements occur in the bridge system. It is possible for the peak displacements in each direction to occur at different times with little to no displacement in the orthogonal direction, meaning the system is performing uniaxially along each of the axes. One of the primary goals of this project was to assess the performance of ABC systems under biaxial loading. To determine if the bridge model movements were coupled, a coupling index developed by Saiidi et al. (2013) was used. The focus of this evaluation was on the particle movements on top of the center point in the bent cap.

The bent particle displacements in the longitudinal and transverse directions were calculated by averaging the north and south total column displacements presented in section 6.7.1. The transverse and longitudinal displacement histories for each run were plotted against each other so the coupling index could be calculated. The particle displacements for each run are shown in figures 7.1 to 7.3. The peak displacements in the longitudinal or transverse directions were used to form the outer bounds of a square as indicated by the dashed gray squares in figures 7.1 to 7.3. In this application, the longitudinal displacement controlled the peak displacement in each run, which was expected due to larger input acceleration in the longitudinal direction. Recall that the earthquake motion components were oriented in this way to induce larger moment in the superstructure-to-cap beam connections and to place maximum demand on the column-to-cap beam socket connections in the out-of-plane direction for the bent. Diagonals were connected between opposing corners of the square, and the outermost intersection between the particle displacement history and the diagonal was set as the peak displacement for that quadrant. An example of calculating the coupling index and the quadrants is shown in figure 7.4. The coupling index was calculated for each quadrant by dividing the distance between the origin and the peak particle displacement (for example, the red line in the first quadrant in figure 7.4) in the respective quadrant by the diagonal length between the origin and square corner (for example, the bold black line plus red line in figure 7.4). A fully coupled system, where peak longitudinal and transverse displacement are the same and occur simultaneously, would result in a coupling index of

1.0. The coupling index for each quadrant and each run are listed in table 7.1. The average coupling index for each run was also calculated to represent the overall coupling observed in each run.

The coupling indices for each quadrant were between 0.19 and 0.73 for all runs. The maximum coupling index for the cumulative displacement histories was 0.55 (figure 7.3). The average coupling index for all runs and quadrants was 0.38 and the average peak coupling index for all runs was 0.48. These values indicate the system was moderately coupled and the bridge system did indeed undergo significant simultaneous biaxial movements. The maximum coupling index did not remain in the same quadrant for all runs. When damage to the columns was low during early runs, the maximum coupling index occurred in the same quadrant. As damage progressed, the displacement response changed, and the peak coupling index shifted quadrants. This indicates the coupling index depends on the damage state of the columns and is not exclusively related to the ground motion characteristics.

7.3 Bent Displacement Ductility

The bent displacement ductility was calculated by idealizing the force-displacement envelopes presented in section 6.9 with elasto-plastic curves. Commonly, the force-displacement envelope is taken from the positive and negative direction and averaged to form an average envelope prior to calculating the idealized curve. However, because the applied ground motion was asymmetric, one direction was dominant in each of the longitudinal and transverse directions. The dominant direction was selected for calculation of the idealized curve as it is more indicative of the ultimate limit state.

Strain data was used to determine the point of first yield in each direction, which was required to idealize the force-displacement envelopes. The reinforcing bars in the axes of interest were evaluated for determining first yield. However, because of the biaxial behavior of the columns and the yielding being dominated by longitudinal translation, strain data indicated a yield displacement that was artificially large for the transverse and resultant directions. To account for this, the displacement at one-half of the peak base shear was assumed to be the point of first yield. In the longitudinal direction, the first yield occurred during run 2 at 0.72 in (18.3 mm) of displacement. The area under the envelope and the idealized curve were equated to calculate the plastic shear. The effective yield displacement was 1.1 in (27.9 mm), 0.63 in (16.0 mm), and 1.05 in (26.7 mm) for the longitudinal, transverse and resultant directions, respectively, resulting in displacement ductilities of 3.6, 4.1, and 4.6. The idealized curves superimposed on the envelopes for each direction are presented in figure 7.5, and the general properties are listed in table 7.2. Note that because the bridge testing was not terminated due to column failure, the ultimate displacement capacity and displacement ductility capacity were not determined in the tests. The maximum displacement ductilities stated in table 7.2 are those measured based on the test results and do not constitute capacities.

7.4 Energy Dissipation

A critical component of bridge systems in seismic regions is the ability to dissipate the earthquake energy through stable formation of plastic hinges in critical members. Energy dissipation in the bridge system was observed in the hysteresis loops shown in figure 6.53. The total energy dissipated during each run was determined by calculating the area within each hysteresis loop. The total energy dissipated for each run and the cumulative dissipated energy for the longitudinal and transverse directions are shown in figures 7.6 and 7.7, respectively. A larger amount of energy was dissipated during longitudinal movement compared to the transverse due to the larger displacement and wider hysteresis loops in that direction. The total energy dissipation in the longitudinal and transverse direction was 1793 kip-in (203 kN-m) and 821 kip-in (91 kN-m), respectively. Increasing dissipated energy with each successive run demonstrated stable damage progression in the column plastic hinges and provided further evidence that the ABC connections allowed for formation of plastic hinges in the columns and maintained integrity between components even under large ground motions.

7.5 Average Strains and Curvatures in Superstructure-to-Cap Beam Connection

Moments developed in the bent at the superstructure-to-cap beam connection due to seismic forces that occurred during the shake table tests primarily due to longitudinal movement of the bridge model. The spans were continuous for seismic excitation; therefore, the upper region on each side of the bent was subjected to positive or negative moment depending on the direction of the superstructure movement. The girder-to-cap beam connection utilized projected steel strands from the girders to resist the tension in the lower region of the cap beam face due to positive moment. Shear friction between the cap beam and the girders served as a secondary moment transfer mechanism. The lap spliced projected deck reinforcement encased in UHPC resisted tension in the upper region of the superstructure in the upper part of the cap beam. Evaluation of the force distribution within the superstructure-to-cap beam connections was performed by analyzing strain data in the deck reinforcement for the negative moment transfer and the projected steel strands for the positive moment transfer.

Strains were measured in the deck and projected girder reinforcement on each side faces of the cap beam in an exterior and an interior girder. The instrumented locations are shown in figures 4.6 to 4.8. The average measured tensile strain histories for each run are presented in figures 7.8 to 7.15. No steel yielded in either connection, which validates the design methodology that each connection was a capacity protected member. Peaks in the strain histories along the deck reinforcement and projected girder reinforcement occurred simultaneously but in opposing directions, meaning when one connection was undergoing compression, the other was subjected to tension and vice versa. This indicates that the connections contributed to moment resistance as a force couple. The strand strains were higher than their deck reinforcement counterparts, particularly in later runs. This is attributed to the different neutral axis depths for opposing moment directions as shown in figure 7.16. Since these strains occur in the superstructure, it can be assumed that the materials remain elastic. The compression block is assumed to be in the deck for positive moment because of the large effective width provided by the deck. This results in a small depth to the neutral axis, which places large strains on the steel (girder strands). The neutral axis for negative moment would be in the girder, which is relatively narrow and therefore the compressive block is relatively large. As can be seen in the strain diagram for negative moment, the steel strain (deck bars) would be smaller than the steel strain (girder strands) for positive moment under comparable maximum concrete strains. Additionally, there was a larger amount of steel in the deck panel connection over the pier relative to the superstructure-to-cap beam connection, and the deck bars were encased in UHPC that has intrinsic tensile capacity contributing to tensile resistance in the upper region of the cap beam. The deck reinforcement strains at each instrumented location exhibited minor increases in strain as earthquake intensity increased, again suggesting that UHPC may have significantly contributed to the tensile capacity at the top of the cap beam. The girder strand strains had similar response histories at each location but varied in the peak tensile strain. The interior girder of the west span had a peak tensile strain in the girder strands of 575 με, which nearly double that of the corresponding deck bar strain of 289 με. This was in contrast to the exterior girder in the west span that had a peak tensile strain in the girder strands of 1575 με, which was almost eight times larger than the peak deck bar strain of 200 με. The same difference in peak strains between the interior and exterior girder was not observed in the east span with both the girders experiencing peak tensile strains of approximately 1150 με and 350 με in the girder strands and deck reinforcement, respectively. The unbalanced strains between the two girders in the west span imply that uneven moment distribution occurred in the cap beam, specifically in the west span. This may have been caused by asymmetric placement of the superstructure or superimposed mass, or strong friction forces between the exterior girder and abutment may have induced axial forces along that girder placing additional demand on the connection. In-plane rotation of the superstructure during strong ground motions lends additional evidence to this theory.

The superstructure-to-cap beam connection was further evaluated by calculating the curvature in the superstructure adjacent to the cap beam face. The curvature was calculated by taking the difference of the average strain in the deck reinforcement and strands and dividing it by the vertical distance between them. The curvature histories are shown in figures 7.17 and 7.18. Positive curvature indicates positive internal bending moment in the section with tension at the bottom of the cap beam and compression at the top. The peak curvatures occurred in the positive direction. This is consistent with the strain data showing higher tensile strains in the girder strands. The curvatures of the exterior girder in the west span were much higher than that of the other three girders. Limited data was available in this location as only three strain gauges along one strand functioned during the shake table tests. Therefore, the higher strains observed at this location may have been caused by a local force concentration in the single instrumented strand rather than larger curvature in that region. This is supported by the lower curvatures observed on the opposing face of the cap beam along the same girder. The peak curvatures for each run at each location are shown in figure 7.19. In general, larger curvatures were observed in the exterior girders, particularly during later runs. Also, much higher peaks were observed in the positive direction. Curvature generally increased with each run with only minor increases observed in later runs. The decrease in rate of change of the peak curvature in late runs correlates with the bent force-displacement relationships presented in section 6.9. As column damage increased and the plastic moment capacity in the columns was reached, the moment transmitted to the cap beam did not increase significantly as exhibited by the stabilization in peak base shear shown in figure 6.53. Because the superstructure-cap beam connections were elastic, the relatively constant moment led to a relatively constant curvature.

The peak curvatures in the interior girder were similar in each direction suggesting symmetrical bending in the cap beam. The peak curvatures in the exterior girders were not well correlated, but this may have been caused by limited girder strand data at that location as mentioned previously. The curvatures suggest that both the girder-to-cap beam connection and the deck connection over the bent contributed to moment resistance in the cap beam.

7.6 Positive Moment Resisting Mechanisms in Superstructure-to-Cap Beam Connection

Two mechanisms resisted tension in the lower region of the cap due to positive seismic moment; the first was the projected girder strands and the second was shear friction between the cast-in-place cap beam concrete and the girders. The positive moment resistance contribution from shear friction at each instrumented location was calculated using the method proposed by Vander Werff et al. (2015). For this approach, the shear contribution of dowel action from the headed bars and adhesion and aggregate interlock between cap beam and girder concrete are multiplied by the moment arm projected from the center of rotation to calculate the positive moment resistance. The force contribution of the headed bars was calculated by multiplying the strains at the time of maximum curvature and the headed bar area, modulus of elasticity for steel, and the shear friction coefficient, which was taken as 0.6. The force contribution from friction and aggregate interlock was calculated by multiplying the concrete area engaged in interface shear, A_{cv}, and the cohesion factor, c, which is equal to 0.075 ksi (517 kPa) according to AASHTO LRFD Eq. 5.8.4.1-3 (2017). This approach assumes that no degradation in the headed bar bond or aggregate interlock takes place. The contribution from the top and bottom headed bars and the adhesion and aggregate interlock were doubled to account for shear friction on both sides of the girder.

The approach used by Benjumea et al. (2019) to estimate the strand contribution to positive moment resistance was adopted for this application. A sectional analysis of the girders assuming full composite action between the deck and girders was performed using Xtract (TRC, 2006) to estimate the moment associated with the peak measured curvature. The measured test-day properties were used for the girder materials and deck bars. The UHPC layer of the deck was modeled using an elastic element with a modulus of elasticity of 8,000 ksi (56 GPa) (Russell and Graybeal, 2013). The moment corresponding with the peak curvature at each location was established as the strand contribution to positive moment resistance for that region.

The calculated positive moments at each location are listed in tables 7.3 and 7.4. As expected because of the relatively high girder strand strains, the exterior girder on the west side of the cap beam had the highest contribution to positive moment resistance at 51%. The average exterior girder strand and shear friction contribution was 45% and

55%, respectively. Strand contribution was much lower for the interior girders with an average positive moment contribution of 20% compared to 80% for the shear friction contribution. These values were similar to those found by Vander Werff et al. (2015) where the strand contribution was between 35% and 65% prior to yielding for a girder-to-cap beam component test. The relatively low strand contribution for the positive moment resistance suggest that the girder-to-cap beam connection could have incorporated the minimum required three strands per girder, rather than the conservative four strands that was used. The connection behavior indicates that the girder-to-cap beam connection performed within the bounds of the design and verified the findings from component level testing

7.7 Assessment of Overall Seismic Performance of ABC Bridge System and Connections

7.7.1 ABC Bridge System

The global system level performance of Calt-Bridge 2 during shake table testing was satisfactory. Collapse did not occur, and stability was maintained even after experiencing extensive yielding. Yielding occurred exclusively in the plastic hinge regions of seismic critical members (i.e. columns and base hinges) and all capacity protected members remained essentially elastic, even for ground motions substantially stronger than the design level earthquake. Calt-Bridge 2 exhibited ductile behavior undergoing a maximum displacement ductility of 4.6 (table 7.2). Note that this ductility was not the ultimate displacement ductility capacity because the columns did not fail, and the bridge model testing was not stopped due to column failure but because of concerns for unseating at the abutments. Stable plastic hinging was observed with no abrupt drops in base shear. Spalling of the column cover concrete and large strains in the column longitudinal reinforcement were observed, but bar rupture did not take place. Force-displacement relationships showed good energy dissipation in all runs for both the longitudinal and transverse translation of the bridge. Biaxial response of components was observed indicating the bridge system was subjected to biaxial or coupled forces, meeting one of the primary goals of this study. Substantial in-plane rotation likely caused by asymmetric distribution of friction at the bearing pads, induced large transverse displacements at the abutments, ultimately leading to the termination of the test to avoid potential unseating of the superstructure. Due to these displacement limits, the ultimate limit state of the bridge columns was not reached, although near unseating could be considered as the ultimate limit state of the bridge system itself. However, base shear had begun to decrease in both directions, suggesting that column failure could be imminent.

7.7.2 ABC Connections

Six ABC connection types were implemented in Calt-Bridge 2 to assess their performance when integrated in a single bridge system subjected to biaxial horizontal seismic excitations. These connections were incorporated at: (1) the column-to-footing pocket connection, (2) column-to-cap beam connection, (3) girder-to-cap beam connection, (4) deck panel connection over the pier, (5) deck-to-girder connection, and (6) deck panel-to-panel connection. The performance of each connection type is assessed in the following sections.

7.7.2.1 Rebar Hinge Connection
The column-to-footing connections consisted of a hinge reinforcement cage that was precast with the footing and connected to the column via an opening left in the precast columns. The observed condition of the rebar hinge under different levels of seismic simulation indicated the hinge performed satisfactorily with no rupture of longitudinal bars even under 225% of the design level earthquake. The pocket connection maintained integrity during all earthquake runs and did not experience significant damage. Spalling occurred in the cover grout at the hinge throat due to the amount of rotation experienced in this zone during lateral translation of the superstructure. No shear failure or excessive shear deformation at the hinge was observed.

The maximum hinge strains demonstrated good ductility, with the maximum measured longitudinal reinforcement strain of 17.5 times the yield strain. Reduction of longitudinal bar strains within the pockets away from the hinge was observed, which attests to the effectiveness of the anchorage provided at the connection. The rebar hinge is designed to limit yielding to the hinge element and reduce local forces in regions connected to the hinge. Some yielding spread into adjacent sections under high amplitude ground motions, but the strains were significantly reduced from those measured at the rebar hinge throat. This is the behavior expected from conventional cast-in-place rebar hinges. Therefore, the pocket ABC connection provided at the column base hinges proved to be emulative of conventional bridge behavior.

A primary purpose of the rebar hinge is to keep moment and shear in connecting members low. Significant base shear reduction was achieved, which was due to the reduction in the plastic moment capacity at the base. The base shear was reduced by approximately 40% of what would be expected from a fixed base condition. This demonstrates that the rebar hinge with pocket connection was successful in providing hinge like behavior at the column base and reducing system forces.

The provided hinge gap was sufficient to accommodate the imposed rotations from seismic displacements. Neither column came into contact with the footing, meaning the proposed design method for hinge throat thickness was adequate even for bridge systems subjected to bidirectional earthquakes. The overall performance of the hinges in both bridges indicates the design method developed by Cheng, et al. (2010) was satisfactory for rebar hinge applications in ABC bridge systems even though it was developed for CIP conventional bridges.

Significant relative displacement was observed between the bottom of the column and footing, taking place over the hinge throat. This is attributed to softening of the hinge throat due to degradation and spalling of the grout within the pocket connection under cyclic loading. Had concrete, rather than grout, been used in the hinge, the degradation in the connection would be less pronounced. However, changing the material from grout to concrete would have necessitated the connection type be changed from “pocket” to “socket” connection types, per definition of AASHTO LRFD Guide Specifications for ABC (2018).

7.7.2.2 Column-to-Cap Beam Socket Connection
The column-to-cap beam connections consisted of two precast columns being fit into an opening within the cap beam via a socket connection. This connection is labeled as “socket” connection per definition of the AASHTO LRFD Guide Specifications for ABC (2018) because the columns were fully precast with no exposed column bars protruding

into the cap beam opening. The socket connection provided good anchorage and allowed for formation of plastic hinges in the columns directly adjacent to the cap beam interface, while the cap beam remained capacity protected. Some minor spalling was observed in the grout between the column and cap beam under larger excitations, but no cracking or extensive spalling occurred in the connection. Large strains in the column longitudinal reinforcement were observed at the cap beam interface but dissipated when moving into the capacity protected element. Slippage in the connection was not observed. The column and cap beam performed as would be expected for cast-in-place components subjected to earthquakes, which suggests the socket connections fulfilled their purpose as a fixed connection between prefabricated elements for ABC applications in seismic regions.

7.7.2.3 Superstructure-to-Cap Beam and Deck Panel over Pier Connections

The superstructure-to-cap beam connection consisted of projected girder strands with couplers and headed bars with crossties. The deck panel connection over the pier incorporated relatively long lap-spliced deck bars that were embedded in UHPC. These connections remained elastic for all earthquake runs and resisted the applied seismic moments. No separation was observed between the deck panels and UHPC or the superstructure and cap beam. No cracking was observed at the joint interfaces and the components and connections remained capacity protected as designed. The measured rotations between the superstructure and cap beam were insignificant, which implied full connectivity within the superstructure connections.

7.7.2.4 Deck Panel-to-Girder and Deck Panel-to-Panel Connections

The deck joints incorporated short lap spliced deck bars in the joints filled with UHPC. The panel-to-girder connection consisted of projected steel studs from the girders that were fit into pockets in the deck panels and connected via grout. No damage was observed in either connection type. Cracking of the deck panels or joints, or separation of the deck panels did not occur. The superstructure appeared to have performed as a capacity protected member due to the absence of damage. Relative displacements between the deck panels and girders implied good connectivity between the components and suggested that composite action was provided.

7.8 Assessment of Connection Design Methods

Calt-Bridge 2 and the six ABC connections were designed using a combination of existing guidelines for cast-in-place construction and other documents from the literature as described in chapter 2. These connections had not been incorporated in a bridge system utilizing ABC methods. The Calt-Bridge 2 shake table test data provides an opportunity to assess the seismic performance of these connections relative to the design criteria to possibly identify any necessary refinement in the methods. This section summarizes the design implications based on the findings from shake table testing of Calt-Bridge 2.

7.8.1 Column Base Connection

- Pocket connections with pockets in the columns provided complete connectivity for rebar hinges in the column bases. Relative horizontal displacement was observed at the hinges between the bottom of the full column section and the top of the footing during strong ground motions, a part of which was attributed to degradation of the hinge pocket grout under cyclic loading. The other part was due to degradation of the hinge throat itself that is expected. Utilizing a precast concrete hinge stem with socket connection between the footing and column is recommended to alleviate the pocket grout degradation problem.

- The design procedure for rebar hinges developed by Cheng et al. (2009) based on uniaxial loading of cast-in-place hinges led to satisfactory performance for precast ABC hinges subjected to biaxial ground motions with no modifications required.
- Shear design for the rebar hinge provided sufficient capacity to resist the applied biaxial shear for multiple ground motions. Shear failure was not observed in the hinges even when extensive yielding had occurred in the hinge throat.
- The embedment length for the hinge reinforcement in the pocket connection and footing provided sufficient development of the longitudinal reinforcement, which allowed for formation of plastic hinges and large sustained reinforcement strains within the hinge throat.
- The hinge throat thickness was sufficiently large to allow rotation of the rebar hinges without contact between the column edges and footing. This prevented large moments from developing in the foundation due to bearing of the column on the footing during hinge gap closure, which could damage the foundation and increase the column plastic shear.
- Joint integrity was maintained at the column bases under all ground motions even after the hinge longitudinal bar strains and hinge rotations were large. No damage was observed in the pocket connection or footing except for some degradation of the grout in the lower part of the pocket.

7.8.2 Column-to-Cap Beam Connection

- Socket connections in the column-to-cap beam connection provided sufficient anchorage for the columns. Slippage between the columns and cap beam was insignificant.
- The socket connection guidelines developed by Tazarv & Saiidi (2015) were successfully incorporated for bridge systems implementing ABC methodologies. The design procedure for the socket connections and cap beam dimensions resulted in satisfactory joint behavior for both in-plane and out-of-plane superstructure translation. The performance of the precast cap beam, columns, and socket connections was emulative of conventional bridge behavior.
- Embedment depths of 1.25 times the column diameter allowed for full transfer of biaxial forces between the superstructure and columns. Whether this depth can be reduced to 1.0 times the column diameter as suggested by a recent proposed AASHTO guideline (Saiidi, et al. 2020) could not be assessed in the present study.
- Cap beam widths equal to the column diameter plus 15 inches (381 mm) on each side of the column at the prototype level as recommended by Tazarv & Saiidi (2015) allowed for insertion of the precast columns into the socket connections with sufficient clearance. The recently released proposed AASHTO guideline (Saiidi, et al. 2020) calls for a minimum of 12 inches (254 mm) on each side of the column for cap beam width. The cap beam width in Calt-Bridge 2 was

sufficiently large to allow for large column displacements in the bent out-of-plane and in-plane directions while keeping the cap beam capacity protected.

- Joint integrity was maintained for all ground motions. No damage was observed in the cap beam or socket connections, which implies that the socket connection transferred the loads to the columns, allowed plastic hinges to develop in the column tops, and kept the capacity protected members essentially elastic even for strong ground motions.

7.8.3 Girder-to-Cap Beam Connection

- The extended strand bent with free end detail developed by Vander Werff et al. (2015) was successfully implemented in a bridge system and provided full positive moment transfer between the spans and cap beam.
- Tension in the cap beam from positive superstructure moment was resisted by two mechanisms: the girder strands, and shear friction between the cast-in-place portion of the cap beam and girders. The strands were utilized more in the exterior girders relative to the interior girders with 45% and 20% of the tension resisted by the exterior and interior girder prestress strands, respectively. During design, it was assumed that 80% of tension was resisted by the girder strands with the remaining 20% resisted by shear friction. Shear friction contributed a minimum of 49% to the tensile resistance in the cap beam with contributions as high as 80% observed in the interior girders, which implies that the girder strands were overdesigned and the demand on the strands may be reduced.
- No slippage was observed between the spans and the cap beam. This demonstrates that the girder-to-cap beam connection and embedment length for the spans provided sufficient anchorage for the superstructure within the cap beam.

7.8.4 Deck Connection over Pier

- The projected deck reinforcement over the bent encased in UHPC remained elastic even under strong ground motions. The design procedure for the deck reinforcement in this region was satisfactory in resisting the tension from negative superstructure moment.
- Long lap spliced joints embedded in UHPC demonstrated strong bond between the spliced reinforcement and provided full connectivity. Lap sliced deck bars with UHPC placed over the entire width of the cap beam provide ample resistance and are recommended for ABC even though current design guidelines do not allow lap splices over the cap beam.
- Some tension in the upper region of the cap beam may have been resisted by UHPC as it has intrinsic tensile resistance as exhibited by lower deck bar strains relative to the girder strands. Despite the UHPC having significant tensile resistance, it is recommended that the longitudinal deck reinforcement be designed to resist all negative moment, while neglecting any contribution from the UHPC. This results in conservative tensile capacity in the upper region of the cap beam and helps ensure that the connection remains capacity protected.

7.8.5 Deck-to-Girder Connection

- No damage was observed in the deck-to-girder connections, including the deck panel pockets, pocket grout, and UHPC.
- Slippage did not occur between the deck panel and girders, even at locations with the peak interface shear. No differences were observed in the measured slippage between the deck and the exterior or interior girders. This indicated that the steel studs in precast pockets within the deck panels (exterior girders) and the steel studs along a longitudinal deck joint cast in UHPC (interior girders) both provided good shear resistance between the connected elements. This connection can be used to develop composite action between the deck panels and girders.
- The design procedure for the size and spacing for the projected steel studs in the girders developed by Shrestha et al. (2017) resulted in composite action between the deck panels and girders for a bridge system.

7.8.6 Deck Panel-to-Panel Joints

- The deck panel-to-panel joints remained free of cracking and debonding under all ground motions. The joints transferred all longitudinal and transverse deck forces, while remaining capacity protected even under strong ground motions.
- Short lap-spliced joints cast with UHPC were found to adequately transfer deck forces over a short interface. The development lengths for short lap-splices cast in UHPC proposed by Yuan & Graybeal (2014) were found to be sufficient for ABC bridge system applications.

Chapter 8. Posttest Analysis of Bridge Model

8.1 Introduction

The response of Calt-Bridge 2 during seismic excitation was predicted using an analytical model in Opensees as discussed in chapter 5 prior to finalizing the bridge model design and the shake table testing protocol. After the shake table testing, the measured data was first compared to the predicted response from the pretest analytical model to assess the analytical model accuracy. Various assumptions were made in the pretest analytical model, including the use of target acceleration records and expected material properties. The assumed records and material properties differed from the achieved accelerations and measured material properties from the shake table tests. The differences resulted in significant differences between the measured and predicted data. Several modifications were made to the input data and the pretest model to determine if the response of Calt-Bridge 2 could be reasonably captured using dynamic analysis. These modifications included: using the actual ground motion records from the shake table tests, incorporating measured material properties, and adjusting the modeling of the ABC connections. The adjustments to the model and comparison of the final analytical and measured results are presented in this chapter.

8.2 Comparison of Pretest Model and Measured Results

The force-displacement response of Calt-Bridge 2 for the loading protocol was predicted using the pretest analytical model as shown in figures 5.10 to 5.12. These plots were superimposed on the measured force-displacement curves that were presented in figure 6.53 to compare the hysteretic response and determine if the predicted responses were in the same range as the actual responses and quantify the differences. This comparison is important as bridges designed in practice are modeled using a similar procedure as used in the pretest analysis, but validation of these models using bridge system testing is not likely. Therefore, engineers must rely exclusively on dynamic analyses to predict bridge response during earthquakes. Shake table testing of Calt-Bridge 2 presents an opportunity to assess the relative accuracy of dynamic analyses using standard modeling procedures and to make recommendations to better capture the system response.

The measured and pretest force-displacement relationships for the longitudinal and transverse directions are shown in figures 8.1 and 8.2, respectively. The peak measured and predicted displacements and base shears for the longitudinal and transverse directions are listed in tables 8.1 through 8.4, respectively. Differences between the measured and calculated displacements were quantified using the percent difference between the results. Note that run 8 was not included in the pretest analysis as this run was added during the shake table test after it was determined that the bridge model still had reserved capacity after run 7.

The displacement response in the longitudinal direction was dominant in the negative direction for the pretest analysis but was mostly symmetric for the measured results. This resulted in the pretest model consistently indicating larger displacements than the measured data in the negative direction and underestimating the displacement response in the positive direction. The correlation for the measured and calculated longitudinal displacements was relatively poor in early runs with a difference of 37% and 20% in the first two runs. The correlation improved in runs 3 through 6 with the differences ranging from 1% to 14%. The relationship between the measured and calculated data was poor in run 7, which was caused by the asymmetric response of the pretest model. The predicted and measured hysteresis curves had similar shapes and widths, which showed that the behavior of Calt-Bridge 2 was largely captured in the longitudinal direction.

Large differences between the measured and calculated longitudinal peak base shears were observed in run 1 with an average difference of 58% (table 8.3). However, the correlation was good in the remaining runs with the differences ranging from 1% to 16%. The discrepancy in the force data in run 1 was caused by the achieved ground motion acceleration not meeting the target acceleration, and the actual friction forces at the abutments reducing the force demand on the bent, an effect that was neglected in the analytical model. After run 2, larger lateral forces overcame the abutment friction that had locked the bridge ends during run 1. Additionally, as base shear increased the column plastic shear was reached and remained nearly unchanged due to plastic hinging in the columns and base hinges. The plastic moment capacity of flexure-dominated columns is generally captured well by analytical models, resulting in good correlation between the measured and predicted base shear after the columns and hinges have yielded.

The displacement response in the transverse direction was overestimated by the pretest analytical model in all runs. The correlation of measured and calculated peak transverse displacements was poor in all runs with differences as high as 105% observed (table 8.2). This was likely caused by the achieved spectral accelerations in the transverse direction not meeting the target values (table 6.2). Therefore, the bridge was not excited as strongly in the transverse direction as was predicted. Better correlation was observed between the target and achieved spectral accelerations in the longitudinal direction, which explains the better prediction in that direction. Additionally, friction studies presented in chapter 9 indicated that friction effects may have been more significant in the transverse direction, which would have suppressed the transverse displacement response.

Base shear was well correlated in the transverse direction in runs 3 through 7. The columns reached their plastic moment capacity during these runs. The base shear in flexure dominated bents is controlled by the plastic moment capacity of the columns and rebar hinges once significant yielding of the column longitudinal bars occur. The good correlation between the measured and calculated base shears indicate that the analytical model estimated the flexural capacity of the columns well. Some differences in the measured and calculated base shears were expected due to the use of expected material properties in the pretest model rather than the measured material properties.

Overall, the general response of Calt-Bridge 2 was captured by the pretest model. However, some significant differences were observed between the pretest model and measured displacements. This demonstrates that even sophisticated analytical models when used at the design stage only provide an estimate of the peak displacements. While the information is useful in comparing different alternative designs for a bridge, the estimated results should not be considered as very accurate.

8.3 Modifications to the Pretest Analytical Model

Results from the pretest model indicated that modifications could be made to better capture the measured behavior of Calt-Bridge 2. Input parameters were changed to represent the actual material properties and ground motion characteristics from shake table testing of Calt-Bridge 2 Furthermore, the modeling of the ABC connections was refined to better represent the local behavior of each connection as explained in subsequent sections.

8.3.1 Earthquake Loading

The Northridge earthquake recorded at Sylmar station, was used as the input record for the pretest model for Calt-Bridge 2. This record was retrieved from NGA West (2013), which is a ground motion attenuation model and ground motion record database for the west coast. The Northridge acceleration record was also used as the input motion in the shake table tests for Calt-Bridge 2. However, the shake tables do not perfectly replicate the input ground motion accelerations, which leads to differences between the input and measured accelerations. Table acceleration was recorded during the shake table tests using feedback sensors in the actuators. As a result, the actual motions are affected by the interaction between the shake table and the test model. The input ground motion record was changed to the measured ground motions from the shake table tests to subject the analytical model to the same ground motions as were applied to Calt-Bridge 2.

8.3.2 Material Properties

The actual material properties were not known during formulation of the pretest model. Therefore, expected material properties based on the specified nominal strength for each material type were incorporated in the model. After shake table testing was concluded, the measured test day properties were determined for the concrete and steel as reported in section 3.5. The inputs for the material models were adjusted to represent these rather than the measured properties. Furthermore, strain rate effects were included to account for increased material strength resulting from rapid loading.

8.3.2.1 Steel

Steel02 was used as the constitutive model for the column and rebar hinge steel reinforcement in the posttest model. The measured yield and ultimate strength of the #6 bars was 75.8 ksi (523 MPa) and 106 ksi (727 MPa), rather than 68 ksi (469 MPa) and 95 ksi (655 MPa), which were the assumed expected strengths incorporated in the pretest model.

The measured material properties were modified to account for the strain rate effect using the method developed by Kulkarni and Shah (1998). In this method, the yield and ultimate strength are adjusted based on the strain rate. Calculation of the strain rate factor is performed as shown in equations 8-1 through 8-3. The strain rate properties are listed in table 8.5. The static strain rate was assumed to be 250 $\mu\varepsilon$/s and the dynamic strain rate was assumed to be the average tensile strain rate of 12,073 $\mu\varepsilon$/s as described in section 6.12. However, because the yield strength of the steel was above 75 ksi, equations 8-1 and 8-2 did not apply because these equations use linear interpolation to find the strain rate factor between 45 ksi (310 MPa) and 75 ksi (517 MPa). Since the yield strength of the column steel was close to 75 ksi, the strain rate factor calculated from eq. 8-3 was assumed to be that of the column reinforcement. This resulted in a strain rate factor for steel of 1.01. The factored yield strength and ultimate strength for steel including dynamic strain rate effects was 76.5 ksi (527 MPa) and 106.4 ksi (734 MPa), respectively.

$$SRF_S = SRF_{45} + \frac{SRF_{75} - SRF_{45}}{30} * (f_y - 45) \quad (8\text{-}1)$$

$$SRF_{45} = 0.0328 \ln\left(\frac{\dot{\varepsilon}}{\dot{\varepsilon}_{st}}\right) + 0.9873 \quad (8\text{-}2)$$

$$SRF_{75} = 0.0124 \ln\left(\frac{\dot{\varepsilon}}{\dot{\varepsilon}_{st}}\right) + 0.9632 \quad (8\text{-}3)$$

Where:

f_y: measured yield stress of steel bars, ksi.

SRF_S: strain rate factor for steel with yield stress, f_y.

SRF_{45}, SRF_{75}: strain rate factor for steel with yield stress of 45 ksi (310 MPa) and 75 ksi (517 MPa), respectively.

$\dot{\varepsilon}$, $\dot{\varepsilon}_{st}$: dynamic and static strain rates, respectively, με/s

8.3.2.2 Concrete

The Concrete02 material constitutive relationship was used to model the column and rebar hinge fiber sections. The concrete strength was adjusted based on the results from the concrete cylinder compressive tests presented in section 3.6, which indicated a concrete compressive strength of 7.3 ksi (50.3 MPa). This was significantly higher than the expected concrete strength of 5.2 ksi (35.9 MPa). Mander's model for confined concrete (1988) was used to determine the concrete compressive strength for the column core fibers. The unconfined grout strength for the rebar hinge was set at 8.1 ksi (56.2 MPa). The confined properties were calculated using the same procedure presented in section 5.2.3. Concrete compressive strength was adjusted to account for the strain rate effects from rapid loading of the column sections. Perfect bond was assumed between the steel and concrete, which allowed for the use of the compressive strain rate measured from the column longitudinal bars in section 6.12 (10,997 με/s). The static strain rate was assumed to be 8.65 με/s . The compressive strengths of the column concrete and rebar hinge grout were factored based on the calculated strain rate factor, which resulted in compressive strengths of 8.4 ksi (58.2 MPa) and 9.4 ksi (64.9 MPa), respectively.

The cap beam was modeled using the elasticBeamColumn element using expected material properties for the modulus of elasticity for the pretest model. The modulus of elasticity was updated using the measured compressive concrete strength for the bent, which resulted in a modulus of elasticity of 4872 ksi (33.6 GPa). The gross section stiffness of the cap beam (I_g)was reduced by 30 percent (I_{eff}) to account for cracking of concrete under service load. This is in accordance with section 6.6.3.1.1 of ACI 318-14 (2014) for columns, which accounts for the reduction in sectional stiffness due to concrete cracking in the tensile region of the column. The value for columns was used rather than the $0.35I_g$ factor recommended for building beams, because the cap beam was heavily reinforced to satisfy the capacity protected provision for superstructure elements, which reduces the depth of cracking in the section. The effective moment of inertia for superstructures and cap beams is estimated between $0.5I_g$ - $0.75I_g$ with the upper bound representing heavily reinforced sections according to the Caltrans SDC (2019).

8.3.2.3 Bond-slip Rotation Effects

Bond-slip rotation effects were modeled as uncoupled rotational springs at the column ends to account for rotation in the joints due to slippage between the reinforcing steel and concrete. The bond-slip model developed by Wehbe et al. (1999) was incorporated in the posttest model, which entails placing zero-length rotational elements with specified moment-rotation properties at the top and base of the columns. The moment and rotation at yield and rupture are used to define a bilinear moment-rotation relationship for the zero-length springs based on moment-curvature analysis of the sections (figure 2.4). These properties were used to formulate a hysteretic material model. The column section properties were used to define the springs connecting the column to the cap beam and the rebar hinge section properties were used for the springs connecting the hinge to the foundation. The yield point of the section was defined by the intersection of a line extending from the origin through the point of first yield, and the post-yield stiffness as shown in figures 8.3 and 8.4.

The hinge reinforcement was embedded in the footing and in the pocket connection in the column, both of which are substantially more rigid than the hinge. Consequently, bond-slip rotations developed in two regions: in the hinge reinforcement embedded in the footing concrete directly beneath the hinge-footing interface, and in the hinge reinforcement embedded in the pocket connection grout directly above the hinge-footing interface. Therefore, the bond-slip rotations in the hinge throat were doubled to account for reinforcement deformation in both zones.

8.3.3 Refinement of Modeling ABC Connections

ABC connection measured performance was assessed to verify the connections behaved as modeled in the pretest configuration. The measured data from section 6.13 through 6.17 was used to validate the design assumptions.

8.3.3.1 Rebar Hinge

The rebar hinge was modeled using a fiber section element extending from the footing to the base of the column section in the pretest model. This resulted in a rebar hinge element length that was taken the same as the hinge throat thickness (the gap between the column and footing) with a height of 1.5 in (38.1 mm). Implicit in this simple assumption is that all the plastic deformation at the column base occurs over the short length of the hinge throat and there is no spreading of plasticity into the column. A more accurate modeling procedure for the rebar hinge was incorporated where the hinge reinforcement was included in the column base to allow for spread of the strains along the full length of the longitudinal hinge bars. Additionally, it was unrealistic to include the column bars in the column base as the longitudinal column reinforcement had not been adequately developed in this region. The hinge and column elements were modeled as three different fiber sections as shown in figure 8.5. The hinge throat region was modeled with the hinge fiber section extending from the top of the footing to the base of the full column section (section A-A). The column base (section B-B) was modified to include the hinge reinforcement to allow for strain distribution along the longitudinal bars but did not include the column reinforcement as it was not developed in this zone. The concrete properties for the column base fiber section were the same as those used for the typical column section. The modified column section was extended 19 inches (483 mm), which was equal to the tension development length for #6 rebar from section 5.11.2.1 of the AASHTO LRFD Bridge Design Specifications (2012). This discretization allowed for the full length of the hinge reinforcement to be incorporated in the model. The full column section (C-C) was included beyond the section at which the column longitudinal reinforcement had fully developed. The material properties for each fiber section were modified as discussed in section 8.3.2.

8.3.3.2 Other Connections

The remaining connections, including the socket connections at the top of the columns, were modeled as rigid joints in the pretest model. The measured data for the column-to-cap beam socket connections (section 6.17), superstructure-to-cap beam connections (section 6.16), and deck connections (section 6.15), was assessed to determine the level of fixity provided at the respective connection, and validate the modeling assumption of a rigid joint at each of these locations. The measured results from each of these ABC connections demonstrated rigid connections between the joined elements for all earthquake runs during the shake table tests. Consequently, no adjustments were made to the modeling of these connections and each was modeled as a rigid joint in the posttest model.

8.4 Comparison of Posttest Analytical Model and Measured Results

The posttest analyses were conducted using the measured material properties, measured input acceleration records and the refined model described in the previous sections. Run 8 was included in the posttest analytical studies for a complete comparison of the model results and measured data. To evaluate the adequacy of the analytical modeling method, two important macroscopic and one key microscopic response parameters were evaluated: Bent displacement and shear, superstructure in-plane rotation, and column base hinge rotations.

8.4.1 Bent Displacement

The measured and calculated displacement and base shear histories were compared to assess the capability of the posttest analytical model in capturing the global seismic behavior of Calt-Bridge 2. The superimposed measured and calculated force-displacement hysteresis curves are shown in figures 8.6 through 8.11. The measured and calculated hysteretic responses are nearly matched in the longitudinal directions, particularly for later runs. The elastic stiffness of the bent was overestimated in the posttest model as exhibited in the difference of the measured and calculated force-displacement slopes in runs 1 and 2. This was likely caused by relative deformations in connections among elements, resulting in the system being more flexible in reality compared to the idealized condition of perfectly rigid connections assumed in the posttest model. Once plastic hinges formed in the columns and hinges (run 3 and on), the model more accurately captured the measured response of Calt-Bridge 2, because the post-yield properties of the columns and hinges were accounted for through the material constitutive relationship. The calculated response exhibited nearly symmetric behavior as was observed in the measured results, which contrasts with the behavior of the pretest model where longitudinal displacement was dominant in one direction. The hysteresis curves exhibited comparable energy dissipation between the two methods as demonstrated by the overlapping curves. The correlation between the two approaches is not as strong in the transverse direction with the peak displacements still being overestimated by the analytical model. However, the hysteresis curves are of similar width and shape for the posttest model, showing a stronger fit between the measured and calculated results for the transverse direction than that observed in the pretest analysis. The calculated elastic stiffness was also overestimated in the transverse direction, again attributed to small slippage between elements as explained for the longitudinal direction. The peak displacements were overestimated by the analytical model in the transverse direction in all runs, which was likely caused by the absence of friction forces at the abutments that resisted superstructure translation during the shake table tests. This topic is discussed further in section 8.4.3.

The displacement and base shear histories were evaluated for each run to determine how well the analytical model captured the trends and peaks in the response histories. The displacement and base shear histories are shown in figures 8.11 through 8.17. The measured and calculated peak displacements and base shears are compared in tables 8.6 through 8.9. Displacement and base shear trends were not captured accurately by the model during the smaller runs. This was attributed to the relative deformations in connections and the friction effects at the abutments, as mentioned previously. As acceleration amplitude increased, the correlation between the displacement and base shear histories improved in each direction. The posttest model accurately captured the behavior of Calt-Bridge 2 at the design level earthquake (run 3) and stronger runs. Even in these runs, the correlation between the measured and calculated results was weak for the portion of the ground motion with small acceleration. This was likely caused by the force calculation method for the measured results. If the direction of motion changed, the friction force from the table actuators would change sign and cause an abrupt change in base shear, which was not realistic behavior for the actuator friction forces. Therefore, the force trends for the measured results were less reliable for the regions where smaller acceleration caused rapid changes in translation direction. The calculated peak displacements in both directions were close to the measured results with several runs having error of approximately 10%. Peak base shears were nearly identical between the two models in the longitudinal direction but with approximately 10% error in the transverse direction.

The results from the posttest analytical model demonstrated that the global behavior of a bridge built with ABC techniques and connections subjected to earthquakes can be estimated with reasonable accuracy using an available structural analysis software. Each ABC connection was modeled in Opensees and exhibited similar behavior to what was measured in the shake table tests. This illustrates that conventional modeling techniques for CIP concrete structures may be adopted for ABC bridges in some applications. The difference between the pretest and posttest analysis results highlights the importance of implementing accurate material models and ground motion records for predicting bridge behavior for seismic loading.

8.4.2 Hinge Rotation

Analytical models are often used in practice to predict system level response of bridges such as the bent force-displacement response. Column characteristics dominate the bent hysteretic response, however microscopic response of joints and interaction among components also influence the bridge behavior. Posttest modeling of Calt-Bridge 2 resulted in improved correlation between the measured and calculated force-displacement response as discussed in section 8.4.1, which showed that macroscopic response of bridge elements could be reasonably captured using Opensees. In addition to these comparisons, it is useful to evaluate the capability of the model to capture microscopic characteristics such as joint behavior under dynamic loading to establish the boundaries of the level of detail that can be estimated by the analytical model. Many of the ABC connections behaved as near rigid elements during the shake table tests. The small relative deformations in these connections, although present, could not contribute significantly to the overall bridge response. Therefore, comparing the measured and calculated deformations in these connections would not serve any purpose. The two-way column hinges at the column-to-footing connections were an exception as the hinges were expected to undergo relatively large rotations due to their small cross section and yielding of the hinge longitudinal bars during the shake table tests. The results from section 6.14 demonstrated that the rebar hinges did indeed experience large rotations and allowed for comparison of measured and calculated connection behavior. The nodal rotations at the top of the hinge throats (nodes 3 and 4, figure 5.1) were compared to determine the correlation between the measured and calculated results.

The measured and calculated peak hinge rotations at the base of both columns were compared in each direction and are listed in table 8.10 and 8.11 for the longitudinal and transverse directions, respectively. Note that the direction in which the measured peak rotations occurred varied among the runs. The comparison was made between the measured peak rotation regardless of the direction and the corresponding calculated peak rotation.

The hinge rotations were generally overpredicted by the analytical model and correlation with the measured results was poor with percent differences ranging between 3% and 95% for all directions. Agreement was slightly better in the longitudinal direction with an average percent difference of 35% compared to 48% in the transverse direction. This is consistent with the trends observed in the bent hysteretic response with better matching achieved in the longitudinal direction relative to the transverse. The calculated hinge rotations were closer to the measured rotations in early runs with an average percent difference of 34% in runs 1-3 compared to 51% in runs 4-8. This implies the model was better at predicting hinge rotation when the elements were still essentially elastic but was not as good in reproducing the peak rotations when the rebar hinges had experienced substantial yielding. These differences highlight the limitations of analytical modeling of microscopic effects in Opensees. The macroscopic characteristics such as column displacement and base shears can be reasonably predicted as demonstrated in section 8.4.1. However, the microscopic response of connections such as interaction between the rebar hinge grout and column pocket connection cannot be correctly modeled in Opensees. For applications where accurate prediction of connection performance is required, a finite element model capable of capturing microscopic interaction between elements would be necessary.

The rebar hinge rotation histories were also evaluated to determine the trend during the earthquake simulations. The design level run (run 3) and 200% of the design earthquake (run 7) were selected to identify the trends for limited and extensive yielding and damage cases. The longitudinal and transverse hinge rotation histories for runs 3 and 7 are shown in figures 8.20 and 8.21, respectively. It was observed that the rotational behavior of the rebar hinges in Calt-Bridge 2 was largely captured by the analytical model with the rotation history trends being well matched between the measured and calculated results, especially for the strong portion of each ground motion. The analytical model often overpredicted the rotational response of the hinge as also demonstrated in the comparison of peak hinge rotations in each run; however, the peaks were in phase for the main portion of the ground motions in each direction, meaning the hinge rotational behavior was mostly captured in the model. These results indicate that connection behavior during ground motions can be approximated in Opensees with fairly accurate response trends. However, prediction of the peak hinge rotations was not accurate, and therefore the response histories generated from a macroscopic bridge system model are limited in application and should only be used as an estimate of local connection behavior, rather than precise prediction of peak deformations.

8.4.3 Superstructure In-plane Rotation

Large in-plane superstructure rotations were observed during shake table testing of Calt-Bridge 2 as shown in figure 6.42, which ultimately limited the displacement response of the structure due to termination of testing to prevent superstructure unseating at the abutments. The same trend was observed in testing Calt-Bridge 1 (Benjumea et al., 2019). The in-plane rotation of the posttest model was calculated to determine if the rotational effects were captured using dynamic analysis. The transverse displacement of each girder was averaged at each abutment to calculate the superstructure displacement at that abutment. The in-plane rotation was calculated by taking the difference between the superstructure displacements at the abutments and dividing by the total superstructure length (70 ft, 21.3 m).

The in-plane rotation for all eight runs is shown in figure 8.22. Calculated in-plane rotation was small in runs 1 and 2 but increased during run 3 as was also observed in the measured response. However, significant residual in-plane rotation was observed in Calt-Bridge 2 in run 3 and later runs, which was not captured by the posttest model. The peak calculated in-plane rotation was 0.004 radians in run 5 with only slight increases observed in each successive run with a peak in-plane rotation of 0.005 radians calculated during run 8. The calculated in-plane rotation was much less than the measured in later runs with a peak difference of 0.0188 radians in run 8, a percent difference of 376%.

It is believed that the analytical model was not able to capture the in-plane rotation of Calt-Bridge 2 because the friction forces at the abutments were not included, but rather the superstructure-interface was modeled using frictionless roller supports. In-plane rotation of the superstructure likely occurred from uneven distribution of horizontal forces at the abutments. When friction is accounted for at the stainless steel on PTFE interface, the horizontal forces are not constant due to the change in abutment reactions due to longitudinal translation of the superstructure. As the superstructure moves longitudinally, uplift is produced at one abutment, while downforce is generated at the opposite end. This creates uneven frictional forces at the abutments and can cause the superstructure end experiencing downforce to lock up, while the superstructure moves transversely at the opposing abutment, which produces in-plane rotation. As explained in previous chapters, the abutments were essentially locked during the first run because the earthquake forces were not sufficient to overcome abutment friction. Longitudinal displacement was small in run two, which resulted in relatively even distribution of friction forces and consequently small in-plane rotations. However, as the longitudinal superstructure displacement increased in later runs, the difference in vertical load at the abutments increased, resulting in relatively large differences in the frictional forces between the east and west abutments, and large in-plane rotations. Since the same ground motion record was used for each run, only differing in acceleration scale factors, transverse displacement was initiated under locked conditions at the opposite abutment repeatedly causing in-plane rotation to progressively increase. Eventually, the difference between the vertical abutment reactions was expected to stabilize as the bent plastic shear was reached. The rate of increase in in-plane rotation among the runs would be expected to remain the same for this damage state if the ground accelerations remained constant. However, transverse displacements continued to increase due to larger ground accelerations in successive runs, which explains the continued increase in in-plane rotation relative to the previous run. This phenomenon was explored using a detailed parametric study of friction effects on in-plane rotation and is presented in chapter 9.

Chapter 9. Parametric Study of Abutment Friction Effects

9.1 Introduction

Several modifications were made to the pretest analytical model to improve correlation between the calculated and measured results (chapter 8). The measured force-displacement response and displacement histories were reasonably estimated by the posttest model. However, the in-plane rotation measured in Calt-Bridge 2 was not captured most likely due to friction forces at the abutments not being accounted for in the model. Flat slider bearing elements were incorporated in OpenSees between the abutment and girder base to simulate friction effects at the abutment ends. Multiple analyses were conducted with varying friction coefficients and friction locations to determine the case that best captured in-plane rotation. The force-displacement response of the model with friction effects included was also evaluated to ensure that in-plane rotation of the superstructure had been captured without compromising the model accuracy that was achieved through the posttest model.

9.2 Modifications to Posttest Analytical Model

9.2.1 Modeling of Friction Elements

FlatsliderBearing elements (Opensees, 2014a) were incorporated in the posttest Opensees model to simulate the effects of abutment friction. Even though Calt-Bridge 2 was symmetric, differential friction forces could develop at the abutments because of uneven reactions at abutments caused by the longitudinal movement of the bridge model. The flatsliderBearing element can have zero length and utilizes coupled friction properties for the shear deformations in the longitudinal and transverse directions and uses material models to represent the element stiffnesses in the vertical and rotational directions. The uplift effect is accounted for by not allowing for tensile forces develop during uplift of the superstructure. A velocity dependent friction model (Opensees, 2014b) was incorporated in the flatSliderBearing element to represent the polytetrafluoroethylene (PTFE) on stainless steel interface. This model was selected because of its inherent dynamic properties allowing the user to specify the friction coefficient at low and high velocities, which was representative of the bearing interface at the abutments in shake table testing of Calt-Bridge 2. The axial stiffness of the element in the direction of gravity was modeled using an Elastic material model with high stiffness to prevent relative vertical movement at the abutment seats. The flatSliderBearing elements were modeled with no stiffness in the rotational degrees of freedom.

Fixed nodes were placed at the same location as the girder base nodes at the ends to represent the abutment. The friction model was incorporated using zero length flatSliderBearing elements between the abutment nodes and the girder base nodes. The girder nodes were fixed to prevent vertical displacement in the model to represent the fixity provided by the abutments, however this condition was removed for the friction studies as the abutment stiffness was implicit in the bearing element. The element was oriented such that the i-node (first specified node) was the abutment node and the j-node (second specified node) was the girder base as recommended in the element description.

9.2.2 Friction Model Configurations

Friction effects on superstructure in-plane rotation were modeled at the abutments in three different configurations (figure 9.1). These models included friction at both abutments (FM-1), friction at the east abutment (FM-2), and friction at the west abutment (FM-3). Results from the post-test model with no friction effects included (NF) were used as a benchmark. These three friction configurations were selected to investigate which of two factors were the primary cause of the in-plane rotation: (1) differences between the vertical reactions at the abutments (caused by the frame action of the bridge under longitudinal displacements), or (2) differences between the friction coefficients between the two abutments. The latter could be a result of uneven variation in construction of the bearings and damage in the PTFE bearing pads.

9.2.3 Selection of Friction Coefficients

The velocity dependent friction model was defined using friction coefficients for low (f_{min}) and high velocity (f_{max}), and the transition rate from f_{min} to f_{max}. Initially friction coefficients calculated for Calt-Bridge 1 (Benjumea et al., 2019) were incorporated, which had coefficients of friction at low velocity (f_{min}) and high velocity (f_{max}) of 0.02 and 0.05, respectively. The transition rate from f_{min} to f_{max} was assumed to be 0.635 s/in (25 s/m), which was the average rate for unfilled PTFE reported by Constantinou et al. (1999). The three friction models were analyzed using these friction coefficients for run 7 and the cumulative runs, with run 7 representing the effect of one strong earthquake on a bridge without any damage from prior earthquakes and the cumulative runs simulating the effect of the actual shake table loading history.

The in-plane rotation histories (for the 0.02/0.05 friction coefficients) are shown in figures 9.2 and 9.3. All the models resulted in lower in-plane rotations in run 7 than were measured during the shake table tests suggesting that the 0.02/0.05 coefficient combination was perhaps not sufficiently large, although FM-3 exhibited closer correlation to the measured peak rotation response.

To investigate if increasing the friction coefficient would lead to higher in-plane rotations, the friction coefficients were varied to determine the sensitivity of calculated in-plane rotation to the friction coefficients. Five friction variations were incorporated in FM-1 including friction coefficients of: very low (f_{min} = 0.02, f_{max} = 0.05), low (f_{min} = 0.05, f_{max} = 0.08), medium (f_{min} = 0.10, f_{max} = 0.13), high (f_{min} = 0.15, f_{max} = 0.18), and very high (f_{min} = 0.25, f_{max} = 0.28). The difference between f_{min} and f_{max} was retained for all friction variations.

The in-plane rotations for different friction coefficients were calculated for the FM-1 configuration and are shown in figure 9.4. The peak and residual in-plane rotations increased as the friction coefficient increased. The relationship between peak in-plane rotation and the low velocity friction coefficient is shown in figure 9.5. The in-plane rotation was increased by over 80 percent when the friction coefficient was changed from 0 to 0.02 showing that even incorporating small friction forces at the abutments can have significant impact on the system response. Peak in-plane rotation increased linearly for small friction coefficients. However, as the friction coefficient became large the slope decreased, which demonstrated that increasing the friction coefficient can improve the response only to certain extent.

After evaluating the sensitivity of in-plane rotation to the friction coefficient, the individual (run 7) and cumulative ground motions were applied to each friction model (FM-1, FM-2, and FM-3) with the high friction coefficient variation (f_{min} = 0.15, f_{max} = 0.18). These friction coefficients were selected because it resulted in large peak in-plane rotations in run 7, while maintaining realistic friction coefficients for a stainless-steel on PTFE bearing surface. Increasing the high friction coefficients by 0.1 for the very strong friction case resulted in only slightly higher peak superstructure in-plane rotations, which demonstrated that using a very high friction coefficient would not affect the response and may lead to unrealistically high shear forces at the abutments. The "high" friction coefficients were larger than the recommended value of 0.1 for unfiled PTFE at room temperature with the minimum listed contact stress of 0.5 ksi (3.4 MPa) as listed in table 14.7.2.5-1 in the AASHTO LRFD Bridge Design Specifications (2012). However, the contact stress in the bearing pads for Calt-Bridge 2 was only 0.06 ksi (0.414 MPa). The low bearing stress was a result of PTFE pad width to meet the seat width requirement, a service condition, rather than the strength requirements. Contact stress is inversely proportional to the friction coefficient for stainless-steel on PTFE interfaces; therefore, the friction coefficient was expected to be larger than 0.1. Additionally, some damage was observed in the PTFE pads during shake table testing, which would also lead to larger friction forces at the bearing.

9.3 Effects of Friction Forces at Abutments

9.3.1 In-Plane Rotation

Parametric studies of friction effect on superstructure in-plane rotation were conducted using dynamic analyses in Opensees . The in-plane rotation history in run 7 for each model is shown in figure 9.2. Note that the measured residual in-plane rotation that was present prior to the start of run 7 has been removed. Inclusion of abutment friction increased the calculated in-plane rotation compared to the case of no friction; however, none of the models estimated the in-plane rotations accurately. The in-plane rotation trend for FM-1 most closely resembled the measured trend, but the peak in-plane rotation was 0.0037 radian compared to 0.0078 radian for the measured results. FM-3 had the highest peak in-plane rotation of 0.0055 radian, but the residual displacement was much lower than the peak, a trend that not observed in the measured data. FM-2 and NF did not experience significant in-plane rotation in run 7.

A dynamic analysis using the cumulative achieved ground motion record was applied to all the configurations for comparison of the cumulative calculated and measured data (figure 9.3). Again, none of the models captured the in-plane rotations that were observed during shake table testing of Calt-Bridge 2. Rapid increases in in-plane rotation were calculated for FM-1 in each run, but the peak and residual in-plane rotations were much less than the measured response. FM-2 experienced more in-plane rotation in the cumulative analysis than was observed for a single run and the peak in-plane rotations were larger. FM-2 had nearly identical peak in-plane rotations as the NF model, which indicated that friction effects at the east abutment did not have a significant impact. Conversely, FM-1 and FM-3 had similar in-plane rotation trends but with lower peak in-plane rotations. The small in-plane rotations calculated in each of the friction configurations indicated that the friction coefficient was likely much higher during the shake table tests than was assumed using the low friction coefficients of 0.02 and 0.05.

The dynamic analyses were repeated using the high friction coefficients (f_{min} = 0.15, f_{max} = 0.18) for both the individual run and the cumulative runs (figures 9.6 and 9.7). Peak calculated in-plane rotations were higher than those from the low friction models in run 7, but the peak in-plane rotation was still underestimated relative to the measured data. The in-plane rotation trend for FM-1 was the same for both low and high friction variations, but larger in-plane rotations were observed in the high friction variation of the model. Distinct jumps in the in-plane rotation were observed in all the runs for FM-1, but not to the same extent as those in the measured in-plane rotation. The high friction variation of FM-2 also resulted in larger peak in-plane rotations, but residual in-plane rotation was much lower than was observed in the shake table tests and followed a similar trend to the NF model and low friction variation of FM-2. The residual in-plane rotation in run 8 was much larger than that of the previous seven runs; however, this is attributed to run 8 being incomplete, resulting in the system not rebounding fully. The in-plane rotation increased in FM-2 when the friction coefficient was increased, which indicated that friction at the east abutment did have a small impact on the superstructure rotational response, but not to the same extent as friction at the west abutment. In-plane rotation of FM-3 had the closest correlation with the measured data, exhibiting a particularly close match in runs 1 through 6. Residual in-plane rotation only increased by 0.002 radian in run 7 and decreased in run 8, compared to an increase of 0.006 radian and 0.008 radian in runs 7 and 8 for the measured results, respectively. The correlation in the in-plane rotation between FM-3 and the measured data indicated that friction at the west abutment was the largest contributor to superstructure rotation. In-plane rotation was presumed to be initiated by longitudinal translation of the superstructure towards the abutment followed by transverse displacement, while the abutment was in an instantaneous locked condition. Therefore, when multiple ground motions were applied in subsequent runs with varying acceleration amplitude, the locking was repeated at the same location. This meant that the mechanism inducing in-plane rotation in the superstructure would be more dependent on the friction characteristics at one abutment rather than both.

Friction at the west abutment had a clear impact on the rotational response of the superstructure. The good correlation between FM-3 and the measured response implies that the frictional behavior at the stainless steel on PTFE interface was inconsistent during shake table testing, particularly during later runs. Incorporation of a high friction coefficient at the west abutment with no friction at the east abutment resulted in good estimation of in-plane rotation in runs 1 through 6, which infers the bearing interface at the west abutment may have had inconsistencies in the bearing contact surface, in addition to large transverse displacements occurring during longitudinal superstructure displacement towards the west abutment. Additionally, the measured residual in-plane rotation was much closer to the peak rotation for runs 7 and 8, which may have resulted from damage in the bearings causing the system to not rebound to the same extent as earlier runs. Some possibilities that may have caused additional friction include: uneven contact of the stainless steel plate with the PTFE pad, which could cause the corners of the steel plate to bear into the PTFE pad rather than slide across it; or the girder bases could have been at slightly different elevations resulting in one or more girders not contacting the PTFE pad, resulting in uneven bearing of the superstructure on the abutment. These factors explain the initiation of in-plane rotation in lower runs, but it was likely that the damage to one or more of the PTFE pads in run 6 or 7 that caused the in-plane rotation to greatly increase. This explains why the model captured the in-plane rotation behavior of Calt-Bridge 2 for early runs but poorly estimated the in-plane rotation in runs 7 and 8.

9.3.2 Fundamental Periods

The effect of friction on the system rotational response was further evaluated using modal analyses of the friction models. A modal analysis was conducted for each friction model with only gravity loads applied using initial properties of the elements. The calculated fundamental periods were compared to those from the pretest analytical model and the analytical models without friction effects. These results are listed in table 9.1. The periods associated with in-plane rotation in models with friction were much shorter than those from the pretest and frictionless models; suggesting coupling between the translational and rotational mode shapes may have been present during the shake table tests.

From the data in Table 9.1, it is evident that the fundamental periods from the no-friction models were longer than those measured in Calt-Bridge 2, which implied the system was stiffer than was calculated by these models. However, when friction effects were included, the longitudinal and transverse mode periods became close to those measured during the shake table tests, particularly for FM1 in which friction was included at both abutments. These results demonstrate that friction had a significant effect on the dynamic characteristics of Calt-Bridge 2. Additionally, the in-plane rotational mode period became very close to the longitudinal and transverse vibration periods in FM1, indicating that friction at both abutments led to highly coupled response in the longitudinal, transverse, and rotation directions. This may explain the absence of in-plane rotation in the no-friction analytical models and prominence of in-plane rotation in the measured data and friction models.

9.3.3 Force-Displacement Response

Incorporation of friction effects at the abutments improved correlation between the calculated and measured superstructure in-plane rotations, particularly for FM-3. However, it was important to assess the analytical models to ensure the hysteretic response in the posttest model had been retained after modifying the abutment properties. The force-displacement relationships for the cumulative ground motions were evaluated for the three friction models to determine if the measured response of Calt-Bridge 2 was still captured with reasonable accuracy that was shown in Ch. 8. Only the high friction variations of the friction models were evaluated as the in-plane rotations showed better correlation to the measured data for this configuration.

The hysteretic responses of the analytical models are shown in figures 9.8 to 9.10. The force-displacement response from the posttest model with no friction effects is shown in figures 8.6 to 8.11. The peak base shears in the bent did not change among the three models; however, the friction forces at the abutments reduced the displacements. Consequently, the peak bent displacements in the longitudinal and transverse directions were smaller than the NF model. In all three friction models, the longitudinal displacement response in the negative direction was much less than the measured response. However, the peak response in the positive direction was mostly retained. The calculated longitudinal displacements from FM-1 were smaller than the measured displacements in both directions, whereas the peak displacements were matched well with the measured data for FM-2 and FM-3. FM-1 was expected to have smaller displacements compared to the those from the other friction models because the friction forces were included at both abutments resulting in twice as much friction resistance than that of FM-2 and FM-3. The same trends were observed in the transverse direction with FM-1 underestimating the peak displacements, and FM-2 and FM-3 showing particularly good correlation with the measured data.

Evaluation of the base shears and displacements from the three friction models showed that including friction did not affect the calculated hysteretic response drastically. The displacement response from FM-2 and FM-3 was improved from the posttest model described in chapter 8, exhibiting better correlation of the hysteretic response between the calculated and measured results in the positive longitudinal direction, and both negative and positive transverse directions. This again supports that strong friction forces were concentrated at one abutment, rather than distributed over both. The longitudinal displacements were slightly underestimated, which implies that friction may have been stronger in the transverse direction and not have influenced the longitudinal direction as significantly. This was supported by the observation of transversely oriented scratches in the PTFE bearing pads at the conclusion of testing for Calt-Bridge 2. The correlation of calculated displacements, base shears, and in-plane rotation from FM-3 and the measured data validate that significant friction forces occurred at the west abutment inducing the in-plane rotation of the superstructure that was observed in the test.

Chapter 10. Comparison of Seismic Performance of Three ABC Bridge Models

10.1 Introduction

Three 0.35 scale, two-span bridge models were tested in succession on the shake tables in the Earthquake Engineering Laboratory (EEL) at the University of Nevada, Reno. All bridges were constructed using ABC methods, specifically utilized prefabricated elements and systems (PBES), and incorporated ABC connections between elements. The purpose of each project was to implement several ABC connections that had performed well in past component studies and determine the overall bridge and connection performance when subjected to biaxial forces as part of a bridge system. The following three bridge models were tested: (1) the first bridge was tested by Benjumea et al. (2019) and was labeled Calt-Bridge 1, which consisted of concrete components including prestressed precast girders, (2) the second bridge model was labeled ABC-UTC and was tested by Shoushtari et al. (2019), which was a steel girder bridge with reinforced concrete bent and precast deck panels, (3) and the third bridge model was labeled Calt-Bridge 2 and is the subject of this report (prestressed concrete girder bridge, reinforced concrete bent, and precast deck panels). Detailed information regarding Calt-Bridge 1 is in Benjumea et al. (2019) and ABC-UTC is in Shoushtari et al. (2019). Because the bridges had the same overall geometry and target ground motion histories, there was an opportunity to assess the performance of bridges relative to each other. This chapter presents a comparison of the key aspects of three bridge models including the design and shake table performance and test results. Some ABC connections were used in two or more of the bridge models. In these cases, the connection performance in each model was compared to determine any differences in the connection response among the bridges. Other connections were incorporated in the same joint location, (e.g. column-to-cap beam connection), but the connection detail differed, (e.g. grouted duct connection for Calt-Bridge 1 and ABC-UTC, socket connection for Calt-Bridge 2). In these cases, the relative joint performance was compared and recommendations for one or both connections were made based on the design criteria for the respective joint.

10.2 Overview of Bridge Models

The purpose of this chapter is to compare the ABC connections incorporated in the same joint locations. The bridge model properties, loading protocol, and shake table test results are briefly summarized in this section to establish a baseline for comparison of the bridge systems and hence, the ABC connections.

10.2.1 Bridge Models Properties

The three bridge models were scaled versions of a prototype bridge representative of a typical two-span highway bridge. Scaled versions of the prototype bridge were used for these studies due to geometric and weight limitations imposed by the shake tables and EEL building. The prototype bridge details for Calt-Bridge 1 and Calt-Bridge 2 are summarized in section 2.2. A version of this prototype incorporating steel girders was utilized for the design of ABC-UTC. Three dimensional schematics of Calt-Bridge 1 and ABC-UTC are shown in figure 10.1 and 10.2, respectively, and the construction planset for Calt-Bridge 2 is presented in Appendix A. A summary of the scaled bridge model properties is listed in table 10.1. Calt-Bridge 1 and Calt-Bridge 2 had the same superstructure component configurations and dimensions, which caused the seismic weight to be nearly identical between the two structures. The small difference in weight was a result of the wider cap beam in Calt-Bridge 2 to accommodate the column-to-cap beam socket connection. ABC-UTC was significantly lighter than the other two bridges due to the use of steel girders. Consequently, the diameter of the columns and the longitudinal and transverse column reinforcement area was smaller. However, the axial load indices of Calt-Bridge 1 and Calt-Bridge 2 were smaller than that of ABC-UTC because the payload limitations of the shake tables prevented placement of additional superimposed weight on the superstructure of the concrete girder bridges.

10.2.2 ABC Connections

Six ABC connections were incorporated in each bridge model. The design of the ABC connections in Calt-Bridge 2 is discussed in section 2.6 but the connections are listed here for convenience: (1) a rebar hinge precast with the footing connected to the column via a pocket for the column-to-footing connection, (2) a fully precast socket connection for the column-to-cap beam connection. (3) extended strands and headed bars enclosed in the cast-in-place (CIP) portion of the cap beam for the girder-to-cap beam connection, (4) lap spliced straight bars embedded in ultra-high performance concrete (UHPC) for the deck connection over the pier, (5) precast deck panels to girder connection using deck pockets and projected steel studs from precast concrete girders, and (6) short embedment length lap spliced straight bars for female-to-female deck panel-to-panel connection.

Calt-Bridge 1 incorporated the following ABC connections: (1) base pipe-pins to attach the columns to the footing, (2) column to cap beam connection formed by grouted duct connections between the column and a precast segment of the cap beam with the column bars extended into the CIP part of the cap beam, (3) extended strands and headed bars enclosed in the cast-in-place portion of the cap beam for the girder-to-cap beam connection, (4) lap spliced straight bars embedded in ultra-high performance concrete (UHPC) for the deck connection over the pier, (5) precast deck panels to girder connection using deck pockets and projected steel studs from precast concrete girders, and (6) short embedment length lap spliced straight bars for female-to-female deck panel-to-panel connection.

The following ABC connections were utilized in ABC-UTC: (1) rebar hinge with socket connection in the footing, (2) grouted duct connection for the column-to-cap beam connection, (3) seismic simple for dead continuous for live (SDCL) girder-to-cap beam connection, (4) lap spliced straight bars embedded in ultra-high performance concrete (UHPC) for the deck connection over the pier, (5) precast deck panels to girder connection using deck pockets and projected steel studs from steel girders, and (6) short embedment length lap spliced straight bars for female-to-female deck panel-to-panel connection.

The same rebar hinge design procedure was used for the column-to-footing connection in Calt-Bridge 2 and ABC-UTC. However, the connection in ABC-UTC consisted of a rebar hinge precast with the column, which was fit into an opening in the footing to form a socket connection. This was different from the detail utilized in Calt-Bridge 2 where the rebar hinge was projected from the footing and connected via a pocket in the column base that was filled with grout. The same grouted duct detail was used to connect the columns to the cap beam in Calt-Bridge 1 and ABC-UTC. The four superstructure connections (3-6 in the above lists) were utilized in both Calt-Bridge 1 and Calt-Bridge 2. The main difference between these two bridge models consisted of the column connections with pipe-pin vs. rebar hinge incorporated at the column bases, and grouted duct vs. socket connection at the column tops. This allowed for direct comparisons of the column top and bottom connection performance and assessment of the connections impact on the bridge system response.

Precast deck panels were used in all three bridges with similar deck panel-to-panel and panel-to-girder connections utilized in each case. The same panel layout was incorporated in Calt-Bridge 1 and Calt-Bridge 2. The deck panel configuration differed for ABC-UTC with only transversely oriented deck panels utilized. This resulted in no longitudinal deck joints in ABC-UTC.

10.2 Seismic Performance of Bridge Models

10.2.1 Loading Protocols

The bent capacities for each bridge model were calculated in the longitudinal and transverse directions using pushover analyses in Opensees. The capacities and displacement demands for each bridge are listed in table 10.2. The idealized capacity curves were calculated by using the displacement and base shear at first yield to calculate the effective elastic bent stiffness. The effective yield displacement and plastic base shear were determined by equating the areas under the idealized and calculated capacity curves. Note that the ultimate displacement in Calt-Bridge 2 was assumed to be equal to 8% drift, which differed from the approach used to calculate the ultimate displacement in ABC-UTC and Calt-Bridge 1. In those two cases, the ultimate displacement was taken as either when the longitudinal column reinforcement had ruptured, or core concrete strains of 1.25 times the confined ultimate strain capacity, ε_{cu}, were observed. This approach was modified for Calt-Bridge 2 because crushing of concrete within one fiber does not immediately result in bent failure, and additional capacity was still observed in the calculated capacity curve after the other material limits had been exceeded. The displacement demand, displacement ductility capacity, and displacement ductility demand were calculated for each bridge in the longitudinal and transverse directions.

Calt-Bridge 2 was the stiffest bridge, which was a result of the relatively large moment capacity of the rebar hinge at the column base compared to that of the pipe-pin incorporated in Calt-Bridge 1, and larger, stiffer column sections than those in ABC-UTC. Calt-Bridge 1 was the most flexible system, which attests to the pin-like behavior provided by the pipe-pin connection because of reduced moment in the column base. Despite having large differences in seismic mass and effective stiffness, Calt-Bridge 2 and ABC-UTC had similar effective periods and spectral accelerations, which resulted in nearly equal displacement demands in both bridges. The displacement demand in Calt-Bridge 1 was larger because of the relatively small effective bent stiffness. The resultant displacement demand was calculated using the procedure described in section 5.3.2.

The 1994 Northridge earthquake measured at Sylmar station was used as the input ground motion with horizontal components SCS052 and SCS142 assigned to the longitudinal and transverse directions, respectively for all the bridges. The time history was compressed by the square root of the geometric scale factor to account for scaling effects. Nonlinear dynamic analysis was performed in Opensees using 3-D grillage models to calculate the peak resultant displacement for the applied ground motion. The acceleration record was scaled such that the peak resultant displacement of the analytical model was equal to the calculated displacement demand. The ground motion record utilizing these scaled accelerations was defined as the design level earthquake. Loading protocols were generated that incorporated multiple earthquake runs of varying scale factor to capture different limit states. The final loading protocols for each bridge are listed in table 10.3. Note that the design earthquake was run 3 for ABC-UTC and Calt-Bridge 2 and run 4 for Calt-Bridge 1.

10.2.2 Shake Table Test Results

Eight earthquake runs were applied to each bridge, beginning with run 1 and concluding with run 8 (table 10.3). Shake table testing of Calt-Bridge 1 and Calt-Bridge 2 was terminated during run 8 after the peak input acceleration had been applied due to concerns about unseating of the superstructure at the abutments that resulted from in-plane rotation. However, because the peak accelerations of the ground motions in run 8 had been applied, the results from that run were still deemed indicative of the effect of the 200% and 225% design level earthquake for Calt-Bridge 1 and Calt-Bridge 2, respectively. Bridge system ultimate state was caused by excessive superstructure displacements at the abutments and not by failure of the columns. Therefore, the ultimate capacity of the bents was not determined. However, reduction in peak base shear during the last runs suggests that failure was imminent in both bridge models. In contrast to Calt-Bridge 1 and 2, the bent in ABC-UTC did reach its near failure state during run 8 due to buckling of column longitudinal bars and extensive column core damage.

The peak bent displacements and drift ratios in each run for each bridge are listed in table 10.4, and the peak drift ratio in each run is shown in figure 10.3. The hysteresis curves for the longitudinal and transverse directions for all runs are shown in figure 10.4. Calt-Bridge 2 was the stiffest of the three bridges as exhibited by the relatively low drift ratios in both directions as well as relatively high base shears, particularly in later runs. This behavior was expected due to the larger column sections than those in ABC-UTC and larger column base moment capacity than Calt-Bridge 1. ABC-UTC experienced constant increases in peak displacements in runs 1 through 6 but the peak longitudinal displacements decreased in runs 7 and 8. However, the peak resultant displacement still increased in the last two runs because of large increases in peak transverse displacement. Calt-Bridge 1 displayed stable increases in displacement and base shear as runs progressed. In all three bridges ductile column plastic hinges were formed with no strength degradation as exhibited by the sustained plastic base shear in the hysteresis curves (figure 10.4). Wide hysteresis loops showed that energy dissipation was maintained in all runs, which implied that progressive yielding occurred in the bridge systems while the force and displacement demands were resisted by the bridge components and connections during the shake table tests.

10.3 Comparison of ABC Connection Performance

The bridge models incorporated ABC connections at the following locations: (1) the column-to-footing connection, (2) column-to-cap beam connection, (3) girder-to-cap beam connection, (4) deck panel connection over the pier, (5) deck-to-girder connection, and (6) deck panel-to-panel connection. The ABC connections at the same joint locations were compared against each other to determine relative joint performance. Connection behavior was assessed using the following parameters: (1) the ability of the joint to transfer loads between connected elements, (2) the amount of relative displacement or slippage between joined elements, and (3) visual inspection of joint integrity particularly for capacity protected members or when adjacent to plastic hinges. ABC connection performance was evaluated for each connection relative to its intended function, and connection details incorporated at the same joint type were compared to determine if any offered considerably better behavior for ABC bridge systems.

10.3.1 Column Base Connection

A pipe-pin connection based on the detailing recommendations by Mehraein & Saiidi (2016) and Mehrsoroush & Saiidi (2014) was incorporated at the base of the columns in Calt-Bridge 1. Rebar hinges were designed according to the procedure developed by Cheng et al. (2009) as described in section 2.6.1 and were incorporated in the column base connections in ABC-UTC and Calt-Bridge 2. However, the hinge connection detail differed between the two bridges as ABC-UTC incorporated socket connections with opening in the footing, while Calt-Bridge 2 used pocket connections with pocket in the column base. The details for the rebar hinge in each bridge are shown in figure 10.5. The differences between socket and pocket connections for rebar hinges is explored in section 10.3.1.1 and their seismic performance is compared to the pipe-pin connection in section 10.3.1.2.

10.3.1.1 Comparison of Socket and Pocket Connections for Rebar Hinges at Column Base

Ten inch (254 mm) diameter rebar hinges were incorporated at the column bases for ABC-UTC and Calt-Bridge 2. The hinge reinforcement consisted of 6-#5 longitudinal bars with a 1.5 in (38.1 mm) pitch #3 spiral in ABC-UTC, and 6-#6 longitudinal bars with a 1.5 in (38.1 mm) pitch #3 spiral in Calt-Bridge 2. A 1.5 in (38.1 mm) gap was provided between the bottom of the column and the top of the footing for both bridges, which will hereafter be referred to as the "hinge throat" (see figure 10.5). The rebar hinges in ABC-UTC were precast with the columns, which made the hinge a reinforced concrete section that was connected to the footing via a socket connection, as defined in (Saiidi et al., 2020). In contrast, pocket connections (as defined in Saiidi et al. ,2020) were used to connect the exposed rebar hinge stem and the columns in Calt-Bridge 2. Therefore, the rebar hinge material consisted of the grout used to form the pocket connection. This resulted in the rebar hinge throat consisting of grout rather than concrete. The hinges in both bridges were designed to withstand the base shear and axial load demand for the respective bridge. Using the test results for the two bridge, the hinge performance was compared and the influence of socket versus pocket connections on the joint behavior was determined.

10.3.1.1.1 Visual Assessment of Hinge Performance

The apparent damage state for the rebar hinges was assessed after each earthquake test run. Pictures of each rebar hinge at the conclusion of the shake table tests are shown in figure 10.6. Formation of plastic hinges in the rebar hinges was visually confirmed by inspection of the hinge throats and was evident by the presence of significant spalling of concrete or grout at the throats. In ABC-UTC, no flexural or shear cracks were observed on or near the face of the column adjacent to the hinge. Significant spalling was observed in the cover concrete of the hinge throat with the spiral reinforcement becoming visible after run 8. No rupture of the longitudinal hinge reinforcement was observed. In Calt-Bridge 2, there was significant spalling of the cover grout in the hinge throat with the spalling extending a short distance into the lower part of the pocket connection. The hinge spiral reinforcement was exposed during run 5 but no longitudinal bar rupture was observed during the shake table tests. The column edges did not bear on the footings for either bridge, meaning the hinge gap was sufficiently thick to allow for column rotation without gap closure. In both cases, the rebar hinges experienced significant damage during strong ground motions and would need to be repaired potentially by injecting grout to replace the spalled concrete. However, damage was prevented in the footing and column base, and hinge integrity was maintained for all earthquake runs, which illustrated the rebar hinges fulfilled the design purpose.

10.3.1.1.2 Measured Strains

The rebar hinges were instrumented with many strain gages to detect yielding and damage propagation in critical parts of the bridge model as the earthquake intensity increased. Each hinge was instrumented at three heights including mid-depth of the hinge throat, and 6 in (152 mm) above and below that level, along the longitudinal rebar in the north, south, northwest, and southeast edges (figure 4.3). In addition, the spiral reinforcement was instrumented at the north, south, east, and west edges at the footing-hinge base interface, and 6 in (152 mm) above the interface (figure 4.4). The peak hinge strain profiles normalized to the respective yield strain for both bridges for each run are presented in figure 10.7. Level "0" indicates the mid-depth of the hinge throat. The yield strain is indicated by a dashed red line in both strain profiles. No yielding was observed for ABC-UTC during the first run, but significant yielding occurred from run 2 onwards. The peak strain for the longitudinal hinge bars was 22.3 times the yield strain for ABC-UTC. The strain profile trends show that as the earthquake intensity increased, the peak strains in the rebar hinge longitudinal bars continued to increase. Peak strains were concentrated at the footing-hinge base interface at which essentially all the base rotation took place. There was significant strain dissipation when moving up into the column or down into the footing, which implied that the rebar hinge stem was properly anchored within the column and footing via the socket connection. The peak measured strain in the transverse bars was 81% of the yield strain, meaning the spirals did not yield at any point during the test, which helped maintain the integrity of the hinge and socket connection.

Strains in the hinge longitudinal bars in Calt-Bridge 2 followed a similar trend as that seen in ABC-UTC. No yielding occurred in the hinge reinforcement during the first run, but the peak strains exceeded the yield strain during run 2 and afterwards. The peak strains continued to increase with each successive earthquake run, achieving 17.5 times the yield strain during the final run. Significant strain dissipation was observed when moving into the pocket connection or into the footing, attesting to the good anchorage provided by the pocket connection. The yield strain was slightly exceeded in one of the hinge spirals during the final run, meaning the connection remained essentially elastic for all ground motions, and maintained the joint and hinge integrity.

The longitudinal reinforcement strains in both connection types greatly exceeded the yield strain at the rebar hinge-footing interfaces. The connection type and opening location (whether in the footing or the column) appeared to have little to no effect on the hinges ability to develop large strains and form plastic hinges.

10.3.1.1.3 Hinge Deformations

Local deformation within the rebar hinge was measured in each bridge using several displacement transducers (figure 4.9). These displacement transducers measured the relative displacement between the hinge and footing owing to shear as well as the angle of twist and rotation of the hinge owing to longitudinal and transverse translation of the bridge. In ABC-UTC, the peak relative horizontal displacement between the hinge and the footing was 0.26 in (6.6 mm) and 0.18 in (4.6 mm) in the transverse and longitudinal directions, respectively. The peak relative horizontal displacement in Calt-Bridge 2 was 0.54 in (13.6 mm) and 0.46 in (11.6 mm) in the transverse and longitudinal directions, respectively. It was observed that the maximum relative displacement between the footing and hinge was about twice as large in Calt-Bridge 2 compared to that of ABC-UTC.

Because the force-displacement responses of the two bridges were different, the effective shear stiffness was calculated to determine whether the additional relative horizontal displacement in Calt-Bridge 2 was a result of larger shear forces. The maximum lateral forces in the transverse and longitudinal directions of Calt-Bridge 2 were 54.7 k (243 kN) and 74.3 k (330 kN), respectively; compared to 48.2 k (214 kN) and 56.6 k (252 kN) in ABC-UTC, respectively. The effective shear stiffness at the interface was calculated by dividing the peak base shear by the peak relative horizontal displacement in each direction. The effective shear stiffness of the hinges in Calt-Bridge 2 was 101 k/in (17.7 kN/mm) and 161 k/in (28.2 kN/mm), in the transverse and longitudinal directions, compared to 185 k/in (32.4 kN/mm) and 314 k/in (55.0 kN/mm) for ABC-UTC. The rebar hinges in ABC-UTC were significantly stiffer than those of Calt-Bridge 2 indicating that the hinge socket connection provided a higher shear stiffness than that of the hinge pocket connection. This topic is discussed further in section 10.3.1.1.4.

As shown in table 10.4, the peak bent displacements in ABC-UTC and Calt-Bridge 2 were not equal. Therefore, the slippage (relative to bent cap displacement) was normalized relative to the peak drift ratios. The relationship between the peak drift ratio and peak normalized horizontal slippage is shown in figure 10.8. Note that runs 6 and 7 were not included for ABC-UTC due to damage to the displacement transducers caused by spalling concrete from the column top plastic hinge region. Two clear trends are visible in figure 10.8: (1) the slippage in ABC-UTC remained almost constant, whereas it increased in Calt-Bridge 2 as the total drift ratio of the bent increased; and (2) the maximum normalized hinge slippage in Calt-Bridge 2 was more than twice that in ABC-UTC. These trends are attributed to softer two-way hinges in Calt-Bridge 2, which was caused by the lower stiffness of the grout in the column pockets, in addition to the extension of damage into the lower portion of the pocket connection.

As the stiffness of the rebar hinge was lower than that of the column, longitudinal and transverse translation of the superstructure imposed rotations on the hinge due to hinge flexure and twist angle due to torque at the hinge. As mentioned previously, the flexural rotations were accounted for in design by providing a gap between the columns and footing that was sufficiently thick to prevent gap closure. The rotation to close the gap was 0.093 radian and 0.083 radian in ABC-UTC and Calt-Bridge 2, respectively. The maximum rotations in ABC-UTC and Calt-Bridge 2 were 0.06 radian and 0.0515 radian, respectively, indicating that there was ample margin to prevent contact between the column and footing even under very strong earthquakes.

Because the hinge rotations were imposed by superstructure translation, the peak drift ratio and peak hinge rotations were compared to determine the rotational stiffness provided by the pocket and socket connections as shown in figure 10.9. The relationship between peak drift ratio and hinge rotation for each run was mostly linear, meaning that translation at the top induced rotation in the base with little change in rotational stiffness as the runs progressed. Socket and pocket connections in the column base provided sufficient connectivity and allowed the hinges to undergo large rotations.

The torsional behavior of the rebar hinge as affected by the connection type was also of interest. As the torsional stiffness of the hinge was low, the hinge would be expected to undergo some twist angles during the shake table tests. The maximum angle of twist in ABC-UTC was 0.03 radian, which was nearly equal to the peak twist of 0.028 radian that was measured in Calt-Bridge 2, indicating that the connection type did not affect the twist angle appreciably.

10.3.1.1.4 Recommendations for Rebar Hinge Connections

Most hinge performance parameters including measured strains, and hinge deformation were unaffected by the connection type. Two primary differences were observed between the pocket connections and socket connections: (1) some damage extended into the grout in the pocket connections in Calt-Bridge 2, while the socket connections in ABC-UTC remained essentially damage free in all earthquake runs, and (2) larger relative horizontal displacements were observed between the hinge base and footing in the pocket connections in Calt-Bridge 2. Recall that the rebar hinge connection used in Calt-Bridge 2 consisted of a pocket connection with the opening inside the column that was filled with grout. The larger relative horizontal displacements were attributed to spalling of the grout around the hinge extending into the opening inside the column. As the hinges and the pocket connections were composed of grout, the cyclic loading applied to the hinge led to deterioration of the grout around the steel reinforcement and into the pocket. This led to reductions in the horizontal stiffness of the hinges that in turn led to larger relative displacements between the hinge column base and the footing. One potential solution to mitigate this loss of stiffness would be to cast concrete rather than grout around the hinge bars and create a precast concrete stem. The stem would then be inserted into the column opening and the space between the concrete stem and column would be filled with grout in much the same way the connection with a footing socket was constructed. This adjustment of course would change the "pocket" connection used in Calt-Bridge 2 to a "socket" connection. Formwork could be placed around the hinge stem before casting of the footing, which would make the entire footing and hinge precast. In this detail, grout would solely be used to bond the components together rather than replacing concrete for the hinge. This detail would be similar to the one used in

ABC-UTC but the opening would be in the column rather than the footing. Adjusting the pocket connection to a socket connection is expected to lead to reduction in hinge slippage owing to increased concrete material stiffness. Either opening locations, in the footing, or in the column are recommended for implementation in ABC bridge projects with column base hinges. However, only socket connections are recommended to avoid excessive deterioration in the grout at the hinge throat and the opening.

10.3.1.2 Comparison of Rebar Hinge and Pipe-Pin Connection for Column Base
Calt-Bridge 1 and Calt-Bridge 2 were nearly identical except for the column top and base connections. The column top connection was designed to be rigid in both bridges. Although the connection types at top of columns were different, they utilized conventional materials. The column-footing connections in both bridges were designed to perform as "hinges" with relatively small moment capacity. However, these connections incorporated very different materials and detailing. The test data provided an opportunity to compare the performance of the two column base connection details.

The details for the pipe-pin connection implemented in Calt-Bridge 1 are shown in figure 10.10. This connection consisted of an upper and lower metal pipe that is connected using a threaded rod that passes through both pipes. An elastomeric bearing pad is placed in the hinge throat to allow for column base rotations and to reduce the flexural stiffness of the connection. A precast concrete pedestal with the same diameter as the column diameter was incorporated in the lower part of the column to accommodate the pipe-pin connection.

10.3.1.2.1 Visual Assessment of Column Base Connection
Minimal cracking was observed in the columns near the pipe-pin connections, indicating that the pipe-pin was effective in reducing the flexural demand at the column base. The elastomeric bearing pad incorporated in the hinge throat was damaged during the shake table tests due to being underdesigned for the impact moment; however, this did not affect the bent response, and the hinge gap did not close during shake table testing. Evaluation of the strain data indicated that the upper and lower pipe and the threaded rod remained essentially elastic during testing. This behavior contrasts with that observed in the rebar hinge connection as significant yielding was observed in the hinge.

10.3.1.2.2 Column Base Deformations
Limited slippage in the pipe-pin connections occurred due to translation of the lower pipe within the upper pipe during the shake table tests. The lower pipe was free to move until contacting the upper pipe, after which slippage was constrained. The maximum slippage observed in the pipe-pin connections was 0.33 in (8.4 mm) in the longitudinal direction, and 0.37 in (9.40 mm) in the transverse direction. These values were smaller than the provided gap between the upper and lower pipes of 3/8" (9.5 mm), meaning that slippage did not take place once the gap between the pipes had closed. The measured horizontal slippage in the pipe-pin connection was smaller than that measured in the rebar hinge in Calt-Bridge 2. This was a result of the rebar hinge experiencing significant yielding and spalling of the pocket connection grout, which resulted in lower shear stiffness between the hinge base and the footing.

Rotation of the pipe-pin was controlled by superstructure translation with peak rotations of 0.077 radian and 0.049 radian measured in the longitudinal and transverse directions during run 8, respectively. The maximum rotation measured in the rebar hinge in Calt-Bridge 2 was 0.0515 radian. The peak rotations in the pipe-pin connection were expected to be larger than those in the rebar hinge because of the reduced flexural capacity in the pipe-pin relative to the rebar hinge. The hinge gap rotation limit was 0.083 radian in Calt-Bridge 1. Because of the larger rotations measured in the pipe-pin, the margin for hinge gap closure was much tighter for Calt-Bridge 1 with only 0.006 radian remaining before bearing of the column base on the footing would occur. This suggests that the column base may have possibly contacted the footing if the ultimate bent capacity was reached. The peak angle of twist was 0.029 radian, which was approximately equal to the peak angle of twist in the rebar hinges in Calt-Bridge 2, indicating similar torsional performance.

10.3.1.2.3 Recommendations for Pipe-Pin and Rebar Hinge Connections

The pipe-pin connection provided many advantages over the rebar hinge connection. The pipe-pin connection remained essentially elastic even under strong earthquakes, meaning the connection does not need to be repaired or replaced after an earthquake. Flexural capacity was significantly reduced from that of the rebar hinge, which means the moment applied to the substructure was smaller than that of the rebar hinge. Consequently, near pin-like behavior was achieved using the pipe-pin connection, whereas the rebar hinge had significant column base moment, which caused Calt-Bridge 2 to be much stiffer. Relatively low plastic shear was observed in Calt-Bridge 1 as a result of the implementation of the pipe-pin connection, which would result in lower column transverse reinforcement than was used in Calt-Bridge 2.

There are many benefits to the use of pipe-pins in column base connections, however, some drawbacks exist. The pipe-pin has reduced stiffness from other two-way hinge options, which is ideal for reducing base shear and the seismic demand on the structure, but this results in larger displacements that must be accounted for in design (e.g. increasing hinge throat thickness to prevent bearing of the column base on the footing, providing sufficient seat lengths at the abutments). Additionally, the construction of the pipe-pin connection is more complicated than that of a rebar hinge. Changing the column base connection from a rebar hinge to pipe-pin resulted in an additional connection between the precast pedestal and the footing, as well as tight tolerances during placement of the upper and lower pipes. Rebar hinges are relatively simple connection details that reduce moment at the column end without requiring additional components and design steps.

Pipe-pins are a connection that can be incorporated in ABC applications, which provide effective reductions in column base moment and will remain essentially elastic during earthquakes. Pipe-pins are the recommended option for engineers aiming to reduce column base moment and bent forces through the incorporation of a two-way hinge. Rebar hinges provide satisfactory performance for ABC applications in seismic regions with little damage observed during the design level earthquake. The relative simplicity of the rebar hinge makes it a desirable option if the contractor or designer experience is limited.

10.3.2 Column-to-Cap Beam Connection

Grouted duct connections are moment connections consisting of projected column reinforcement into corrugated ducts in the adjoining elements. These connections were used in ABC-UTC and Calt-Bridge 1 to connect the columns to the precast cap beams. The column-to-cap beam connection in Calt-Bridge 2 was different because it used a socket detail. This section compares the grouted duct performance in ABC-UTC and Calt-Bridge 1 and highlights any differences between the behavior of the two. Subsequently the grouted duct connection performance in Calt-Bridge 1 is compared with the socket connection utilized in Calt-Bridge 2. Recommendations are made based on the findings form these comparisons.

10.3.2.1 Comparison of Grouted Duct Performance in Calt-Bridge 1 and ABC-UTC

Grouted duct connections were used to form moment connections at the column tops in ABC-UTC and Calt-Bridge 1. This connection was formed by passing projected column reinforcement through the precast beam and filling the ducts with grout. The full anchorage of column reinforcement was achieved through bond in the grouted ducts in addition to bond within the CIP portion of the cap beam above the precast part. These connections are compared using the visual assessments of the damage during shake table testing, measured strains in the connections, and relative displacements between the cap beam and columns.

10.3.2.1.1 Visual Assessment of Grouted Duct Connection

Plastic hinges developed in the column tops near the grouted duct connections in both bridges. No cracking was observed in the cap beam. Minor spalling of the grout in the cap beam ducts was observed in ABC-UTC but did not appear to have any impact on the connection performance. Bar pullout was not observed in the connections. In ABC-UTC, the grouted duct connection provided sufficient capacity to buckle the longitudinal bars without damaging the grouted duct connection. Judging from the lack of any damage, it is expected that the same would occur in Calt-Bridge 1 had it not been for the early termination of testing to prevent unseating at the abutments.

10.3.2.1.2 Measured Strains

The peak strain ductilities (defined as the ratio of the strain to the yield strain) in the column top regions in the three bridges are shown in figure 10.11. The column reinforcement did not yield during run 1 in ABC-UTC, but significant yielding was observed from run 2 and onward. The peak measured strain ductility was 18.2 in run 8. The large ductility in the column reinforcement illustrated the ability of the grouted duct connection to develop extensive yielding in the plastic hinge of the column. Significant strain dissipation was observed when moving into the cap beam, which indicates good anchorage provided by the grouted duct connection. The same trend was observed in Calt-Bridge 1 where the maximum column reinforcement strain ductility was 28.8. Again, significant strain dissipation was observed when moving away from the column-cap beam interface.

10.3.2.1.3 Recommendations for Grouted Duct Connections

Grouted duct performance was satisfactory in providing moment connections at the column tops in ABC-UTC and Calt-Bridge 1. Although this conclusion is the same as that observed in previous research, it is particularly significant because both bridges were subjected to bi-directional loading, whereas previous studies focused on behavior only in the strong direction of the bent. The connection provided sufficient anchorage to prevent pullout of the column longitudinal bars during strong earthquakes and to allow formation of plastic hinges in the column tops. The cap beam and grouted ducts remained capacity protected in all earthquake runs, while maintaining joint integrity between the columns and cap beam. Incorporation of the grouted duct connection in ABC-UTC and Calt-Bridge 1 resulted in good joint performance in both cases and the connection. The grouted duct connection is recommended for implementation in ABC bridge systems.

10.3.2.2 Comparison of Grouted Duct and Socket Connections in Column-to-Cap Beam Connections

The moment connections in the column tops were grouted duct connections in Calt-Bridge 1 and socket connections in Calt-Bridge 2. The superstructure and column dimensions were the same between Calt-Bridge 1 and Calt-Bridge 2; therefore, the performance of the moment connections could be directly compared. Note that the cap beam was wider in Calt-Bridge 2 than in Calt-Bridge 1 to accommodate the opening for the socket connection. Additionally, the cap beam longitudinal bars in the precast portion of Calt-Bridge 2 were bundled along the sides to allow for placement of the precast columns in the socket connections with no interference. The performance of the two connection types is compared using the visual assessments of the connections during shake table testing, the measured strains in the connections, relative displacements between the cap beam and columns, and the measured curvatures in the column plastic hinges.

10.3.2.2.1 Visual Comparison of Column-to-Cap Beam Connections

Visual assessments of the socket connection in Calt-bridge 2 during the shake table tests are discussed in section 6.4.4.1. The socket connections remained virtually damage free with only some excess grout spalling observed during the later runs. Plastic hinges formed in the column tops beneath the cap beam interface and the yielding spread further into the column as earthquake runs progressed, which implied that good anchorage was provided by the socket connection. The distribution of damage seen in the column tops as well as the conservation of joint integrity indicated that the socket connection led to satisfactory, full moment connection behavior.

No large differences were observed between the behavior of grouted duct and socket connections. Both connections allowed for distribution of damage into the columns, which provided good energy dissipation in the bent. Additionally, good joint integrity was maintained in both connections as exhibited by the absence of cracking in the joint grout.

10.3.2.2.2 Measured Strains in Column-to-Cap Beam Connections

The peak strain ductility profiles in the column longitudinal reinforcement are shown in figure 10.11 for Calt-Bridge 1 and Calt-Bridge 2. Strain dissipation was observed in both connections when moving away from the interface, either towards the cap beam or into the column. Peak strain ductilities in the column longitudinal reinforcement embedded within the cap beam were reduced to 37% and 53% of the peak strain at the interface in run 8 in Calt-Bridge 1 and Calt-Bridge 2, respectively. This confirmed the trends observed in the visual assessment of the connections with large strains or damage measured near the column-cap beam interface but limited yielding in the cap beam connection. Much larger strains were observed in Calt-Bridge 1 than Calt-Bridge 2, with column longitudinal strain ductilities of 28.8 and 14.5, respectively. The difference in strain ductility between the bridges was a result of the larger column displacements in Calt-Bridge 1 relative to Calt-Bridge 2, rather than an inability of the socket connection to develop large strains in the plastic hinges. Both connections provided desired performance for a moment connection.

10.3.2.2.3 Relative Displacements and Curvatures in Column Plastic Hinges

The relative displacements between the columns and cap beam for the socket connection are summarized in section 6.17. It was determined that slippage between the columns and cap beam did not occur due to the limited relative displacement between the elements, even under strong earthquake runs. The relative displacement between the columns and cap beam was not evaluated for Calt-Bridge 1 but rather the curvature in the plastic hinge section was used to determine connection fixity. Curvature in the plastic hinge region was calculated as summarized in section 6.13 and the peak curvature profiles for the column plastic hinges are shown in figure 10.12 for Calt-Bridge 1 and Calt-Bridge 2. The curvature distribution in both connection types exhibited similar trends. The curvature was concentrated at the column top adjacent to the cap beam interface, which shows that joint integrity was maintained allowing rotation of the columns without local deformations or damage in the joint. Again, the measured data for both the grouted duct and socket connection suggest that both connections provided full moment transfer between the cap beam and columns.

10.3.2.2.4 Recommendations for Grouted Duct and Socket Connections

The grouted duct connection and socket connections both provided effective moment transfer between the columns and cap beam, while maintaining joint integrity. No significant differences in connection behavior were observed between the two connection types, however, the grouted duct connection was easier to construct and assemble in these studies. These conclusions are made for bridge models that were subjected to the more demanding biaxial loading making them particularly important. Similar conclusions had been reached in previous research under the less demanding uniaxial loading. Both connection types are recommended for incorporation in ABC bridge systems.

10.3.3 Girder-to-Cap Beam Connection

The extended strand with bent free end (ESBF) girder-to-cap beam connection detail was incorporated in Calt-Bridge 1 and Calt-Bridge 2. The connection details were the same in the two bridges, which presented the opportunity to assess the performance of the connection in two separate bridge models. The ESBF connection was designed to resist positive superstructure moment above the cap beam. Therefore, an evaluation of the positive moment resistance mechanism in both bridges would highlight the connection behavior under strong earthquake motions.

The SDCL connection incorporated in ABC-UTC was specifically a detail for steel girder bridges, while the ESBF girder-to-cap beam connection was exclusively for prestressed concrete girder bridges. Consequently, a comparison of these two connections would not lead to additional insight beyond what was summarized by Shoushtari et al. (2019) for the SDCL connection because of the difference in application.

Therefore, a comparison of the SDCL connection to the ESBF connection is not included in this section.

10.3.3.1 Comparison of Positive Superstructure Moment Transfer in ESBF Connections

Tension in the cap beam stemming from positive superstructure moment was resisted by the extended prestress strands and concrete shear friction between the cast-in-place cap beam concrete and embedded prestressed concrete girders. The positive moment contribution from each component was calculated for both bridges according to the method presented in section 7.6. The contributions by the prestress strands and shear-friction to positive moment resistance were on average approximately 22% and 78%, respectively, in Calt-Bridge 1. This was nearly identical to the distribution calculated for the interior girders in Calt-Bridge 2 where prestress strand and shear friction contributions were an average of 20% and 80%, respectively. However, strand contribution was found to be higher for the exterior girders in Calt-Bridge 2 with an average distribution of 45% compared to 55% for shear friction. Recall that limited strain data was available for the exterior girders in Calt-Bridge 2 due to damaged strain gages. Therefore, it was unknown whether the strain data for the prestress strands was reliable in those locations. The correlation between the positive moment resistance mechanisms in the interior girders of Calt-Bridge 2 with the average contributions in Calt-Bridge 1 suggest that the strain data in the exterior girders may have been inflated due to small sample size.

In the draft version of the Caltrans design approach for this connection, prestress strands are assumed to provide 80% of the connection strength, compared to 20% provided by shear friction (Caltrans, 2016). The findings from component (Vander Werff et al., 2015) and system level studies of this connection suggest that shear friction provides significantly greater positive moment resistance than was assumed in design. These results suggest the demand requirements for the prestress strands may be relaxed.

10.3.3.2 Relative Slippage Between Superstructure and Cap Beam

The fixity provided by the superstructure-to-cap beam connection was assessed by evaluating the measured slippage between the superstructure and cap beam side faces. Displacement transducers were placed at the bottom of the girders and top of the superstructure (figure 4.10) in both Calt-Bridge 1 and Calt-Bridge 2 to measure any relative displacement between the elements. The largest measured relative displacements in Calt-Bridge 1 and Calt-Bridge 2 was 0.077 in (0.196 mm) and 0.0105 in, respectively, which were insignificant in both cases implying that the connection was essentially fixed and maintained good integrity during all earthquake runs. Furthermore, the rotation in the superstructure was calculated by dividing the difference between the displacements at the top and bottom of the section by the vertical distance between them. The maximum superstructure rotation at the cap beam interface was 0.0005 radian and 0.0007 radian in Calt-Bridge 1 and Calt-Bridge 2, respectively. This implied that the superstructure was fixed for both translation and rotation at the cap beam interface, and the connection performed as designed in both bridges.

10.3.4 Deck Connection over Pier

The same lap spliced straight bars embedded in UHPC connection detail was incorporated for the deck connection over the bent in all three bridges. This connection was designed to remain capacity protected and resist the tension from negative superstructure moment owing to phase 2 superimposed weight and negative seismic moment. The peak strains in the deck reinforcement within the connection were 14%, 36%, and 40% of yield strain in ABC-UTC, Calt-Bridge 1, Calt-Bridge 2, respectively. Therefore, none of the reinforcement yielded in the connection, satisfying the capacity protected design criteria in each case. Low strains could mean slippage. But slippage would be accompanied with significant cracks at the joint. The assessment of the connection indicated that there were no cracks in or adjacent to the UHPC in any of the bridge models, which implies that the UHPC maintained good bond with the deck reinforcement and allowed for force transfer between the superstructure and the cap beam even under strong earthquakes. No significant differences were observed in the behavior of the deck connection over the pier incorporated in the two bridges.

10.3.5 Deck-to-Girder Connection

The same design principle was incorporated in the deck-to-girder connections in each bridge, which consisted of steel studs projected into grouted deck panel pockets. Some differences were present between the concrete girder bridges (Calt-Bridge-1, Calt-Bridge 2) and the steel girder bridge (ABC-UTC) including the use of longitudinally oriented deck joints along the interior girders, which were filled with UHPC instead of grout in Calt-Bridge 1 and Calt-Bridge 2. The composite action between the girders and deck was evaluated using displacement transducers to measure the relative displacement between the girders and deck panels (figure 4.11). The maximum slippage between the deck and girders was 0.0036 in (0.09 mm), 0.0096 in (0.24 mm), and 0.0119 in (0.30 mm) for ABC-UTC, Calt-Bridge 1, and Calt-Bridge 2, respectively. These slippages were all insignificant, which implied that composite action was maintained in the deck panels and girders in all earthquake runs. Visual assessment of the joints at the conclusion of shake table testing also attested to the maintenance of joint integrity with no damage observed in the deck panels, deck pockets, or girders in any bridge. This suggests that the steel shear connectors, deck panels and grouted pockets remained elastic under all earthquake runs. No differences in slippage were observed in the interior girders with shear connectors projected into a longitudinal joint cast with UHPC in Calt-Bridge 1 and Calt-Bridge 2. These results suggest that the shear connector spacing, and number of connectors was sufficient to create composite action between the deck panels and girders in grouted deck panel pockets and connectors projected into longitudinal joints cast with UHPC.

10.3.6 Deck Panel-to-Panel Joints

Relatively short lap spliced straight bars deck panel-to-panel joints filled with UHPC was implemented in each bridge. This connection was not explicitly instrumented in any of the bridge models, therefore, assessment of the connection behavior was limited to visual inspection of the joints. Signs of joint distress in these connections would include pullout of the deck reinforcement from the UHPC, delamination of the deck panels from the UHPC joint, or cracking in the deck panels or UHPC surrounding the female-to-female shear key. None of these damage states were observed in any joints in the bridges. The short embedment length lap spliced deck panel-to-panel connection cast in UHPC was deemed to provide sufficient load transfer between adjacent panels and remain elastic even under strong earthquakes.

Chapter 11. Summary and Conclusions

11.1 Summary

Increases in traffic demand combined with the rapid approach of the end of the design service life of a large population of US bridges has placed an increased interest on accelerated bridge construction (ABC). With ABC, prefabricated elements are used to assemble bridges on-site, which removes or reduces construction time associated with formwork and curing of concrete. Benefits associated with ABC include improved constructability, improved project delivery time, and improved work-zone safety for the traveling public, all while also reducing traffic impact and onsite construction time [FHWA (2019)]. While there are many benefits associated with the use of ABC, maintaining integrity of connections between precast components under seismic loads has led to design challenges for moderate and high seismic zones. Incorporation of ABC connections in component tests has shown promise for the future of ABC in seismic regions with results indicating equal or superior performance to cast-in-place (CIP) counterparts. However, these tests have not included biaxial forces or system interaction among the connections as would be experienced in realistic conditions, leaving questions regarding the viability of ABC connections for bridge systems in seismic regions.

A 0.35 scale two-span bridge model (Calt-Bridge 2) implementing ABC methods and connections was tested at the Earthquake Engineering Laboratory at the University of Nevada, Reno. The bridge was symmetric and supported on a two-column bent with seat type abutments designed to freely slide. Biaxial shake table testing was conducted to assess the seismic performance of six ABC connections when incorporated at the system level; to gain additional confidence in the integrity and resilience of ABC for seismic regions and recommend the tested ABC connections for engineering practice. Experimental and analytical studies were used to: (1) assess the performance of the ABC connections and bridge system when subjected to multiple bi-directional ground motions of varying intensity, (2) review the current design procedure for each connection type and revise said procedure based on findings from the experimental results to account for interaction within the bridge system or for bi-axial ground motions, (3) determine if the behavior of the bridge system under biaxial seismic loading can be captured using existing modeling methods, (4) evaluate various parameters for the scaled bridge model that were not tested during the shake table tests, and (5) compare the behavior of three bridge systems utilizing ABC connections and make recommendations based on relative connection performance.

Six ABC connection types were implemented in the scaled bridge model: (1) a rebar hinge precast with the footing connected to the column via a pocket for the column-to-footing connection, (2) a fully precast pocket connection for the column-to-cap beam connection. (3) extended strands and headed bars enclosed in the cast-in-place portion of the cap beam for the girder-to-cap beam connection, (4) lap spliced straight bars embedded in ultra-high performance concrete (UHPC) for the deck connection over the pier, (5) precast deck panels to girder connection using deck pockets and projected steel studs from precast concrete girders, and (6) short embedment length lap spliced straight bars for female-to-female deck panel-to-panel connection. The first two connections were utilized to connect precast columns to adjacent members and were expected to allow formation of plastic hinges adjacent to the connection. The last four connections were incorporated in "capacity protected" elements and were expected to remain essentially elastic during shake table testing. Of the six connection types, three (Types 1, 2, and 4) had not been studied in previous research even at the component level. No previous studies had been conducted on Type 1. Past studies of Type 2 were limited to uniaxial testing of socket connections. Type 4 is technically dis-allowed in current seismic guidelines because it utilized lap splices, but was modified in the current study by embedding the splices in UHPC.

The 1994 Northridge earthquake measured at Sylmar station was used as the input motion for the shake table tests. Eight earthquake runs ranging from 30% to 225% of the design level earthquake were applied to the bridge model in succession. The global and local bridge response including displacements, strains, accelerations, and forces was monitored during the earthquake runs using 362 data channels. The measured data was used to assess system behavior and local connection performance, which was compared to the intended design performance as well as expected behavior for CIP counterparts. Three-dimensional nonlinear analyses in Opensees were used to predict the bridge response prior to shake table testing to examine the feasibility of the test. The analytical model was refined subsequent to the tests to better represent the actual material properties and the actual shake table records and study the correlation between the calculated and measured response. Large in-plane rotations were measured during shake table testing of the bridge even though the bridge was symmetric. The rotations were attributed to friction between the girders and abutments. Because these rotations were not captured in the analytical model using conventional analyses, a parametric study evaluating abutment friction effects on the in-plane rotation was conducted. Finally, the behavior of the ABC connections in Calt-Bridge 2 was compared to that of two other ABC bridges (Calt-Bridge 1 and ABC-UTC) tested previously and recommendations were made for ABC connections based on the relative connection performance in three bridges.

11.2 Observations

The key observations from the experimental work, analytical studies, and ABC connection comparison are summarized in this section.

11.2.1 Experimental Studies

1) The seismic performance of Calt-Bridge 2 was emblematic of the performance expected from conventional CIP bridges. Plastic hinges were formed in the seismic critical members, (i.e. columns and hinges) and relatively small strains were developed in the capacity protected elements (i.e. cap beam, girders, and deck panels) meaning those components remained essentially elastic even under strong earthquake runs.
2) Column plastic hinges were stable and ductile exhibiting no strength degradation. This led to a ductile system response, which is the primary performance objective for bridges subjected to strong earthquakes.
3) The hysteretic response of the bridge exhibited good energy dissipation in both horizontal directions owing to the stable and non-degrading column plastic hinges.

4) Large superstructure in-plane rotations were measured during the shake table tests, which progressively became larger as acceleration amplitude increased even though the bridge geometry was symmetrical. These in-plane rotations were attributed to friction forces at the abutments in conjunction with unbalanced vertical abutment reactions caused by the frame action of the bridge in the longitudinal direction of the bridge. This caused the friction forces to be larger at one end, essentially locking that end against transverse displacement, while the other end was free to translate.
5) Construction and assembly of Calt-Bridge 2 was quick and greatly reduced the "site" construction time. Thus, the prefabricated elements and connections allowed for fulfillment of ABC method objectives.
6) Joint integrity was maintained in all the ABC connections, and all damage in seismic critical members took place outside of the joints. The ABC connections provided full load transfer between joined elements and provided a stable load path from the superstructure to the substructure.
7) Specifically, the performance of three of the connection types incorporated in Calt-Bridge 2 with unknown history was satisfactory. The pocket connections of the column hinge bases resisted seismic forces with controlled damage, although the local deformation exceeded that of CIP connections. The socket connection between the columns and the cap beam provided full fixity with no damage even under the biaxial earthquake loading. The UHPC embedded lap splices over the cap beam maintained the connection integrity with small bar strains and no damage, indicating successful performance of lap splices when embedded in UHPC.
8) Precast rebar hinges with pocket connection in the column base provided a reduced moment section at the base, which allowed for significant rotation about the column base from superstructure translation while maintaining integrity between the column and footing. Rebar hinges can be incorporated in ABC bridges with no adjustments to the design procedure that has been developed for CIP hinges.
9) The girder-to-cap beam connection sufficiently resisted the positive superstructure moment through the prestress strands and shear friction mechanisms. The demand on the prestress strands was much less than anticipated in design, suggesting that the design requirements for the strands may be relaxed.
10) The deck panel-to-girder connection provided composite action between the precast deck panels and prestressed concrete girders. No slippage was measured between the deck and girders, and the grouted pockets and UHPC filled longitudinal joints did not crack during the shake table tests.

11.2.2 Analytical Studies

1) The pretest analysis of Calt-Bridge 2 using a 3-D grillage model in Opensees resulted in reasonable prediction of the seismic response of the bridge. The displacement and force histories can be estimated using expected material properties and real ground motion records.
2) Modifications to the Opensees model including the use of measured test day material strengths in the material models, achieved ground motions, and refinement of local connection response, resulted in greatly improved correlation

between the calculated and measured data. The displacement response of the structure was well captured by the post-test analytical model

3) In-plane rotation of the superstructure was underestimated when using roller supports at the abutments. The incorporation of friction effects at the abutments resulted in improved prediction of superstructure in-plane rotation as well as the displacement response.
4) Measured in-plane rotation was captured most accurately when friction effects were included at one abutment. Evaluation of the measured and calculated residual rotations indicated that some damage likely occurred in the PTFE pads during the last two or three runs, which inhibited rebound of the superstructure.

11.2.3 Comparison of Seismic Performance of Three Bridge Models

1) Socket connections or pocket connections provided full development of the rebar hinge and allowed for extensive yielding to occur in the hinge throat. However, some relative horizontal displacements were measured between the footing and column base in the rebar hinge pocket connection. It is recommended that socket connections be used whether the opening is in the column or the footing.
2) The behavior of pipe-pins is more emblematic of pure pinned supports at the column base than rebar hinges due to the relatively low moment capacity of the connection. Pipe-pins offer performance benefits over rebar hinges including decreased moment applied to the foundation and essentially elastic response to strong earthquakes, but this comes at the cost of larger superstructure displacements and relatively complicated design and construction.
3) Socket and grouted duct connections both provided full moment transfer between precast columns and cap beams. Both connections are recommended for implementation in ABC applications.
4) The measured shear friction and prestress strand contribution to positive moment resistance in the girder-to-cap beam connection in Calt-Bridge 1 and Calt-Bridge 2 suggest that the design requirements for the prestress strands may be relaxed.
5) Lap spliced straight bars embedded in UHPC sufficiently transferred forces among the deck panels regardless of superstructure configuration in the bridge models. UHPC encased lap splices remained elastic during strong earthquakes
6) The deck panel-to-girder connection provided composite action between the precast deck panels and girders for both steel and concrete girder configurations. The projected steel stud into precast deck panel pocket connection is recommended for ABC applications with steel or concrete girders.

11.3 Conclusions

The following conclusions were drawn from the experimental and analytical studies of Calt-Bridge 2 and assessment of the relative performance of Calt-Bridge 1, ABC-UTC bridge, and Calt-Bridge 2:

12) Bridge systems utilizing prefabricated elements and the six ABC connections utilized in this study meet the seismic requirements for CIP bridges in current design codes and can be implemented in the field with confidence.
13) The implemented ABC connection details and design guidelines resulted in satisfactory seismic performance even under strong earthquakes. Many of these

methods have been incorporated in the newly released proposed AASHTO seismic guidelines for seismic design of ABC connections providing tools to implement the results of the present study in practice.

14) The behavior of rebar hinges precast with the footing and connected via column pocket connections resembles that of CIP hinges, providing reduction in the moment transferred to the footing in addition to reducing column plastic shear forces. Pocket connections cast with grout for the hinge material experience limited damage and relative horizontal displacements between joined elements when subjected to dynamic loading. Socket connections are recommended as an alternative to mitigate these issues.
15) Socket connections provide a full moment connection between prefabricated elements and allow plastic hinges to form in connected seismic critical members.
16) Extended strand bent with free end anchorage in the girder-to-cap beam connections are practical and provide sufficient positive superstructure moment resistance. The superstructure behaves as a continuous span over the supports after casting of the integral cap beam, and results in a fixed connection between the bent and superstructure.
17) UHPC provides good continuity for lap spliced bars between precast elements due to its large bond strength and intrinsic tensile capacity even in capacity-protected connections where lap splices are disallowed.
18) Steel studs projected from girders into precast deck panels provide composite action between the deck and girders and maintain their integrity during seismic events.
19) Analytical models can reasonably capture the macroscopic seismic response of bridges constructed with precast elements and ABC connections.
20) Accounting for friction effects at the abutments can lead to better correlation between measured and calculated system response.
21) Pipe-pins provide pin-like behavior when incorporated at the column base and are recommended over rebar hinges because of relatively low column base moment and essentially elastic response during strong earthquakes.
22) No significant differences were observed between the seismic response of socket connections and grouted duct connections. Both are recommended for implementation in moment connections for ABC applications.

References

Aktan, H., & Attanayake, U. (2013). *Improving Bridges with Prefabricated Precast Concrete Systems.* Kalamazoo, MI: Western Michigan University. Report No. RC-1602

American Association of State Highway and Transportation Officials (AASHTO). (2017). *AASHTO LRFD Bridge Design Specifications* (8^{th} Ed.). Washington D.C.: American Association of State Highway and Transportation Officials.

American Association of State Highway and Transportation Officials (AASHTO), (2018). "AASHTO LRFD Guide Specification for Accelerated Bridge Construction," 2018.

American Concrete Institute (ACI). (2014). *Building Code Requirements for Structural Concrete (ACI 318-14).* Farmington Hills, MI: American Concrete Institute

Amirihormozaki, E., Pekcan, G., & Itani, A. (2015). "Analytical Modeling of Horizontally Curved Steel Girder Highway Bridges for Seismic Analysis". *Journal of Earthquake Engineering, 19(2),* pp. 220-248

Badie, S. S, and Tadros, M. K, (2008). "Full-Depth Precast Concrete Bridge Deck Panel Systems", National Cooperative Highway Research Program, Report No. 584.

Benjumea, J., Saiidi, M., & Itani, I. (2019). *Experimental and Analytical Seismic Studies of a Two-Span Bridge System with Precast Concrete Elements and ABC Connections.* Reno, NV: Center for Civil Engineering Earthquake Research, Department of Civil and Environmental Engineering, University of Nevada, Reno. Report No. CCEER 19-02

Caltrans. (2004). Bridge Design Details 14: Prestressed, Precast. Sacramento, CA: Department of Transportation - State of California. Retrieved from http://www.dot.ca.gov/des/techpubs/bdd.html

Caltrans. (2008). MTD 10-20 Attachment 2: Table 10-20.1(a) Deck Slab Thickness and Reinforcement Schedule. Sacramento, CA: Department of Transportation - State of California.

Caltrans. (2016a). xs1-123: PC/Pretensioned Wide Flange Girder (Debonded Strands). Sacramento, CA: Department of Transportation - State of California. Retrieved from http://www.dot.ca.gov/hq/esc/techpubs/manual/bridgemanuals/bridge-standard-

Caltrans. (2016b). ABC Design Example – Draft V2. Sacramento, CA: Department of Transportation – State of California

Caltrans. (2017). Caltrans ARS Online: Version 2.3.09. Accessed August 20, 2019. from http://dap3.dot.ca.gov/ARS_Online/

Caltrans. (2019). Caltrans Seismic Design Criteria: Version 2.0. Sacramento, CA: Department of Transportation – State of California

Chadwell, C. B., & Imbsen, R. A. (2002). XTRACT-cross section analysis software for structural and earthquake engineering. *TRC, Rancho Cordova, CA, ⟨http://www.imbsen.com/xtract. htm⟩ (Aug. 30, 2011).*

Cheng, Z., Saiidi, M., and Sanders, D. (2009) "Seismic Design Method for Reinforced Concrete Two-Way Column Hinges" *ACI Structural Journal*, V. 107, No. 5, September-October 2010, pp. 572-579.

Constantinou, M., Tsopelas, P., Kasalanati, A., & Wolff, E. (1999). *Property Modifcation Factors for Seismic Isolation Bearings.* Buffalo, NY: Multidisciplinary Center for Earthquake Engineering Research, University at Buffalo, State University of New York

Cruz-Noguez, C., and Saiidi, M. (2010). *Experimental and Analytical Seismic Studies of a Four-Span Bridge System with Innovative Materials.* Reno, NV: Center for Civil Engineering Earthquake Research, Department of Civil and Environmental Engineering, University of Nevada, Reno, Report No. CCEER 10-4

Federal Highway Administration (2019a), "Accelerated Bridge Construction", https://www.fhwa.dot.gov/bridge/abc/

Federal Highway Administration. (2019b), "Prefabricated Bridge Elements and Systems" https://www.fhwa.dot.gov/bridge/prefab/

Graybeal, B. (2010). *Behavior of Field-Cast Ultra-High Performance Concrete Bridge Deck Connections Under Cyclic and Static Structural Loading*. McLean, VA: Federal Highway Administration. Report No. FHWA-HRT-11-023.

Graybeal, B. (2014). "Ultra-high-performance concrete connections for precast concrete bridge decks". *PCI Journal*, *59*(4), 48‑62.

Haraldsson, O.S., Janes, T.M., Eberhard, M.O, and Stanton, J.F. (2013). "Seismic Resistance of Socket Connection between Footing and Precast Column", *Journal of Bridge Engineering, ASCE,* Vol. 18, No. 9, pp. 910-919.

Haroun, M., Pardoen, G., Shepherd, R., Kazanjy, R. & Salama, A. (1994). "Shear Capacity of Bridge Pinned Columns". Transportation Research Board, Report No. FHWA/CA/UCI-95-02, 192 pp.

Johnson, N, M Saiidi, and D Sanders. 2006. "Large-Scale Experimental and Analytical Seismic Studies of a Two-Span Reinforced Concrete Bridge System." Reno, NV: Center for Civil Engineering Earthquake Research, Department of Civil and Environmental Engineering, University of Nevada, Reno. Report No. CCEER-06-02.

Johnson, N., Ranf, T., Saiidi, M., Sanders, D., & Eberhard M. (2008), "Seismic Testing of a Two-Span Reinforced Concrete Bridge," *Journal of Bridge Engineering*, *13*(2), pp. 173-182.

Jones, J., Ryan, K., & Saiidi, M. (2016). *Toward Successful Implementation of Prefabricated Deck Panels to Accelerate the Bridge Construction Process*. Reno, NV: Center for Civil Engineering Earthquake Research, Department of Civil and Environmental Engineering, University of Nevada, Reno, Report No. CCEER 16-05, 280 pp.

Kavianpour, F., & Saiidi, M. (2013). "Experimental and Analytical Seismic Studies of a Four-Span Bridge System with Composite Piers". University of Nevada, Reno, Department of Civil and Environmental Engineering. Center for Civil Engineering Earthquake Research.

Kulkarni, M, and S Shah. 1998. "Response of Reinforced Concrete Beams at High Strain Rates." *ACI Structural Journal* 95 (6): 705–15.

Larosche, A., Cukrov, M., Sanders, D., and Ziehl, P. (2014). "Prestressed Pile to Bent Cap Connections: Seismic Performance of a Full-Scale Three Pile Specimen," *Journal of Bridge Engineering, ASCE,* Vol. 19, No. 3, 04013012, 10 pp.

Lee, G., Huang, C., Song, J., & O' Connor, J. (2014). *Seismic Performance Evaluation of Precast Girders with Field-Cast Ultra High Performance Concrete (UHPC) Connections*. Buffalo, NY: Multidisciplinary Center for Earthquake Engineering Research, University at Buffalo, State University of New York. Report No. MCEER-14-0007.

Lim, K., and McLean, D. & Henley, E (1991). "Moment-Reducing Hinge Details for the Bases of Bridge Columns". Transportation Research Record, No. 1275, pp 1-11

Mander, J.B., Priestley, M. J. N., & Park, R. (1988). "Theoretical Stress-Strain Model for Confined Concrete. *Journal of Structural Engineering, 114(8),* pp. 1804-1826

Matsumoto, E., Waggoner, M., Kreger, M., Vogel, J., & Wolf, L. (2008). "Development of a Precast Concrete Bent-Cap System". *PCI Journal, May-June 2008,* pp. 74-99

Mehraein, M., & Saiidi, M. (2016). "Seismic Performance of Bridge Column-Pile-Shaft Pin Connections for Application in Accelerated Bridge Construction". Center for Civil Engineering Earthquake Research, Department of Civil and Environmental Engineering, University of Nevada, Reno. Report No. CCEER-16-01.

Mehrsoroush, A., & Saiidi, M. (2016). "Cyclic Response of Precast Bridge Piers with Novel Column-Base Pipe Pins and Pocket Cap Beam Connections". *Journal of Bridge Engineering*, *21*(4), 04015080.

Mehrsoroush, A., Saiidi, M., Ryan, K. (2017). "Development of Earthquake-Resistant Precast Pier Systems for Accelerated Bridge Construction in Nevada". Transportation Research Board, Report No. 555-14-803, 578 pp.

Mohebbi, A., Saiidi, M., & Itani, A. (2017). “Development and Seismic Evaluation of Pier Systems w/Pocket Connections, CFRP Tendons, and ECC/UHPC Columns”. Center for Civil Engineering Earthquake Research, Department of Civil and Environmental Engineering, University of Nevada, Reno, Report No. CCEER 17-02.

Mohebbi, A., Saiidi, M., & Itani, A. (2018a). “Shake Table Studies and Analysis of a PT-UHPC Bridge Column with Pocket Connection”. *Journal of Structural Engineering*, *144*(4)

Mohebbi, A., Saiidi, M., & Itani, A. (2018b). “Shake Table Studies and Analysis of a Precast Two-Column Bent with Advanced Materials and Pocket Connections”. *Journal of Bridge Engineering*, *23*(7)

Mortensen, J., and M. Saiidi, "A Performance-Based Design Method for Confinement in Circular Columns," Civil Engineering Department, University of Nevada, Reno, Report No. CCEER 02-07, November 2002.

Motaref, S., Saiidi, M., & Sanders, D. (2011). *Seismic Response of Precast Bridge Columns with Energy Dissipating Joints.* Reno, NV: Center for Civil Engineering Earthquake Research, Department of Civil and Environmental Engineering, University of Nevada, Reno. Report No. CCEER 11-01

Opensees. (2006). What is Opensees. Accessed August 20, 2019. from http://opensees.berkeley.edu/

OpenseesWiki. (2009). Concrete04 Material –Popovics Concrete Material. Accessed August 20, 2019. from http://opensees.berkeley.edu/wiki/index.php/Concrete04_Material_--_Popovics_Concrete_Material

Opensees. (2014a). Flat Slider Bearing Element, Retrieved May 11, 2020, from https://opensees.berkeley.edu/wiki/index.php/Flat_Slider_Bearing_Element

Opensees. (2014b). Velocity Dependent Friction, Retrieved May 11, 2020, from https://opensees.berkeley.edu/wiki/index.php/Velocity_Dependent_Friction

Pacific Earthquake Engineering Research Center. (2013). *PEER Ground Motion Database – NGA-West2.* https://ngawest2.berkeley.edu/.

Precast Concrete Institute (PCI), (2011a). “Full Depth Deck Panels Guidelines for Accelerated Bridge Deck Replacement or Construction”, Report No. PCINER-11-FDDP, Second Edition.

Precast Concrete Institute (PCI), (2011b). “State-of-the-Art Report on Full-Depth Precast Concrete Bridge Deck Panels”. First Edition.

Restrepo, J., Tobolski, M., & Matsumoto, E. (2011). “Development of a Precast Bent Cap System for Seismic Regions”. Washington, D.C.: National Cooperative Highway Research Program. NCHRP Report 681.Tazarv, M., & Saiidi, M. (2015). “UHPC-

Filled Duct Connections for Accelerated Bridge Construction of RC Columns in High Seismic Zones". *Engineering Structures*, *99*, pp. 413–422.

Russell, H., & Graybeal, B. (2013). *Ultra-High Performance Concrete: A State-of-the-Art Report for the Bridge Community*. McLean, VA: Federal Highway Administration. Report No. FHWA-HRT-13-060.

Sadeghnejad, A., & Azizinamini, A. (2018). *Extending Application of Simple for Dead and Continuous for Live Load Steel Bridge System to ABC Applications in Seismic Regions-Phase II Experimental ABC-UTC.* Miami, FL: Department of Civil and Environmental Engineering, Florida International University. Final Report.

Saiidi, M., Vosooghi, A., & Nelson, R. (2013). Shake-Table Studies of a Four-Span Reinforced Concrete Bridge. *Journal of Bridge Engineering*, *139*(8), 1352–1361.

Saiidi, M., M. Mehraein, G. Shrestha, E. Jordan, A. Itani, M. Tazarv, T. Murphy, M. Reno, and M. Pohll, (2020). "Proposed AASHTO Seismic Specifications for ABC Column Connections," National Cooperative Highway Research Program, NCHRP Report 935, Transportation Research Board, Washington, DC, April 2020.

Shoushtari, E., Saiidi, M., Itani, A. & Moustafa, M. (2019). *Shake Table Studies of a Steel Girder Bridge System with ABC Connections.* Reno, NV: Center for Civil Engineering Earthquake Research, Department of Civil and Environmental Engineering, University of Nevada, Reno. Report No. CCEER 19-04

Shrestha, G., Itani, A., & Saiidi, M. (2016). Preliminary Results of Shear and Pullout Test of Anchors. Reno, NV. Retrieved from https://wolfweb.unr.edu/homepage/saiidi/caltrans/BridgeDeck/PDFs/PreliminaryResultsofShearandPulloutTestofAnchors.pdf

Shrestha, G., Itani, A., & Saiidi, M. (2017). *Seismic Performance of Precast Full-Depth Decks in Accelerated Bridge Construction.* Reno NV: Center for Civil Engineering Earthquake Research, Department of Civil and Environmental Engineering, University of Nevada, Reno. Report No. CCEER 17-05

Tazarv, M. and Saiidi, M.S. (2015). "Design and Construction of Precast Bent Caps with Pocket Connections for High Seismic Regions," Reno, NV: Center for Civil Engineering Earthquake Research, Department of Civil and Environmental Engineering, University of Nevada, Reno, Report No. CCEER-15-06, 101 pp.

TRC. (2006). XTRACT. Rancho Cordova, CA: TRC Bridge Design Software.

Vander Werff, J., Peggar, R., Cheng, Z., & Sritharan, S. (2015). "Seismic Performance of Precast Girder-to-Cap Connections for Accelerated Bridge Construction of Integral Bridges". Ames, IA: Iowa State University. Report CA16-2265.

Varela, S., & Saiidi, M. (2016). *Resilient Earthquake-Resistant Bridges Designed for Disassembly.* Reno, NV: Center for Civil Engineering Earthquake Research, Department of Civil and Environmental Engineering, University of Nevada, Reno. Report No. CCEER 16-02

Wehbe, N., Saiidi, M. & Sanders, D. (1998). "Seismic Performance of Rectangular Columns with Moderate Confinement". *ACI Structural Journal, 96(*2), March-April 1999, pp 248-258

Yuan, J., & Graybeal, B. (2014). *Bond Behavior of Reinforcing Steel in Ultra-High Performance Concrete*. McLean, VA: Federal Highway Administration. Report No. FHWA-HRT-14-090.

Yuan, J., & Graybeal, B. (2015). "Bond of Reinforcement in Ultra-High-Performance Concrete. *ACI Structural Journal, 112(6),* pp. 851-860

Zadeh, M., and M. Saiidi. 2007. "Effect of Strain Rate on Stress-Strain Properties and Yield Propagation in Steel Reinforcing Bars." Reno, NV: Center for Civil Engineering Earthquake Research, Department of Civil and Environmental Engineering, University of Nevada, Reno. Report No. CCEER-07-02.

Tables

Table 2.1 Gravity loads for each component, hand calculated

Prototype Bridge DC Loads		
Girder	711	kips
Cap Beam	243.3	kips
Deck	597	kips
Int. Diaphragm	0.00	kips
Column	75.4	kips
Barrier	158.3	kips
DC Load =	1785	kips
Prototype Bridge DW Loads		
DW Load =	217	kips
Total Dead Load		
DC + DW =	2002	kips

Table 2.2 Comparison of gravity load analysis from hand calculations and CSiBridge

Dead Load Comparison		
CSiBridge	1958.1	kips
Hand Calculations	2001.8	kips
Difference	2%	

Table 2.3 Modal periods for prototype bridge

Mode Type	Period (s)
Vertical	0.32
Transverse	1.04
Longitudinal	1.15
In-plane Rotation	6.67

Table 2.4 Summary of bent properties from iterative analysis, (Benjumea et. al, 2019)

	Case	ρ_L	ρ_S	T_{eff} (s)	Sa (g)	Δ_D [in (cm)]	Δ_Y [in (cm)]	Δ_C [in (cm)]	μ_C	μ_D	C/D (Δ_C/Δ_D)	Bent Shear (F_Y) [kip (kN)]	Shear Design ΦVn/Vu
D_{col}= 4.0 ft (1.2 m) ALI^{top}=7.9% Hc/Dc= 5.0	A	1.38% (16-#11)	1.39% (#7 @ 4.0")	1.22	0.89	12.94 (32.4)	2.14 (5.4)	12.16 (30.4)	5.7	6.0	0.93	326 (1,449)	Ccol: 3.07 Tcol: 3.00
	B	1.72% (20-#11)	1.22% (#8 @ 6.0")	1.16	0.92	12.01 (30)	2.27 (5.7)	10.72 (26.8)	4.7	5.3	0.89	384 (1,710)	Ccol: 2.26 Tcol: 2.03
	C	1.72% (20-#11)	1.63% (#8 @4.5")	1.17	0.91	12.14 (30.4)	2.33 (5.8)	13.80 (34.5)	5.9	5.2	1.14	387 (1,723)	Ccol: 2.89 Tcol: 2.69
D_{col}= 4.5 ft (1.35 m) ALI^{top}= 6.2% Hc/Dc= 4.44	D	1.77% (18-#14)	1.07% (#8 @6")	0.94	1.06	9.24 (23.1)	2.12 (5.3)	8.62 (21.6)	4.1	4.4	0.93	568 (2,526)	Ccol: 1.74 Tcol: 1.57
	E	1.77% (18-#14)	1.30% (#8 @5")	0.94	1.06	9.32 (23.3)	2.15 (5.4)	9.86 (24.7)	4.6	4.3	1.06	571 (2,539)	Ccol: 2.03 Tcol: 1.85
	F	1.77% (18-#14)	1.61% (#8 @4")	0.95	1.06	9.40 (23.5)	2.20 (5.5)	12.13 (30.3)	5.5	4.3	1.29	574 (2,556)	Ccol: 2.89 Tcol: 2.30
	G	1.77% (18-#14)	2.00% (#8 @3")	0.96	1.05	9.53 (23.8)	2.28 (5.7)	17.39 (43.5)	7.6	4.2	1.82	578 (2,572)	Ccol: 2.85 Tcol: 2.33

Table 2.5 Column shear demand and capacities for dead load, and dead load plus overturning effects

Tension Column (33 k - T)		
$M_{P, Col}$ =	2132	k-in
$M_{P, RH}$ =	642	k-in
$V_{u, Col}$ =	33.0	k
$\phi V_{n, column}$ =	49.9	k
Compression Column (137 k - C)		
$M_{P, Col}$ =	2871	k-in
$M_{P, RH}$ =	829	k-in
$V_{u, Col}$ =	44.0	k
$\phi V_{n, column}$ =	80.1	k
DL Column (50 k - C)		
$M_{P, Col}$ =	2291	k-in
$M_{P, RH}$ =	750	k-in
$V_{u, Col}$ =	36.2	k
$\phi V_{n, column}$ =	80.1	k

Table 3.1 Measured compressive strength of concrete test cylinders for 7, 28, and test day

Calt - Bridge 2 Concrete Properties	7-day Strength - psi (MPa)		28-day Strength - psi (MPa)		Test-day Strength - psi (MPa)	
Footing, Columns, Precast Cap Beam	3565	(24.6)	5261	(36.3)	7307	(50.4)
Girders	7825	(54.0)	8886	(61.3)	-	-
Deck Panels	4062	(28.0)	6533	(45.0)	6807	(46.9)
Diaphragms	4199	(29.0)	6575	(45.3)	6680	(46.1)
CIP Cap Beam	2754	(19.0)	3944	(27.2)	3944	(27.2)

Table 3.2 Measured compressive strength of grout cubes for 7, 28, and test day

Calt - Bridge 2 Grout Properties		7-day Strength psi (MPa)		28-day Strength psi (MPa)		Test-day Strength psi (MPa)	
Bent	Pocket Connections	6642	(45.8)	7954	(54.8)	8148	(56.2)
Superstructure	Deck Panel Pockets	7000	(48.3)	6532	(45.0)	7359	(50.7)

Table 3.3 Measured compressive strength of UHPC cylinders for 7, 28, and test day

Calt - Bridge 2 UHPC Properties		7-day Strength psi (MPa)		28-day Strength psi (MPa)		Test-day Strength psi (MPa)	
Superstructure	Deck Joints	13274	(91.5)	16933	(116.7)	18504	(127.6)
CIP Cap Beam	Closure Pour	13253	(91.4)	16915	(116.6)	16915	(116.6)

Table 3.4 Measured yield stress, ultimate stress, yield strain, and ultimate strain

Calt - Bridge 2 Steel Properties		σ_y, ksi (Mpa)		σ_u, ksi (Mpa)		ε_y	ε_u
#3 - Deck	Bar 1	65.6	452	105.3	726	0.23%	-
	Bar 2	65.2	450	105.3	726	0.22%	17.5%
	Bar 3	65.3	450	105.6	728	0.23%	-
	Average	65.4	451	105.4	727	0.23%	17.5%
#3 - Diaphragm	Bar 1	62.6	432	105.7	729	0.22%	17.6%
	Bar 2	63.8	440	105.6	728	0.22%	18.1%
	Bar 3	63.5	438	105.2	725	0.22%	17.8%
	Average	63.3	436	105.5	727	0.22%	17.8%
#3 - Bent	Bar 1	71.1	490	110.8	764	0.25%	17.4%
	Bar 2	71.0	490	111.2	767	0.24%	17.6%
	Bar 3	70	483	109.5	755	0.24%	17.0%
	Average	70.7	487	110.5	762	0.24%	17.3%
#4 - Deck	Bar 1	70.6	487	99.9	689	0.24%	21.4%
	Bar 2	71.7	494	96.7	667	0.25%	-
	Average	71.2	491	98.3	678	0.25%	19.5%
# 5 - Footing	Bar 1	69.7	481	96.9	668	0.25%	19.5%
	Bar 2	70.4	485	95.3	657	0.25%	21.3%
	Bar 3	70.3	485	95.3	657	0.25%	14.7%
	Average	70.1	484	95.8	661	0.25%	18.5%
# 6 - Column, Rebar Hinge, Cap Beam	Bar 1	74.6	514	105.2	725	0.25%	16.9%
	Bar 2	77.3	533	105.9	730	0.25%	18.3%
	Bar 3	75.6	521	105.3	726	0.25%	26.3%
	Average	75.8	523	105.5	727	0.25%	20.5%

Table 4.1 Target and achieved peak ground accelerations

Camera #	Camera Type	Area of Interest
1	GoPro Hero5	Global Superstructure (Top)
2	Video Camera	Global Bridge (Elevation N)
3	Video Camera	Global Bridge (Elevation S)
4	GoPro Hero5	Bent (Elevation N)
5	GoPro Hero5	Bent (Elevation S)
6	GoPro Hero5	E. Abutment (Elevation Long.)
7	GoPro Hero5	W. Abutment (Elevation Long.)
8	GoPro Hero5	E. Abutment (Elevation Trans.)
9	GoPro Hero5	W. Abutment (Elevation Trans.)
10	GoPro Hero5	Bent (Elevation E Trans.)
11	GoPro Hero5	Bent (Elevation W Trans.)
12	GoPro Hero2	N. Column Top (NE)
13	GoPro Hero2	N. Column Top (SW)
14	GoPro Hero2	S. Column Top (NE)
15	GoPro Hero2	S. Column Top (SW)
16	GoPro Hero2	N. Column Bottom (NE)
17	GoPro Hero2	N. Column Bottom (SW)
18	GoPro Hero2	S. Column Bottom (NE)
19	GoPro Hero2	S. Column Bottom (SW)
20	GoPro Hero1	Exterior girder-cap beam interface
21	GoPro Hero1	Girder-Cap beam interface (1-2)
22	GoPro Hero1	Girder-Cap beam interface (2-3)
23	GoPro Hero1	Girder-Cap beam interface (3-4)

Table 5.1 Comparison of reactions at abutments and column bases from gravity analysis and hand calculations

East Abutment				
Girder	Opensees		Hand	
	k	kN	k	kN
1	5.1	22.7	5.5	24.3
2	14.7	65.4	16.6	73.7
3	14.7	65.4	16.6	73.7
4	5.2	23.1	5.3	23.4
Total	39.7	176.6	43.9	195.1
West Abutment				
Girder	Opensees		Hand	
	k	kN	k	kN
1	4.3	19.1	5.5	24.3
2	15.2	67.6	16.6	73.7
3	15.2	67.6	16.6	73.7
4	4.4	19.6	5.5	24.3
Total	39.1	173.9	44.0	195.9
Bent				
Column	Opensees		Hand	
	k	kN	k	kN
North	54.3	241.7	50.0	222.4
South	53.9	240.0	50.0	222.4
Bent Total	108.3	481.7	100.0	444.9
BRIDGE TOTAL	187.1	832.2	187.9	835.9

Table 5.2: Fundamental periods of Opensees bridge model using distributed mass and lumped mass models

Distributed Mass Periods (s)		
Mode 1	1.42	In-plane Rotation
Mode 2	0.30	Longitudinal
Mode 3	0.29	Transverse
Mode 4	0.11	Vertical
Lumped Mass Periods (s)		
Mode 1	1.40	In-plane Rotation
Mode 2	0.29	Longitudinal
Mode 3	0.28	Transverse
Mode 4	0.11	Vertical

Table 5.3 Effective properties of transverse and longitudinal pushover analyses

	Longitudinal		Transverse	
Displacement at first yield	0.38 in	9.65 mm	0.38 in	9.65 mm
Effective yield, Δ_y	0.56 in	14.2 mm	0.56 in	14.2 mm
Maximum Disp. From Pushover, Δ_u	6.72 in	171 mm	6.72 in	171 mm
Plastic Base Shear, F_y	72.7 k	323 kN	71.8 k	319 kN
Effective Stiffness, k_e	130.2 k/in	22.8 kN/mm	128.6 k/in	22.5 kN/mm
Displacement Ductility Capacity, μ_c	$12 < \mu_c$		$12 < \mu_c$	
Effective Period, T_{eff}	0.38		0.39	
Spectral Acceleration, S_a	1.18 g		1.18 g	
Displacement Demand, Δ_d	1.79 in	45.5 mm	1.82 in	46.2 mm
Displacement Ductility Demand, μ_d	2.47		2.47	
Disp. Capacity/ Disp. Demand	3.8 < C/D		3.7 < C/D	

Table 5.4 Target loading protocol and PGAs for Calt-Bridge 2

Run #	% Design Earthquake	Scale Factor	PGA	
			Transverse	Longitudinal
WN1-L	-			
WN1-T				
1	30%	0.137	0.085	0.125
WN2-L	-			
WN2-T				
2	65%	0.296	0.183	0.271
WN3-L	-			
WN3-T				
3	100%	0.455	0.281	0.417
WN4-L	-			
WN4-T				
4	125%	0.569	0.351	0.521
WN5-L	-			
WN5-T				
5	150%	0.683	0.421	0.626
WN6-L	-			
WN6-T				
6	175%	0.796	0.491	0.729
WN7-L	-			
WN7-T				
7	200%	0.91	0.561	0.833
WN8-L	-			
WN8-T				

Table 5.5 Pretest calculated peak longitudinal displacements

Peak Displacements - Longitudinal Direction				
Run #		Calculated		
		(in)	(mm)	Drift Ratio
1	Max.	0.21	5.4	0.30%
	Min.	-0.19	-4.8	-0.20%
2	Max.	0.77	19.5	0.90%
	Min.	-0.93	-23.6	-1.10%
3	Max.	1.6	40.6	1.90%
	Min.	-1.59	-40.4	-1.90%
4	Max.	2.02	51.3	2.40%
	Min.	-2.17	-55.2	-2.60%
5	Max.	2.02	51.4	2.40%
	Min.	-2.91	-73.9	-3.50%
6	Max.	2.11	53.5	2.50%
	Min.	-3.81	-96.8	-4.50%
7	Max.	2.38	60.5	2.80%
	Min.	-4.76	-121	-5.70%

Table 5.6 Pretest calculated peak transverse displacements

Peak Displacements - Transverse Direction				
Run #		Calculated		
		(in)	(mm)	Drift Ratio
1	Max.	0.11	2.8	0.10%
	Min.	-0.14	-3.6	-0.20%
2	Max.	0.49	12.6	0.60%
	Min.	-0.74	-18.7	-0.90%
3	Max.	0.61	15.6	0.70%
	Min.	-1.65	-42	-2.00%
4	Max.	1.05	26.6	1.20%
	Min.	-2.25	-57	-2.70%
5	Max.	1.44	36.5	1.70%
	Min.	-2.76	-70.2	-3.30%
6	Max.	1.96	49.7	2.30%
	Min.	-3.16	-80.2	-3.80%
7	Max.	2.57	65.4	3.10%
	Min.	-3.43	-87.1	-4.10%

Table 5.7 Pretest calculated peak resultant displacements

Peak Displacements - Resultant			
Run #	Calculated		
	(in)	(mm)	Drift Ratio
1	0.22	5.6	0.30%
2	0.99	25.2	1.20%
3	2.18	55.4	2.60%
4	2.86	72.6	3.40%
5	3.27	83	3.90%
6	3.91	99.3	4.70%
7	4.91	124.6	5.80%

Table 5.8 Pretest calculated peak longitudinal base shear

Peak Base Shear - Longitudinal Direction			
Run #		Calculated	
		(k)	(kN)
1	Max.	32.8	146
	Min.	-31.3	-139
2	Max.	51	226.7
	Min.	-58.8	-261.4
3	Max.	59.1	262.9
	Min.	-57.7	-256.5
4	Max.	59.9	266.5
	Min.	-58.1	-258.4
5	Max.	63.6	282.8
	Min.	-59	-262.3
6	Max.	66.3	294.8
	Min.	-53	-235.6
7	Max.	69.1	307.5
	Min.	-56.5	-251.3

Table 5.9 Pretest calculated peak transverse base shear

Peak Base Bent Shear - Transverse Direction			
Run #		Calculated	
		(k)	(kN)
1	Max.	28	124.5
	Min.	-22.7	-100.9
2	Max.	56.1	249.7
	Min.	-48.9	-217.7
3	Max.	56.5	251.2
	Min.	-49	-218.1
4	Max.	57.2	254.5
	Min.	-53.2	-236.5
5	Max.	59	262.4
	Min.	-55.6	-247.3
6	Max.	62.3	277.1
	Min.	-56.9	-253.3
7	Max.	60.9	270.7
	Min.	-59.8	-266.2

Table 6.1 Target and achieved peak ground accelerations

Run #	Longitudinal Direction			Transverse Direction			Average Ratio
	Target (g)	Measured (g)	Measured/ Target	Target (g)	Measured (g)	Measured/ Target	
1	0.125	0.171	137%	0.085	0.086	101%	119%
2	0.271	0.276	102%	0.183	0.162	89%	95%
3	0.417	0.320	77%	0.281	0.226	80%	79%
4	0.521	0.370	71%	0.351	0.291	83%	77%
5	0.626	0.415	66%	0.421	0.372	88%	77%
6	0.729	0.500	69%	0.491	0.451	92%	80%
7	0.833	0.577	69%	0.561	0.563	100%	85%
8	0.938	0.686	73%	0.632	0.684	108%	91%

Table 6.2 Target and achieved spectral accelerations

Run #	Longitudinal Direction			Transverse Direction			Average Ratio
	Target (g)	Measured (g)	Measured/ Target	Target (g)	Measured (g)	Measured/ Target	
1	0.198	0.190	96%	0.157	0.108	69%	82%
2	0.428	0.370	86%	0.341	0.258	76%	81%
3	0.659	0.566	86%	0.520	0.345	66%	76%
4	0.820	0.725	88%	0.650	0.549	84%	86%
5	0.985	0.880	89%	0.785	0.715	91%	90%
6	1.15	1.12	97%	0.915	0.855	93%	95%
7	1.31	1.401	107%	1.045	0.985	94%	101%
8	1.47	1.63	111%	1.174	1.125	96%	103%

Table 6.3 Peak longitudinal accelerations along superstructure for all runs

Run #		Longitudinal Direction				
		AL1	AL2	AL3	AL4	AL5
1	Max.	0.073	0.074	0.075	0.071	0.067
	Min.	-0.116	-0.114	-0.113	-0.115	-0.122
2	Max.	0.240	0.240	0.244	0.243	0.235
	Min.	-0.278	-0.285	-0.292	-0.284	-0.288
3	Max.	0.295	0.305	0.301	0.297	0.294
	Min.	-0.337	-0.341	-0.346	-0.336	-0.348
4	Max.	0.333	0.341	0.340	0.333	0.341
	Min.	-0.327	-0.324	-0.323	-0.326	-0.329
5	Max.	0.359	0.366	0.366	0.360	0.358
	Min.	-0.287	-0.273	-0.279	-0.287	-0.275
6	Max.	0.361	0.355	0.365	0.360	0.361
	Min.	-0.259	-0.265	-0.256	-0.257	-0.266
7	Max.	0.351	0.354	0.358	0.354	0.362
	Min.	-0.274	-0.276	-0.277	-0.269	-0.276
8	Max.	0.335	0.339	0.340	0.335	0.336
	Min.	-0.281	-0.277	-0.277	-0.275	-0.280

Table 6.4 Peak transverse accelerations along superstructure for all runs

Run #		Transverse Direction				
		AT1	AT2	AT3	AT4	AT5
1	Max.	0.060	0.063	0.067	0.065	0.064
	Min.	-0.071	-0.072	-0.071	-0.075	-0.085
2	Max.	0.239	0.203	0.217	0.196	0.251
	Min.	-0.259	-0.221	-0.235	-0.238	-0.264
3	Max.	0.320	0.302	0.317	0.278	0.387
	Min.	-0.365	-0.307	-0.326	-0.316	-0.342
4	Max.	0.286	0.253	0.262	0.262	0.392
	Min.	-0.300	-0.267	-0.287	-0.279	-0.306
5	Max.	0.290	0.238	0.242	0.251	0.301
	Min.	-0.266	-0.257	-0.260	-0.267	-0.289
6	Max.	0.266	0.226	0.236	0.248	0.272
	Min.	-0.273	-0.238	-0.241	-0.245	-0.266
7	Max.	0.239	0.231	0.238	0.248	0.280
	Min.	-0.257	-0.223	-0.211	-0.221	-0.240
8	Max.	0.232	0.238	0.230	0.244	0.270
	Min.	-0.233	-0.198	-0.202	-0.205	-0.234

Table 6.5 Peak vertical accelerations along superstructure for all runs

Peak vertical acceleration along superstructure						
Run #		Vertical Direction				
		AV1	AV2	AV3	AV4	AV5
1	Max.	0.027	0.050	0.028	0.060	0.023
	Min.	-0.014	-0.054	-0.022	-0.059	-0.025
2	Max.	0.020	0.080	0.041	0.083	0.029
	Min.	-0.020	-0.085	-0.040	-0.101	-0.045
3	Max.	0.040	0.129	0.059	0.149	0.035
	Min.	-0.040	-0.147	-0.056	-0.136	-0.043
4	Max.	0.026	0.178	0.051	0.154	0.045
	Min.	-0.030	-0.166	-0.074	-0.188	-0.058
5	Max.	0.043	0.228	0.043	0.173	0.029
	Min.	-0.018	-0.185	-0.073	-0.165	-0.043
6	Max.	0.043	0.186	0.058	0.188	0.025
	Min.	-0.048	-0.175	-0.062	-0.169	-0.038
7	Max.	0.051	0.150	0.055	0.190	0.046
	Min.	-0.044	-0.167	-0.080	-0.169	-0.030
8	Max.	0.035	0.149	0.057	0.167	0.037
	Min.	-0.048	-0.159	-0.069	-0.168	-0.040

Table 6.6 Abutment seat absolute displacement

Run #		Longitudinal Displacement				Transverse Displacement			
		East Abutment		West Abutment		East Abutment		West Abutment	
		(in)	(mm)	(in)	(mm)	(in)	(mm)	(in)	(mm)
1	Max.	0.04	1.1	0.03	0.8	0.03	0.8	0.00	0.1
	Min.	-0.04	-1.1	-0.04	-1.0	-0.01	-0.3	-0.01	-0.3
2	Max.	0.05	1.3	0.03	0.7	0.04	1.1	0.01	0.3
	Min.	-0.05	-1.3	-0.04	-1.1	-0.03	-0.7	-0.01	-0.2
3	Max.	0.04	1.0	0.02	0.5	0.04	1.0	0.00	0.1
	Min.	-0.04	-1.0	-0.04	-1.0	-0.02	-0.4	-0.02	-0.5
4	Max.	0.03	0.7	0.02	0.4	0.05	1.2	0.01	0.2
	Min.	-0.02	-0.6	-0.04	-1.0	-0.01	-0.2	-0.02	-0.5
5	Max.	0.03	0.8	0.02	0.5	0.04	1.1	0.03	0.7
	Min.	-0.02	-0.6	-0.04	-0.9	-0.01	-0.2	-0.02	-0.5
6	Max.	0.03	0.8	0.02	0.6	0.05	1.4	0.01	0.3
	Min.	-0.01	-0.2	-0.03	-0.7	-0.01	-0.2	-0.03	-0.8
7	Max.	0.03	0.9	0.02	0.5	0.06	1.5	0.02	0.6
	Min.	-0.01	-0.2	-0.03	-0.9	0.00	0.1	-0.05	-1.2
8	Max.	0.03	0.9	0.02	0.5	0.05	1.2	0.00	0.1
	Min.	-0.01	-0.3	-0.09	-2.3	0.02	0.4	-0.03	-0.9

Table 6.7 Transverse superstructure displacement at abutments, bent, and midspan

Run #		DT7 (East)		DT6		DT5		DT3		DT1 (West)	
		(in)	(mm)	(in)	(mm)	(in)	(mm)	(in)	(mm)	(in)	(mm)
1	Max.	0.16	4.1	0.15	3.7	0.13	3.3	0.13	3.2	0.12	3.0
	Min.	-0.15	-3.8	-0.17	-4.2	-0.16	-4.1	-0.18	-4.6	-0.20	-5.1
2	Max.	0.58	14.7	0.53	13.6	0.59	14.9	0.71	18.0	0.80	20.3
	Min.	-0.91	-23.1	-0.81	-20.5	-0.66	-16.7	-0.58	-14.8	-0.55	-14.0
3	Max.	0.93	23.6	0.95	24.0	0.95	24.1	1.62	41.2	2.10	53.3
	Min.	-2.44	-62.0	-1.93	-49.1	-1.29	-32.7	-0.93	-23.7	-0.92	-23.4
4	Max.	0.44	11.2	0.72	18.4	1.09	27.7	2.39	60.7	3.31	84.1
	Min.	-3.49	-88.6	-2.64	-67.2	-1.49	-37.7	-1.05	-26.8	-0.71	-18.0
5	Max.	-0.17	-4.3	0.39	9.9	1.43	36.4	3.26	82.7	4.41	112.0
	Min.	-4.51	-114.6	-3.22	-81.7	-1.65	-41.8	-0.97	-24.7	0.20	5.1
6	Max.	-1.76	-44.7	-0.03	-0.8	1.82	46.3	4.35	110.5	4.50	114.3
	Min.	-4.30	-109.2	-4.04	-102.5	-1.96	-49.9	-0.80	-20.3	2.07	52.6
7	Max.	-3.49	-88.6	-0.74	-18.8	2.12	53.9	6.03	153.1	6.90	175.3
	Min.	-7.03	-178.6	-5.71	-145.0	-2.31	-58.7	-0.22	-5.7	3.51	89.2
8	Max.	-6.56	-166.6	-2.30	-58.5	2.24	56.8	7.94	201.7	11.09	281.7
	Min.	-10.7	-271.8	-7.67	-194.8	-2.73	-69.4	1.09	27.7	6.29	159.8

Table 6.8 Peak and residual in-plane rotation of superstructure

Run #	Peak Rotation (rad)	Residual Rotation (rad)
1	-0.0002	-0.0001
2	-0.0004	0.0001
3	0.0027	0.0013
4	0.0053	0.0031
5	0.0076	0.0052
6	0.0104	0.009
7	0.0165	0.0161
8	0.0249	0.0242

Table 6.9 Longitudinal superstructure displacement measured at the abutments

Run #		DL1		DL3		DL5		DL8		Average	
		(in)	(mm)	(in)	(mm)	(in)	(mm)	(in)	(mm)	(in)	(mm)
1	Max.	0.29	7.4	0.28	7.1	0.21	5.4	0.22	5.5	0.25	6.3
	Min.	-0.21	-5.3	-0.21	-5.4	-0.30	-7.5	-0.28	-7.2	-0.25	-6.4
2	Max.	0.92	23.4	0.86	21.9	0.90	22.9	1.00	25.5	0.92	23.4
	Min.	-0.87	-22.2	-0.98	-24.8	-0.94	-23.9	-0.86	-21.9	-0.91	-23.2
3	Max.	1.76	44.8	1.55	39.3	1.44	36.4	1.81	46.0	1.64	41.6
	Min.	-1.38	-35.1	-1.77	-44.9	-1.78	-45.3	-1.54	-39.1	-1.62	-41.1
4	Max.	2.79	71.0	2.18	55.5	1.38	34.9	2.15	54.6	2.13	54.0
	Min.	-1.28	-32.5	-2.09	-53.1	-2.79	-70.9	-2.17	-55.0	-2.08	-52.9
5	Max.	3.75	95.4	2.78	70.5	1.40	35.6	2.15	54.6	2.52	64.0
	Min.	-1.33	-33.8	-2.11	-53.6	-3.71	-94.2	-2.73	-69.4	-2.47	-62.8
6	Max.	4.56	115.9	3.10	78.7	1.68	42.6	2.89	73.5	3.06	77.7
	Min.	-1.54	-39.2	-2.82	-71.5	-4.45	-113.0	-3.02	-76.6	-2.96	-75.1
7	Max.	5.38	136.7	2.99	76.0	1.92	48.8	3.92	99.6	3.55	90.3
	Min.	-1.63	-41.4	-3.75	-95.1	-5.08	-129.0	-2.76	-70.1	-3.30	-83.9
8	Max.	6.35	161.3	2.72	69.0	2.03	51.5	5.10	129.6	4.05	102.9
	Min.	-1.43	-36.3	-4.68	-118.9	-5.67	-144.1	-2.21	-56.1	-3.50	-88.8

Table 6.10 Vertical superstructure displacement along north girder

Run #		Abutment - East (DV9)		Mid-span - East (DV7)		Bent (DV5)		Mid-span - West (DV3)		Abutment - West (DV1)	
		(in)	(mm)	(in)	(mm)	(in)	(mm)	(in)	(mm)	(in)	(mm)
1	Max.	0.03	0.66	0.07	1.73	0.01	0.30	0.06	1.42	0.01	0.30
	Min.	-0.02	-0.53	-0.03	-0.84	-0.01	-0.20	-0.05	-1.20	-0.02	-0.51
2	Max.	0.06	1.52	0.14	3.60	0.08	1.94	0.16	4.01	0.05	1.16
	Min.	-0.06	-1.62	-0.07	-1.81	-0.01	-0.15	-0.08	-2.09	-0.03	-0.76
3	Max.	0.10	2.63	0.19	4.86	0.15	3.83	0.21	5.33	0.06	1.51
	Min.	-0.08	-2.06	-0.08	-1.94	0.00	0.10	-0.10	-2.63	-0.04	-1.12
4	Max.	0.08	2.11	0.23	5.86	0.18	4.60	0.21	5.33	0.05	1.23
	Min.	-0.05	-1.17	-0.08	-1.96	0.03	0.65	-0.12	-3.07	-0.06	-1.61
5	Max.	0.14	3.46	0.25	6.32	0.24	5.99	0.18	4.52	0.04	1.07
	Min.	-0.10	-2.41	-0.08	-2.03	0.04	1.01	-0.14	-3.66	-0.08	-2.00
6	Max.	0.15	3.69	0.23	5.81	0.29	7.28	0.18	4.62	0.07	1.66
	Min.	-0.12	-2.97	-0.10	-2.64	0.05	1.26	-0.19	-4.94	-0.09	-2.29
7	Max.	0.24	6.11	0.15	3.93	0.35	8.78	0.13	3.38	0.13	3.41
	Min.	-0.12	-2.92	-0.14	-3.63	0.06	1.52	-0.27	-6.73	-0.14	-3.55
8	Max.	0.34	8.60	0.07	1.84	0.38	9.65	0.03	0.84	0.15	3.80
	Min.	-0.12	-3.14	-0.30	-7.59	0.06	1.54	-0.61	-15.53	-0.23	-5.86

Table 6.11 Vertical superstructure displacement along south girder

Run #		Abutment - East (DV10)		Mid-span - East (DV8)		Bent (DV6)		Mid-span - West (DV4)		Abutment - West (DV10)	
		(in)	(mm)	(in)	(mm)	(in)	(mm)	(in)	(mm)	(in)	(mm)
1	Max.	0.01	0.33	0.07	1.88	0.01	0.35	0.06	1.45	0.02	0.45
	Min.	-0.02	-0.43	-0.04	-0.91	-0.01	-0.15	-0.04	-0.96	-0.02	-0.44
2	Max.	0.05	1.21	0.14	3.61	0.09	2.28	0.17	4.36	0.07	1.73
	Min.	-0.03	-0.75	-0.10	-2.45	0.00	-0.10	-0.06	-1.58	-0.03	-0.72
3	Max.	0.08	2.11	0.19	4.93	0.18	4.55	0.24	6.09	0.10	2.66
	Min.	-0.05	-1.17	-0.10	-2.52	0.01	0.15	-0.07	-1.83	-0.03	-0.85
4	Max.	0.10	2.42	0.23	5.81	0.21	5.28	0.26	6.51	0.12	3.03
	Min.	-0.04	-1.07	-0.12	-3.01	0.04	0.94	-0.07	-1.66	-0.03	-0.80
5	Max.	0.10	2.45	0.25	6.24	0.22	5.61	0.22	5.61	0.11	2.87
	Min.	-0.04	-0.94	-0.11	-2.83	0.05	1.25	-0.07	-1.89	-0.04	-1.09
6	Max.	0.18	4.65	0.24	5.97	0.25	6.42	0.23	5.84	0.17	4.25
	Min.	-0.05	-1.21	-0.16	-4.06	0.06	1.54	-0.08	-2.03	-0.05	-1.18
7	Max.	0.33	8.27	0.17	4.37	0.30	7.65	0.22	5.62	0.28	7.16
	Min.	-0.07	-1.73	-0.24	-6.03	0.06	1.64	-0.13	-3.38	-0.09	-2.22
8	Max.	0.52	13.15	0.10	2.49	0.36	9.22	0.15	3.70	0.30	7.63
	Min.	-0.05	-1.30	-0.49	-12.42	0.06	1.58	-0.24	-6.01	-0.08	-1.96

Table 6.12 Peak longitudinal total displacements in columns and bent

Run #		North Column			South Column			Bent		
		(in)	(mm)	Drift Ratio	(in)	(mm)	Drift Ratio	(in)	(mm)	Drift Ratio
1	Max.	0.21	5.4	0.3%	0.22	5.5	0.3%	0.22	5.5	0.3%
	Min.	-0.31	-7.9	-0.4%	-0.30	-7.5	-0.4%	-0.30	-7.7	-0.4%
2	Max.	0.91	23.0	1.1%	1.01	25.7	1.2%	0.96	24.3	1.1%
	Min.	-0.95	-24.2	-1.1%	-0.88	-22.3	-1.0%	-0.91	-23.2	-1.1%
3	Max.	1.45	36.9	1.7%	1.84	46.6	2.2%	1.64	41.7	2.0%
	Min.	-1.78	-45.3	-2.1%	-1.55	-39.3	-1.8%	-1.66	-42.3	-2.0%
4	Max.	1.42	36.1	1.7%	2.21	56.2	2.6%	1.82	46.1	2.2%
	Min.	-2.80	-71.1	-3.3%	-2.16	-55.0	-2.6%	-2.48	-63.0	-3.0%
5	Max.	1.51	38.3	1.8%	2.26	57.5	2.7%	1.88	47.9	2.2%
	Min.	-3.74	-94.9	-4.4%	-2.73	-69.4	-3.3%	-3.23	-82.1	-3.8%
6	Max.	1.83	46.5	2.2%	3.06	77.7	3.6%	2.45	62.1	2.9%
	Min.	-4.48	-113.9	-5.3%	-3.00	-76.3	-3.6%	-3.74	-95.1	-4.5%
7	Max.	2.12	53.8	2.5%	4.15	105.5	4.9%	3.14	79.6	3.7%
	Min.	-5.13	-130.3	-6.1%	-2.74	-69.7	-3.3%	-3.94	-100.0	-4.7%
8	Max.	2.20	56.0	2.6%	5.36	136.2	6.4%	3.78	96.0	4.5%
	Min.	-5.75	-146.1	-6.8%	-2.21	-56.0	-2.6%	-4.20	-101.1	-4.7%

Table 6.13 Peak transverse total displacements in columns and bent

Run #		North Column			South Column			Bent		
		(in)	(mm)	Drift Ratio	(in)	(mm)	Drift Ratio	(in)	(mm)	Drift Ratio
1	Max.	0.16	4.2	0.2%	0.16	4.2	0.2%	0.16	4.2	0.2%
	Min.	-0.13	-3.3	-0.2%	-0.13	-3.3	-0.2%	-0.13	-3.3	-0.2%
2	Max.	0.66	16.8	0.8%	0.66	16.8	0.8%	0.66	16.8	0.8%
	Min.	-0.59	-15.0	-0.7%	-0.59	-15.0	-0.7%	-0.59	-15.0	-0.7%
3	Max.	1.29	32.8	1.5%	1.29	32.8	1.5%	1.29	32.8	1.5%
	Min.	-0.95	-24.1	-1.1%	-0.95	-24.1	-1.1%	-0.95	-24.1	-1.1%
4	Max.	1.49	37.8	1.8%	1.49	37.8	1.8%	1.49	37.8	1.8%
	Min.	-1.10	-27.9	-1.3%	-1.10	-27.9	-1.3%	-1.10	-27.9	-1.3%
5	Max.	1.65	41.9	2.0%	1.65	41.9	2.0%	1.65	41.9	2.0%
	Min.	-1.43	-36.4	-1.7%	-1.44	-36.5	-1.7%	-1.44	-36.5	-1.7%
6	Max.	1.97	50.0	2.3%	1.97	50.0	2.3%	1.97	50.0	2.3%
	Min.	-1.83	-46.5	-2.2%	-1.83	-46.6	-2.2%	-1.83	-46.5	-2.2%
7	Max.	2.32	59.0	2.8%	2.32	58.9	2.8%	2.32	59.0	2.8%
	Min.	-2.13	-54.1	-2.5%	-2.14	-54.4	-2.5%	-2.14	-54.3	-2.5%
8	Max.	2.73	69.5	3.3%	2.72	69.1	3.2%	2.73	69.3	3.2%
	Min.	-2.25	-57.1	-2.7%	-2.27	-57.7	-2.7%	-2.26	-57.4	-2.7%

Table 6.14 Peak resultant total displacements in columns and bent

Run #	North Column			South Column			Bent		
	(in)	(mm)	Drift Ratio	(in)	(mm)	Drift Ratio	(in)	(mm)	Drift Ratio
1	0.31	8.0	0.4%	0.30	7.7	0.4%	0.31	7.8	0.4%
2	1.84	46.7	2.2%	1.81	46.0	2.2%	1.82	46.3	2.2%
3	1.89	48.1	2.3%	1.99	50.5	2.4%	1.81	46.0	2.2%
4	2.87	72.9	3.4%	2.39	60.7	2.8%	2.56	64.9	3.0%
5	3.78	96.1	4.5%	2.79	71.0	3.3%	3.29	83.5	3.9%
6	4.51	114.4	5.4%	3.12	79.2	3.7%	3.77	95.7	4.5%
7	5.14	130.6	6.1%	4.17	106.0	5.0%	3.95	100.3	4.7%
8	5.78	146.8	6.9%	5.36	136.2	6.4%	4.02	102.0	4.8%

Table 6.15 Peak longitudinal net displacements in columns and bent

Run #		North Column			South Column			Bent		
		(in)	(mm)	Drift Ratio	(in)	(mm)	Drift Ratio	(in)	(mm)	Drift Ratio
1	Max.	0.21	5.4	0.3%	0.22	5.6	0.3%	0.22	5.5	0.3%
	Min.	-0.31	-7.8	-0.4%	-0.30	-7.6	-0.4%	-0.30	-7.7	-0.4%
2	Max.	0.89	22.7	1.1%	1.02	25.9	1.2%	0.96	24.3	1.1%
	Min.	-0.95	-24.1	-1.1%	-0.89	-22.5	-1.1%	-0.92	-23.3	-1.1%
3	Max.	1.40	35.5	1.7%	1.85	46.9	2.2%	1.62	41.2	1.9%
	Min.	-1.78	-45.1	-2.1%	-1.55	-39.4	-1.8%	-1.66	-42.3	-2.0%
4	Max.	1.31	33.3	1.6%	2.23	56.6	2.7%	1.77	44.9	2.1%
	Min.	-2.80	-71.2	-3.3%	-2.16	-54.8	-2.6%	-2.48	-63.0	-3.0%
5	Max.	1.40	35.6	1.7%	2.28	57.9	2.7%	1.84	46.7	2.2%
	Min.	-3.76	-95.6	-4.5%	-2.71	-68.9	-3.2%	-3.24	-82.2	-3.9%
6	Max.	1.66	42.1	2.0%	3.09	78.5	3.7%	2.37	60.3	2.8%
	Min.	-4.54	-115.4	-5.4%	-2.96	-75.3	-3.5%	-3.75	-95.3	-4.5%
7	Max.	1.84	46.7	2.2%	4.21	106.9	5.0%	3.02	76.7	3.6%
	Min.	-5.24	-133.0	-6.2%	-2.66	-67.7	-3.2%	-3.95	-100.3	-4.7%
8	Max.	1.76	44.8	2.1%	5.43	138.0	6.5%	3.60	91.4	4.3%
	Min.	-5.92	-150.3	-7.0%	-2.08	-52.9	-2.5%	-4.00	-101.6	-4.8%

Table 6.16 Peak transverse net displacements in columns and bent

Run #		North Column (in)	North Column (mm)	North Column Drift Ratio	South Column (in)	South Column (mm)	South Column Drift Ratio	Bent (in)	Bent (mm)	Bent Drift Ratio
1	Max.	0.16	4.1	0.2%	0.15	3.9	0.2%	0.16	4.0	0.2%
	Min.	-0.13	-3.2	-0.2%	-0.12	-3.1	-0.1%	-0.12	-3.2	-0.1%
2	Max.	0.62	15.8	0.7%	0.67	16.9	0.8%	0.68	17.3	0.8%
	Min.	-0.67	-17.0	-0.8%	-0.69	-17.6	-0.8%	-0.64	-16.3	-0.8%
3	Max.	1.21	30.8	1.4%	1.17	29.8	1.4%	1.19	30.3	1.4%
	Min.	-0.95	-24.2	-1.1%	-0.86	-21.8	-1.0%	-0.90	-23.0	-1.1%
4	Max.	1.38	34.9	1.6%	1.34	34.1	1.6%	1.36	34.5	1.6%
	Min.	-1.12	-28.6	-1.3%	-0.99	-25.2	-1.2%	-1.06	-26.9	-1.3%
5	Max.	1.55	39.5	1.8%	1.50	38.1	1.8%	1.53	38.8	1.8%
	Min.	-1.48	-37.5	-1.8%	-1.30	-33.1	-1.6%	-1.39	-35.3	-1.7%
6	Max.	1.82	46.2	2.2%	1.78	45.2	2.1%	1.80	45.7	2.1%
	Min.	-1.89	-47.9	-2.2%	-1.66	-42.2	-2.0%	-1.77	-45.1	-2.1%
7	Max.	2.08	52.9	2.5%	2.09	53.0	2.5%	2.08	52.9	2.5%
	Min.	-2.25	-57.2	-2.7%	-1.93	-49.0	-2.3%	-2.09	-53.1	-2.5%
8	Max.	2.35	59.7	2.8%	2.40	61.0	2.9%	2.37	60.3	2.8%
	Min.	-2.46	-62.6	-2.9%	-2.05	-52.0	-2.4%	-2.26	-57.3	-2.7%

Table 6.17 Peak slippage at column base

Run #		N. Column				S. Column			
		Longitudinal		Transverse		Longitudinal		Transverse	
		(in)	(mm)	(in)	(mm)	(in)	(mm)	(in)	(mm)
1	Max.	0.001	0.028	0.004	0.097	0.003	0.076	0.009	0.236
	Min.	-0.003	-0.086	-0.006	-0.142	-0.002	-0.061	-0.011	-0.290
2	Max.	0.013	0.338	0.015	0.376	0.008	0.198	0.054	1.369
	Min.	-0.007	-0.180	-0.030	-0.772	-0.011	-0.277	-0.053	-1.349
3	Max.	0.057	1.453	0.026	0.658	0.007	0.173	0.093	2.370
	Min.	-0.012	-0.307	-0.079	-2.009	-0.018	-0.450	-0.117	-2.979
4	Max.	0.109	2.779	0.010	0.251	0.005	0.117	0.106	2.700
	Min.	-0.012	-0.312	-0.140	-3.551	-0.026	-0.648	-0.145	-3.683
5	Max.	0.153	3.891	-0.010	-0.246	0.006	0.155	0.135	3.429
	Min.	-0.001	-0.036	-0.207	-5.265	-0.034	-0.864	-0.163	-4.150
6	Max.	0.203	5.166	-0.030	-0.749	-0.005	-0.122	0.171	4.343
	Min.	0.015	0.368	-0.285	-7.242	-0.054	-1.372	-0.189	-4.803
7	Max.	0.291	7.386	-0.067	-1.702	-0.022	-0.569	0.212	5.387
	Min.	0.045	1.135	-0.392	-9.967	-0.088	-2.238	-0.236	-5.987
8	Max.	0.456	11.585	-0.149	-3.795	-0.055	-1.387	0.221	5.618
	Min.	0.102	2.588	-0.537	-13.637	-0.133	-3.383	-0.316	-8.024

Table 6.18 Comparison of longitudinal base shear using force and acceleration-based methods

Run #		Force Based Method		Acceleration Based Method		% Difference
		(k)	(kN)	(k)	(kN)	
1	Max.	22.4	99.8	14.5	64.6	35%
	Min.	-18.4	-81.7	-21.8	-96.8	-18%
2	Max.	51.7	229.8	47.1	209.4	9%
	Min.	-52.0	-231.4	-56.4	-250.7	-8%
3	Max.	64.5	286.9	58.0	258.2	10%
	Min.	-63.2	-281.2	-66.7	-296.5	-5%
4	Max.	70.9	315.2	65.5	291.2	8%
	Min.	-56.7	-252.2	-62.3	-277.0	-10%
5	Max.	72.8	323.9	70.5	313.7	3%
	Min.	-55.2	-245.7	-53.8	-239.4	3%
6	Max.	74.3	330.4	70.4	313.0	5%
	Min.	-59.5	-264.9	-49.4	-219.9	17%
7	Max.	71.2	316.7	69.0	307.0	3%
	Min.	-61.9	-275.4	-53.5	-237.9	14%
8	Max.	70.6	314.1	65.5	291.2	7%
	Min.	-62.7	-278.8	-53.3	-237.2	15%

Table 6.19 Comparison of transverse base shear using force and acceleration-based methods

Run #		Force Based Method		Acceleration Based Method		% Difference
		(k)	(kN)	(k)	(kN)	
1	Max.	15.1	67.1	12.9	57.3	15%
	Min.	-13.9	-61.7	-13.7	-61.1	1%
2	Max.	37.7	167.7	41.9	186.4	-11%
	Min.	-36.9	-164.2	-45.3	-201.5	-23%
3	Max.	49.8	221.5	61.1	271.6	-23%
	Min.	-52.3	-232.5	-62.9	-279.9	-20%
4	Max.	51.1	227.2	50.6	224.9	1%
	Min.	-49.8	-221.5	-55.3	-246.0	-11%
5	Max.	53.4	237.6	46.6	207.5	13%
	Min.	-49.1	-218.6	-50.2	-223.3	-2%
6	Max.	54.6	242.7	45.5	202.2	17%
	Min.	-44.7	-198.8	-46.5	-206.7	-4%
7	Max.	54.7	243.4	45.8	203.7	16%
	Min.	-42.3	-188.1	-40.7	-181.1	4%
8	Max.	54.1	240.7	44.3	196.9	18%
	Min.	-41.4	-184.2	-38.8	-172.8	6%

Table 6.20 Longitudinal and vertical fundamental frequencies and periods

Run #	Longitudinal		Vertical	
	Frequency (Hz)	Period (s)	Frequency (Hz)	Period (s)
WN1-L	6.3	0.16	6.3	0.16
WN2-L	5.8	0.17	6.0	0.17
WN3-L	5.8	0.17	5.8	0.17
WN4-L	5.6	0.18	5.5	0.18
WN5-L	5.5	0.18	5.5	0.18
WN6-L	5.5	0.18	5.5	0.18
WN7-L	5.5	0.18	5.5	0.18
WN8-L	5.5	0.18	5.5	0.18
WN9-L	5.5	0.18	5.5	0.18

Table 6.21 Transverse fundamental frequencies and periods

Run #	Transverse	
	Frequency (Hz)	Period (s)
WN1-L	7.8	0.13
WN2-L	7.0	0.14
WN3-L	6.8	0.15
WN4-L	6.5	0.15
WN5-L	6.5	0.15
WN6-L	6.5	0.15
WN7-L	6.5	0.15
WN8-L	6.3	0.16
WN9-L	6.3	0.16

Table 6.22 Maximum strains and yield ratio in each element

Zone	Rein. Type	Max. Strain (με)	Yield Ratio
Column	Longitudinal North	-26800	10.3
	Spiral North	-1680	0.69
	Longitudinal South	-37900	14.5
	Spiral South	-1080	0.44
Hinge	Longitudinal North	-45600	17.5
	Spiral North	-1040	0.43
	Longitudinal South	-43600	16.7
	Spiral South	-2690	1.10
Deck	Longitudinal	-975	0.40
Bent	Transverse	-1690	0.69
	Headed Bars	838	≈ 0.35
	Crossties	-111	0.05
	Girder Strands	-1670	0.18
	Longitudinal Top	-386	0.15
	Longitudinal Bottom	-1000	0.38
	Pocket Spiral	-1620	0.66

Table 6.23 Peak strains in north column longitudinal bars

North Column Longitudinal Bar Strains (με) (ε_y = 2610 με)								
	Run 1	Run 2	Run 3	Run 4	Run 5	Run 6	Run 7	Run 8
CSGN1	91	117	-83	-104	124	-138	-145	-145
CSGN2	-298	-407	-538	-642	-704	-566	-614	-649
CSGN3	-	-	-	-	-	-	-	-
CSGN4	-	-	-	-	-	-	-	-
CSGN5	718	-2210	-	-	-	-	-	-
CSGN6	201	-1530	-2500	-2890	-3300	-3540	-4230	-4440
CSGN7	960	-1760	-3320	-3760	-7760	-11000	-	-
CSGN8	231	-1210	-2350	-2570	-2710	-2890	-3060	-3360
CSGN9	366	-2550	-3230	-3210	-3750	-13100	-14600	-15100
CSGN10	208	366	525	-442	670	-2680	-1840	-1450
CSGN11	-768	-2440	-3090	-17900	-18400	-21500	-24000	-26500
CSGN12	-524	-1730	-3010	-3400	-4960	-	-	-
CSGN13	-983	-3030	-13600	-	-	-	-	-
CSGN14	390	-1850	-7870	-18300	-19900	-22600	-24900	-25700
CSGN15	-875	-2660	-17000	-19000	-23900	-26800	-	-
CSGN16	-593	-2020	-16000	-	-	-	-	-
CSGN17	235	-2120	-11100	-14100	-16000	-17600	-18500	-18800
CSGN18	192	-1620	2380	-	-	-	-	-
CSGN19	202	-2120	-5370	-11300	-	-	-	-
CSGN20	147	-1490	-2770	-3760	-4970	-10300	-16800	-20000

Table 6.24 Peak strains in south column longitudinal bars

South Column Longitudinal Bar Strains (με) (ε_y = 2610 με)								
	Run 1	Run 2	Run 3	Run 4	Run 5	Run 6	Run 7	Run 8
CSGS1	102	145	97	-117	-131	-159	-172	-172
CSGS2	68	110	-83	-104	-97	-117	-138	-145
CSGS3	-	-	-	-	-	-	-	-
CSGS4	-	-	-	-	-	-	-	-
CSGS5	-520	-3030	-5640	-6360	-6270	-6740	-9780	-13700
CSGS6	256	-1400	-2150	-2190	-2390	-2610	-2850	-3060
CSGS7	-452	-2870	-3960	-4420	-4770	-6170	-9200	-11600
CSGS8	251	-1620	-3030	-3170	-3360	-4660	-12300	-21600
CSGS9	341	-3090	-8810	-14100	-16600	-19600	-26200	-30700
CSGS10	279	-1710	-2790	-3160	-3260	-13100	-15100	-15700
CSGS11	-832	-3180	-6400	-	-	-	-	-
CSGS12	227	-1960	-3590	-9250	-13500	-16600	-18900	-22600
CSGS13	395	-2900	-17100	-19100	-20600	-26100	-33800	-37900
CSGS14	294	-2120	-12400	-	-	-	-	-
CSGS15	-1001	-2820	-18500	-17900	-22100	-23500	-22500	-21900
CSGS16	246	-2200	-7720	-19900	-18500	-20700	-27700	-32800
CSGS17	168	-2120	-2820	-3140	-3780	-6780	-14300	-16700
CSGS18	259	-908	-1880	-2430	-2660	-2710	-2800	-2780
CSGS19	228	-2180	-2840	-3510	-16100	-16600	-18200	-19500
CSGS20	209	-1520	-2800	-2920	-2990	-3090	-10400	-15300

Table 6.25 Peak strains in south column spirals

South Column Spiral Strains (με) (ε_y = 2440 με)								
	Run 1	Run 2	Run 3	Run 4	Run 5	Run 6	Run 7	Run 8
CSGS21	-	-	-	-	-	-	-	-
CSGS22	-	-	-	-	-	-	-	-
CSGS23	128	111	-111	-104	138	-90	-124	-166
CSGS24	22	-62	-97	-104	-83	-90	-104	-110
CSGS25	108	-180	-180	-193	-193	-290	-366	-560
CSGS26	116	124	-131	-152	-152	-200	-269	-414
CSGS27	153	166	-159	-207	-200	-276	-359	-476
CSGS28	-378	-607	-711	-745	-752	-807	-897	-1080
CSGS29	120	131	-145	-214	-311	-407	-518	-469
CSGS30	109	-110	-186	-221	-242	-290	-352	-469
CSGS31	113	-214	-276	-290	-483	-614	-628	-752
CSGS32	108	-104	-235	-290	-331	-469	-476	-380
CSGS33	-348	-373	-380	-414	-366	-538	-635	-794
CSGS34	105	-104	-159	-262	-248	-269	-317	-338
CSGS35	551	594	552	442	373	283	228	-518
CSGS36	70	104	-55	-97	-124	-207	-249	-256
CSGS37	115	131	-221	-256	-242	-235	-214	-207
CSGS38	118	131	-380	-442	-401	-525	-656	-760
CSGS39	83	97	-104	-104	-90	-145	-166	-173
CSGS40	88	97	104	90	-124	-152	-193	-173

Table 6.26 Peak strains in north column spirals

North Column Spiral Strains (με) (ε_y = 2440 με)								
	Run 1	Run 2	Run 3	Run 4	Run 5	Run 6	Run 7	Run 8
CSGN21	60	-76	-145	-166	-152	-179	-207	-235
CSGN22	86	97	-311	-435	-490	-511	-511	-580
CSGN23	-	-	-	-	-	-	-	-
CSGN24	-	-	-	-	-	-	-	-
CSGN25	158	166	-117	-179	-228	-262	-290	-317
CSGN26	101	-173	-283	-297	-317	-449	-552	-676
CSGN27	100	124	-83	-110	-138	-338	-524	-586
CSGN28	48	-69	-228	-248	-221	-255	-283	-324
CSGN29	-535	-656	-746	-794	-911	-1060	-1190	-1270
CSGN30	162	159	110	-97	-173	-380	-725	-656
CSGN31	391	414	373	262	-338	-497	-684	-690
CSGN32	155	186	138	-235	-311	-421	-600	-752
CSGN33	44	-83	-186	-235	-241	-359	-973	-1680
CSGN34	85	-76	-145	-200	-221	-235	-283	-338
CSGN35	160	172	145	124	-207	-262	-379	-483
CSGN36	-124	-200	-352	-414	124	193	255	-318
CSGN37	125	145	117	-297	-393	-435	-476	-483
CSGN38	64	90	-166	-283	-352	-435	-455	-455
CSGN39	-	-	-	-	-	-	-	-
CSGN40	64	-90	-90	-90	-97	-193	-297	-304

Table 6.27 Peak strains in north rebar hinge longitudinal bars

North Column Hinge Longitudinal Strains (με) (ε_y = 2610 με)								
	Run 1	Run 2	Run 3	Run 4	Run 5	Run 6	Run 7	Run 8
HSGN1	-263	-1860	-2200	-2300	-2420	-2540	-2800	-3100
HSGN2	339	-1680	-2110	-2340	-2480	-2810	-3830	-9450
HSGN3	-217	-1410	-1710	-1900	-2060	-2170	-2220	-2290
HSGN4	158	-421	-856	-760	-552	-525	-1270	-1690
HSGN5	-1163	-14800	-16800	-15400	-	-	-	-
HSGN6	-709	-3380	-8170	-	-	-	-	-
HSGN7	-1292	-11900	-19400	-28500	-36000	-40700	-43600	-45600
HSGN8	-868	-7490	-20300	-21900	-23900	-25000	-28000	-30100
HSGN9	-236	-2110	-2220	-2250	-2250	-2270	-2270	-2240
HSGN10	306	-1720	-2060	-1980	-2150	-2290	-2360	-2380
HSGN11	-583	-1880	-2040	-2170	-2310	-2400	-2440	-2430
HSGN12	-269	-1860	-2150	-2270	-2270	-2370	-2450	-2480

Table 6.28 Peak strains in south rebar hinge longitudinal bars

South Column Hinge Longitudinal Strains (με) (ε_y = 2610 με)								
	Run 1	Run 2	Run 3	Run 4	Run 5	Run 6	Run 7	Run 8
HSGS1	321	-1150	1240	1320	1280	1230	1290	-2790
HSGS2	165	-399	1090	-316	-337	-365	-427	-385
HSGS3	-301	-1330	-3290	-2910	-2790	-2870	-2870	-2840
HSGS4	313	-1740	-2240	-2440	-2550	-2740	-3000	-3380
HSGS5	-	-	-	-	-	-	-	-
HSGS6	597	2550	3920	4430	3780	5480	6350	10600
HSGS7	-1069	-6990	5840	12900	12000	11000	8750	-
HSGS8	-1236	-16300	-22700	-26700	-27500	-32700	-38200	-43600
HSGS9	-513	-2220	-2400	-2390	-2290	-2400	-2470	-2560
HSGS10	338	-1520	-1780	-1820	-1870	-1950	-2050	-2110
HSGS11	-545	-2030	-2140	-2190	-2300	-2370	-2400	-2380
HSGS12	-304	-304	-614	-518	531	504	863	-662

Table 6.29 Peak strains in south rebar hinge spirals

South Column Hinge Spiral Strains (με) (ε_y = 2440 με)								
	Run 1	Run 2	Run 3	Run 4	Run 5	Run 6	Run 7	Run 8
HSGN13	-60	104	166	276	-822	-967	-635	766
HSGN14	64	-83	124	207	331	421	670	808
HSGN15	-131	110	138	207	324	-504	-773	-973
HSGN16	-349	-456	-566	-691	-532	-718	-1510	-2690
HSGN17	36	48	90	97	138	145	145	159
HSGN18	79	166	221	235	249	249	249	255
HSGN19	89	90	76	83	138	138	117	131
HSGN20	50	90	97	117	159	152	145	152

Table 6.30 Peak strains in north rebar hinge spirals

North Column Hinge Spiral Strains (με) (ε_y = 2440 με)								
	Run 1	Run 2	Run 3	Run 4	Run 5	Run 6	Run 7	Run 8
HSGN13	69	-110	-463	-753	-1010	-1150	-1100	-1040
HSGN14	62	110	283	303	441	648	869	931
HSGN15	42	269	545	539	421	483	559	490
HSGN16	100	110	131	255	442	573	539	1040
HSGN17	75	97	90	97	117	110	110	110
HSGN18	116	124	138	152	186	186	186	193
HSGN19	-39	-62	-90	76	110	131	145	159
HSGN20	118	138	124	159	186	207	214	-235

Table 6.31 Peak strains in cap beam

Bent Cap Rebar Strains (με) (#3 ε_y = 2440 με) (#6 ε_y = 2610 με)									
	Run 1	Run 2	Run 3	Run 4	Run 5	Run 6	Run 7	Run 8	Rein. Type
BSG1	-	-	-	-	-	-	-	-	Hoop
BSG2	87	378	461	454	-577	-921	-1180	-1260	Hoop
BSG3	123	275	282	296	275	282	302	282	Hoop
BSG4	393	420	420	420	433	426	420	420	Hoop
BSG5	355	399	399	399	419	412	412	406	Hoop
BSG6	-	-	-	-	-	-	-	-	Hoop
BSG7	792	764	674	668	709	702	668	674	Hoop
BSG8	-	-	-	-	-	-	-	-	Hoop
BSG9	94	241	378	378	427	406	-1110	-1690	Hoop
BSG10	68	261	330	-750	-1110	-1360	-1510	-1640	Hoop
BSG59	19	-46	-124	-216	-242	-261	-294	-307	Top Long
BSG60	-34	-85	-137	-157	-144	-196	-275	-314	Top Long
BSG61	-	-	-	-	-	-	-	-	Top Long
BSG62	-35	-98	-170	-216	-203	-242	-288	-314	Top Long
BSG63	-27	-124	-203	-242	-268	-334	-367	-386	Top Long
BSG64	-	-	-	-	-	-	-	-	Top Long
BSG65	-	-	-	-	-	-	-	-	Top Long
BSG66	-	-	-	-	-	-	-	-	Top Long
BSG67	61	69	-158	-227	-282	-337	-358	-378	Bottom Long
BSG68	-	-	-	-	-	-	-	-	Bottom Long
BSG69	147	117	-241	-275	-289	-372	-523	-654	Bottom Long
BSG70	930	1050	1050	970	998	998	984	984	Bottom Long
BSG71	-	-	-	-	-	-	-	-	Bottom Long
BSG72	-399	103	-268	440	-1000	-763	461	-543	Bottom Long
BSG73	178	207	186	138	-117	-179	-241	-289	Bottom Long
BSG74	-	-	-	-	-	-	-	-	Bottom Long
BSG75	-56	-220	-434	-537	-640	-757	-792	-778	Pocket Spiral
BSG76	-557	-1000	-1400	-1440	-1460	-1600	-1650	-1620	Pocket Spiral
BSG77	-502	-688	-984	-1200	-1290	-1310	-1300	-1290	Pocket Spiral
BSG78	-467	-495	-502	-654	-784	-798	-764	-881	Pocket Spiral
BSG79	120	-131	-564	-736	-791	-921	-956	-1000	Pocket Spiral
BSG80	29	-117	-516	-571	-564	-667	-729	-743	Pocket Spiral
BSG81	81	-138	-510	-854	-1030	-1130	-1090	-1030	Pocket Spiral
BSG82	-29	-96.4	-207	-482	-654	-737	-757	-757	Pocket Spiral

Table 6.32 Peak strains in girder-to-cap beam connection, headed bars and crossties

Girder-to-Cap Beam Rebar Strains (με) (#3 ε_y = 2440με) (Strands ε_y = 9379με)									Rein. Type
	Run 1	Run 2	Run 3	Run 4	Run 5	Run 6	Run 7	Run 8	
BSG11	35	-85	196	235	255	242	248	288	Headed Bar
BSG12	-	-	-	-	-	-	-	-	Headed Bar
BSG13	-116	-288	-452	-465	-530	-582	-595	-615	Headed Bar
BSG14	27	-138	-308	-406	-380	-367	-334	-295	Headed Bar
BSG15	-23	-98	-137	-105	-85	-105	-118	-105	Headed Bar
BSG16	-25	-65	-105	-105	-92	-105	-98	-98	Headed Bar
BSG17	49	-137	-229	-216	281	320	366	432	Headed Bar
BSG18	22	-92	-216	-268	-242	-216	-203	-177	Headed Bar
BSG19	-31	-85	-144	-137	-98	-137	-164	-196	Headed Bar
BSG20	-	-	-	-	-	-	-	-	Headed Bar
BSG21	-24	-59	-111	-150	-209	-255	-262	-288	Headed Bar
BSG22	-	-	-	-	-	-	-	-	Headed Bar
BSG23	-24	-52	-72	-79	-59	-85	-111	-118	Headed Bar
BSG24	101	137	150	164	150	157	196	203	Headed Bar
BSG25	-20	-65	-105	-190	-262	-301	-307	-301	Headed Bar
BSG26	18	-72	-124	-176	-261	-288	-307	-327	Headed Bar
BSG27	-24	-39	-59	-46	-20	-33	-52	-52	Crosstie
BSG28	-20	-46	-65	-65	-39	-59	-65	-72	Crosstie
BSG29	-	-	-	-	-	-	-	-	Crosstie
BSG30	-	-	-	-	-	-	-	-	Crosstie
BSG31	-	-	-	-	-	-	-	-	Crosstie
BSG32	-15	-33	-39	-39	-33	-52	-66	-66	Crosstie
BSG33	21	-52	-65	-72	-52	-72	-92	-105	Crosstie
BSG34	-23	-46	-72	-92	-65	-85	-98	-111	Crosstie

Table 6.33 Peak strains in girder-to-cap beam connection, girder strands

Girder-to-Cap Beam Rebar Strains (με) (#3 ε_y = 2440με) (Strands ε_y = 9379με)									Rein. Type
	Run 1	Run 2	Run 3	Run 4	Run 5	Run 6	Run 7	Run 8	
BSG35	46	105	-150	-190	-190	-236	-294	-353	G. Strand
BSG36	21	65	98	137	137	137	177	150	G. Strand
BSG37	34	98	-131	-144	-118	-144	-164	-190	G. Strand
BSG38	-	-	-	-	-	-	-	-	G. Strand
BSG39	-20	59	-79	-177	-222	-281	-301	-294	G. Strand
BSG40	-25	-85	-157	-327	-458	-595	-654	-648	G. Strand
BSG41	23	-111	-196	-222	-314	-373	-432	-386	G. Strand
BSG42	-	-	-	-	-	-	-	-	G. Strand
BSG43	19	-59	-111	-105	-105	-137	-170	-196	G. Strand
BSG44	-25	-79	-111	-242	-321	-406	-438	-445	G. Strand
BSG45	45	92	98	-366	-556	-661	-680	-674	G. Strand
BSG46	25	-79	-137	-399	-582	-706	-733	-713	G. Strand
BSG47	82	157	183	242	-477	-732	-1140	-1370	G. Strand
BSG48	102	177	203	255	-294	-380	-484	-530	G. Strand
BSG49	59	144	-235	-320	-628	-942	-1410	-1670	G. Strand
BSG50	-	-	-	-	-	-	-	-	G. Strand
BSG51	-	-	-	-	-	-	-	-	G. Strand
BSG52	-	-	-	-	-	-	-	-	G. Strand
BSG53	-49	105	-209	-327	-359	-568	-954	-1230	G. Strand
BSG54	-50	-137	-242	-353	-615	-805	-968	-975	G. Strand
BSG55	-44	-92	-150	-222	-406	-622	-923	-1130	G. Strand
BSG56	-35	-98	-308	-511	-622	-655	-655	-655	G. Strand
BSG57	-55	222	-726	-1450	-1970	-2180	-2260	-2320	G. Strand
BSG58	-39	190	-556	-1100	-1450	-1640	-1720	-1770	G. Strand

Table 6.34 Peak strains in deck longitudinal rebar

Deck Rebar Strains (με) (#3 ε_y = 2250) (#4 ε_y = 2450με)								
	Run 1	Run 2	Run 3	Run 4	Run 5	Run 6	Run 7	Run 8
DSG1	-44	-144	-288	-412	-452	-491	-497	-491
DSG2	20	-46	-85	-92	-79	-105	-124	-131
DSG3	87	-177	-340	-340	-308	-288	-288	-249
DSG4	-34	-92	-118	-124	-111	-144	-177	-196
DSG5	-37	-137	-268	-393	-458	-530	-563	-595
DSG6	-21	-59	-98	-118	-111	-144	-164	-164
DSG7	27	-157	-255	-275	-255	-301	-360	-406
DSG8	-29	-79	-118	-131	-124	-163	-190	-216
DSG9	-52	-340	-543	-654	-366	-445	-419	-373
DSG10	-	-	-	-	-	-	-	-
DSG11	-69	-281	-458	-563	-687	-805	-897	-975
DSG12	-46	-92	-118	-137	-105	-144	-183	-196
DSG13	-93	-384	-599	-658	-697	-762	-749	-717
DSG14	-45	-163	-249	-262	-249	-281	-294	-307
DSG15	-45	-157	-268	-360	-484	-569	-681	-759
DSG16	-37	-92	-131	-157	-138	-190	-229	-249

Table 6.35 Tensile strain rates in north column longitudinal bars within plastic hinge

Strain Gage	Average (με/s)	Run of 1st yield
CSGN5	-	-
CSGN6	7228	4
CSGN7	12683	3
CSGN8	7610	5
CSGN9	14289	3
CSGN10	23450	6
CSGN11	15142	3
CSGN12	8985	3
CSGN13	11403	2
CSGN14	9116	3
CSGN15	11416	2
CSGN16	16890	3
CSGN17	16797	3
CSGN18	-	-
CSGN19	13227	3
CSGN20	8420	3
Total	12618	-

Table 6.36 Tensile strain rates in south column longitudinal bars within plastic hinge

Strain Gage	Average (με/s)	Run of 1st yield
CSGS5	9760	2
CSGS6	7614	6
CSGS7	11266	2
CSGS8	8451	3
CSGS9	10768	2
CSGS10	8961	3
CSGS11	12380	2
CSGS12	12491	3
CSGS13	10026	2
CSGS14	21014	3
CSGS15	9807	2
CSGS16	18752	3
CSGS17	12223	3
CSGS18	6898	5
CSGS19	13876	3
CSGS20	8400	3
Total	11528	-

Table 6.37 Compressive strain rates in column longitudinal bars within plastic hinge

Compression strain rates in longitudinal bars within plastic hinge		
Strain Gage	Average (με/s)	Run of 1st yield
CSGN9	10379	2
CSGN13	11614	6
Total	10997	-

Table 6.38 Peak column rotation associated with longitudinal movement of bridge

Run #	North Column		South Column	
	Max (rad)	Min (rad)	Max (rad)	Min (rad)
1	0.0011	-0.0014	0.000959	-0.001
2	0.0046	-0.0050	0.0047	-0.0035
3	0.0089	-0.0116	0.011	-0.0079
4	0.0094	-0.0214	0.0136	-0.0148
5	0.0105	-0.0297	0.0143	-0.0211
6	0.0145	-0.0352	0.0209	-0.0248
7	0.0186	-0.0401	0.03	-0.0247
8	0.0208	-0.0446	0.0394	-0.022

Table 6.39 Peak column rotation associated with transverse movement of bridge

Run #	North Column		South Column	
	Max (rad)	Min (rad)	Max (rad)	Min (rad)
1	0.00034	-0.00033	0.00066	-0.00088
2	0.0011	-0.0160	0.0032	-0.0038
3	0.0017	-0.0039	0.0058	-0.009
4	0.0022	-0.0049	0.0077	-0.0111
5	0.0032	-0.0052	0.011	-0.0122
6	0.0044	-0.0076	0.0142	-0.0155
7	0.0051	-0.0119	0.0162	-0.0194
8	0.0052	-0.0177	0.0162	-0.0238

Table 6.40 Peak hinge rotation associated with longitudinal movement of bridge

Run #		N. Column (rad)	S. Column (rad)
1	Max.	0.0018	0.0018
	Min.	-0.0023	-0.0024
2	Max.	0.0086	0.0094
	Min.	-0.0084	-0.0084
3	Max.	0.0146	0.0172
	Min.	-0.0167	-0.0161
4	Max.	0.0142	0.0195
	Min.	-0.0263	-0.0232
5	Max.	0.0147	0.0195
	Min.	-0.035	-0.0299
6	Max.	0.0182	0.0276
	Min.	-0.0417	-0.0322
7	Max.	0.0215	0.0358
	Min.	-0.0468	-0.0317
8	Max.	0.023	0.0436
	Min.	-0.0515	-0.0293

Table 6.41 Peak hinge rotation associated with transverse movement of bridge

Run #		N. Column (rad)	S. Column (rad)
1	Max.	0.0016	0.0015
	Min.	-0.0012	-0.0012
2	Max.	0.0071	0.0068
	Min.	-0.0065	-0.0064
3	Max.	0.0143	0.014
	Min.	-0.0105	-0.0105
4	Max.	0.0163	0.0162
	Min.	-0.0118	-0.0117
5	Max.	0.018	0.0177
	Min.	-0.0158	-0.015
6	Max.	0.0211	0.021
	Min.	-0.0201	-0.0187
7	Max.	0.0247	0.0248
	Min.	-0.0233	-0.0213
8	Max.	0.0291	0.0293
	Min.	-0.0242	-0.0218

Table 6.42 Peak angle of twist in rebar hinge and in-plane rotation of superstructure

Run #	$\phi_{N. Column}$ (rad)	$\phi_{S. Column}$ (rad)	$\theta_{Superstructure}$ (rad)
1	0.0004	0.0001	-0.0002
2	0.0014	0.0006	-0.0004
3	0.003	0.003	0.003
4	0.006	0.006	0.005
5	0.009	0.009	0.008
6	0.011	0.013	0.010
7	0.014	0.019	0.017
8	0.018	0.028	0.025

Table 6.43 Peak vertical displacement in rebar hinge

Run #	N. Column (in)		S. Column (in)	
	(in)	(mm)	(in)	(mm)
1	0.005	0.13462	0.005	0.11684
2	0.024	0.6096	0.023	0.58928
3	0.048	1.21412	0.049	1.25222
4	0.072	1.82372	0.072	1.82118
5	0.089	2.2479	0.092	2.3368
6	0.095	2.41046	0.122	3.10642
7	0.087	2.21742	0.119	3.01752
8	0.065	1.64338	0.106	2.68224

Table 6.44 Peak relative displacement between deck and interior girder, longitudinal direction

Run #	Interior Girder							
	West (8")		West (54")		East (8")		East (54")	
	(in)	(mm)	(in)	(mm)	(in)	(mm)	(in)	(mm)
1	0.000	0.012	0.000	0.012	0.000	0.010	0.001	0.019
2	0.001	0.023	0.001	0.013	0.002	0.045	0.002	0.039
3	0.001	0.020	0.001	0.013	0.003	0.075	0.002	0.039
4	0.001	0.027	0.001	0.015	0.003	0.082	0.001	0.037
5	0.001	0.032	0.001	0.015	0.004	0.094	0.002	0.042
6	0.002	0.047	0.001	0.013	0.004	0.106	0.002	0.042
7	0.002	0.057	0.001	0.015	0.005	0.129	0.002	0.044
8	0.002	0.062	0.001	0.015	0.006	0.149	0.002	0.050

Table 6.45 Peak relative displacement between deck and exterior girder, longitudinal direction

Run #	Exterior Girder							
	West (8")		West (54")		East (8")		East (54")	
	(in)	(mm)	(in)	(mm)	(in)	(mm)	(in)	(mm)
1	0.001	0.015	0.000	0.010	0.001	0.017	0.001	0.013
2	0.001	0.029	0.001	0.013	0.001	0.034	0.001	0.035
3	0.003	0.086	0.001	0.018	0.005	0.123	0.002	0.042
4	0.003	0.081	0.001	0.017	0.007	0.173	0.002	0.042
5	0.002	0.047	0.001	0.022	0.009	0.224	0.002	0.044
6	0.002	0.039	0.001	0.022	0.010	0.261	0.002	0.044
7	0.002	0.044	0.001	0.024	0.011	0.284	0.002	0.045
8	0.002	0.044	0.001	0.025	0.012	0.301	0.002	0.042

Table 6.46 Peak relative displacement between deck and girder, transverse direction

Run #	Interior Girder				Exterior Girder			
	NT49 (8")		NT55 (8")		NT51 (8")		NT53 (8")	
	(in)	(mm)	(in)	(mm)	(in)	(mm)	(in)	(mm)
1	-	-	0.000	0.010	0.000	0.008	0.000	0.007
2	-	-	0.001	0.013	0.001	0.017	0.001	0.013
3	-	-	0.001	0.027	0.001	0.035	0.001	0.029
4	-	-	0.001	0.027	0.002	0.052	0.003	0.082
5	-	-	0.001	0.030	0.003	0.069	0.006	0.146
6	-	-	0.001	0.032	0.003	0.082	0.007	0.188
7	-	-	0.001	0.037	0.004	0.102	0.008	0.203
8	-	-	0.002	0.047	0.005	0.129	0.009	0.220

Table 6.47 Peak relative displacement between superstructure-cap beam interface, interior girder

Run #	Interior Girder							
	Bottom of Girder				Top of Deck			
	NT41 - E		NT43 - W		NT42 - E		NT44 - W	
	(in)	(mm)	(in)	(mm)	(in)	(mm)	(in)	(mm)
1	0.001	0.029	0.000	0.012	0.001	0.021	0.001	0.020
2	0.003	0.069	0.002	0.049	0.002	0.053	0.002	0.062
3	0.004	0.089	0.003	0.074	0.003	0.065	0.004	0.094
4	0.003	0.086	0.004	0.111	0.004	0.096	0.004	0.099
5	0.004	0.096	0.006	0.141	0.004	0.109	0.005	0.119
6	0.004	0.111	0.006	0.143	0.005	0.118	0.005	0.139
7	0.005	0.118	0.006	0.144	0.005	0.115	0.006	0.160
8	0.005	0.133	0.006	0.161	0.004	0.107	0.007	0.175

Table 6.48 Peak relative displacement between superstructure-cap beam interface, exterior girder

Run #	Exterior Girder							
	Bottom of Girder				Top of Deck			
	NT45 - E		NT47 - W		NT46 - E		NT48 - W	
	(in)	(mm)	(in)	(mm)	(in)	(mm)	(in)	(mm)
1	0.001	0.027	0.001	0.029	0.012	0.314	0.000	0.006
2	0.003	0.069	0.002	0.055	0.014	0.358	0.002	0.045
3	0.005	0.122	0.003	0.072	0.012	0.316	0.004	0.099
4	0.006	0.149	0.003	0.086	0.018	0.450	0.004	0.104
5	0.006	0.164	0.004	0.106	0.009	0.229	0.004	0.104
6	0.008	0.200	0.005	0.116	0.023	0.589	0.004	0.107
7	0.009	0.230	0.004	0.104	0.033	0.831	0.004	0.110
8	0.010	0.267	0.004	0.111	0.005	0.124	0.005	0.117

Table 6.49 Peak rotation between superstructure and cap beam

Run #	Interior Girder		Exterior Girder	
	East	West	East	West
1	0.00009	0.00006	0.00010	0.00061
2	0.00021	0.00021	0.00023	0.00072
3	0.00027	0.00032	0.00038	0.00063
4	0.00032	0.00038	0.00044	0.00088
5	0.00038	0.00045	0.00052	0.00048
6	0.00044	0.00051	0.00060	0.00113
7	0.00044	0.00059	0.00065	0.00159
8	0.00046	0.00065	0.00071	0.00031

Table 6.50 Peak relative vertical displacement between column and cap beam at pocket connection

Run #		N. Column (in)	N. Column (mm)	S. Column (in)	S. Column (mm)
1	Max.	0.00	0.11	0.01	0.22
	Min.	0.00	-0.05	0.00	-0.02
2	Max.	0.01	0.35	0.03	0.77
	Min.	0.00	-0.08	0.00	-0.01
3	Max.	0.05	1.17	0.07	1.67
	Min.	0.00	-0.11	0.00	0.02
4	Max.	0.11	2.70	0.12	2.99
	Min.	0.01	0.15	0.01	0.15
5	Max.	0.15	3.91	0.16	4.15
	Min.	0.02	0.53	0.01	0.37
6	Max.	0.19	4.80	0.20	4.95
	Min.	0.04	1.09	0.03	0.66
7	Max.	0.22	5.63	0.21	5.22
	Min.	0.07	1.86	0.03	0.71
8	Max.	0.27	6.80	0.20	5.12
	Min.	0.11	2.80	0.01	0.15

Table 7.1 Coupling index values for bent particle displacement, all runs

Coupling Index									
	Run 1	Run 2	Run 3	Run 4	Run 5	Run 6	Run 7	Run 8	Cum.
Quadrant A	0.5	0.68	0.73	0.39	0.38	0.38	0.42	0.46	0.46
Quadrant B	0.26	0.19	0.28	0.27	0.25	0.25	0.27	0.32	0.32
Quadrant C	0.41	0.44	0.53	0.37	0.43	0.36	0.32	0.3	0.35
Quadrant D	0.38	0.26	0.26	0.31	0.32	0.38	0.47	0.55	0.55
Average	0.39	0.39	0.45	0.34	0.34	0.34	0.37	0.41	0.42
Maximum	0.5	0.38	0.73	0.39	0.43	0.38	0.47	0.55	0.55
Peak Displacement, in (mm)	0.29 (7.4)	0.95 (24.1)	1.63 (41.4)	2.49 (63.2)	3.22 (81.8)	3.65 (92.7)	3.87 (98.3)	4.01 (102)	4.01 (102)

Table 7.2 Idealized curve properties for longitudinal, transverse, and resultant directions

Idealized Curve Properties			
	Longitudinal	Transverse	Resultant
Displacement at First Yield, Δ_y	0.72 in (18.3 mm)	0.33 in (8.38 mm)	0.7 in (17.8 mm)
Effective Stiffness, k_e	61.4 k/in 10.7 kN/mm	80.3 k/in 14.1 kN/mm	67.9 k/in 11.9 kN/mm
Effective Yield Displacement, Δ_{ye}	1.11 in 28.2 mm	0.63 in 16.0 mm	1.05 in 26.7 mm
Ultimate Displacement, Δ_u	4 in 102 mm	2.6 in 66.0 mm	4.75 in 121 mm
Idealized Peak Base Shear, V_p	68.0 kips 302 kN	50.4 kips 224 kN	71.1 kips 316 kN
Displacement Ductility, μ	3.6	4.1	4.6

Table 7.3 Strand contribution to positive moment resistance in girder-to-cap beam connection, exterior girder

Exterior Girder West		
Headed Bar Contribution		
μ =	0.6	
A_{vf} =	0.22	in^2
E_s =	29000	ksi
$\varepsilon_{dowel, bottom}$ =	0.000327	
$\varepsilon_{dowel, top}$ =	0.000301	
$F_{dowel, bottom}$ =	1.25	kip
$F_{dowel, top}$ =	1.15	kip
Adhesion and Aggregate Interlock Contribution		
c =	0.075	ksi
b =	10.4344	in
h =	16.75	in
F_c =	13.1	k
Center of Rotation		
COR =	1.375	in
Moment Contribution		
$M^+_{Shear\ Friction}$ =	272	k-in
Peak Curvature	0.0001	rad/in
$M^+_{strands}$ =	280	k-in
Strand Contribution	51%	
Shear Friction Contribution	49%	

Exterior Girder East		
Headed Bar Contribution		
μ =	0.6	
A_{vf} =	0.22	in^2
E_s =	29000	ksi
$\varepsilon_{dowel, bottom}$ =	0.000203	
$\varepsilon_{dowel, top}$ =	0.000196	
$F_{dowel, bottom}$ =	0.78	kip
$F_{dowel, top}$ =	0.75	kip
Adhesion and Aggregate Interlock Contribution		
c =	0.075	ksi
b =	10.4344	in
h =	16.75	in
F_c =	13.1	k
Center of Rotation		
COR =	1.375	in
Moment Contribution		
$M^+_{Shear\ Friction}$ =	256	k-in
Peak Curvature	0.00006	rad/in
$M_{strands}$ =	168	k-in
Strand Contribution	40%	
Shear Friction Contribution	60%	

Table 7.4 Strand contribution to positive moment resistance in girder-to-cap beam connection, interior girder

Interior Girder West		
Headed Bar Contribution		
μ =	0.6	
A_{vf} =	0.22	in^2
E_s =	29000	ksi
$\varepsilon_{dowel, bottom}$ =	0.000406	
$\varepsilon_{dowel, top}$ =	0.000615	
$F_{dowel, bottom}$ =	1.55	kip
$F_{dowel, top}$ =	2.35	kip
Adhesion and Aggregate Interlock Contribution		
c =	0.075	ksi
b =	10.4344	in
h =	16.75	in
F_c =	13.1	k
Center of Rotation		
COR =	1.375	in
Moment Contribution		
$M^{+}_{Shear\ Friction}$ =	294	k-in
Peak Curvature	0.00003	rad/in
$M_{strands}$ =	90	k-in
Strand Contribution	23%	
Shear Friction Contribution	77%	

Interior Girder East		
Headed Bar Contribution		
μ =	0.6	
A_{vf} =	0.22	in^2
E_s =	29000	ksi
$\varepsilon_{dowel, bottom}$ =	0.000105	
$\varepsilon_{dowel, top}$ =	0.000288	
$F_{dowel, bottom}$ =	0.40	kip
$F_{dowel, top}$ =	1.10	kip
Adhesion and Aggregate Interlock Contribution		
c =	0.075	ksi
b =	10.4344	in
h =	16.75	in
F_c =	13.1	k
Center of Rotation		
COR =	1.375	in
Moment Contribution		
$M^{+}_{Shear\ Friction}$ =	252	k-in
Peak Curvature	0.000017	rad/in
$M_{strands}$ =	51	k-in
Strand Contribution	17%	
Shear Friction Contribution	83%	

Table 8.1 Measured and calculated (pretest) peak longitudinal displacements

Peak Displacements - Longitudinal Direction						
Run #		Calculated (Pretest)		Measured		% Difference
		(in)	(mm)	(in)	(mm)	
1	Max.	0.21	5.4	0.22	5.5	-5%
	Min.	-0.19	-4.8	-0.3	-7.7	-37%
2	Max.	0.77	19.5	0.96	24.3	-20%
	Min.	-0.93	-23.6	-0.92	-23.3	1%
3	Max.	1.6	40.6	1.62	41.2	-1%
	Min.	-1.59	-40.4	-1.66	-42.3	-4%
4	Max.	2.02	51.3	1.77	44.9	14%
	Min.	-2.17	-55.2	-2.48	-63	-13%
5	Max.	2.02	51.4	1.84	46.7	10%
	Min.	-2.91	-73.9	-3.24	-82.2	-10%
6	Max.	2.11	53.5	2.37	60.3	-11%
	Min.	-3.81	-96.8	-3.75	-95.3	2%
7	Max.	2.38	60.5	3.02	76.7	-21%
	Min.	-4.76	-121	-3.95	-100.3	21%
8	Max.	-	-	3.6	91.4	-
	Min.	-	-	-4	-101.6	-

Table 8.2 Measured and calculated (pretest) peak transverse displacements

Peak Displacements - Transverse Direction						
Run #		Calculated (Pretest)		Measured		% Difference
		(in)	(mm)	(in)	(mm)	
1	Max.	0.11	2.8	0.16	4.1	-31%
	Min.	-0.14	-3.6	-0.13	-3.3	8%
2	Max.	0.49	12.6	0.66	16.8	-26%
	Min.	-0.74	-18.7	-0.59	-15.0	25%
3	Max.	0.61	15.6	1.29	32.8	-53%
	Min.	-1.65	-42	-0.95	-24.1	74%
4	Max.	1.05	26.6	1.49	37.8	-30%
	Min.	-2.25	-57	-1.1	-27.9	105%
5	Max.	1.44	36.5	1.65	41.9	-13%
	Min.	-2.76	-70.2	-1.44	-36.6	92%
6	Max.	1.96	49.7	1.97	50.0	-1%
	Min.	-3.16	-80.2	-1.83	-46.5	73%
7	Max.	2.57	65.4	2.32	58.9	11%
	Min.	-3.43	-87.1	-2.14	-54.4	60%
8	Max.	-	-	2.73	69.3	-
	Min.	-	-	-2.26	-57.4	-

Table 8.3 Measured and calculated (pretest) peak longitudinal base shear

Peak Base Shear - Longitudinal Direction						
Run #		Calculated (Pretest)		Measured		% Difference
		(k)	(kN)	(k)	(kN)	
1	Max.	32.8	146	22.4	99.8	46%
	Min.	-31.3	-139	-18.4	-81.7	70%
2	Max.	51	226.7	51.7	229.8	-1%
	Min.	-58.8	-261.4	-52	-231.4	13%
3	Max.	59.1	262.9	64.5	286.9	-8%
	Min.	-57.7	-256.5	-63.2	-281.2	-9%
4	Max.	59.9	266.5	70.9	315.2	-16%
	Min.	-58.1	-258.4	-56.7	-252.2	2%
5	Max.	63.6	282.8	72.8	323.9	-13%
	Min.	-59	-262.3	-55.2	-245.7	7%
6	Max.	66.3	294.8	74.3	330.4	-11%
	Min.	-53	-235.6	-59.5	-264.9	-11%
7	Max.	69.1	307.5	71.2	316.7	-3%
	Min.	-56.5	-251.3	-61.9	-275.4	-9%
8	Max.	-	-	70.6	314.1	-
	Min.	-	-	-62.7	-278.8	-

Table 8.4 Measured and calculated (pretest) peak longitudinal base shear

Peak Base Bent Shear - Transverse Direction						
Run #		Calculated (Pretest)		Measured		% Difference
		(k)	(kN)	(k)	(kN)	
1	Max.	28	124.5	15.1	67.1	85%
	Min.	-22.7	-100.9	-13.9	-61.7	63%
2	Max.	56.1	249.7	37.7	167.7	49%
	Min.	-48.9	-217.7	-36.9	-164.2	33%
3	Max.	56.5	251.2	49.8	221.5	13%
	Min.	-49	-218.1	-52.3	-232.5	-6%
4	Max.	57.2	254.5	51.1	227.2	12%
	Min.	-53.2	-236.5	-49.8	-221.5	7%
5	Max.	59	262.4	53.4	237.6	10%
	Min.	-55.6	-247.3	-49.1	-218.6	13%
6	Max.	62.3	277.1	54.6	242.7	14%
	Min.	-56.9	-253.3	-44.7	-198.8	27%
7	Max.	60.9	270.7	54.7	243.4	11%
	Min.	-59.8	-266.2	-42.3	-188.1	41%
8	Max.	-	-	54.1	240.7	-
	Min.	-	-	-41.4	-184.2	-

Table 8.5 Strain rate factors for steel and concrete for dynamic loading

Strain Rate Effect (Steel)		
f_y =	75.8	ksi
f_u =	105.5	ksi
ε_{st} =	250	με/s
ε =	12073	με/s
SRF_{45} =	1.11	
SRF_{75} =	1.01	
SRF_S =	1.01	
$f_{y,\ adj}$ =	76.5	ksi
$f_{u,\ adj}$ =	106.4	ksi

Strain Rate Effect (Concrete)		
$f'_{c,\ column}$ =	7307	psi
$f'_{c,\ grout}$ =	8148	psi
ε_{st} =	8.65	με/s
ε =	10997	με/s
SRF_c =	1.15	
$f'_{c,\ column\ adj}$ =	8436	psi
$f'_{c,\ grout,\ adj}$ =	9407	psi

Table 8.6 Measured and calculated (posttest) peak longitudinal displacements

Peak Displacements - Longitudinal Direction						
Run #		Calculated (Posttest)		Measured		% Difference
		(in)	(mm)	(in)	(mm)	
1	Max.	0.26	6.5	0.22	5.6	16%
	Min.	-0.19	-4.8	-0.3	-7.6	-37%
2	Max.	0.71	18.1	0.96	24.4	-26%
	Min.	-0.50	-12.8	-0.92	-23.4	-45%
3	Max.	2.01	50.9	1.62	41.1	24%
	Min.	-1.52	-38.5	-1.66	-42.2	-9%
4	Max.	2.39	60.7	1.77	45.0	35%
	Min.	-2.64	-67.1	-2.48	-63.0	7%
5	Max.	2.27	57.8	1.84	46.7	24%
	Min.	-3.60	-91.5	-3.24	-82.3	11%
6	Max.	2.39	60.6	2.37	60.2	1%
	Min.	-4.30	-109.1	-3.75	-95.3	15%
7	Max.	3.14	79.7	3.02	76.7	4%
	Min.	-4.79	-121.6	-3.95	-100.3	21%
8	Max.	3.92	99.6	3.6	91.4	9%
	Min.	-4.87	-123.6	-4	-101.6	22%

Table 8.7 Measured and calculated (posttest) peak transverse displacements

Peak Displacements - Transverse Direction						
Run #		Calculated (Posttest)		Measured		% Difference
		(in)	(mm)	(in)	(mm)	
1	Max.	0.11	2.9	0.16	4.1	-30%
	Min.	-0.08	-1.9	-0.13	-3.3	-42%
2	Max.	0.49	12.5	0.66	16.8	-25%
	Min.	-0.34	-8.5	-0.59	-15.0	-43%
3	Max.	1.74	44.3	1.29	32.8	35%
	Min.	-1.36	-34.6	-0.95	-24.1	43%
4	Max.	1.89	47.9	1.49	37.8	27%
	Min.	-1.62	-41.1	-1.1	-27.9	47%
5	Max.	1.93	48.9	1.65	41.9	17%
	Min.	-2.13	-54.2	-1.44	-36.6	48%
6	Max.	2.40	61.0	1.97	50.0	22%
	Min.	-2.71	-68.9	-1.83	-46.5	48%
7	Max.	2.54	64.5	2.32	58.9	9%
	Min.	-3.29	-83.7	-2.14	-54.4	54%
8	Max.	2.51	63.8	2.73	69.3	-8%
	Min.	-3.92	-99.6	-2.26	-57.4	74%

Table 8.8 Measured and calculated (posttest) peak longitudinal base shear

Peak Base Shear - Longitudinal Direction						
Run #		Calculated (Posttest)		Measured		% Difference
		(k)	(kN)	(k)	(kN)	
1	Max.	30.2	134	22.4	100	35%
	Min.	-38.3	-170	-18.4	-82	108%
2	Max.	51.9	231	51.7	230	0%
	Min.	-56.6	-252	-52	-231	9%
3	Max.	62.5	278	64.5	287	-3%
	Min.	-58.8	-262	-63.2	-281	-7%
4	Max.	68.7	306	70.9	315	-3%
	Min.	-58.6	-260	-56.7	-252	3%
5	Max.	73.4	327	72.8	324	1%
	Min.	-57.5	-256	-55.2	-246	4%
6	Max.	74.9	333	74.3	330	1%
	Min.	-53.2	-237	-59.5	-265	-11%
7	Max.	76.9	342	71.2	317	8%
	Min.	-59.0	-262	-61.9	-275	-5%
8	Max.	75.5	336	70.6	314	7%
	Min.	-62.6	-279	-62.7	-279	0%

Table 8.9 Measured and calculated (posttest) peak transverse base shear

Peak Base Bent Shear - Transverse Direction						
Run #		Calculated (Posttest)		Measured		% Difference
		(k)	(kN)	(k)	(kN)	
1	Max.	14.4	64	15.1	67.1	-5%
	Min.	-22.8	-102	-13.9	-61.7	64%
2	Max.	44.6	198	37.7	167.7	18%
	Min.	-54.0	-240	-36.9	-164.2	46%
3	Max.	55.8	248	49.8	221.5	12%
	Min.	-68.0	-302	-52.3	-232.5	30%
4	Max.	56.6	252	51.1	227.2	11%
	Min.	-54.5	-242	-49.8	-221.5	9%
5	Max.	59.0	262	53.4	237.6	10%
	Min.	-54.2	-241	-49.1	-218.6	10%
6	Max.	63.2	281	54.6	242.7	16%
	Min.	-53.2	-237	-44.7	-198.8	19%
7	Max.	65.5	291	54.7	243.4	20%
	Min.	-57.9	-257	-42.3	-188.1	37%
8	Max.	67.2	299	54.1	240.7	24%
	Min.	-45.7	-203	-41.4	-184.2	10%

Table 8.10 Measured and calculated (posttest) peak longitudinal hinge rotations

Longitudinal Hinge Rotation						
Run #	N. Hinge (radians)			S. Hinge (radians)		
	Measured	Calculated	Percent Difference	Measured	Calculated	Percent Difference
1	-0.0023	-0.0025	10%	-0.0024	-0.0036	50%
2	0.0086	0.0067	-22%	0.0094	0.0061	-35%
3	-0.0167	-0.0210	26%	0.0172	0.0192	12%
4	-0.0263	-0.0342	30%	-0.0232	-0.0269	16%
5	-0.035	-0.0494	41%	-0.0299	-0.0225	-25%
6	-0.0417	-0.0601	44%	-0.0322	-0.0277	-14%
7	-0.0468	-0.0664	42%	0.0358	0.0700	95%
8	-0.0515	-0.0672	31%	0.0436	0.0712	63%

Table 8.11 Measured and calculated (posttest) peak transverse hinge rotations

Transverse Hinge Rotation						
Run #	N. Hinge (radians)			S. Hinge (radians)		
	Measured	Calculated	Percent Difference	Measured	Calculated	Percent Difference
1	0.0016	0.0017	3%	0.0015	0.0016	6%
2	0.0071	0.0094	32%	0.0068	0.0093	36%
3	0.0143	0.0193	35%	0.014	0.0200	43%
4	0.0163	0.0222	36%	0.0162	0.0226	39%
5	0.018	0.0285	58%	0.0177	0.0286	62%
6	0.0211	0.0356	69%	0.021	0.0353	68%
7	0.0247	0.0426	73%	0.0248	0.0419	69%
8	0.0291	0.0507	74%	0.0293	0.0494	69%

Table 9.1 Fundamental periods from analytical models

Fundamental Periods from Measured Data and Analytical Models (seconds)					
	Pretest	NF	FM1	FM2	FM3
In-plane rotation	1.42	1.51	0.16	0.38	0.38
Longitudinal	0.29	0.30	0.17	0.20	0.20
Transverse	0.28	0.26	0.13	0.16	0.16
Vertical	0.11	0.08	0.08	0.08	0.08

Table 10.1 Bridge model properties for ABC-UTC, Calt-Bridge 1, and Calt-Bridge 2

Bridge Model Properties			
	ABC-UTC	Calt-Bridge 1	Calt-Bridge 2
Scale Factor	0.35	0.35	0.35
# of spans	2	2	2
Span Length	34 ft - 8 in (10.6 m)	34 ft - 8 in (10.6 m)	34 ft - 8 in (10.6 m)
Bridge Width	11 ft (3.35 m)	11 ft (3.35 m)	11 ft (3.35 m)
# of girders per span	4	4	4
Girder Type	Steel plate	Prestressed Concrete	Prestressed Concrete
Column Diameter	16 in (406 mm)	18 in (457 mm)	18 in (457 mm)
Column Clear Height	84.75 in (2.15 m)	84 in (2.13 m)	84 in (2.13 m)
Column Spacing	6 ft - 6 in (1.98 m)	6 ft - 6 in (1.98 m)	6 ft - 6 in (1.98 m)
Column Long. Reinforcement	12 - #5 (A_s = 3.72 in^2, 2400 mm^2), ρ_l =1.83%	10 - #6 (A_s = 4.4 in^2, 2840 mm^2), ρ_l =1.73%	10 - #6 (A_s = 4.4 in^2, 2840 mm^2), ρ_l =1.73%
Column Trans. Reinforcement	#3 @ 2.5 in (63.5 mm), ρ_s =1.25%	#3 @ 1.75 in (44.4 mm), ρ_s =1.65%	#3 @ 1.75 in (44.4 mm), ρ_s =1.65%
Seismic Weight	143 kip (636 kN)	187.2 kip (833 kN)	187.9 kip (836 kN)
Axial Load Index (ALI)	5.7%	4.6%	4.6%

Table 10.2 Parameters from idealized capacity curves and displacement demands for ABC-UTC, Calt-Bridge 1, and Calt-Bridge 2

	ABC-UTC		Calt-Bridge 1		Calt-Bridge 2	
	Longitudinal	Transverse	Longitudinal	Transverse	Longitudinal	Transverse
Displacement at first yield	0.4 in (10.2 mm)	0.44 in (11.3 mm)	0.67 in (17.0 mm)	0.68 in (17.3 mm)	0.38 in (9.65 mm)	0.38 in (9.65 mm)
Effective yield displacement, Δ_y	0.62 in (15.8 mm)	0.6 in (15.2 mm)	1.04 in (26.2 mm)	1.08 in (27.4 mm)	0.56 in (14.2 mm)	0.56 in (14.2 mm)
Maximum Disp. From Pushover, Δ_u	4.64 in (118 mm)	3.71 in (94.2 mm)	4.75 in (121 mm)	4.51 in (115 mm)	6.72 in (171 mm)	6.72 in (171 mm)
Plastic Base Shear, F_y	58.3 kip (259 kN)	57 kip (253 kN)	62.6 kip (279 kN)	61.8 kip (275 kN)	72.7 kip (323 kN)	71.8 kip (319 kN)
Effective Stiffness, k_e	94.0 kip/in (16.5 kN/mm)	95.0 kip/in (16.6 kN/mm)	60.4 kip/in (10.6 kN/mm)	56.9 kips/in (9.97 kN/mm)	130.2 k/in (22.8 kN/mm)	128.6 k/in (22.5 kN/mm)
Displacement Ductility Capacity, μ_c	7.48	6.18	4.59	4.15	> 12	> 12
Effective Period, T_{eff}	0.44	0.41	0.57 s	0.58 s	0.38 s	0.39 s
Spectral Acceleration, S_a	1.15 g	1.15 g	1.05 g	1.04 g	1.18 g	1.18 g
Displacement Demand, Δ_d	1.75 in (44.4 mm)	1.73 in (44.0 mm)	3.26 in (82.8 mm)	3.45 in (87.4 mm)	1.79 in (45.5 mm)	1.82 in (46.2 mm)
Resultant Displacement Demand, Δ_d	2.27 in (57.7 mm)		4.43 in (112 mm)		2.36 in (59.9 mm)	
Displacement Ductility Demand, μ_d	2.82	2.88	3.15	3.16	2.47	2.47
Disp. Capacity/ Disp. Demand	2.65	2.14	1.46	1.31	> 3.8	> 3.7
Calculated Fundamental Periods (s)						
In-Plane Rotation	2.57		3.53		1.42	
Longitudinal	0.58		0.63		0.4	
Transverse	0.48		0.6		0.39	

Table 10.3 Loading protocol for ABC-UTC, Calt-Bridge 1, and Calt-Bridge 2

Run #	ABC-UTC				Calt-Bridge 1				Calt-Bridge 2			
	% Design Earthquake	Scale Factor	PGA		% Design Earthquake	Scale Factor	PGA		% Design Earthquake	Scale Factor	PGA	
			Transverse	Longitudinal			Transverse	Longitudinal			Transverse	Longitudinal
WN1-L WN1-T	-				-				-			
1	30%	0.18	0.278	0.1872	20%	0.107	0.066	0.098	30%	0.137	0.085	0.125
WN2-L WN2-T	-				-				-			
2	65%	0.39	0.602	0.4056	50%	0.268	0.165	0.245	65%	0.296	0.183	0.271
WN3-L WN3-T	-				-				-			
3	100%	0.6	0.926	0.624	75%	0.401	0.248	0.3675	100%	0.455	0.281	0.417
WN4-L WN4-T	-				-				-			
4	125%	0.75	1.158	0.78	100%	0.535	0.33	0.49	125%	0.569	0.351	0.521
WN5-L WN5-T	-				-				-			
5	150%	0.9	1.389	0.936	125%	0.669	0.413	0.6125	150%	0.683	0.421	0.626
WN6-L WN6-T	-				-				-			
6	175%	1.05	1.621	1.092	150%	0.803	0.495	0.735	175%	0.796	0.491	0.729
WN7-L WN7-T	-				-				-			
7	200%	1.2	1.852	1.248	175%	0.936	0.578	0.8575	200%	0.91	0.561	0.833
WN8-L WN8-T	-				-				-			
8	225%	1.35	2.084	1.404	200%	1.07	0.66	0.98	225%	1.02	0.632	0.938
WN9-L WN9-T	-				-				-			

Table 10.4 Peak bent displacements in longitudinal and transverse directions for ABC-UTC, Calt-Bridge 1 and Calt-Bridge 2

Longitudinal Direction						
Run #	ABC-UTC		Calt-Bridge 1		Calt-Bridge 2	
	Bent Displacement	Drift Ratio	Bent Displacement	Drift Ratio	Bent Displacement	Drift Ratio
1	0.85 in (21.5 mm)	1.0%	0.24 in (6.1 mm)	0.3%	0.3 in (7.7 mm)	0.4%
2	1.70 in (43.0 mm)	2.0%	1.28 in (32.5 mm)	1.5%	0.96 in (24.3 mm)	1.1%
3	2.92 in (74.3 mm)	3.4%	2.38 in (60.4 mm)	2.8%	1.66 in (42.3 mm)	2.0%
4	4.41 in (112 mm)	5.2%	3.87 in (98.3 mm)	4.6%	2.48 in (63.0 mm)	3.0%
5	4.87 in (124 mm)	5.7%	4.16 in (106 mm)	5.0%	3.23 in (82.1 mm)	3.8%
6	5.51 in (140 mm)	6.5%	4.12 in (105 mm)	4.9%	3.74 in (95.1 mm)	4.5%
7	5.03 in (128 mm)	5.9%	5.04 in (128 mm)	6.0%	3.94 in (100 mm)	4.7%
8	4.81 in (122 mm)	5.7%	5.88 in (149 mm)	7.0%	4.20 in (107 mm)	4.7%

Transverse Direction						
Run #	ABC-UTC		Calt-Bridge 1		Calt-Bridge 2	
	Bent Displacement	Drift Ratio	Bent Displacement	Drift Ratio	Bent Displacement	Drift Ratio
1	0.42 in (10.8 mm)	0.5%	0.22 in (5.6 mm)	0.3%	0.16 in (4.2 mm)	0.2%
2	1.53 in (38.7 mm)	1.8%	0.8 in (20.3 mm)	3.1%	0.66 in (16.8 mm)	0.8%
3	1.61 in (40.9 mm)	1.9%	1.12 in (28.4 mm)	1.3%	1.29 in (32.8 mm)	1.5%
4	2.03 in (51.7 mm)	2.4%	1.31 in (33.3 mm)	1.6%	1.49 in (37.8 mm)	1.8%
5	2.58 in (65.6 mm)	3.0%	1.92 in (48.8 mm)	2.3%	1.65 in (41.9 mm)	2.0%
6	3.01 in (76.4 mm)	3.6%	2.74 in (69.6 mm)	3.3%	1.97 in (50.0 mm)	2.3%
7	3.60 in (91.5 mm)	4.2%	3.48 in (88.4 mm)	4.1%	2.32 in (59.0 mm)	2.8%
8	4.41 in (112 mm)	5.2%	4.27 in (108 mm)	5.1%	2.73 in (69.3 mm)	3.3%

Figures

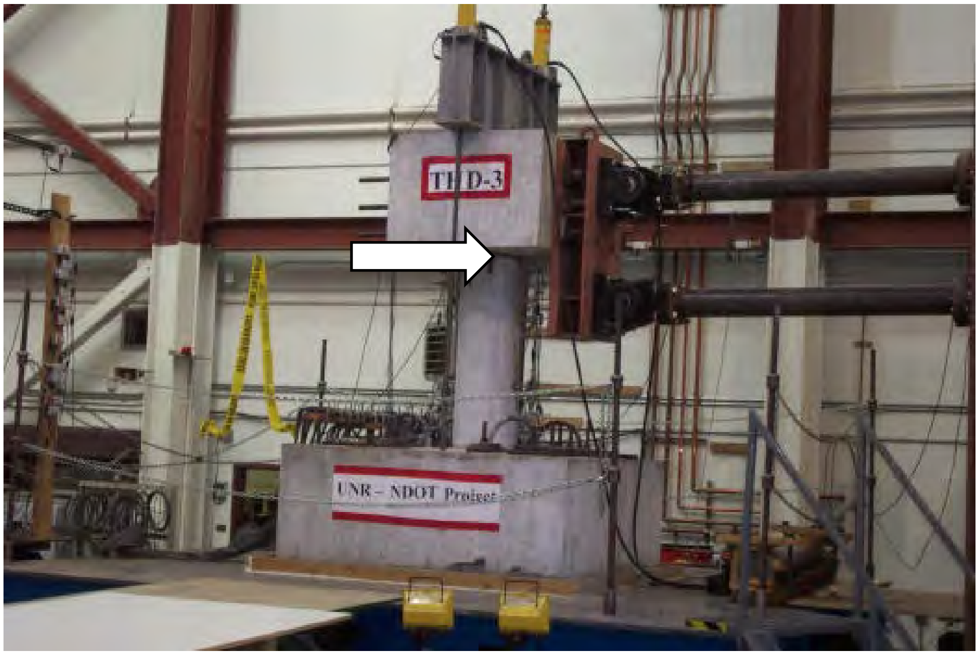

Figure 1.1 Single column shake table test incorporating rebar hinge at the top indicated by arrow, (Cheng et al., 2009)

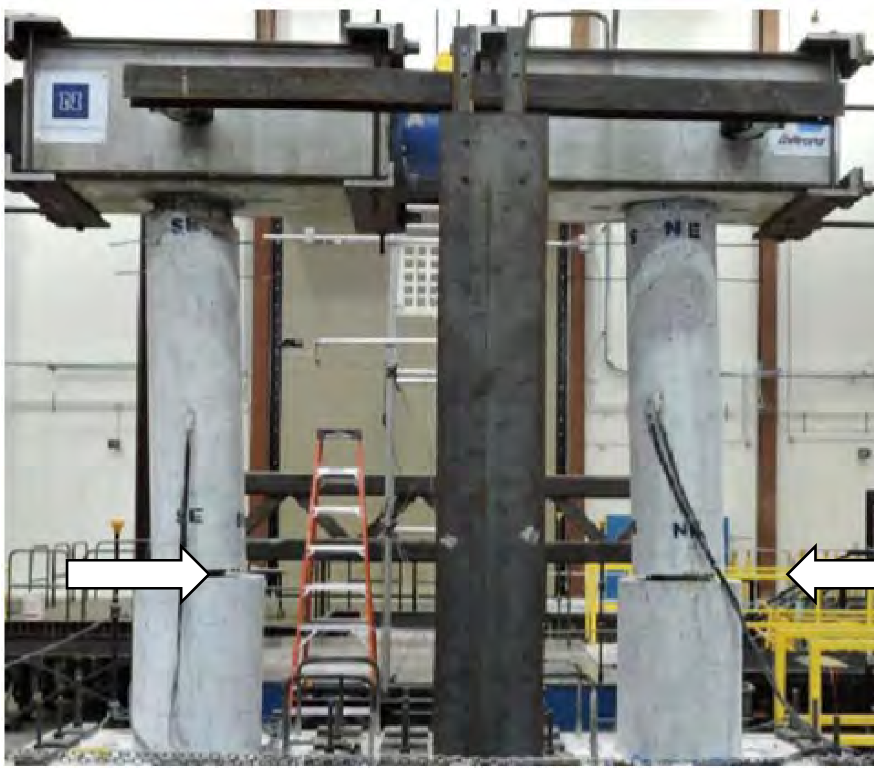

Figure 1.2 Bent with rebar hinge connecting pedestal and column, (Mehraein & Saiidi, 2016)

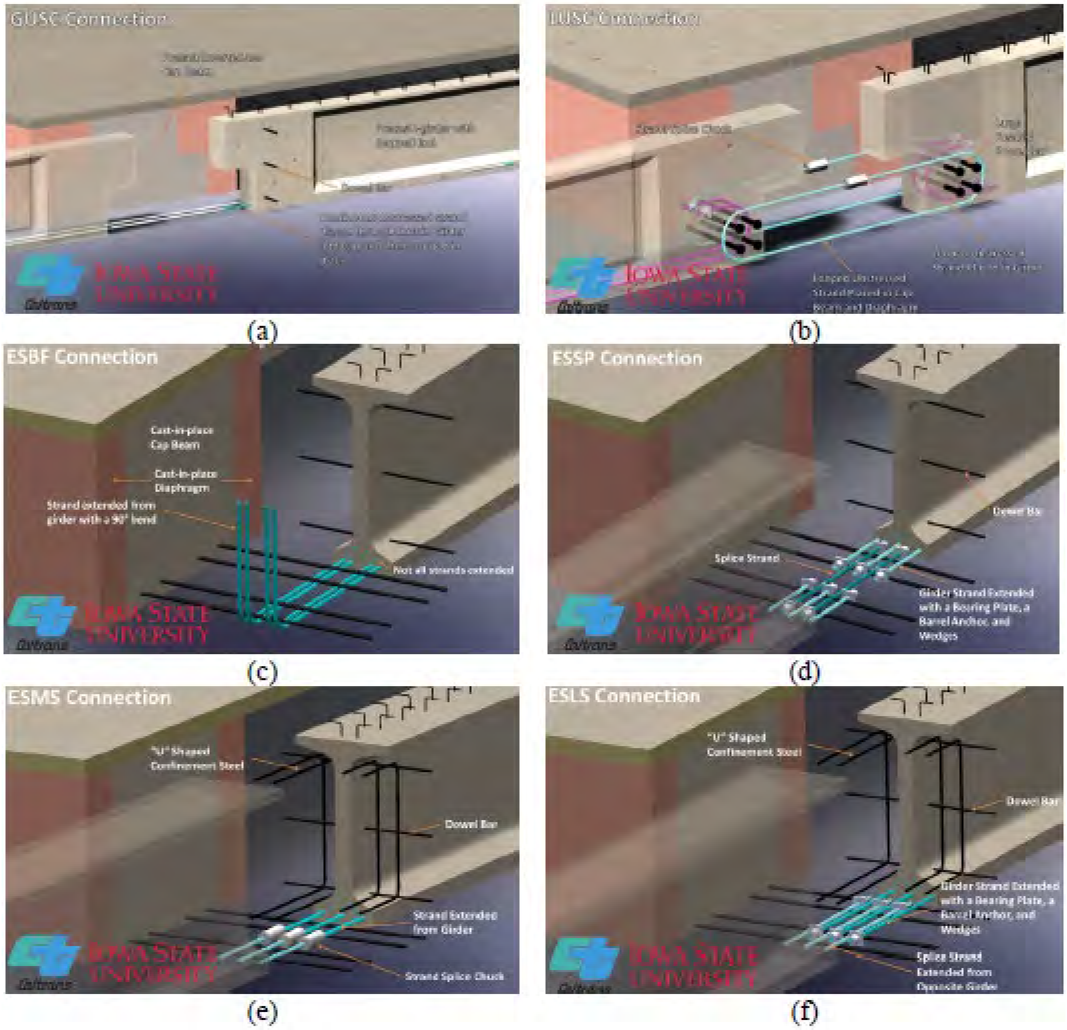

Figure 1.3 Girder-to-cap beam connections developed by Vander Werff et al. (2015), [figure taken from Benjumea et al. (2016)]

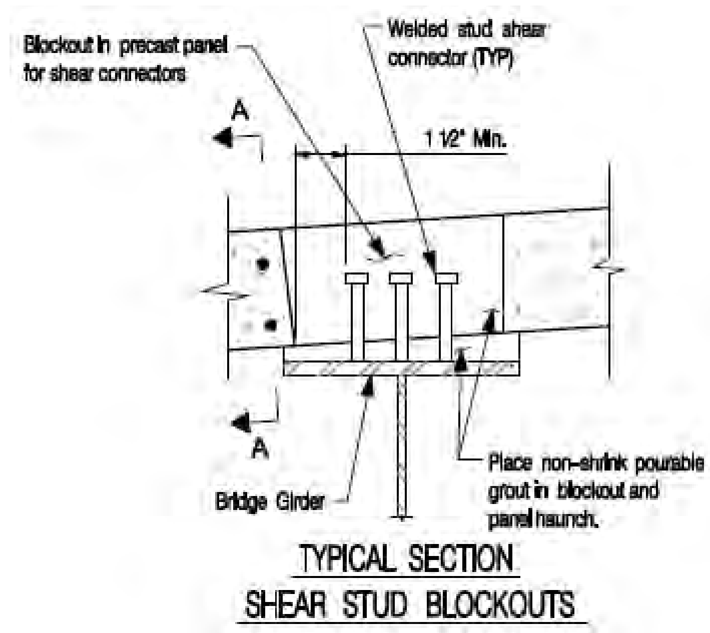

Figure 1.4 Pocket connection with projected studs from steel girder (PCI, 2011a)

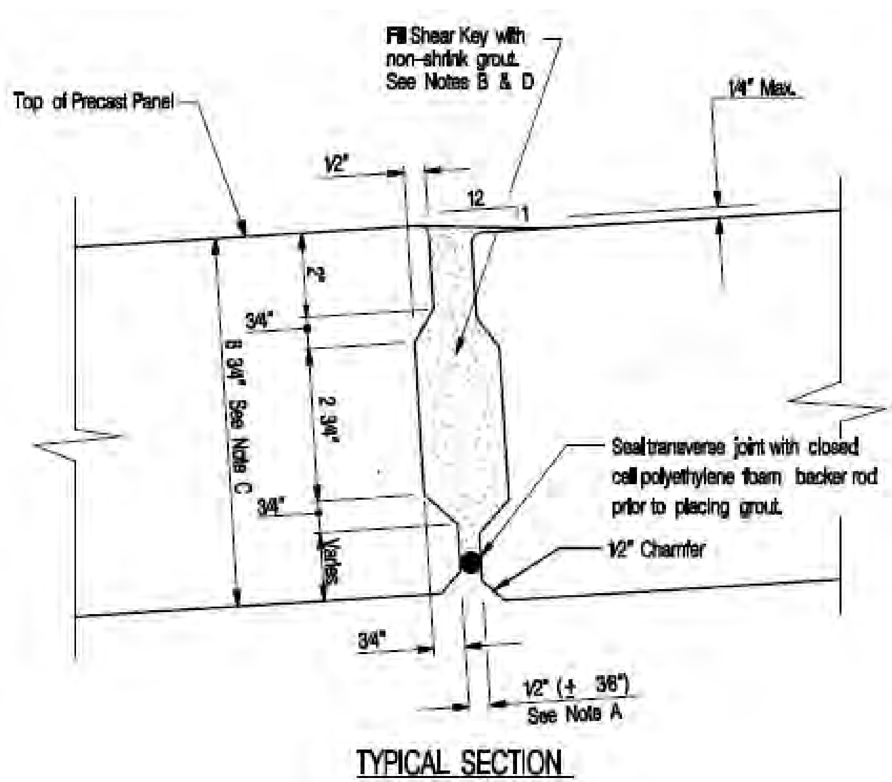

Figure 1.5 Panel to panel connection (PCI, 2011a)

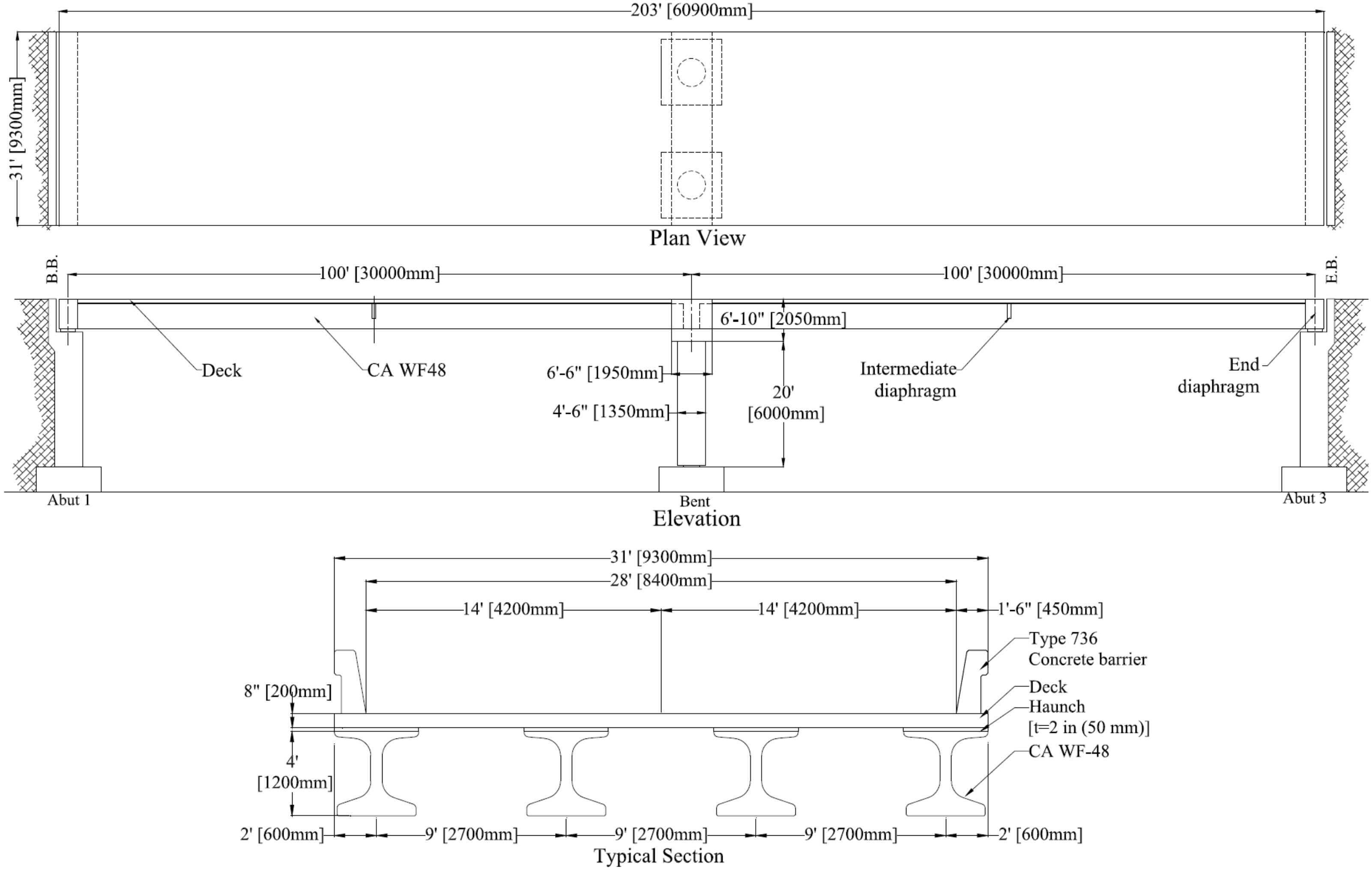

Figure 2.1 Prototype bridge dimensions (Benjumea et. al, 2019)

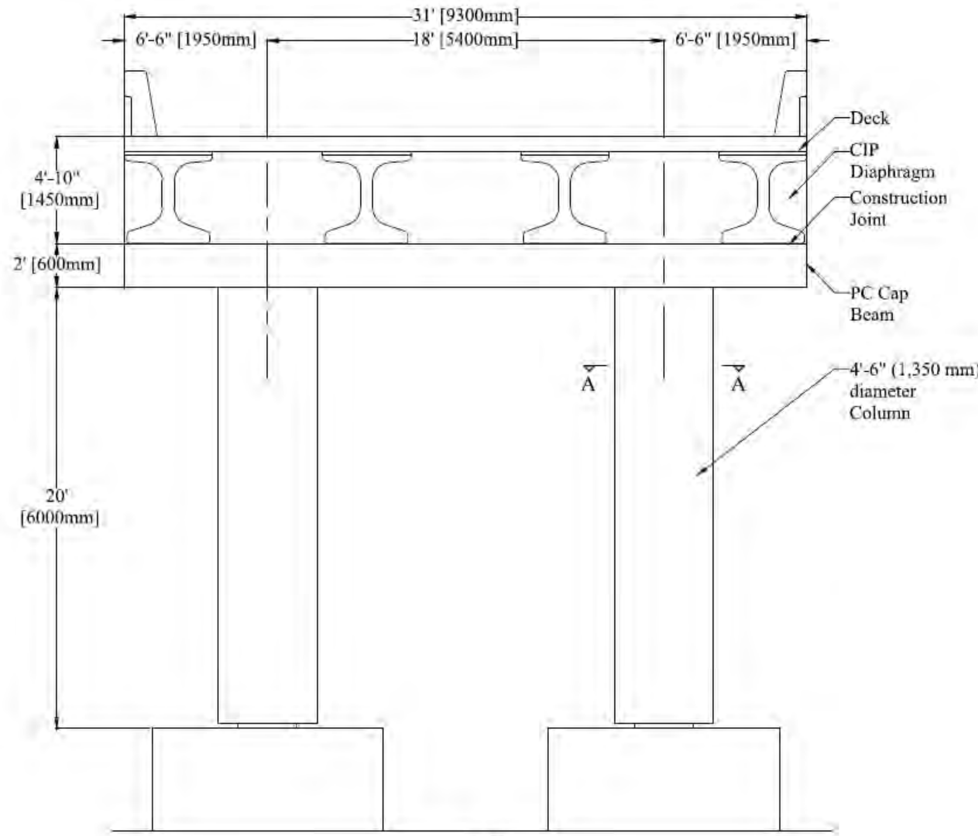

(a)

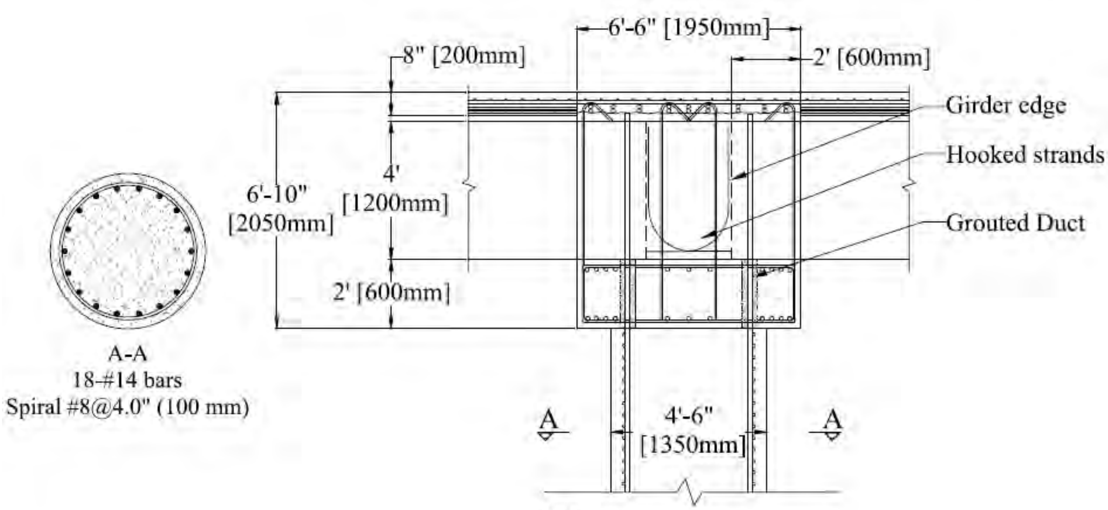

(b)

Figure 2.2 Prototype bent dimensions: (a) elevation view, (b) bent reinforcement, (Benjumea et. al, 2019)

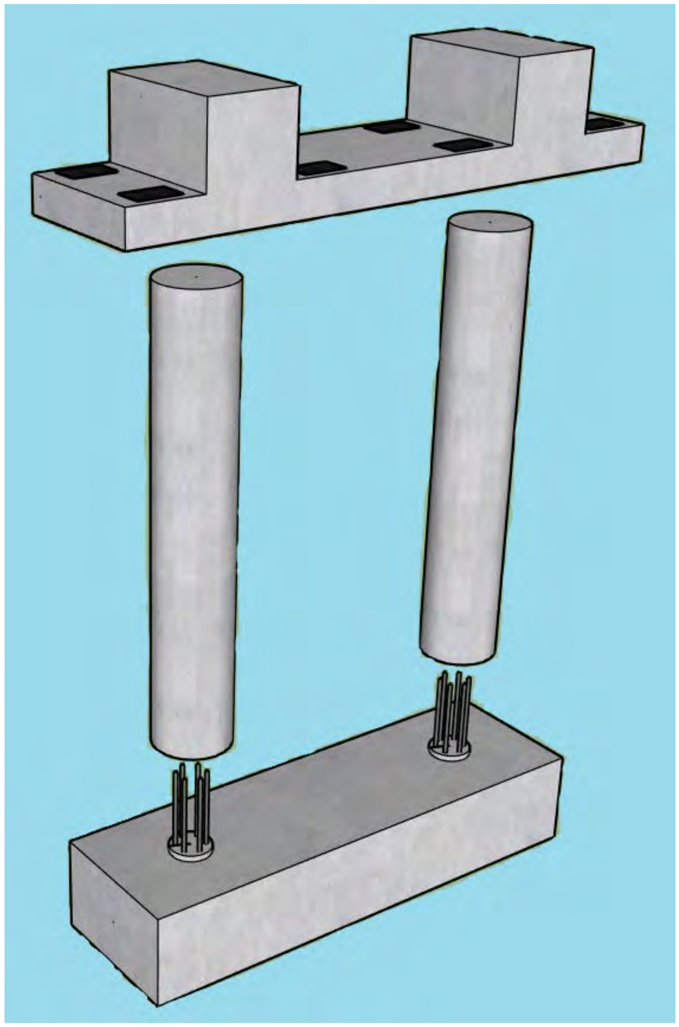

Figure 2.3 Exploded view of bent for Calt-Bridge 2 showing ABC connections

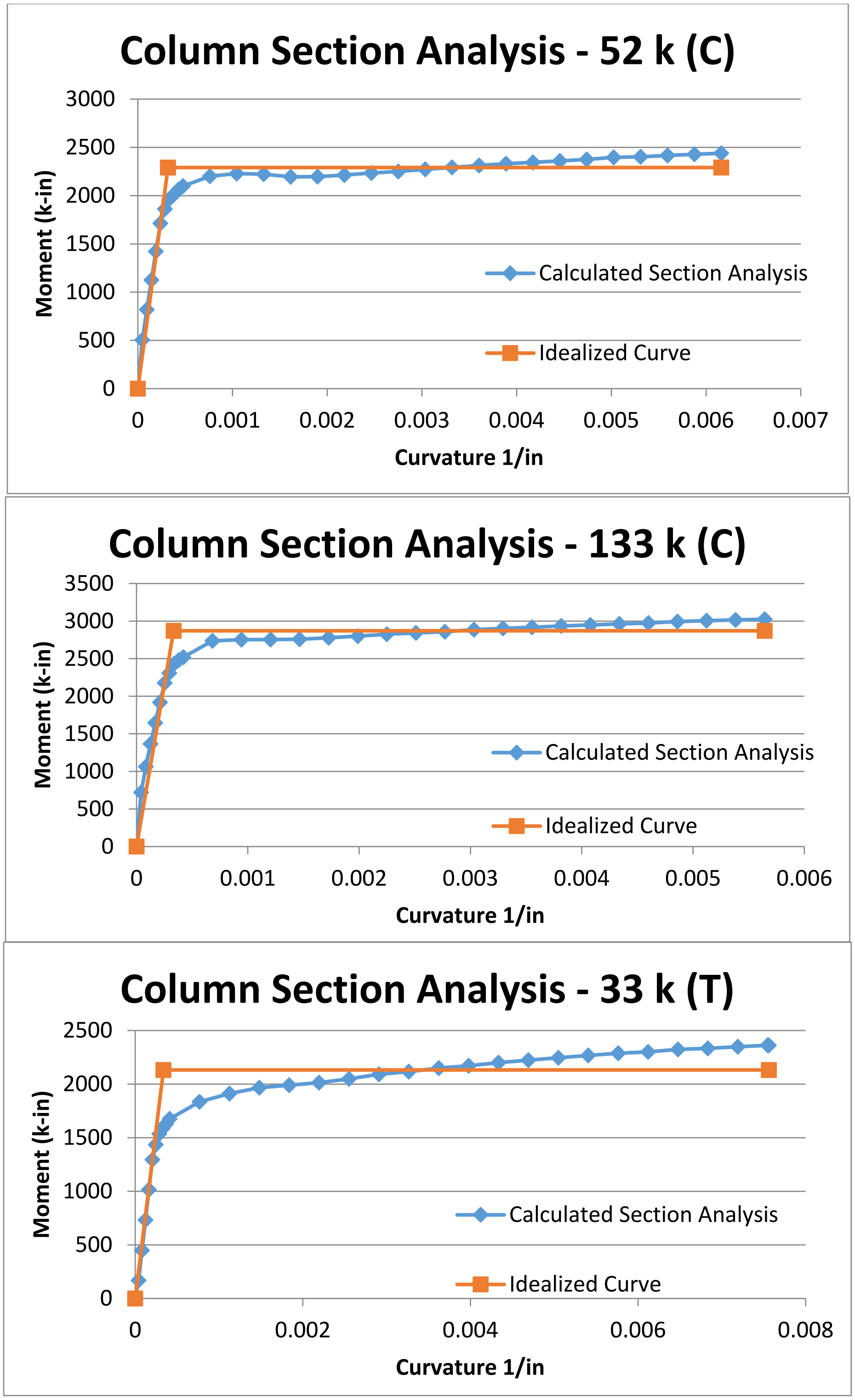

Figure 2.4 Column moment-curvature analysis from Xtract for dead load, dead load plus compression from overturning, and dead load plus tension from overturning

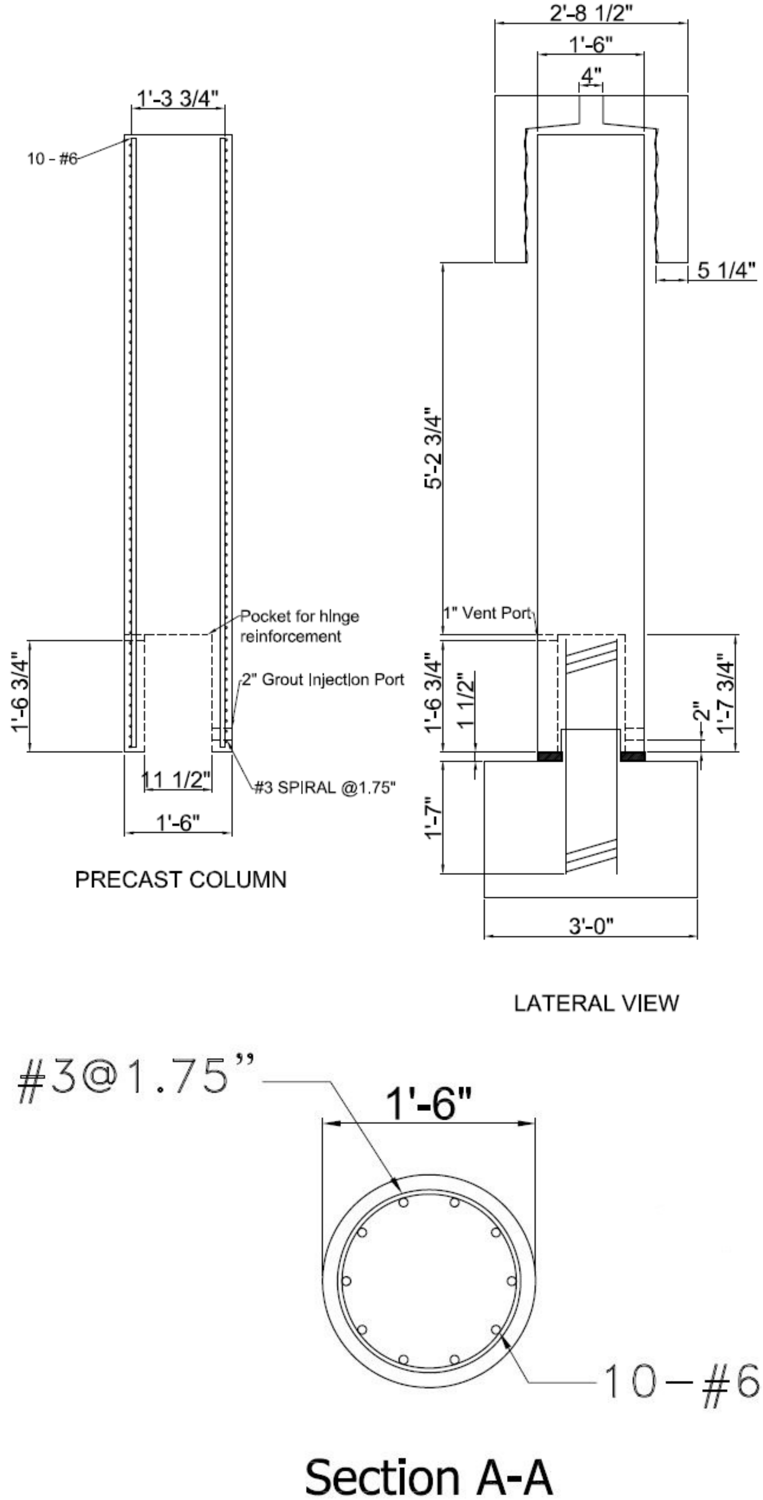

Figure 2.5 Column dimensions and cross section

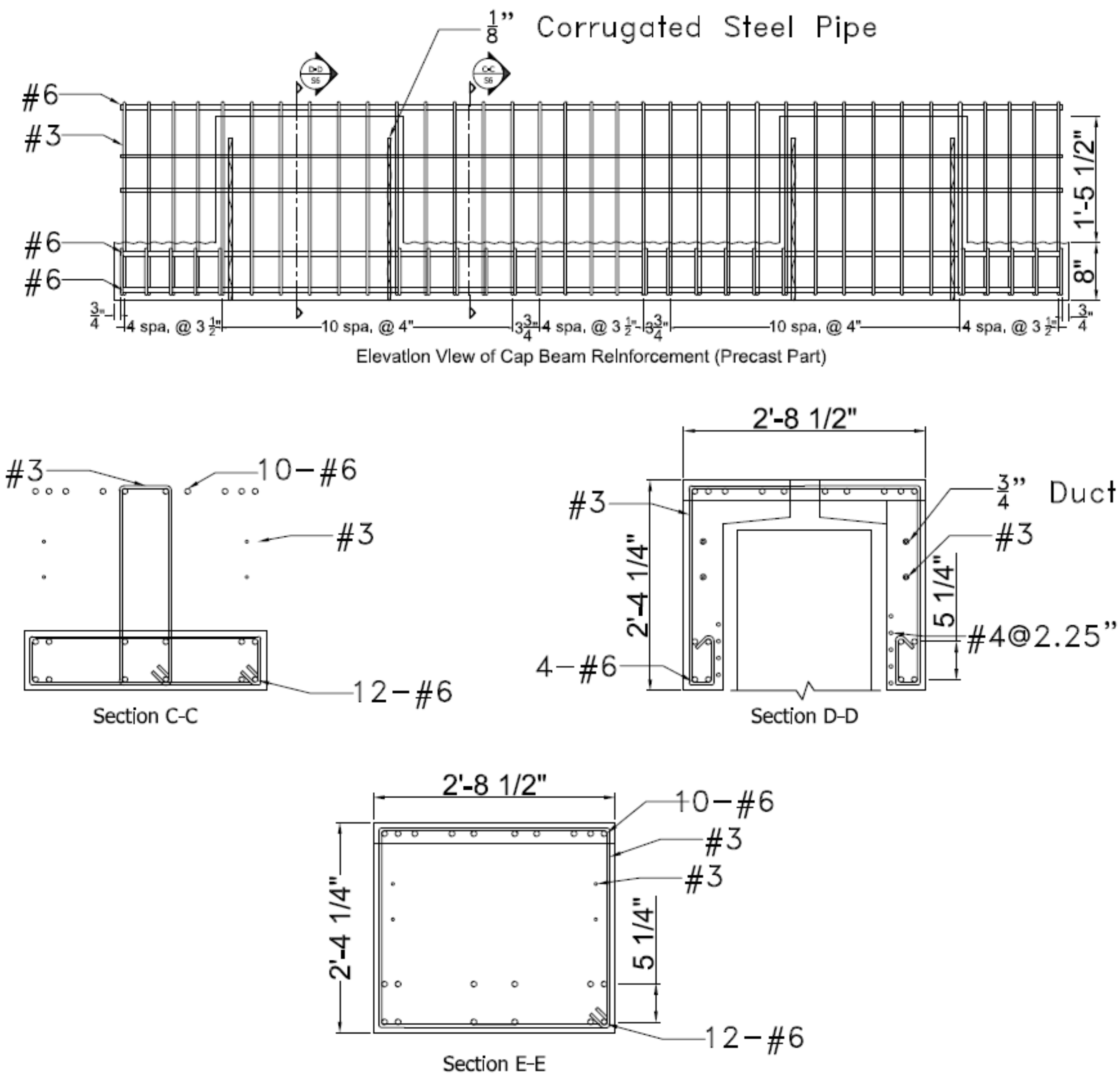

Figure 2.6 View of precast cap beam with reinforcement and cap beam cross sections

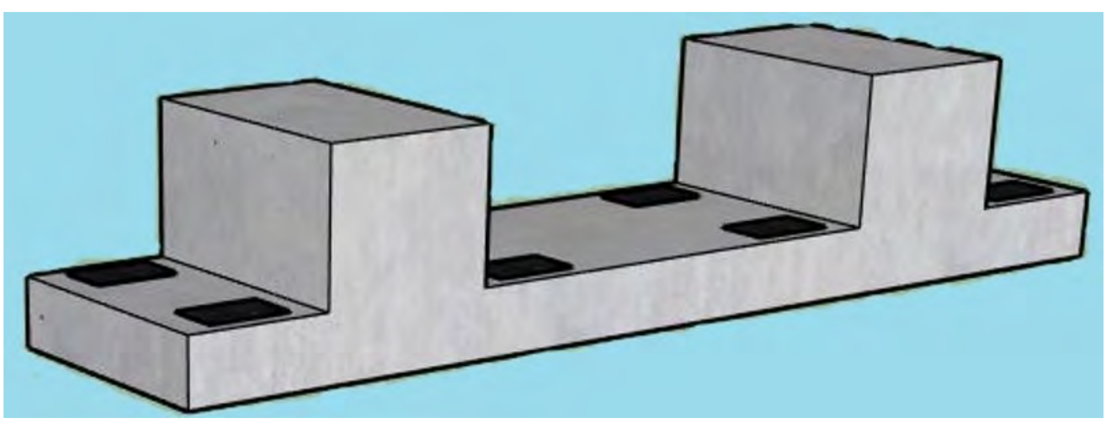

Figure 2.7 Isometric view of cap beam

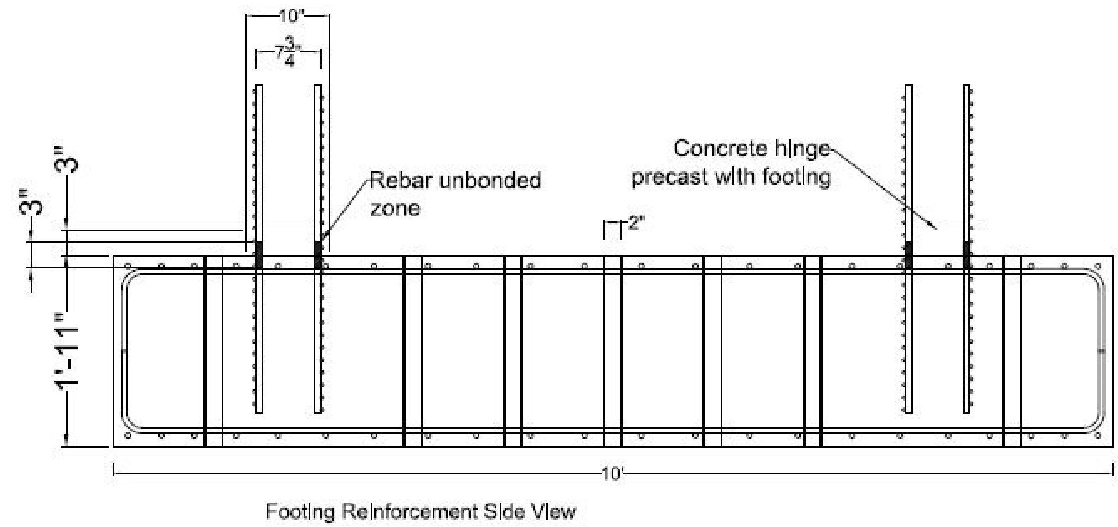

Figure 2.8 Footing dimensions with rebar hinge, elevation view (top) and plan view (bottom)

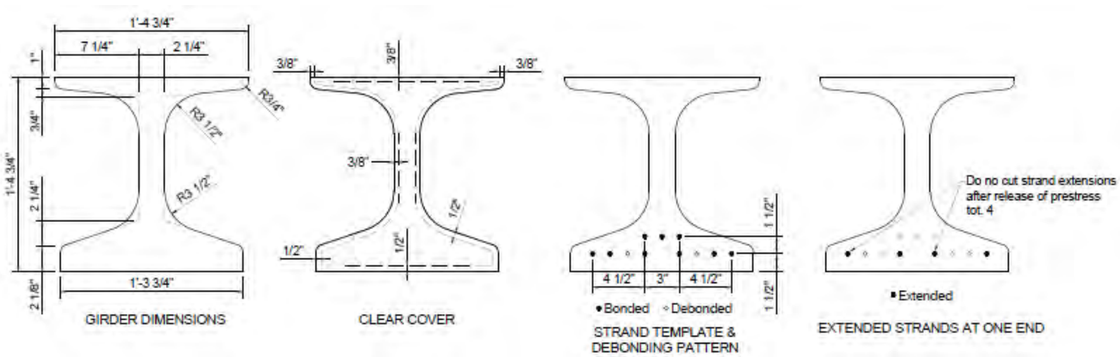

Figure 2.9 Girder dimensions and reinforcement

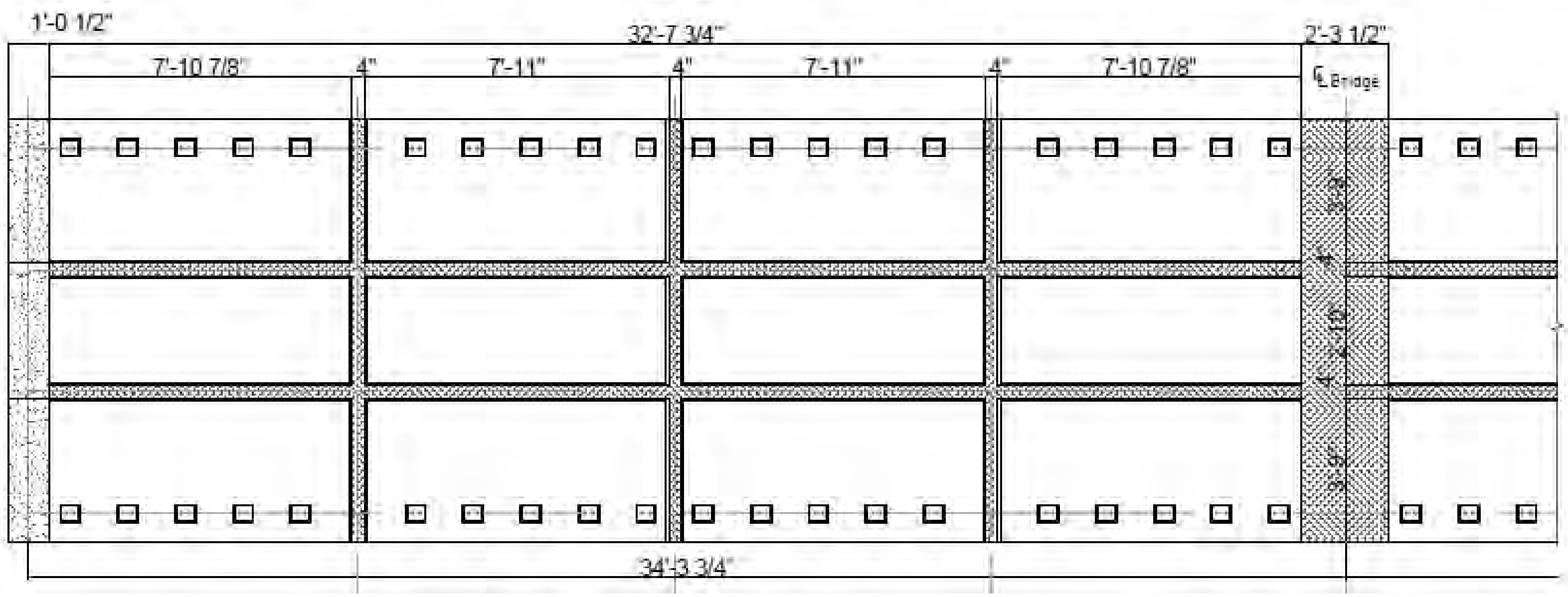

Figure 2.9: Deck panel configuration

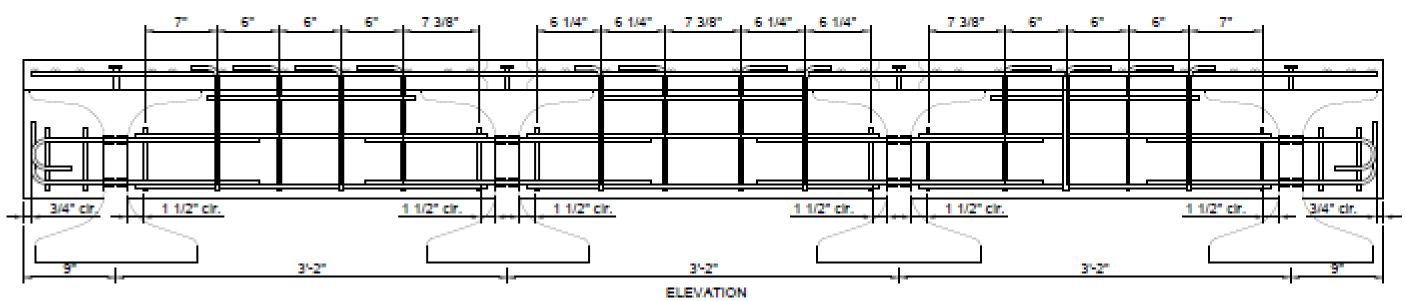

Figure 2.10: Intermediate diaphragm dimensions and reinforcement details

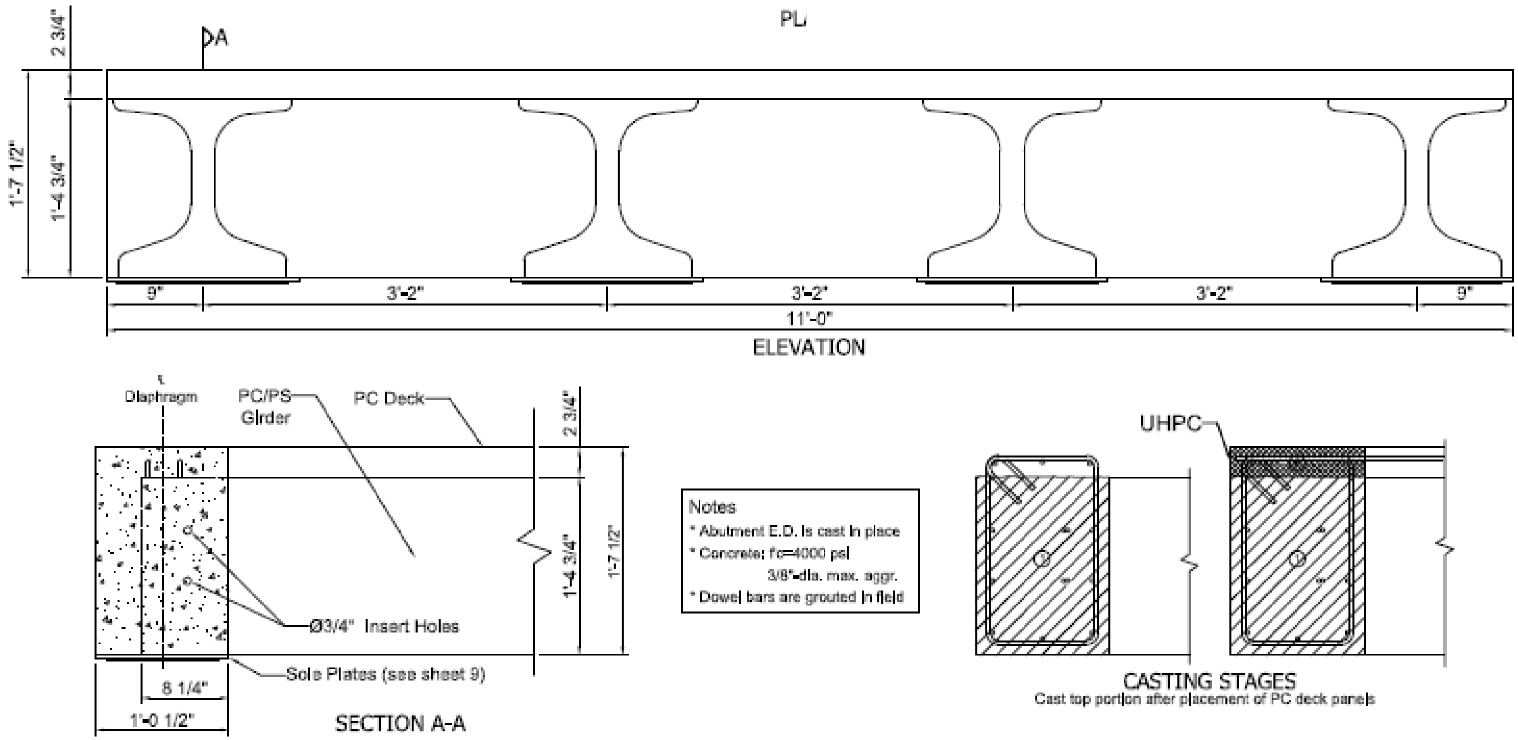

Figure 2.11: End diaphragm elevation view and cross section

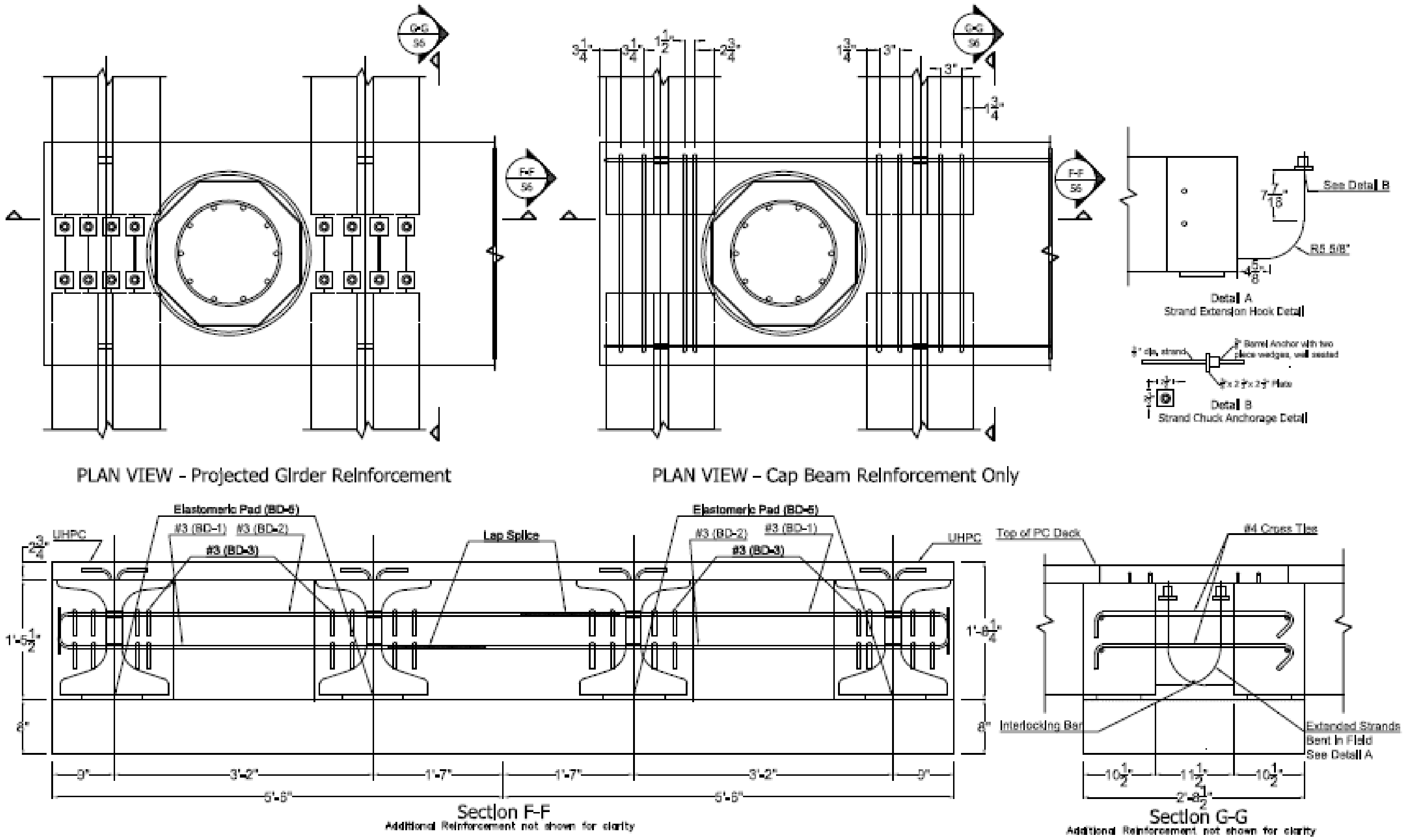

Figure 2.12: Girder-to-cap beam connection details

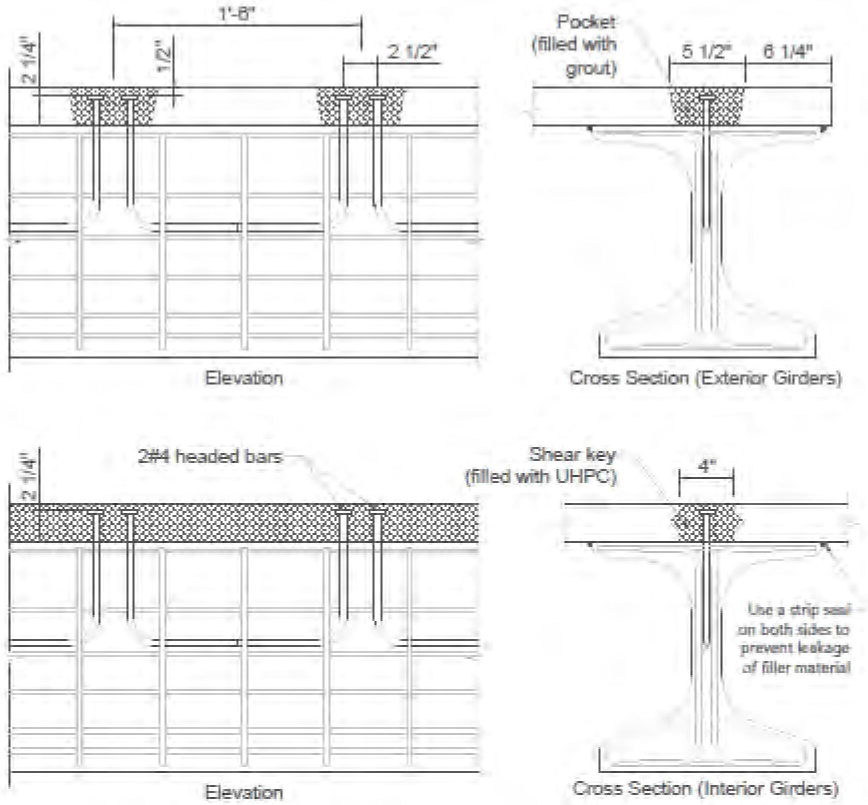

Figure 2.13: Girder-to-deck panel connection details

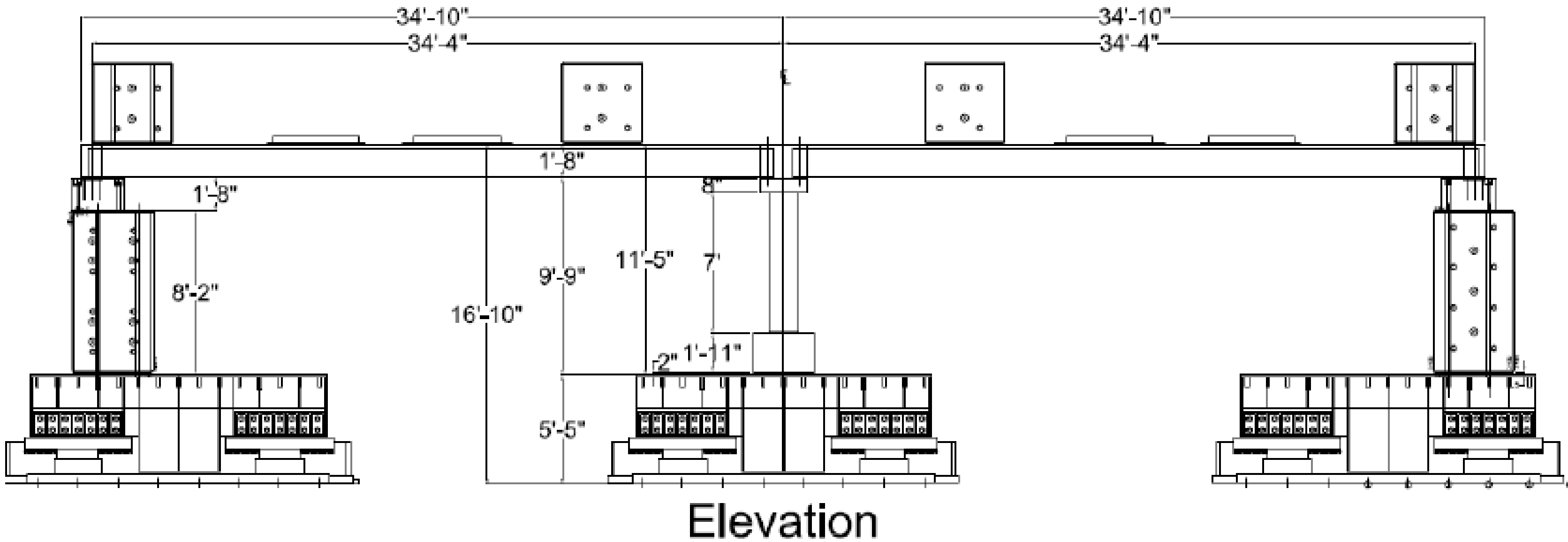

Figure 2.14: Superimposed mass for Calt-Bridge 2

Figure 3.1 Concrete slump for footing, columns, and precast cap beam

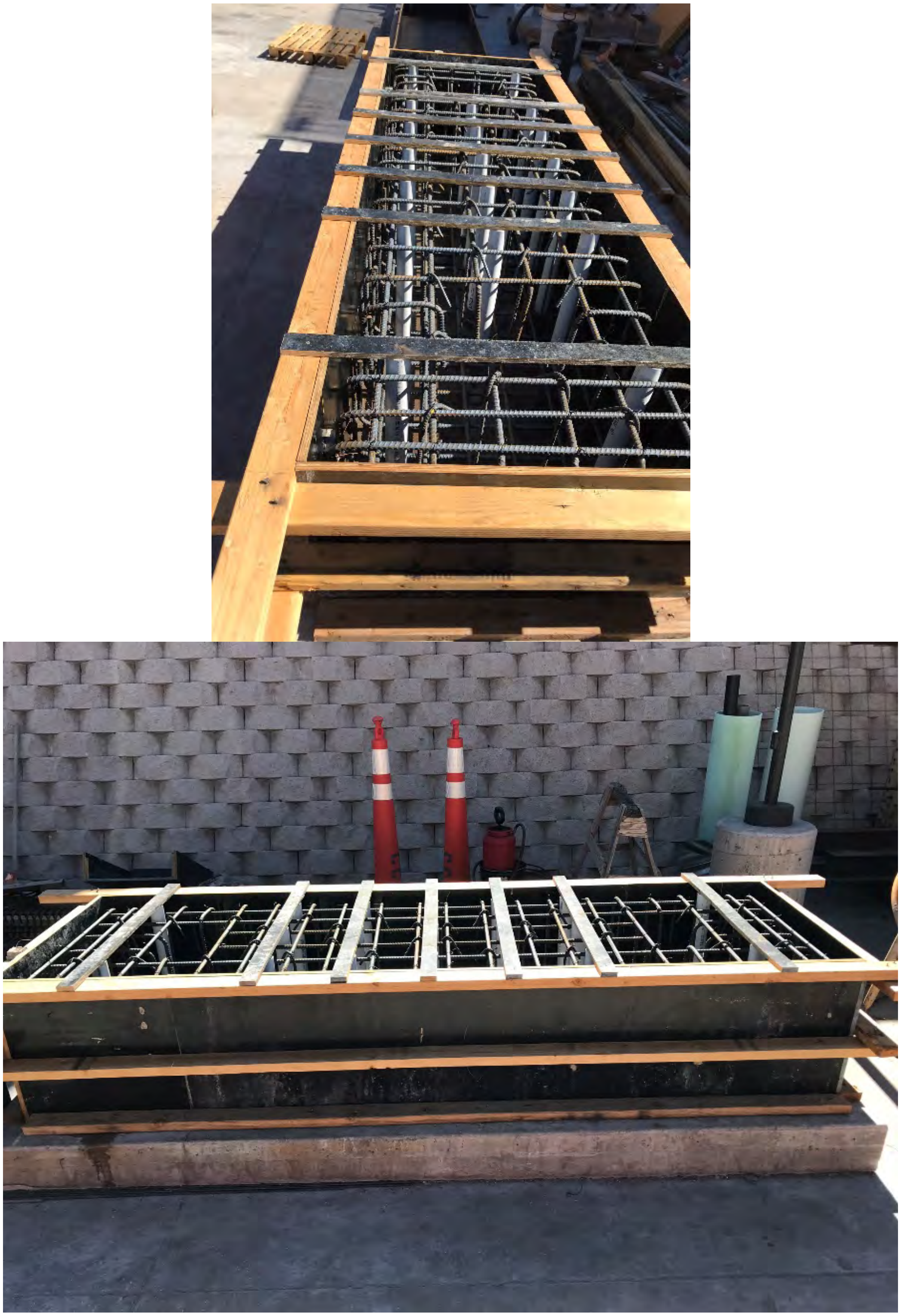

Figure 3.2 Reinforcement and formwork for footing

Figure 3.3 Rebar hinge reinforcement, longitudinal bars and spiral

Figure 3.4 Rebar hinge reinforcement installed in footing

Figure 3.5 Region surrounding rebar hinge after casting of the footing

Figure 3.6 Footing after concrete casting

Figure 3.7 Transportation of footing into EEL

Figure 3.8 Column reinforcement with pocket forms and supports

Figure 3.9 Placement of column concrete using bucket and forklift

Figure 3.10 Column pocket after removal of excess concrete

Figure 3.11 Roughened column top using grinder

Figure 3.12 Bottom longitudinal reinforcement and some transverse hoops for cap beam reinforcement

Figure 3.13 Cap beam reinforcement with all hoops and some top longitudinal bars

Figure 3.14 Cap beam reinforcement and pocket formwork

Figure 3.15 Cap beam with pocket formwork

Figure 3.16 Cap beam pocket and base after casting of concrete

Figure 3.17 Inside view of precast pocket

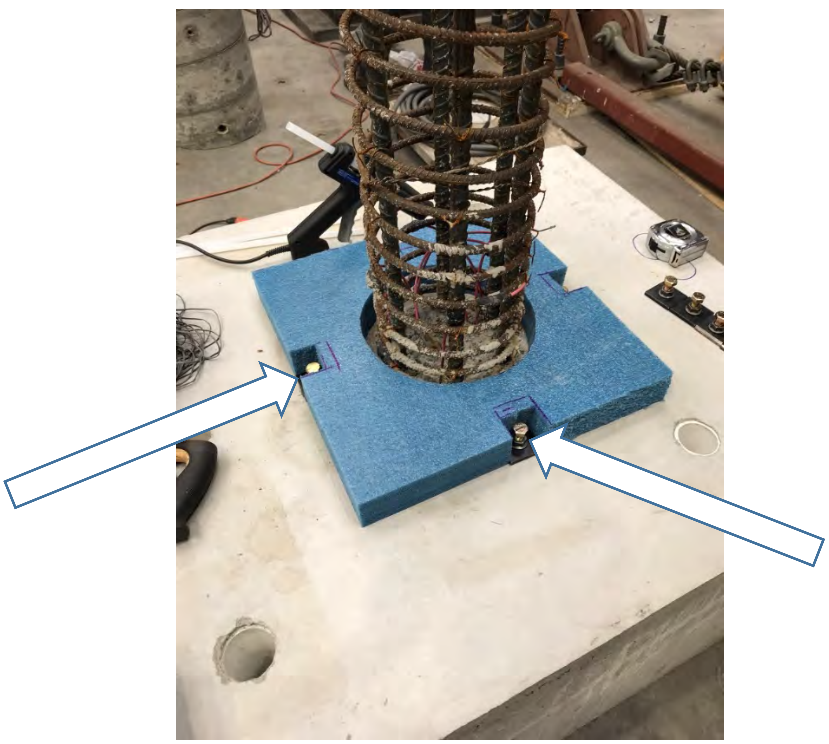

Figure 3.18 Foam base with leveling bolts (indicated by white arrow) for formation of the rebar hinge

Figure 3.19 Column resting on leveling bolts and foam form

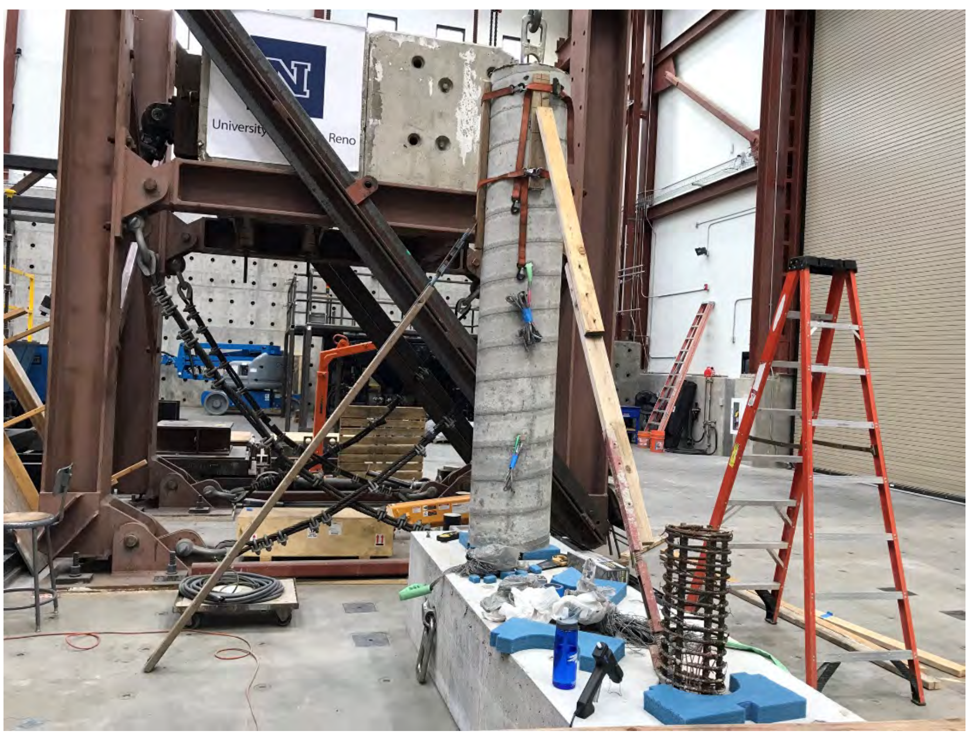

Figure 3.20 Wood bracing to keep column level

Figure 3.21 Column after grout has been applied via ducts for rebar hinge

Figure 3.22 View of rebar hinge after casting of grout and removal of foam form

Figure 3.23 Cap beam pocket formwork for assembly of the bent

Figure 3.24 Placement of cap beam on columns using crane

Figure 3.25 Column inside of cap beam pocket connection with no grout

Figure 3.26 Pouring of grout into the cap beam pocket connection

Figure 3.27 Side of pocket connection after casting of grout

Figure 3.28 Column-cap beam interface after casting of grout in pocket connection

Figure 3.29 Storage of prestressed concrete girders prior to assembly of spans

Figure 3.30 Concrete slump for precast deck panels

Figure 3.31 Casting of precast deck panels

Figure 3.32 Transportation of girders using two forklifts

Figure 3.33 Final setting of girders prior to placement of the precast deck panels

Figure 3.34 Intermediate diaphragm formwork between girders

Figure 3.35 Intermediate diaphragm formwork when viewed from top

Figure 3.36 Intermediate diaphragm formwork on outside edge of exterior girder

Figure 3.37 Embedded steel plate on underside of girder with projected reinforcement

Figure 3.38 End diaphragm formwork with metal bracing

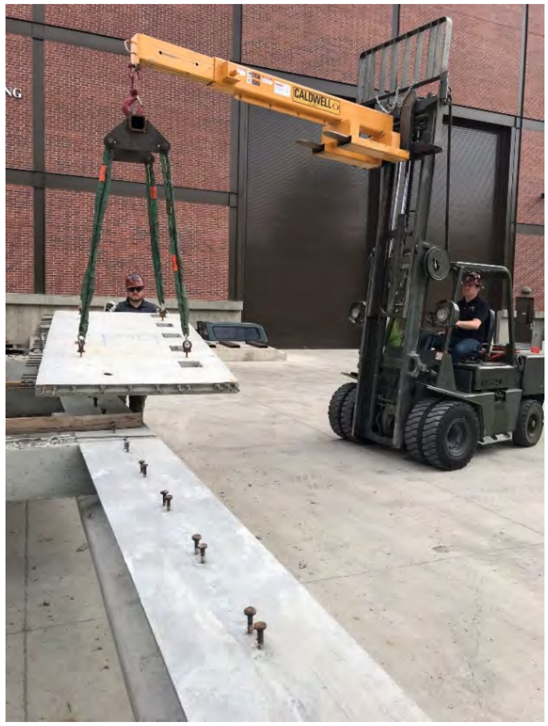

Figure 3.39 Placement of precast deck panels using formwork

Figure 3.40 View of deck panel-to-panel connection after placement of precast deck panels

Figure 3.41 Span after placement of precast deck panels

Figure 3.42 Casting of UHPC in deck joints and over end diaphragm

Figure 3.43 Deck joints after casting of UHPC

Figure 3.44 End diaphragms, deck joints, and deck panel pockets after casting of UHPC and grout

Figure 3.45 Bent after placement on shake table 2

Figure 3.46 Lifting of span on end with end diaphragm using crane

Figure 3.47 Lifting of span with forklift

Figure 3.48 Placement of span on cart for transportation into the EEL

Figure 3.49 Lifting of span using EEL crane

Figure 3.50 Storage of spans prior to placement on shake tables

Figure 3.51 Placement of east span over abutment and bent

Figure 3.52 Placement of west span over abutment and bent

Figure 3.53 Placement of phase 1 mass blocks on superstructure

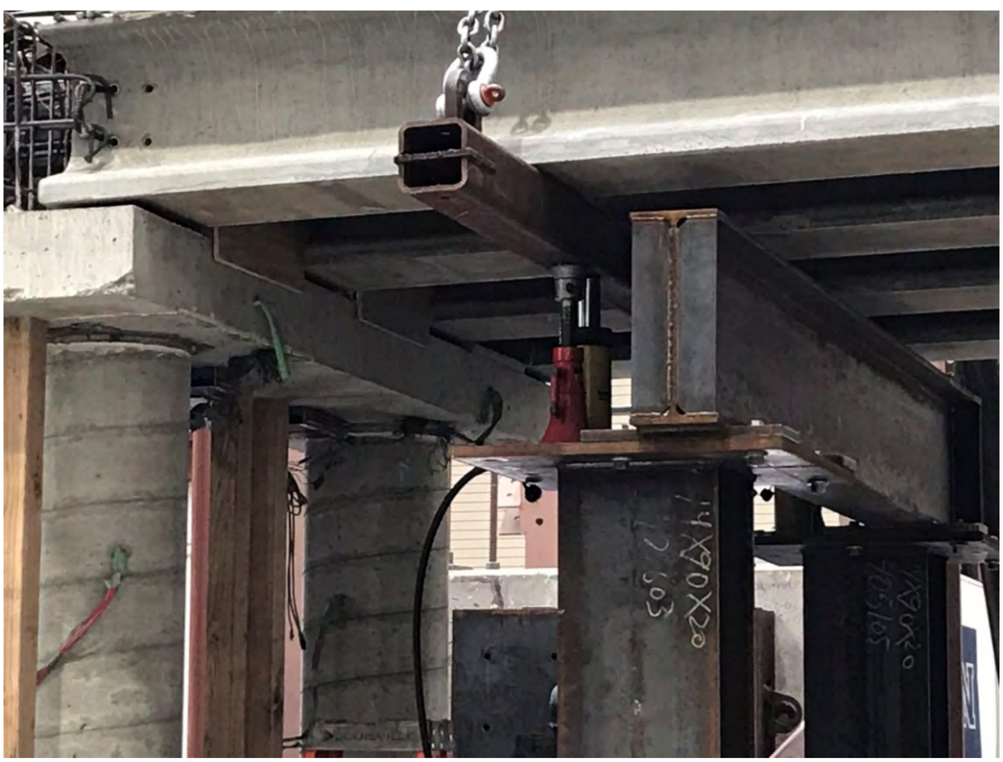

Figure 3.54 Hydraulic jacks used to drop spans onto the cap beam

Figure 3.55 Bent with both spans bearing on cap beam

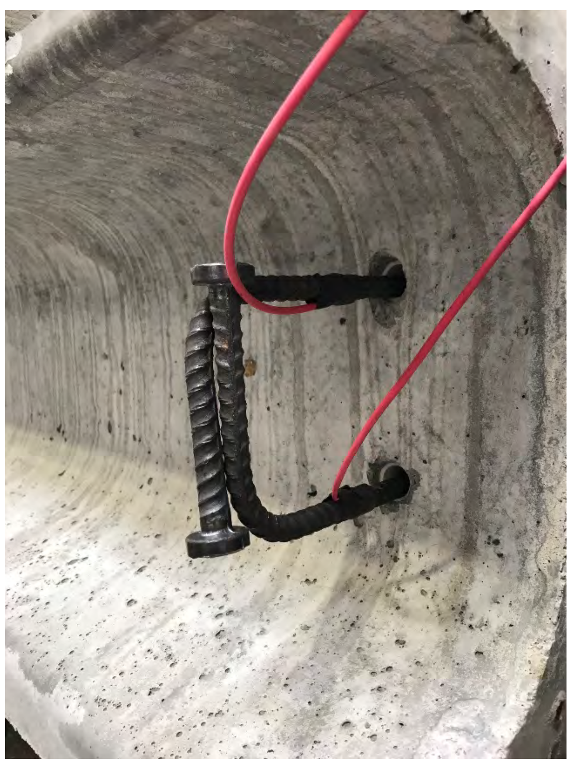

Figure 3.56 Headed bars bent to 90 degrees to allow placement of formwork

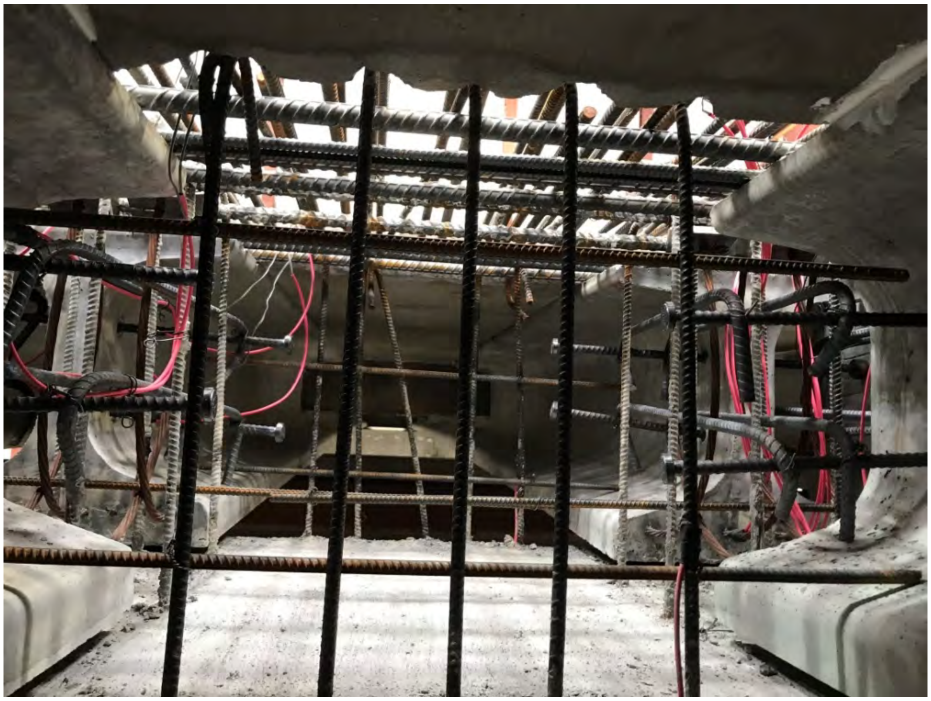

Figure 3.57 View of cap beam reinforcement and girder-to-cap beam connection as seen from side of cap beam

Figure 3.58 Projected deck reinforcement and top longitudinal cap beam bars at top of closure pour

Figure 3.59 Cast-in-place concrete for cap beam after casting

Figure 3.60 UHPC in cap beam closure pour

Figure 3.61 Transportation of UHPC to top of bridge using EEL crane and plastic tubs

Figure 3.62 Voids in cast-in-place concrete as seen after formwork removal

Figure 3.63 Dry packed concrete in location of cap beam voids

Figure 3.64 Placement of phase 2 mass blocks

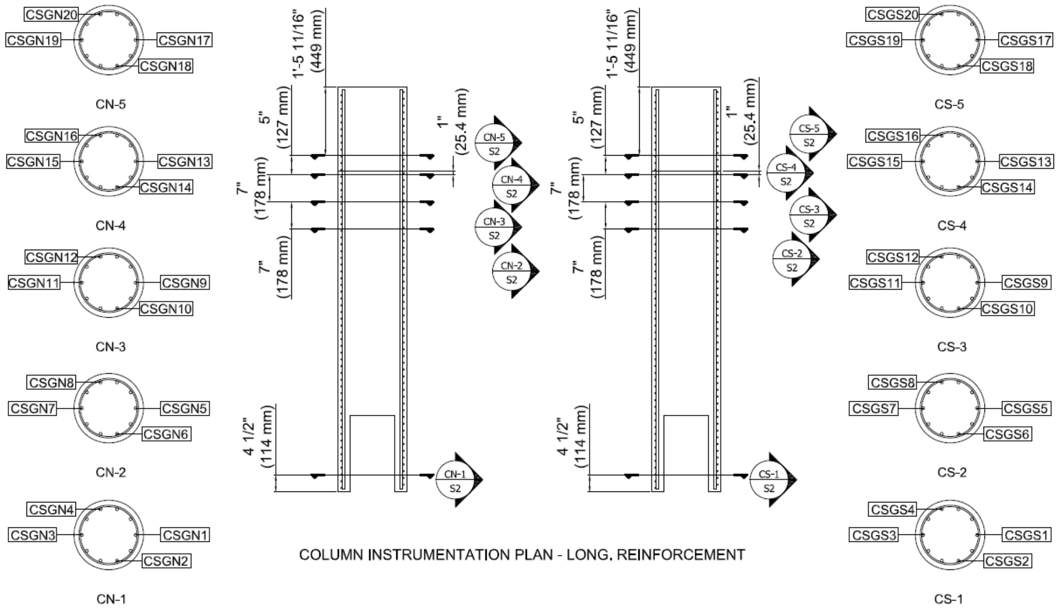

Figure 4.1 Instrumentation planset, longitudinal column reinforcement strain gauges

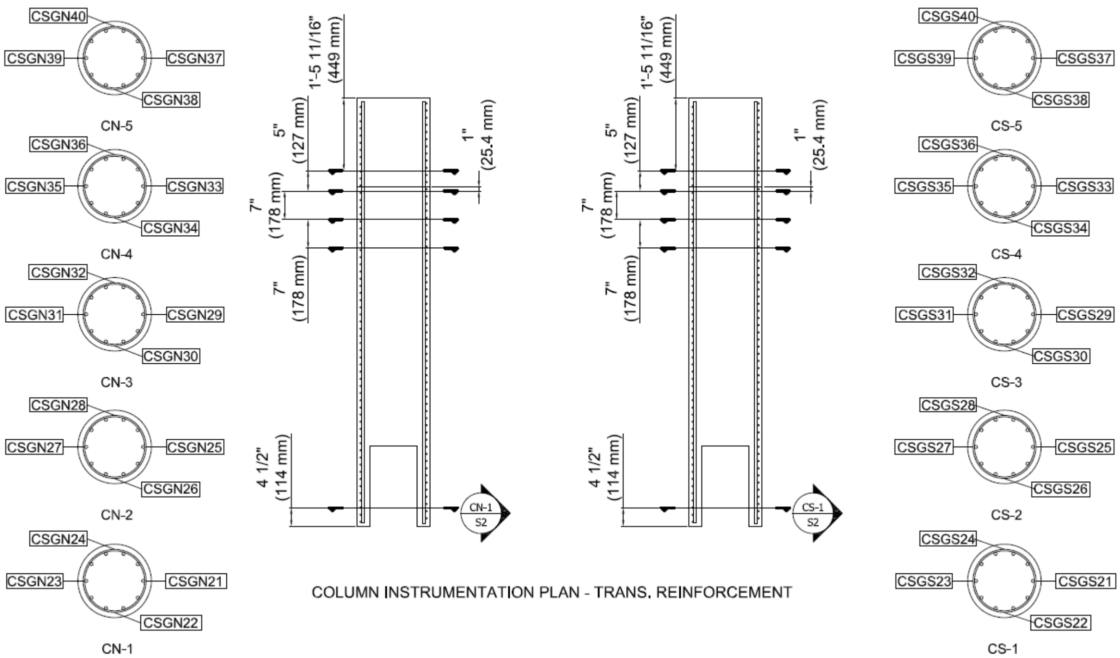

Figure 4.2 Instrumentation planset, spiral column reinforcement strain gauges

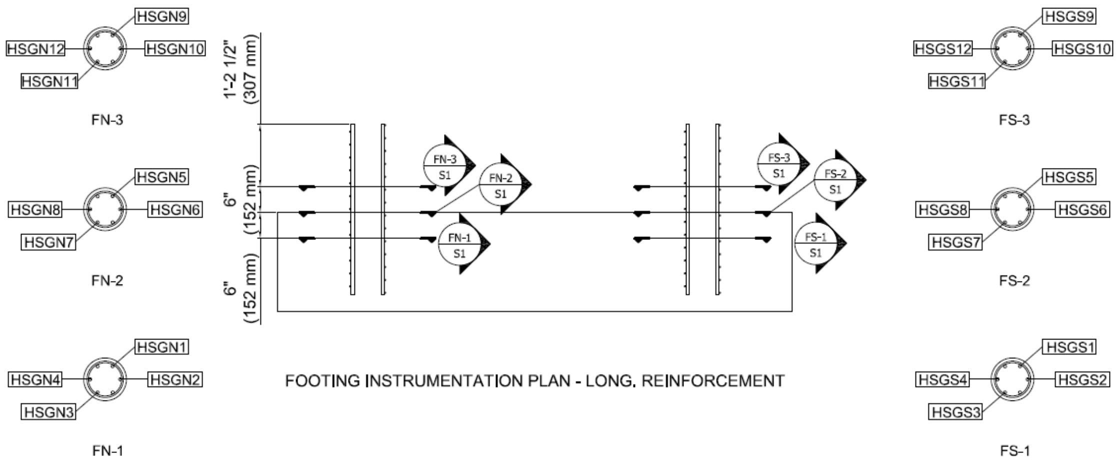

Figure 4.3 Instrumentation planset, longitudinal hinge reinforcement strain gauges

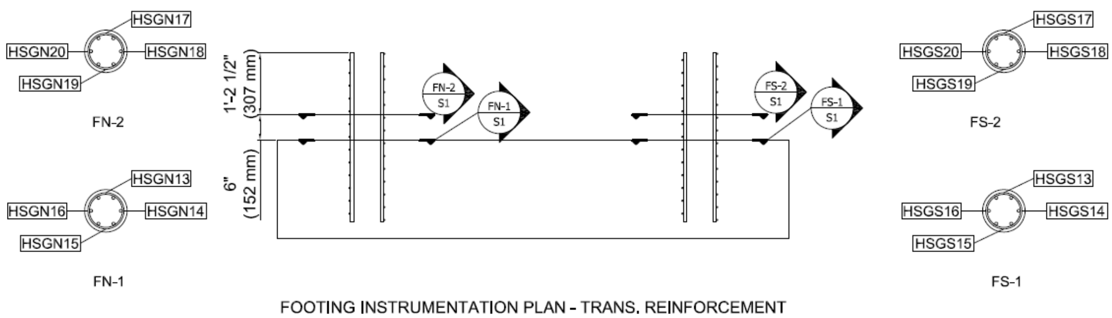

Figure 4.4 Instrumentation planset, transverse hinge reinforcement strain gauges

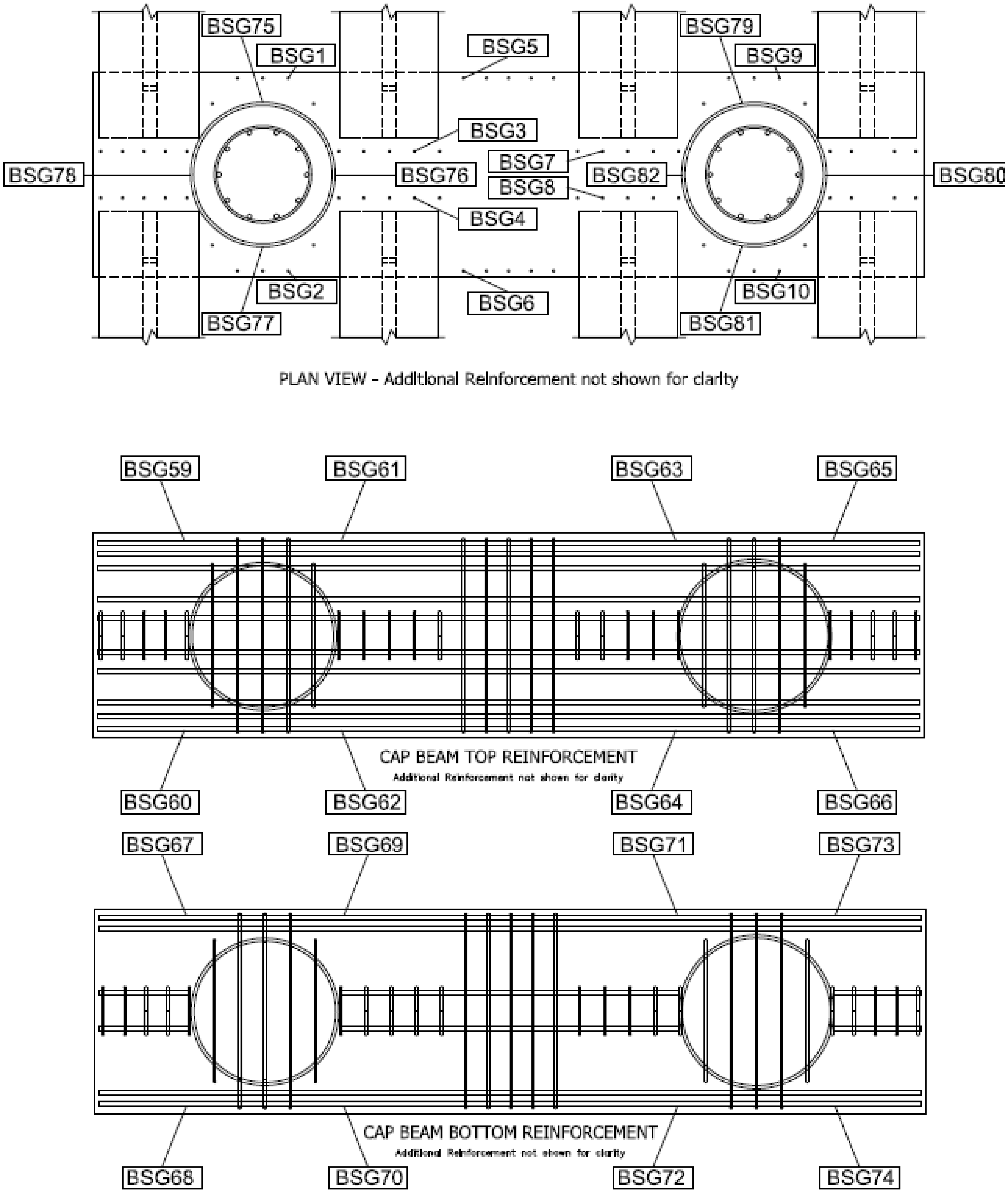

Figure 4.5 Instrumentation planset, cap beam reinforcement strain gauges

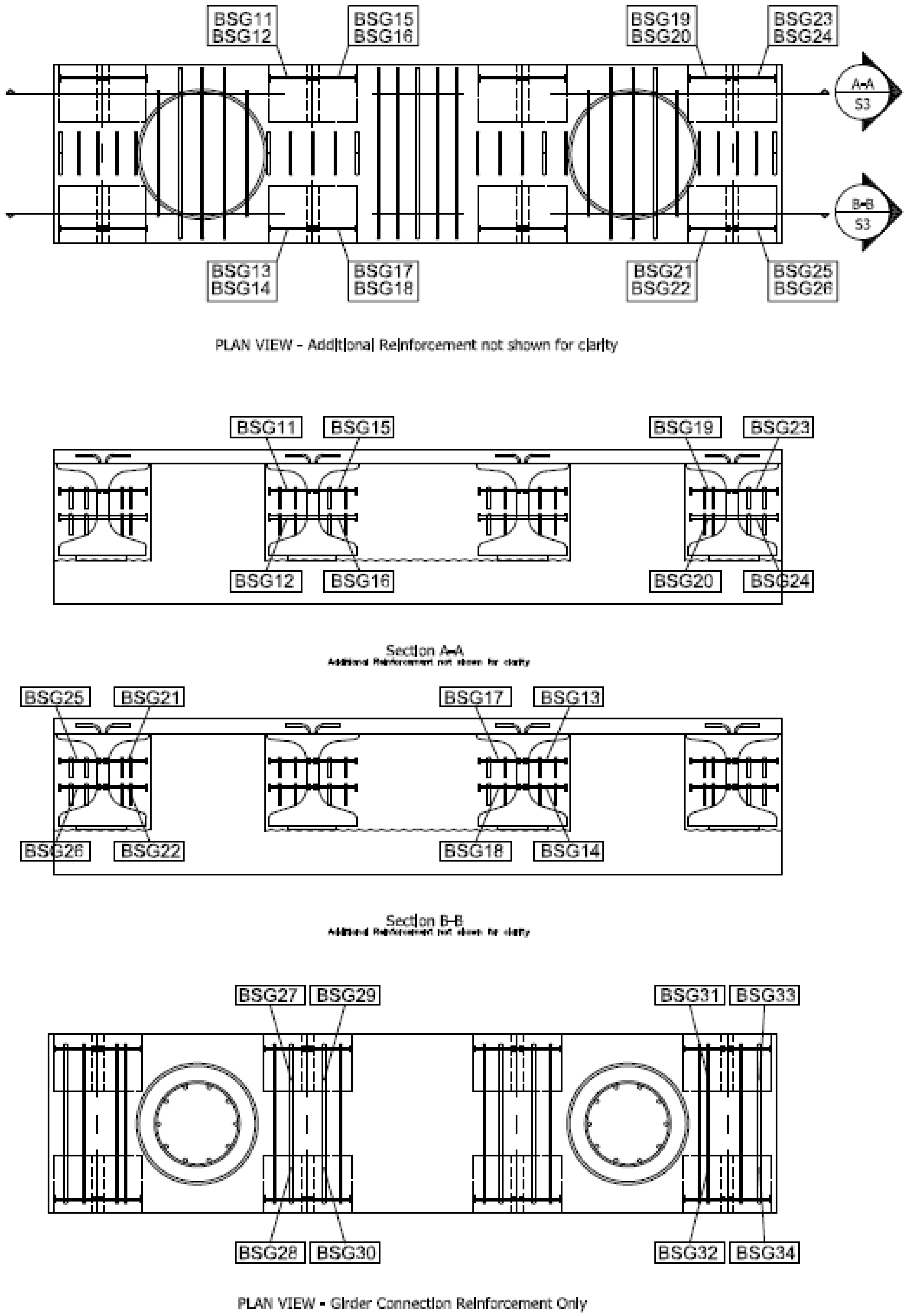

Figure 4.6 Instrumentation planset, cap beam headed bars strain gauges

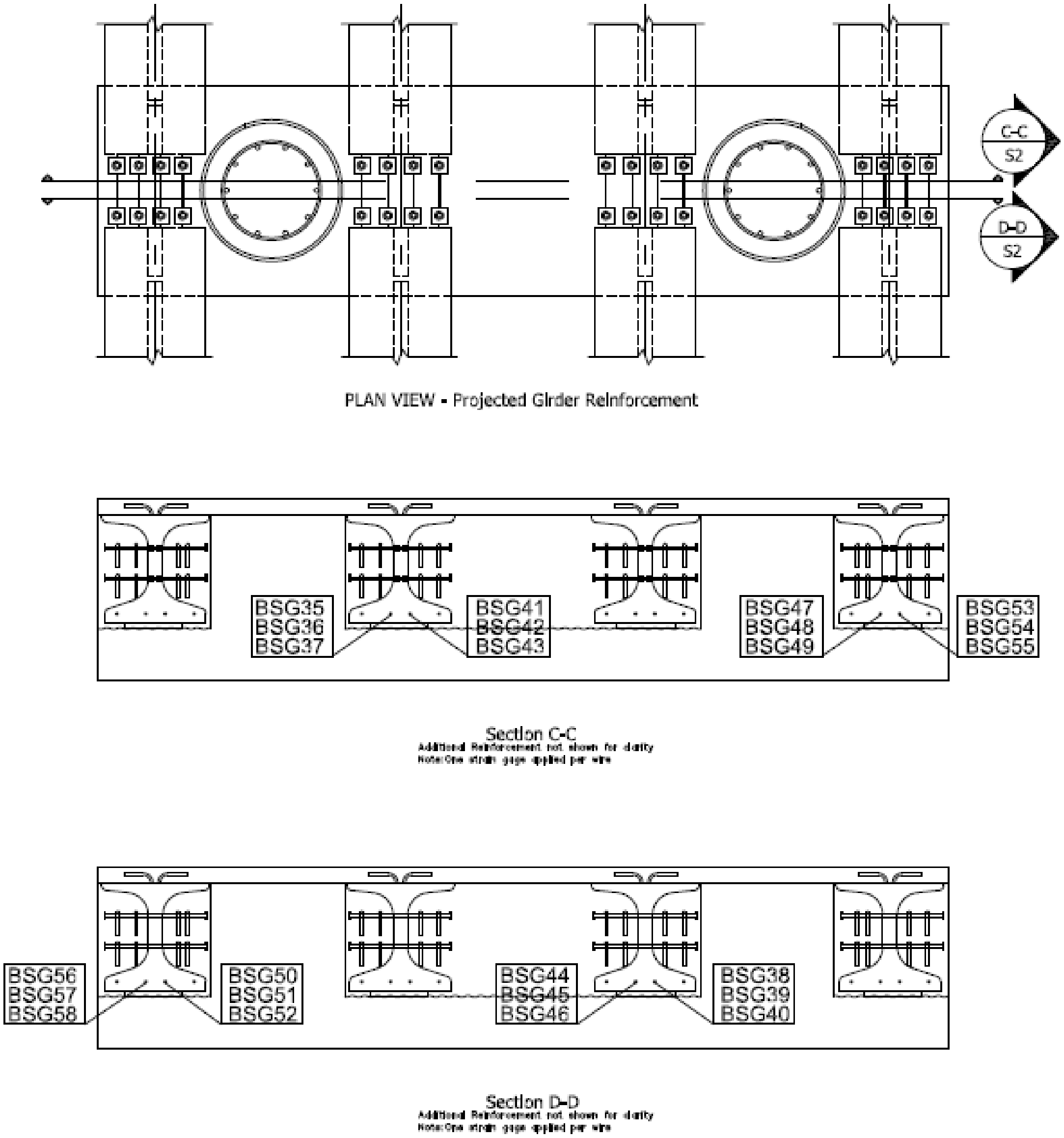

Figure 4.7 Instrumentation planset, girder prestress strands strain gauges

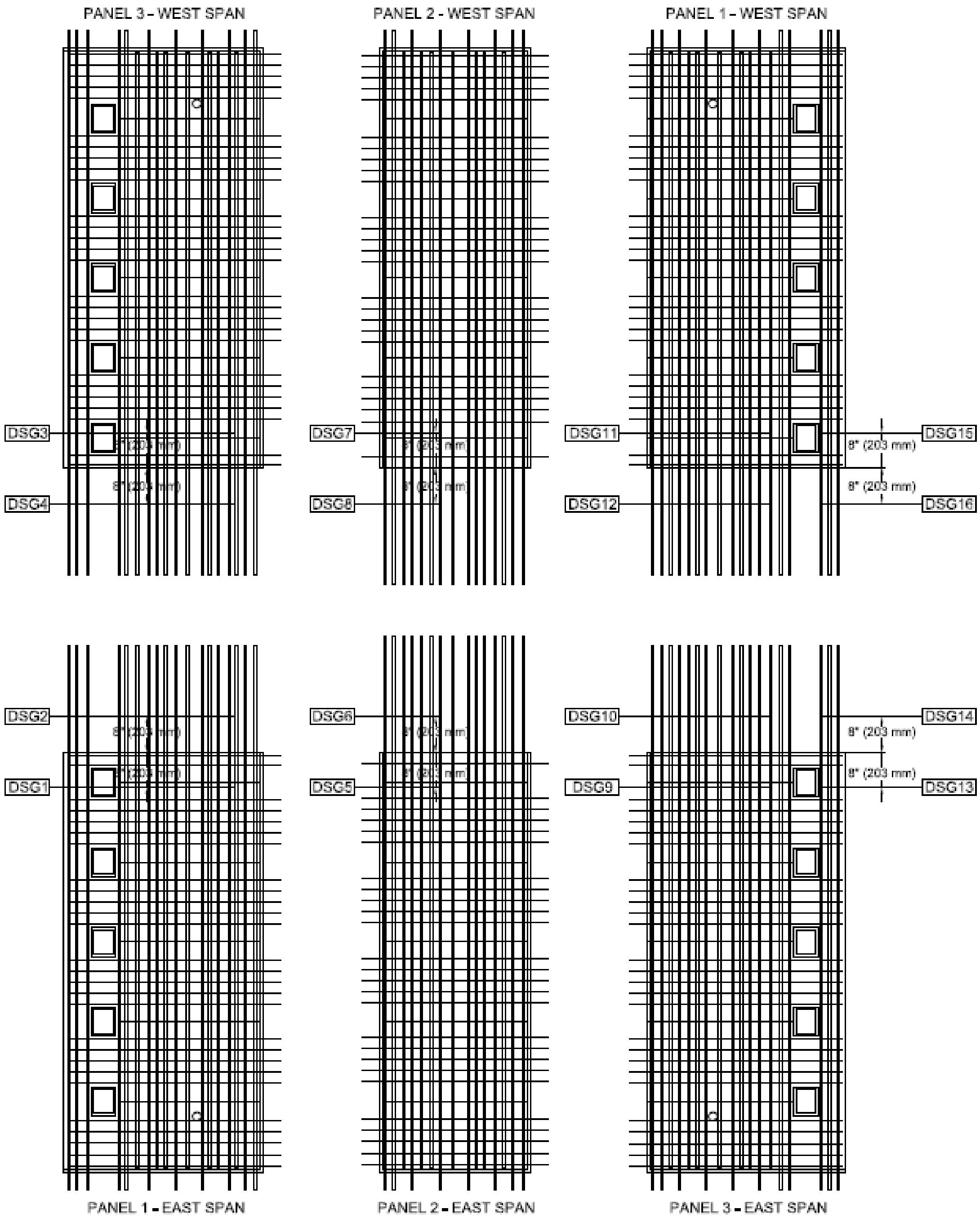

Figure 4.8 Instrumentation planset, deck panel strain gauges

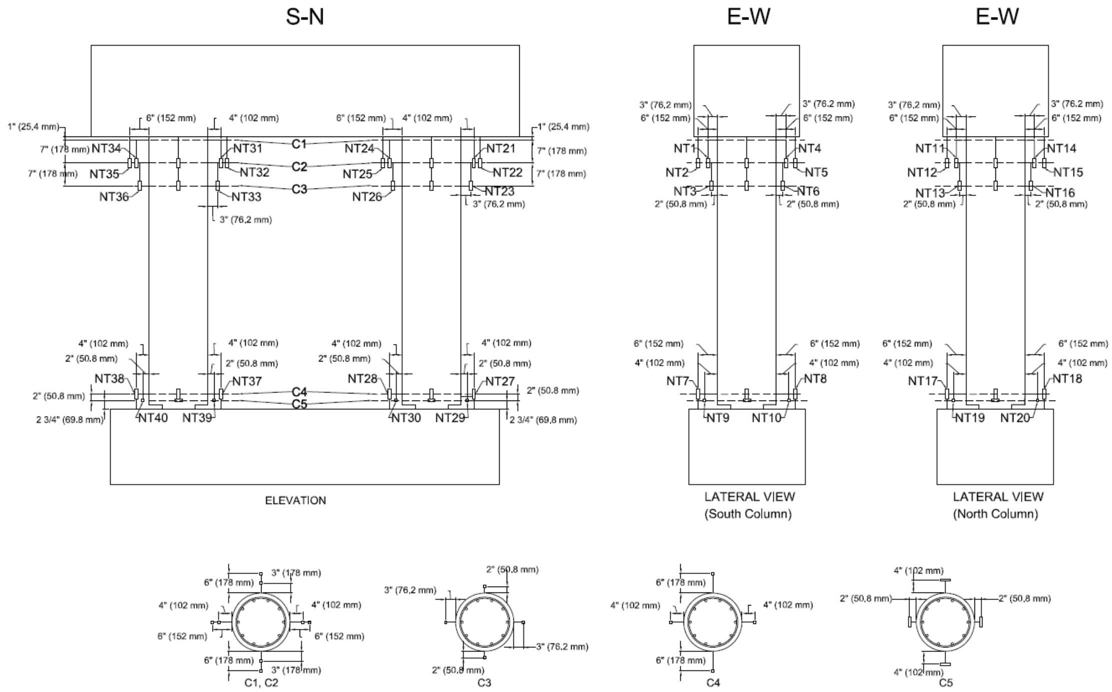

Figure 4.9 Instrumentation planset, column displacement transducer layout

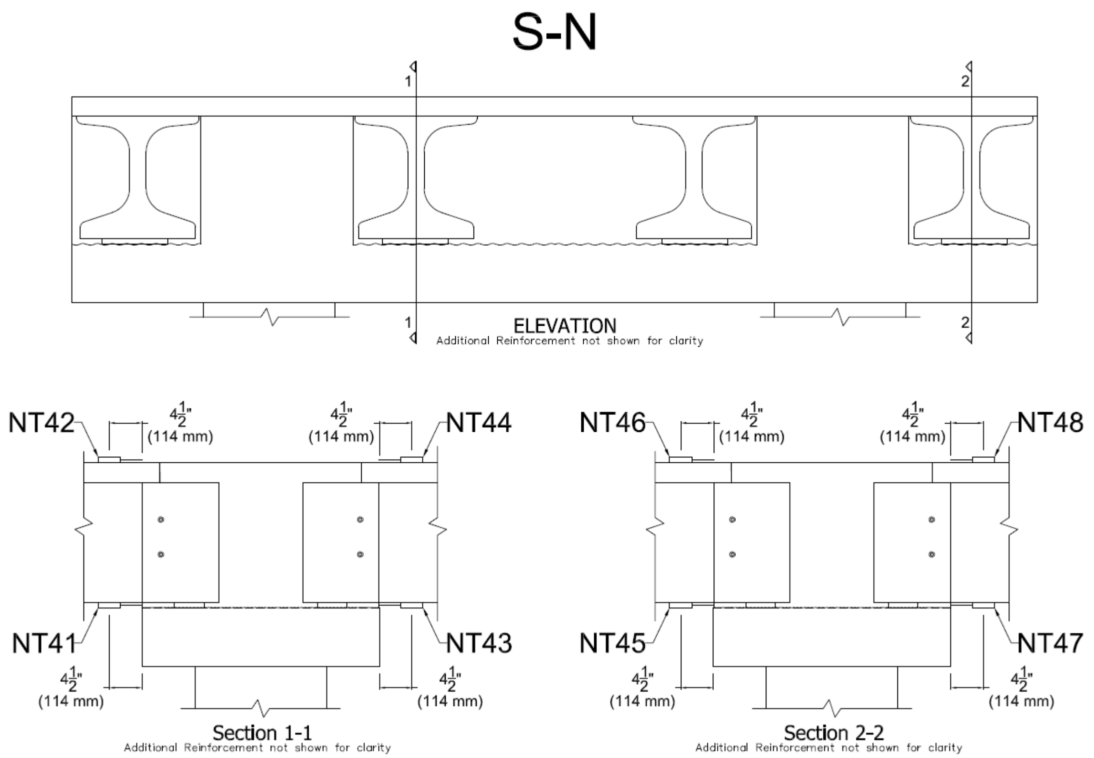

Figure 4.10 Instrumentation planset, superstructure-cap beam displacement transducer layout

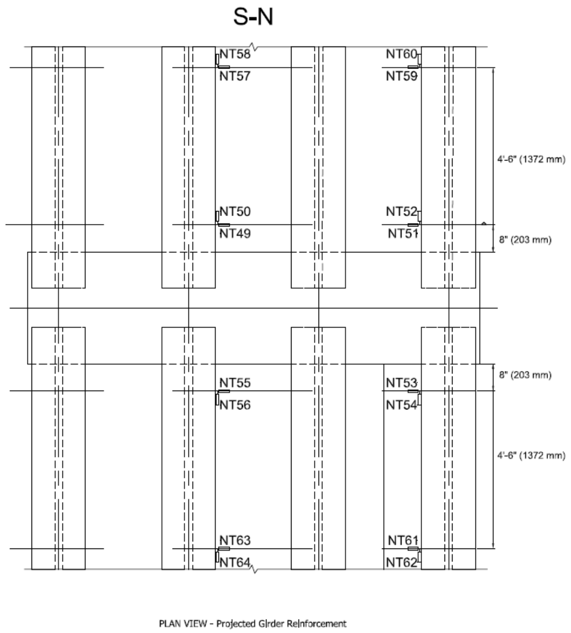

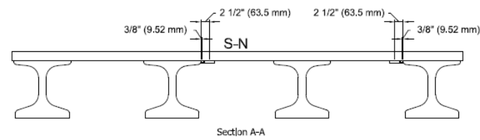

Figure 4.11 Instrumentation planset, deck panel-girder displacement transducer layout

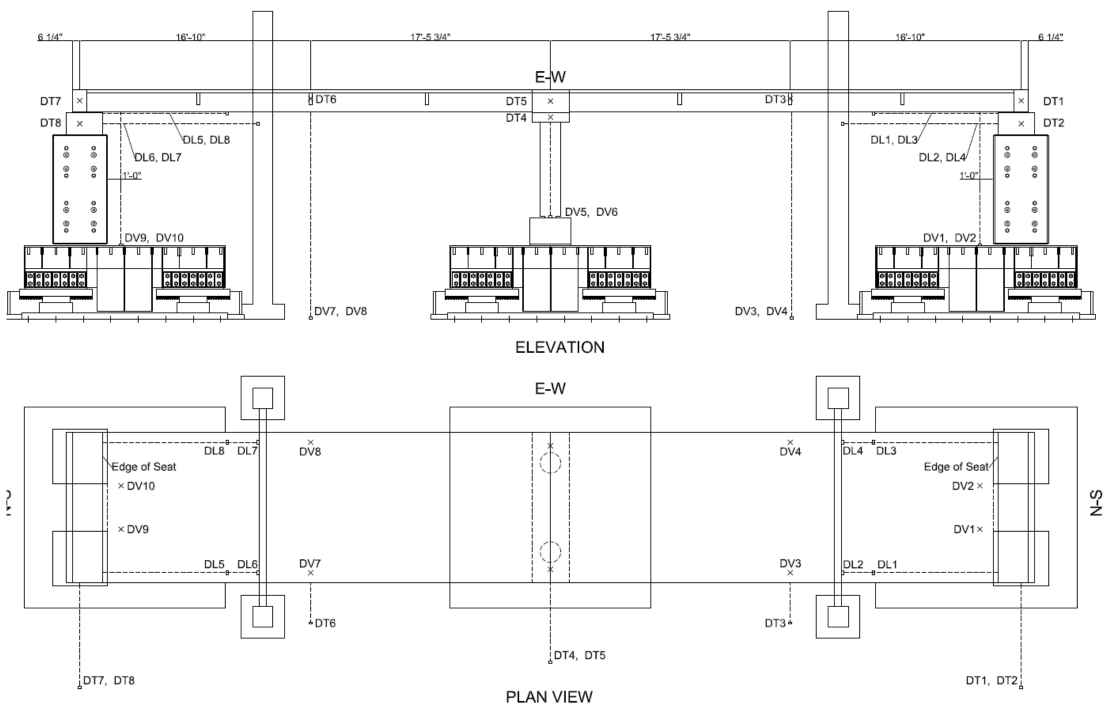

Figure 4.12 Instrumentation planset, string pot layout

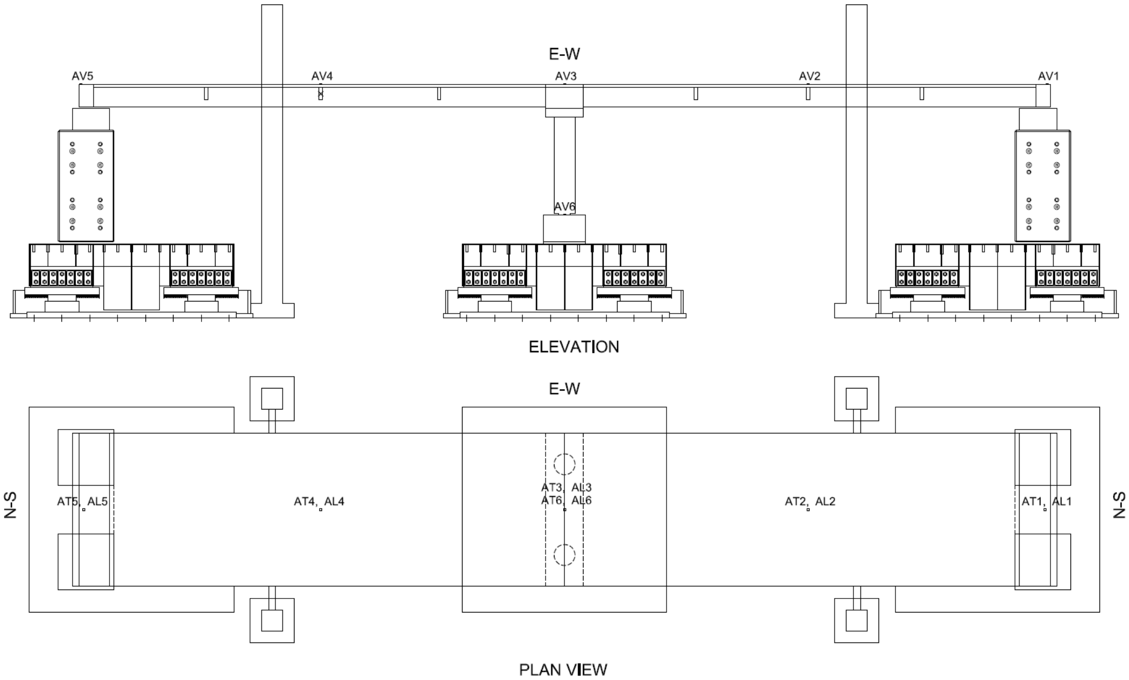

Figure 4.13 Instrumentation planset, accelerometer layout

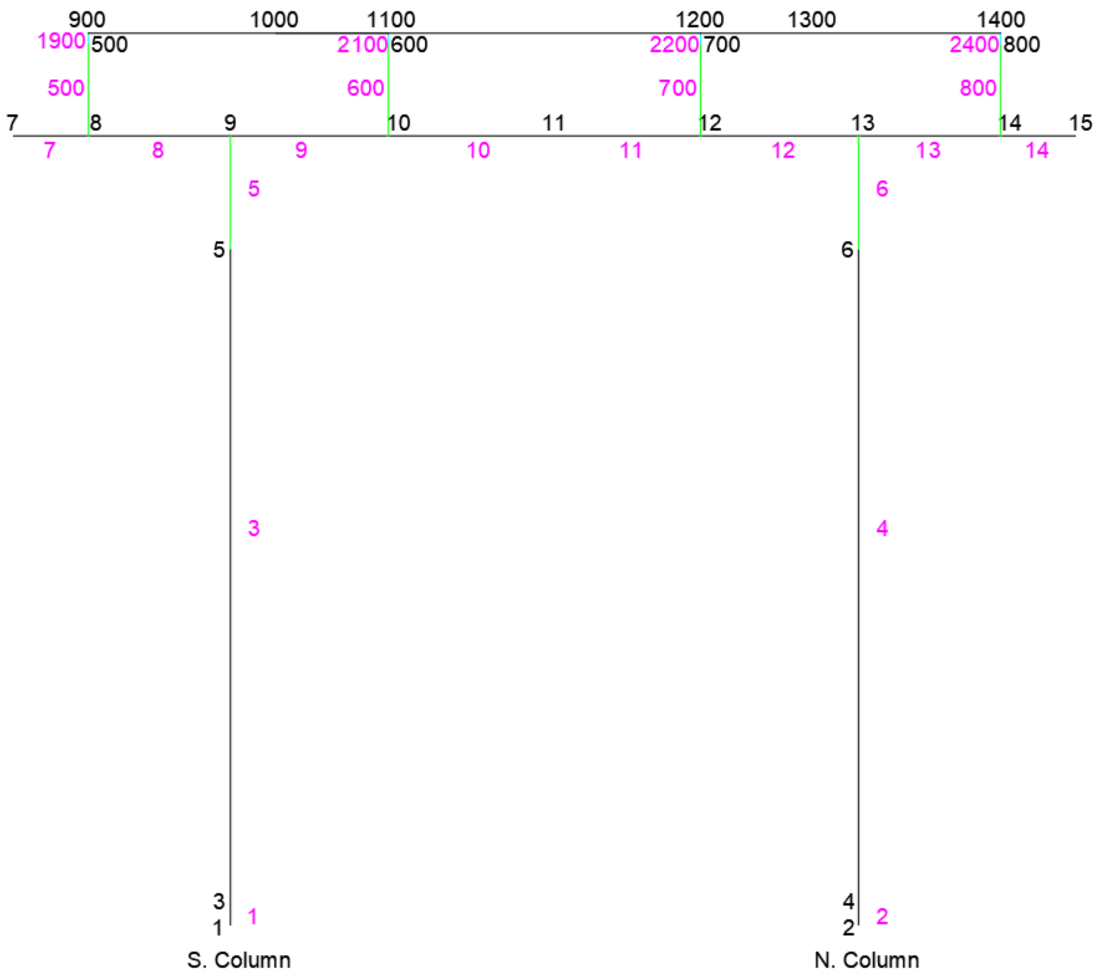

Figure 5.1 Node and element layout of bent (black # - Node, pink # - Element)

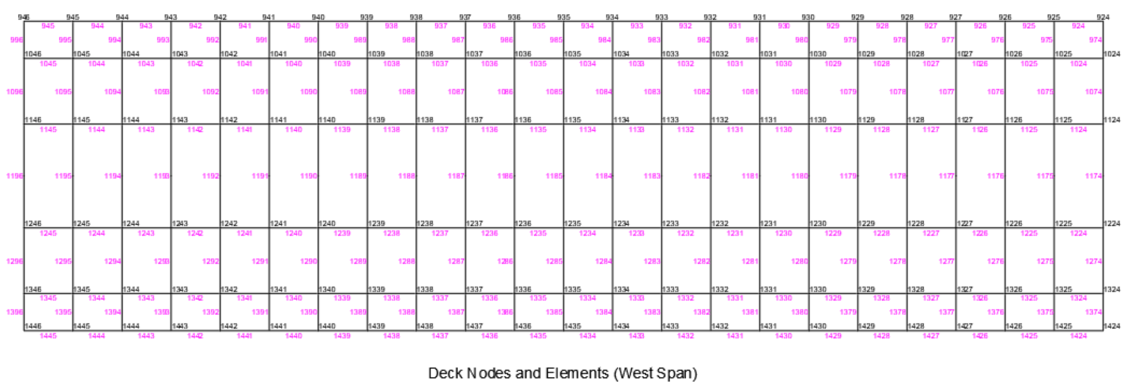

Figure 5.2 Node and element layout of deck along west span (black # - Node, pink # - Element)

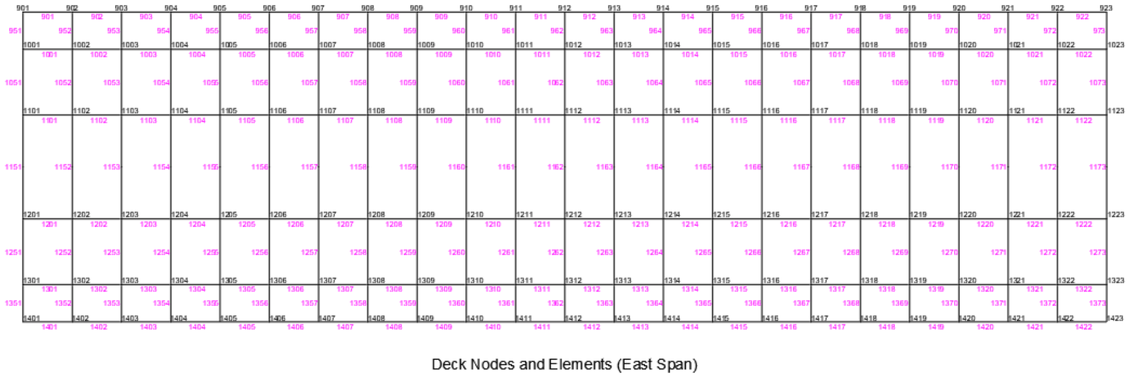

Figure 5.3 Node and element layout of deck along east span (black # - Node, pink # - Element)

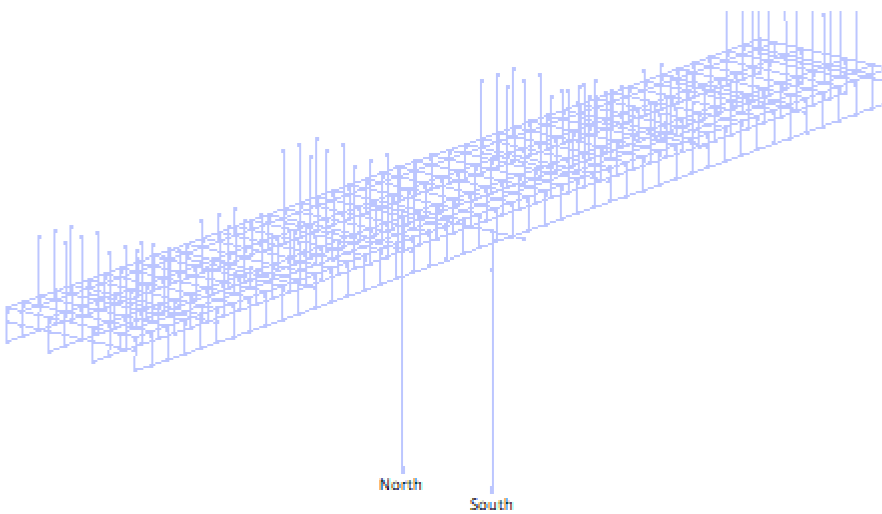

Figure 5.4 View of final model from Opensees display plane

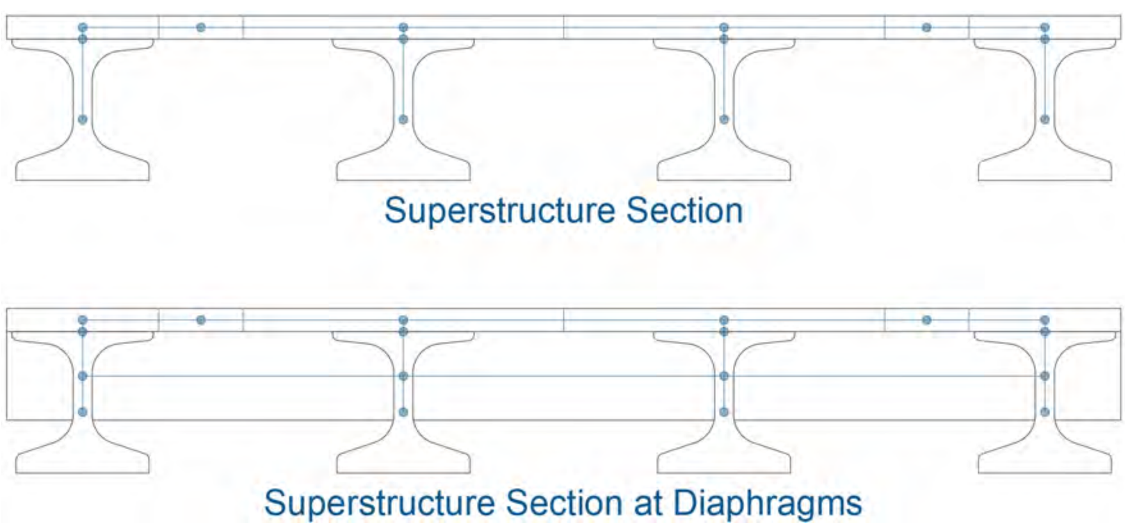

Figure 5.5 Node and element layout, superstructure cross-section

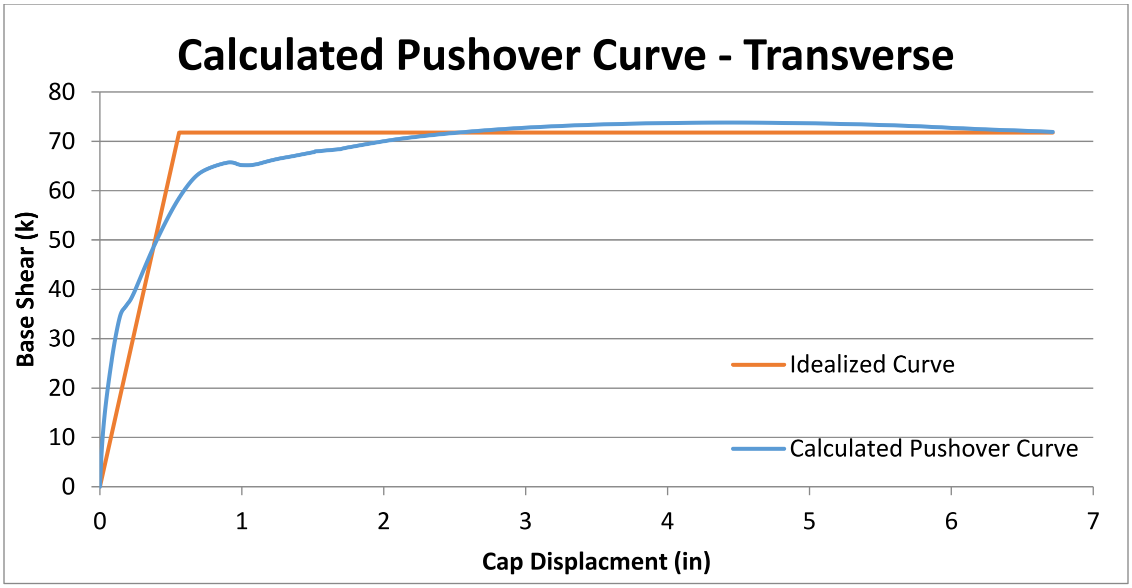

Figure 5.6 Calculated and idealized pushover curve for bridge when pushed transversely

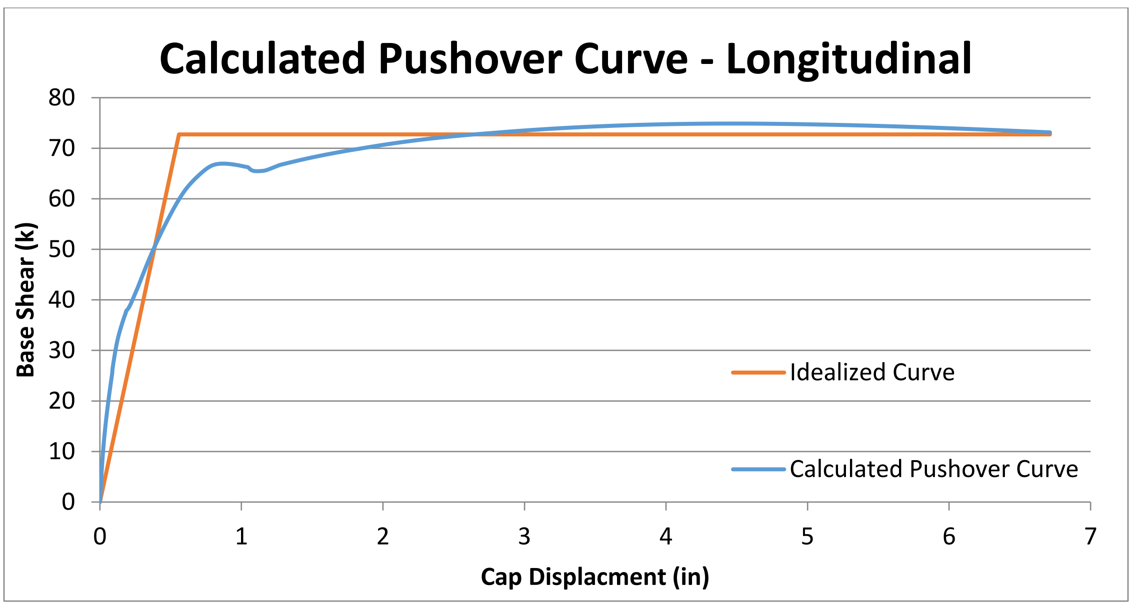

Figure 5.7 Calculated and idealized pushover curve for bridge when pushed longitudinally

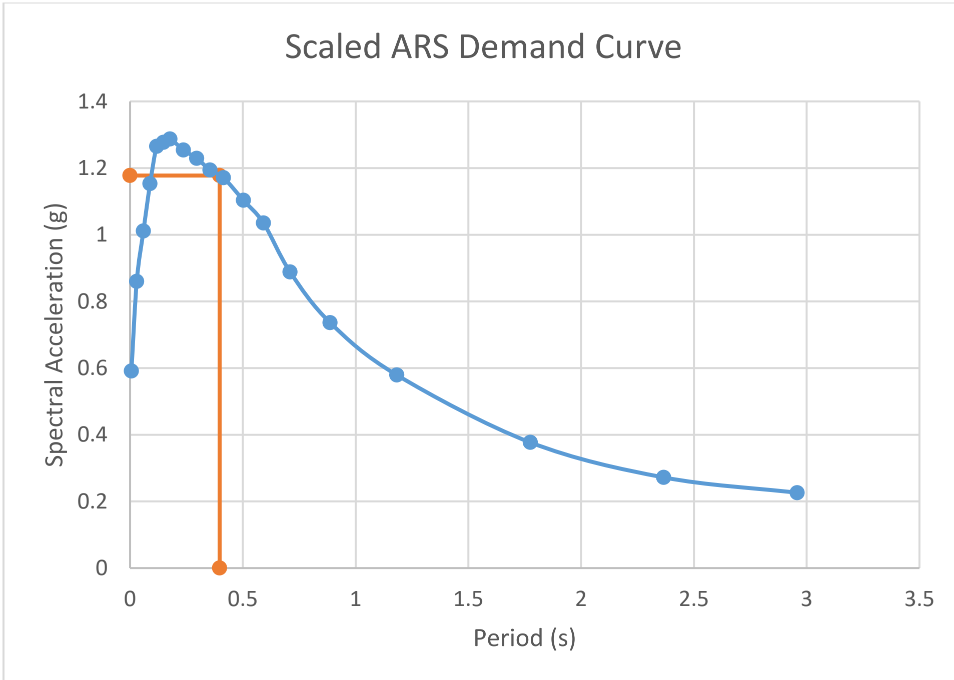

Figure 5.8 Scaled ARS curve at period of interest

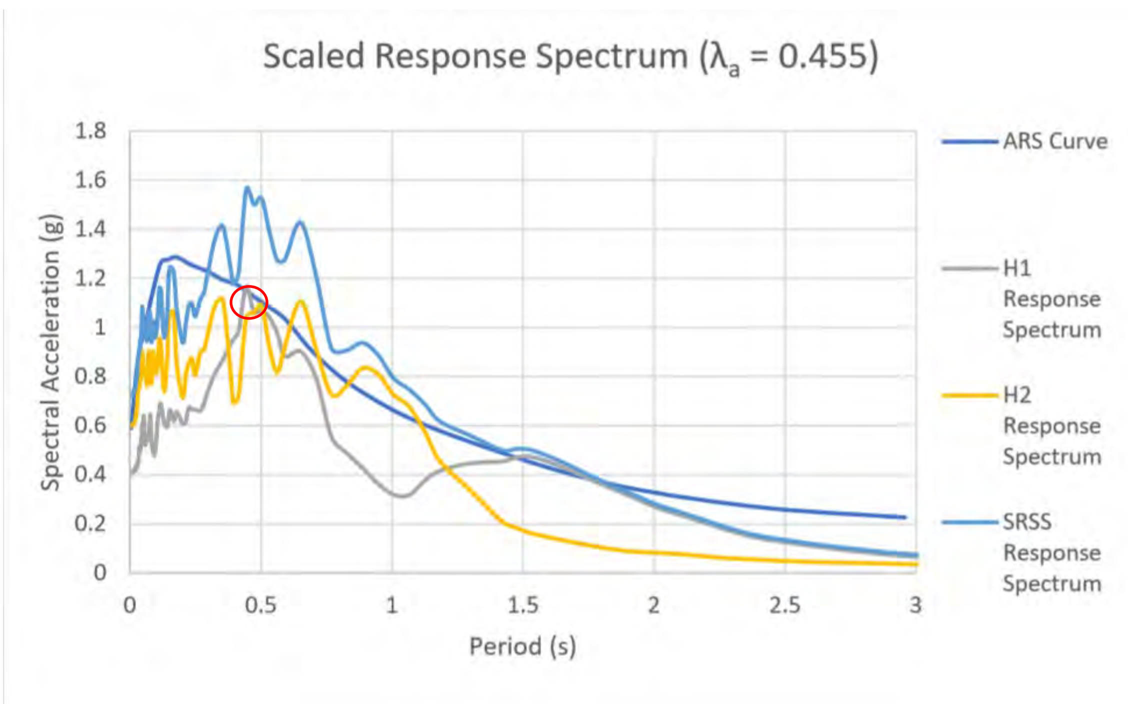

Figure 5.9 Scaled ARS curve with SRSS response spectrum

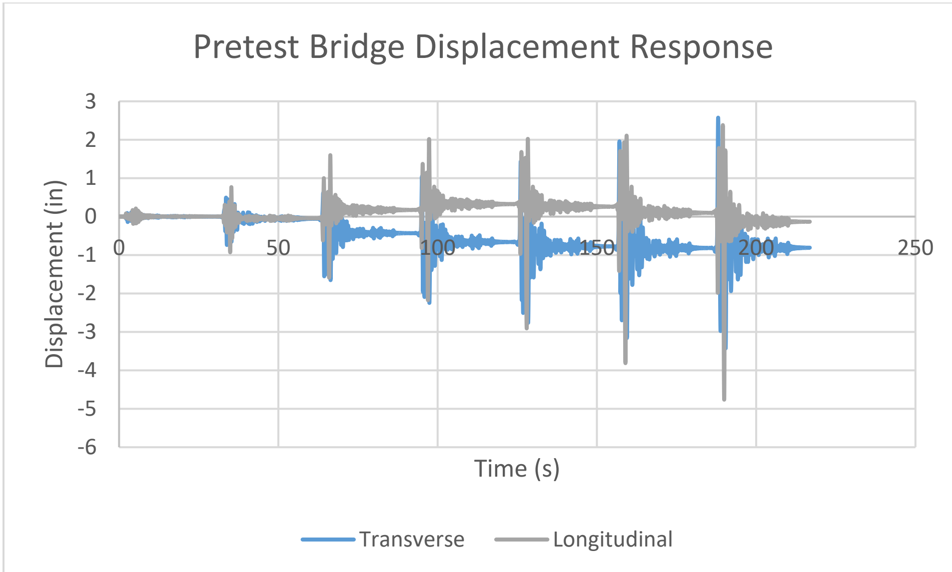

Figure 5.10 Pretest displacement response of bridge to target loading protocol

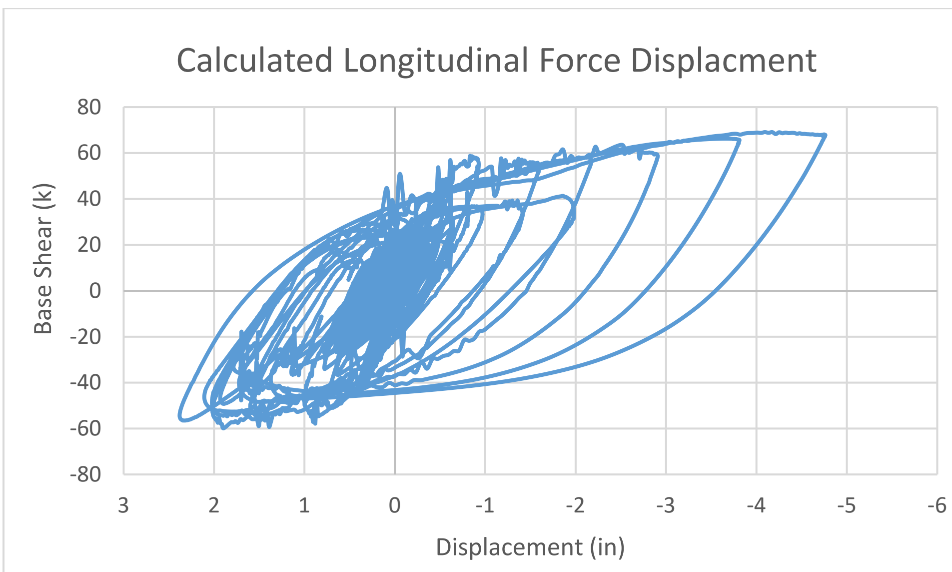

Figure 5.11 Pretest calculated longitudinal force-displacement relationship

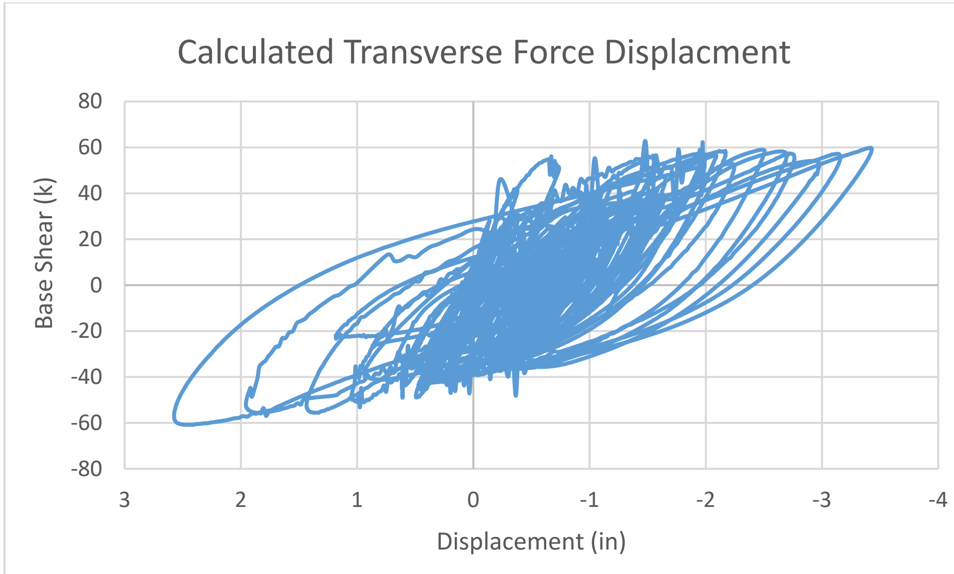

Figure 5.12 Pretest calculated transverse force-displacement relationship

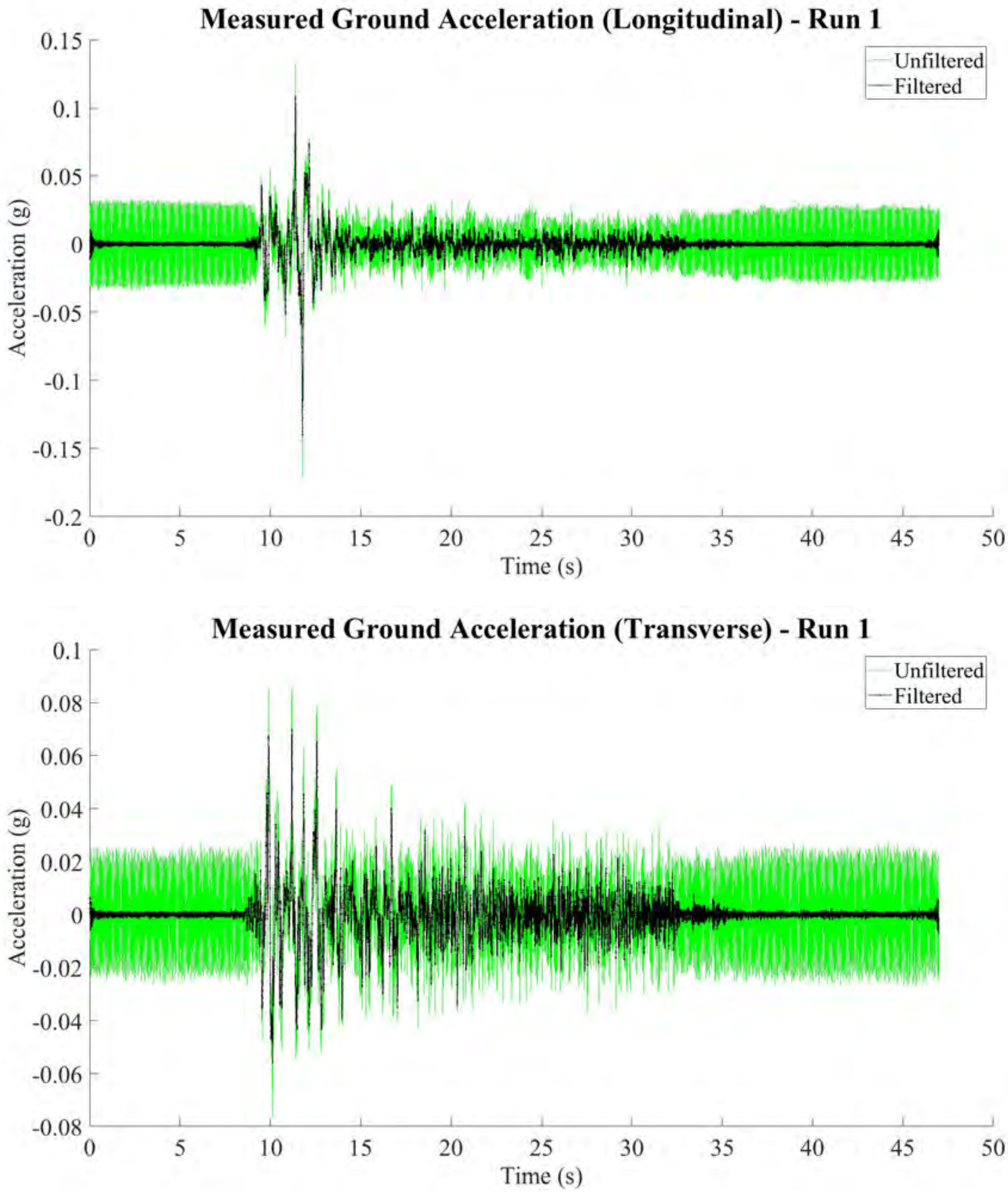

Figure 6.1 Comparison of filtered and unfiltered measured ground acceleration, run 1

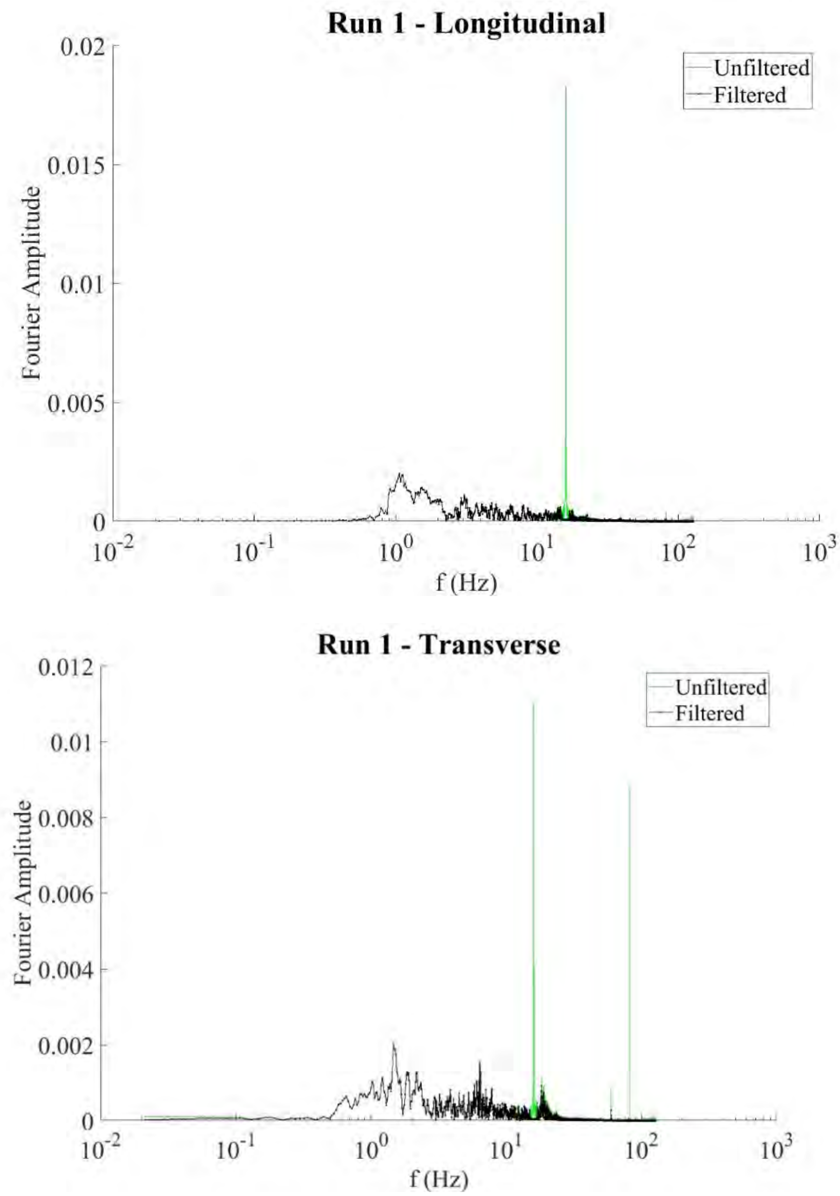

Figure 6.2 Fast Fourier transform amplitude of ground acceleration, run 1

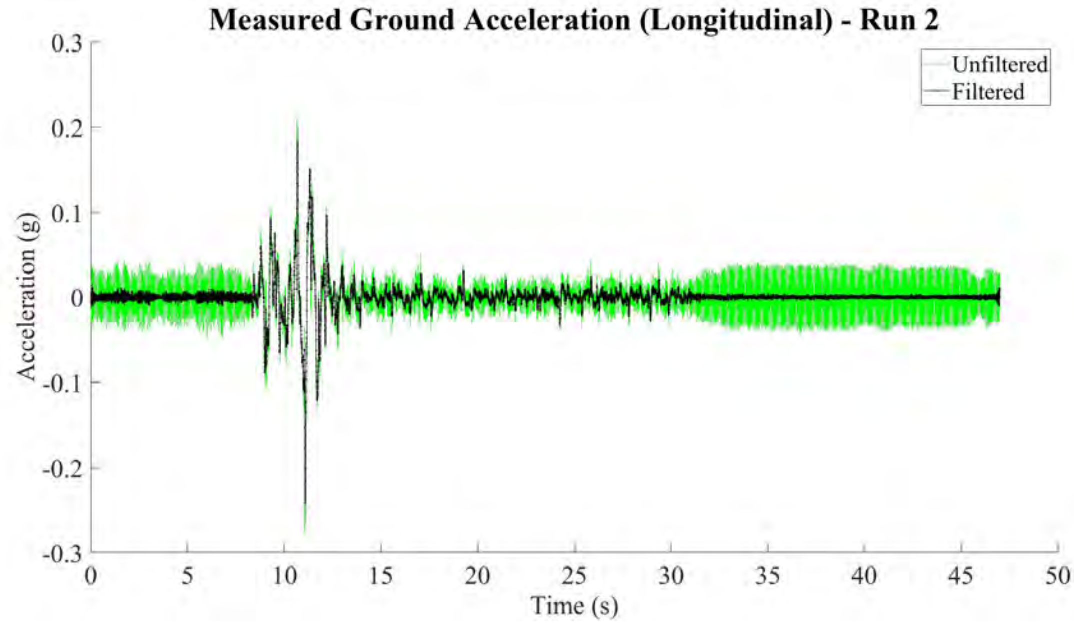

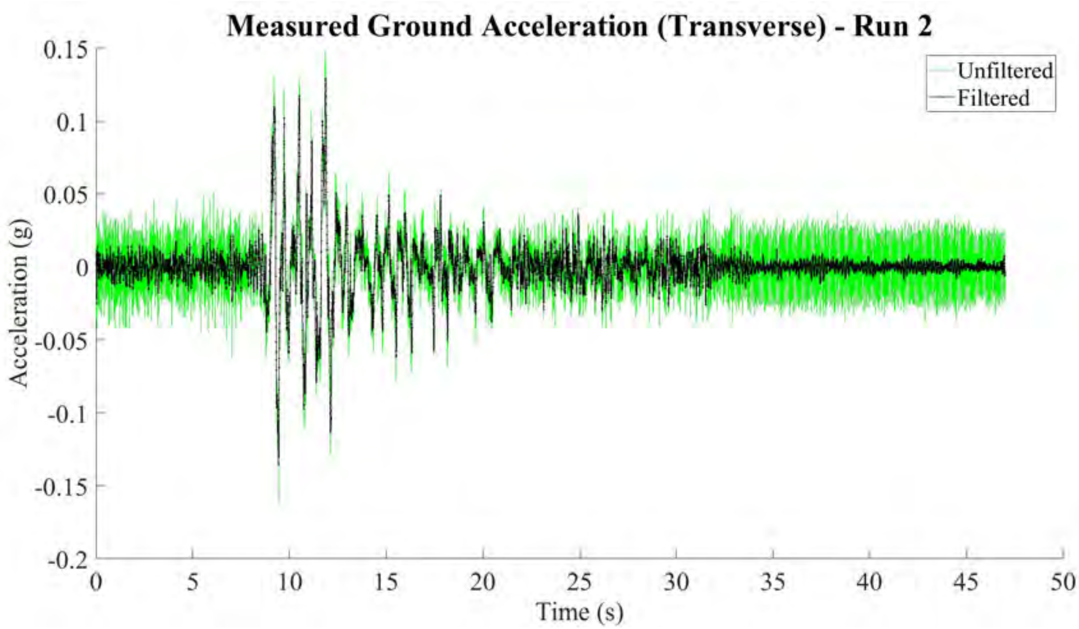

Figure 6.3 Comparison of filtered and unfiltered measured ground acceleration, run 2

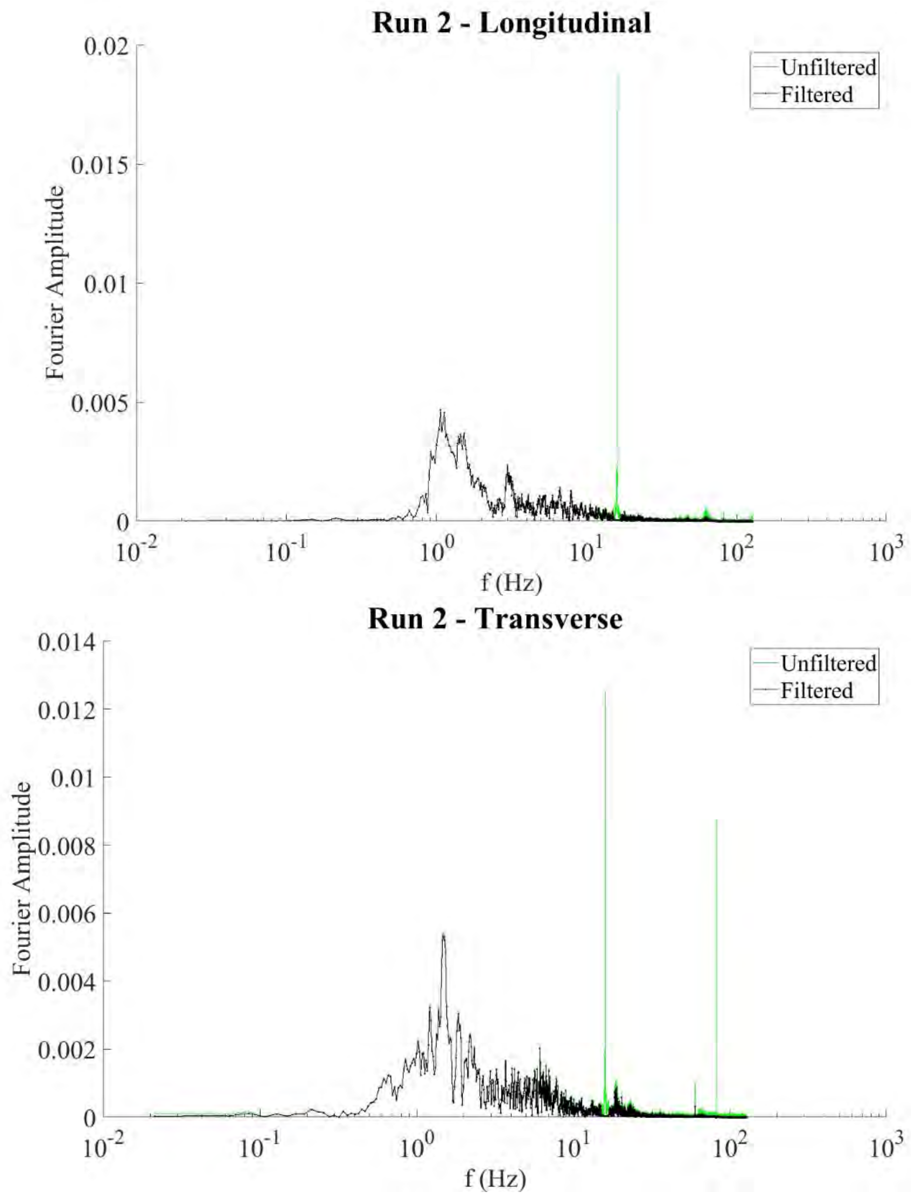

Figure 6.4 Fast Fourier transform amplitude of ground acceleration, run 2

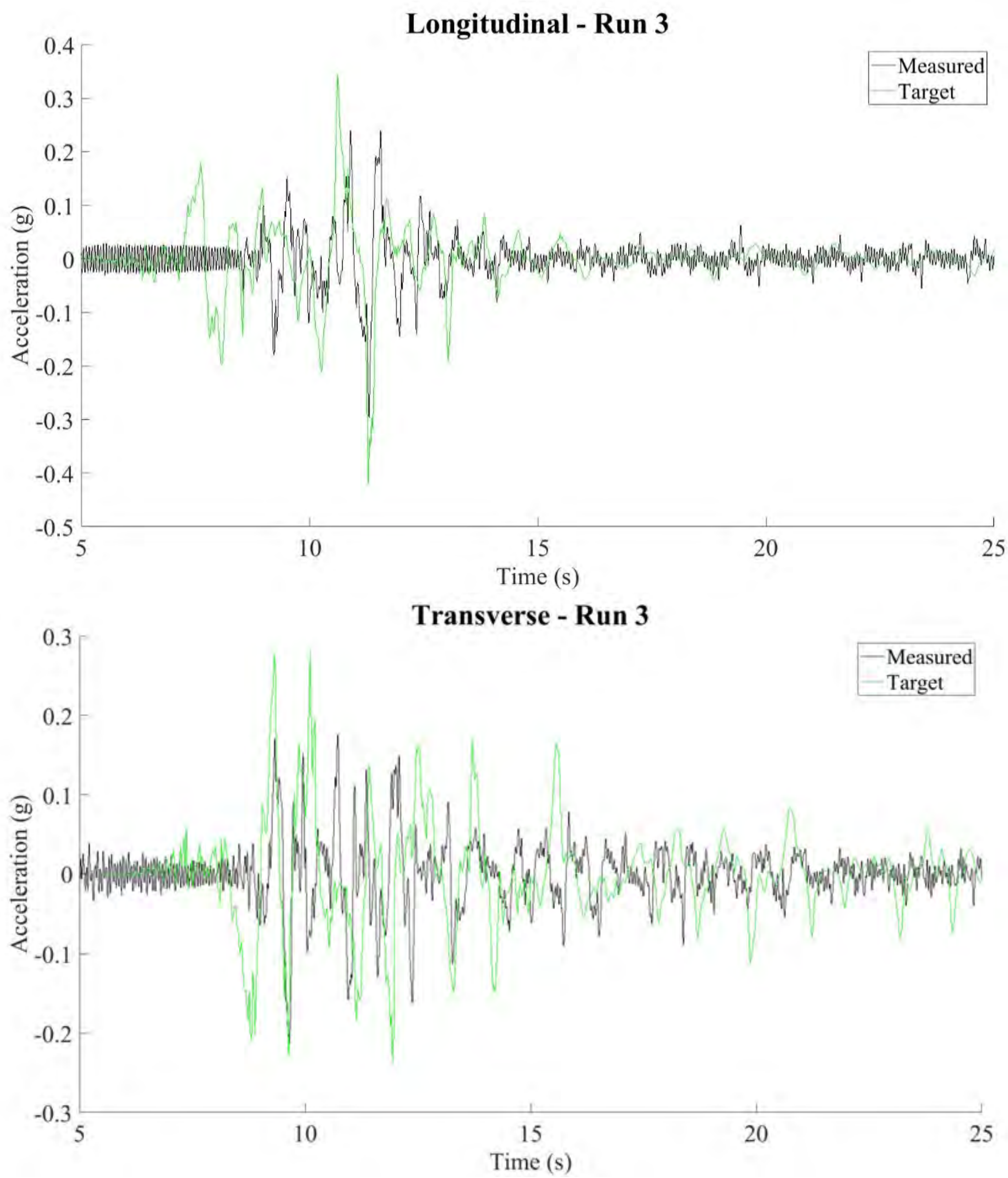

Figure 6.5 Comparison of measured and target ground motions for run 3

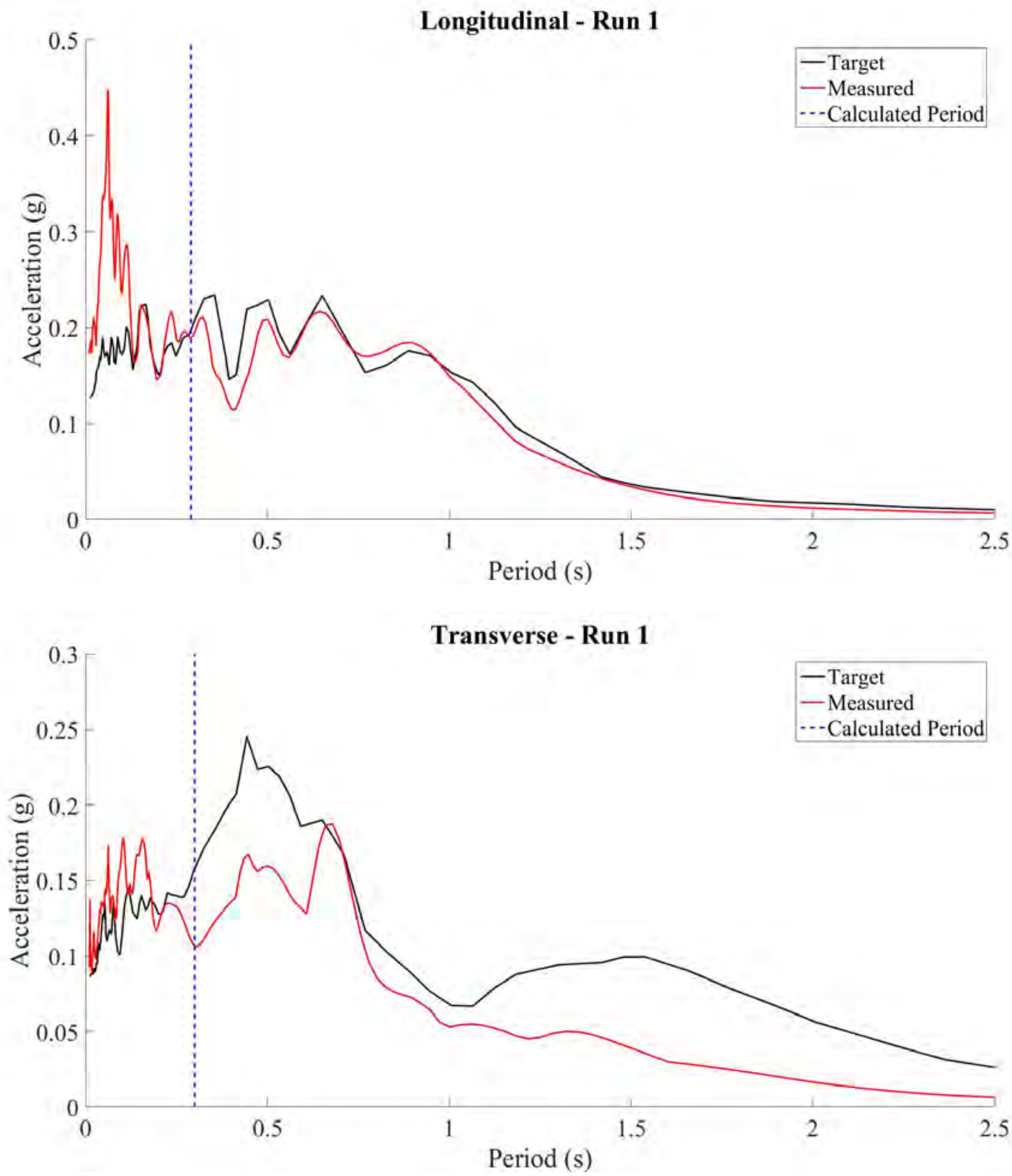

Figure 6.6 Measured vs. target response spectrum at period of interest, run 1

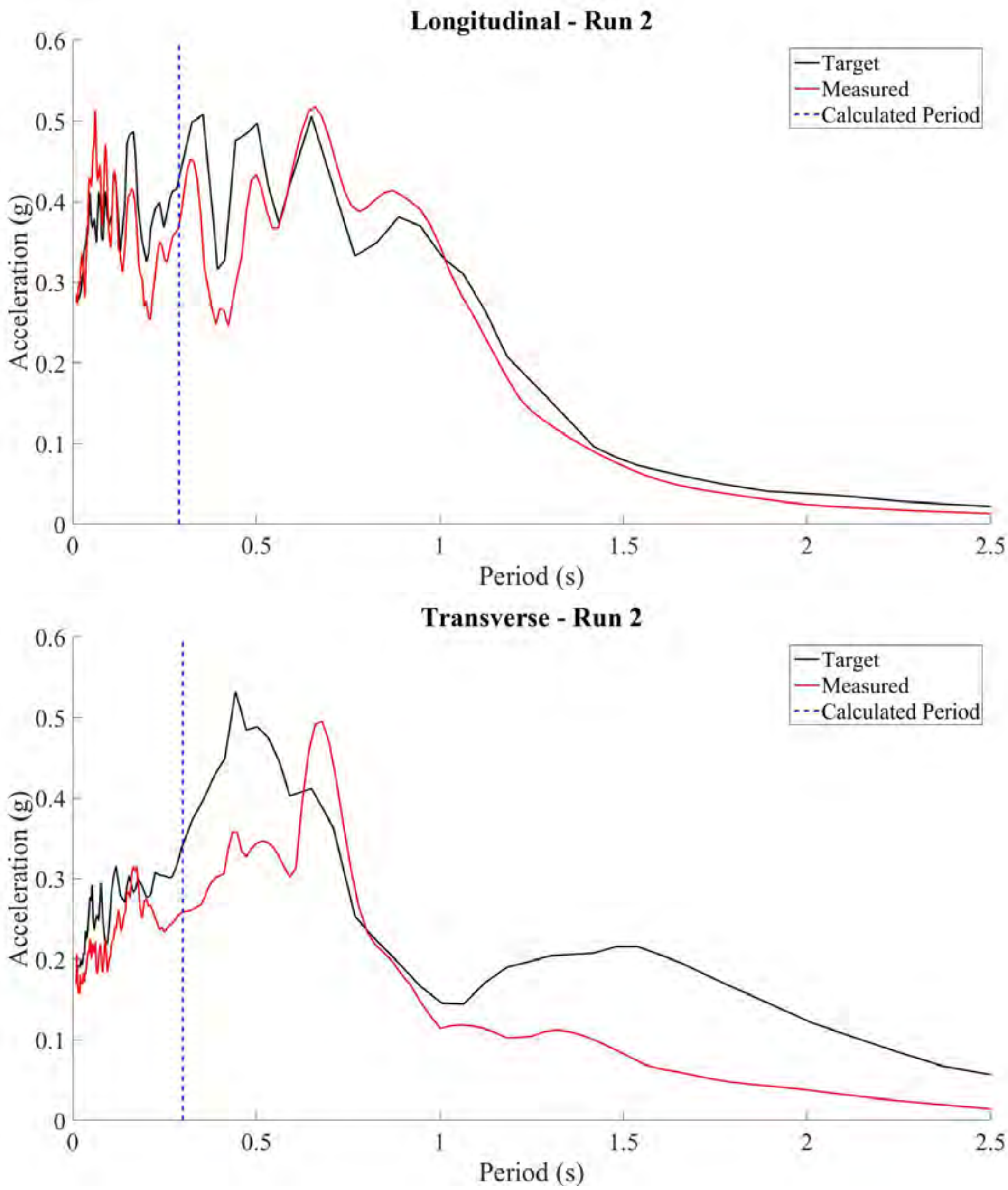

Figure 6.7 Measured vs. target response spectrum at period of interest, run 2

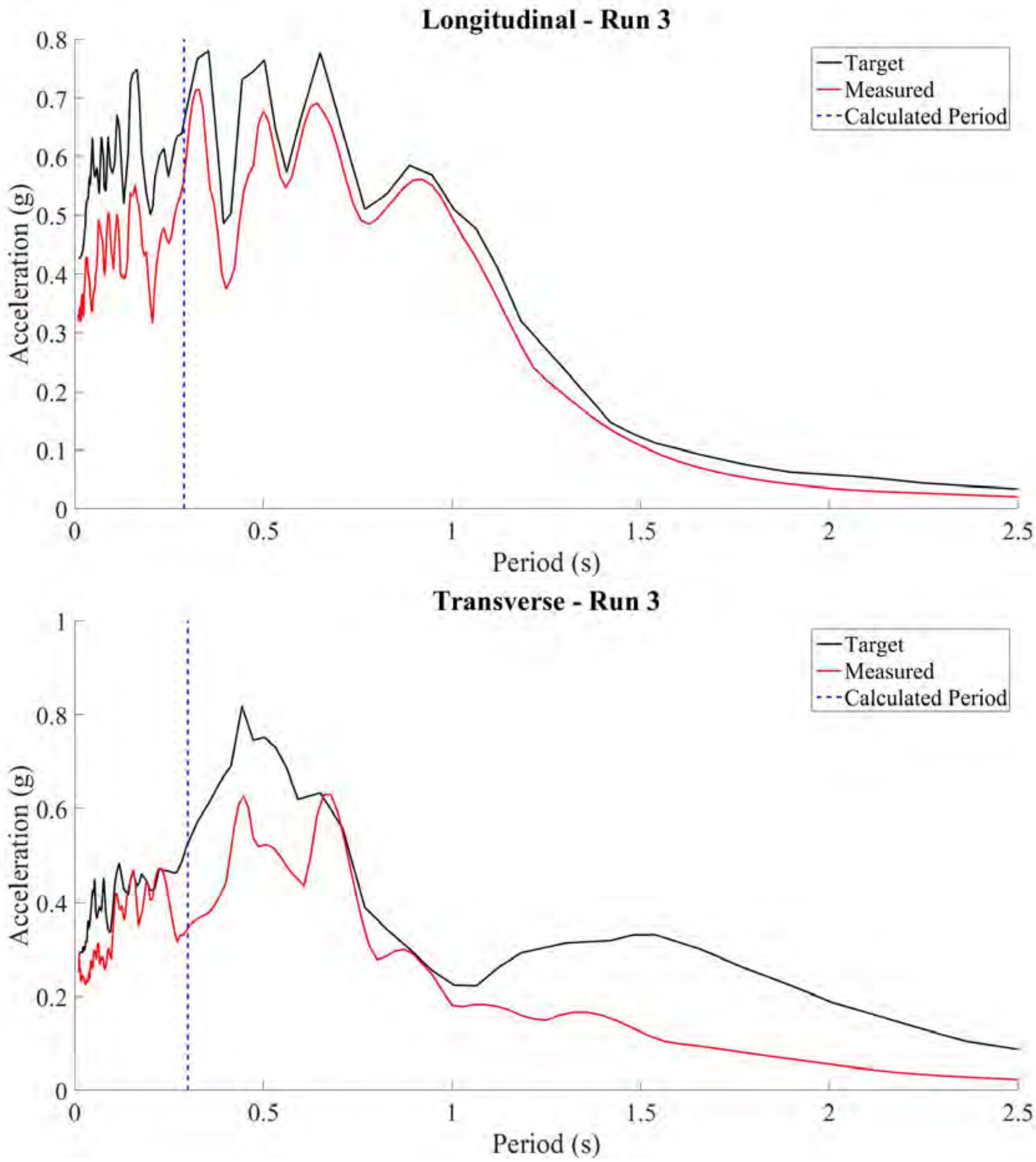

Figure 6.8 Measured vs. target response spectrum at period of interest, run 3

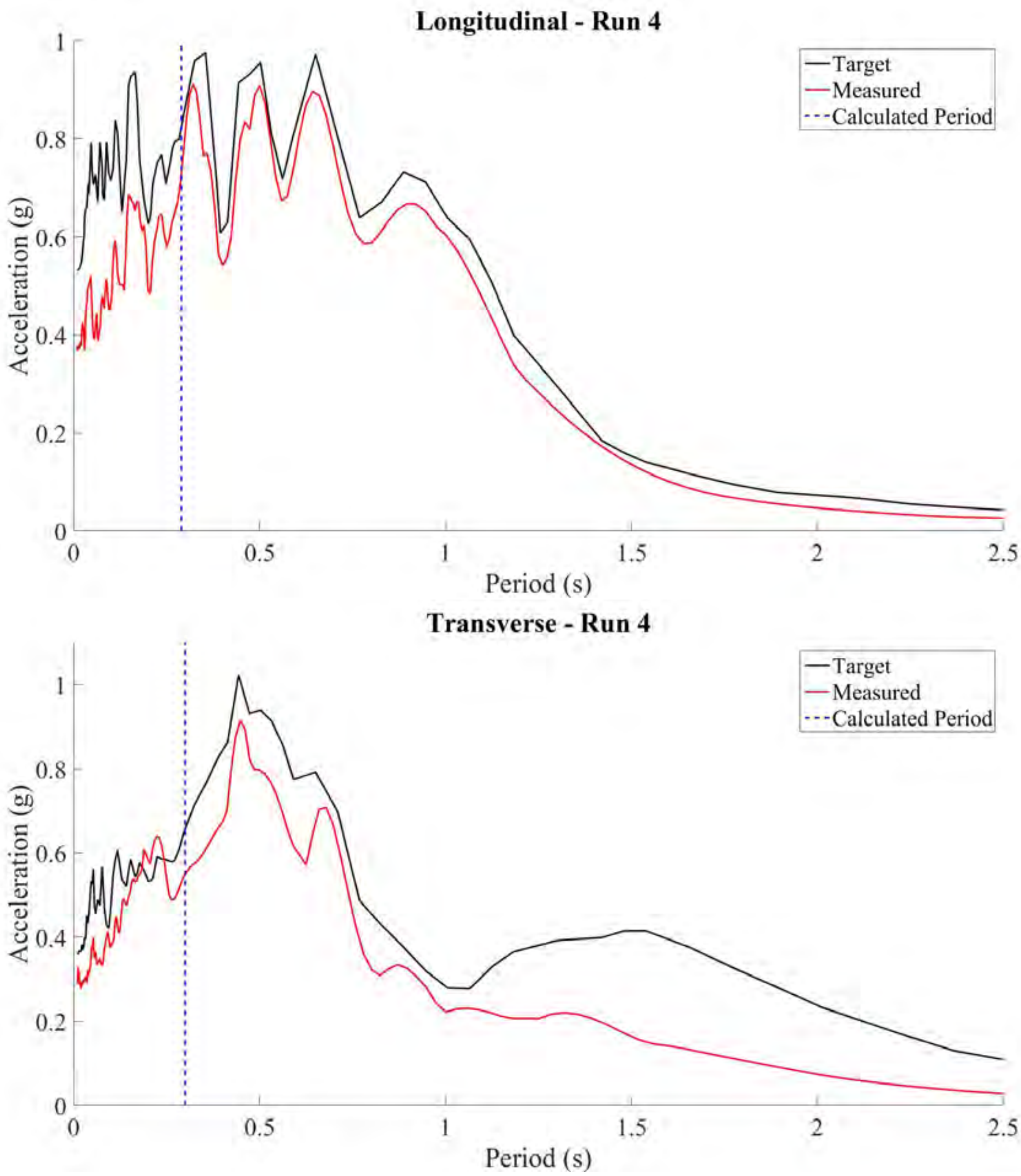

Figure 6.9 Measured vs. target response spectrum at period of interest, run 3

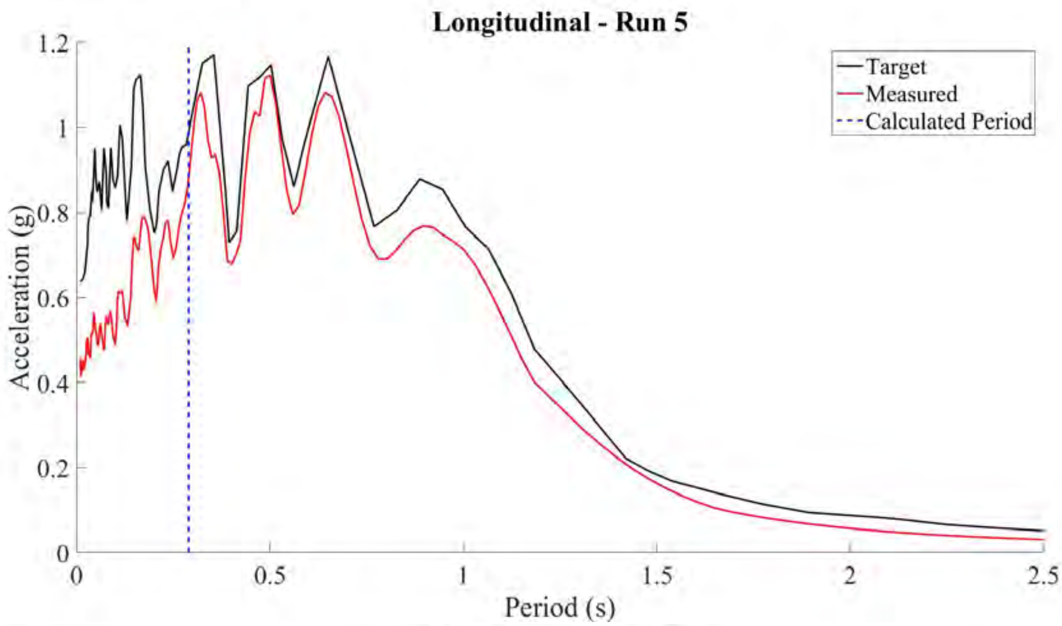

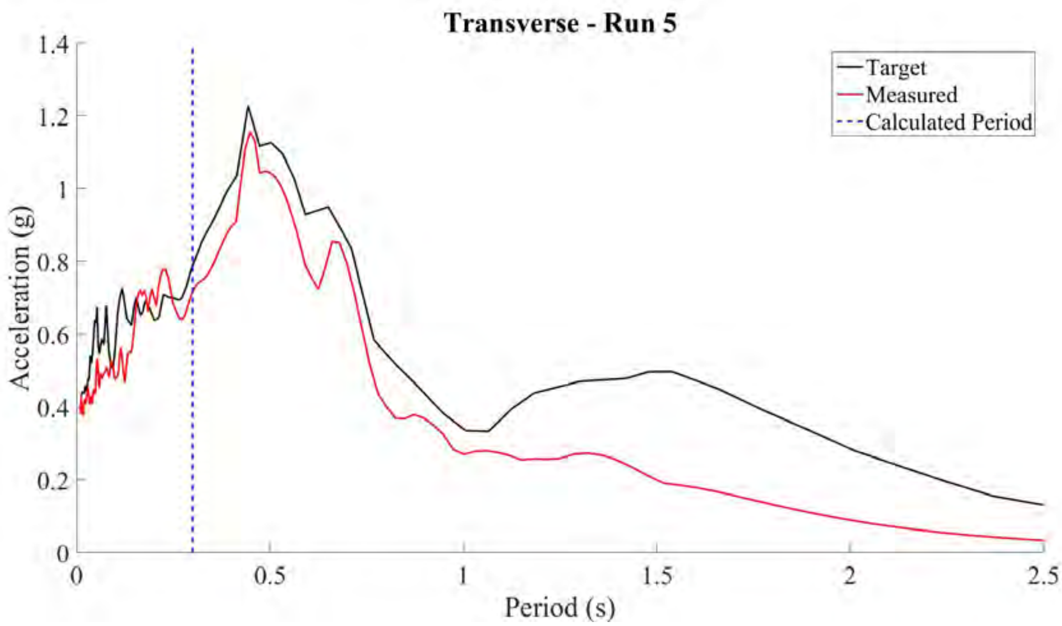

Figure 6.10 Measured vs. target response spectrum at period of interest, run 5

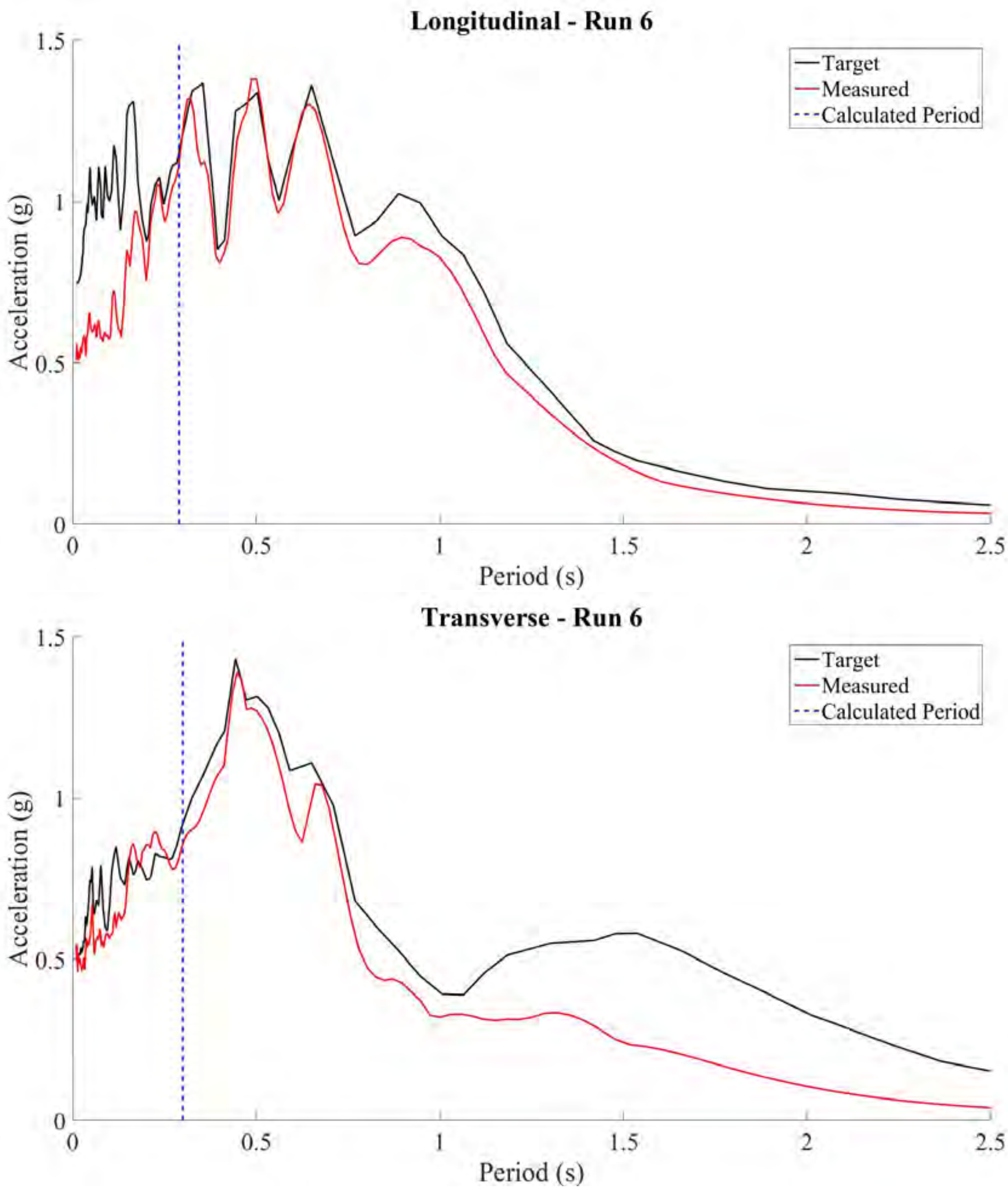

Figure 6.11 Measured vs. target response spectrum at period of interest, run 6

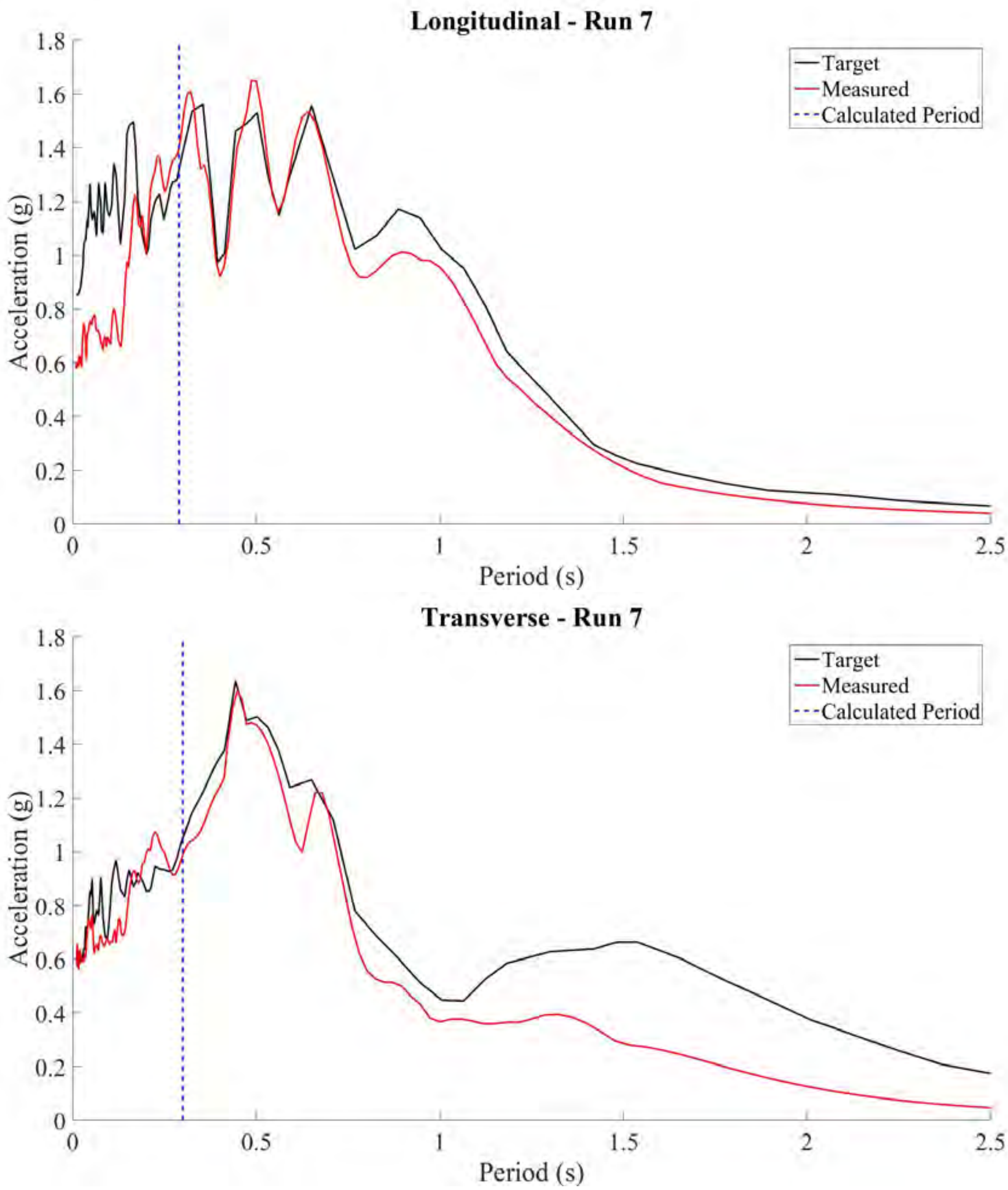

Figure 6.12 Measured vs. target response spectrum at period of interest, run 7

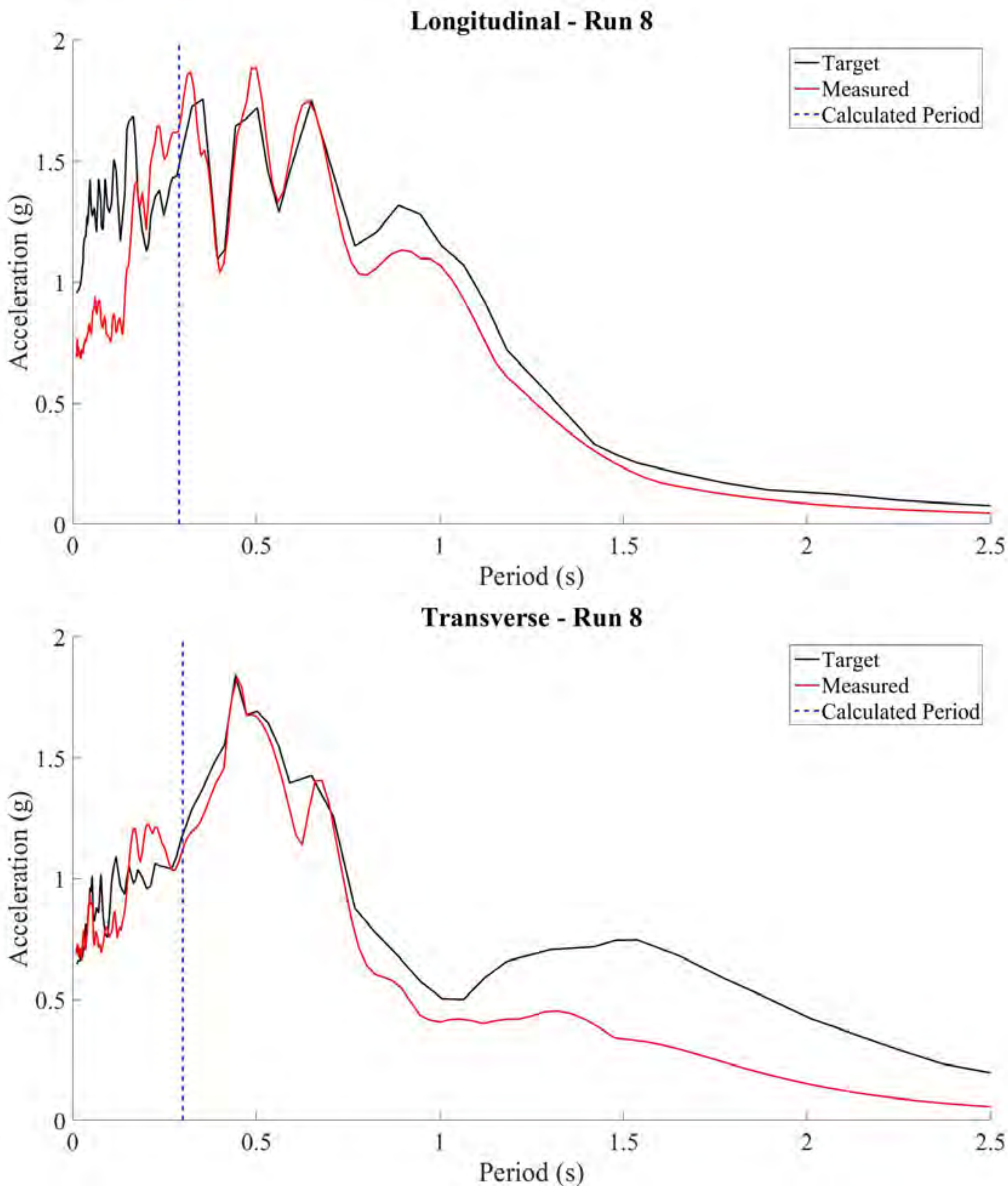

Figure 6.13 Measured vs. target response spectrum at period of interest, run 8

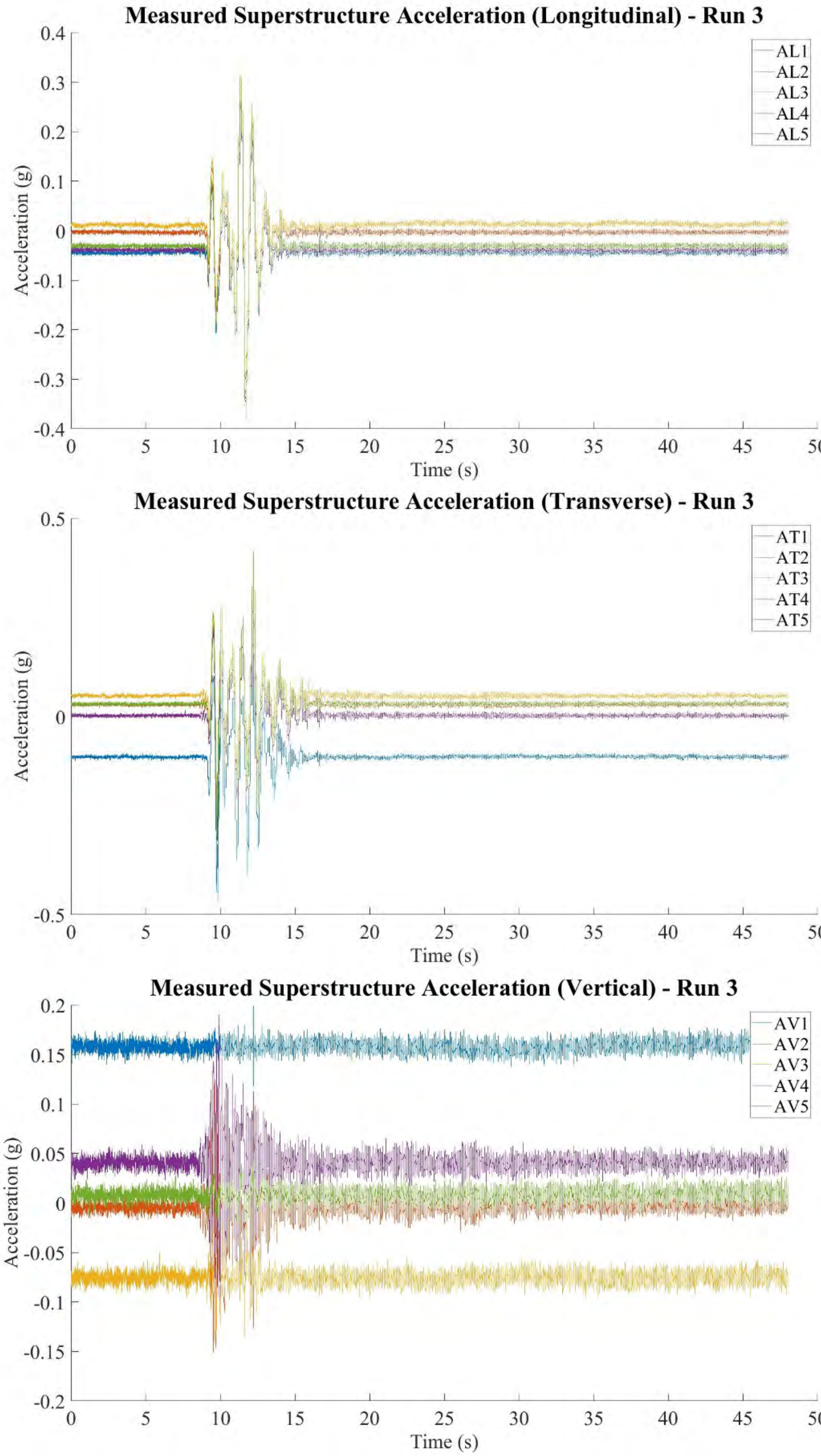

Figure 6.14 As-measured superstructure acceleration for run 3

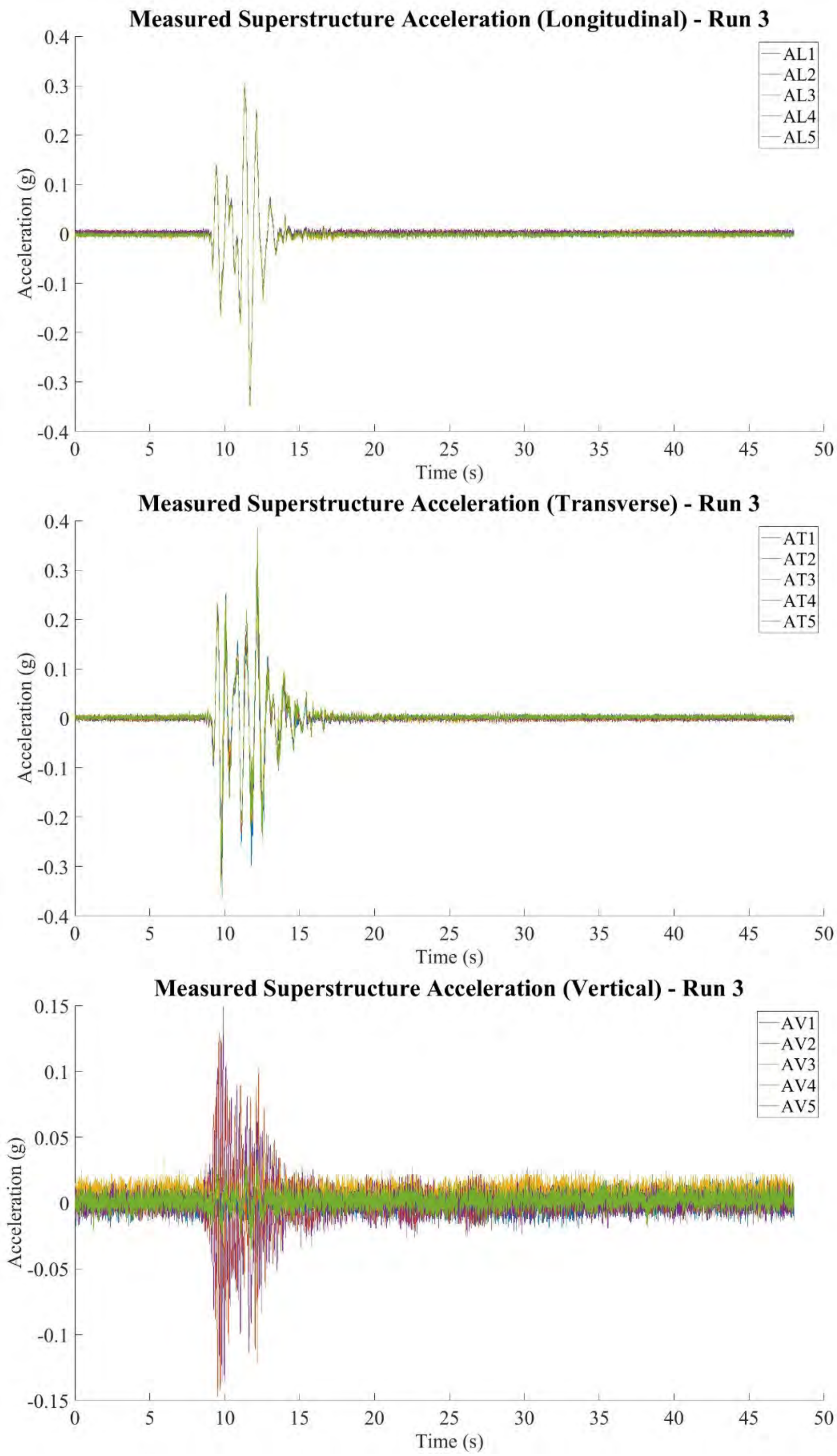

Figure 6.15 Measured superstructure acceleration for run 3 with offsets applied

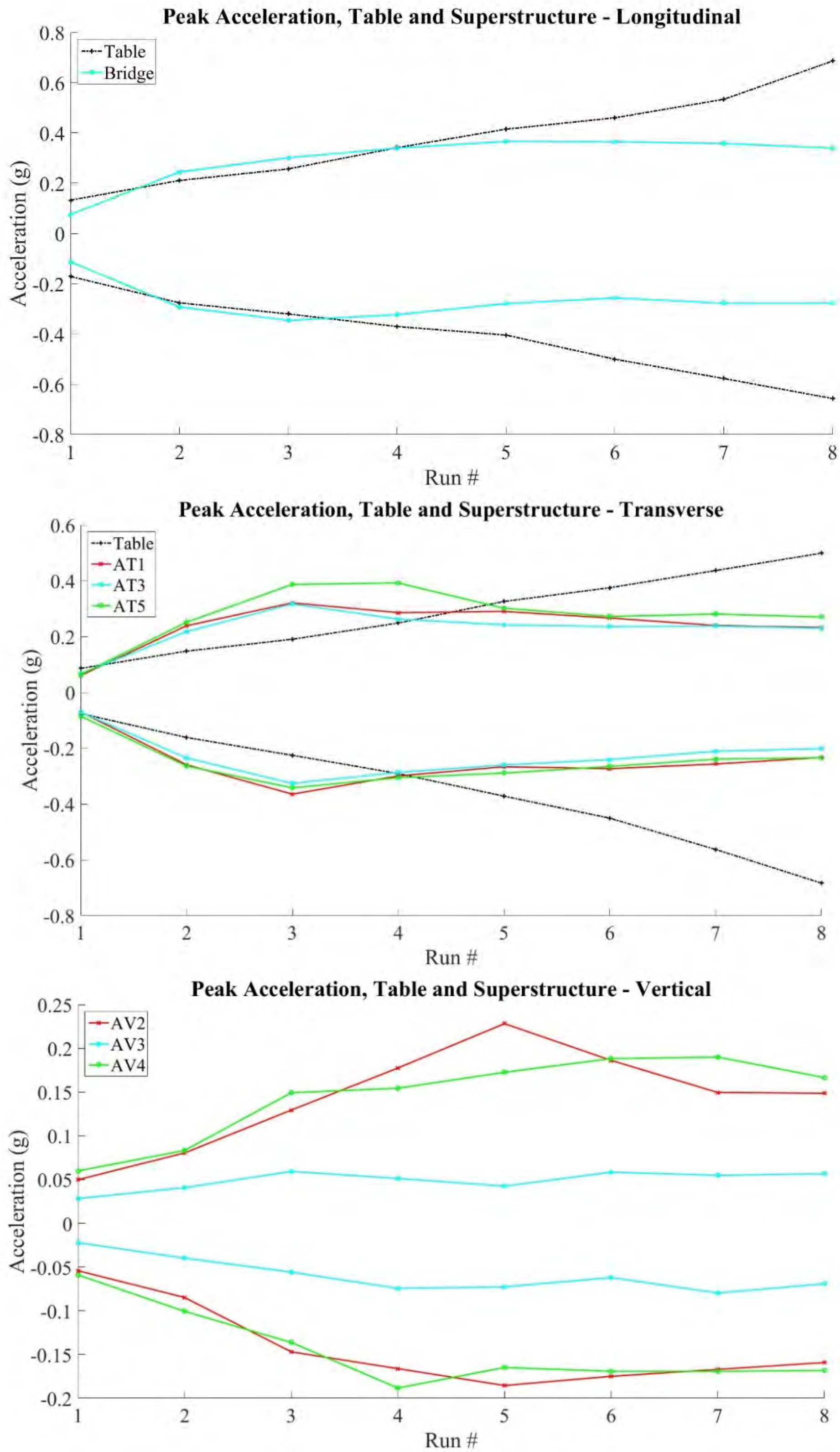

Figure 6.16 Comparison of peak superstructure and table accelerations

Figure 6.17 Damage progression in the northeast region at the top of the north column

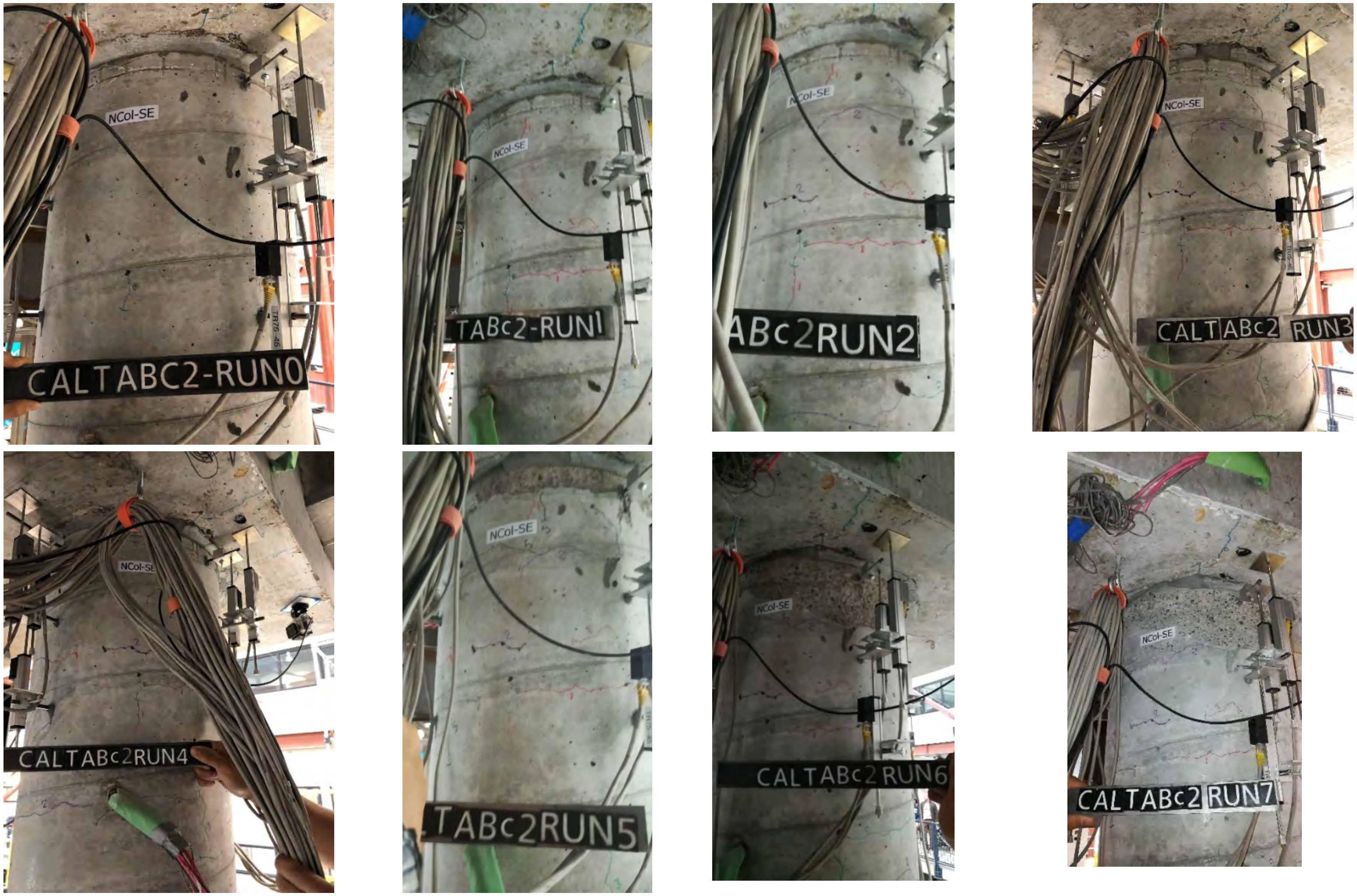

Figure 6.18 Damage progression in the southeast region at the top of the north column

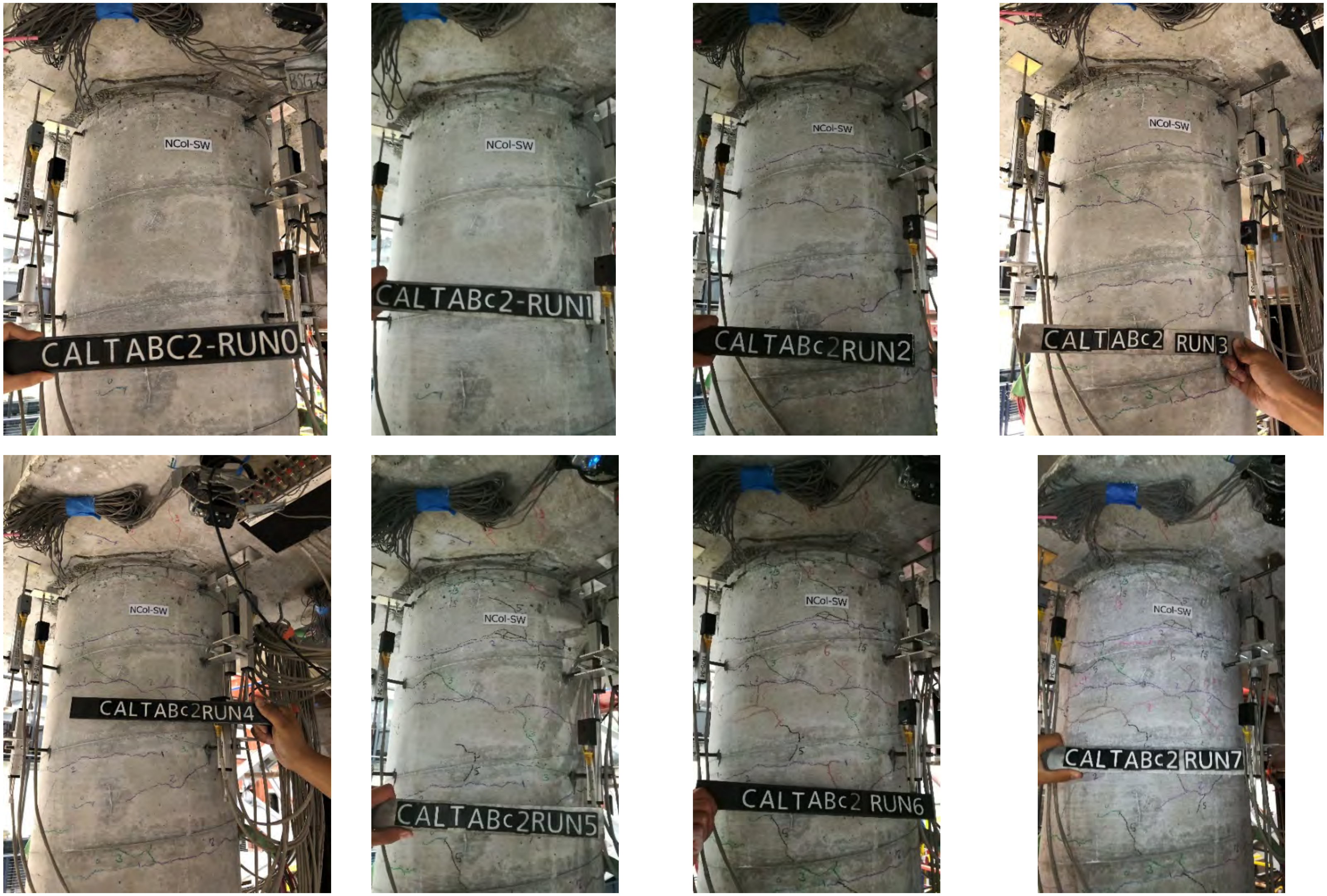

Figure 6.19 Damage progression in the southwest region at the top of the north column

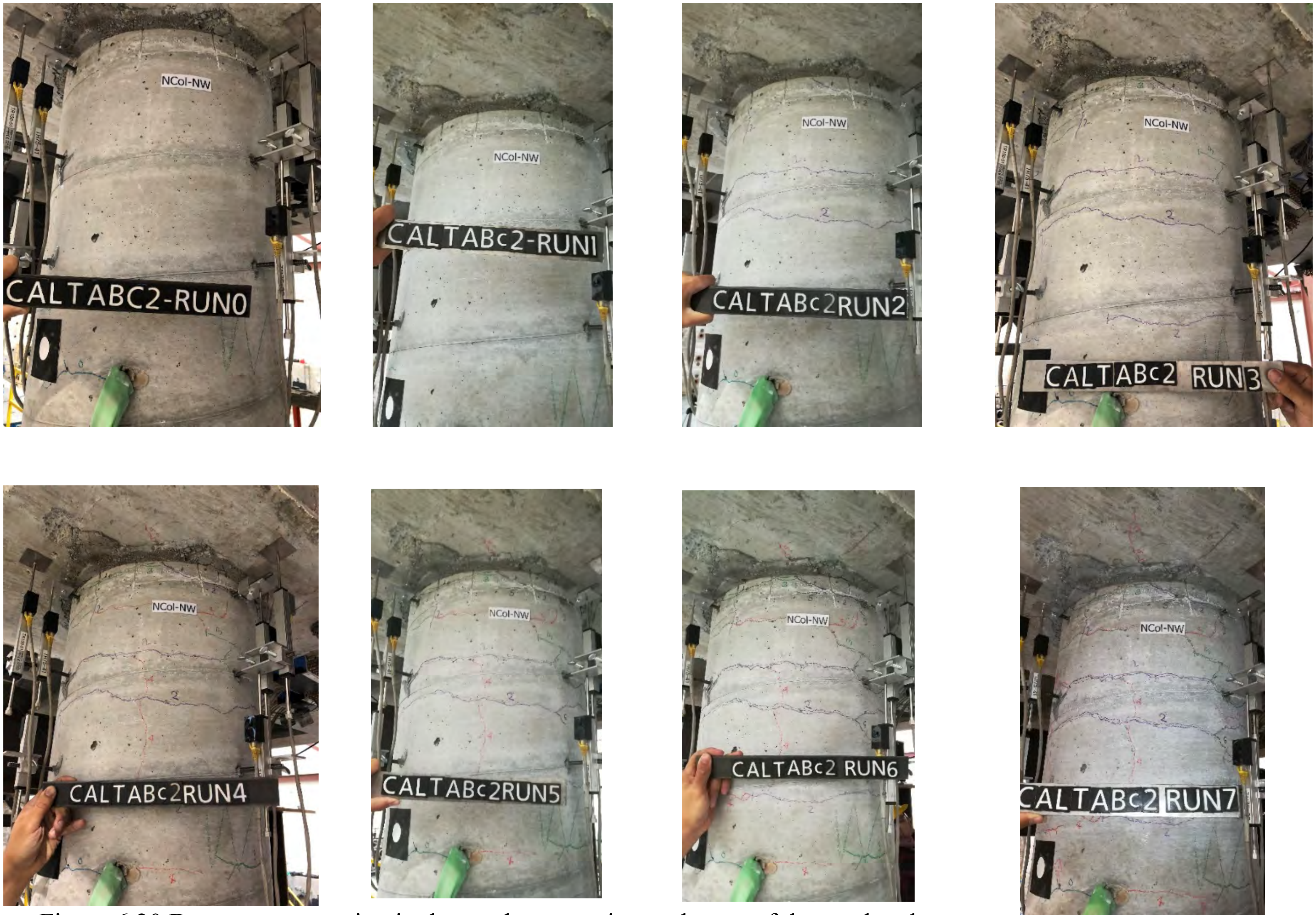

Figure 6.20 Damage progression in the northwest region at the top of the north column

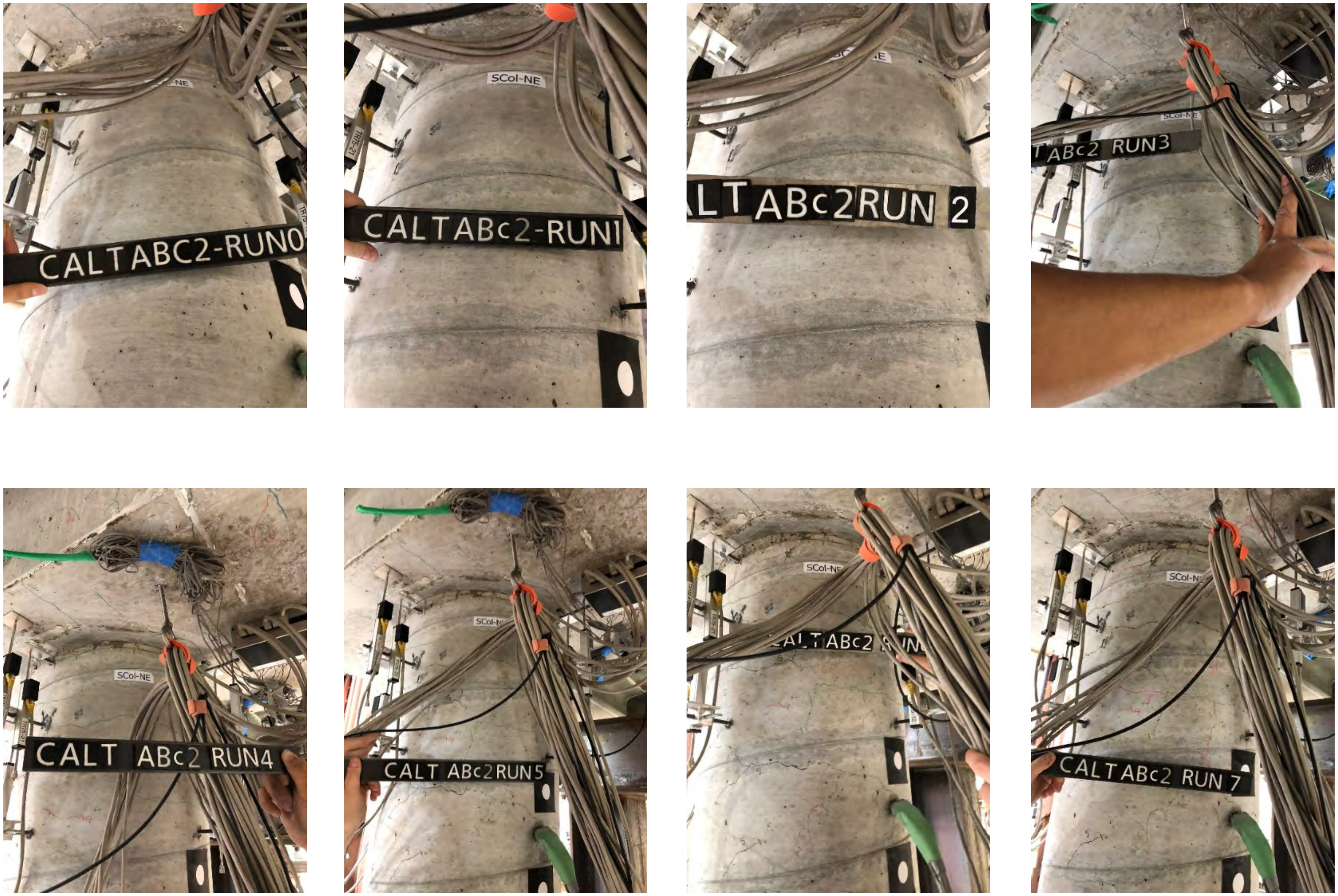

Figure 6.21 Damage progression in the northeast region at the top of the south column

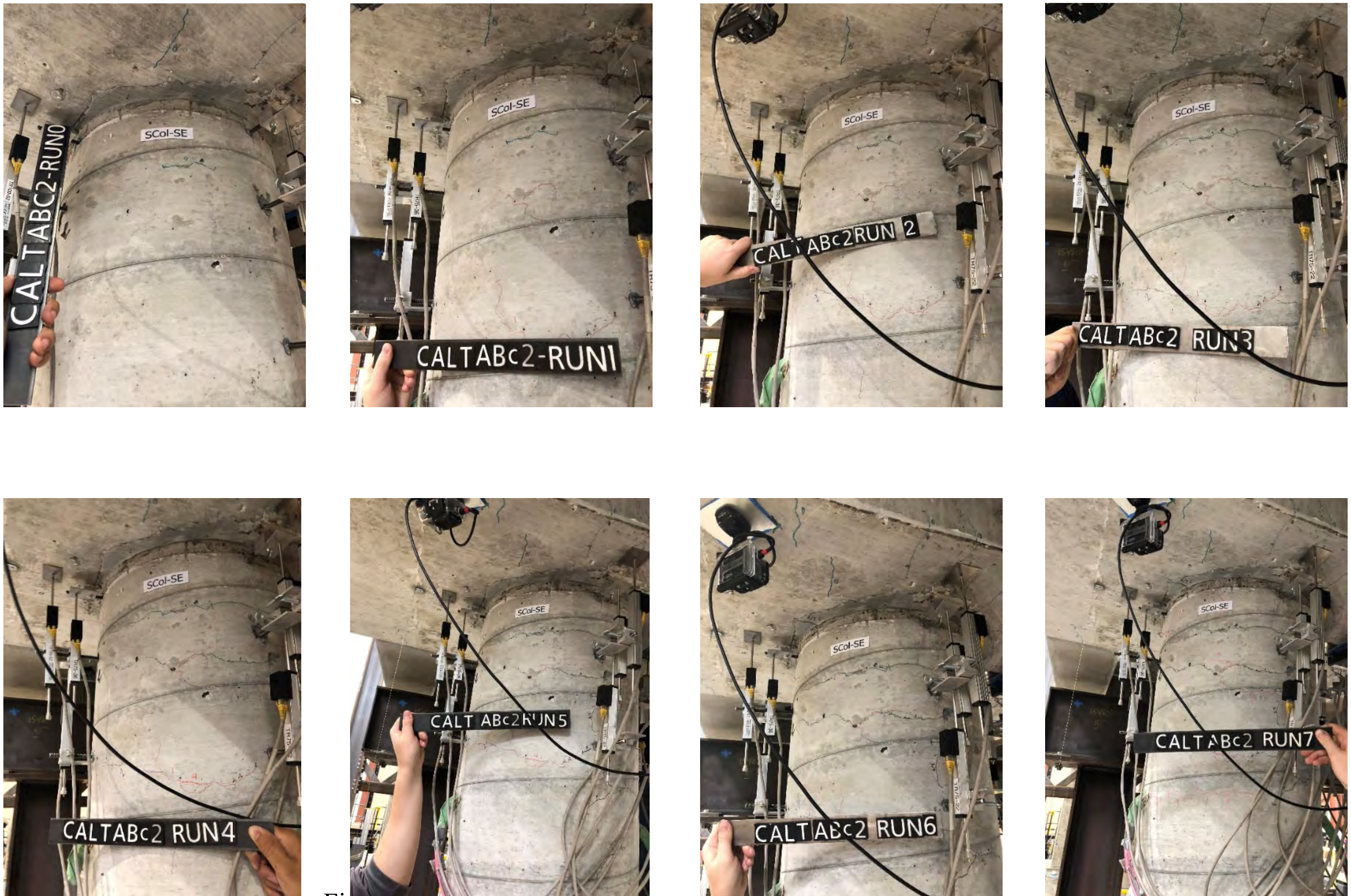

Figure 6.22 Damage progression in the southeast region at the top of the south column

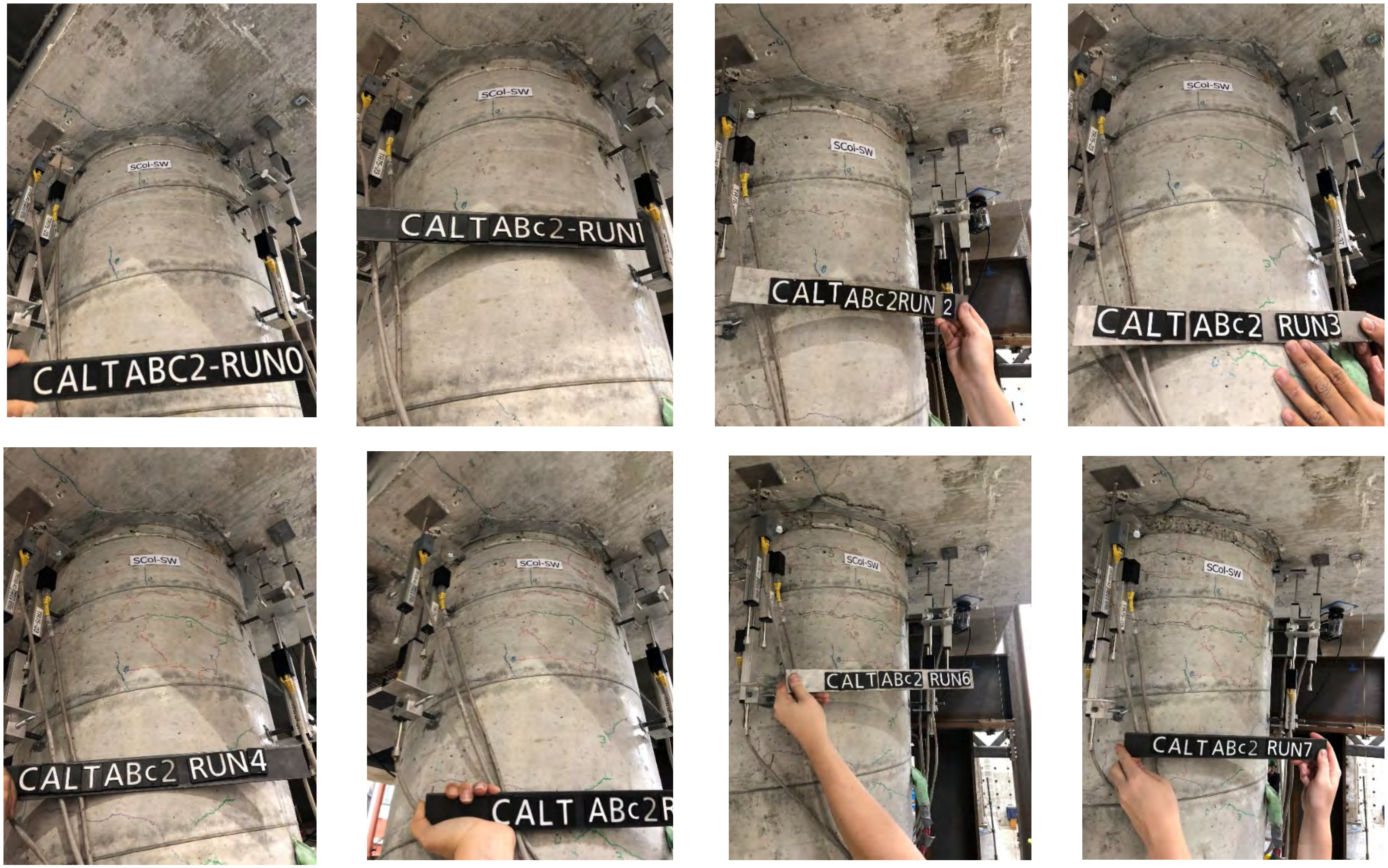

Figure 6.23 Damage progression in the southwest region at the top of the south column

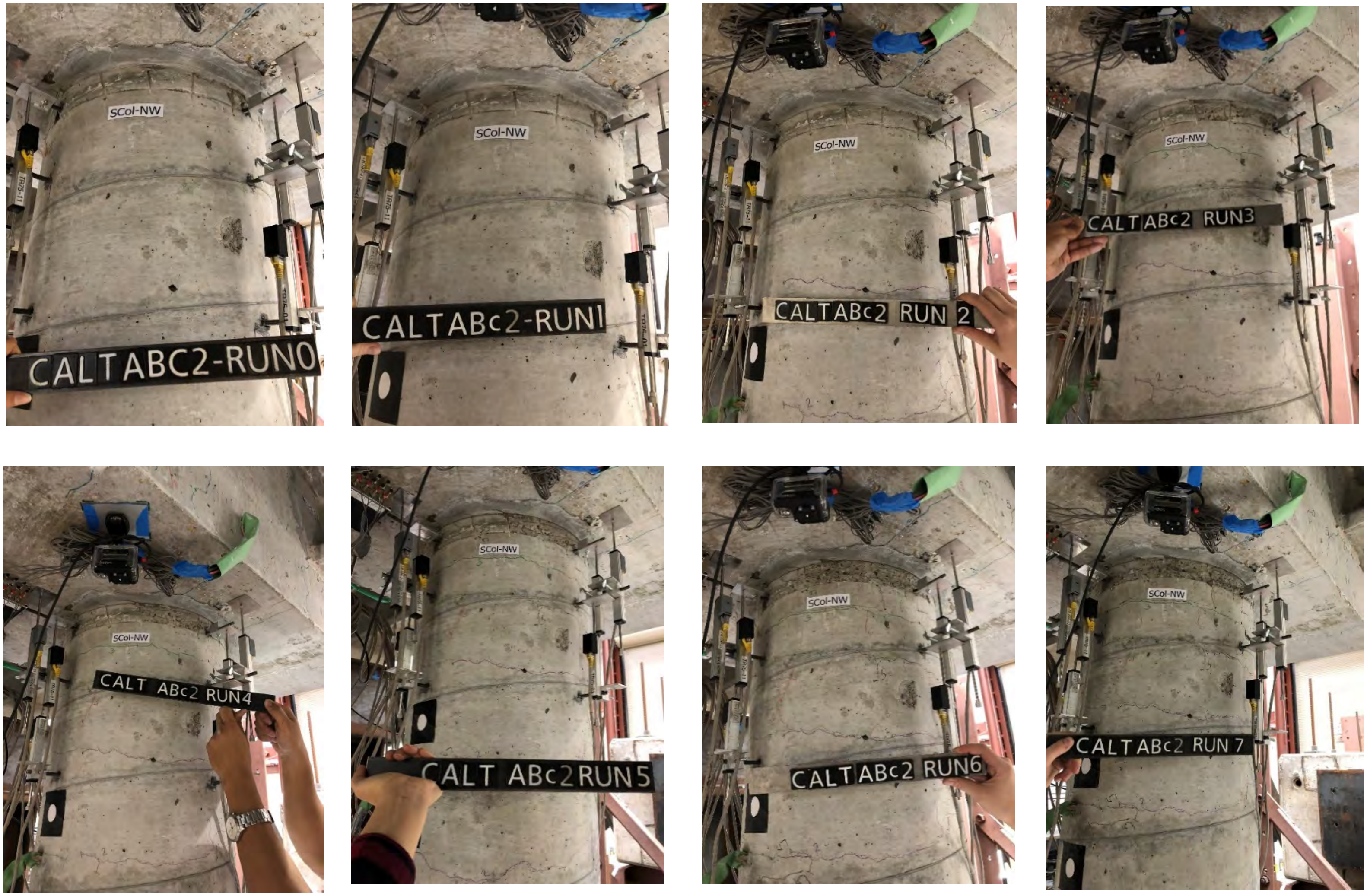

Figure 6.24 Damage progression in the northwest region at the top of the south column

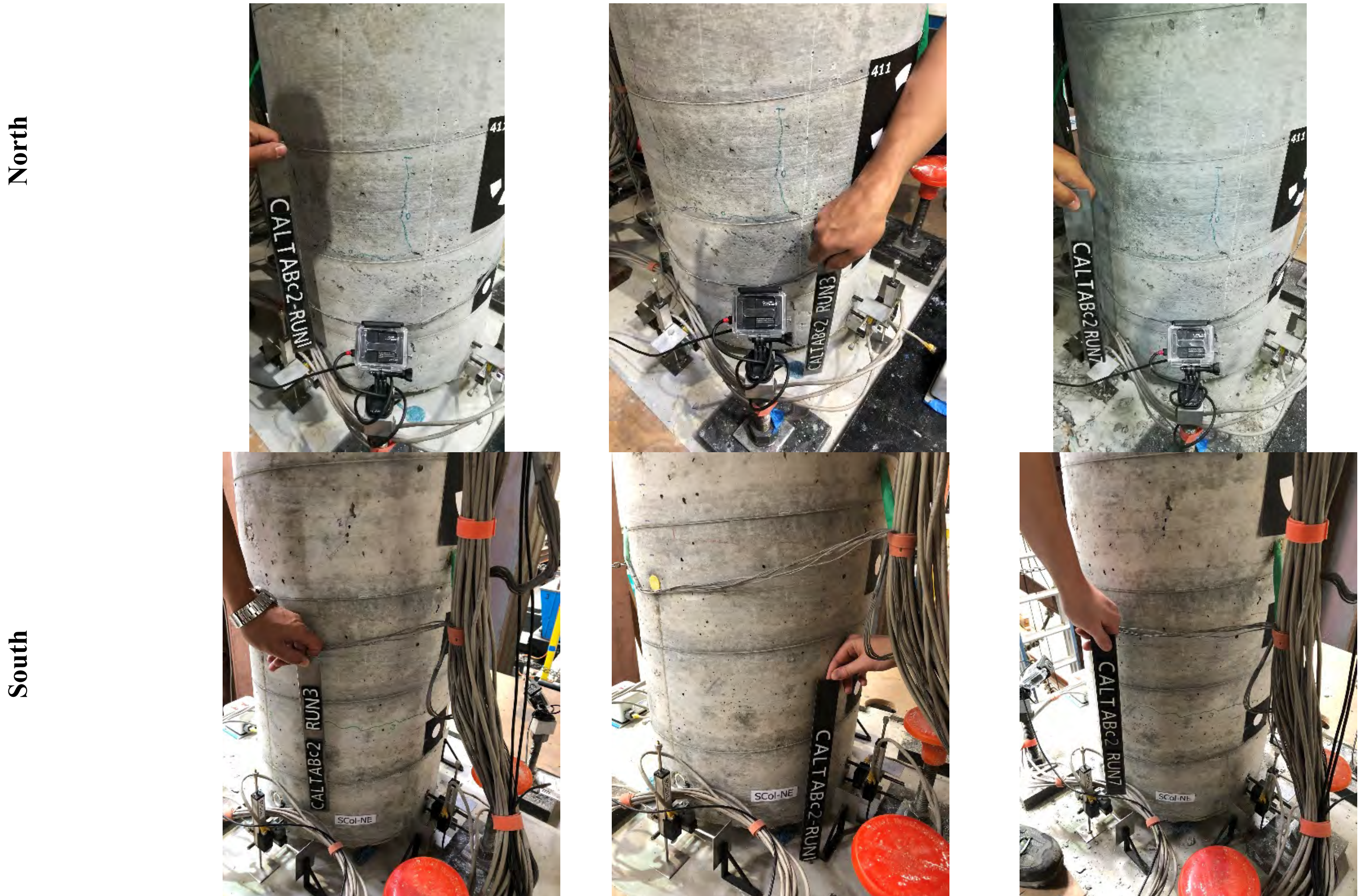

Figure 6.25
Damage progression in the northeast region at the bottom of the north and south column after runs 1, 3, and 7

North

South

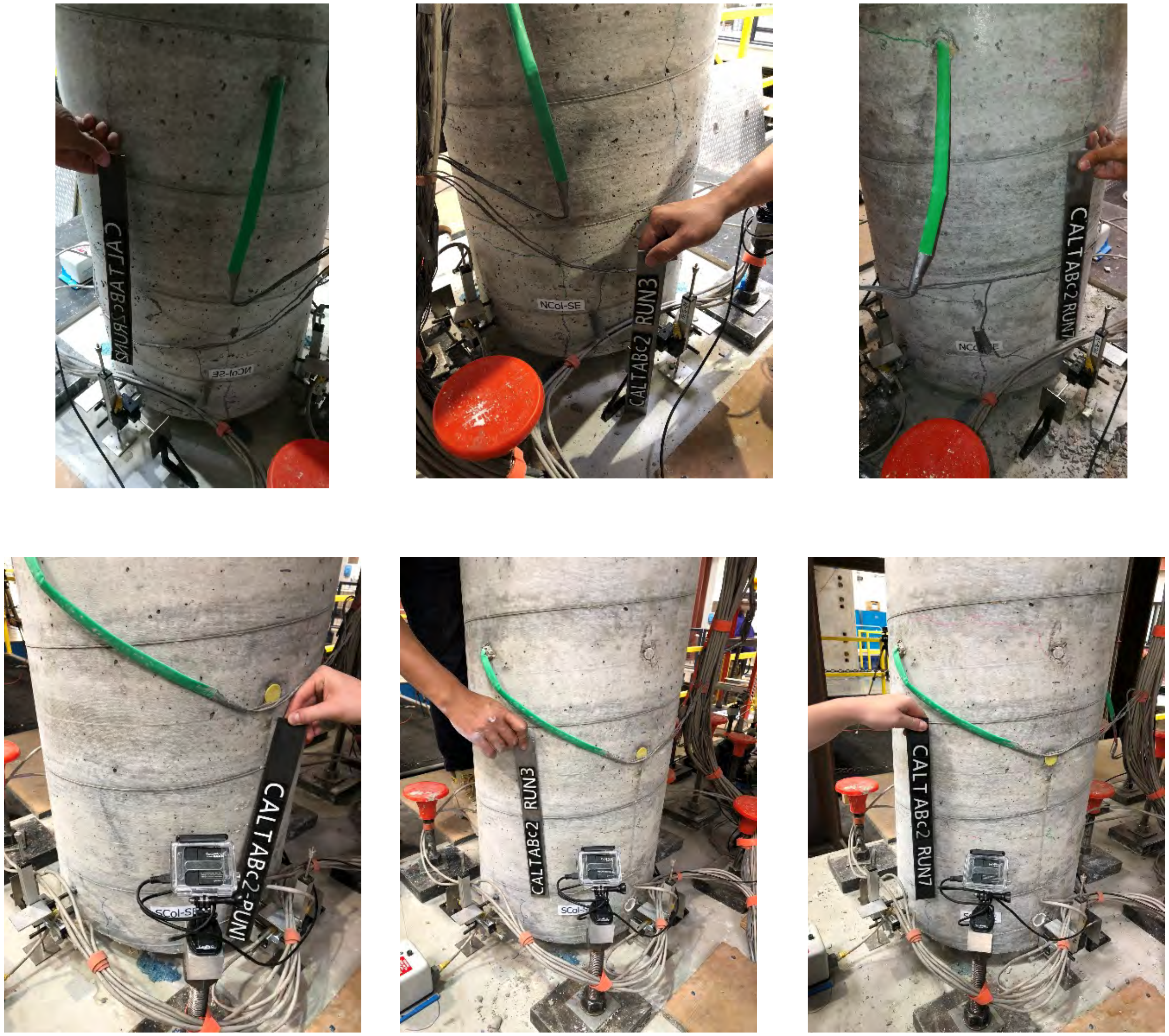

Figure 6.26 Damage progression in the southeast region at the bottom of the north and south column after runs 1, 3, and 7

Figure 6.27 Damage progression in the southwest region at the bottom of the north and south column after runs 1, 3, and 7

North

South

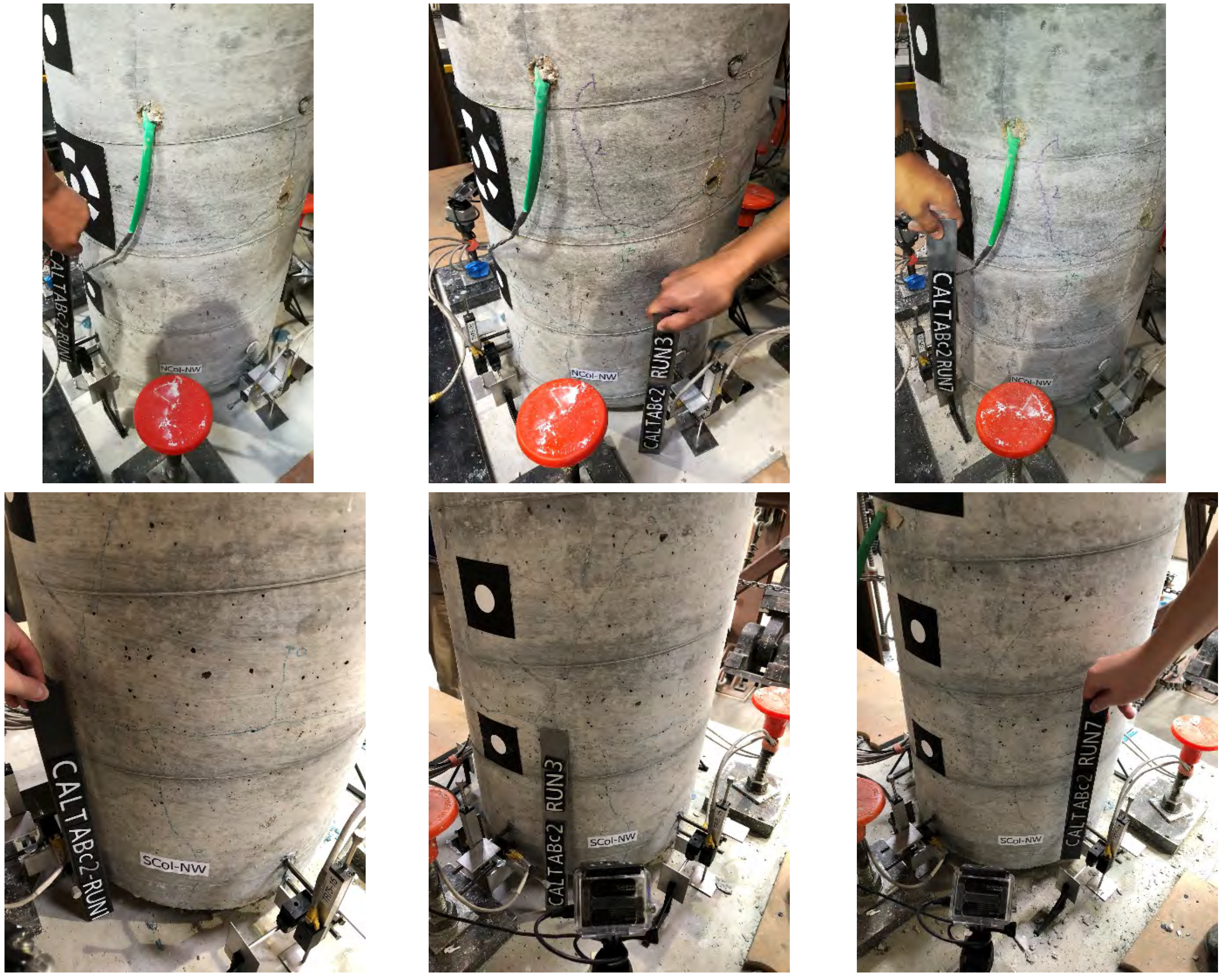

Figure 6.28
Damage progression in the northwest region at the bottom of the north and south column after runs 1, 3, and 7

Figure 6.29 Condition c [illegible] ion of run 7 (bottom)

Run 0-East

Run 7-East

Figure 6.30 Condition of east side of cap beam prior to testing (top) and at the conclusion of run 7 (bottom)

Figure 6.31 Condition of west side of cap beam prior to testing (top) and at the conclusion of run 7 (bottom)

Run 0 **Run 7**

Figure 6.32 Condition of north side of cap beam prior to testing (left) and at the conclusion of run 7 (right)

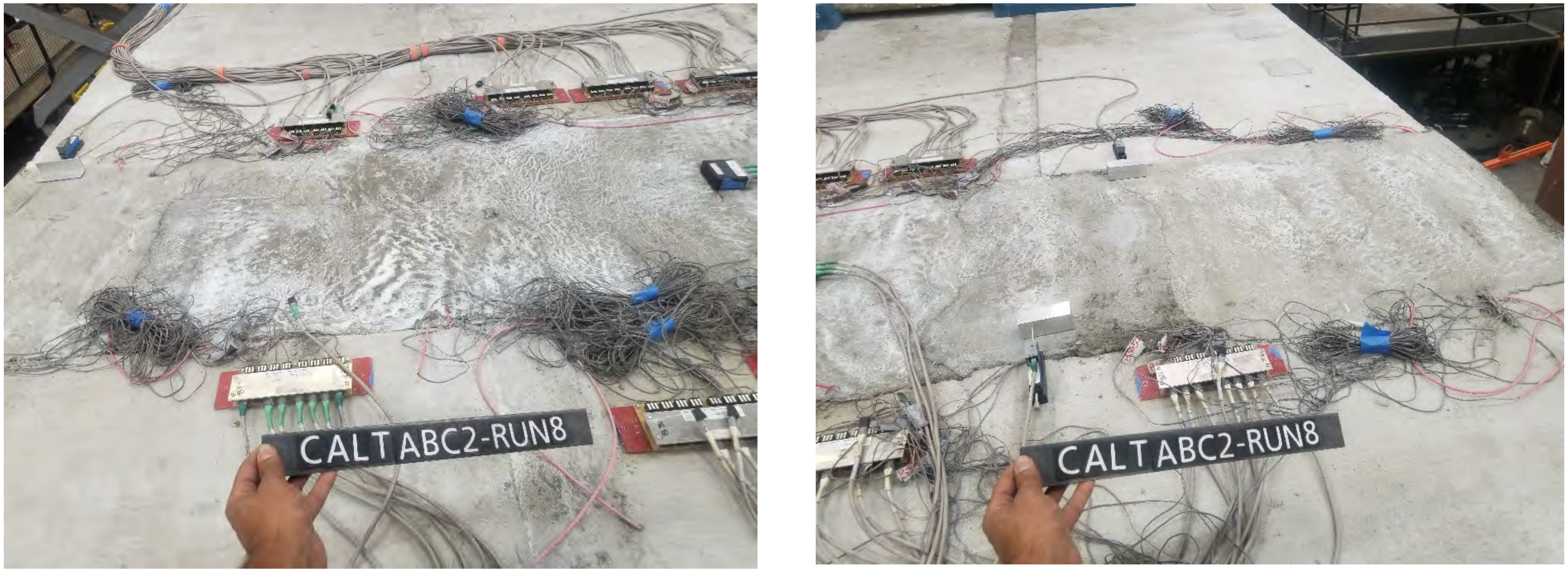

Figure 6.33 Condition of deck joint over the cap beam at the conclusion of run 8

Figure 6.34 Condition of deck joint over the exterior girders at the conclusion of run 8

Figure 6.35 Condition of deck panel connections and connections between the deck and interior girders in the region near the bent after run 8

Abutment-West

Abutment-East

Figure 6.36 Progression of residual transverse displacements at the west (top) and east (bottom) abutments for runs 1 to 4

Abutment-West

Abutment-East

Figure 6.37 Progression of residual transverse displacements at the west (top) and east (bottom) abutments for runs 5 to 7

Girder G1 **Girder G4**

Figure 6.38 Condition of interface between exterior girders and cap beam after Run 7, girder G1 (left), girder G4 (right)

Girder G2 **Girder G3**

Figure 6.39 Condition of interface between interior girders and cap beam after Run 7, girder G2 (left), girder G3 (right)

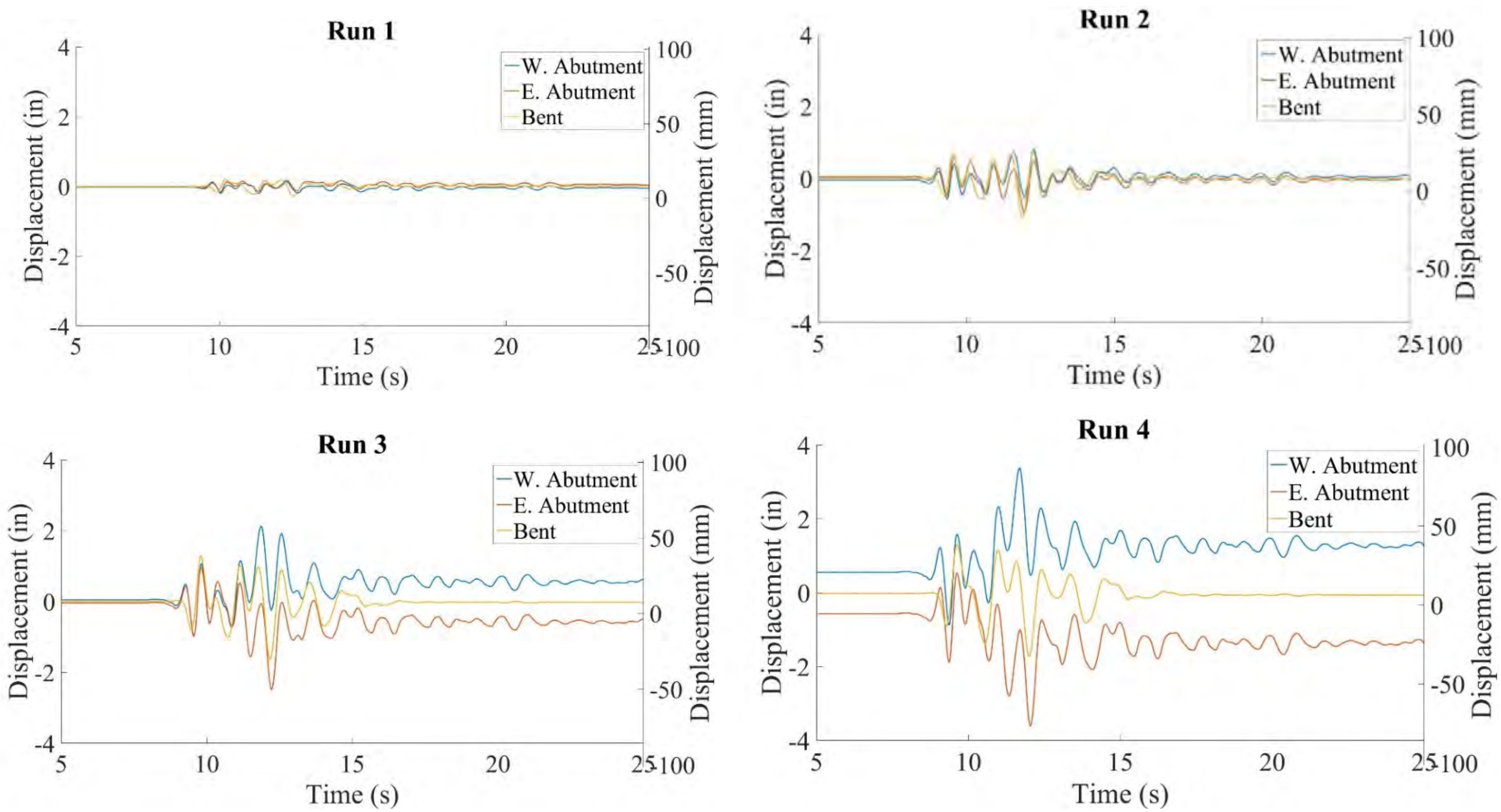

Figure 6.40 Abutment and bent transverse displacement along superstructure, runs 1-4

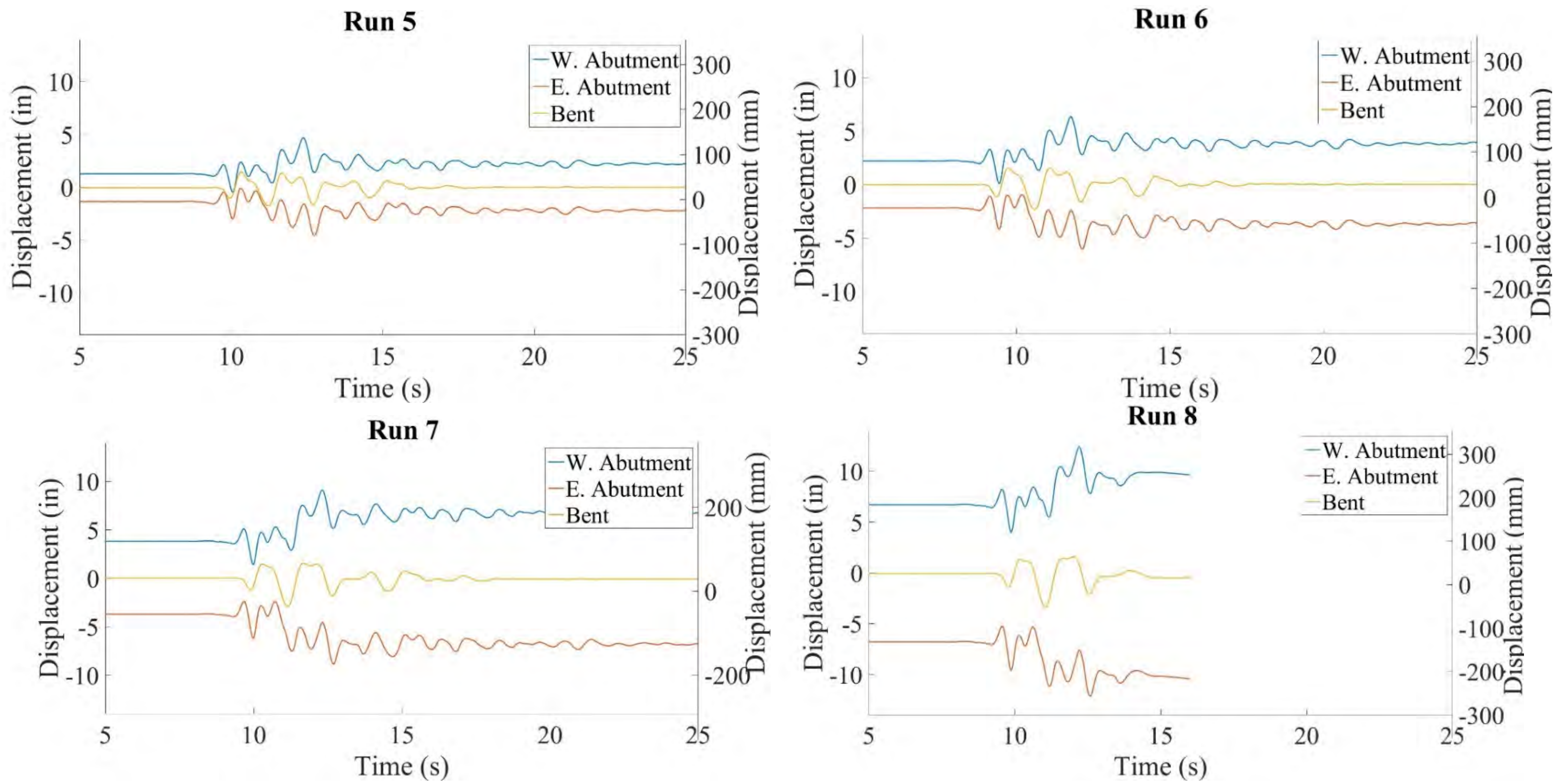

Figure 6.41 Abutment and bent transverse displacement, runs 5-8

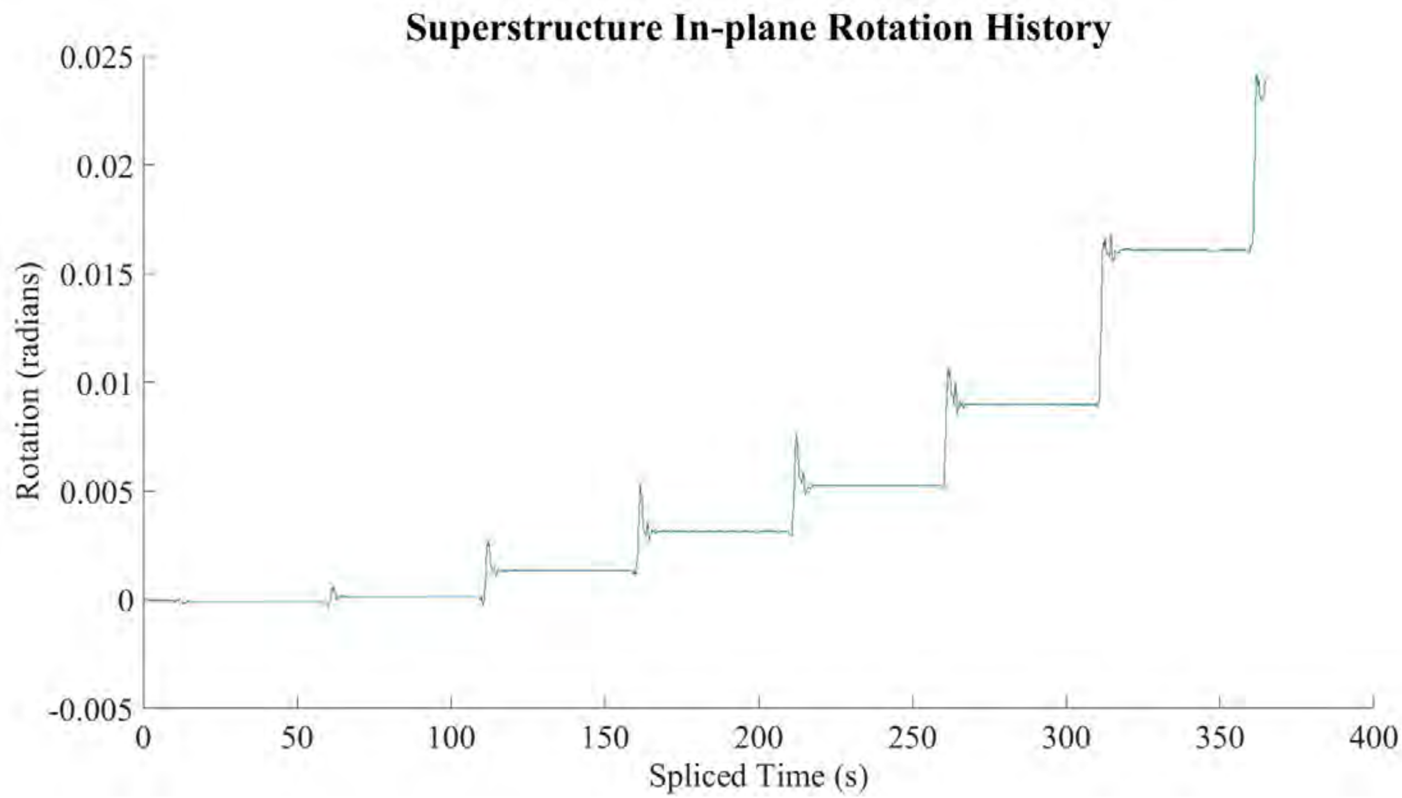

Figure 6.42 Spliced history of superstructure in-plane rotation for all runs

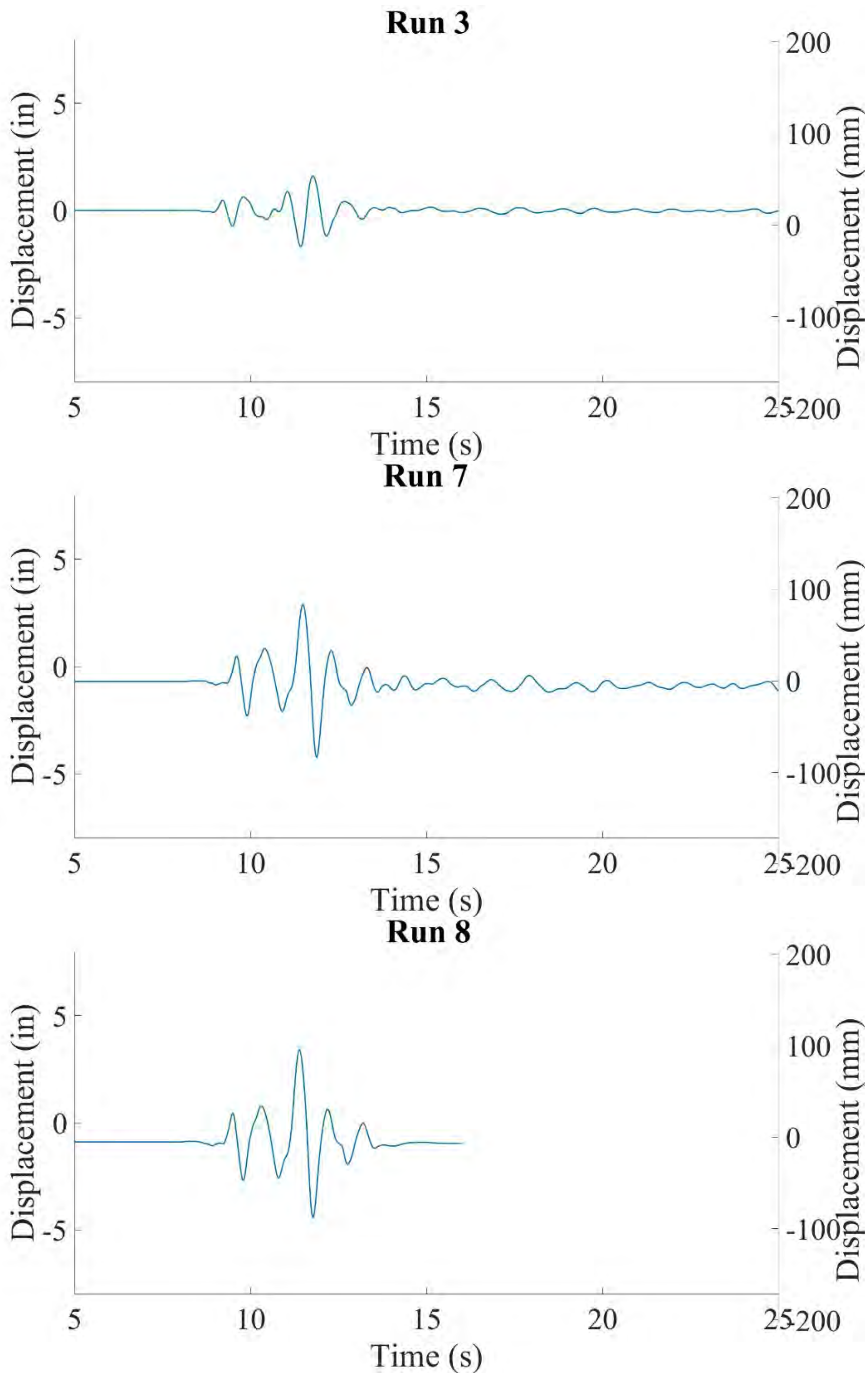

Figure 6.43 Average longitudinal superstructure displacement

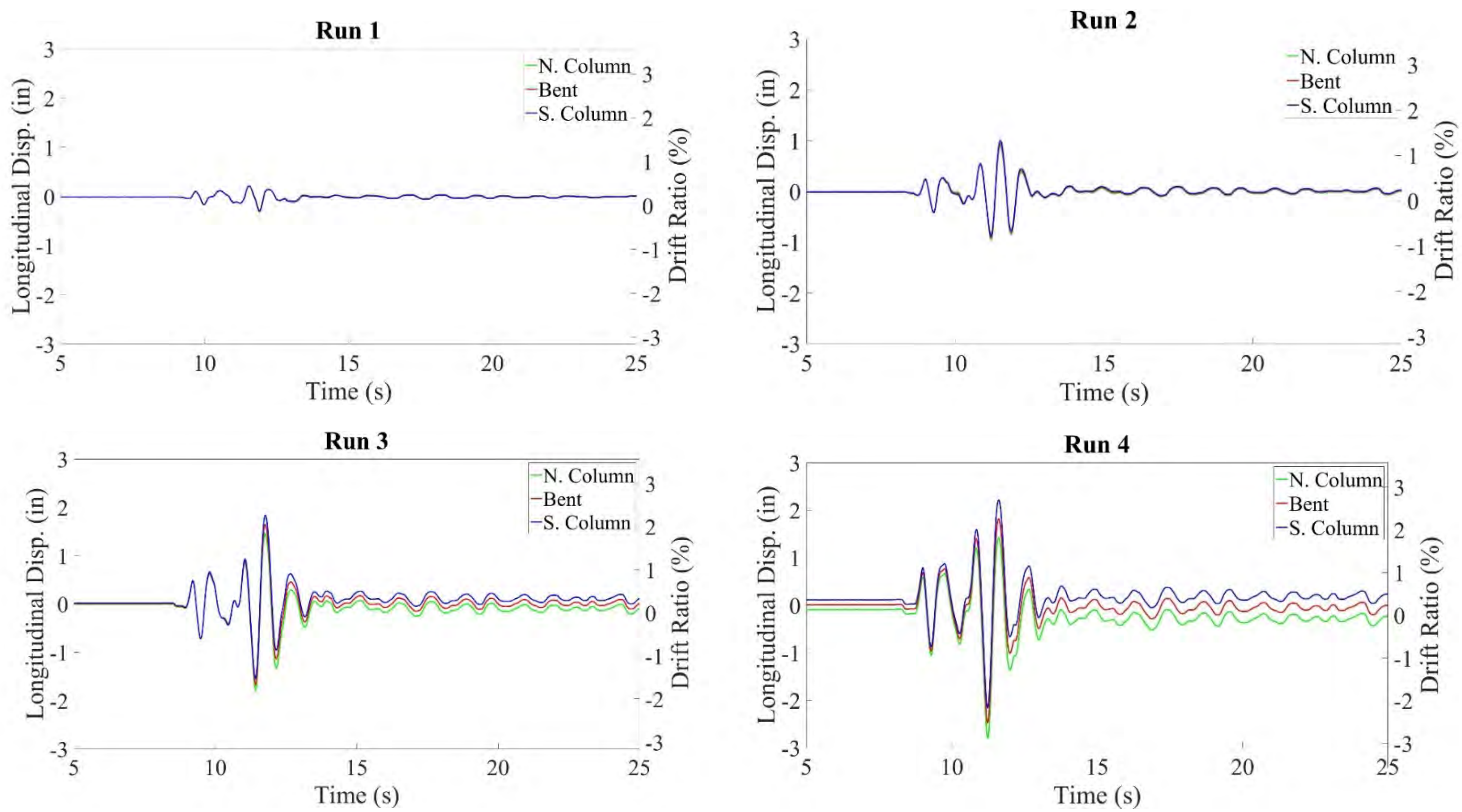

Figure 6.44 Total relative column and bent longitudinal displacement, runs 1-4

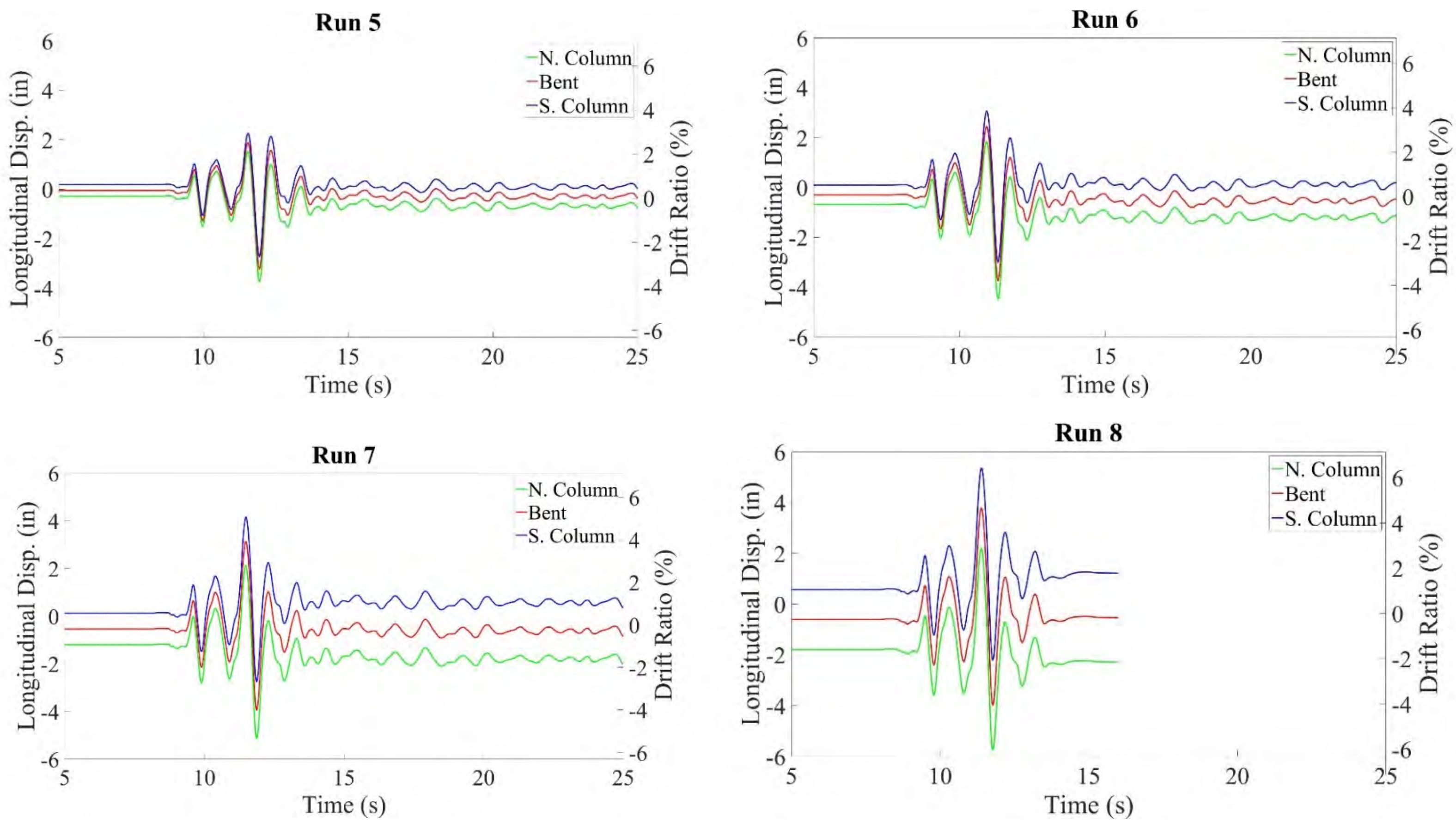

Figure 6.45 Total relative column and bent longitudinal displacement, runs 5-8

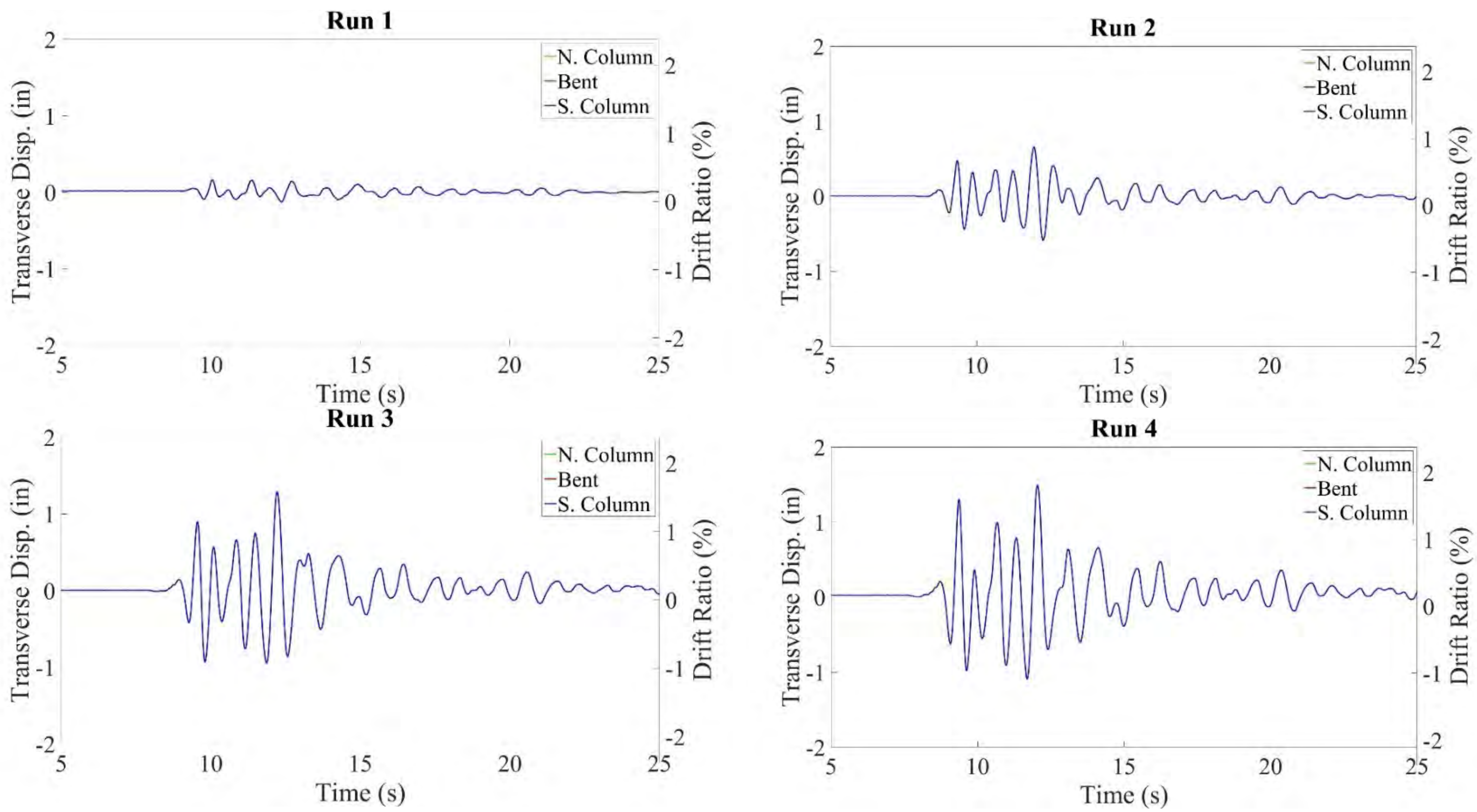

Figure 6.46 Total relative column and bent transverse displacement, runs 1-4

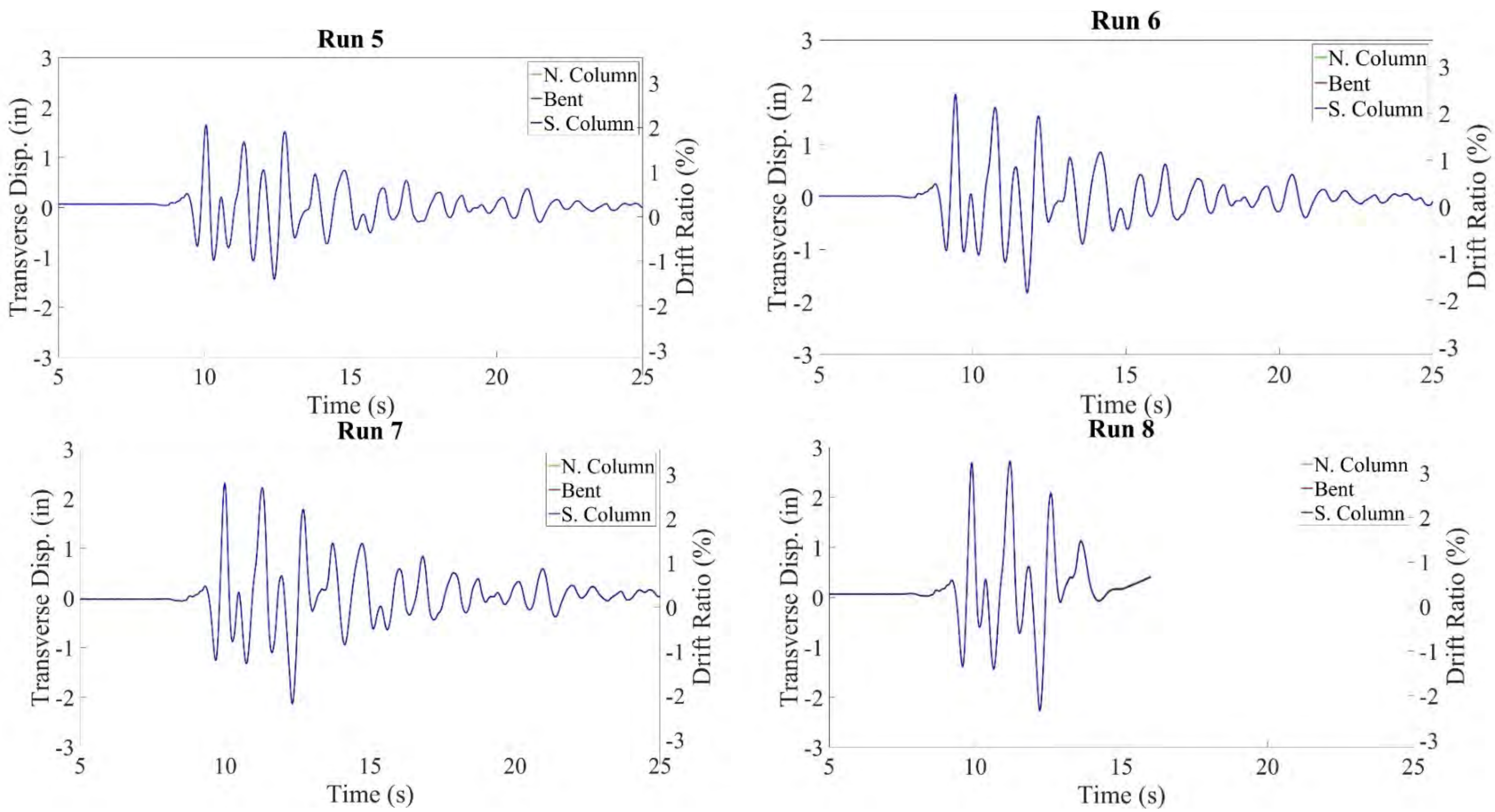

Figure 6.47 Total relative column and bent transverse displacement, runs 5-8

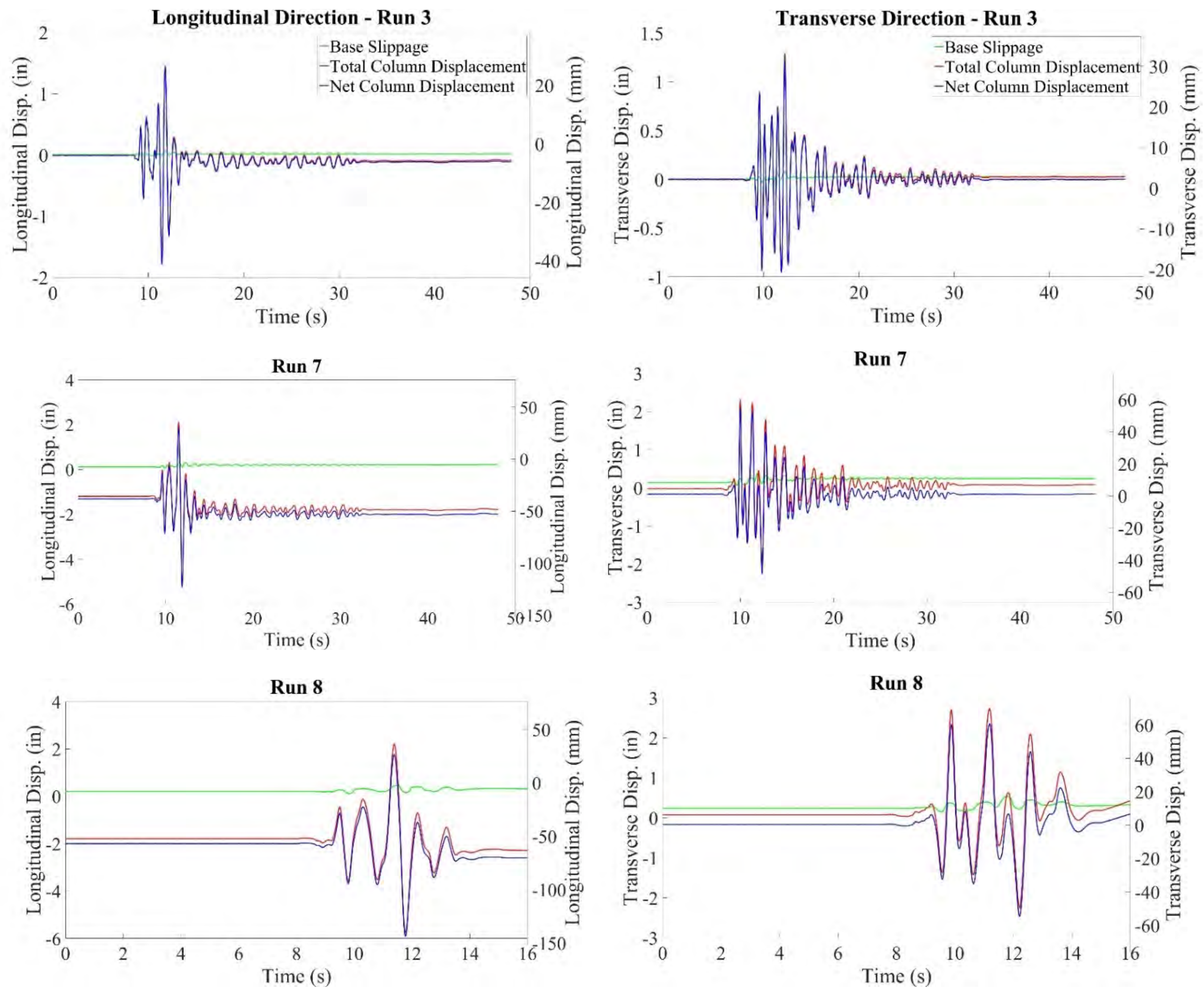

Figure 6.48 Total and net column displacement in north column, runs 3, 7, and 8

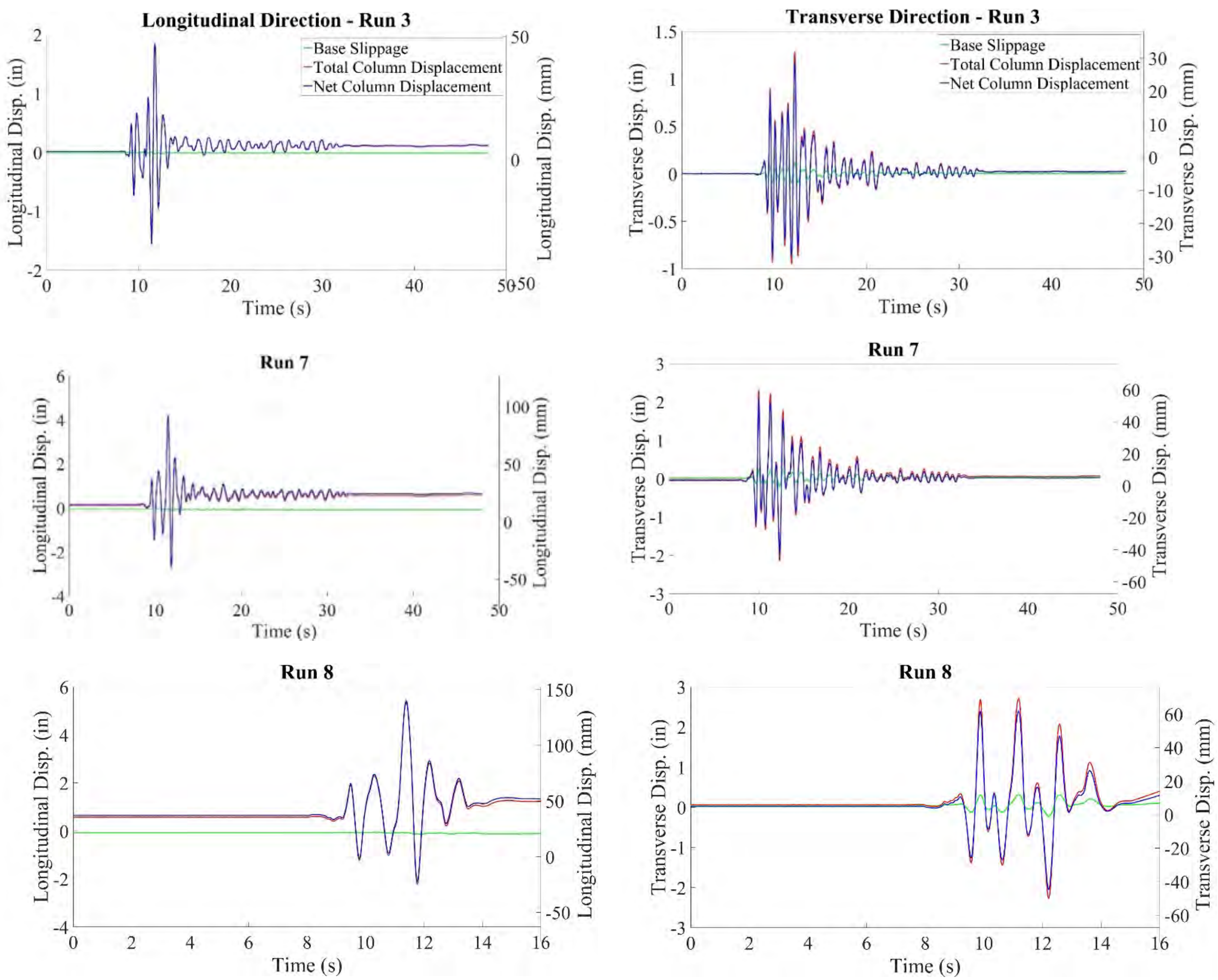

Figure 6.49 Total and net column displacement in south column, runs 3, 7, and 8

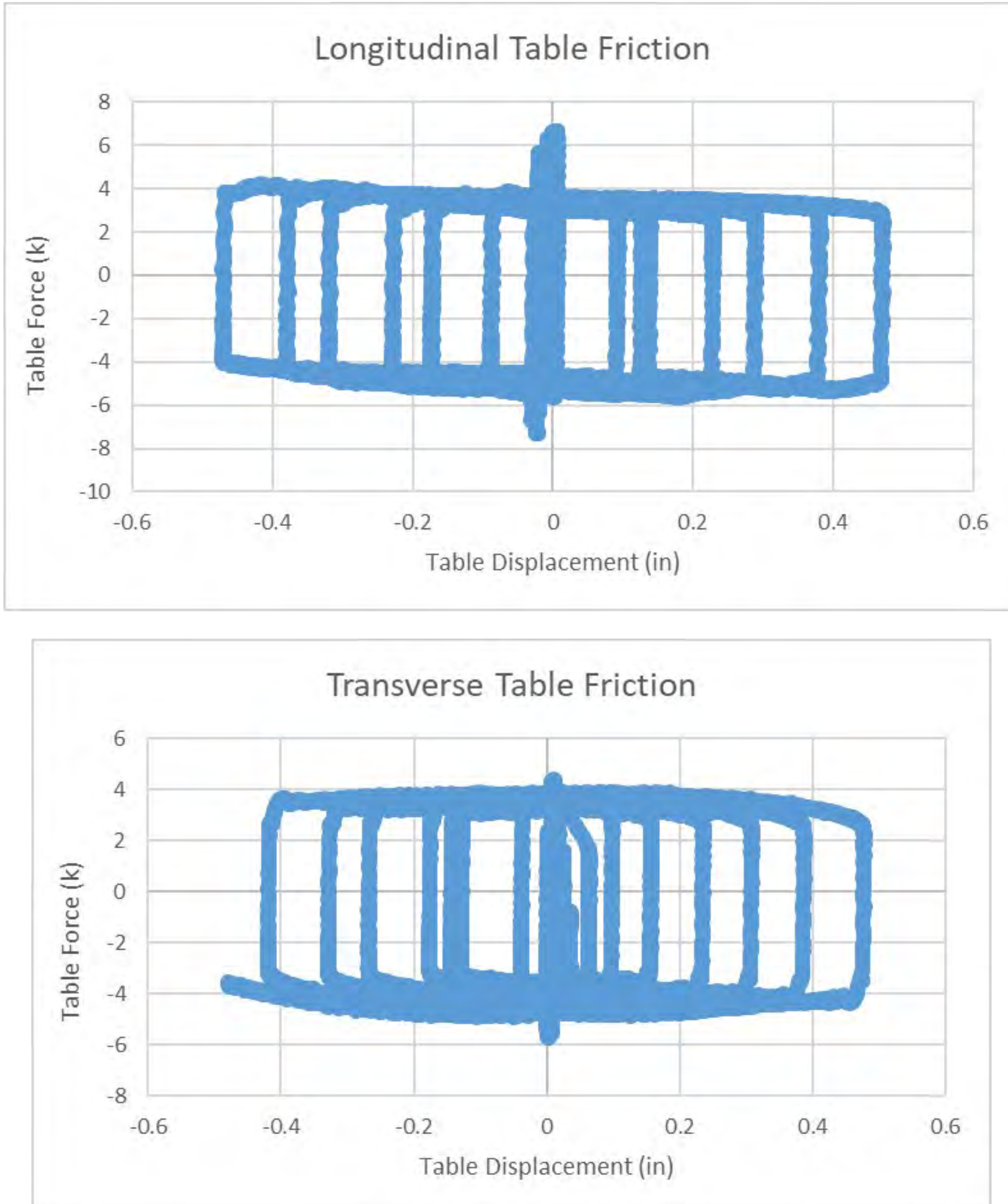

Figure 6.50 Friction in the table actuator during warm-up motion

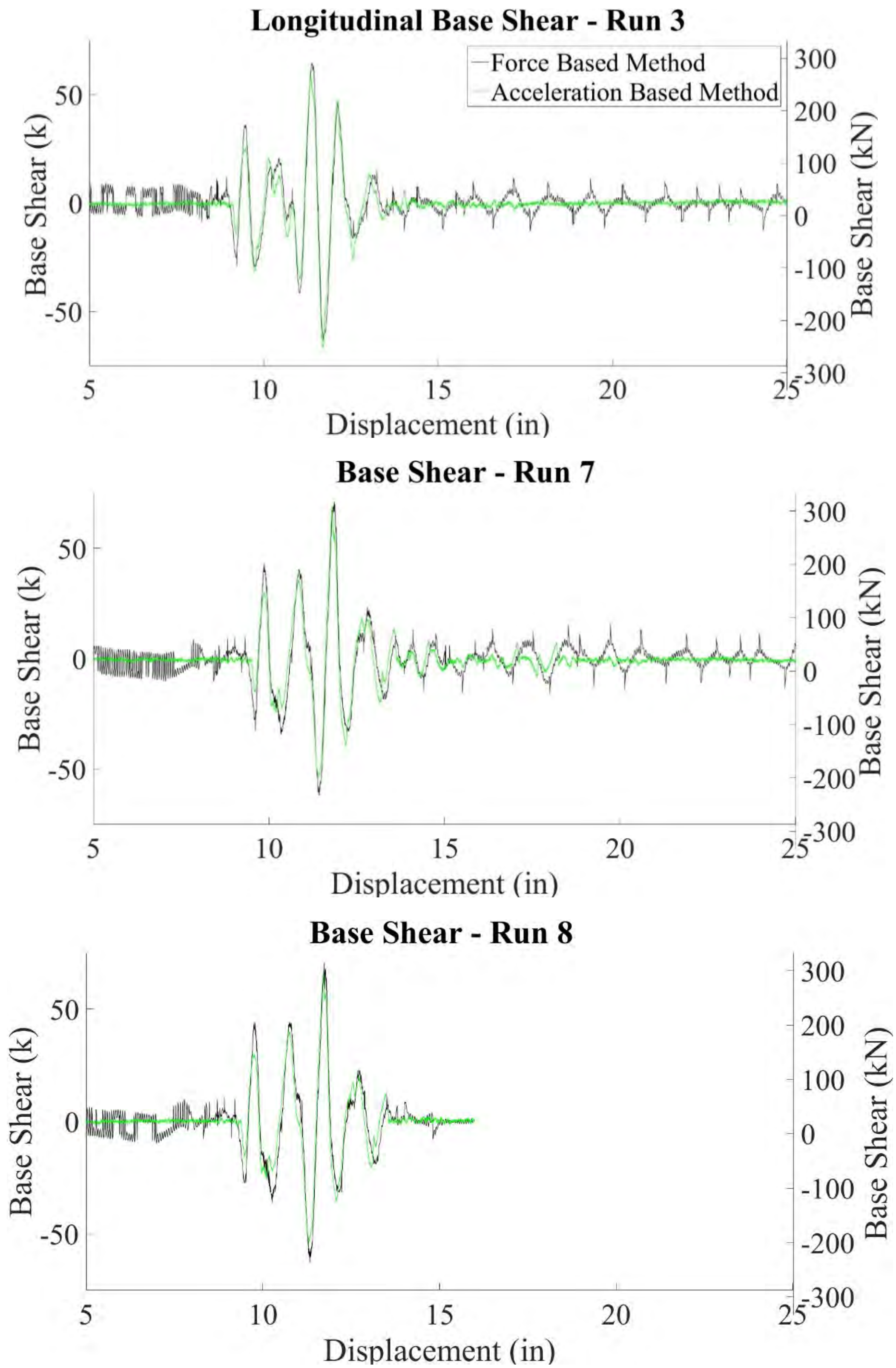

Figure 6.51 Comparison of force-based and acceleration-based base shear, longitudinal

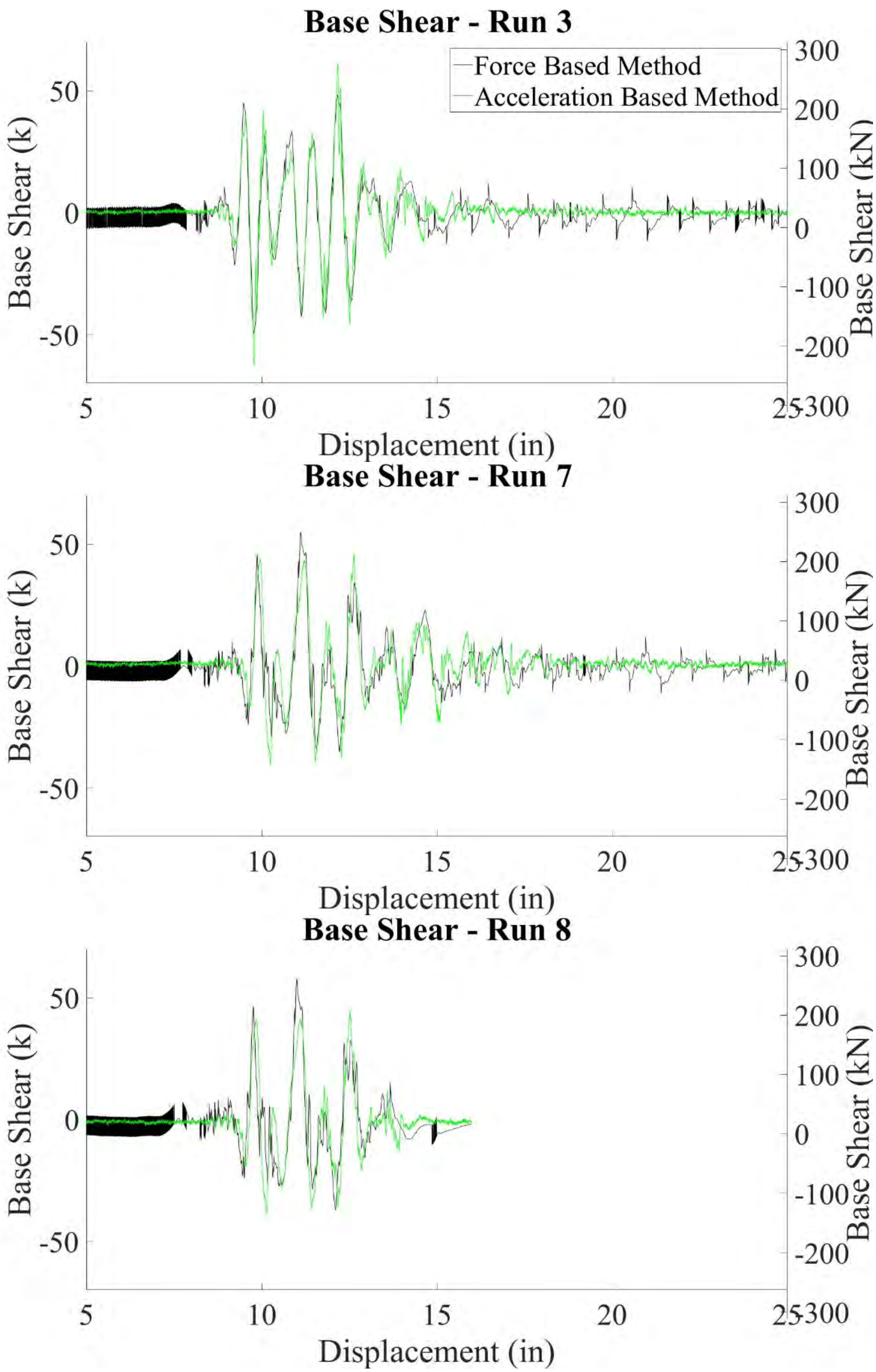

Figure 6.52 Comparison of force-based and acceleration-based base shear, transverse

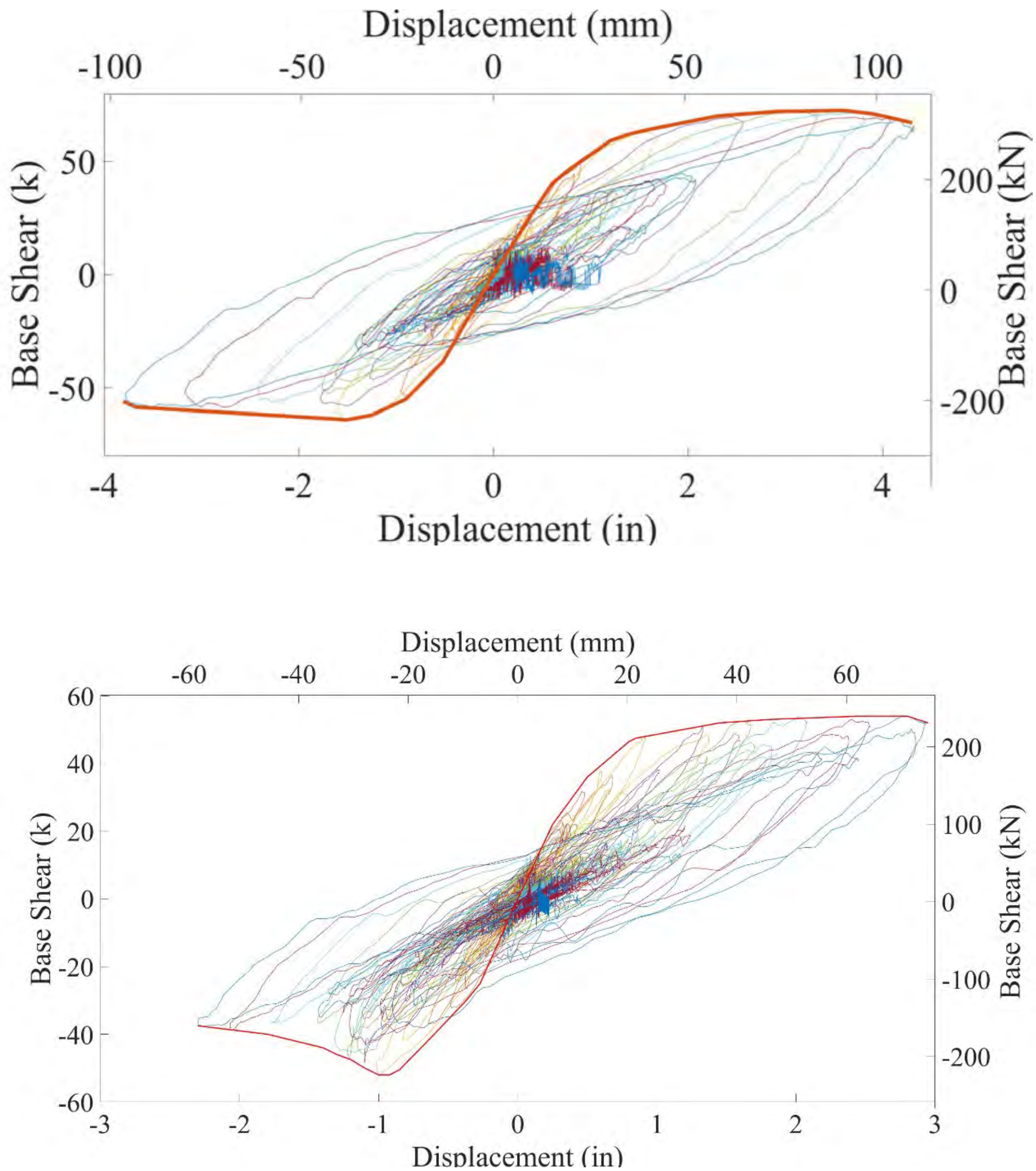

Figure 6.53 Cumulative force-displacement hysteresis curves with envelope in longitudinal (top) and transverse (bottom) directions

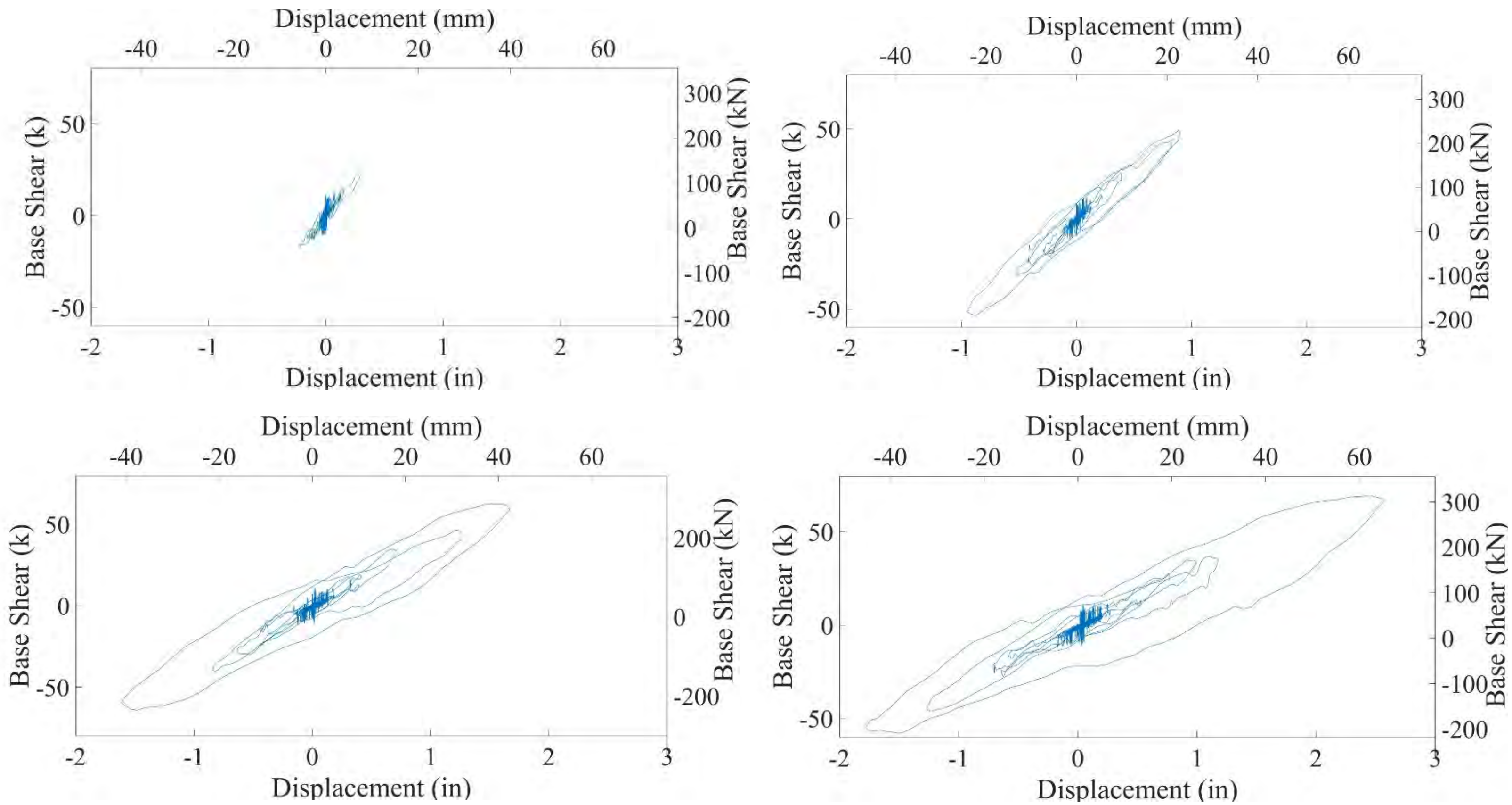

Figure 6.54 Force-displacement hysteresis curves for longitudinal direction, runs 1-4

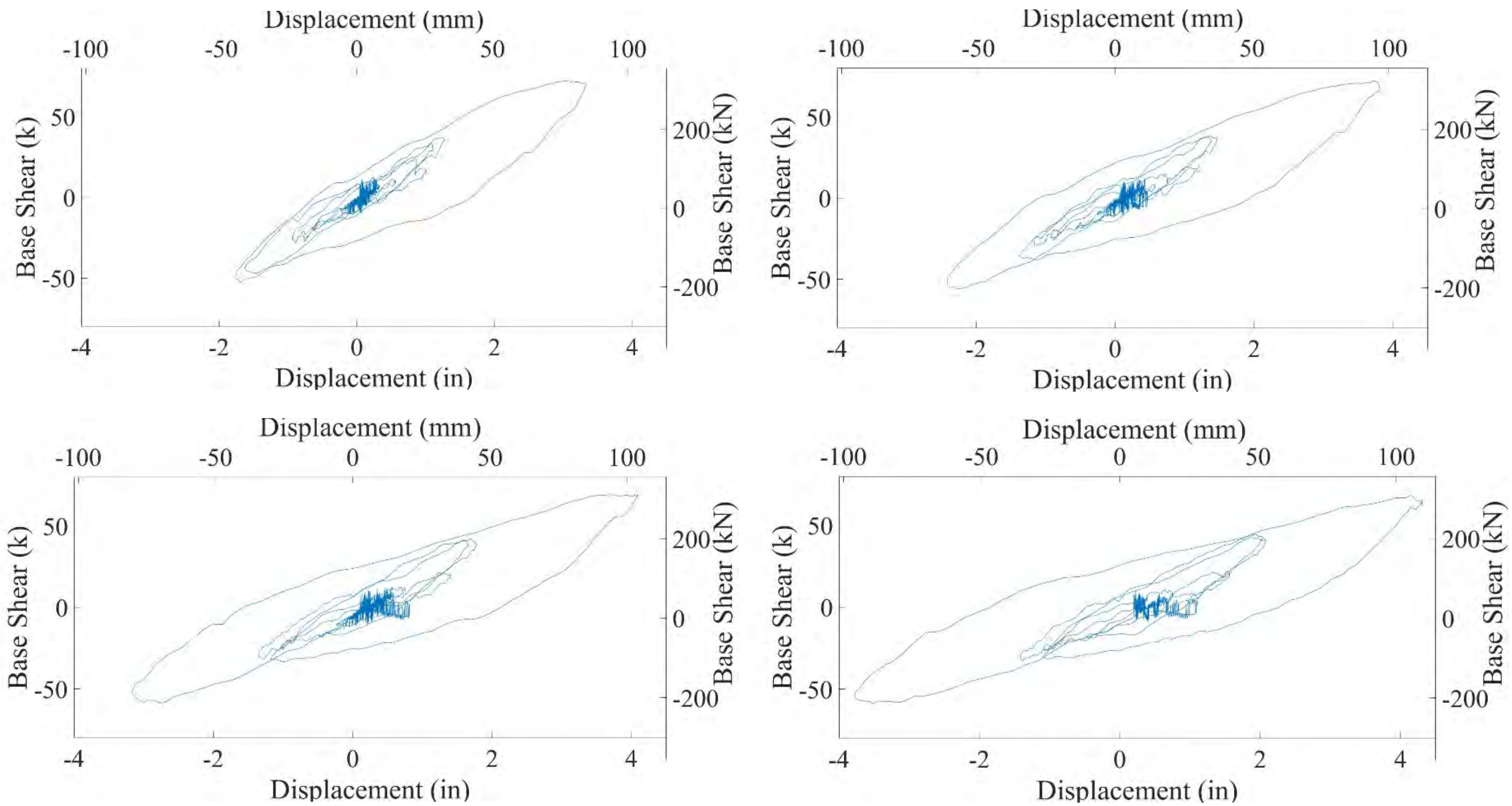

Figure 6.55 Force-displacement hysteresis curves for longitudinal direction, runs 5-8

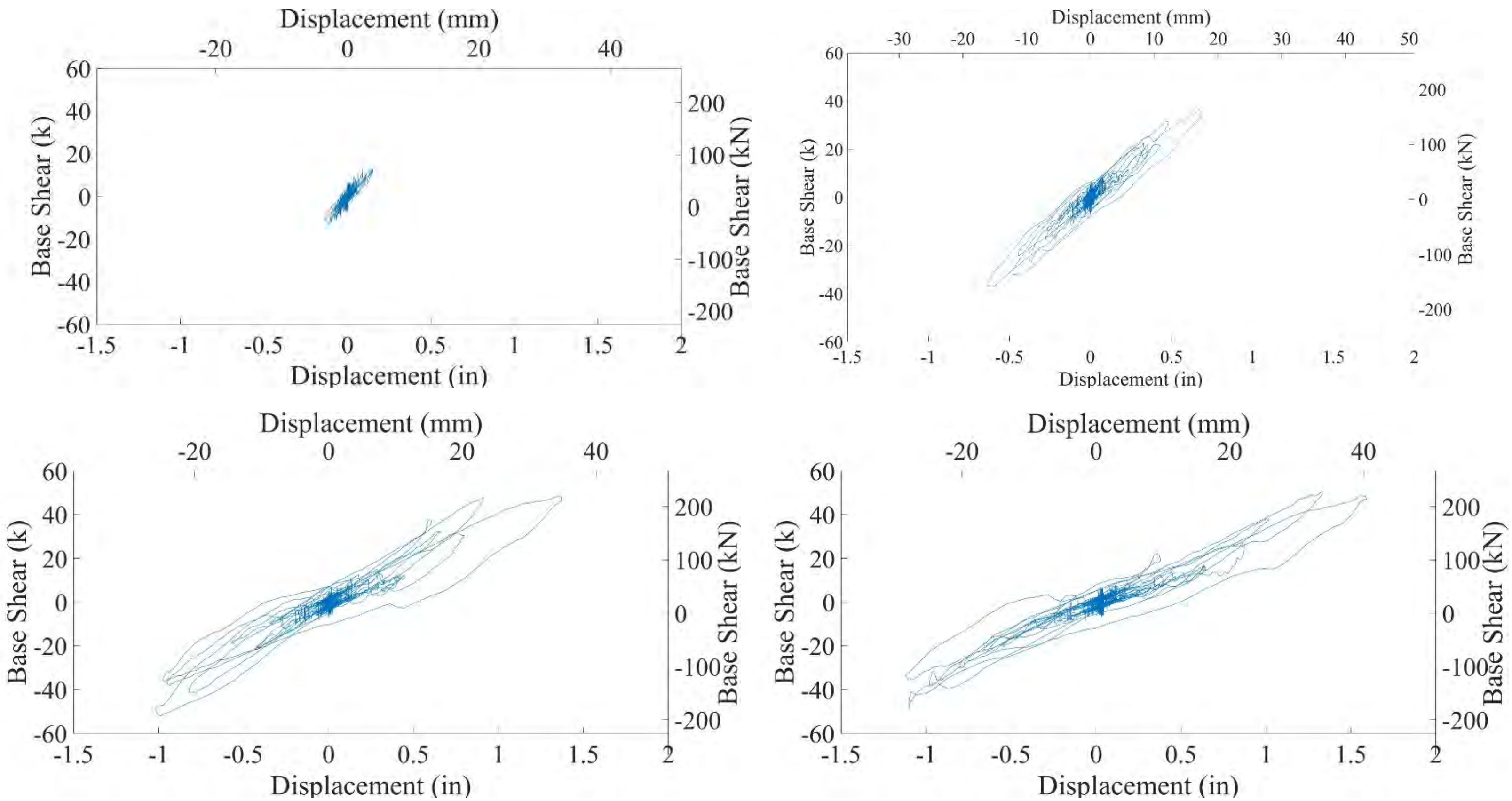

Figure 6.56 Force-displacement hysteresis curves for transverse direction, runs 1-4

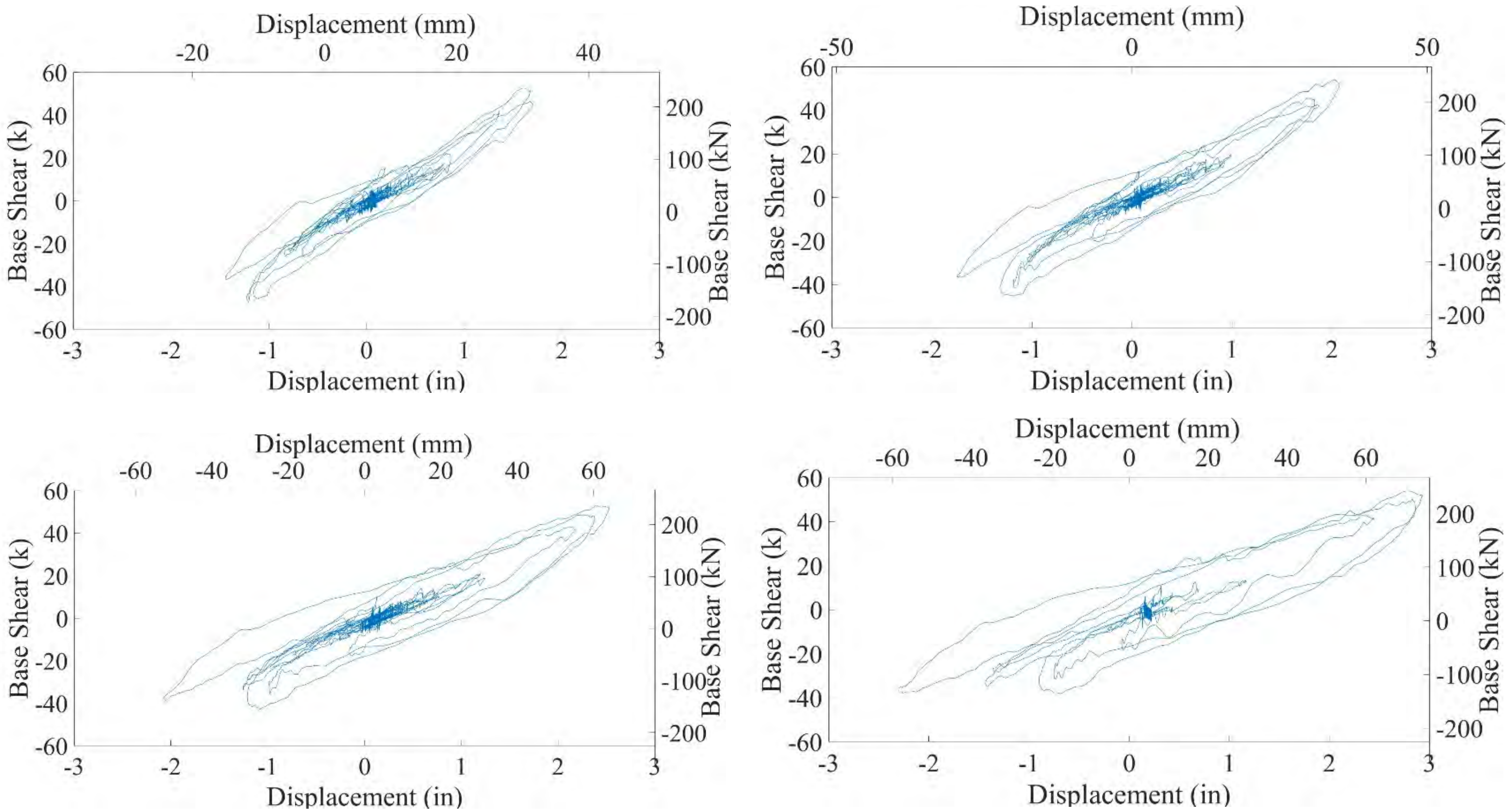

Figure 6.57 Force-displacement hysteresis curves for transverse direction, runs 5-8

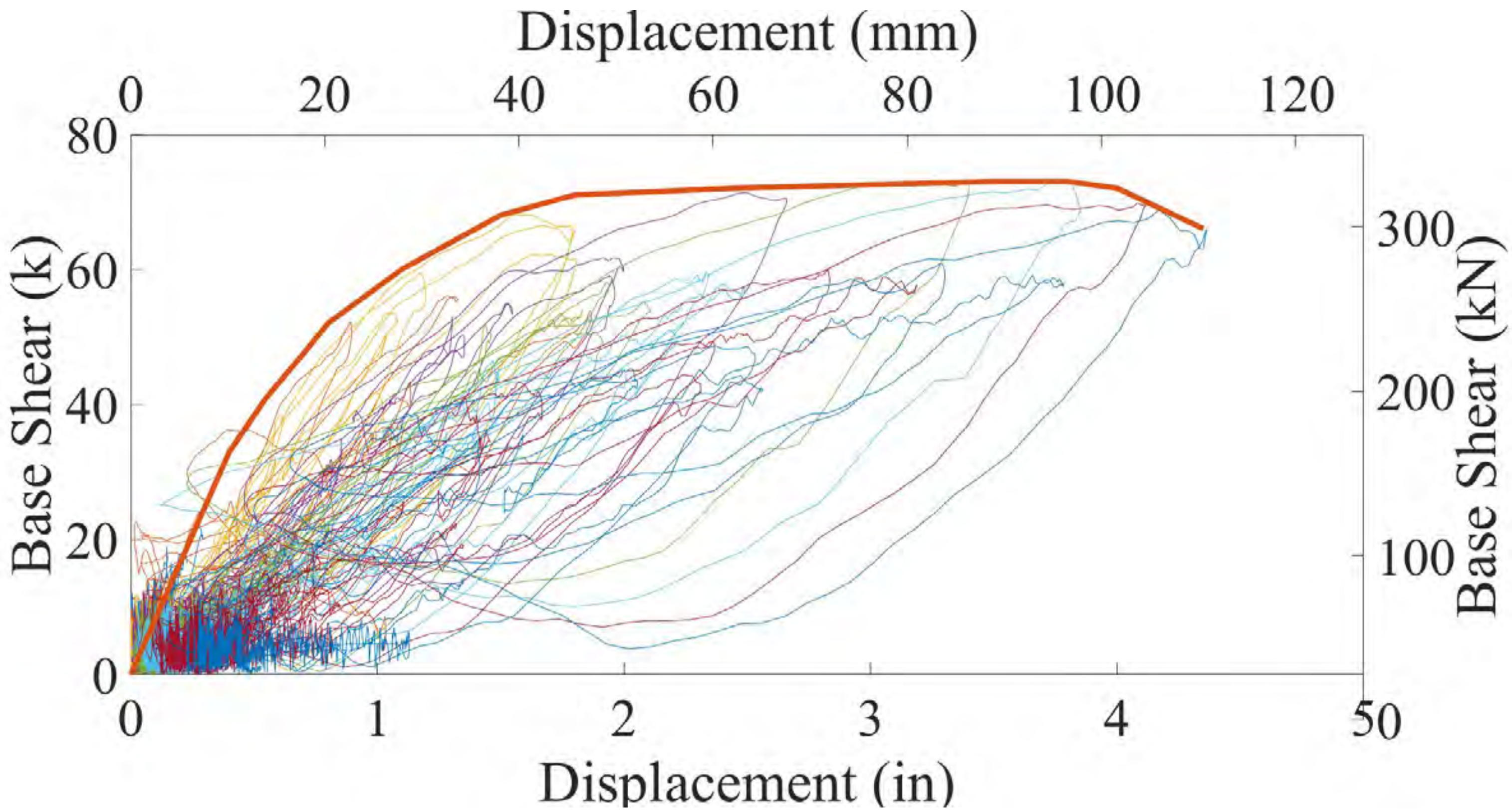

Figure 6.58 Cumulative force displacement hysteresis curve for resultant

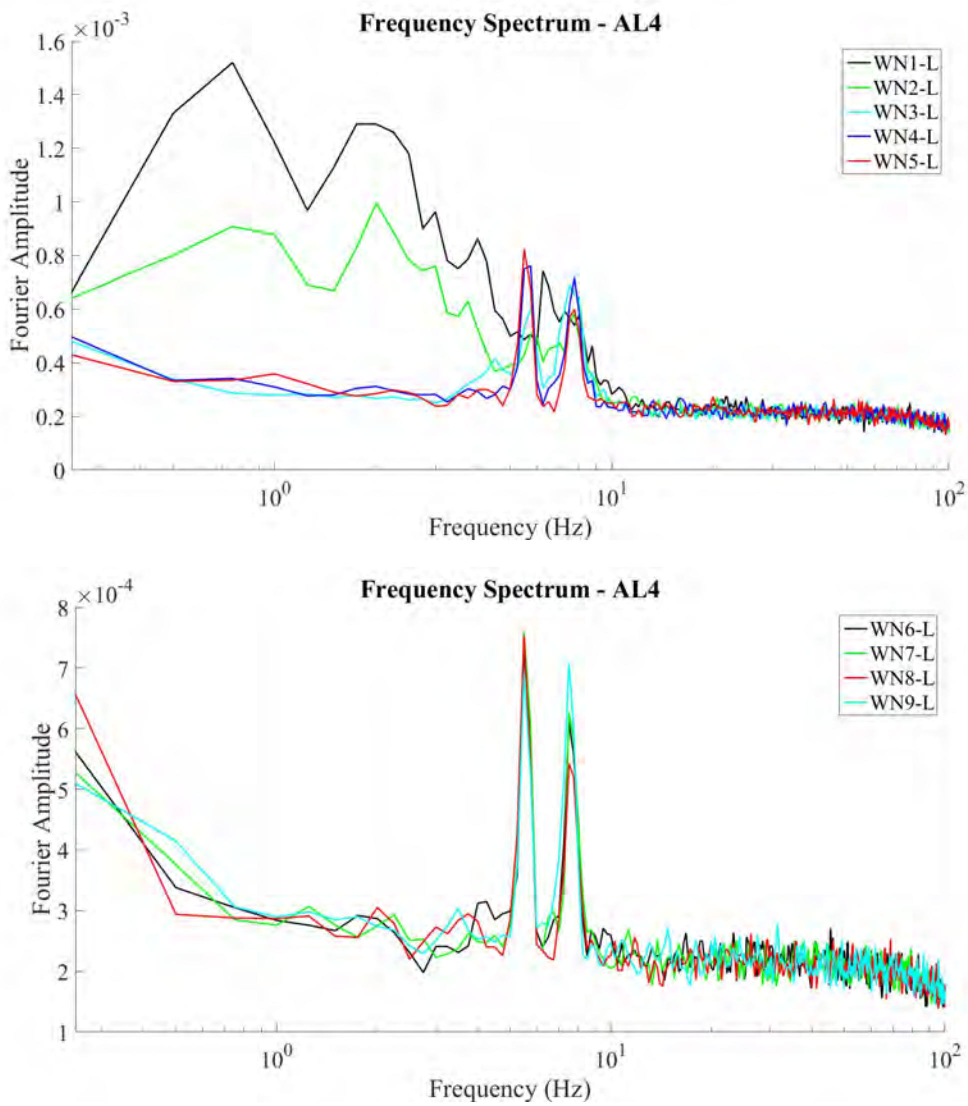

Figure 6.59 Fast-Fourier transform of white noise accelerations for longitudinal direction

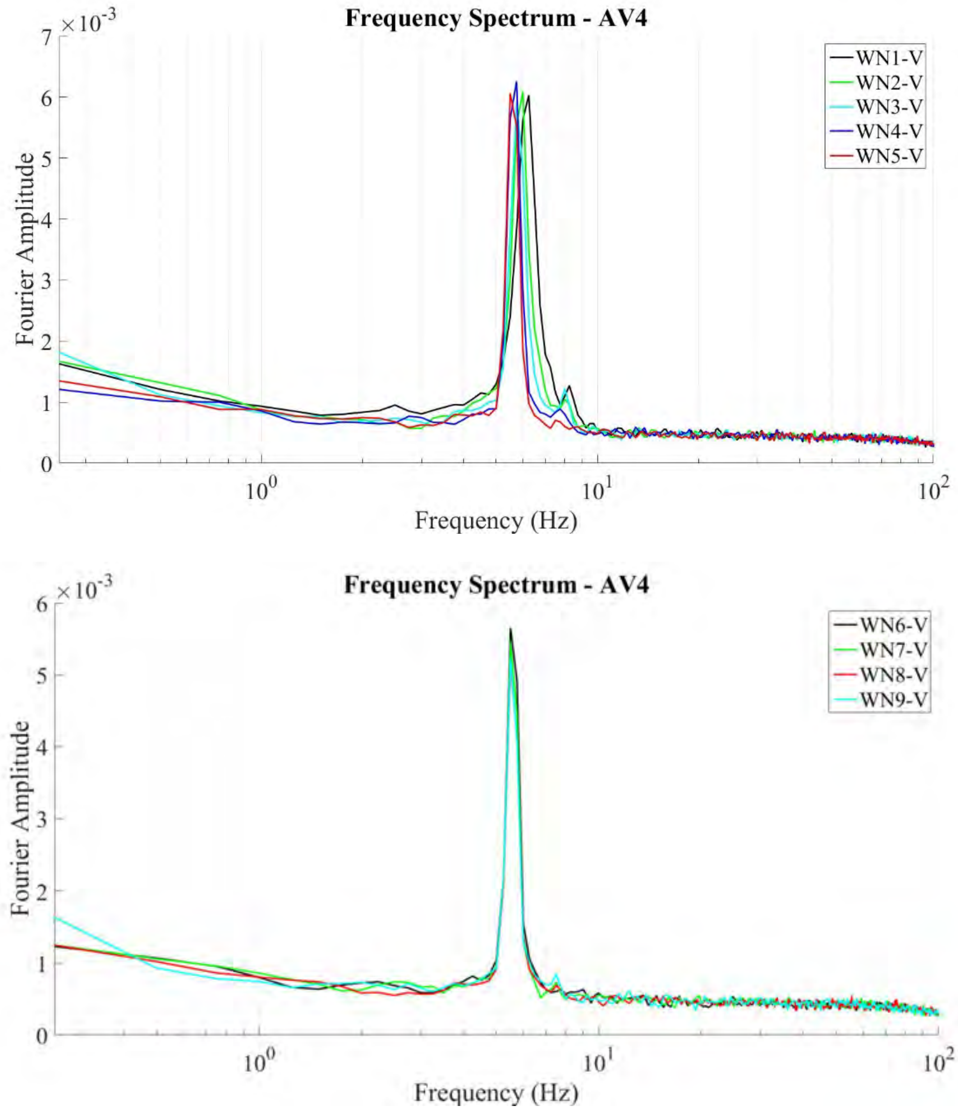

Figure 6.60 Fast-Fourier transform of white noise accelerations for vertical direction

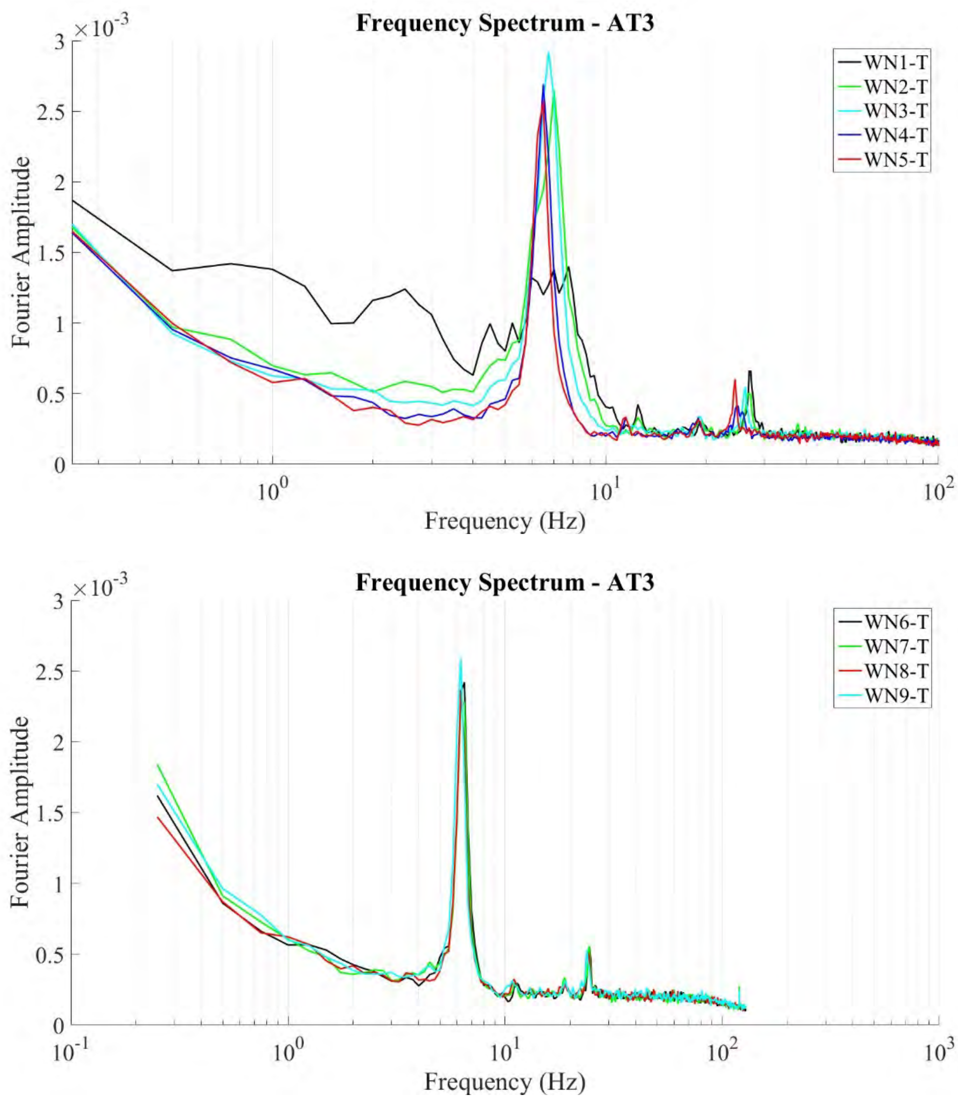

Figure 6.61 Fast-Fourier transform of white noise accelerations for transverse direction

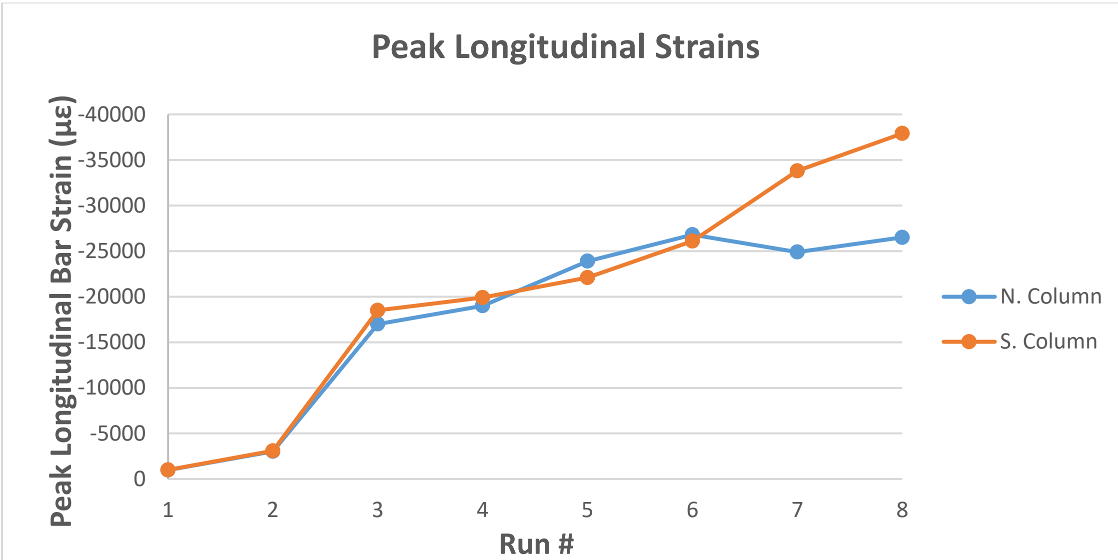

Figure 6.62 Column bar peak strains in different runs

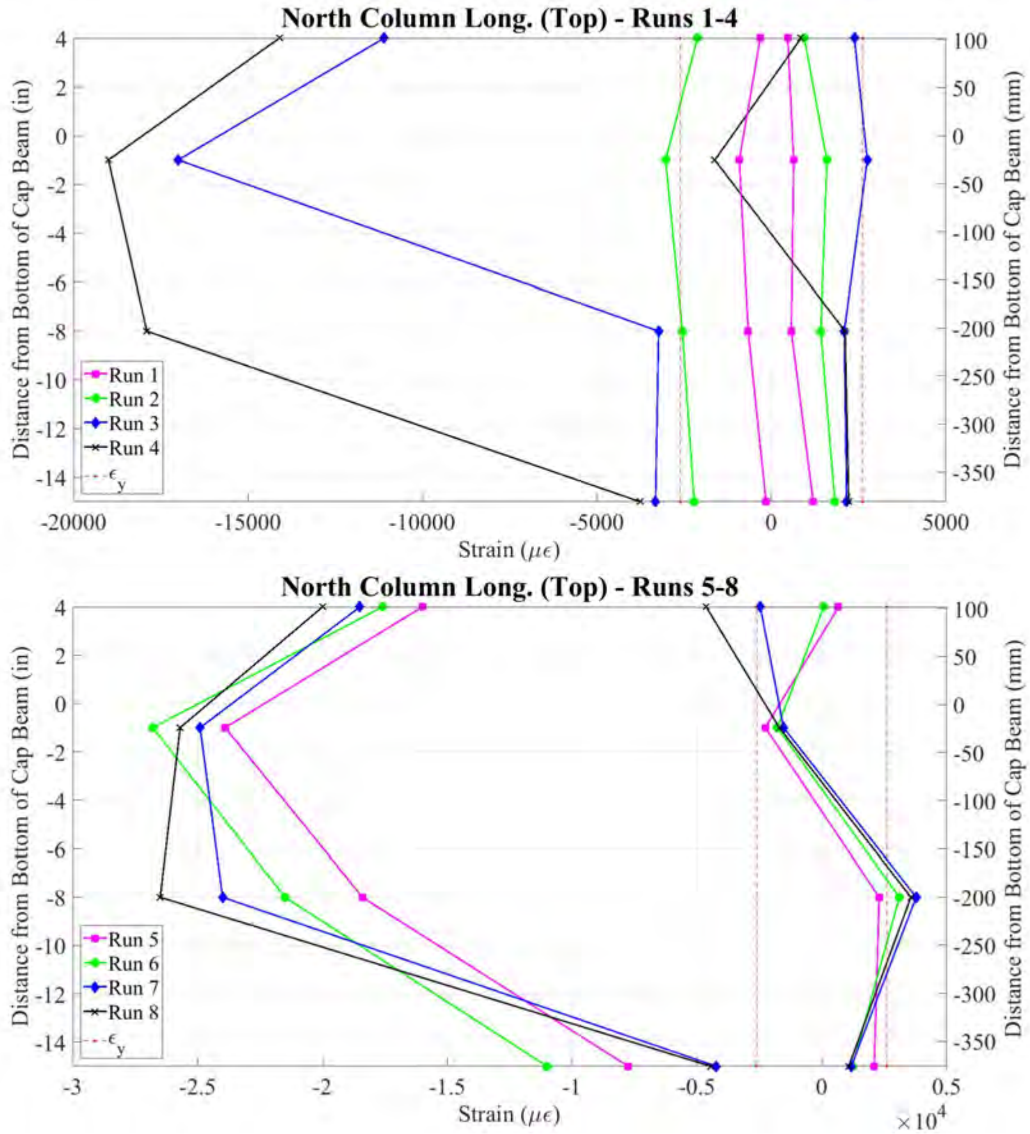

Figure 6.63 Column strain profiles for the longitudinal bars in the top of the north column in the plastic hinge, runs 1-4 (top), runs 5-8 (bottom)

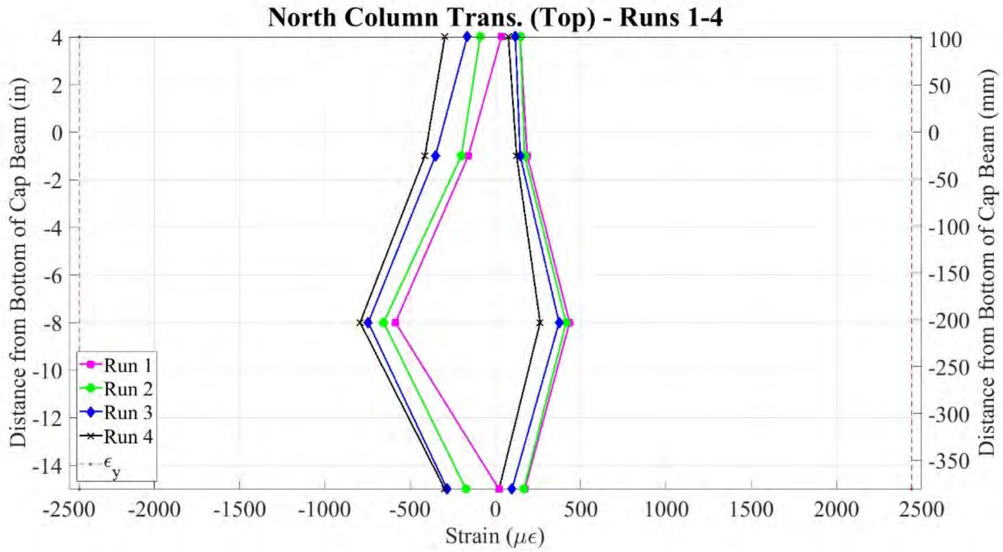

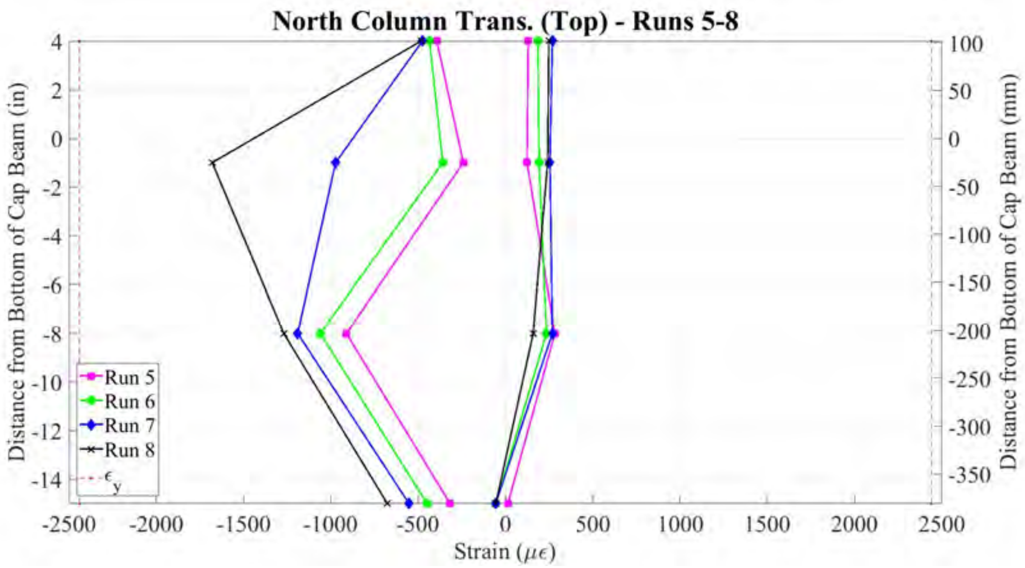

Figure 6.64 Column strain profiles for the spirals in the top of the north column in the plastic hinge, runs 1-4 (top), runs 5-8 (bottom)

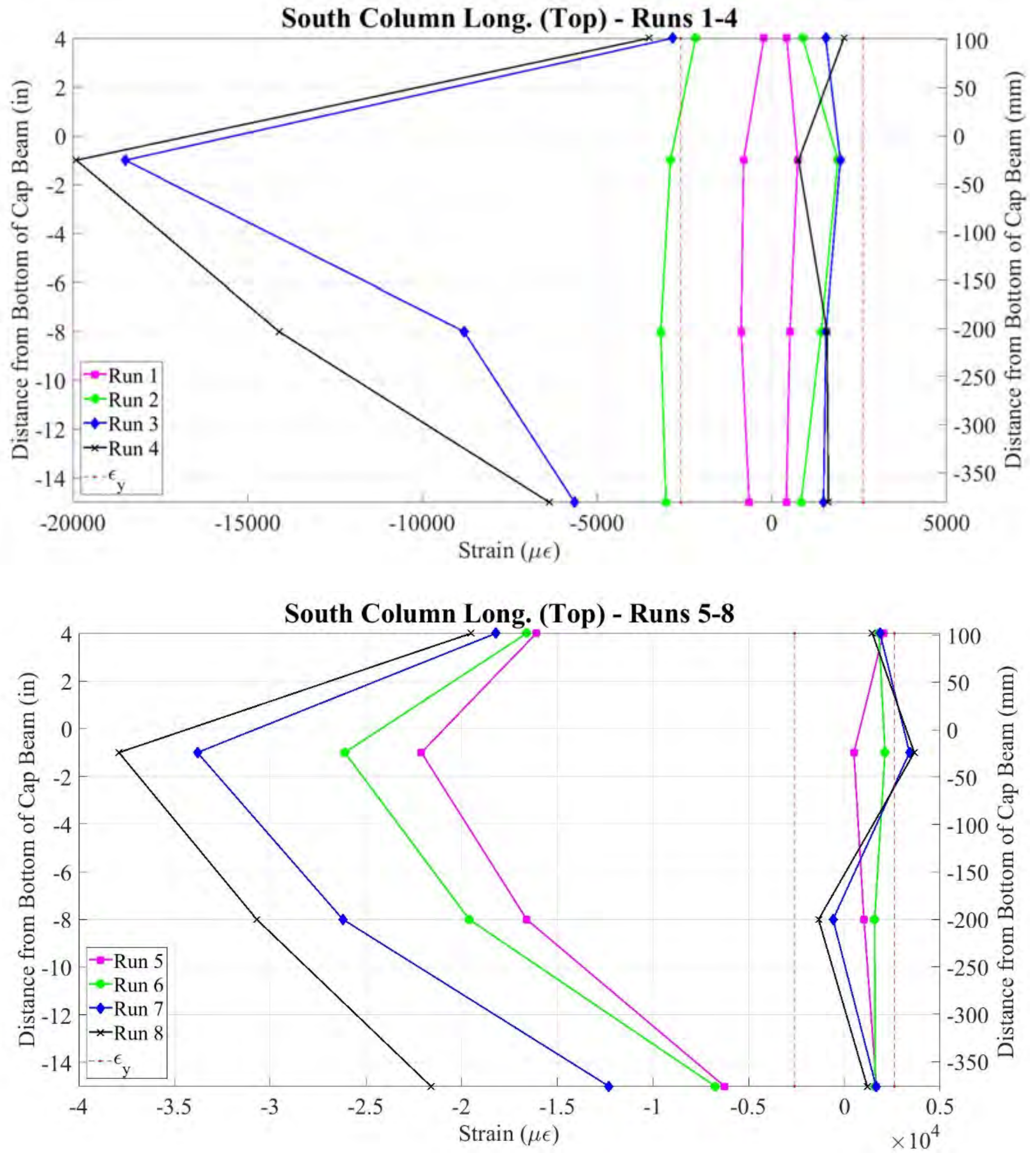

Figure 6.65 Column strain profiles for the longitudinal bars in the top of the south column in the plastic hinge, runs 1-4 (top), runs 5-8 (bottom)

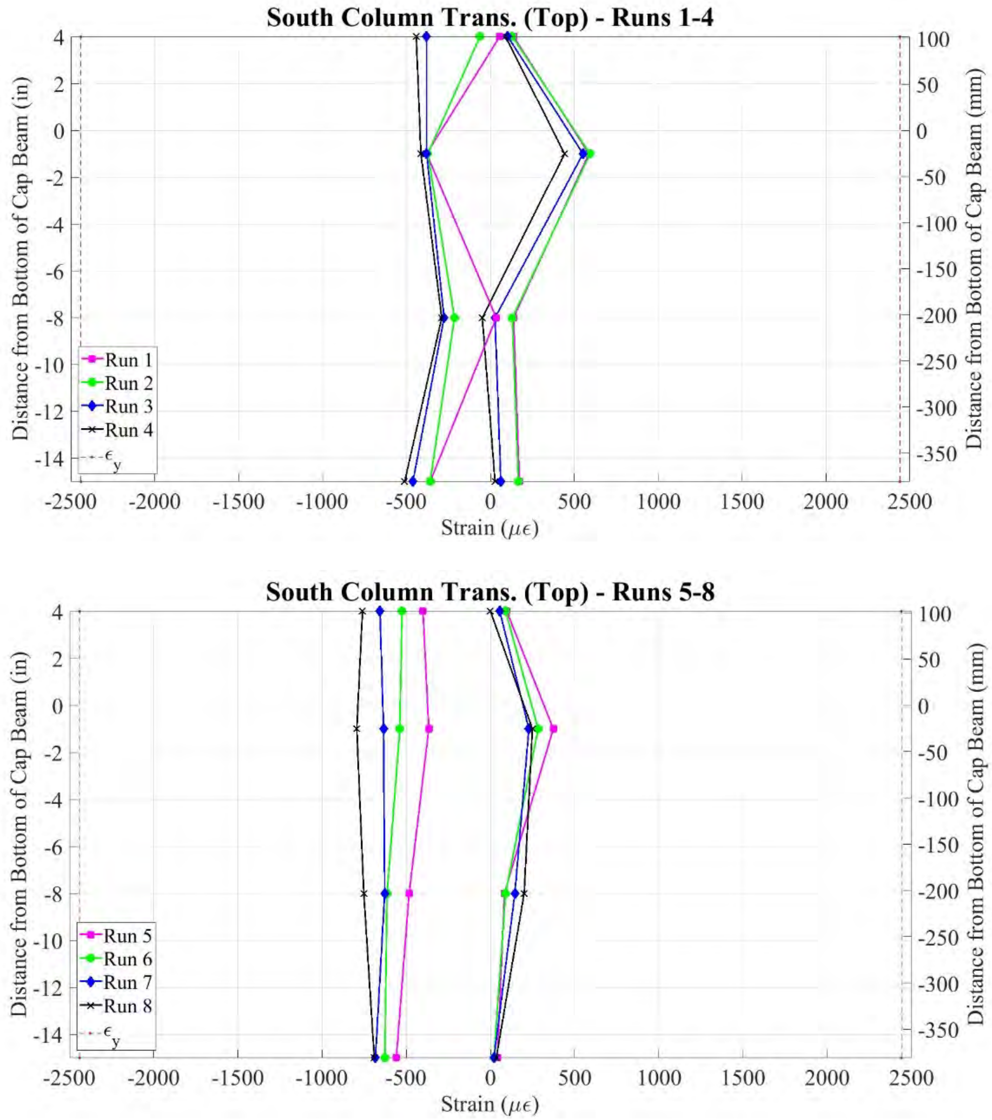

Figure 6.66 Column strain profiles for the spirals in the top of the south column in the plastic hinge, runs 1-4 (top), runs 5-8 (bottom)

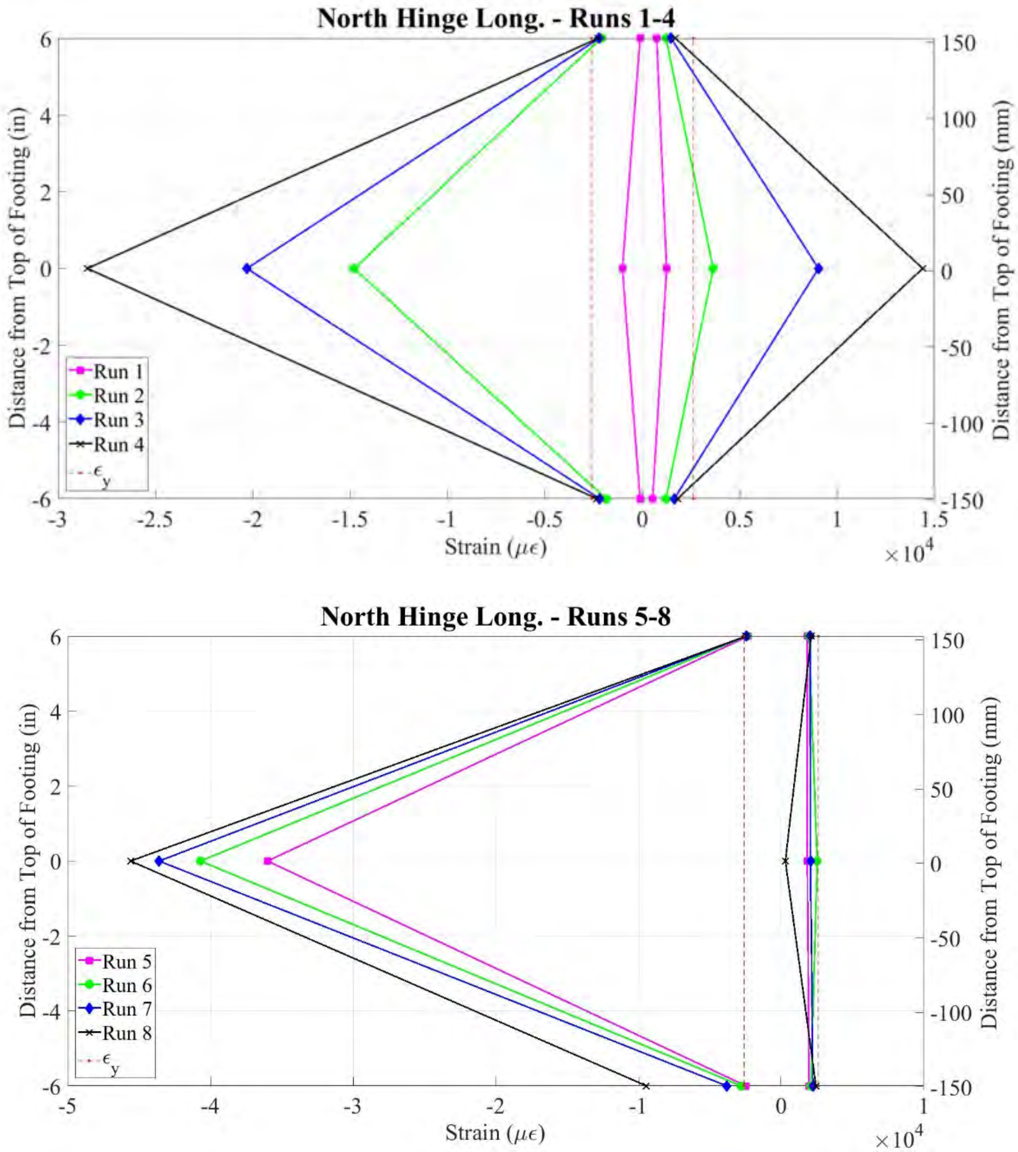

Figure 6.67 Column strain profiles for the longitudinal bars in the north rebar hinge, runs 1-4 (top), runs 5-8 (bottom)

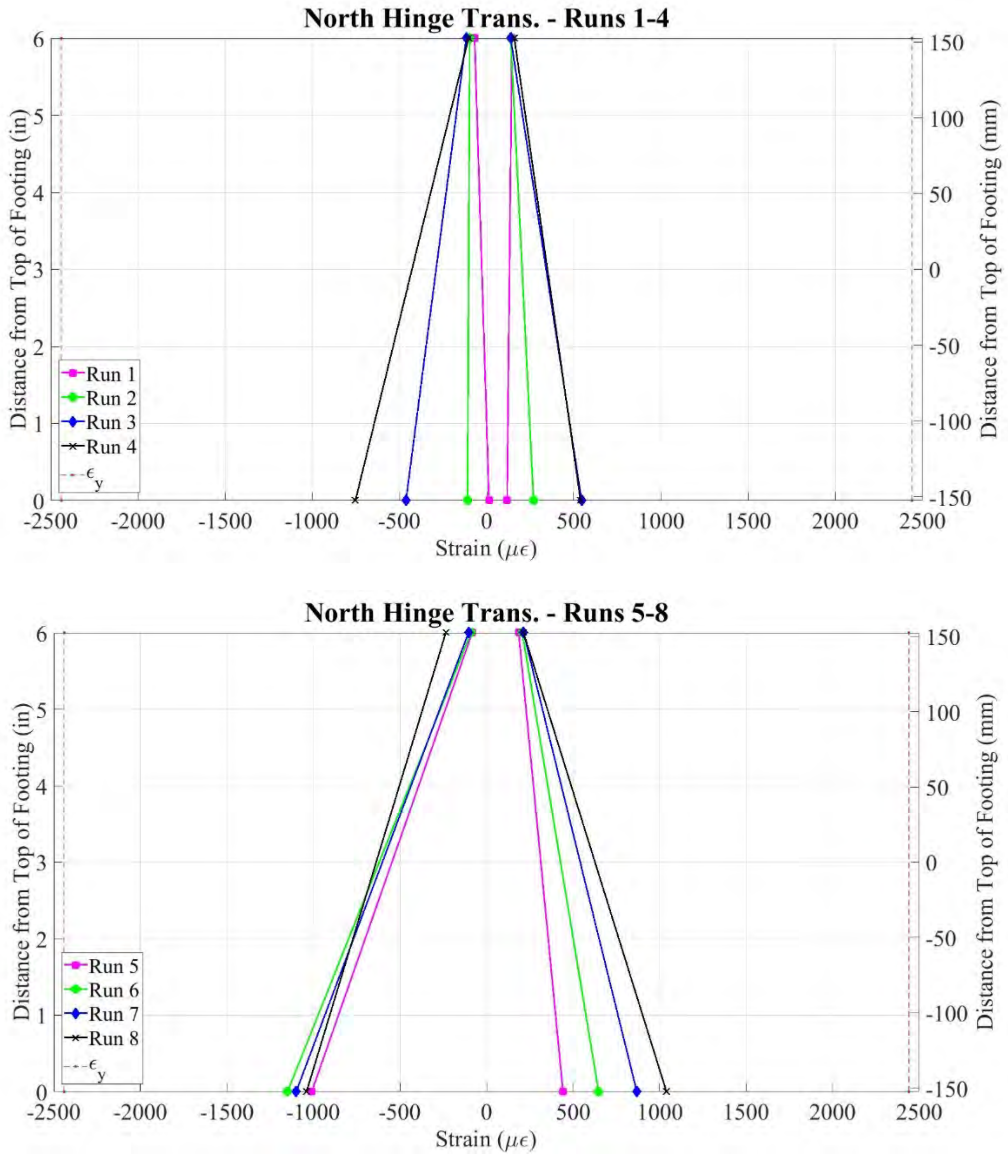

Figure 6.68 Column strain profiles for the spirals in the north rebar hinge, runs 1-4 (top), runs 5-8 (bottom)

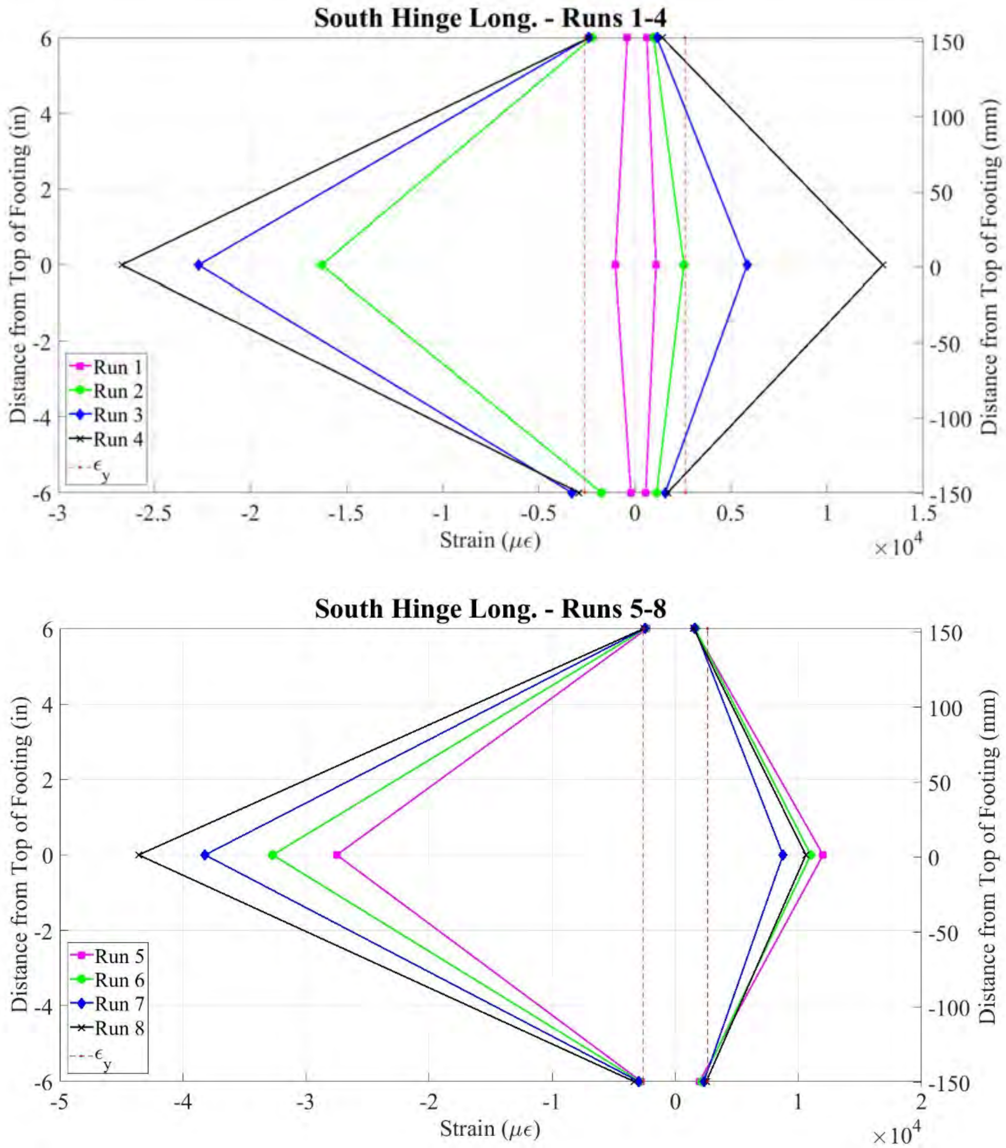

Figure 6.69 Column strain profiles for the longitudinal bars in the south rebar hinge, runs 1-4 (top), runs 5-8 (bottom)

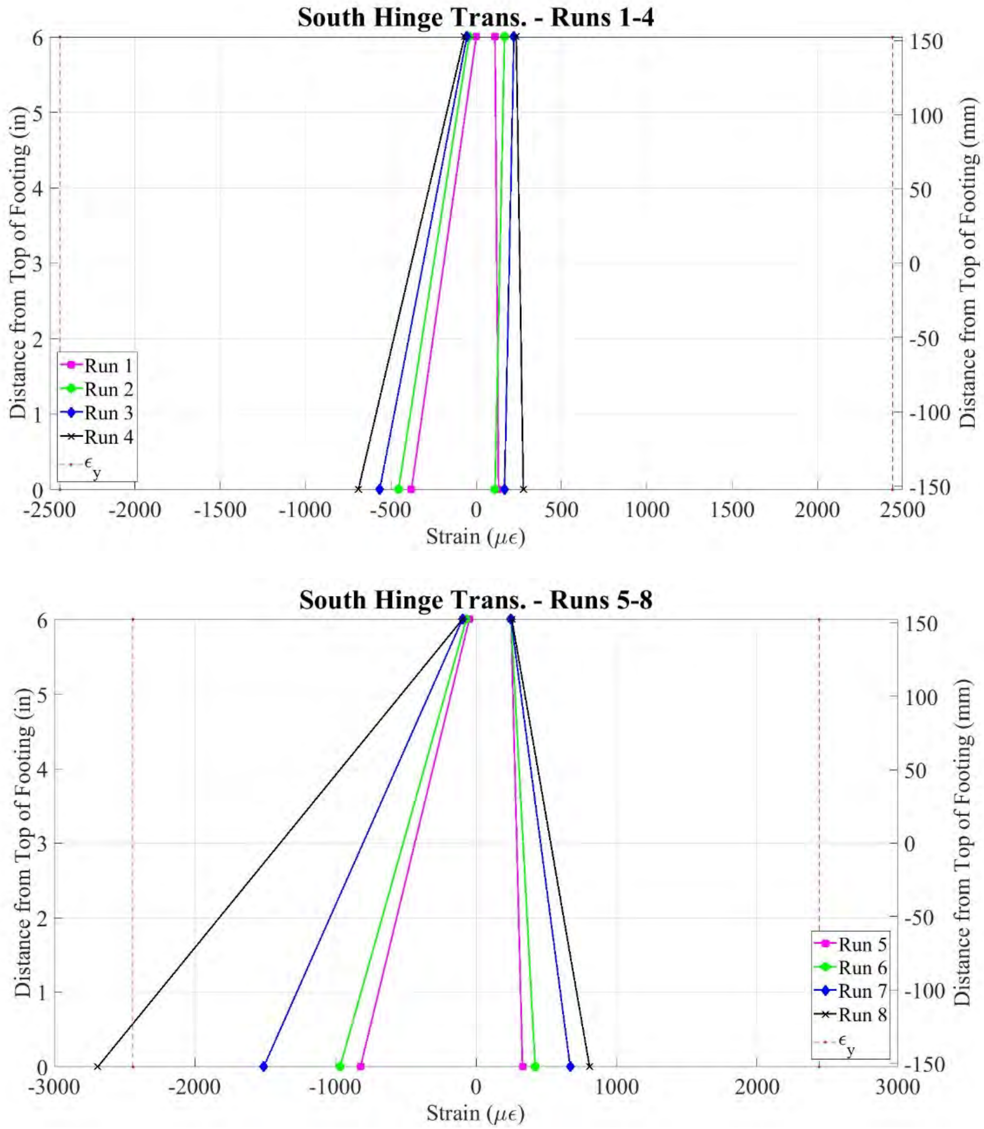

Figure 6.70 Column strain profiles for the spirals in the south rebar hinge, runs 1-4 (top), runs 5-8 (bottom)

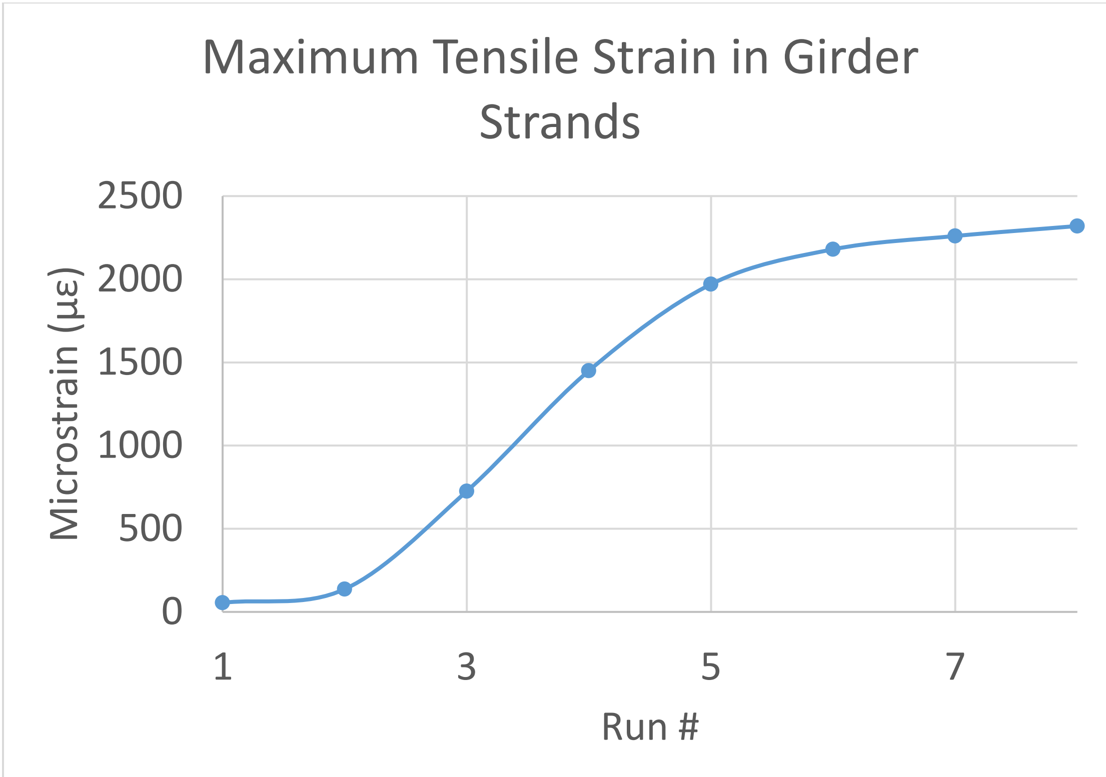

Figure 6.71 Maximum tensile strain in projected girder prestress strands, ε_y = 9379 με

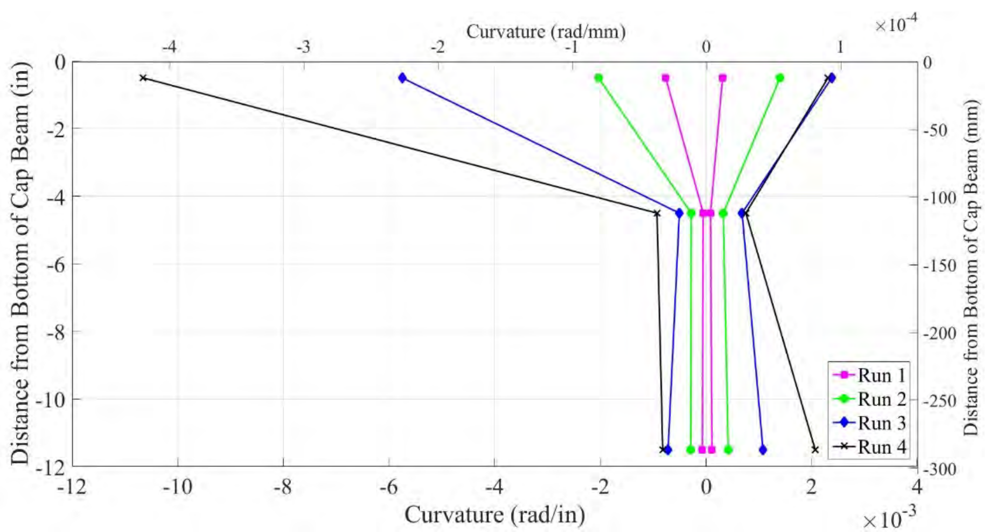

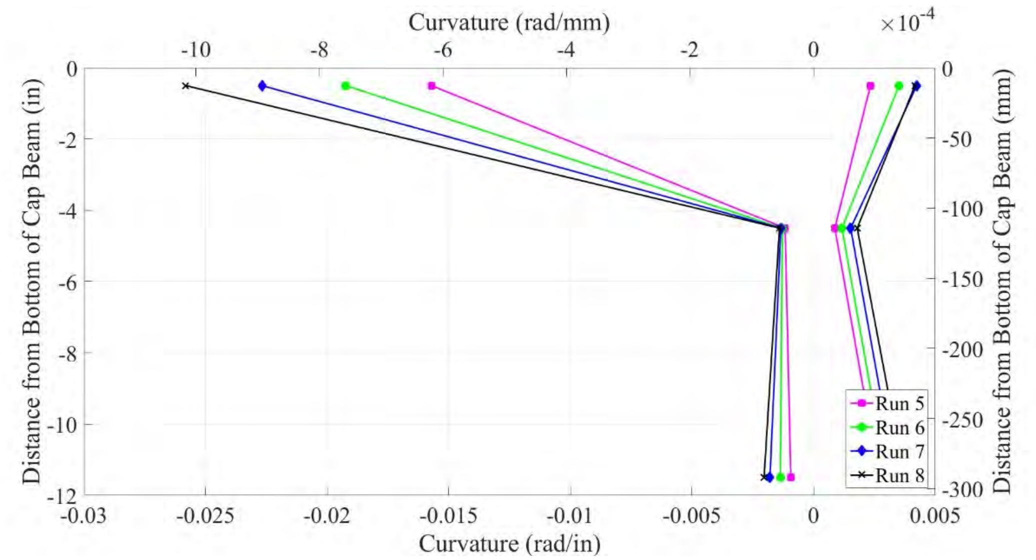

Figure 6.72 Curvature profile in north column plastic hinge associated with longitudinal movement of the bridge, runs 1-4 (top), runs 5-8 (bottom)

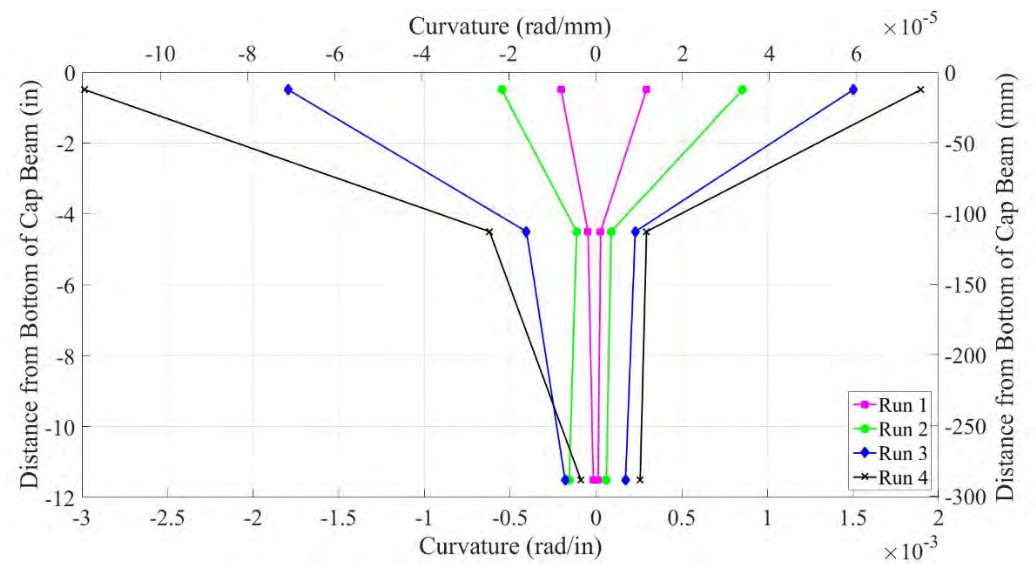

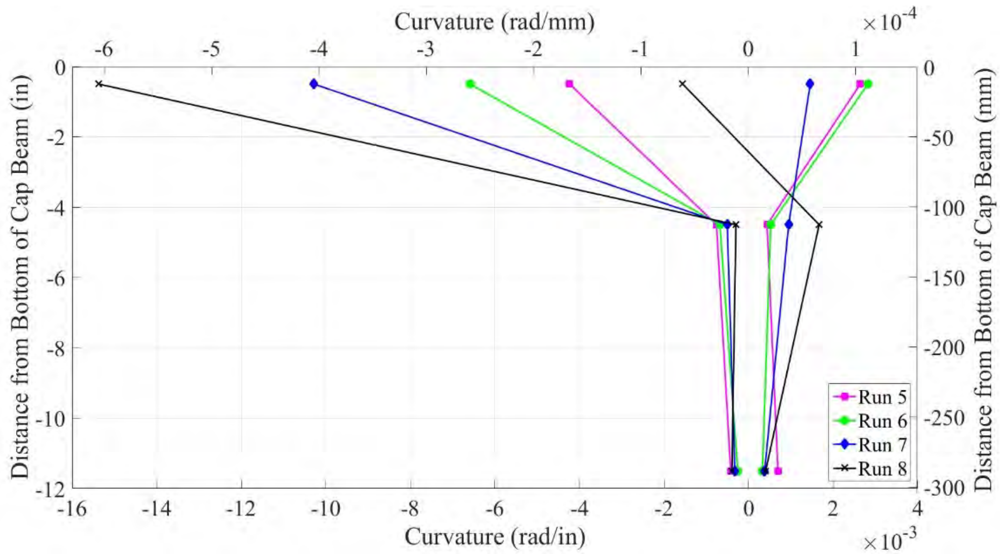

Figure 6.73 Curvature profile in north column plastic hinge associated with transverse movement of the bridge, runs 1-4 (top), runs 5-8 (bottom)

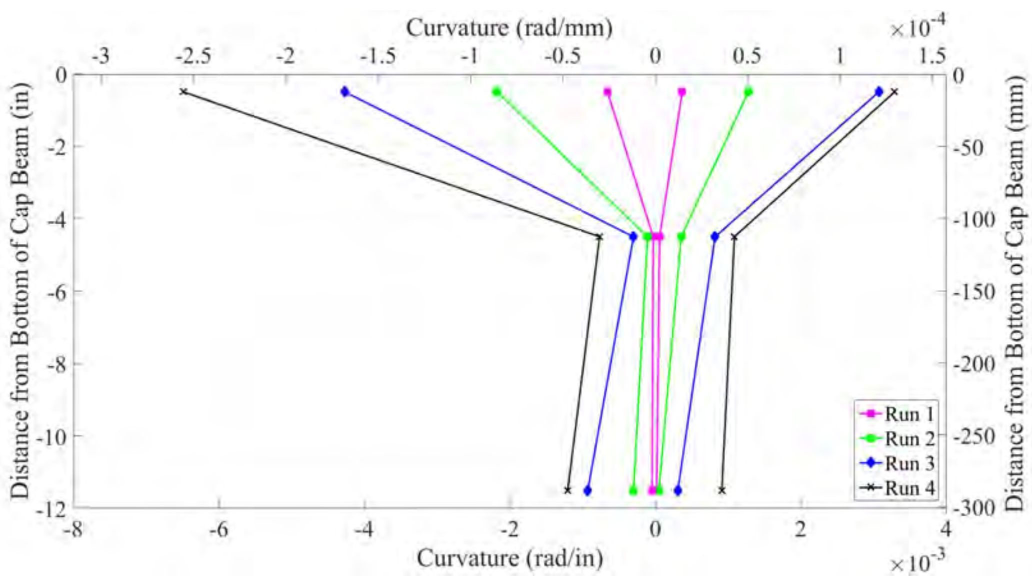

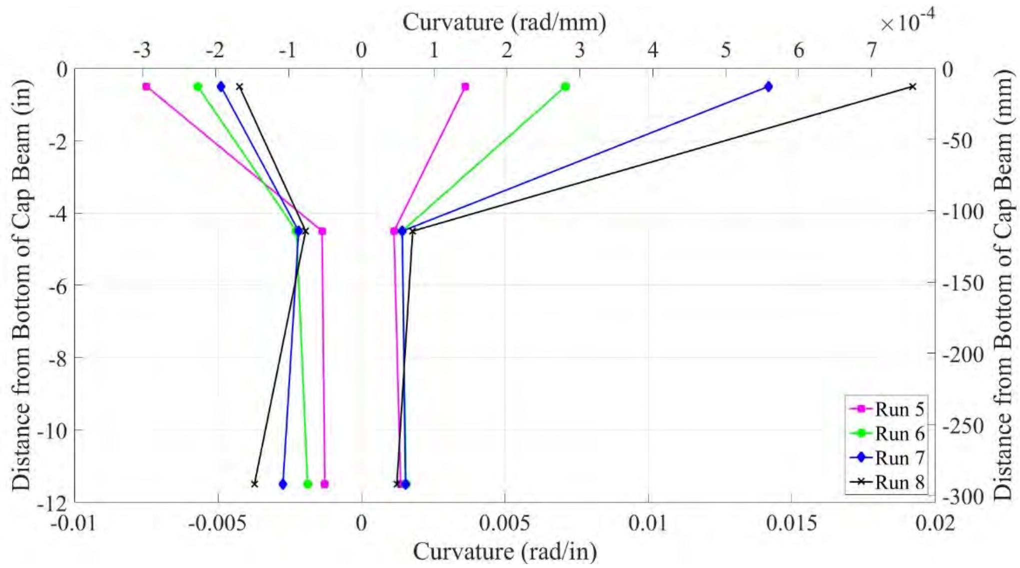

Figure 6.74 Curvature profile in south column plastic hinge associated with longitudinal movement of the bridge, runs 1-4 (top), runs 5-8 (bottom)

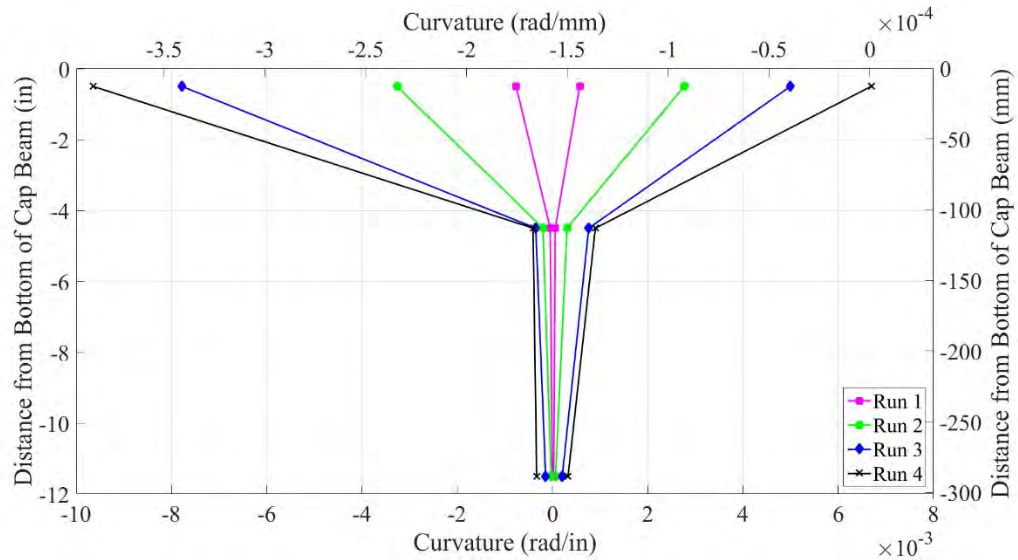

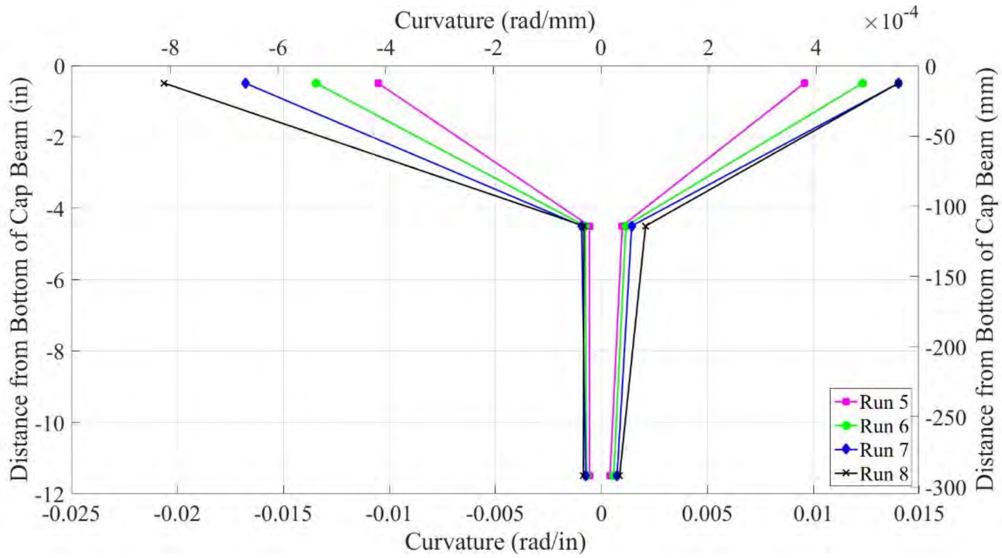

Figure 6.75 Curvature profile in south column plastic hinge associated with transverse movement of the bridge, runs 1-4 (top), runs 5-8 (bottom)

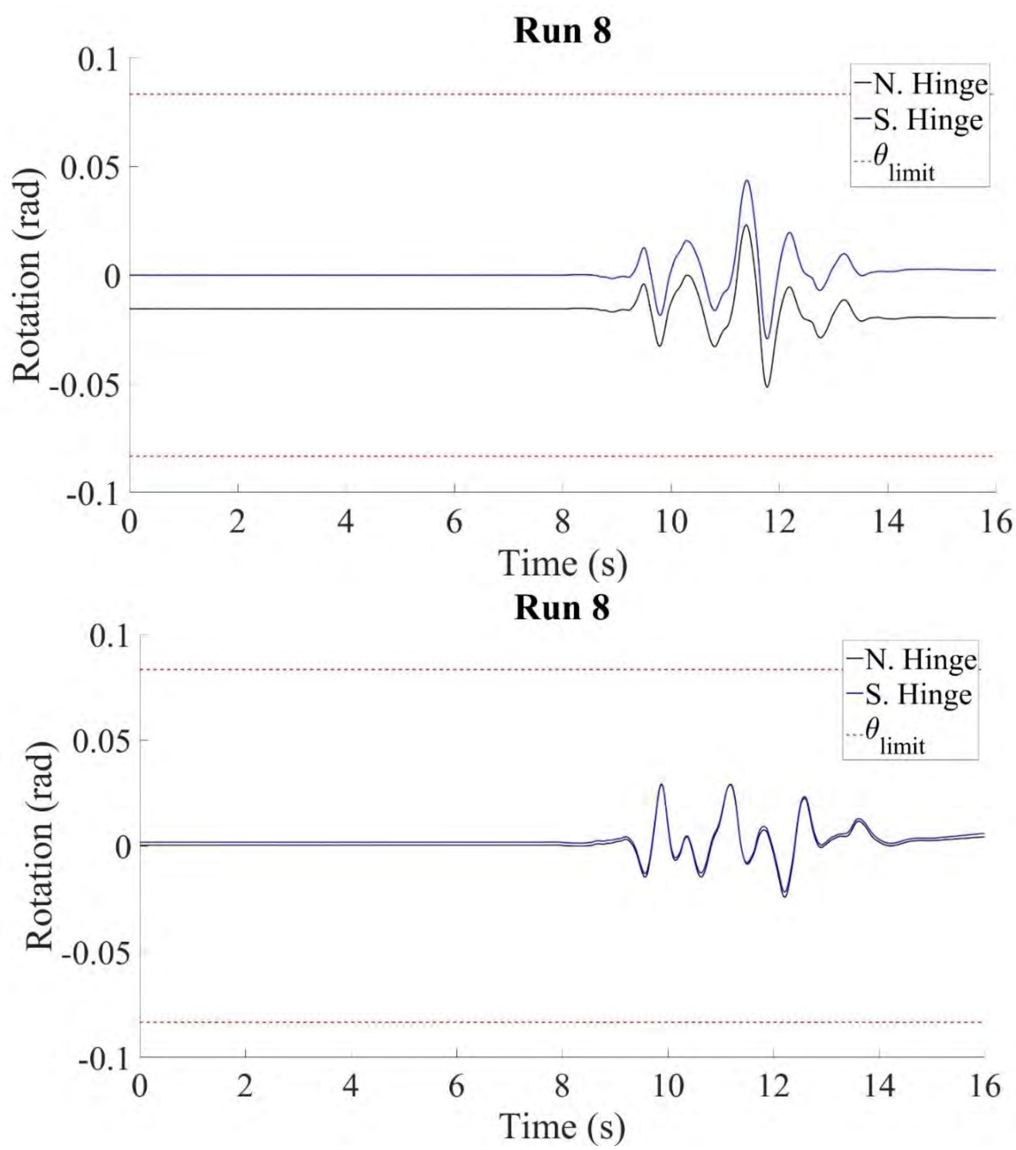

Figure 6.76 Hinge rotation associated with longitudinal (top) and transverse (bottom) movement of bridge, run 8

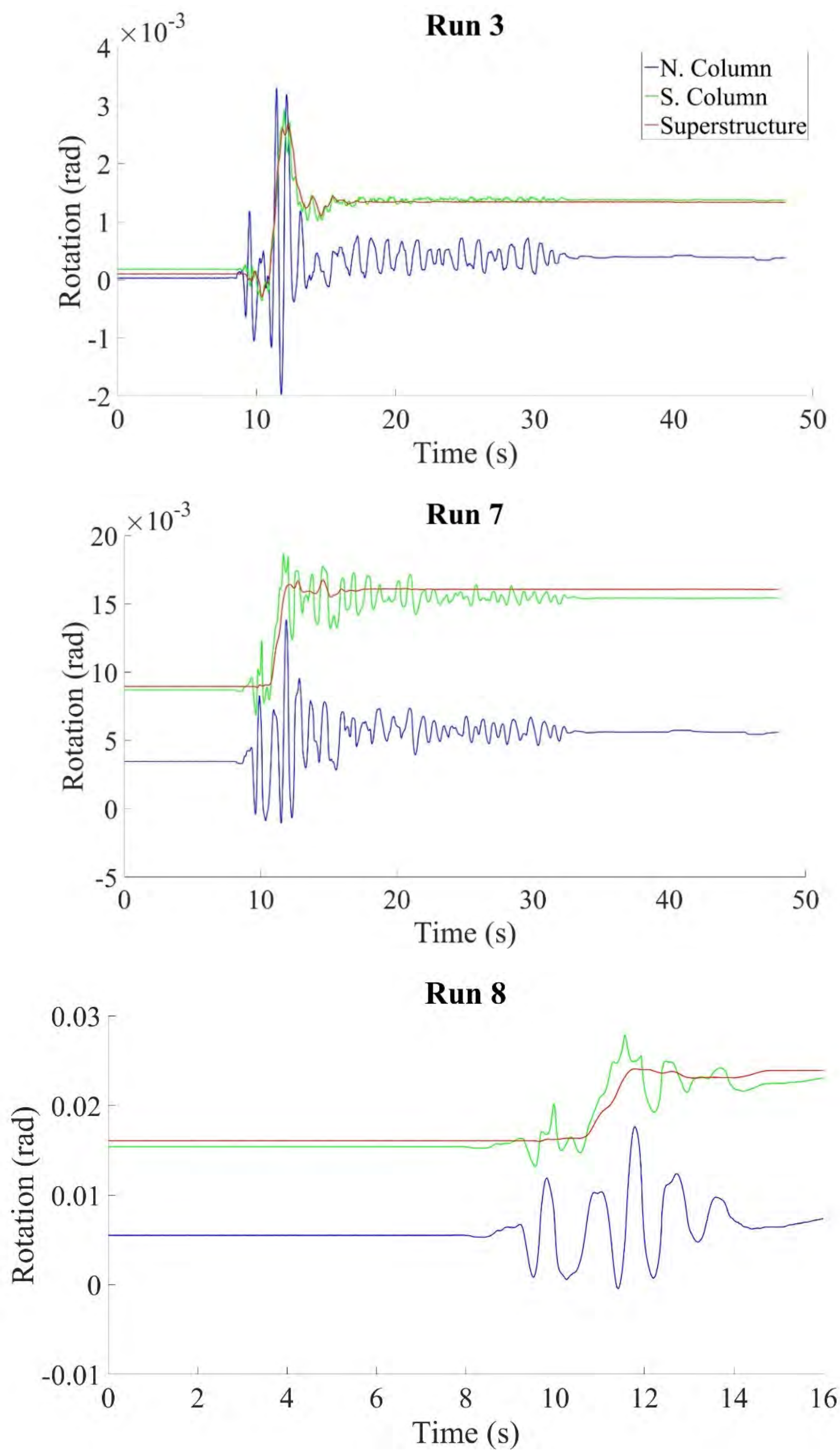

Figure 6.77 Angle of twist for both columns, runs 3, 7, and 8

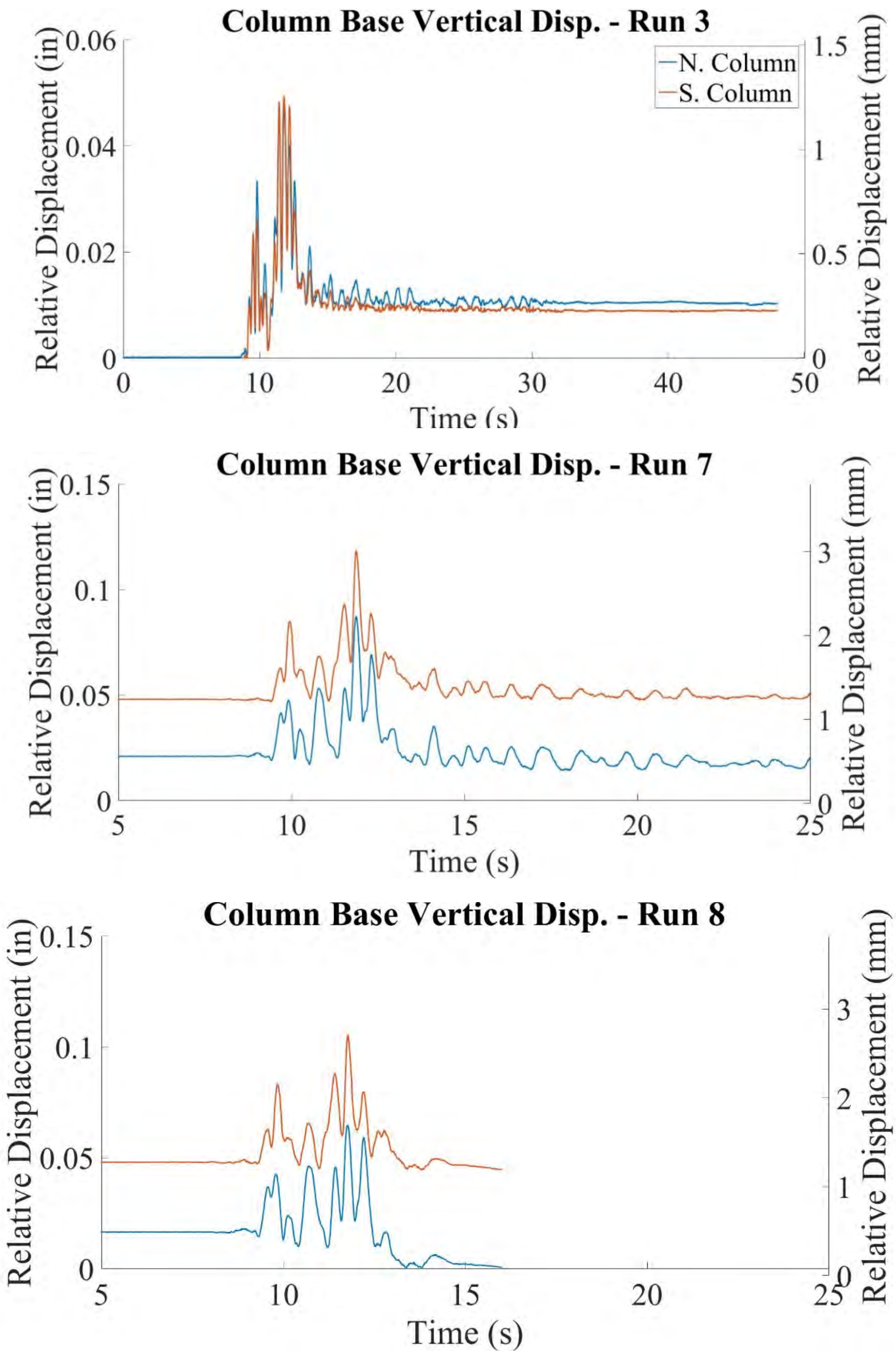

Figure 6.78 Relative vertical displacement at column base for runs 3, 7, and 8

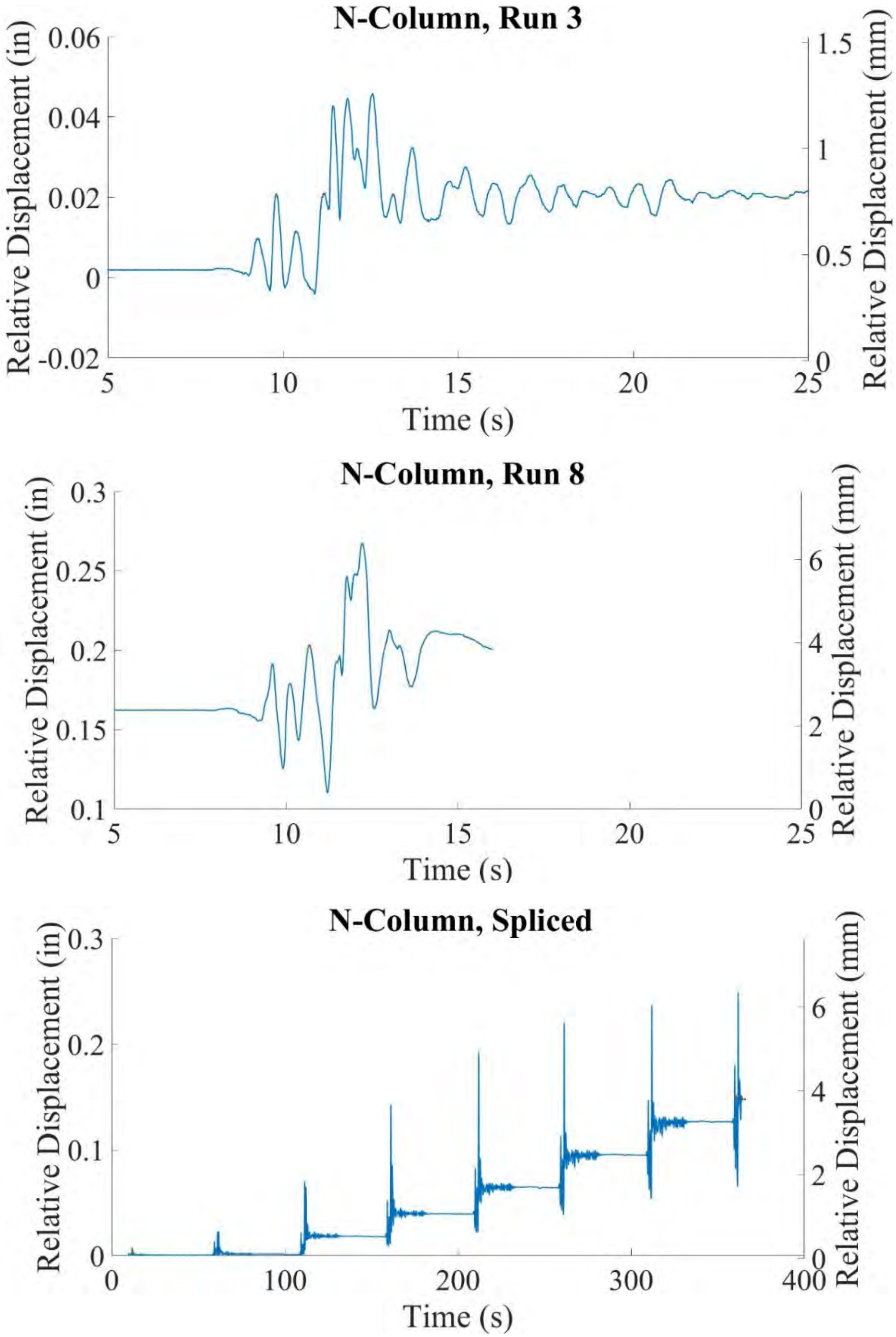

Figure 6.79 Relative displacement between pocket connection and north column runs 3, 8, and spliced

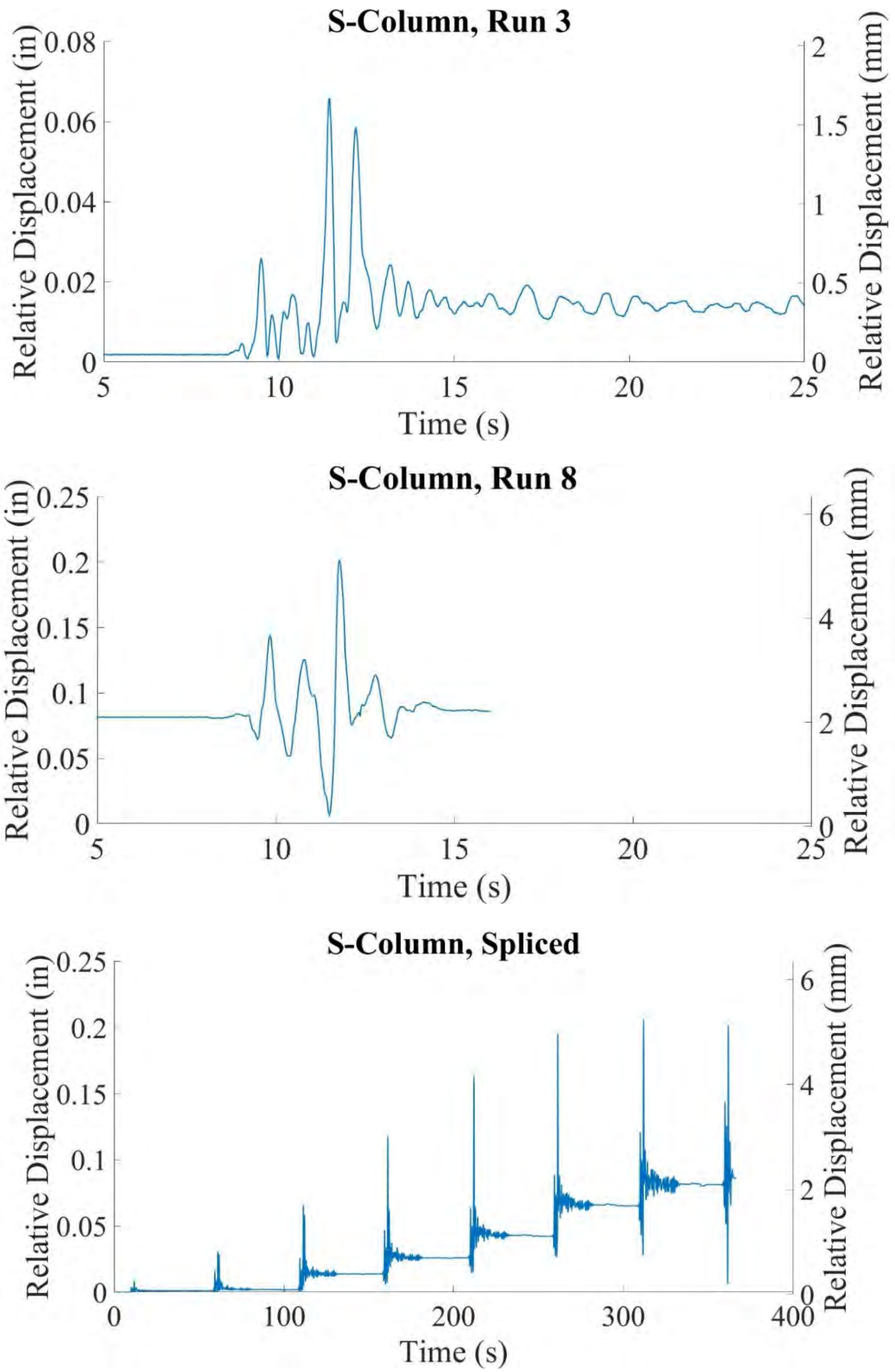

Figure 6.80 Relative displacement between pocket connection and south column runs 3, 8, and spliced

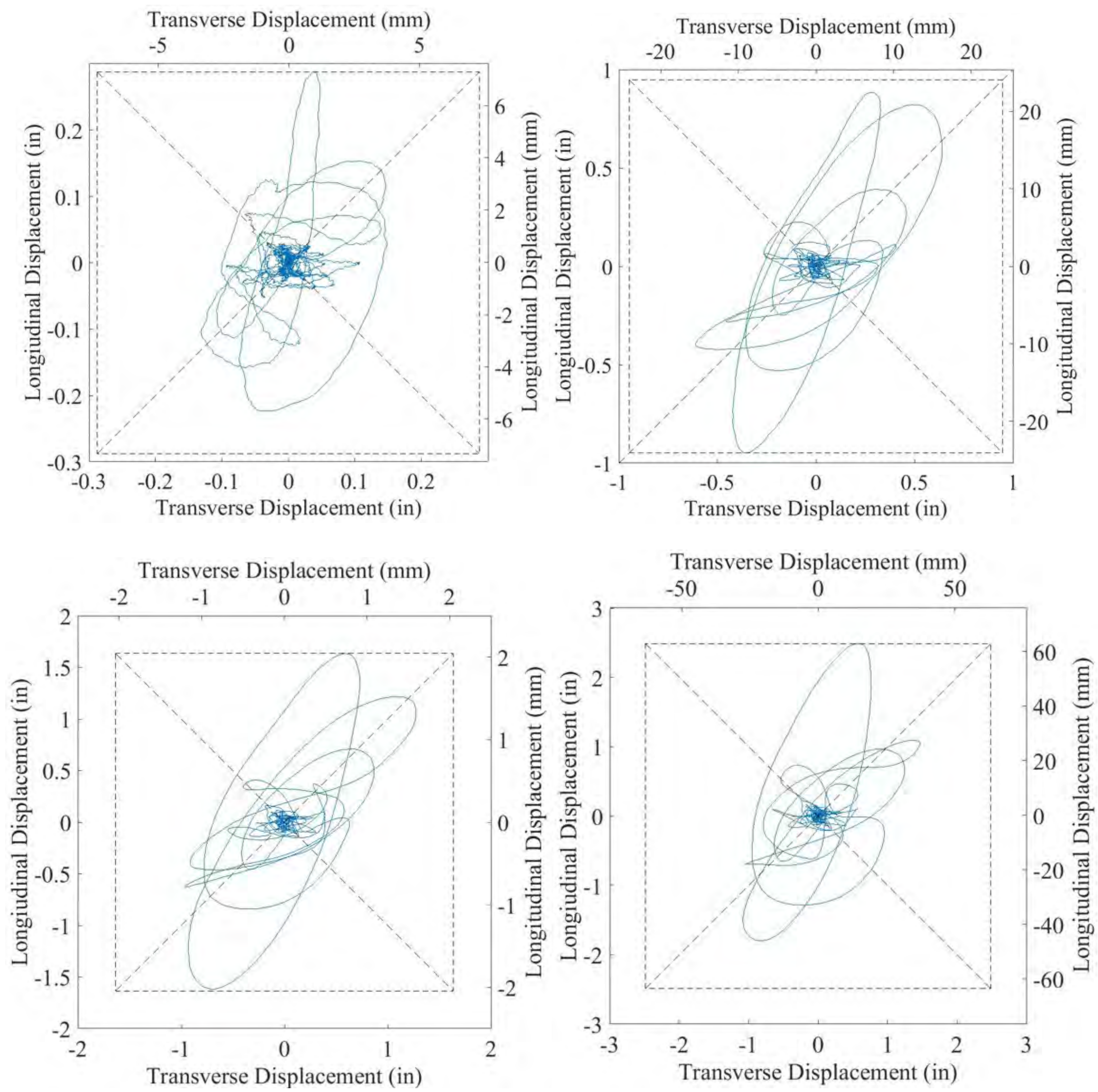

Figure 7.1 Bent particle displacement and coupling index, runs 1-4

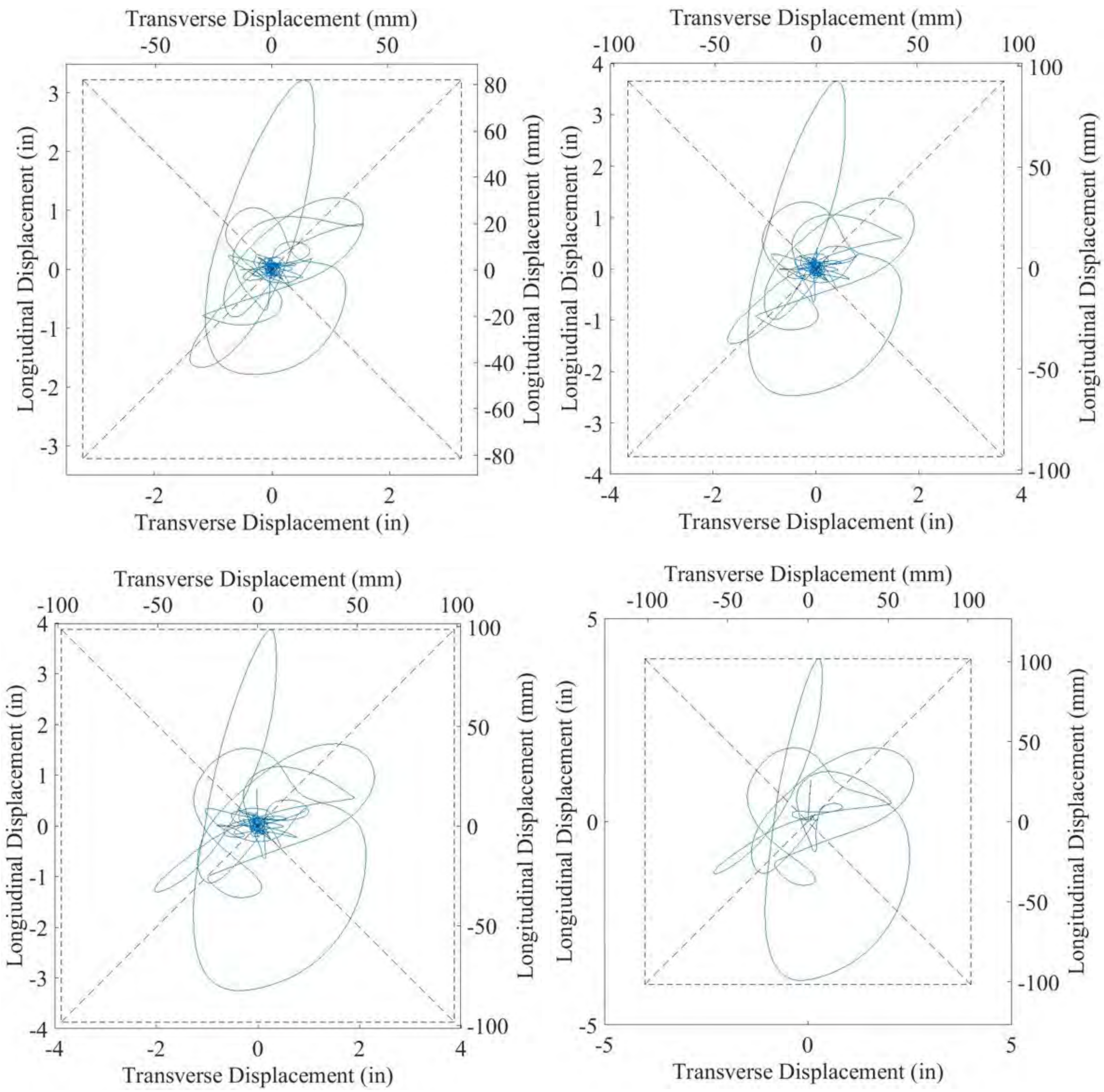

Figure 7.2 Bent particle displacement and coupling index, runs 5-8

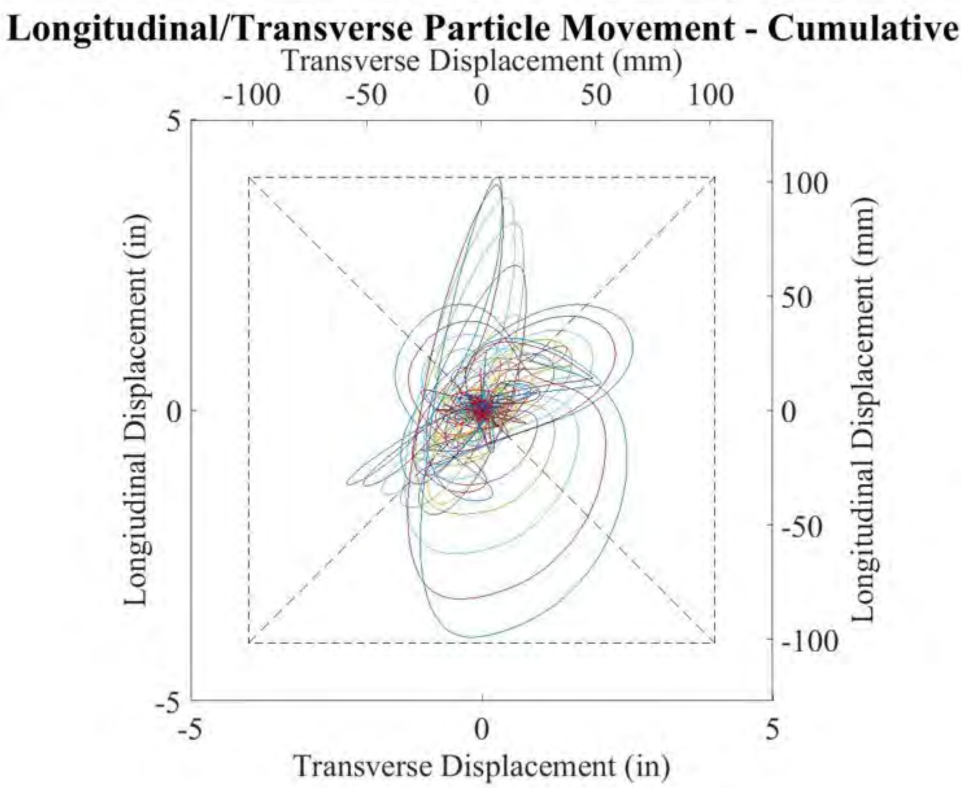

Figure 7.3 Bent particle displacement and coupling index, cumulative

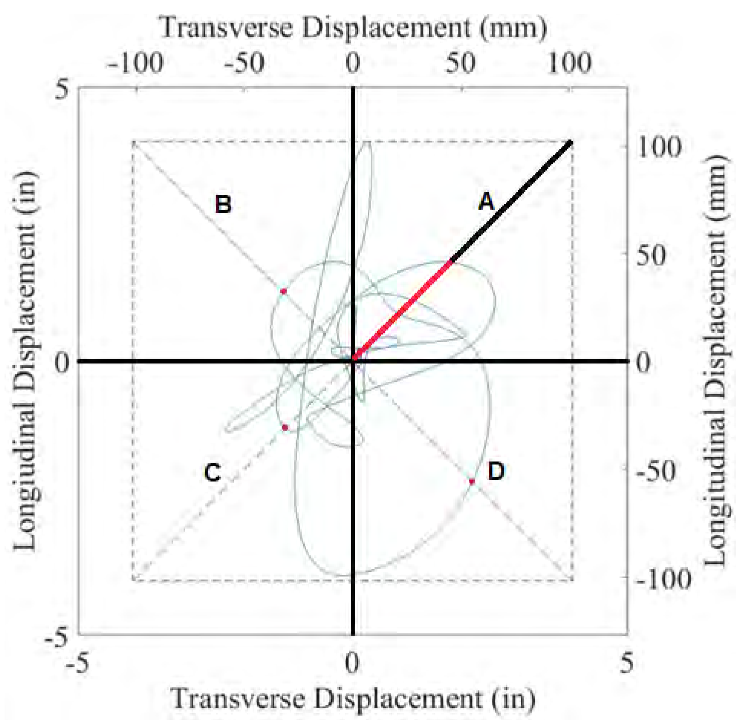

Figure 7.4 Coupling index example and quadrant labels

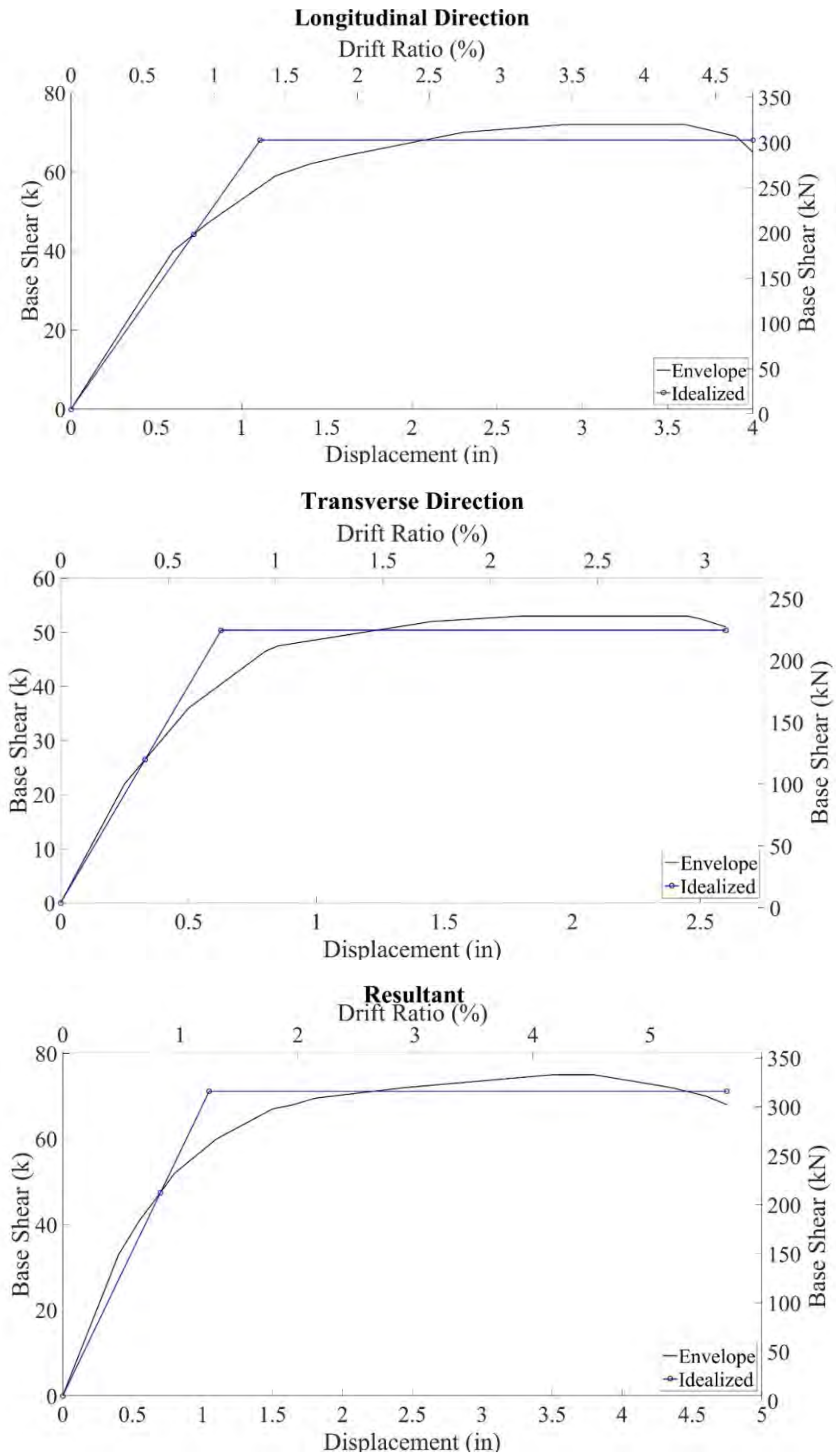

Figure 7.5 Force-displacement envelopes and idealized curves, longitudinal, transverse, and resultant data

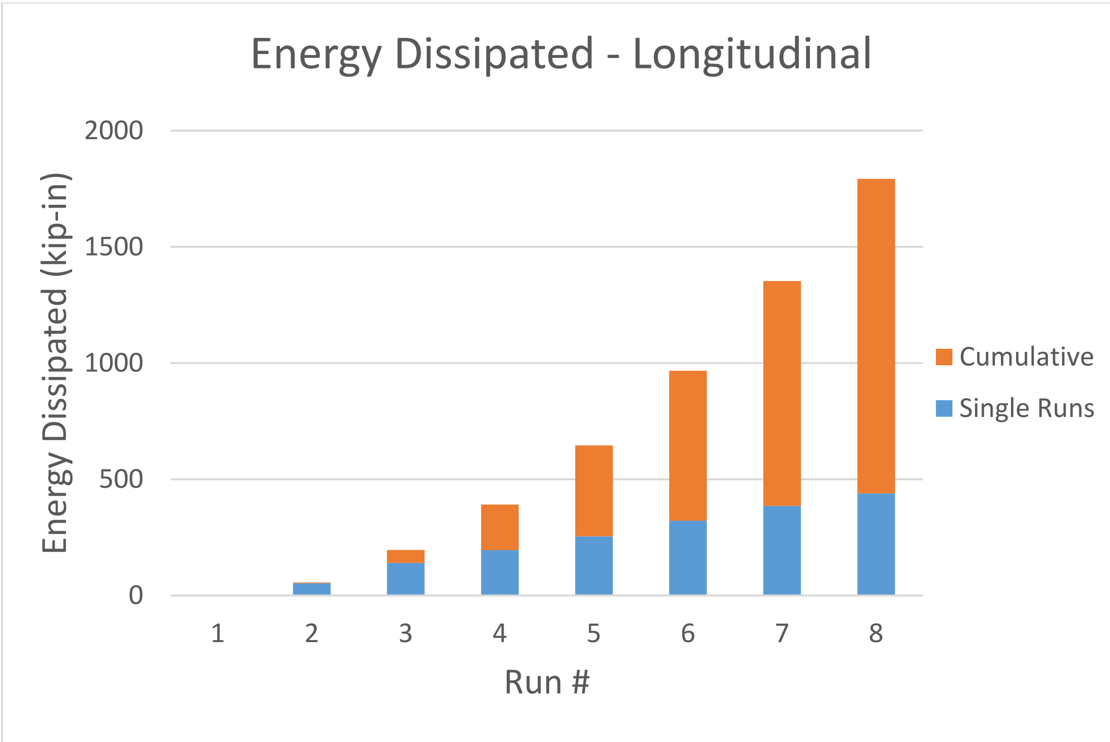

Figure 7.6 Individual and cumulative energy dissipated during for each run, longitudinal direction

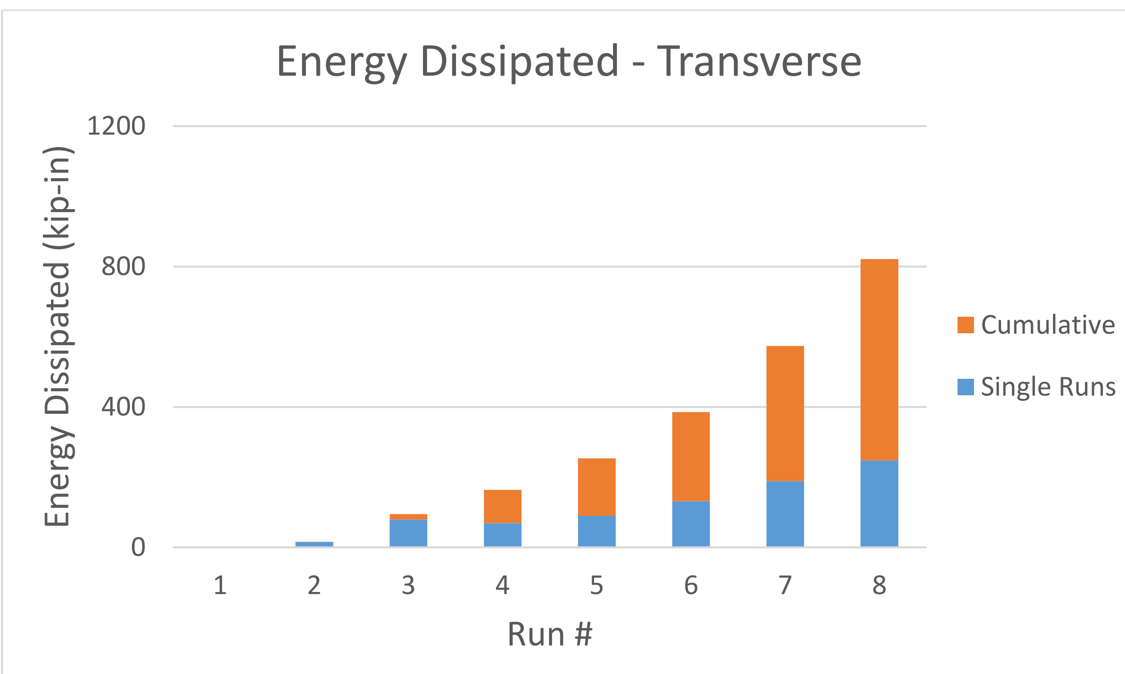

Figure 7.7 Individual and cumulative energy dissipated during for each run, transverse direction

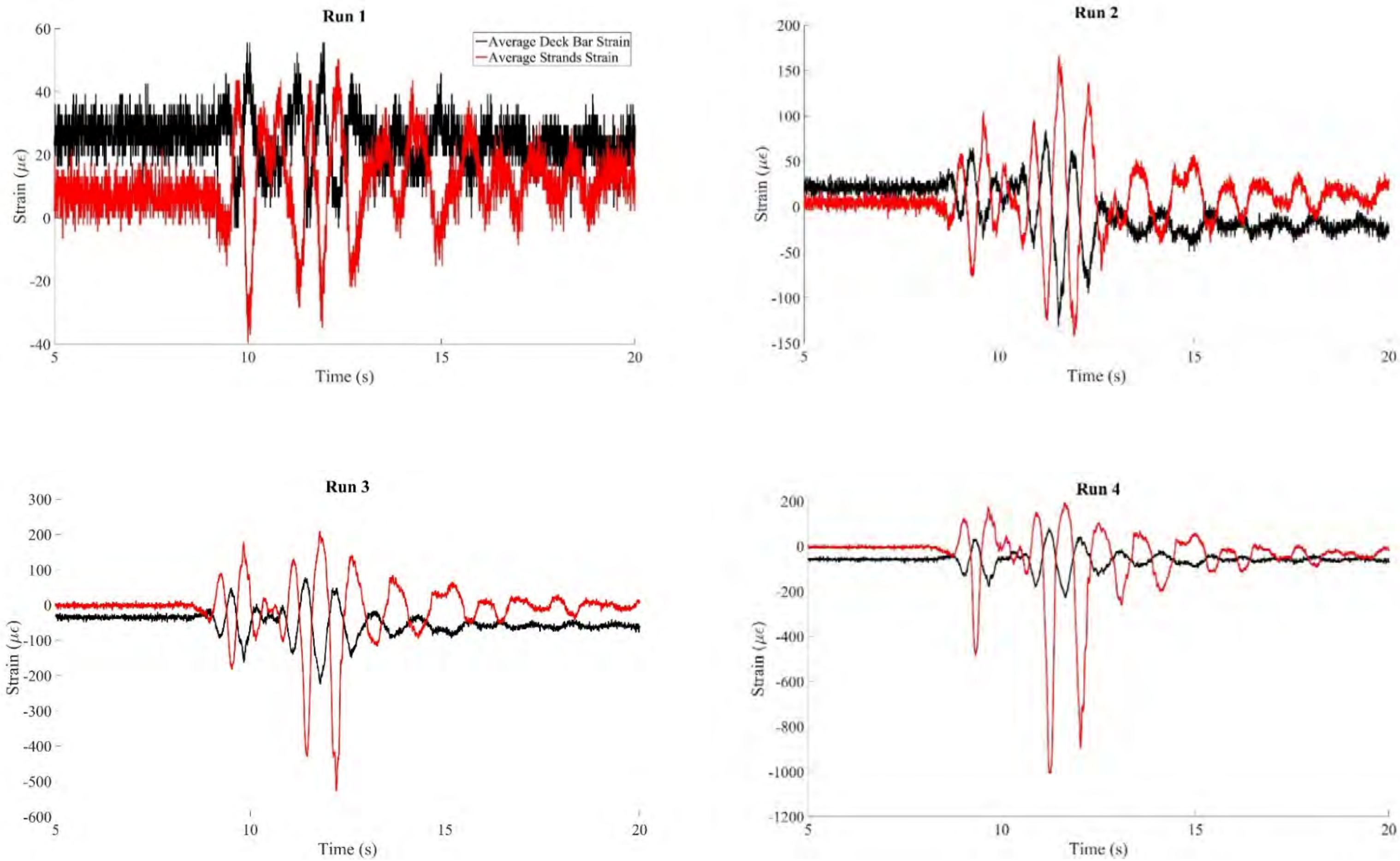

Figure 7.8: Average strains in deck reinforcement and girder strands, exterior girder, west span (runs 1-4)

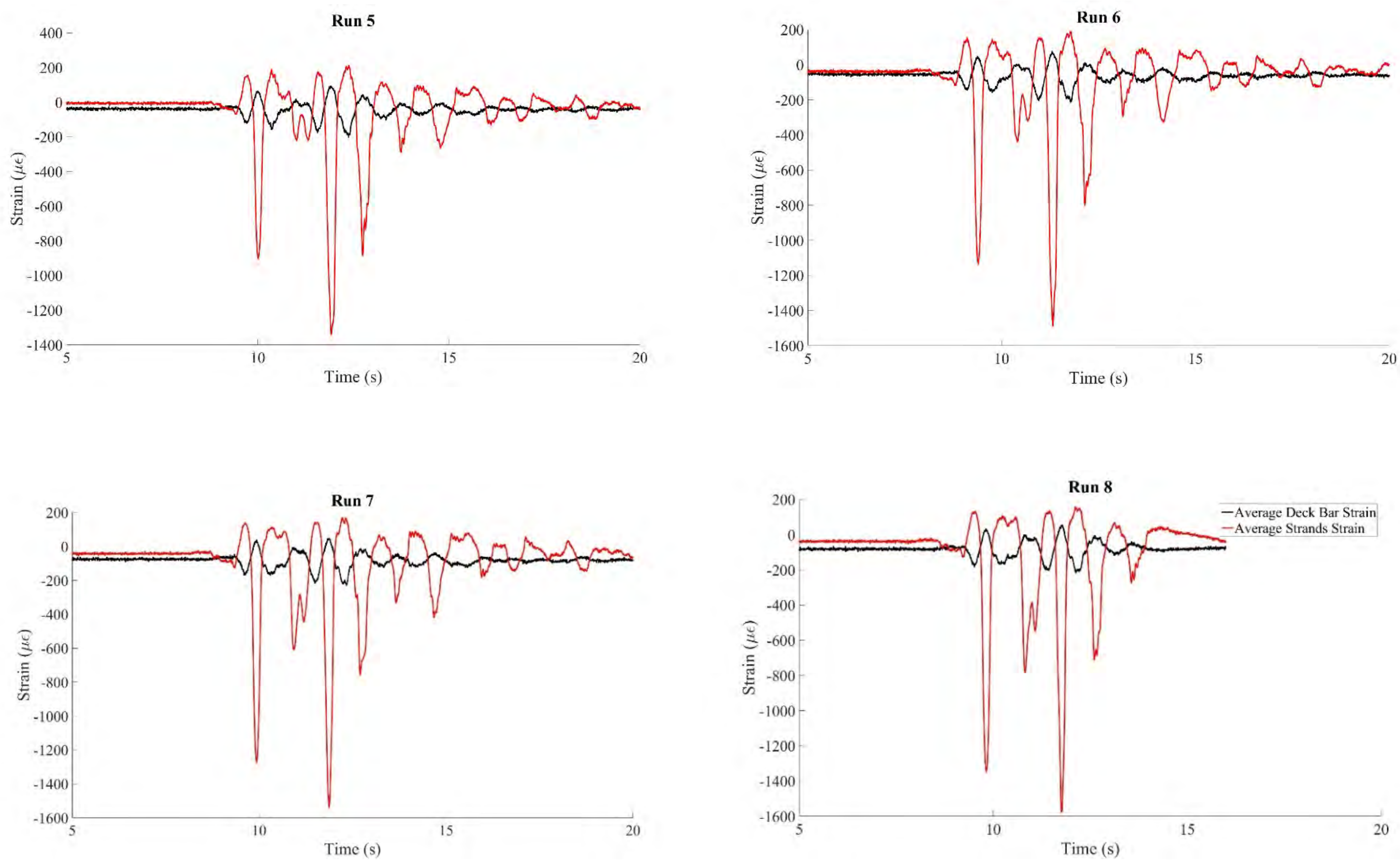

Figure 7.9: Average strains in deck reinforcement and girder strands, exterior girder, west span (runs 5-8)

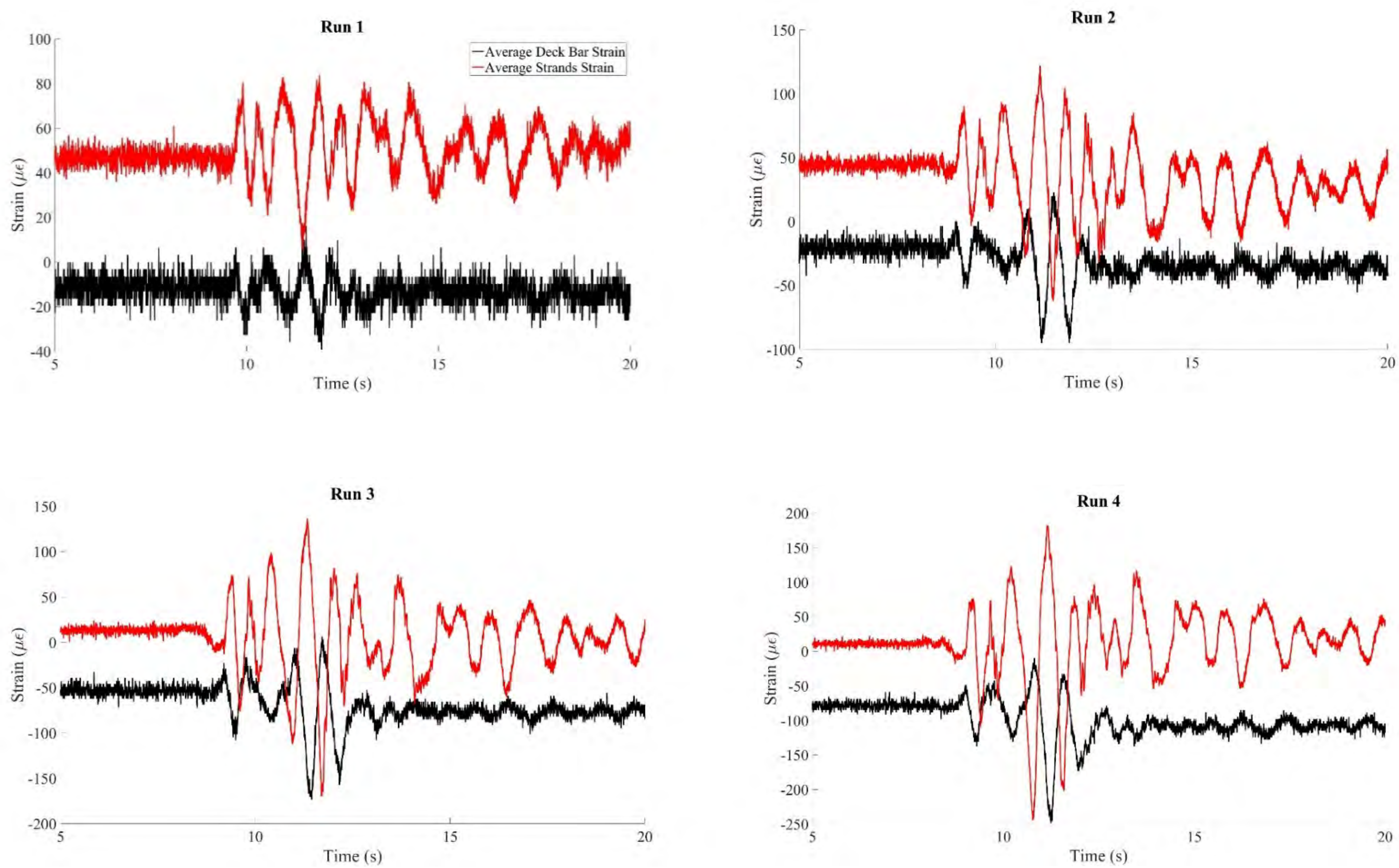

Figure 7.10: Average strains in deck reinforcement and girder strands, exterior girder, east span (runs 1-4)

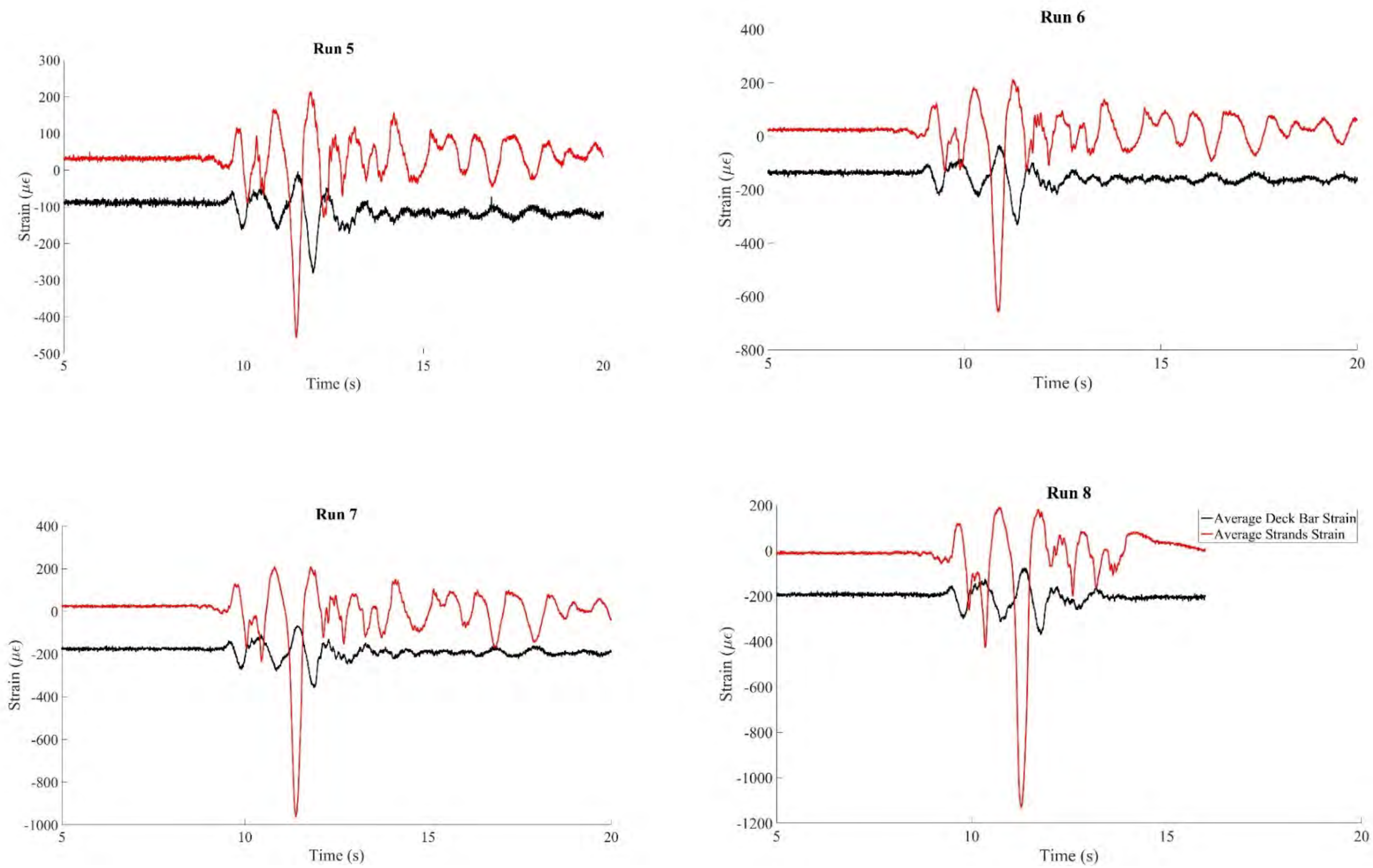

Figure 7.11: Average strains in deck reinforcement and girder strands, exterior girder, east span (runs 5-8)

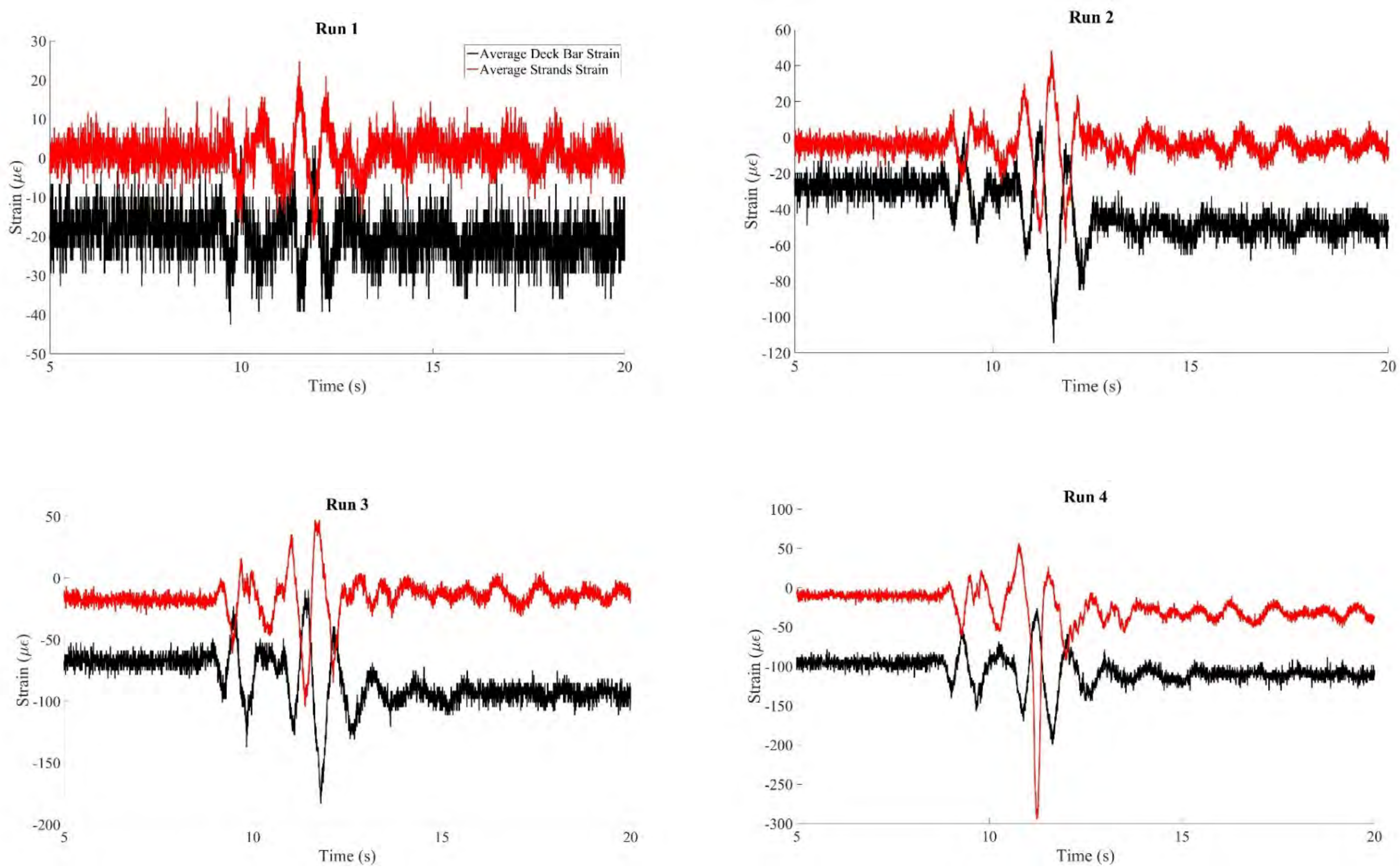

Figure 7.12: Average strains in deck reinforcement and girder strands, interior girder, west span (runs 1-4)

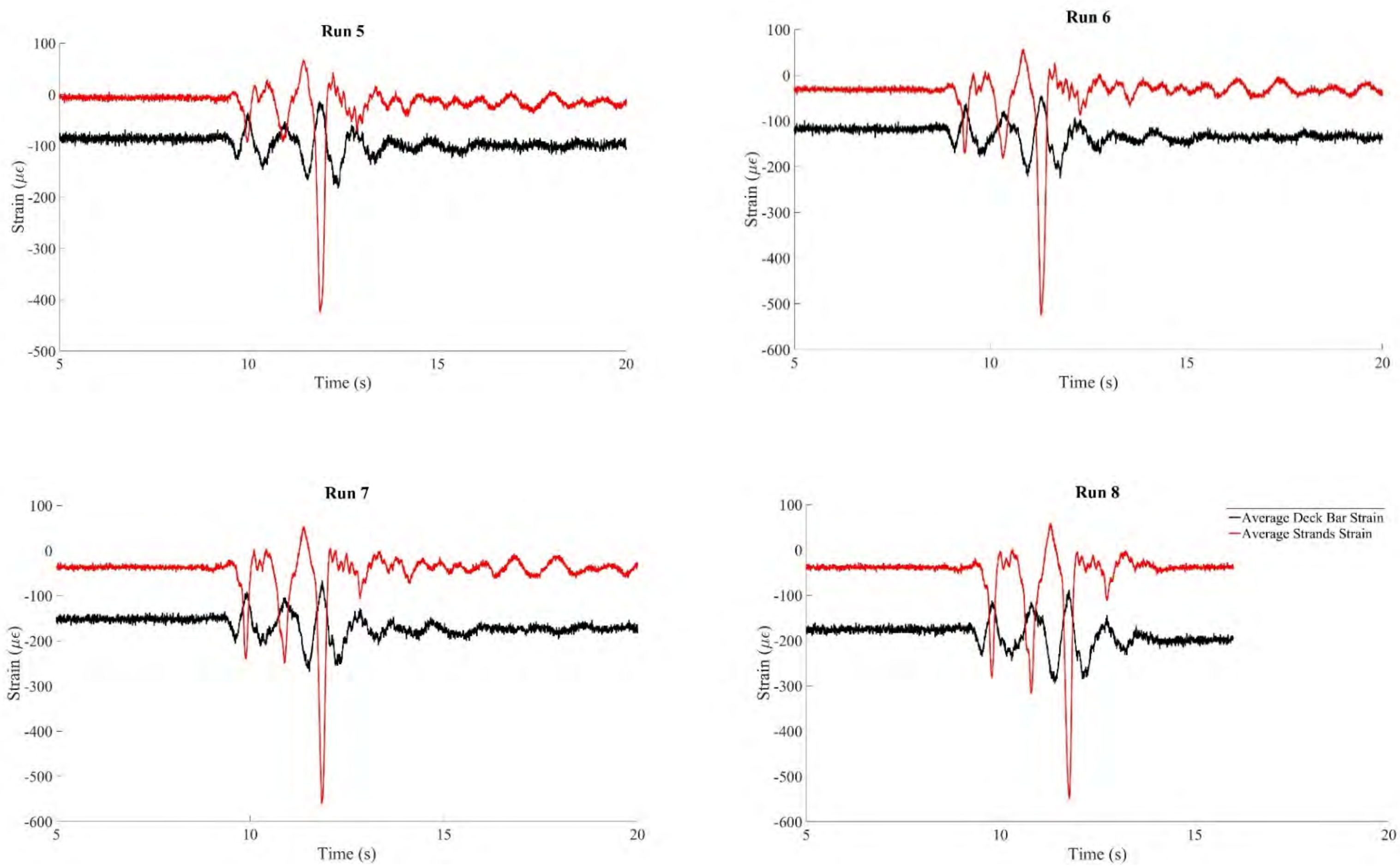

Figure 7.13: Average strains in deck reinforcement and girder strands, interior girder, west span (runs 5-8)

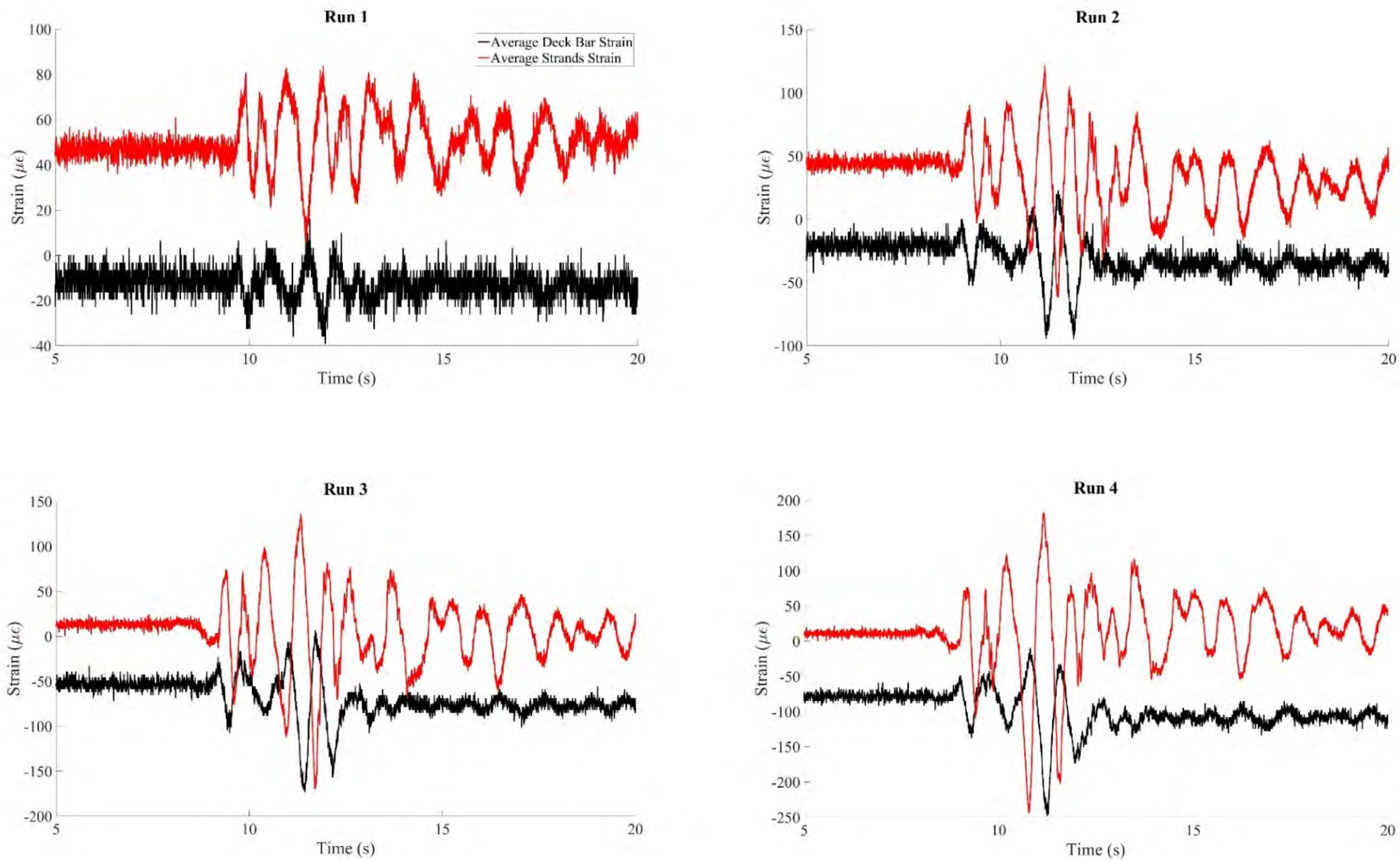

Figure 7.14: Average strains in deck reinforcement and girder strands, interior girder, east span (runs 1-4)

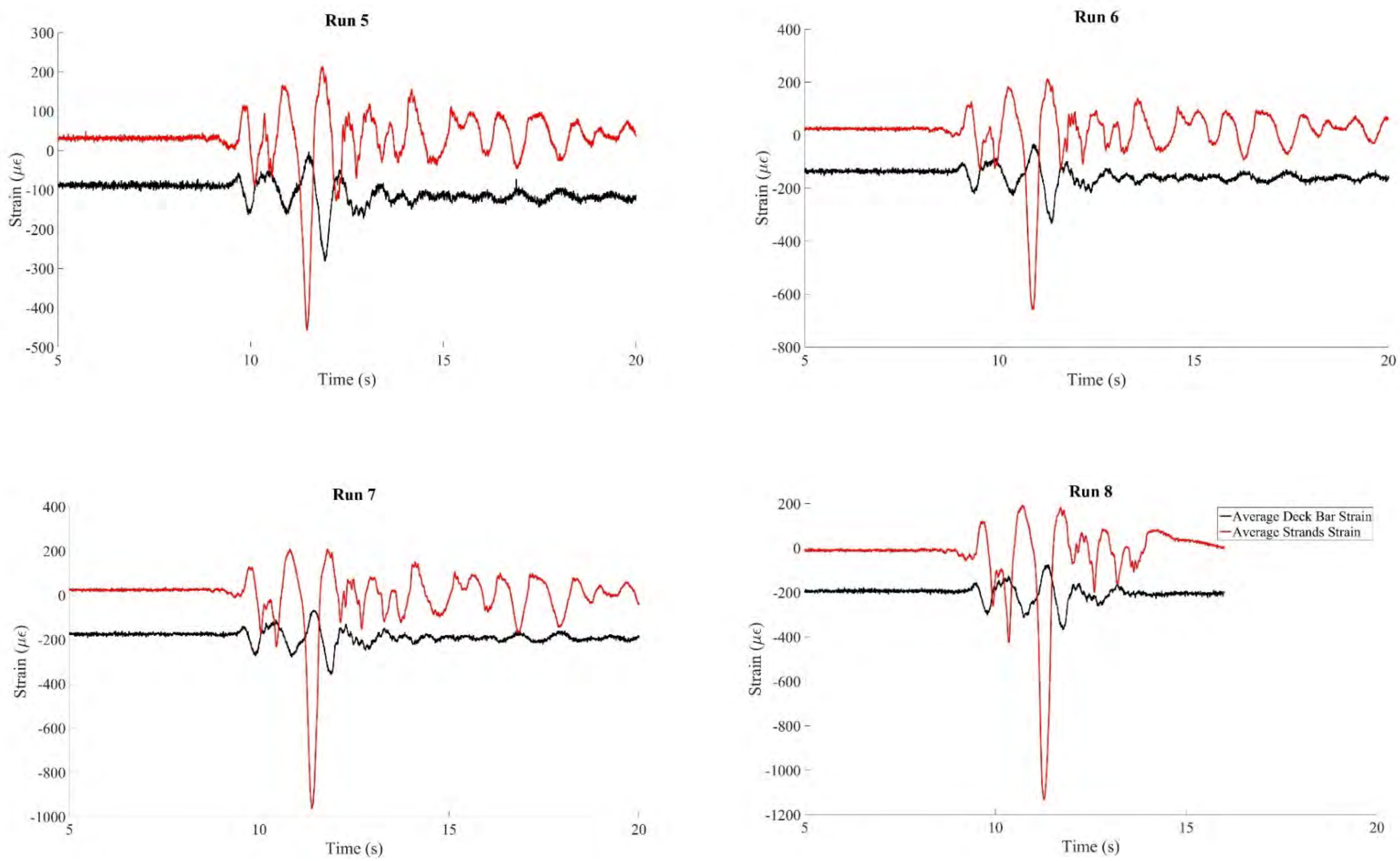

Figure 7.15: Average strains in deck reinforcement and girder strands, interior girder, east span (runs 5-8)

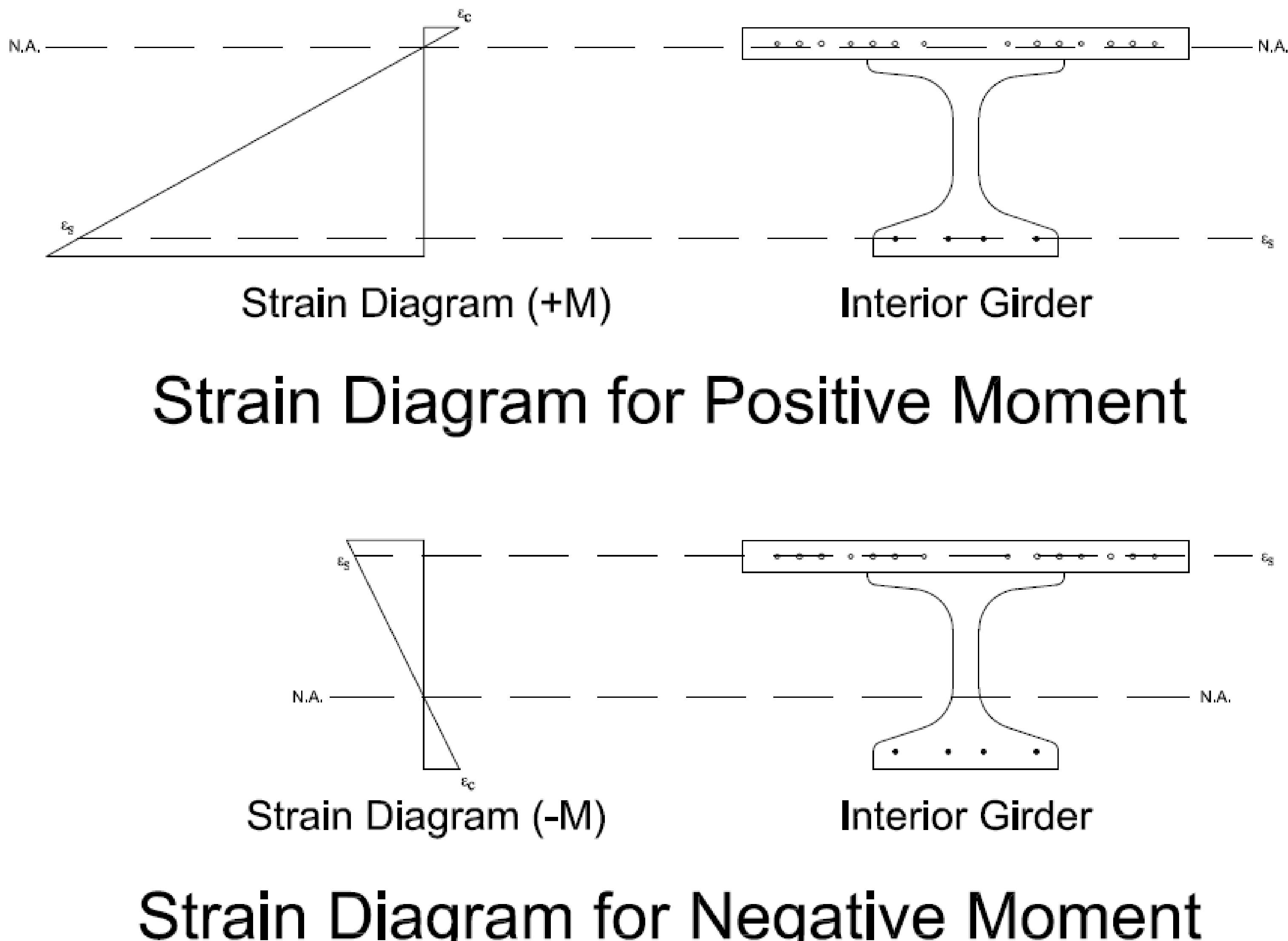

Figure 7.16: Strain diagrams for positive and negative superstructure moment

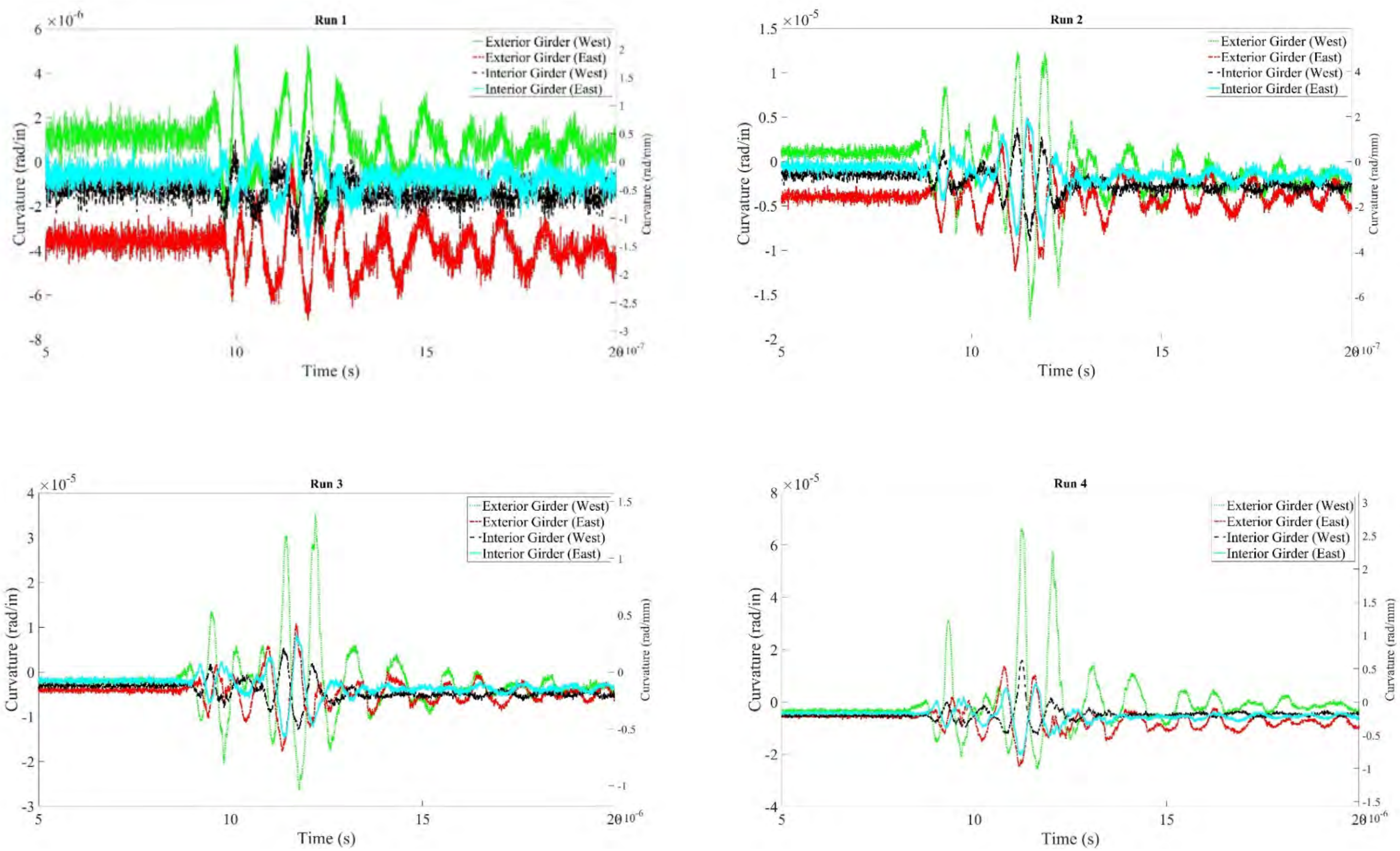

Figure 7.17: Average curvature in the superstructure-to-cap beam connection (runs 1-4)

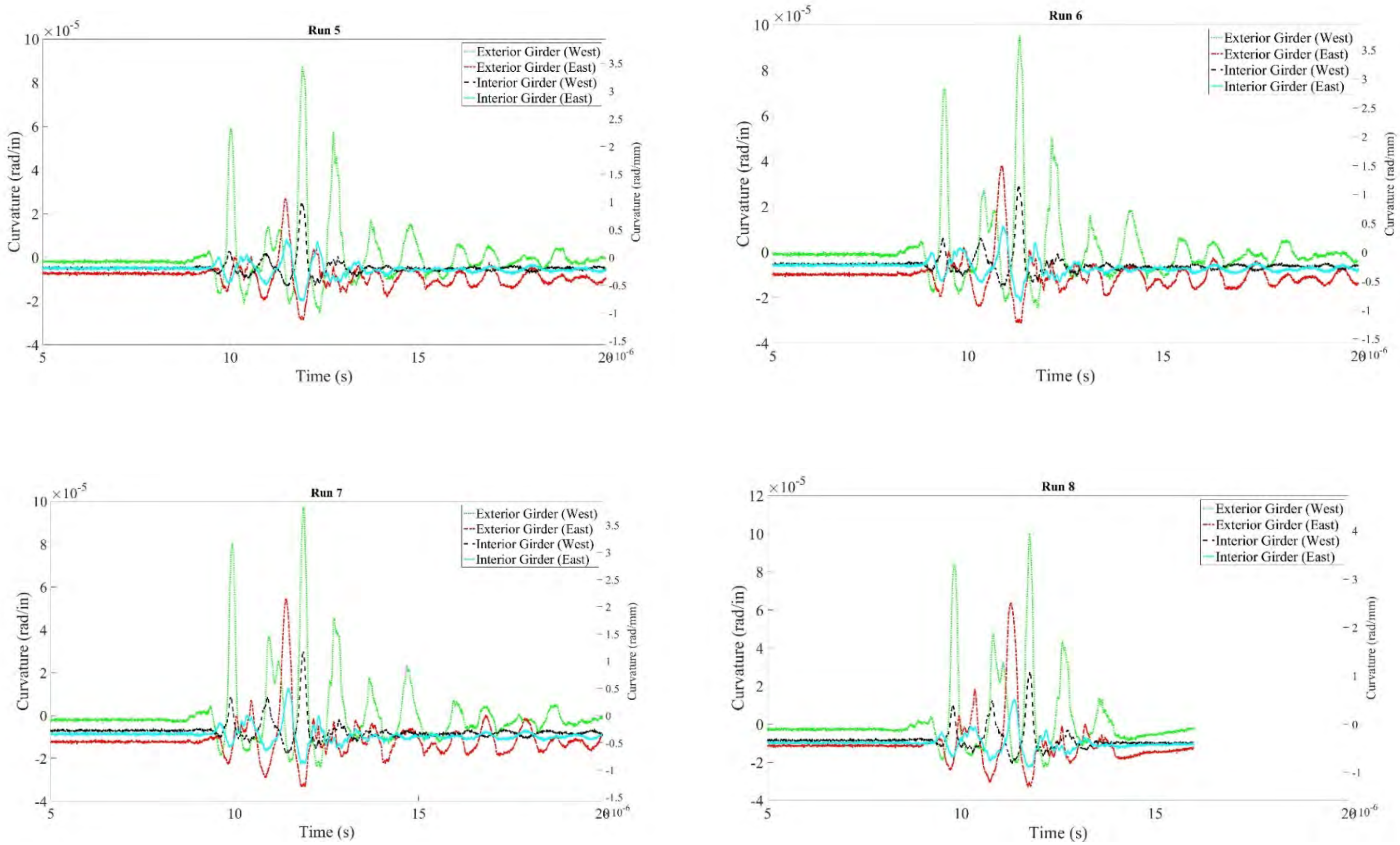

Figure 7.18: Average curvature in the superstructure-to-cap beam connection (runs 5-8)

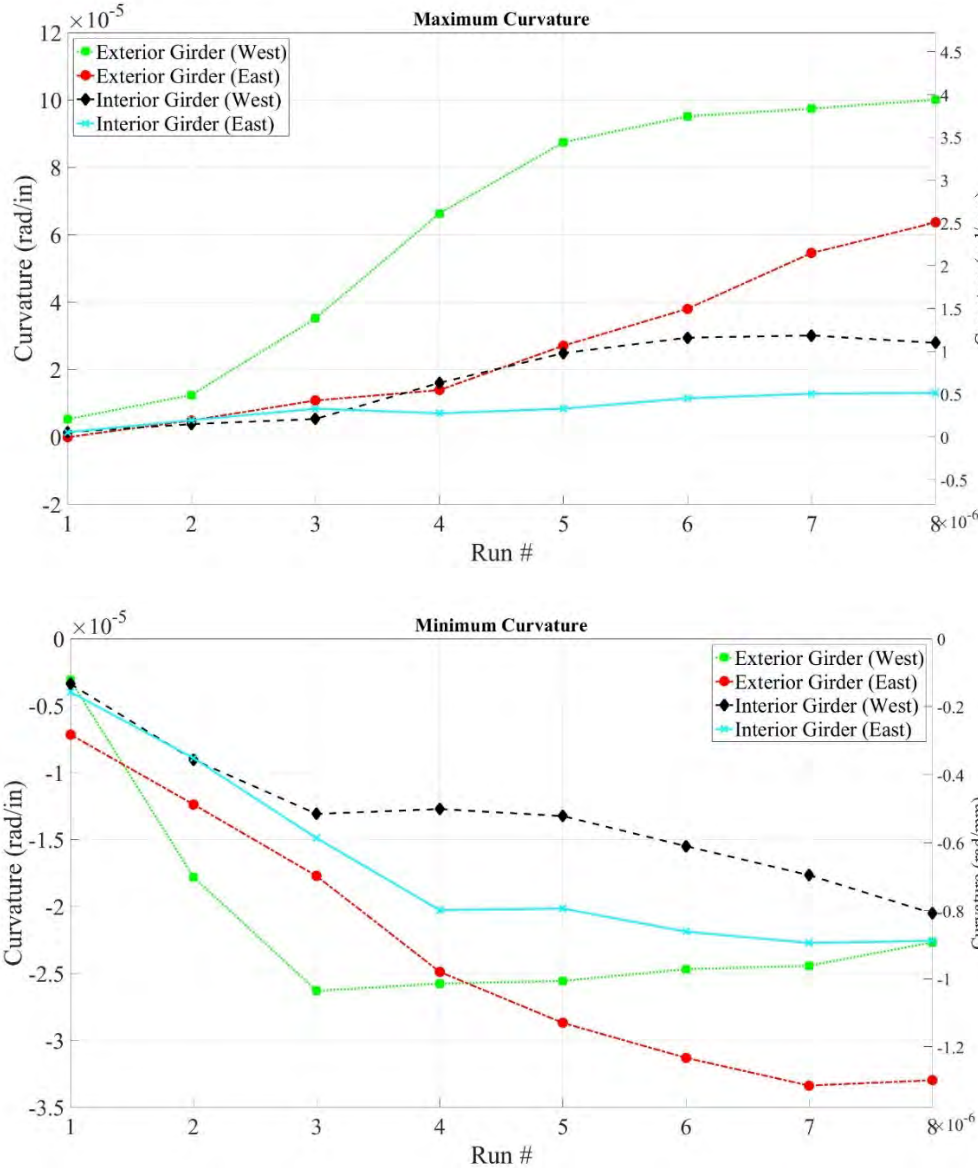

Figure 7.19: Maximum and minimum curvature in each region of the superstructure-to-cap beam connection

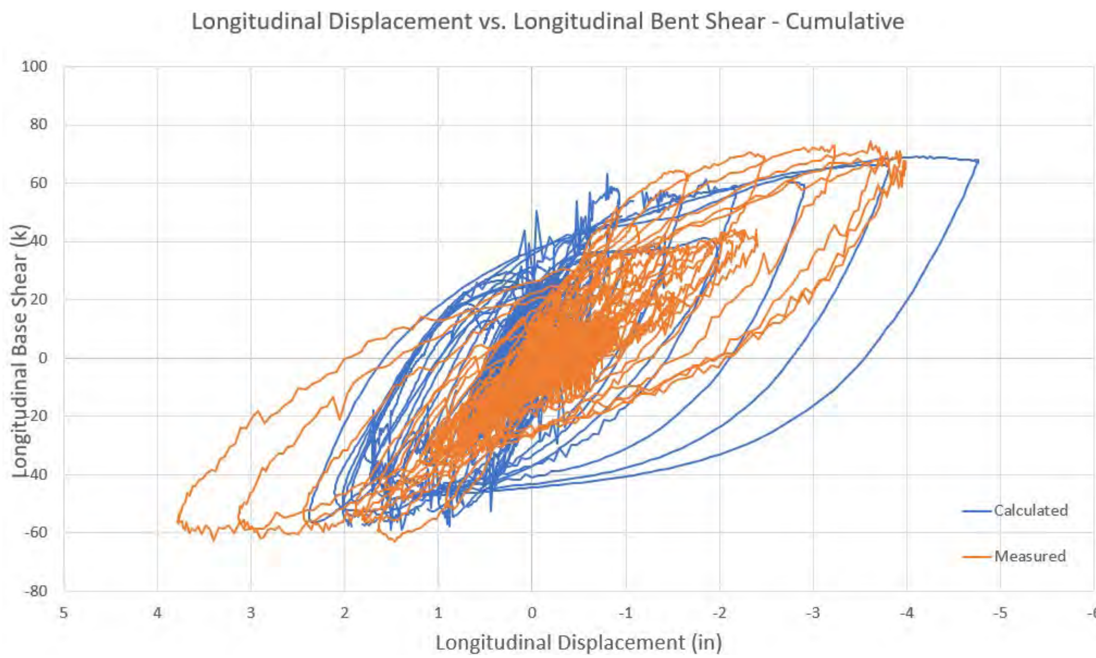

Figure 8.1 Comparison of measured and predicted force-displacement response longitudinal direction, cumulative

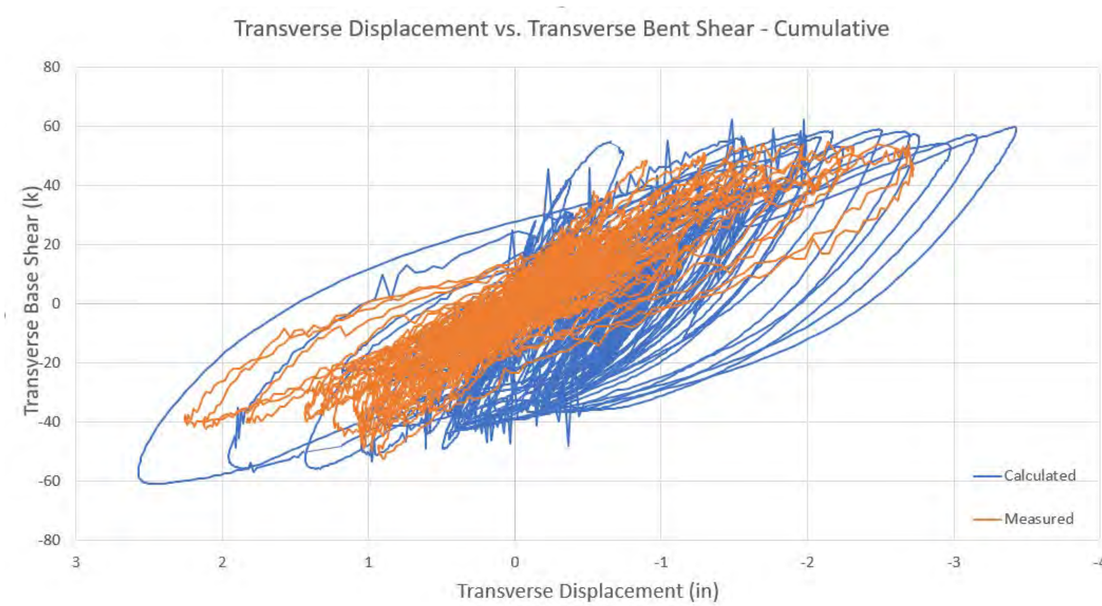

Figure 8.2 Comparison of measured and predicted force-displacement response transverse direction, cumulative

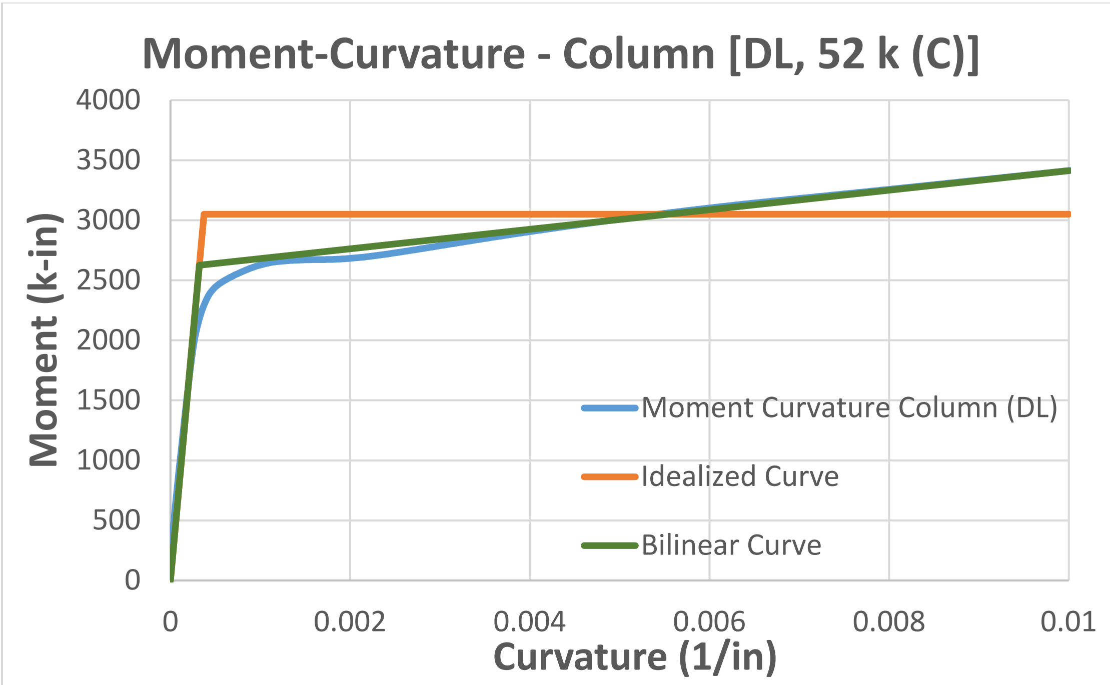

Figure 8.3 Moment-curvature relationship for column under dead load

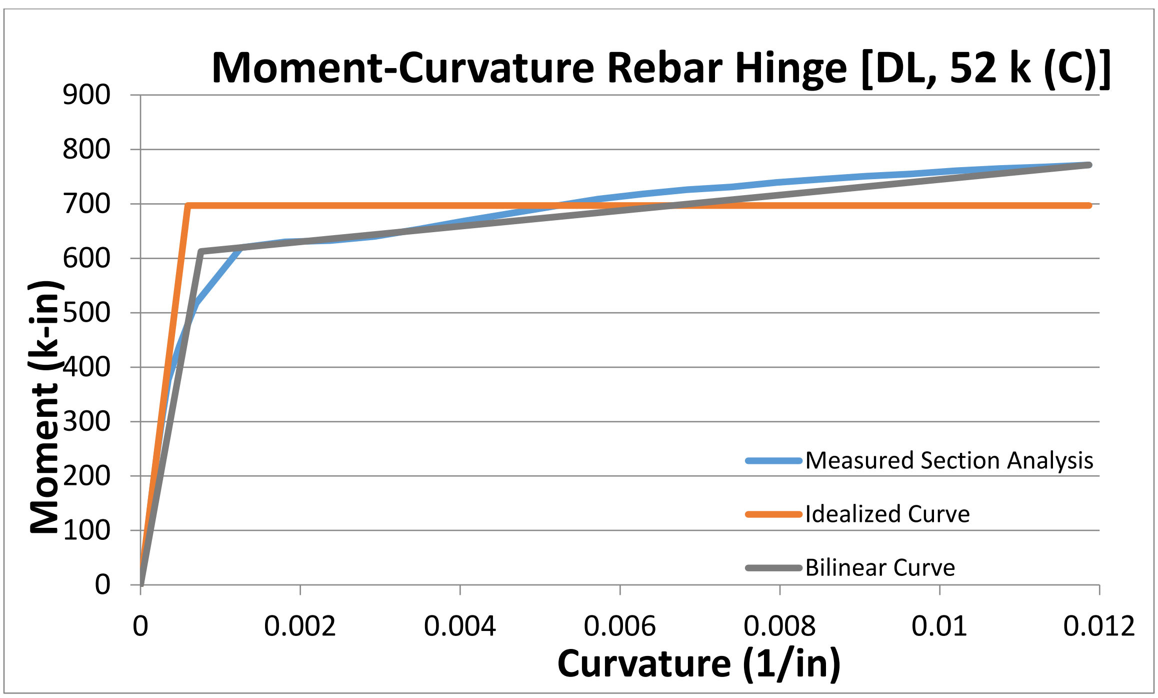

Figure 8.4 Moment curvature analysis for rebar hinge under dead load

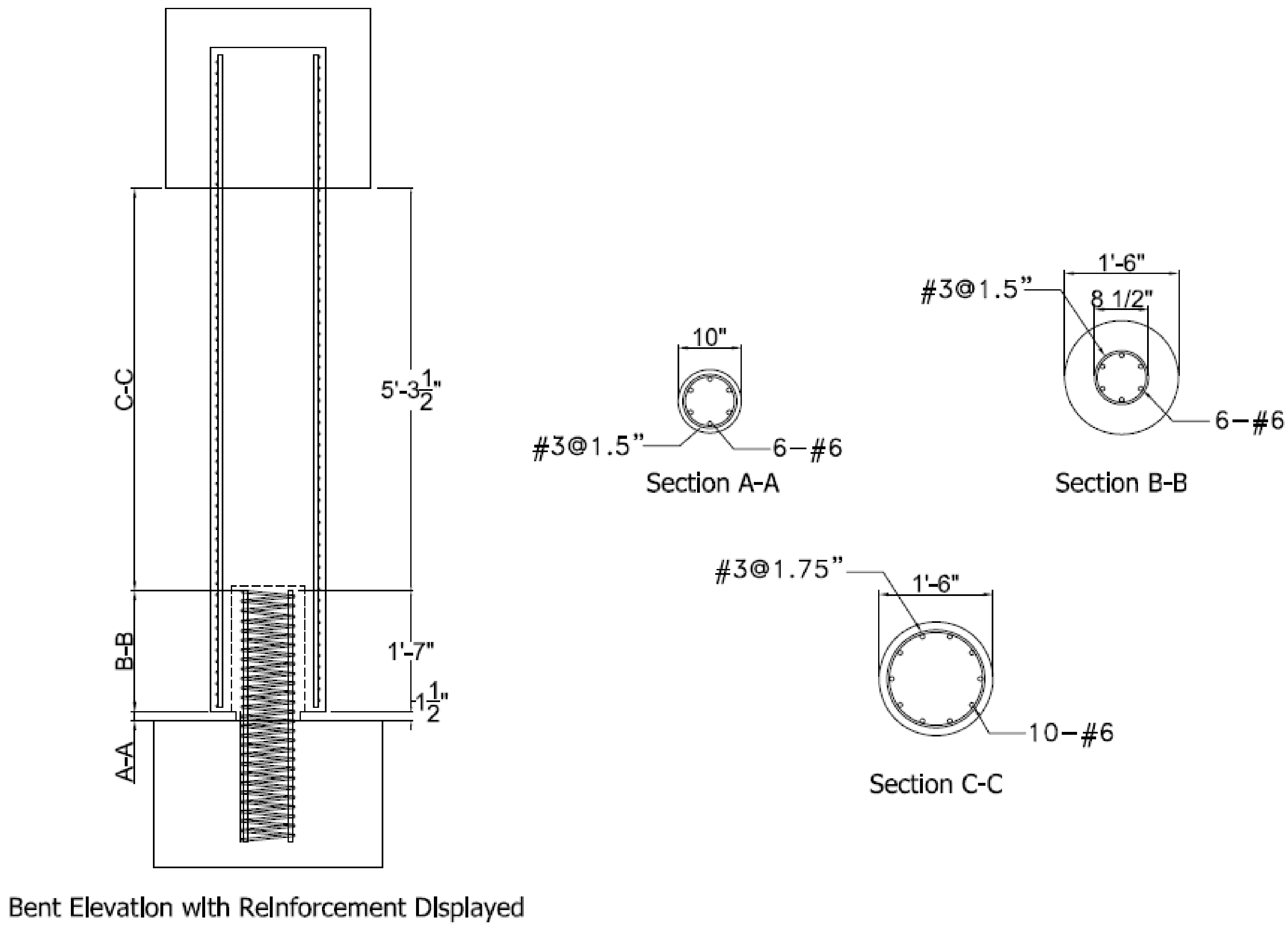

Figure 8.5: Modeling of column and hinge sections for post-test model

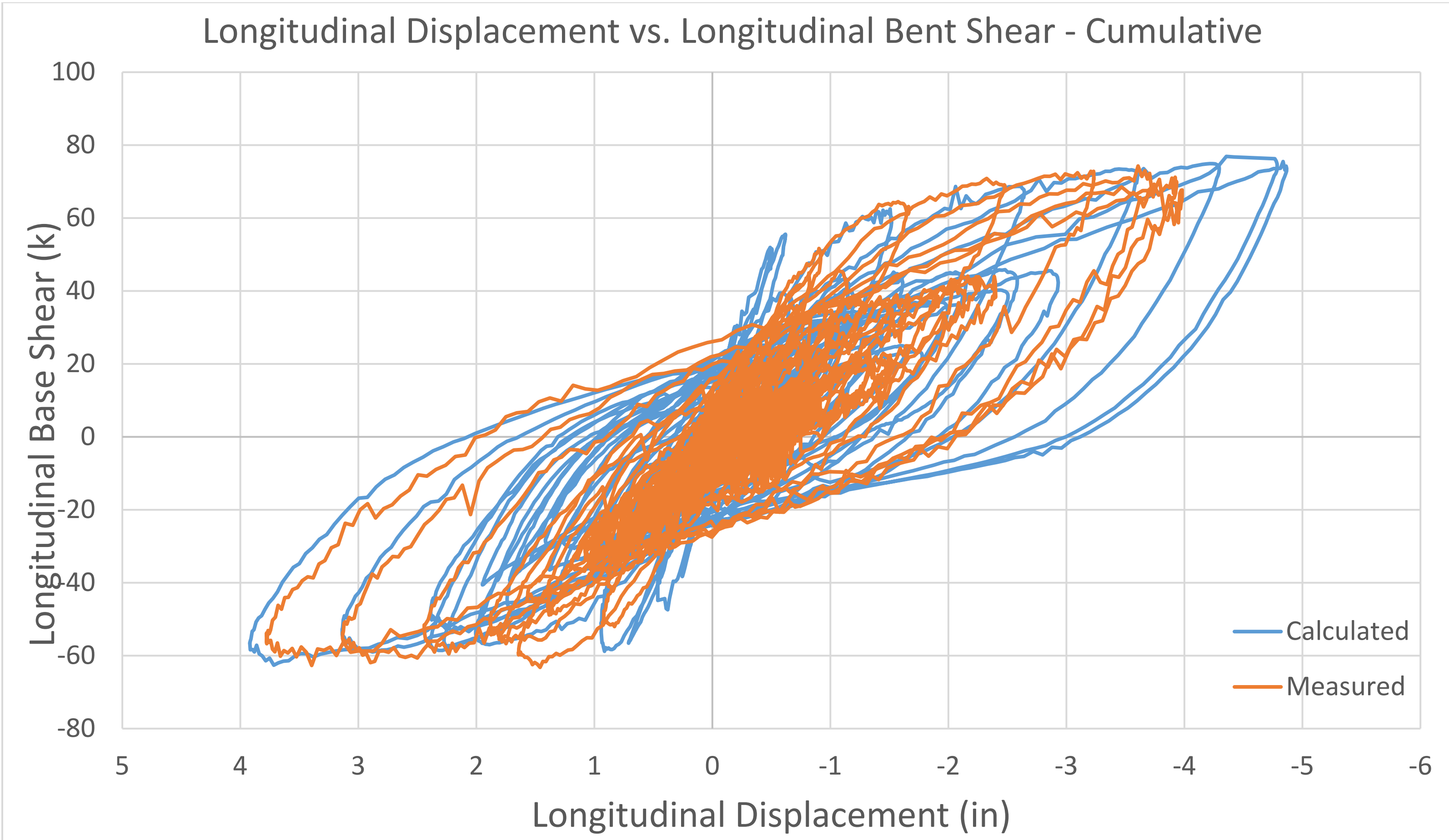

Figure 8.6: Measured and calculated longitudinal bent hysteresis curve, cumulative

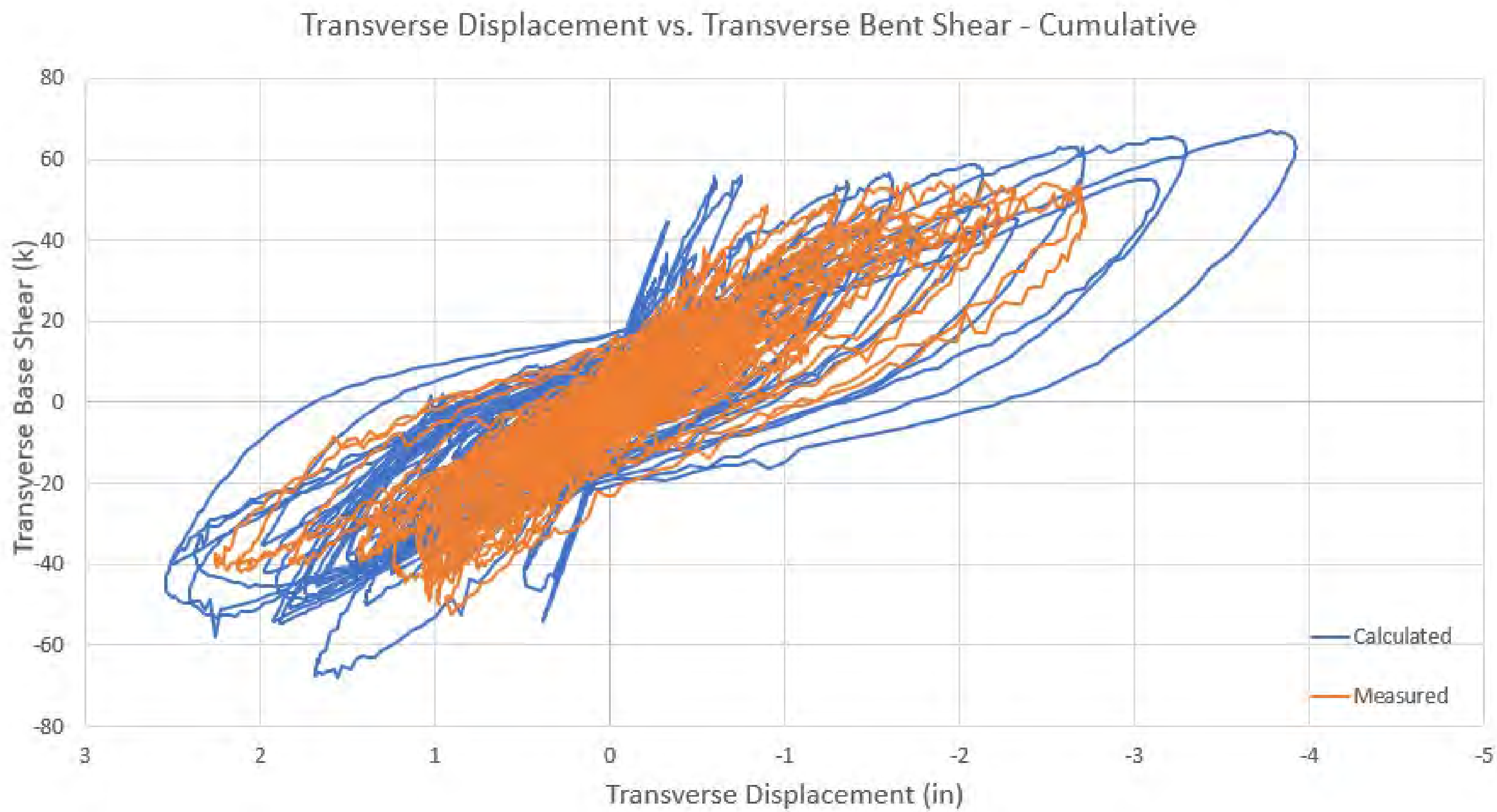

Figure 8.7: Measured and calculated transverse bent hysteresis curve, cumulative

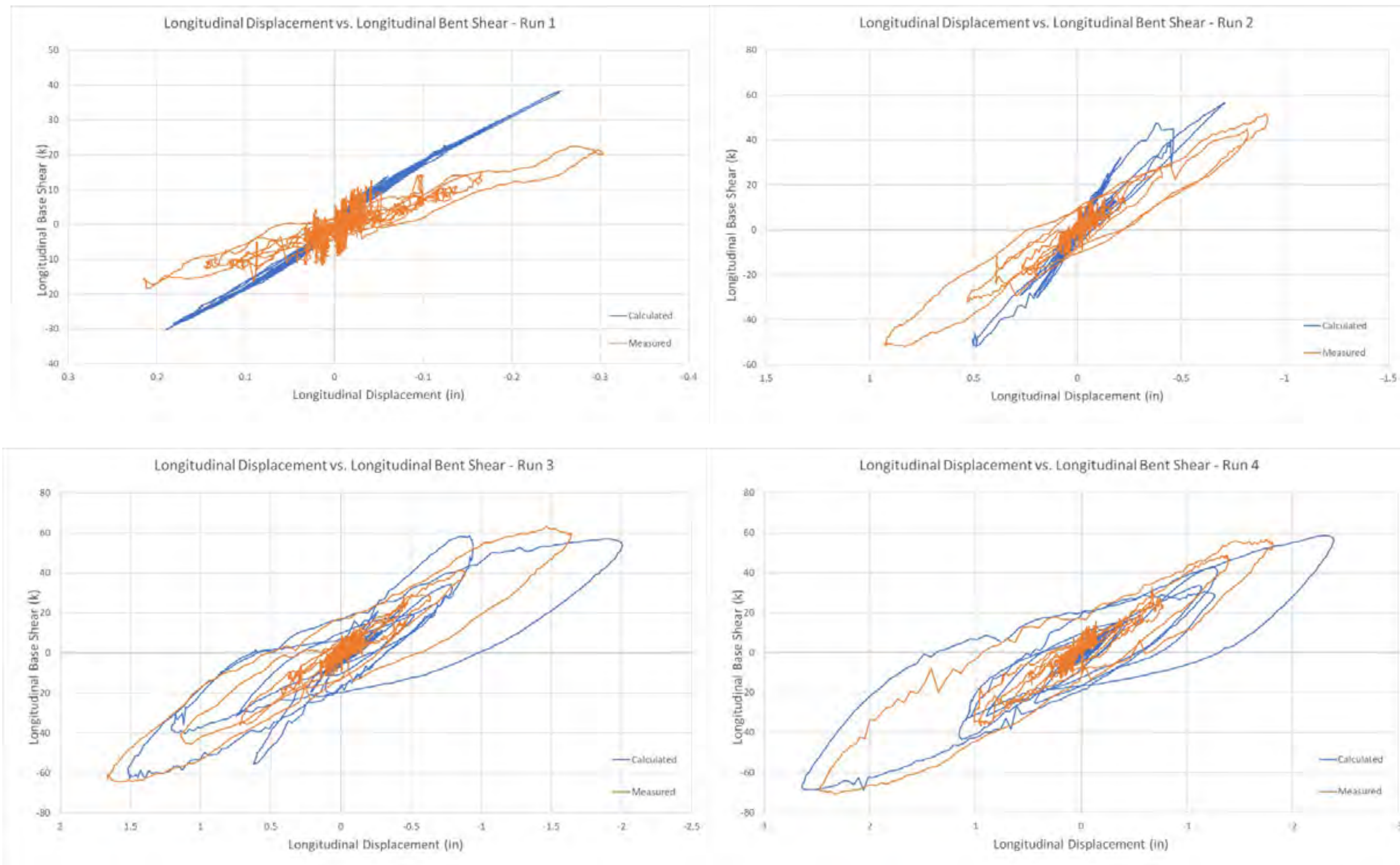

Figure 8.8: Measured and calculated longitudinal bent hysteresis curve, runs 1-4

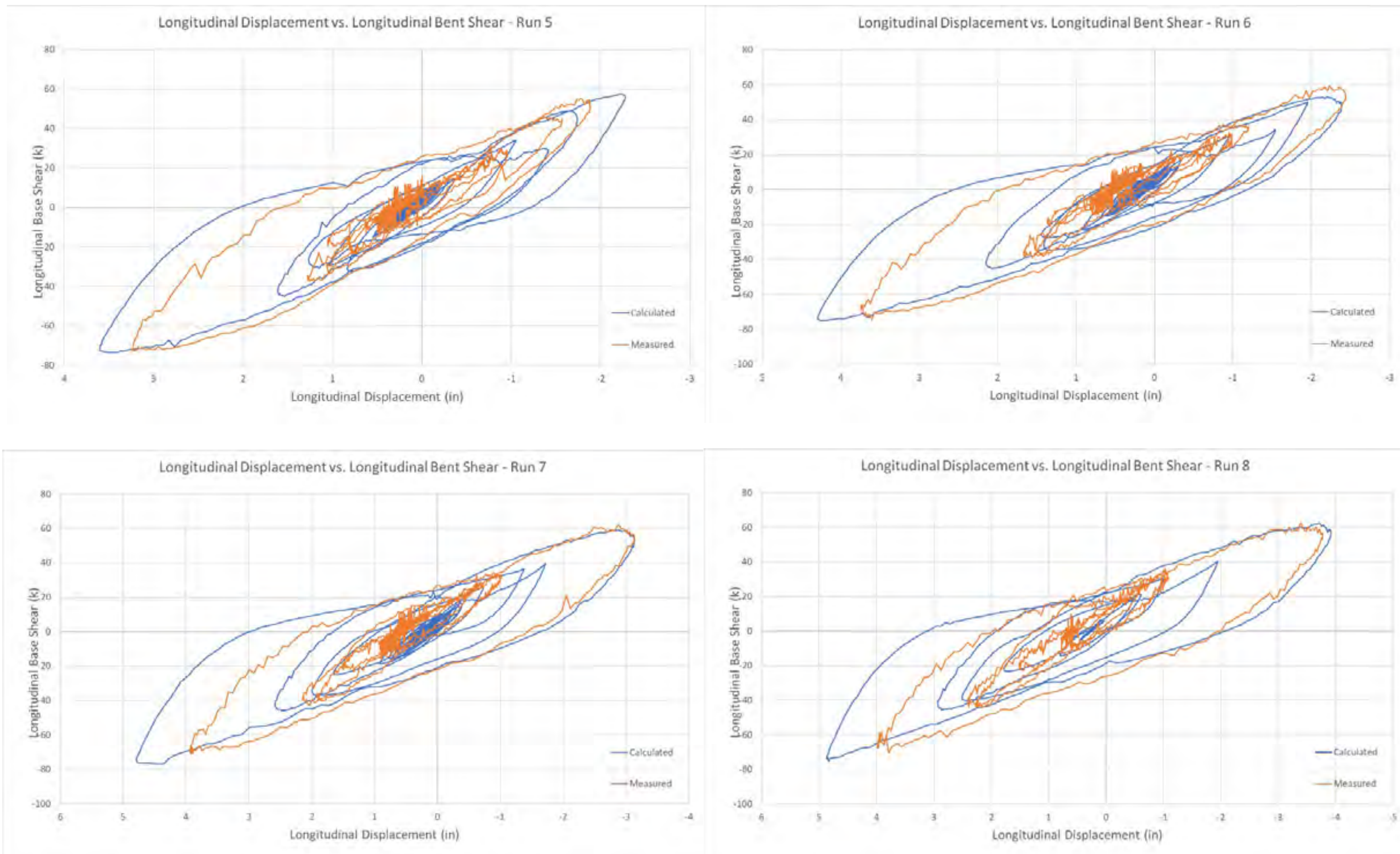

Figure 8.9: Measured and calculated longitudinal bent hysteresis curve, runs 5-8

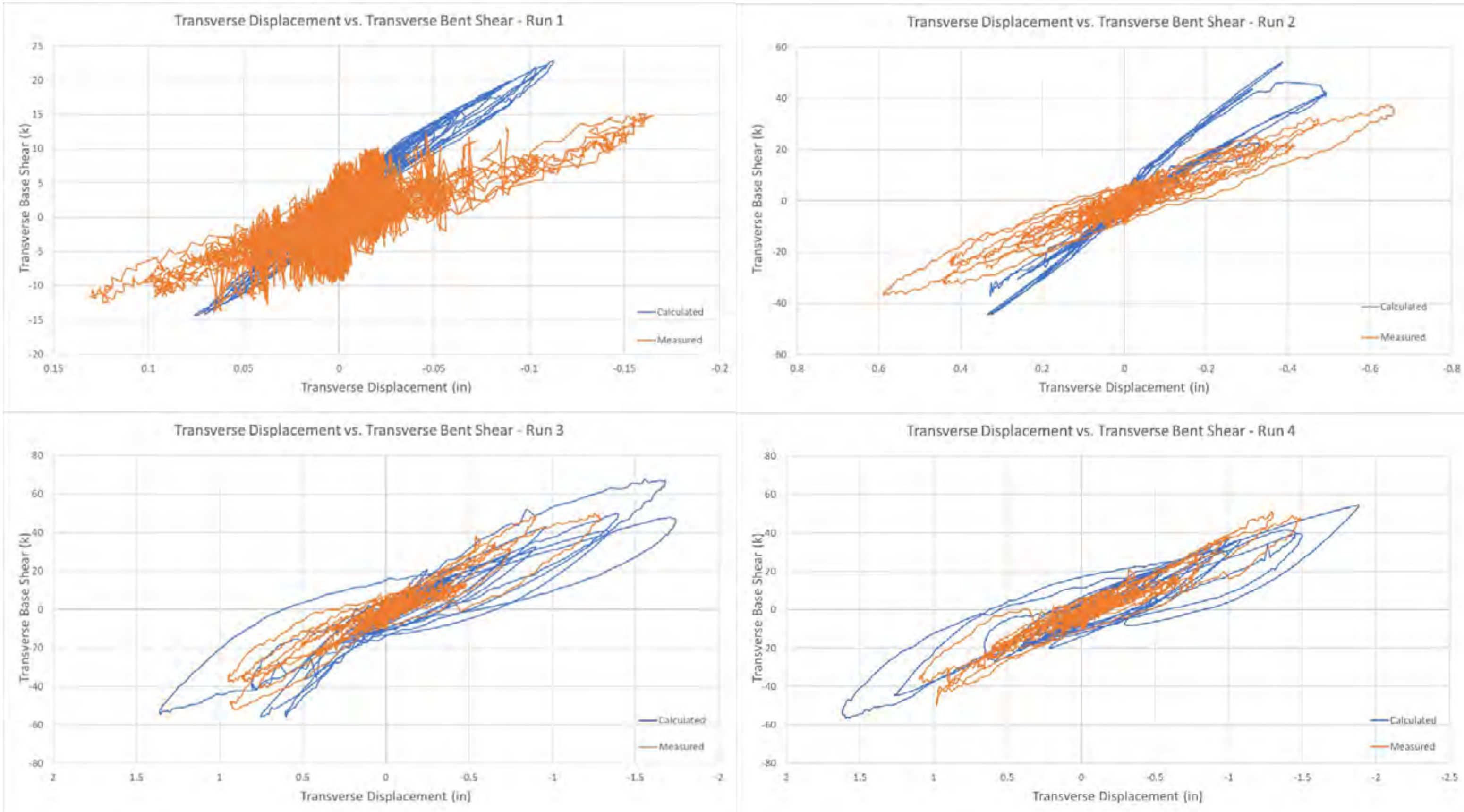

Figure 8.10: Measured and calculated transverse bent hysteresis curves, runs 1-4

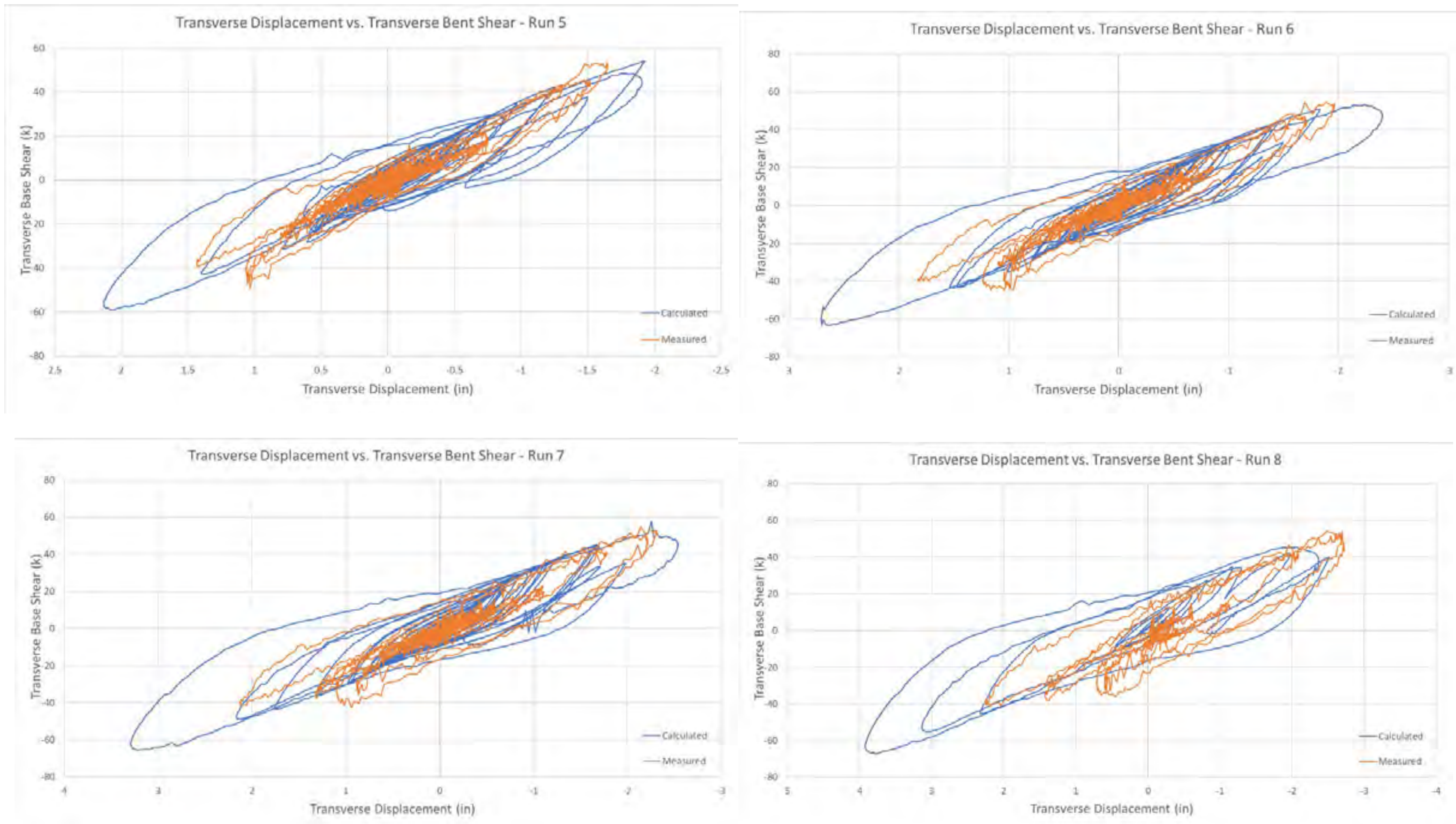

Figure 8.11: Measured and calculated transverse bent hysteresis curves, runs 5-8

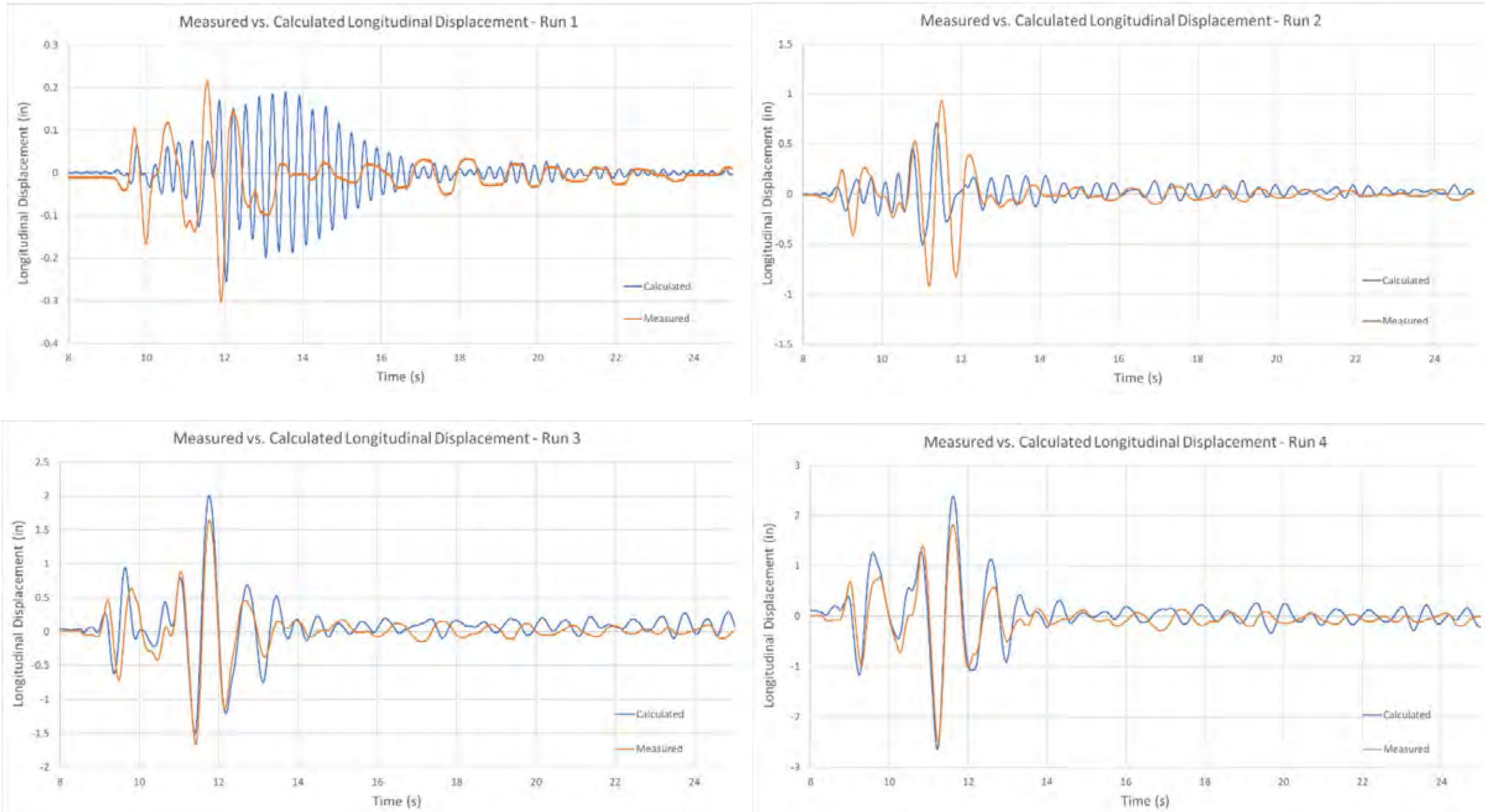

Figure 8.12: Measured and calculated longitudinal displacement history, runs 1-4

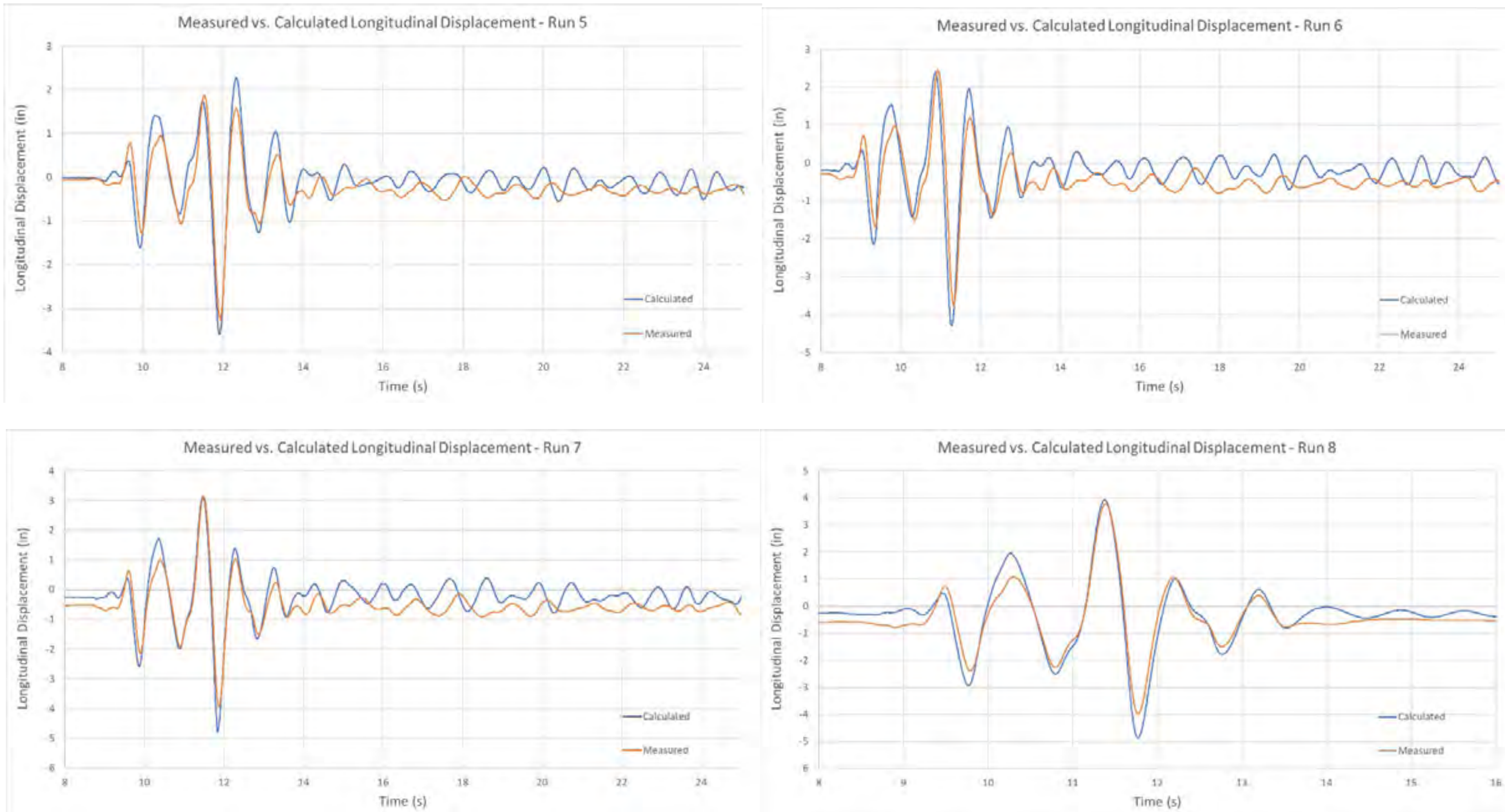

Figure 8.13: Measured and calculated longitudinal displacement history, runs 5-8

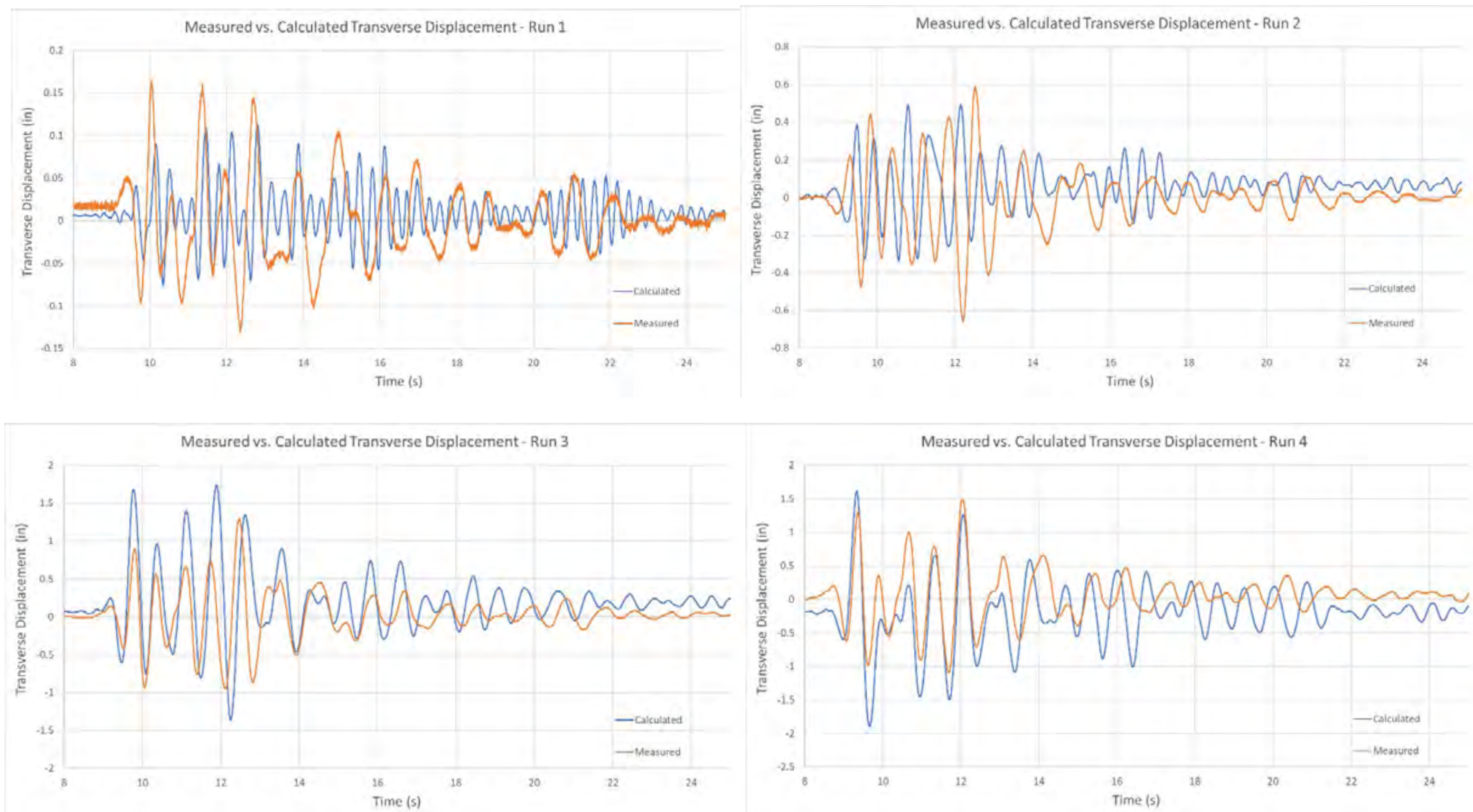

Figure 8.14: Measured and calculated transverse displacement history, runs 1-4

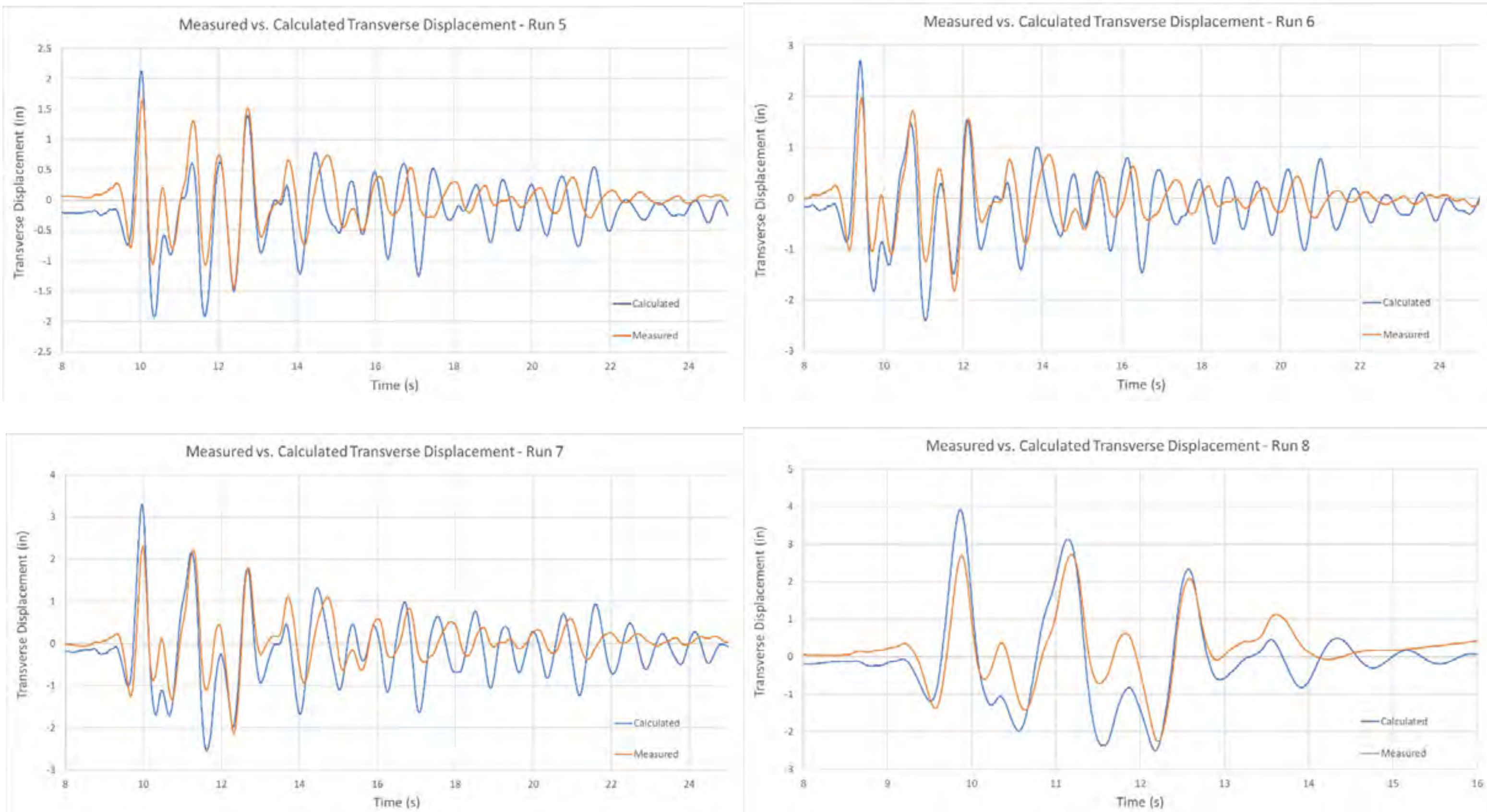

Figure 8.15: Measured and calculated transverse displacement history, runs 5-8

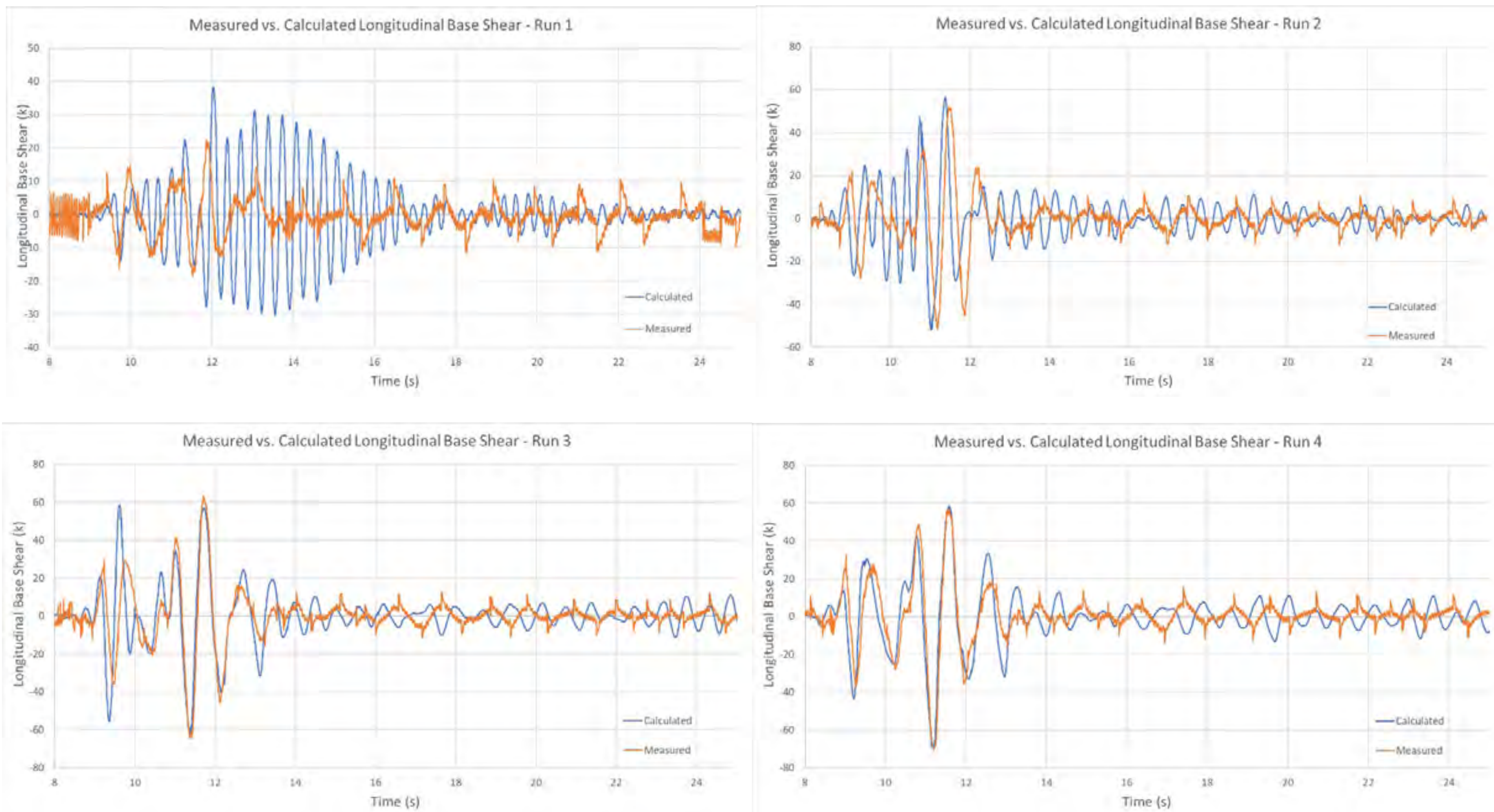

Figure 8.16: Measured and calculated longitudinal base shear history, runs 1-4

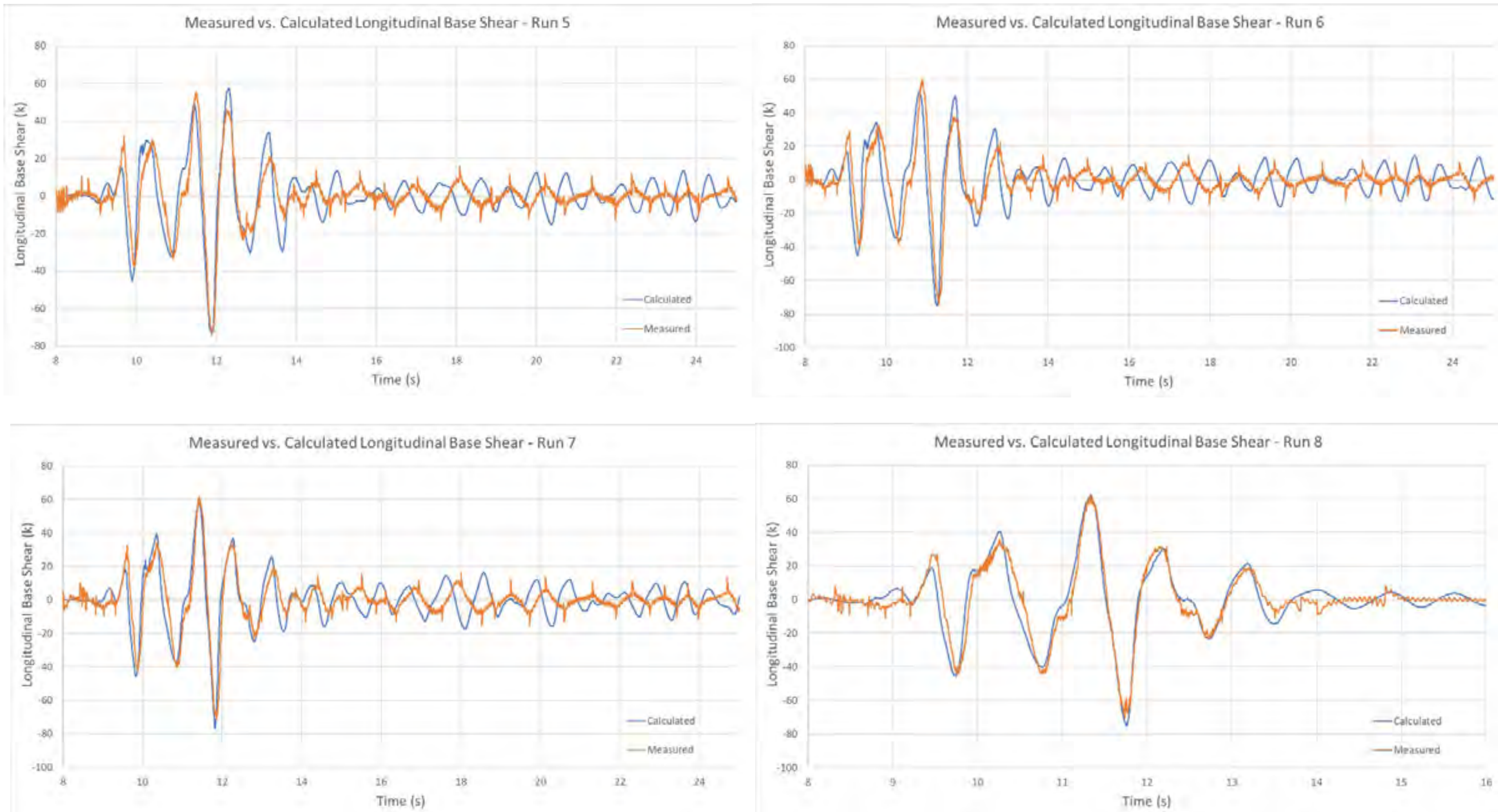

Figure 8.17: Measured and calculated longitudinal base shear history, runs 5-8

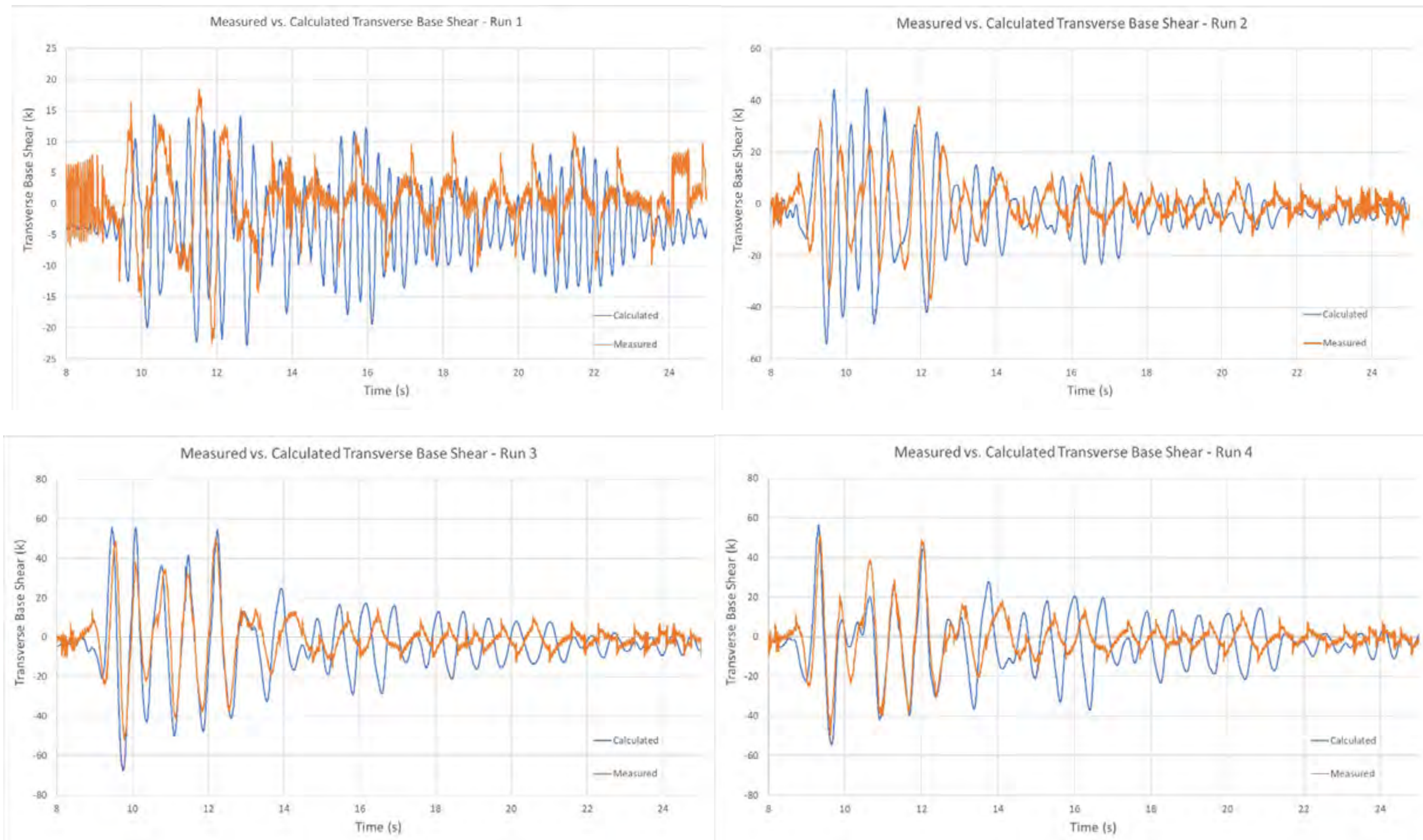

Figure 8.18: Measured and calculated transverse base shear history, run 1-4

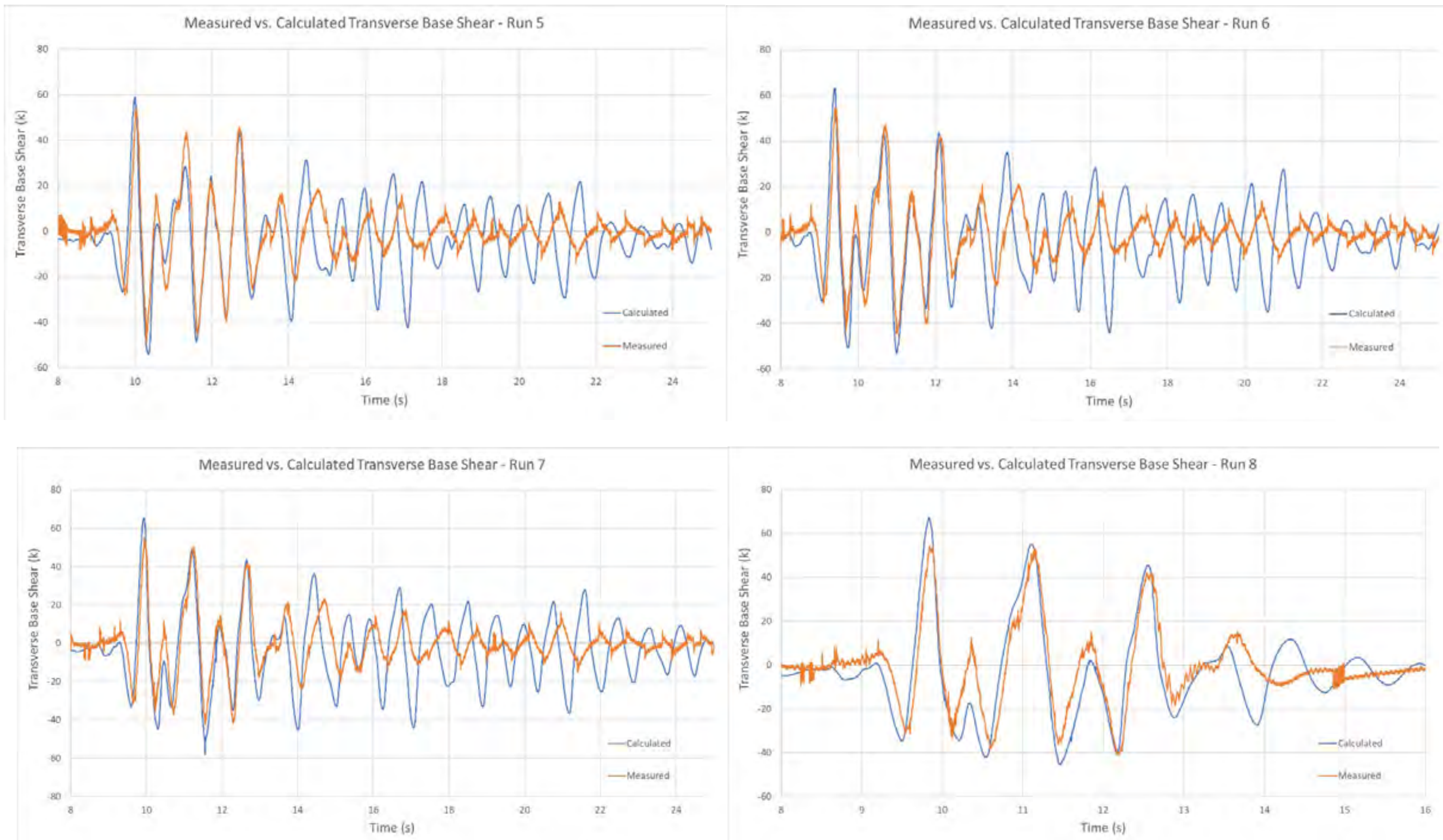

Figure 8.19: Measured and calculated transverse base shear history, runs 5-8

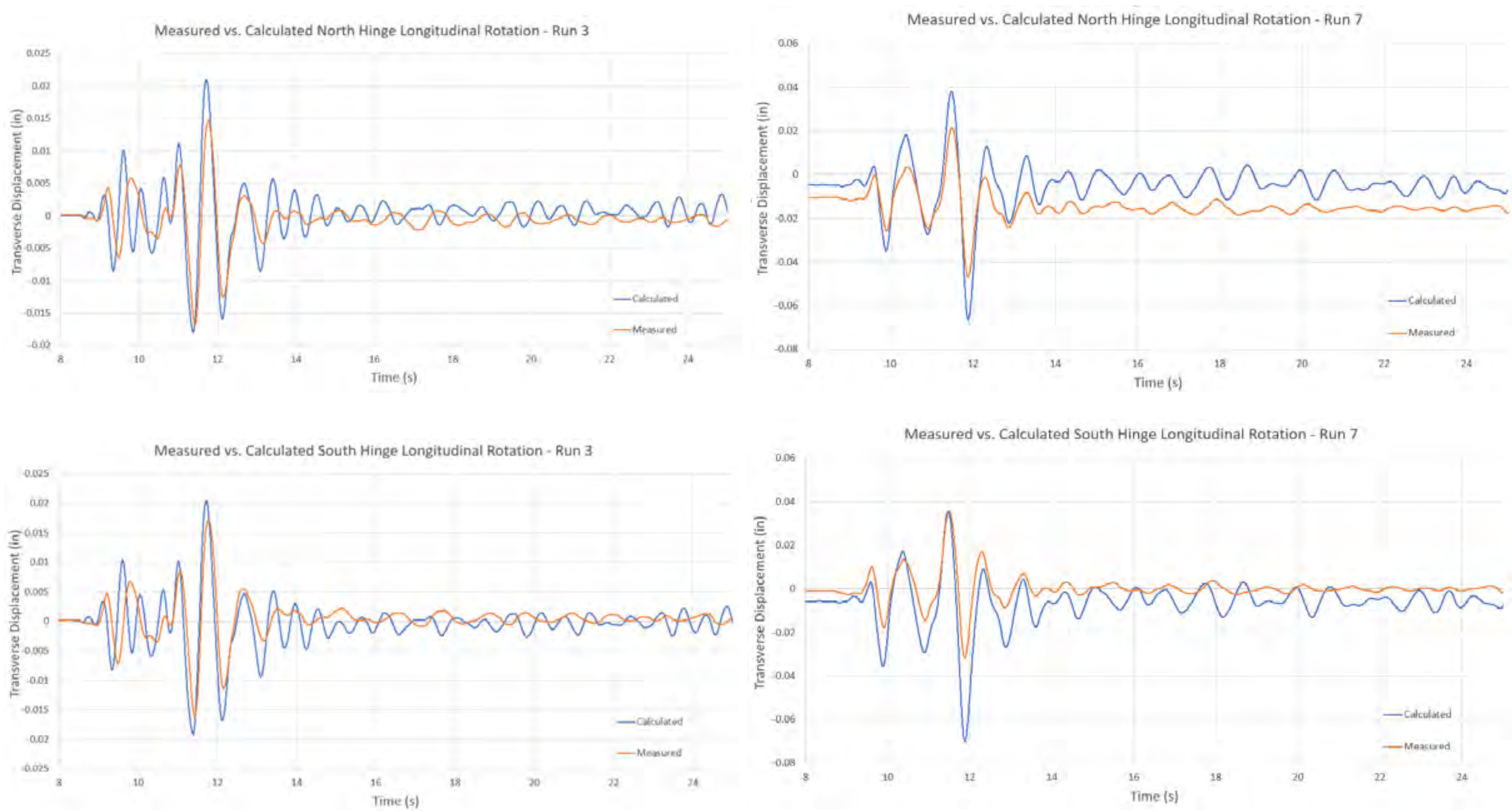

Figure 8.20 Measured and calculated longitudinal hinge rotation for north (top) and south (bottom) hinge, run 3 (left) and run 7 (right)

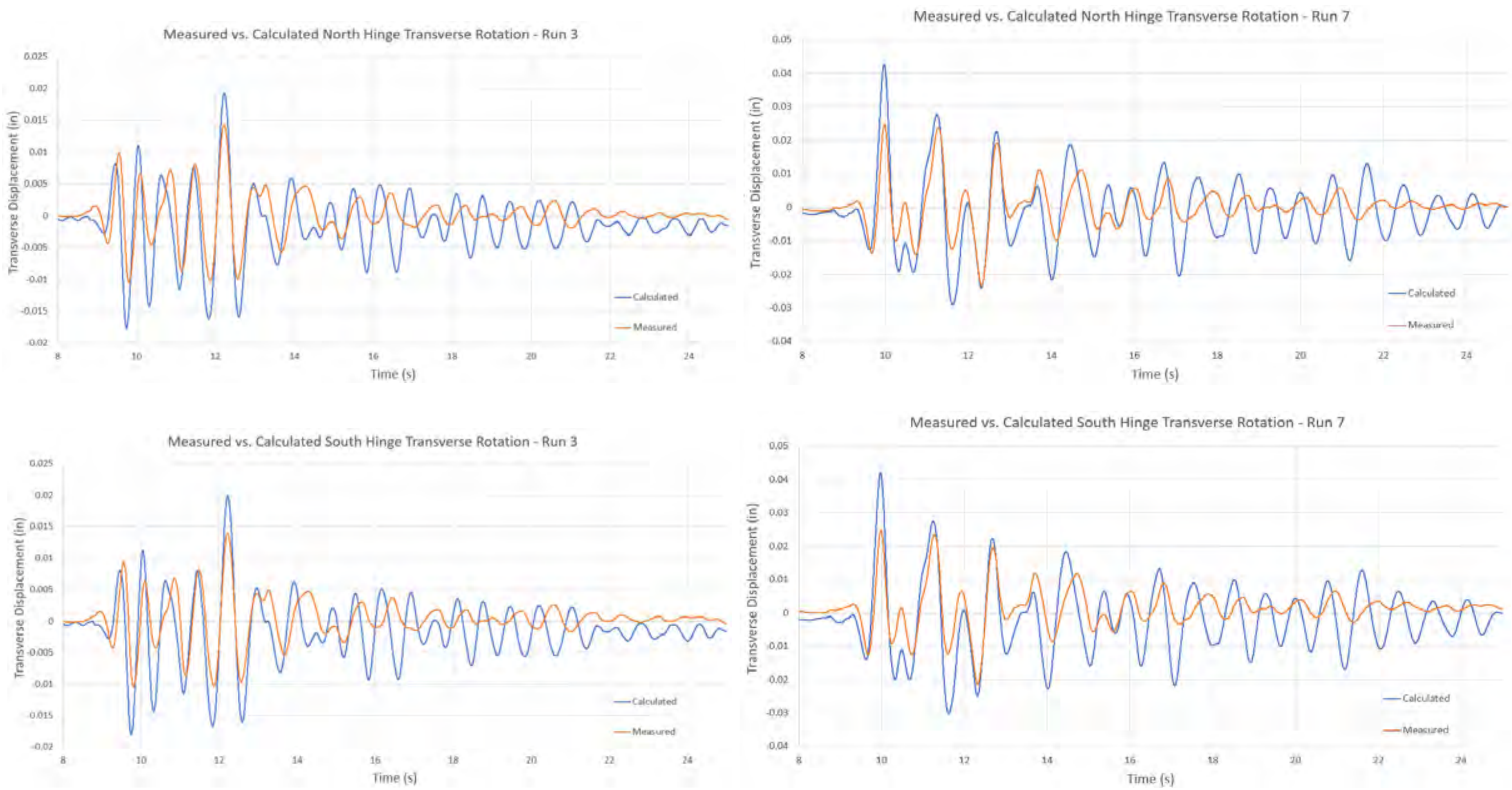

Figure 8.21 Measured and calculated transverse hinge rotation for north (top) and south (bottom) hinge, run 3 (left) and run 7 (right)

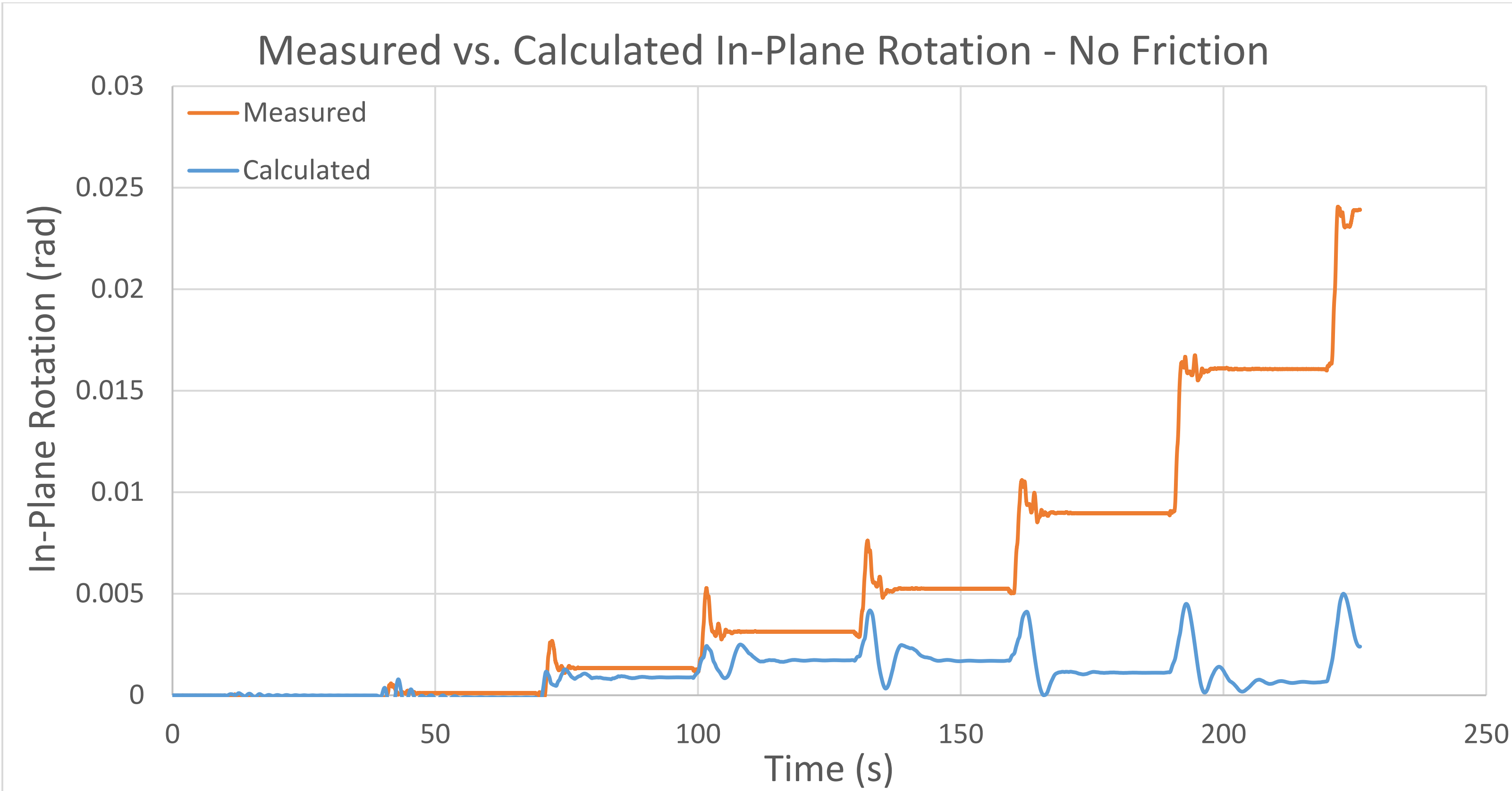

Figure 8.22 Measured and calculated in-plane rotation

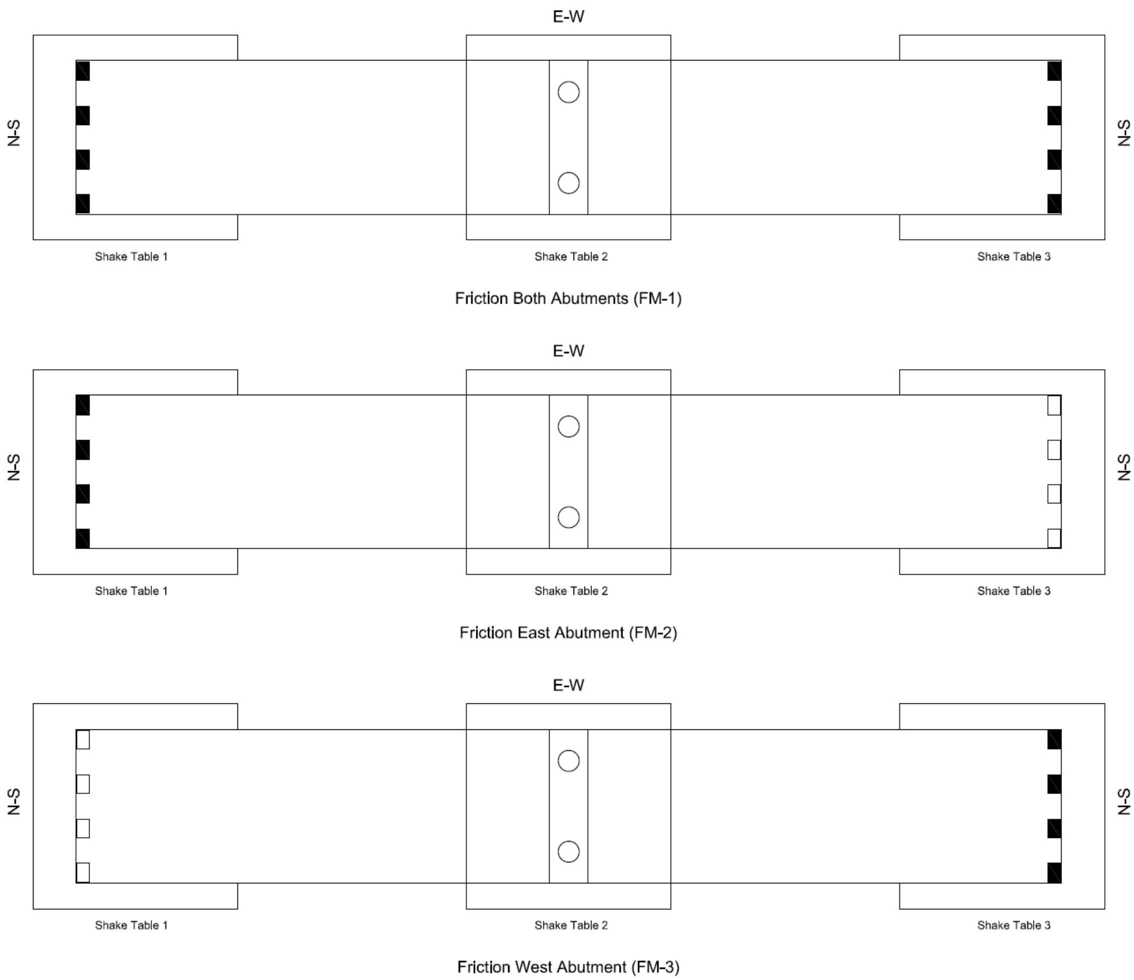

Figure 9.1 Girders with friction effects (indicated by black) for friction at both abutments (FM-1), friction at the east abutment (FM-2), and friction at the west abutment (FM-3)

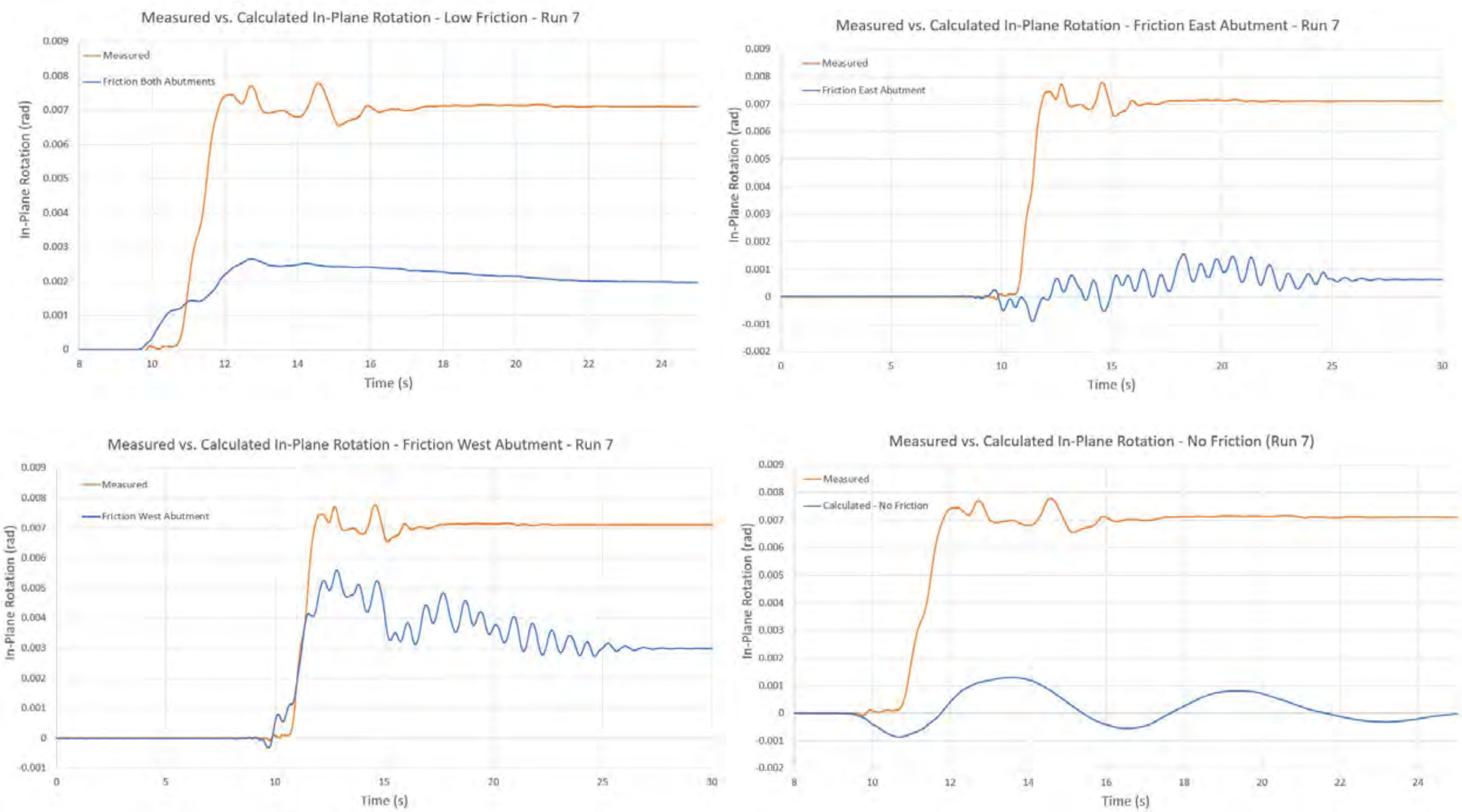

Figure 9.2 Measured and calculated in-plane rotation for FM-1 (top left), FM-2 (top right), FM-3 (bottom left), and NF (bottom right), run 7 (very low friction coefficients)

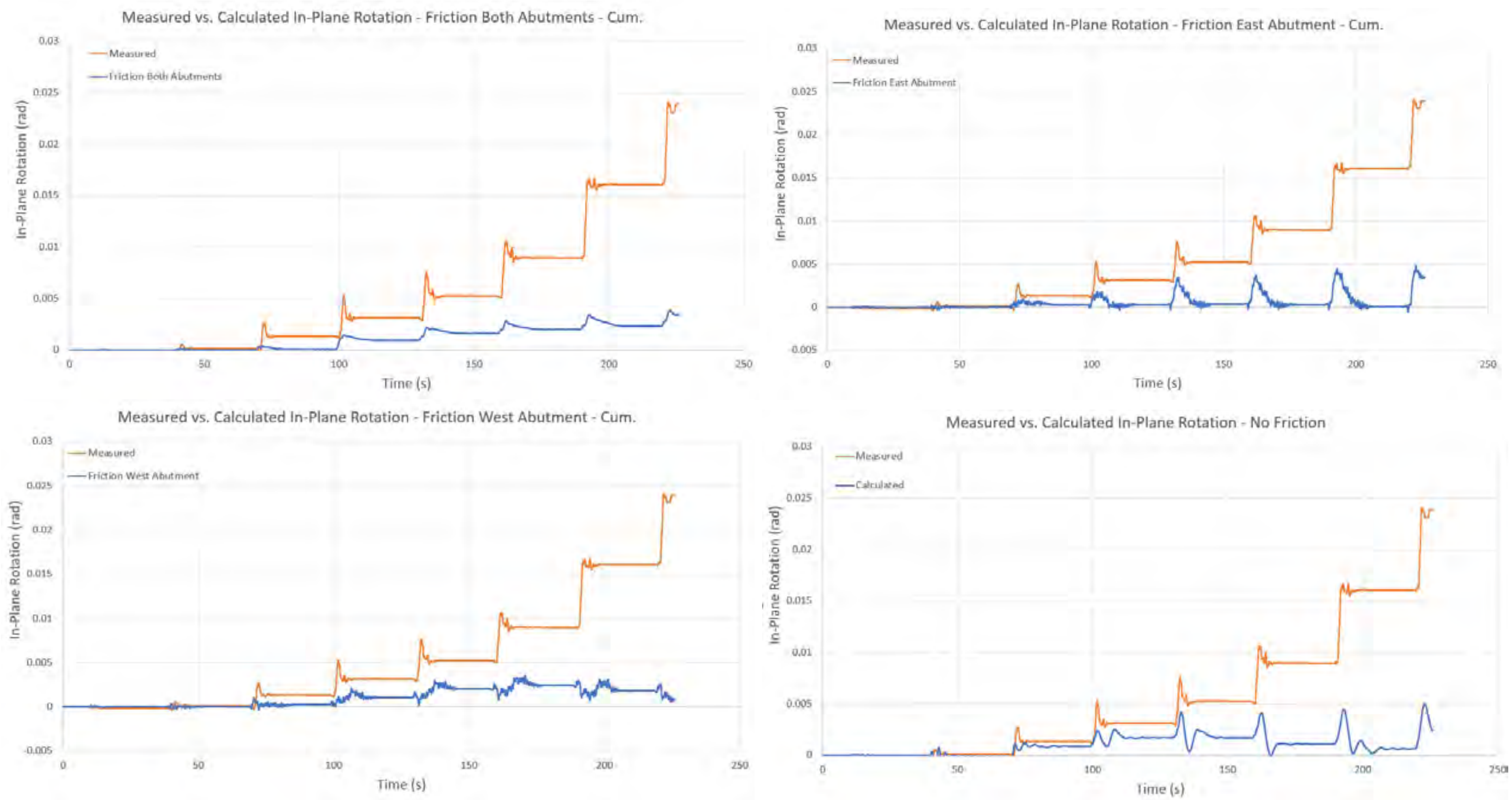

Figure 9.3 Measured and calculated in-plane rotation for FM-1 (top left), FM-2 (top right), FM-3 (bottom left), and NF (bottom right), cumulative (very low friction coefficients)

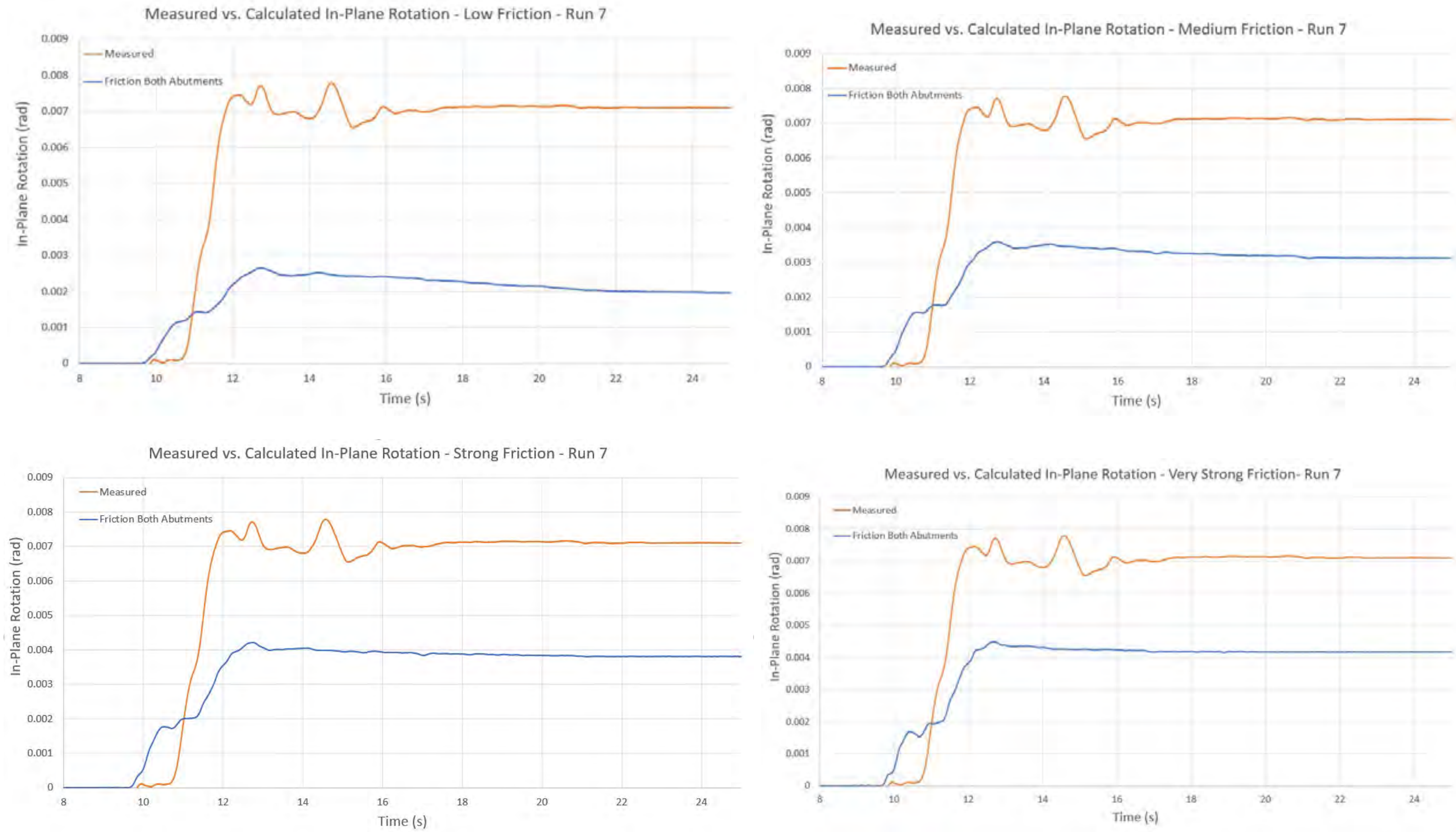

Figure 9.4 Measured and calculated in-plane rotation from FM-1 with low friction (top left), medium friction (top right), strong friction (bottom left), and very strong friction (bottom right), run 7

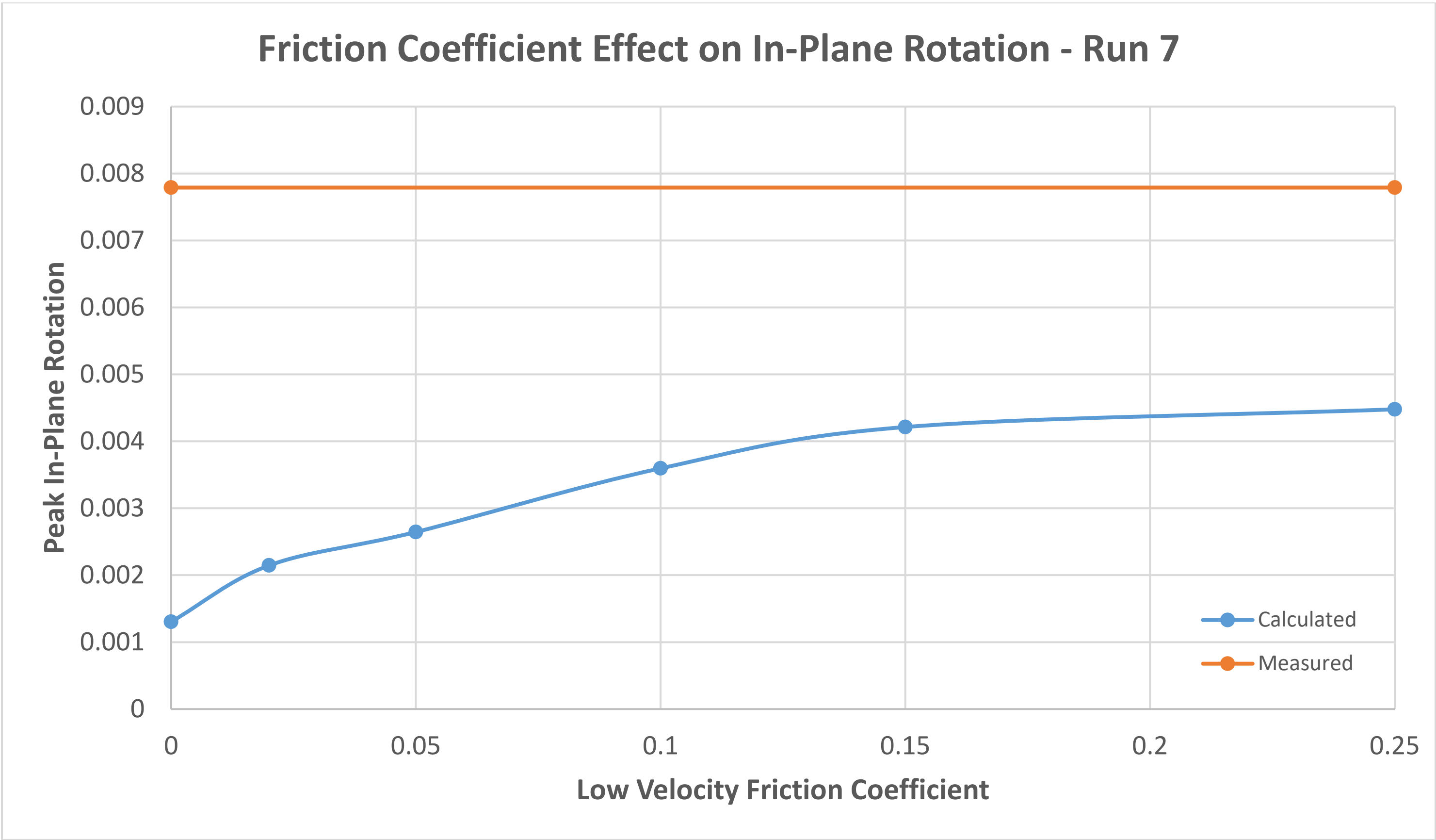

Figure 9.5 Peak in-plane rotations from FM-1 with different friction coefficients, run 7

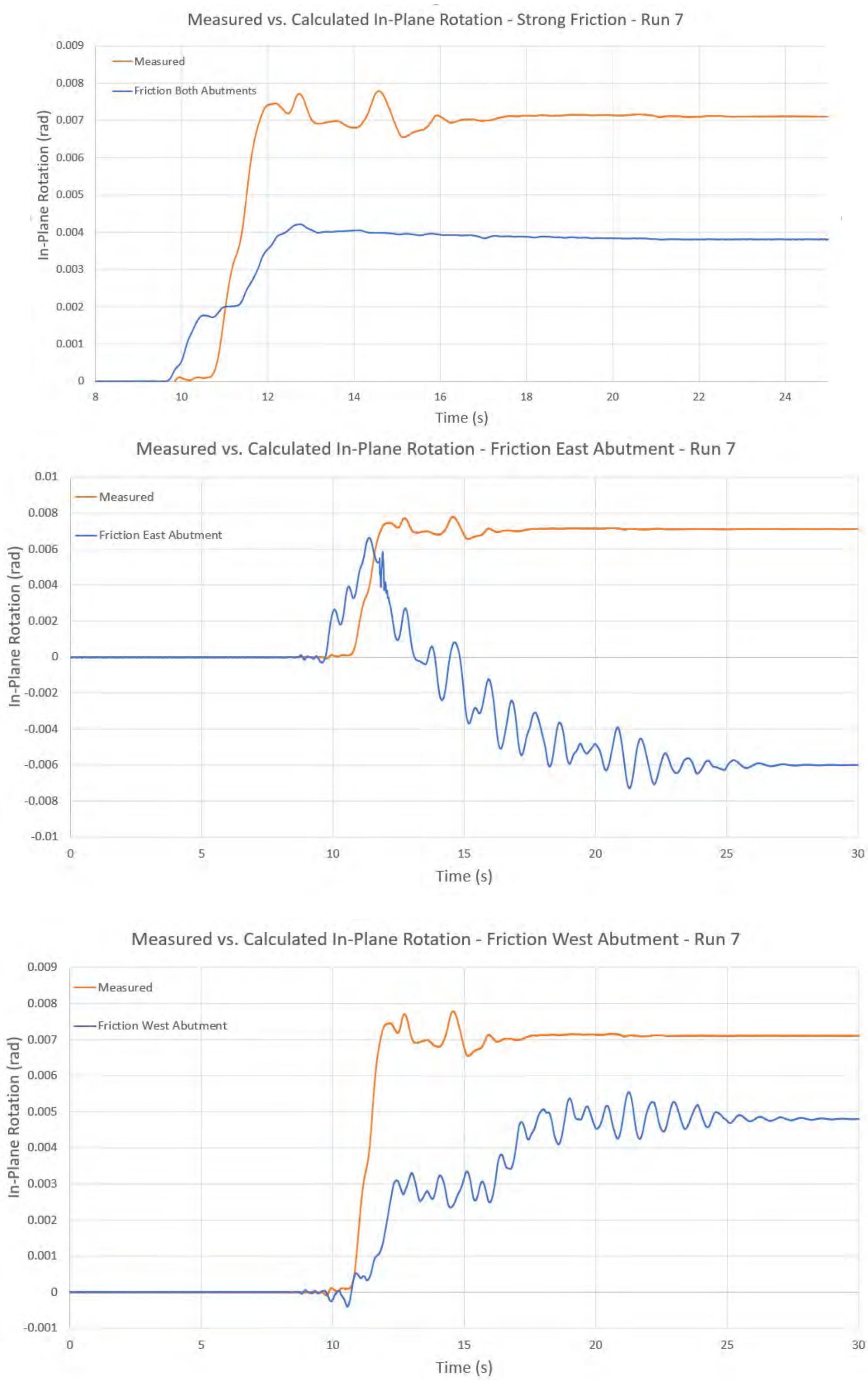

Figure 9.6 Measured and calculated in-plane rotation for FM-1 (top), FM-2 (middle), and FM-3 (bottom), run 7 (high friction coefficients)

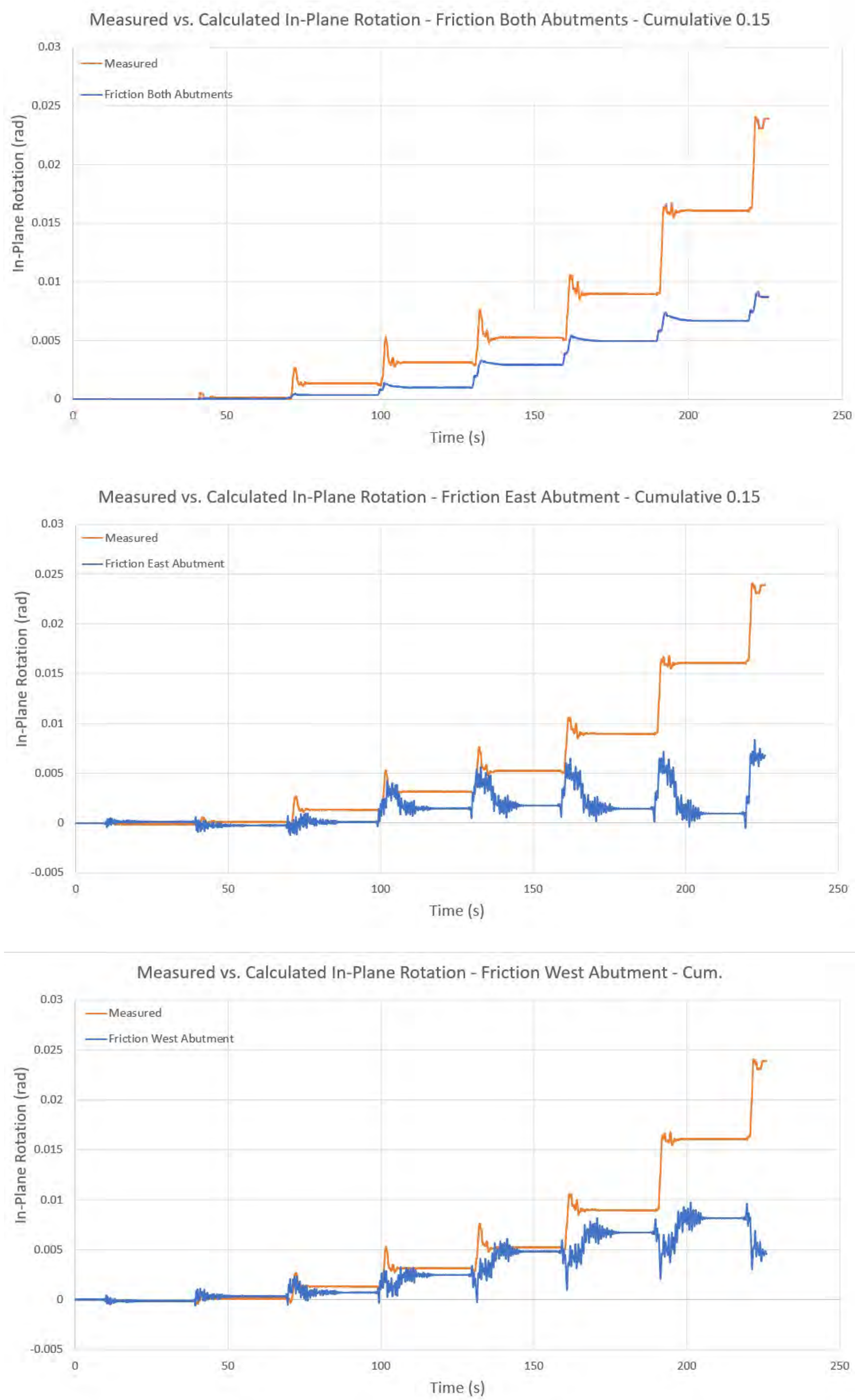

Figure 9.7: Measured and calculated in-plane rotation for FM-1 (top), FM-2 (middle), and FM-3 (bottom), cumulative (high friction coefficients)

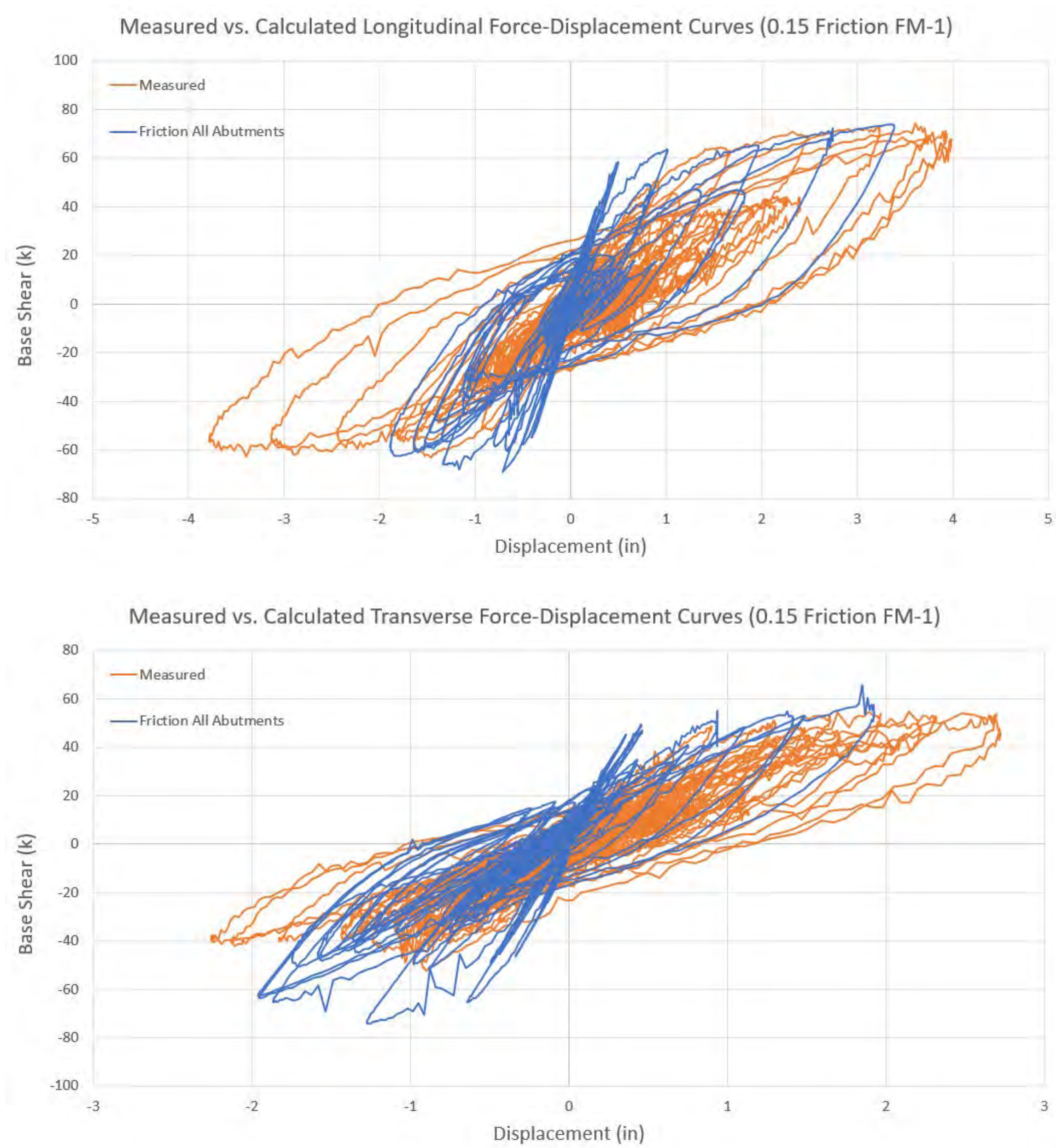

Figure 9.8: Measured and calculated hysteresis curves for FM-1 with 0.15 friction coefficient, longitudinal (top) and transverse (bottom) directions, cumulative

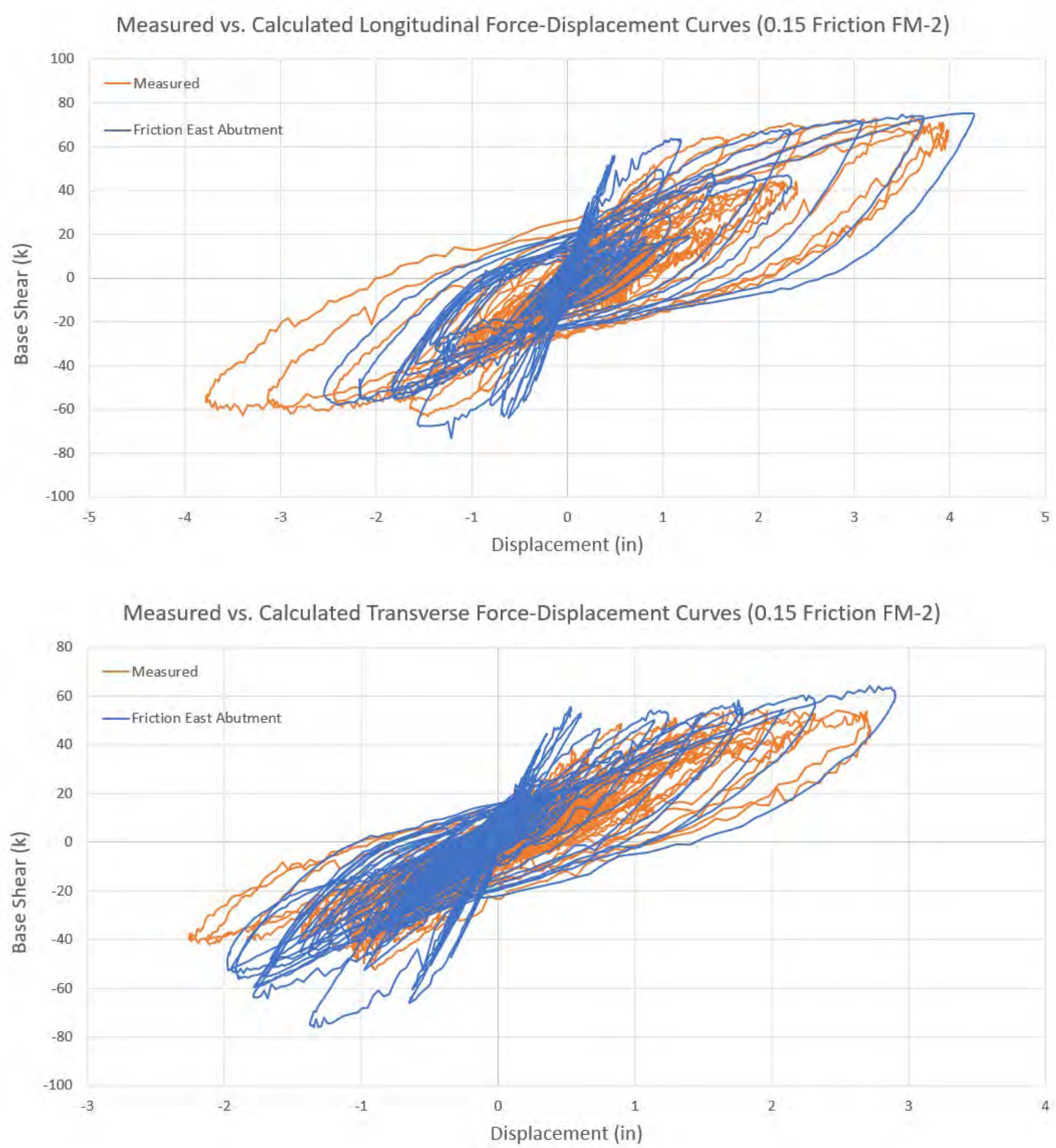

Figure 9.9: Measured and calculated hysteresis curves for FM-2 with 0.15 friction coefficient, longitudinal (top) and transverse (bottom) directions, cumulative

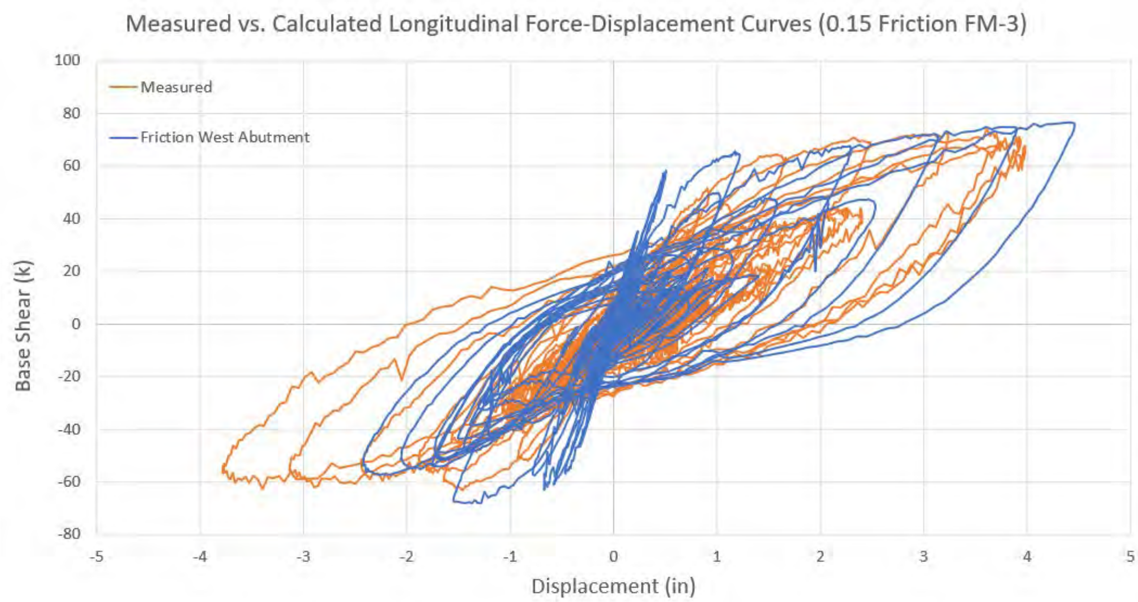

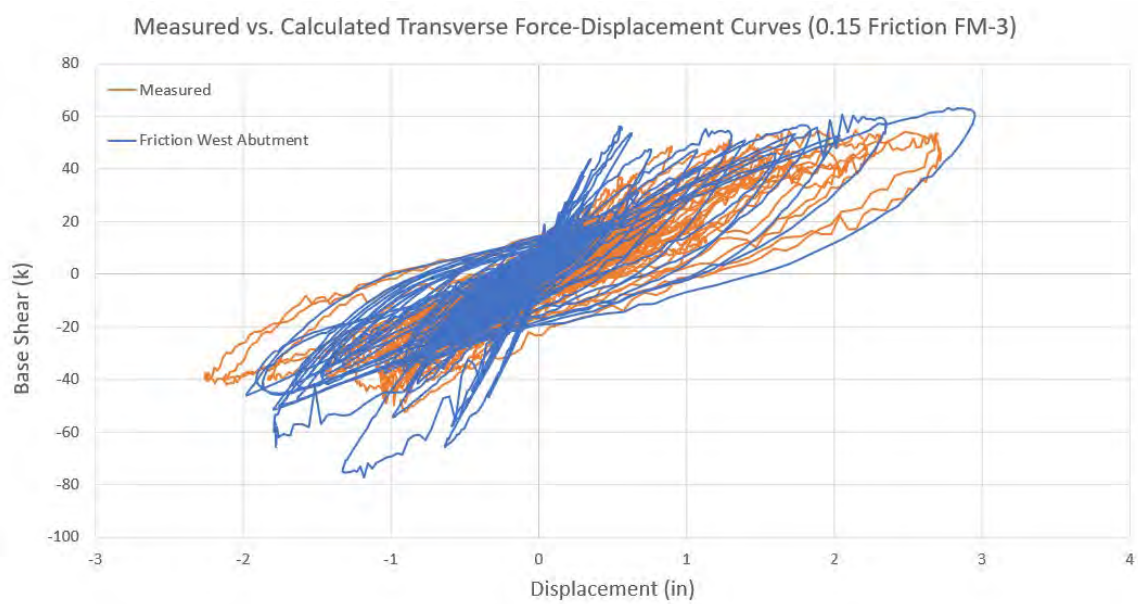

Figure 9.10: Measured and calculated hysteresis curves for FM-3 with 0.15 friction coefficient, longitudinal (top) and transverse (bottom) directions, cumulative

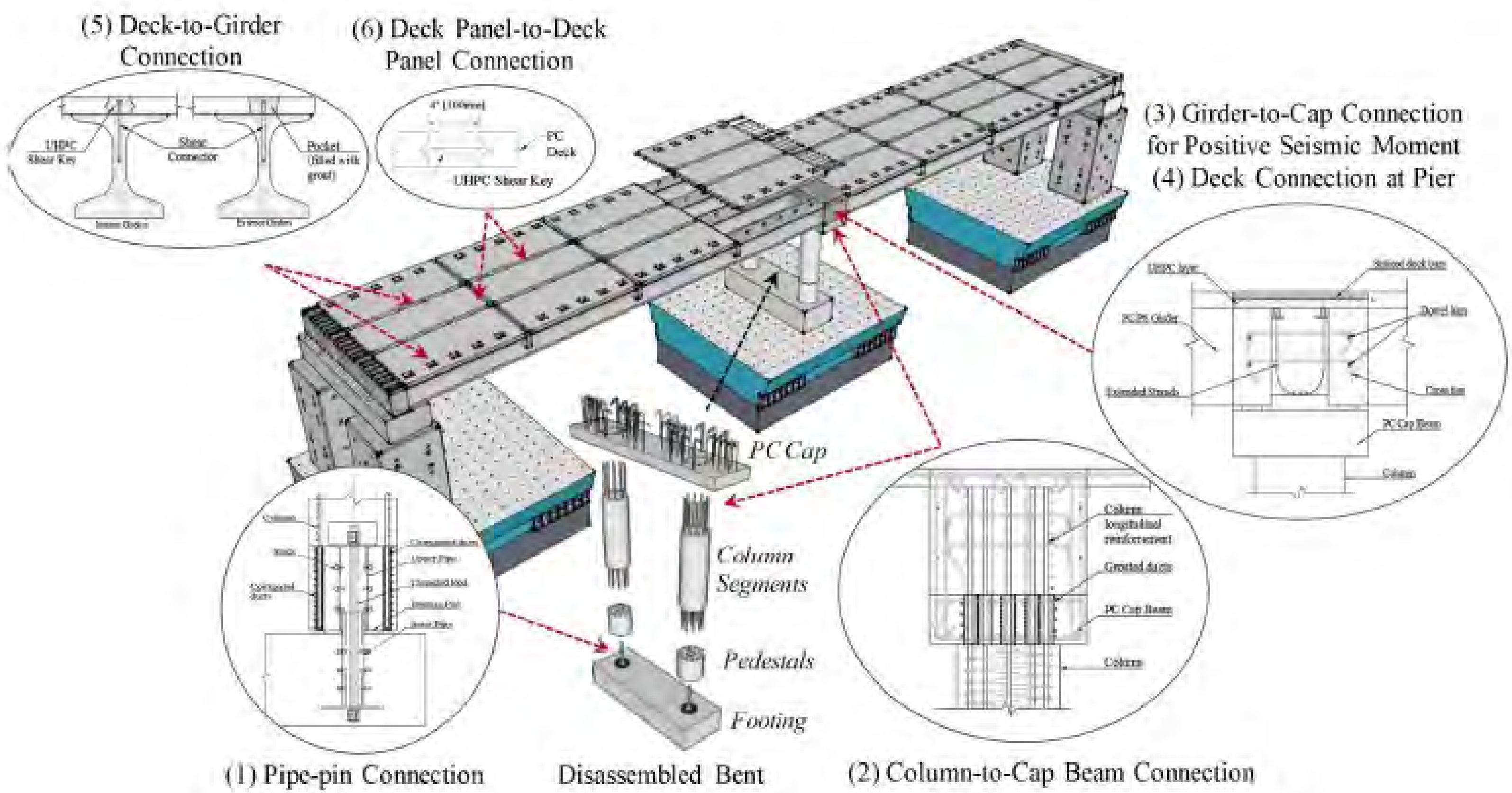

Figure 10.1: 3-D schematic of Calt-Bridge 1 with ABC connection details (Benjumea et al., 2019)

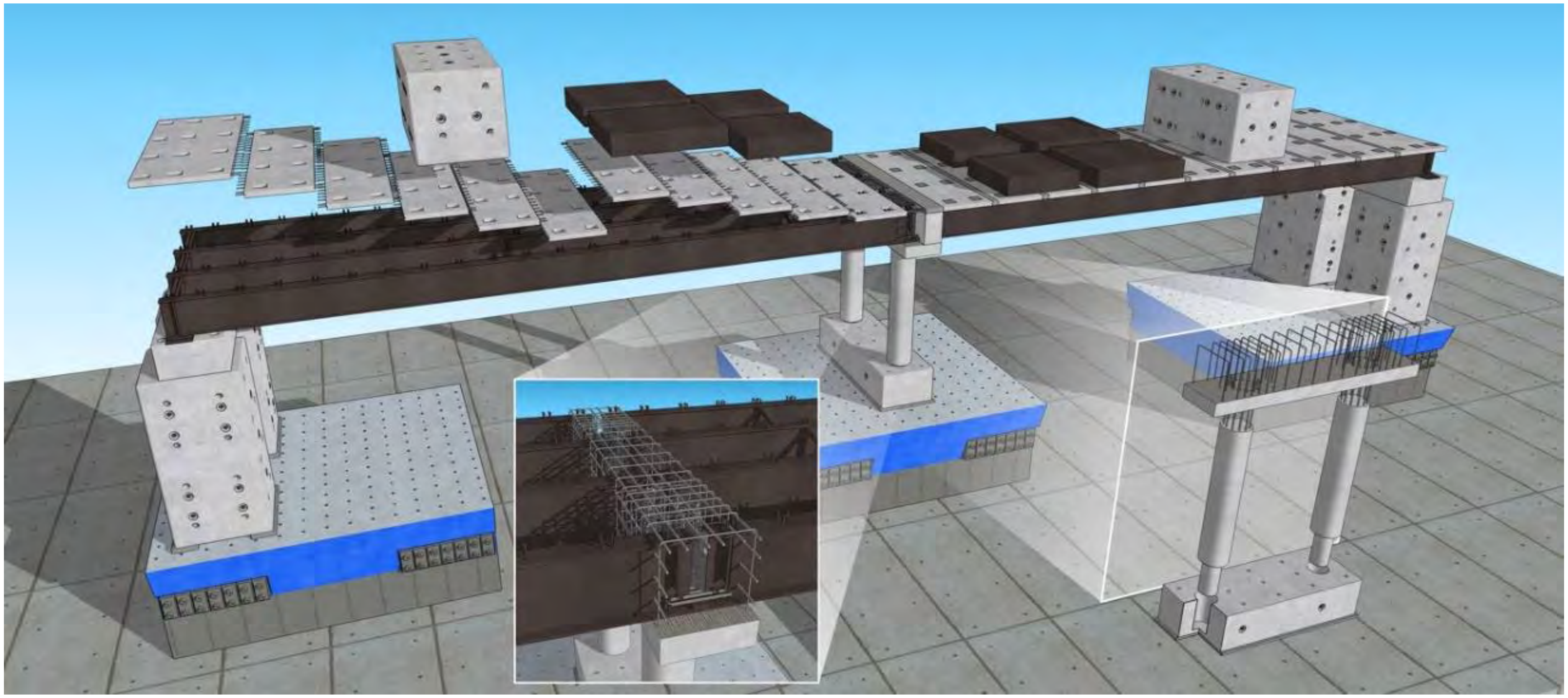

Figure 10.2: 3-D rendering of ABC-UTC, (Shoushtari et al., 2019)

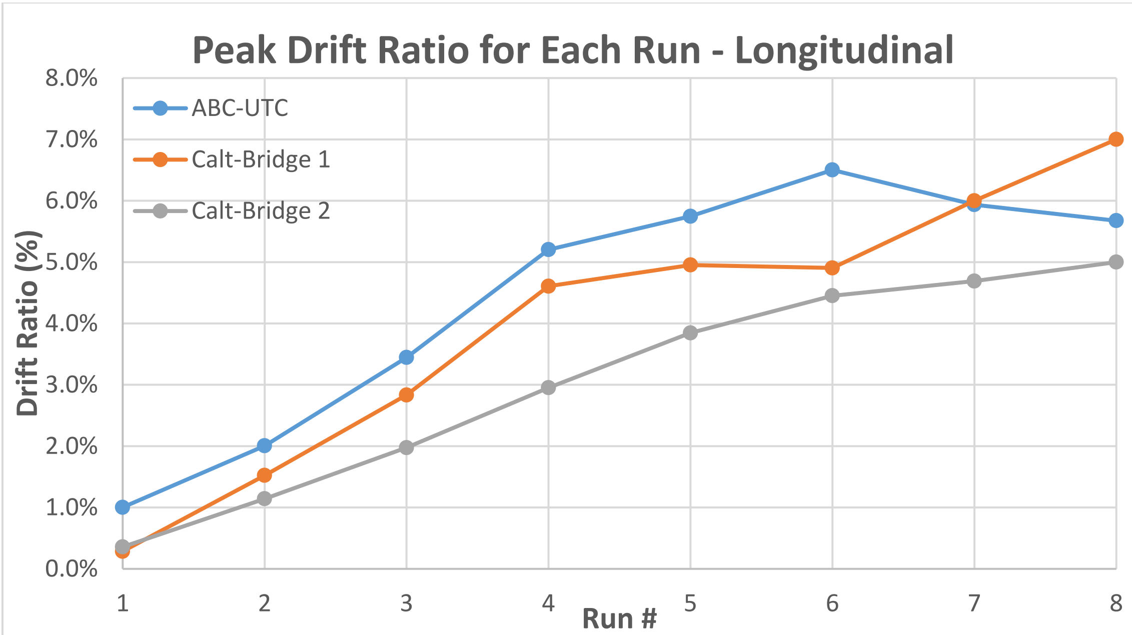

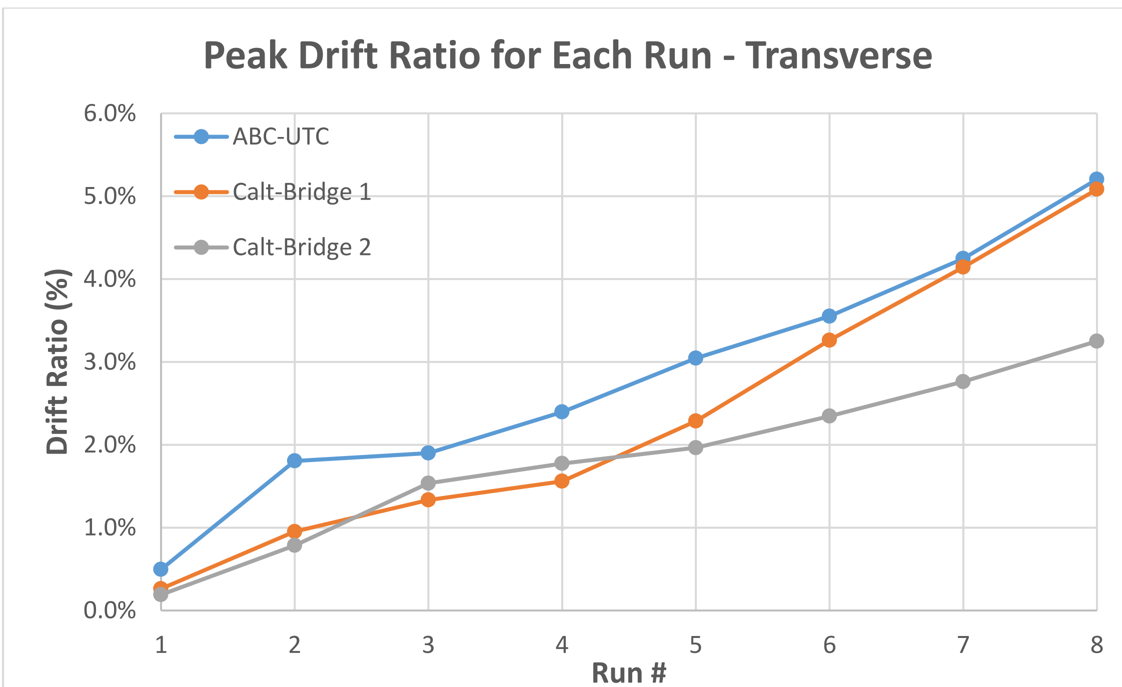

Figure 10.3 Peak drift ratio associated with each run for the three bridges in the longitudinal (top) and transverse (bottom) directions

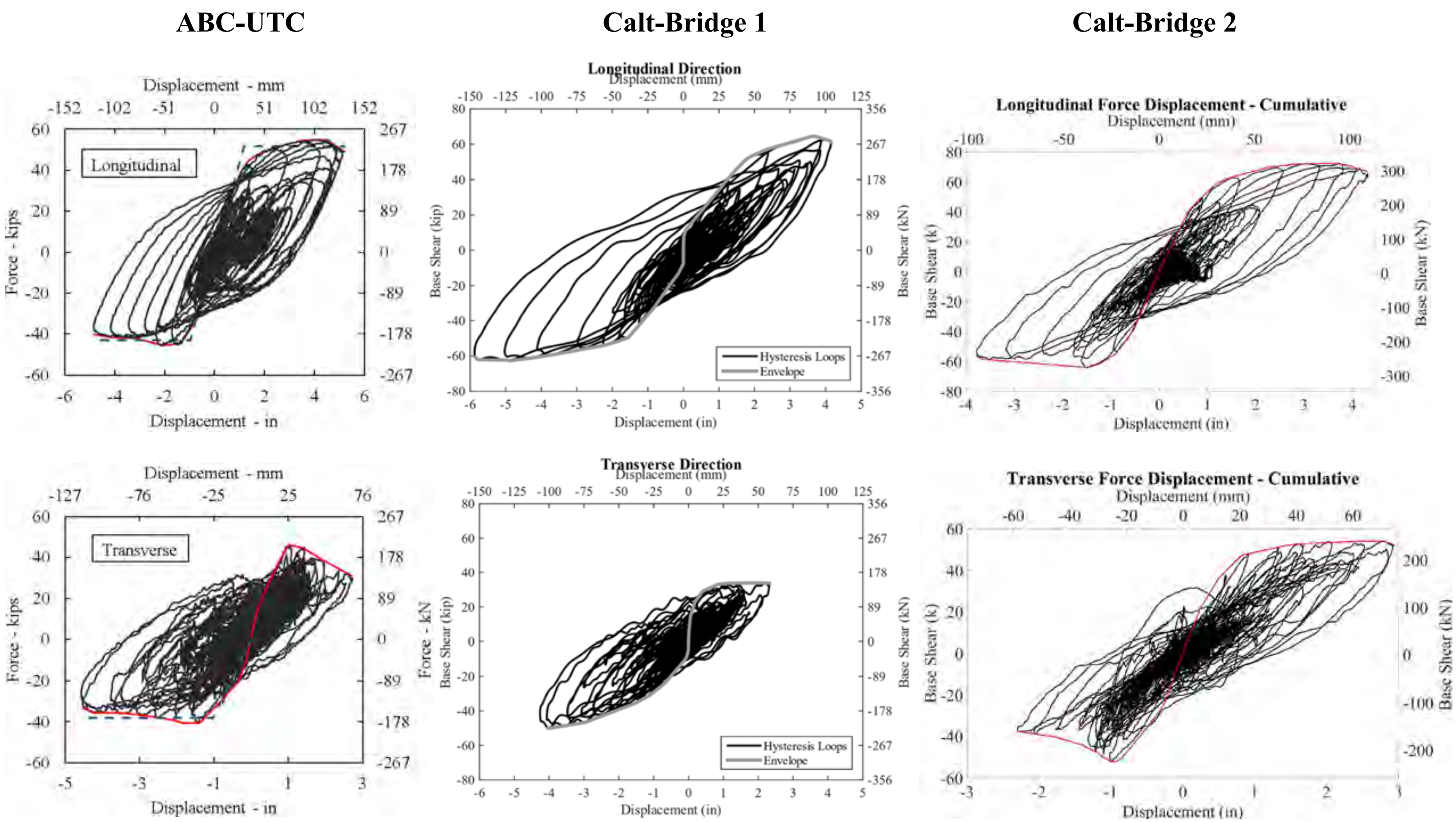

Figure 10.4 Measured force-displacement curves for longitudinal (top) and transverse (bottom) directions for ABC-UTC (Shoushtari et al., 2019), Calt-Bridge 1 (Benjumea et al., 2019), and Calt-Bridge 2

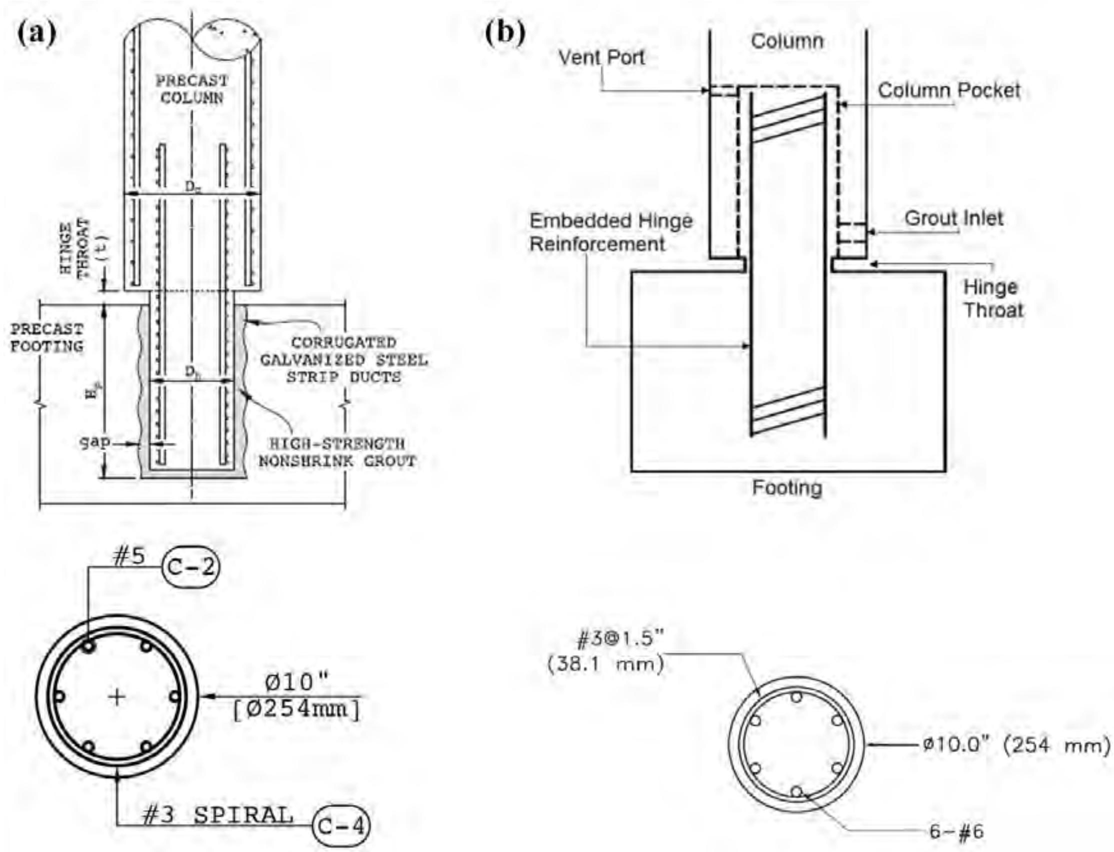

Figure 10.5 Elevation view of the bent and rebar hinge cross sections for ABC-UTC (a) and Calt-Bridge 2 (b)

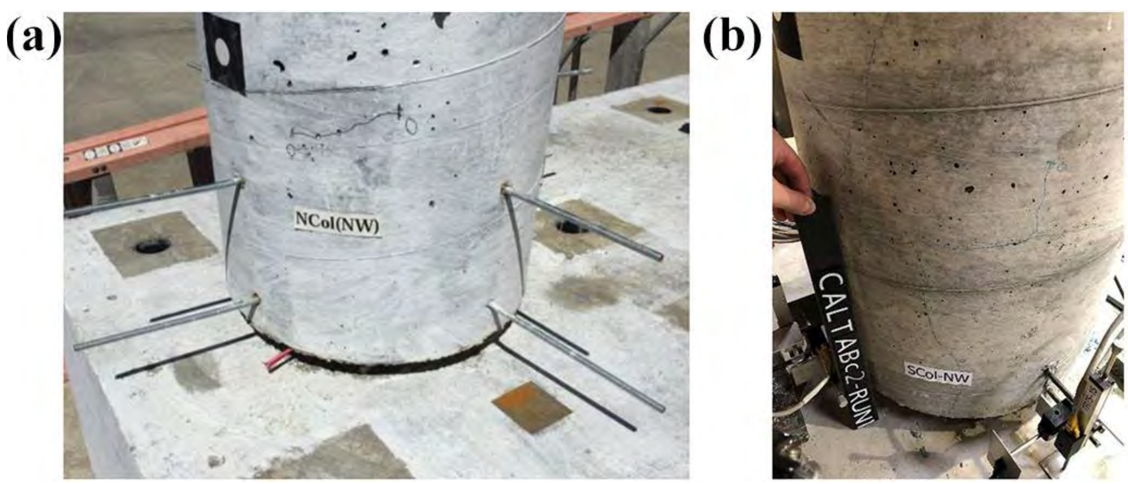

Figure 10.6 Damage state of column and rebar hinge at conclusion of run 8, ABC-UTC (a) and Calt-Bridge 2 (b)

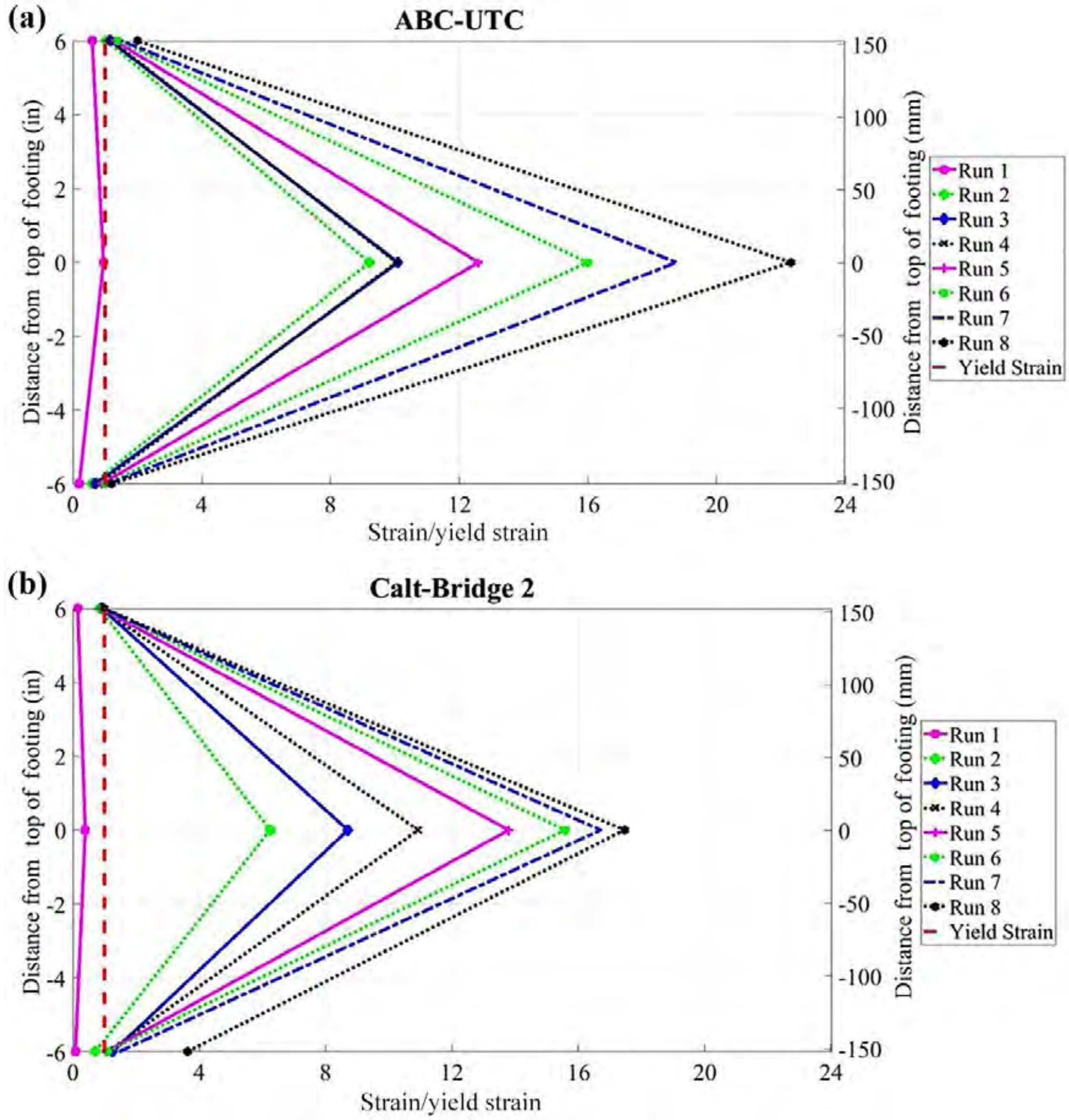

Figure 10.7 Strain profiles within the hinge: ABC-UTC (a), Calt-Bridge 2 (b)

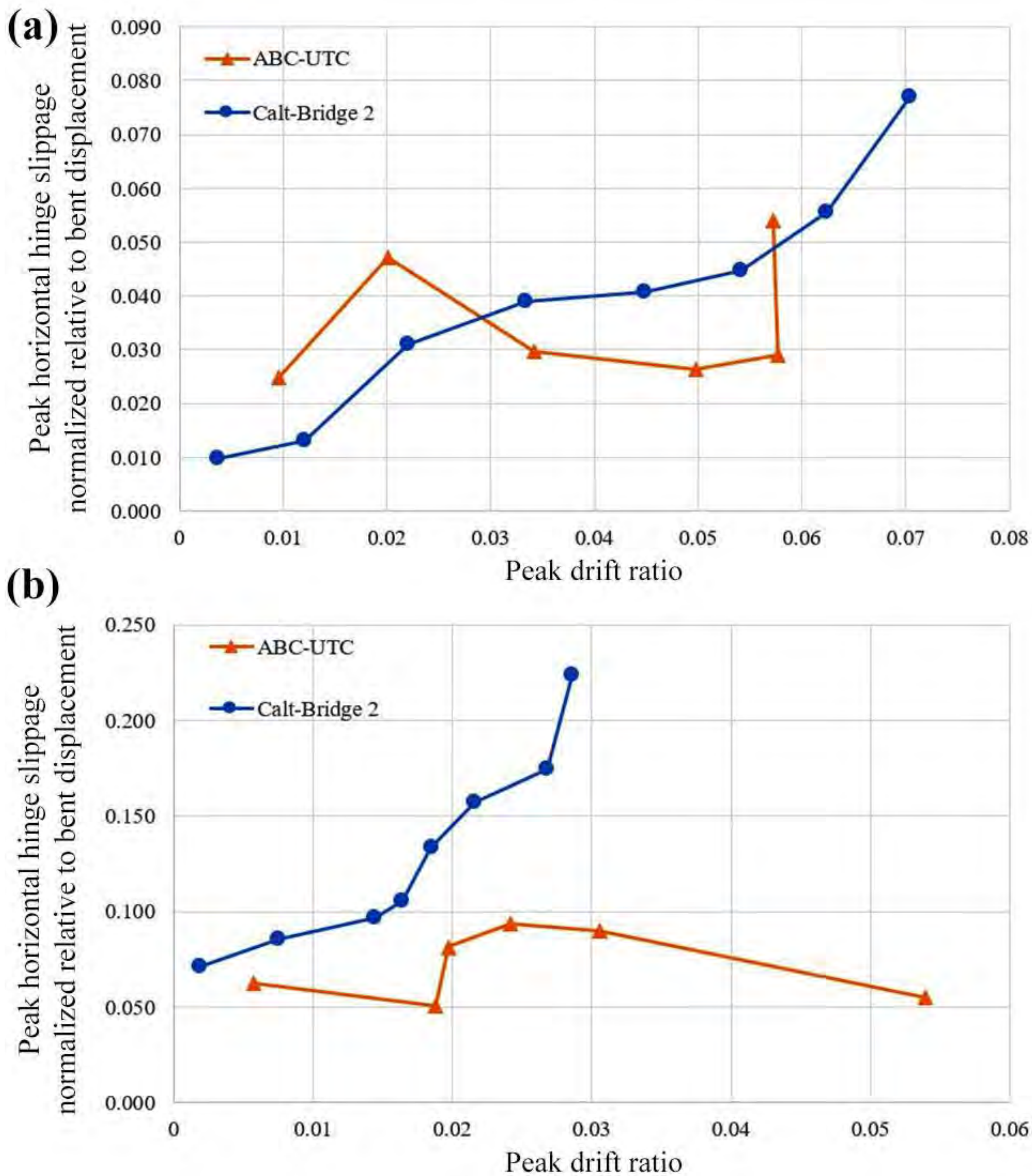

Figure 10.8 Peak drift ratio relative to ratio of hinge slippage to bent displacement for the longitudinal (a) and transverse (b) directions

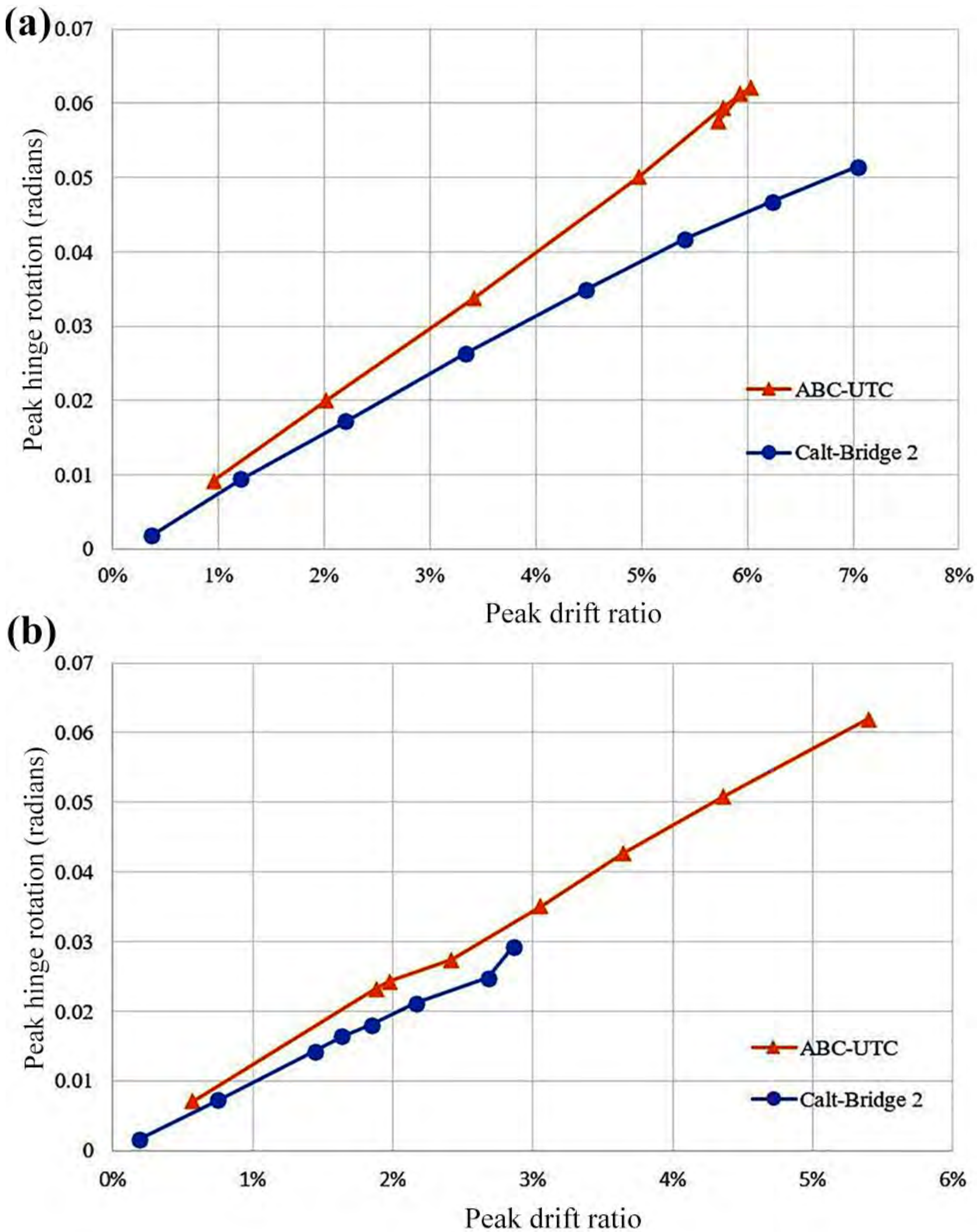

Figure 10.9 Peak drift ratio relative to hinge rotation for the longitudinal (a) and transverse (b) directions

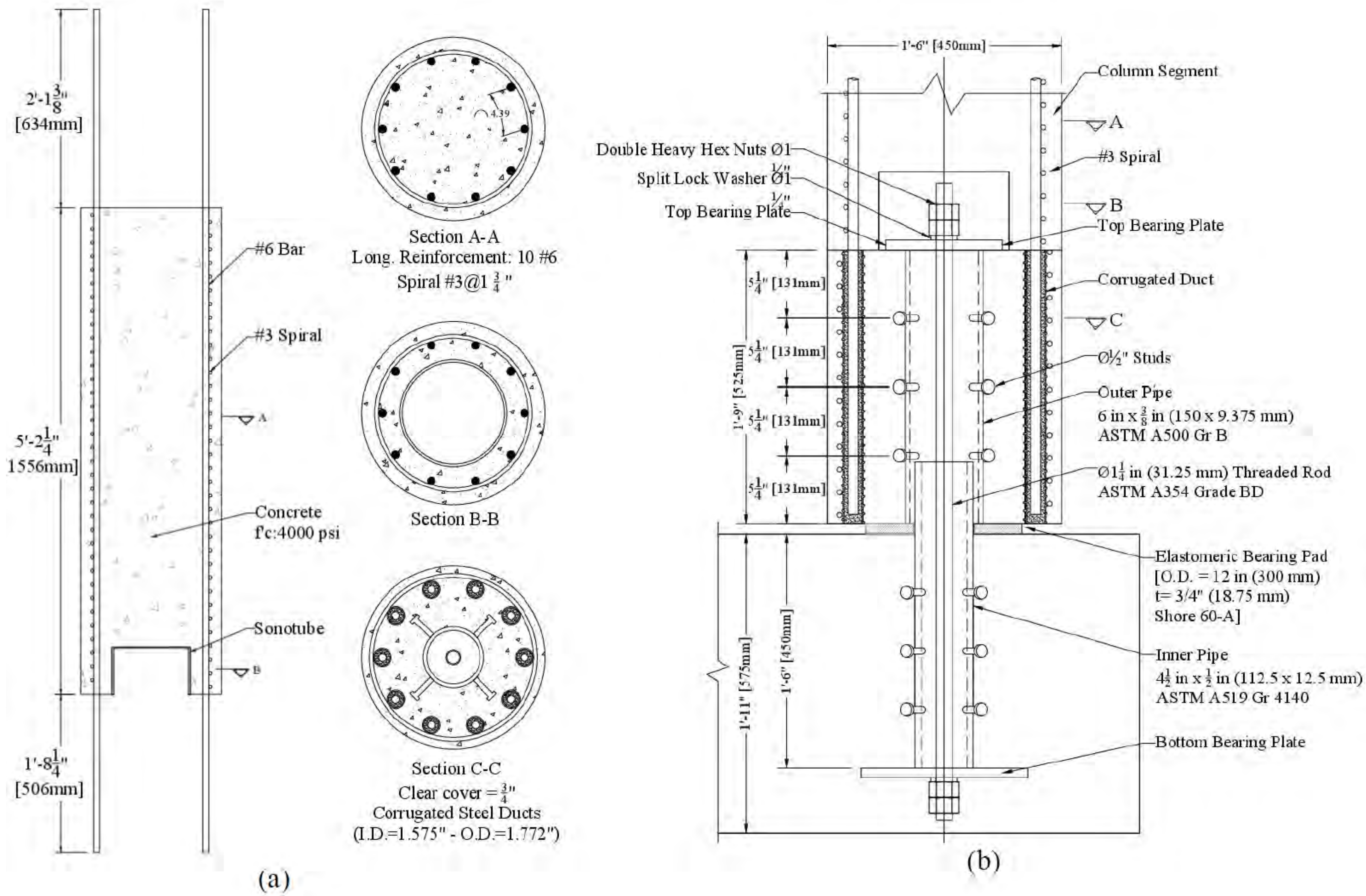

Figure 10.10 Details for precast column segments (a), and pedestals (b) for Calt-Bridge 1 (Benjumea et al., 2019)

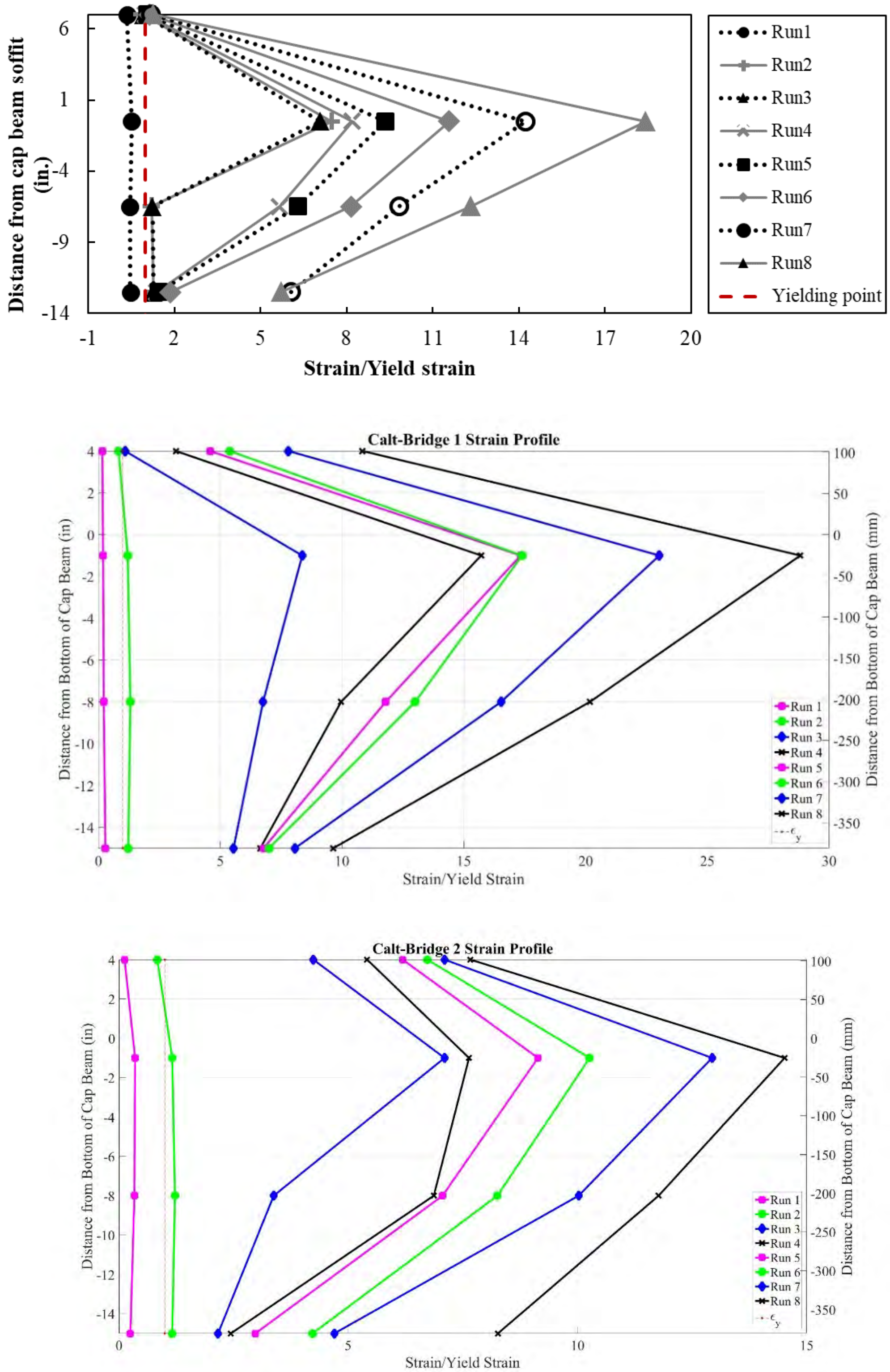

Figure 10.11: Strain profile normalized to yield strain for ABC-UTC (top) (Shoushtari et al., 2019), Calt-Bridge 1 (middle), and Calt-Bridge 2 (bottom)

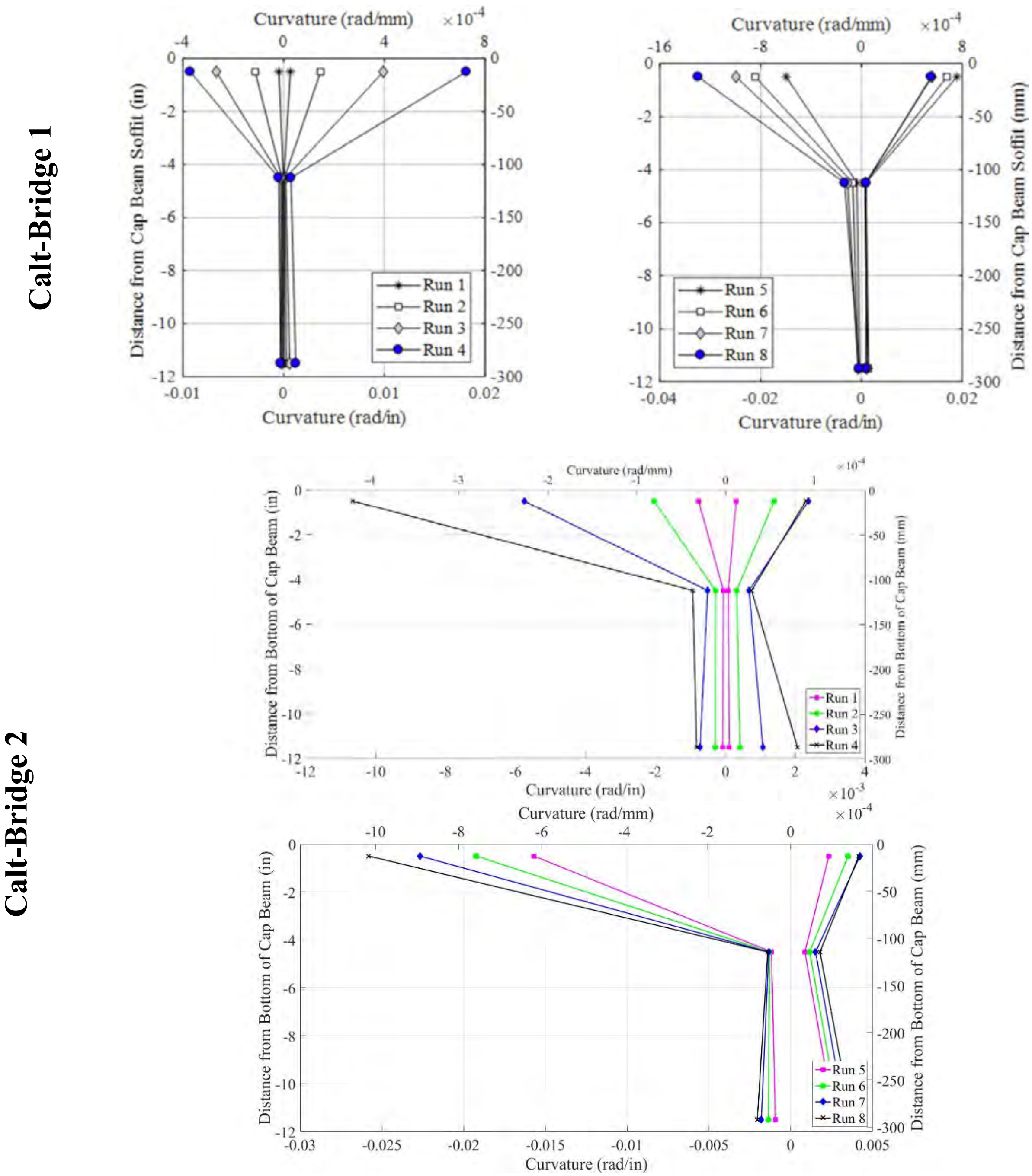

Figure 10.12 Curvature profile associated with longitudinal translation of the bridge for the top of the N. column in Calt-Bridge 1 (Benjumea et al., 2019) (top), and Calt-Bridge 2 (bottom)

Appendix A: Construction Drawings for Calt-Bridge 2

Caltrans ABC Bridge 2
Bent Drawings

Notes:

University of Nevada, Reno / Caltrans	Project: Calt-ABC Bridge 2	
	Contains:	Sheet:
	Designed and Drawn by: Jared Jones	00 of 10
	Scale: N/A — Date: 7/11/2017	

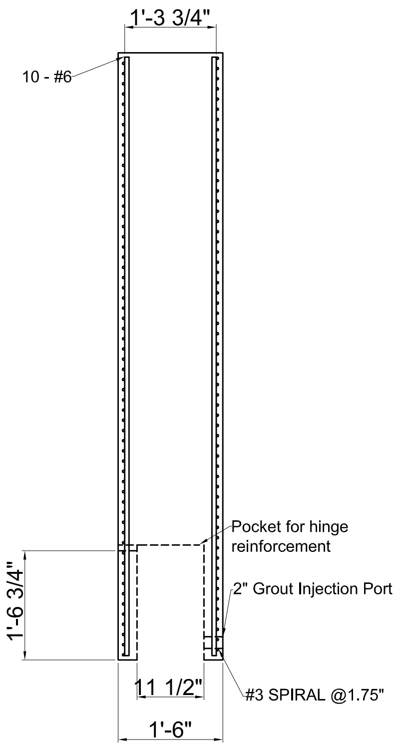

PRECAST COLUMN

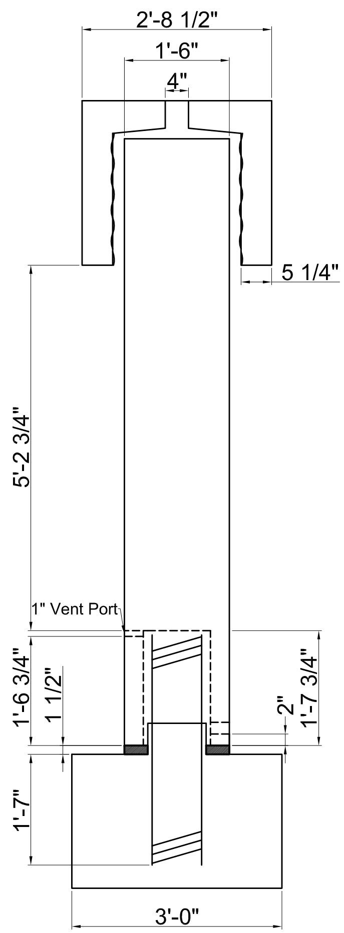

LATERAL VIEW

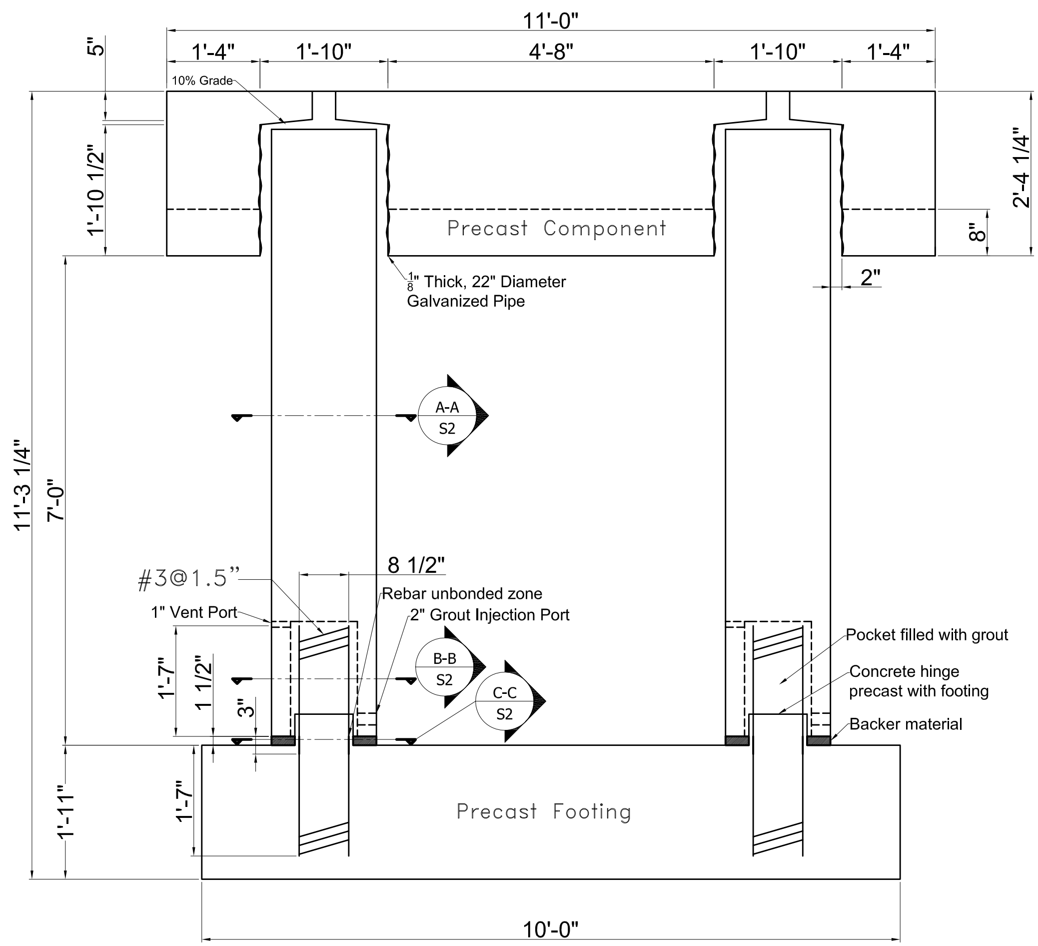

ELEVATION

University of Nevada, Reno
Caltrans

Project: Calt - ABC Bridge 2
Contains: Rebar Hinge Profile
Designed and Drawn by: Jared Jones
Scale: 3/8"=1'-0"
Date: 7/11/2017
Sheet: 01 of 10

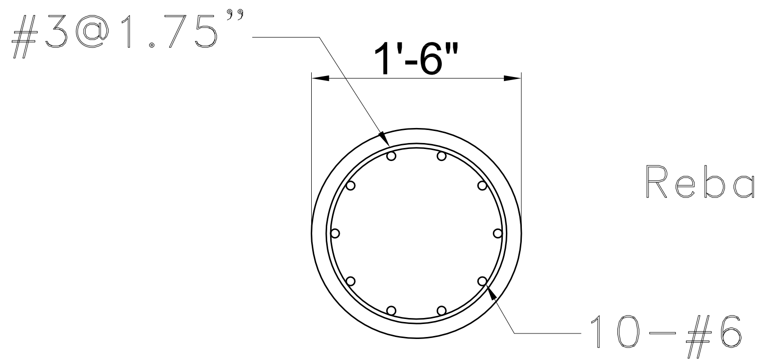

Section A-A

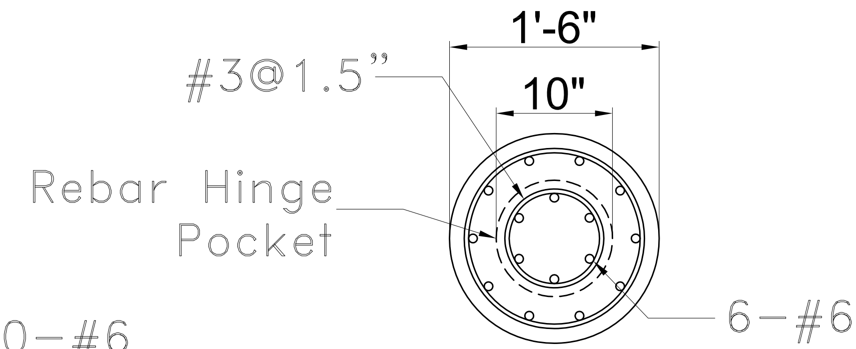

Section B-B

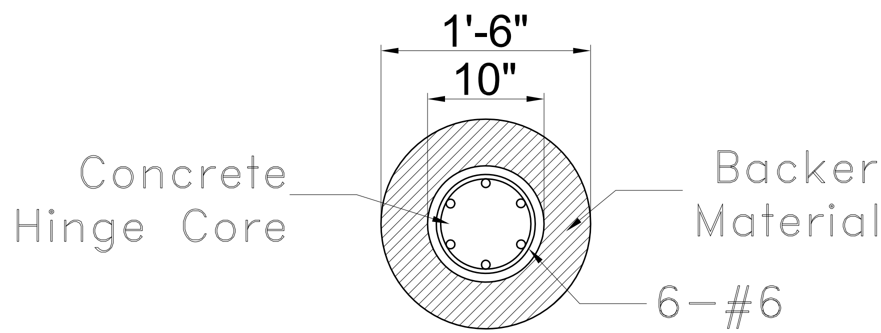

Section C-C

NOTE: 3/4" COVER FOR HINGE SECTIONS

NOTE: 1 1/2" COVER FOR COLUMN SECTIONS

University of Nevada, Reno / Caltrans	Project: Calt - ABC Bridge 2		
	Contains: Rebar Hinge Cross Sections		Sheet:
	Designed and Drawn by: Jared Jones		02 of 10
	Scale: 3/4"=1'-0"	Date: 7/11/2017	

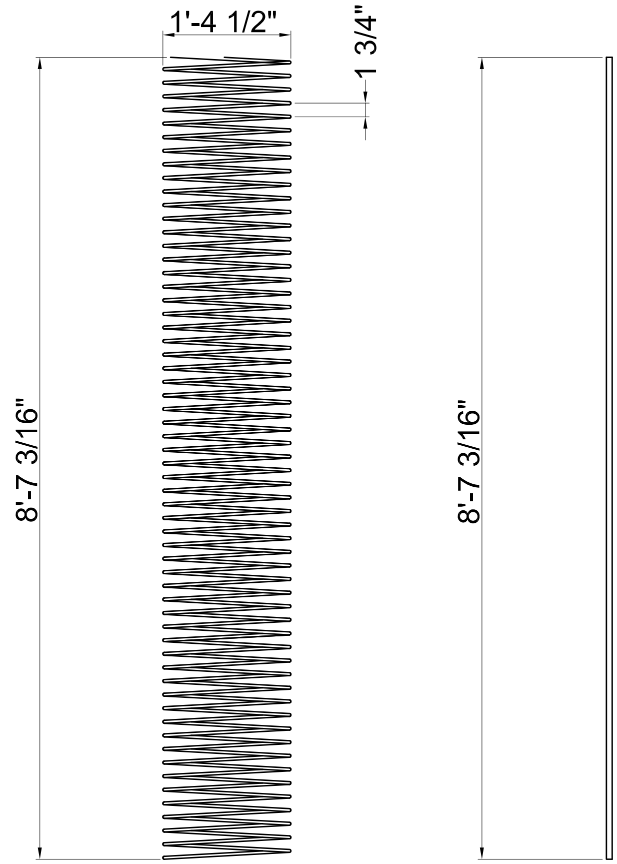

2 #3 Spiral @1.75" Pitch

20 #6 Bar

University of Nevada, Reno / Caltrans	Project: Project: Calt - ABC Bridge 2	
	Contains: Column Reinforcement	Sheet: 03 of 10
	Designed and Drawn by: Jared Jones	
	Scale: 3/4"=1'-0" Date: 7/11/2017	

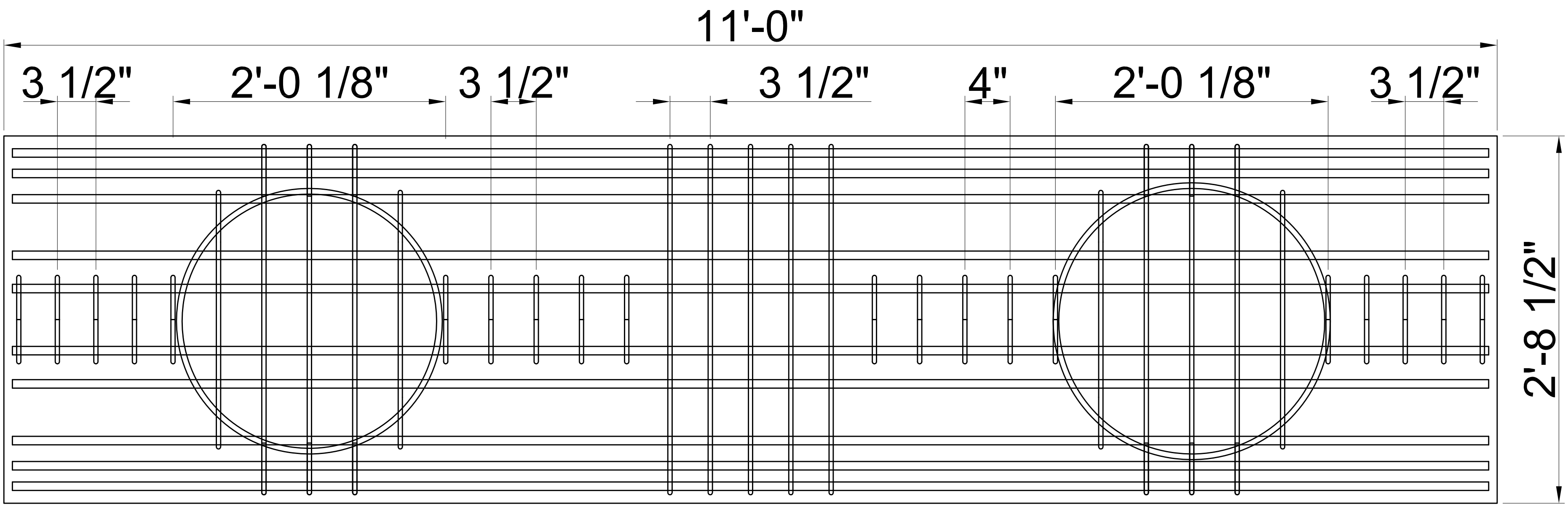

CAP BEAM TOP REINFORCEMENT

University of Nevada, Reno

Caltrans

Project: Calt - ABC Bridge 2	
Contains: Cap Beam Reinforcement - Top View	Sheet:
Designed and Drawn by: Jared Jones	04 of 10
Scale: 1"=1'-0" Date: 7/11/2017	

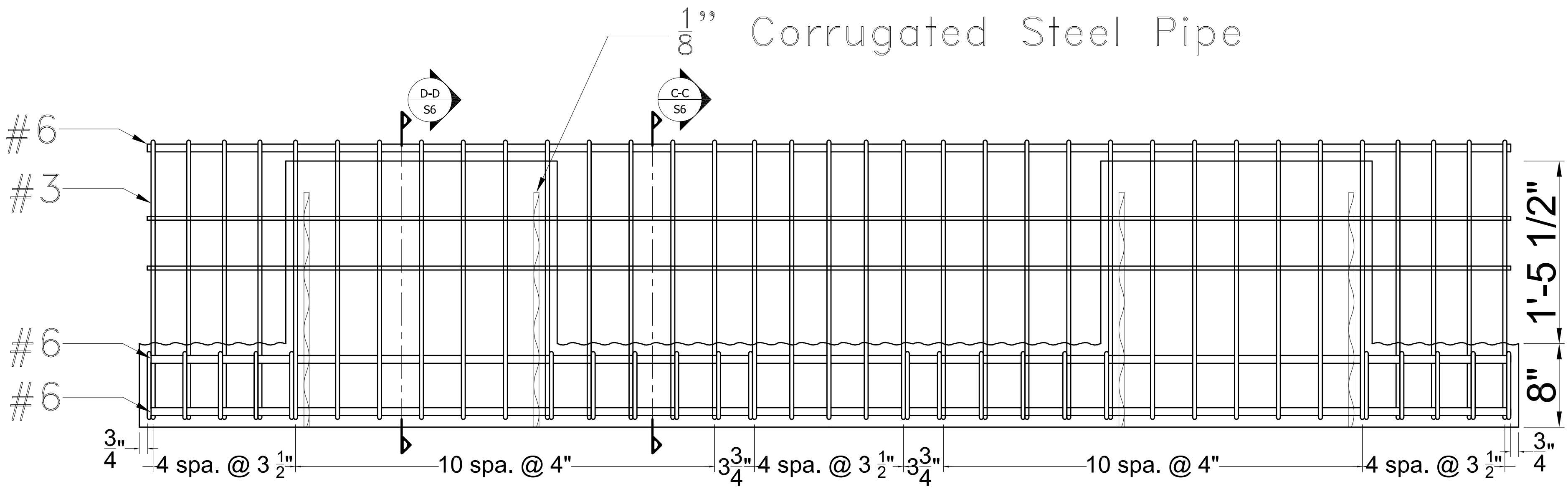

Elevation View of Cap Beam Reinforcement (Precast Part)

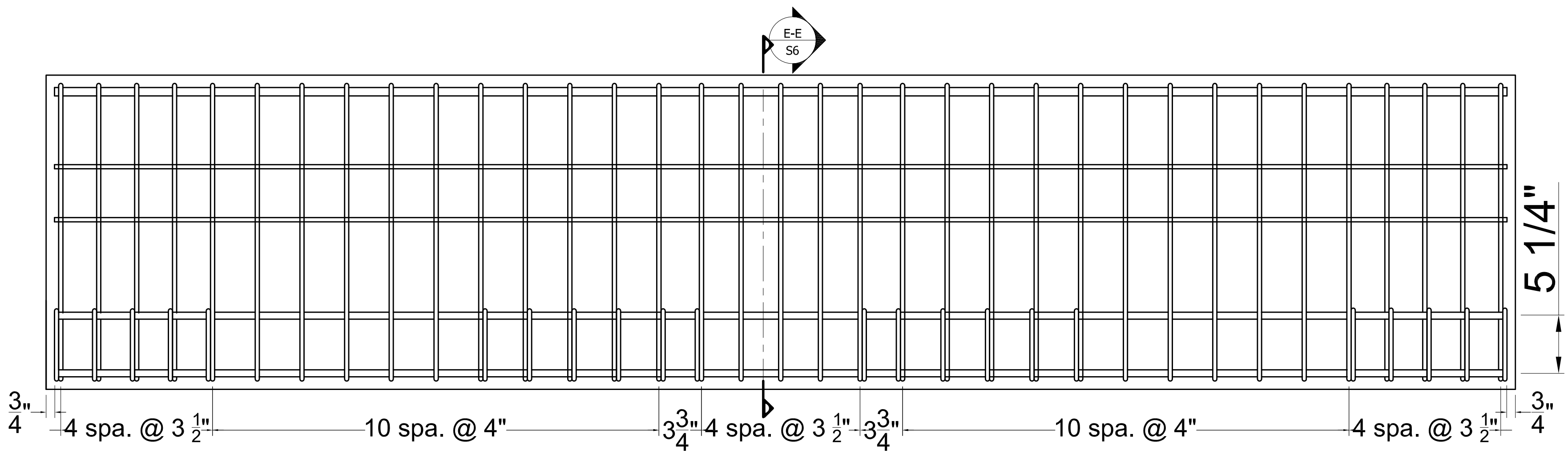

Cap Beam Reinforcement (Combined Precast and Cast-In-Place Parts)

University of Nevada, Reno — Caltrans	Project: Calt - ABC Bridge 2	
	Contains: Cap Beam Reinforcement - Elevation View	Sheet:
	Designed and Drawn by: Jared Jones	05 of 10
	Scale: 1"=1'-0" Date: 7/11/2017	

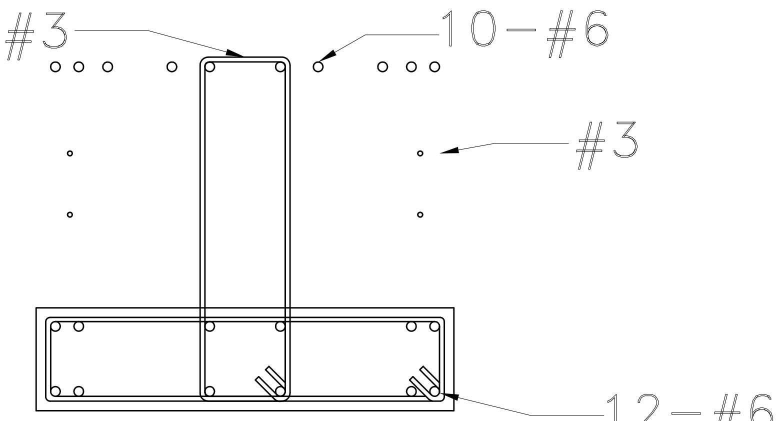

Section C-C

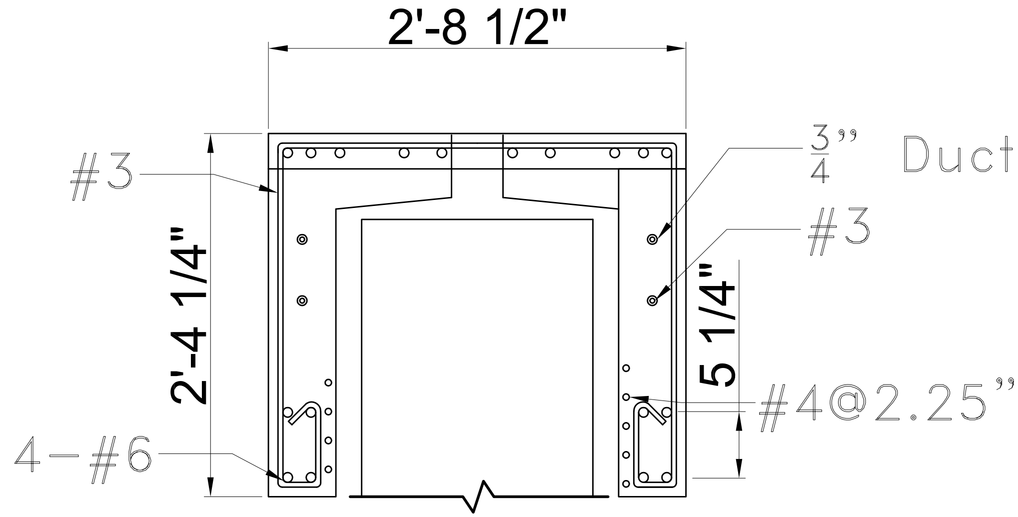

Section D-D

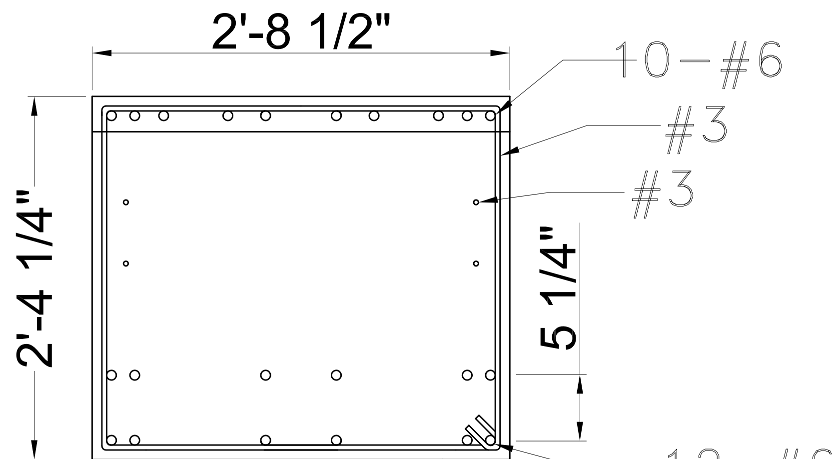

Section E-E

University of Nevada, Reno
Caltrans

Project: Calt - ABC Bridge 2	
Contains: Cap Beam Reinforcement Cross Sections	Sheet:
Designed and Drawn by: Jared Jones	06 of 10
Scale: 1 1/2"=1'-0" Date: 7/11/2017	

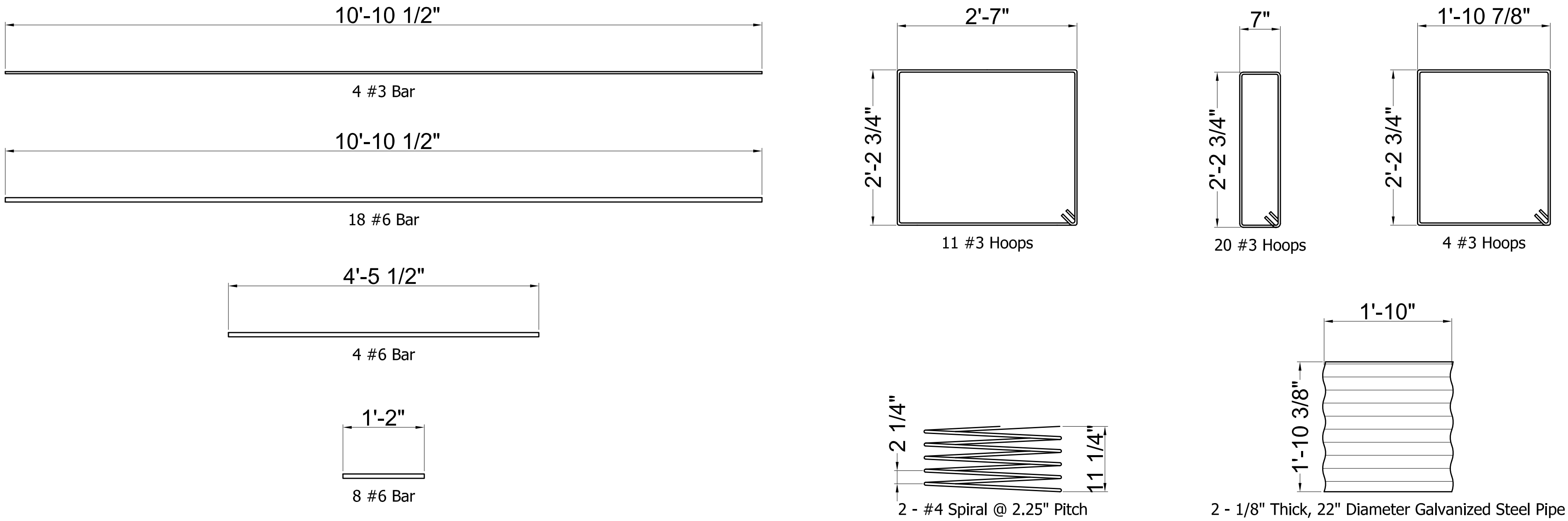

University of Nevada, Reno / Caltrans	Project: Calt - ABC Bridge 2	
	Contains: Girder Connection Details	Sheet:
	Designed and Drawn by: Jared Jones	07 of 10
	Scale: NTS / Date: 7/11/2017	

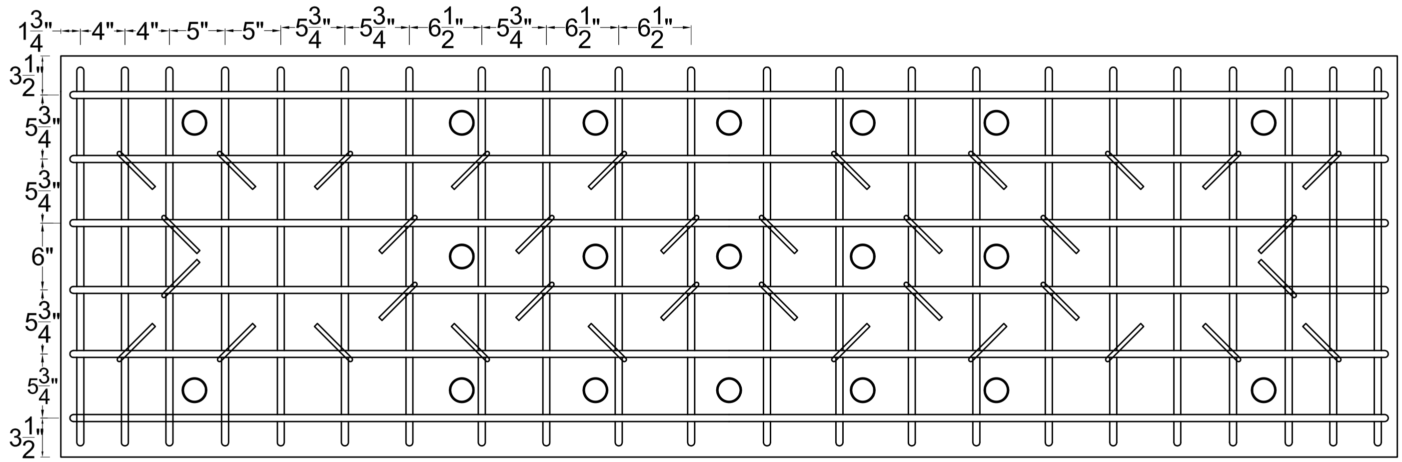

Footing Reinforcement - Bottom Bars

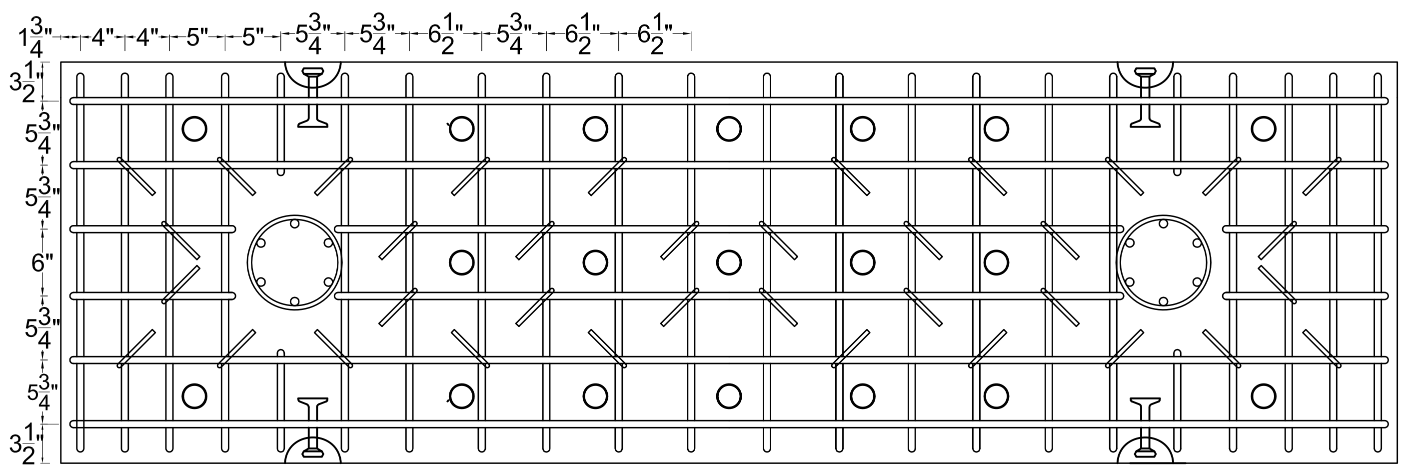

Footing Reinforcement Top Bars

University of Nevada, Reno / Caltrans	Project: Calt - ABC Bridge 2	
	Contains: Footing Reinforcement - Plan View	Sheet:
	Designed and Drawn by: Jared Jones	08 of 10
	Scale: NTS / Date: 7/11/2017	

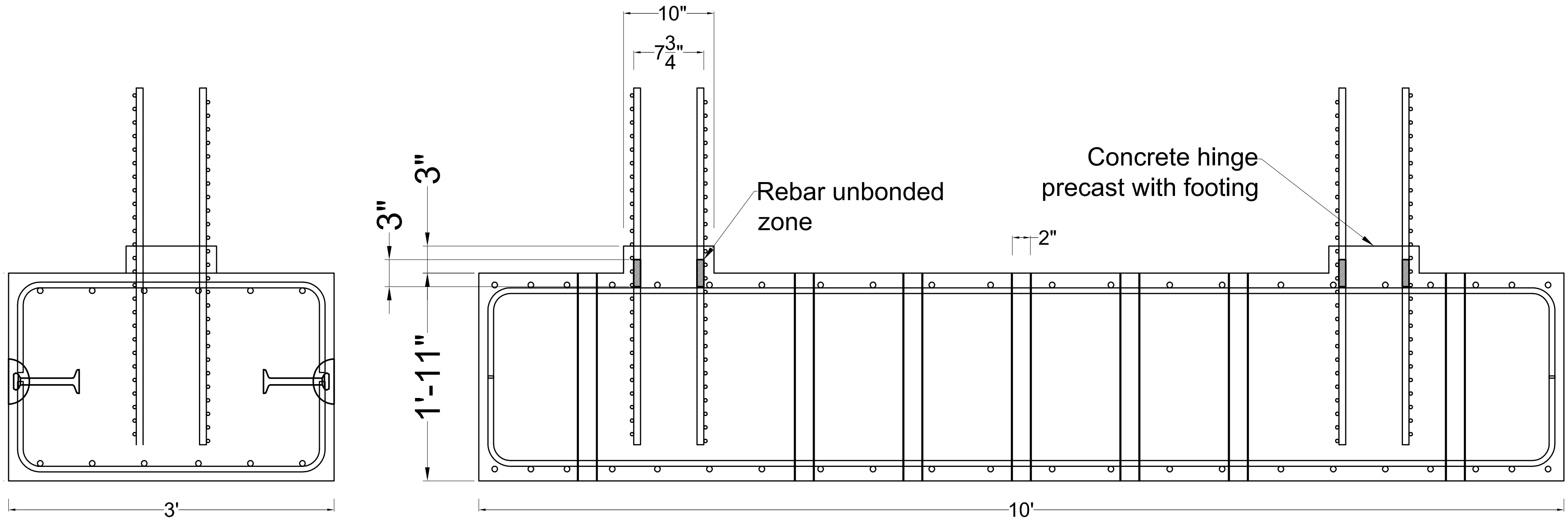

Footing Reinforcement Side View

Note: Stirrups removed for clarity

Project: Calt - ABC Bridge 2		
Contains: Footing Reinforcement - Side View		Sheet:
Designed and Drawn by: Jared Jones		09 of 10
Scale: NTS	Date: 7/11/2017	

University of Nevada, Reno
Caltrans

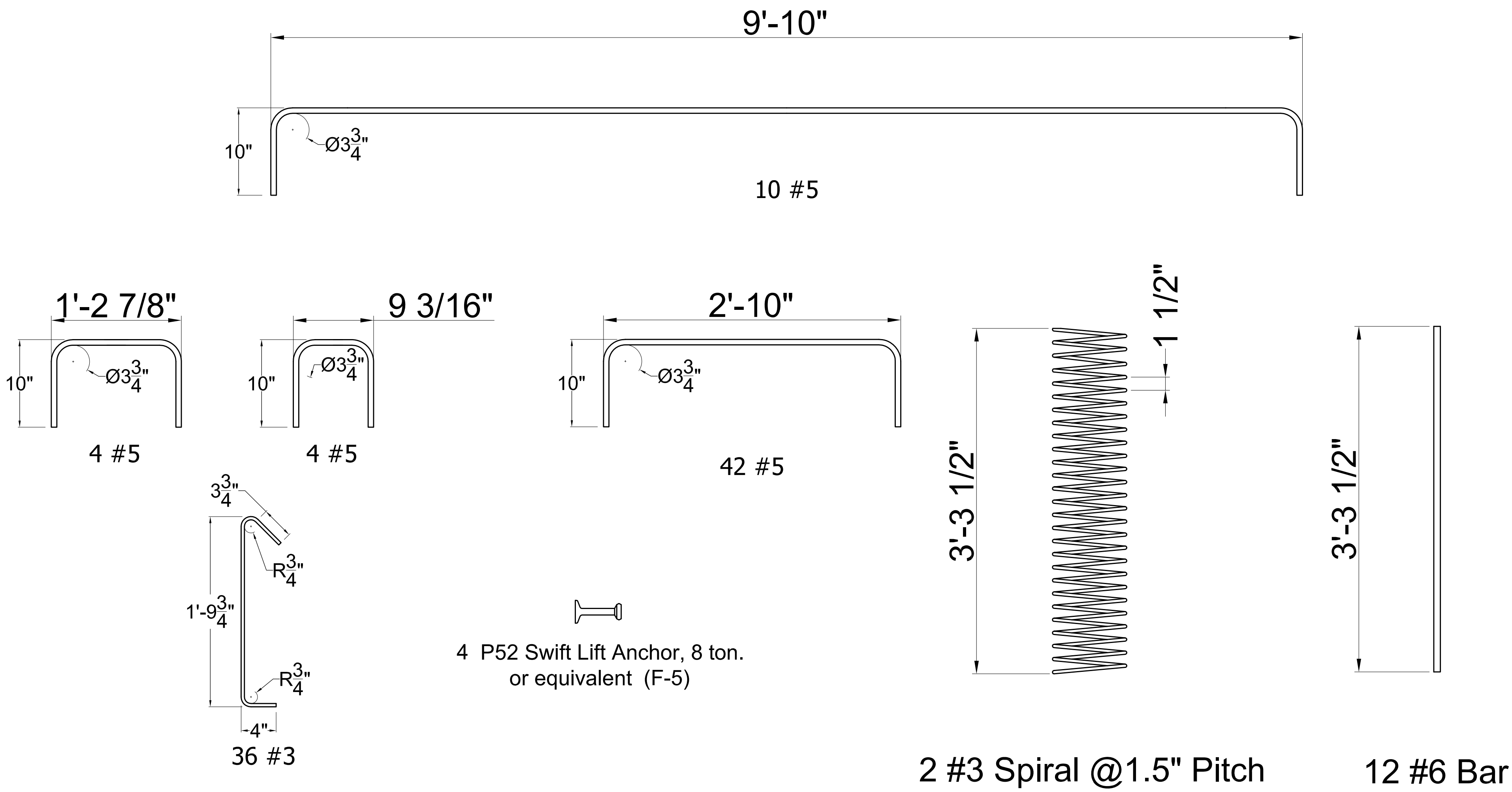

University of Nevada, Reno / Caltrans	Project: Calt - ABC Bridge 2	
	Contains: Footing Reinforcement	Sheet:
	Designed and Drawn by: Jared Jones	10 of 10
	Scale: NTS / Date: 7/11/2017	

Deck Panel Drawings

Notes:

University of Nevada, Reno Caltrans

Project: Calt-ABC Bridge 2		
Contains:		Sheet:
Designed and Drawn by:		00 of 16
Scale: N/A	Date: 10/3/2017	

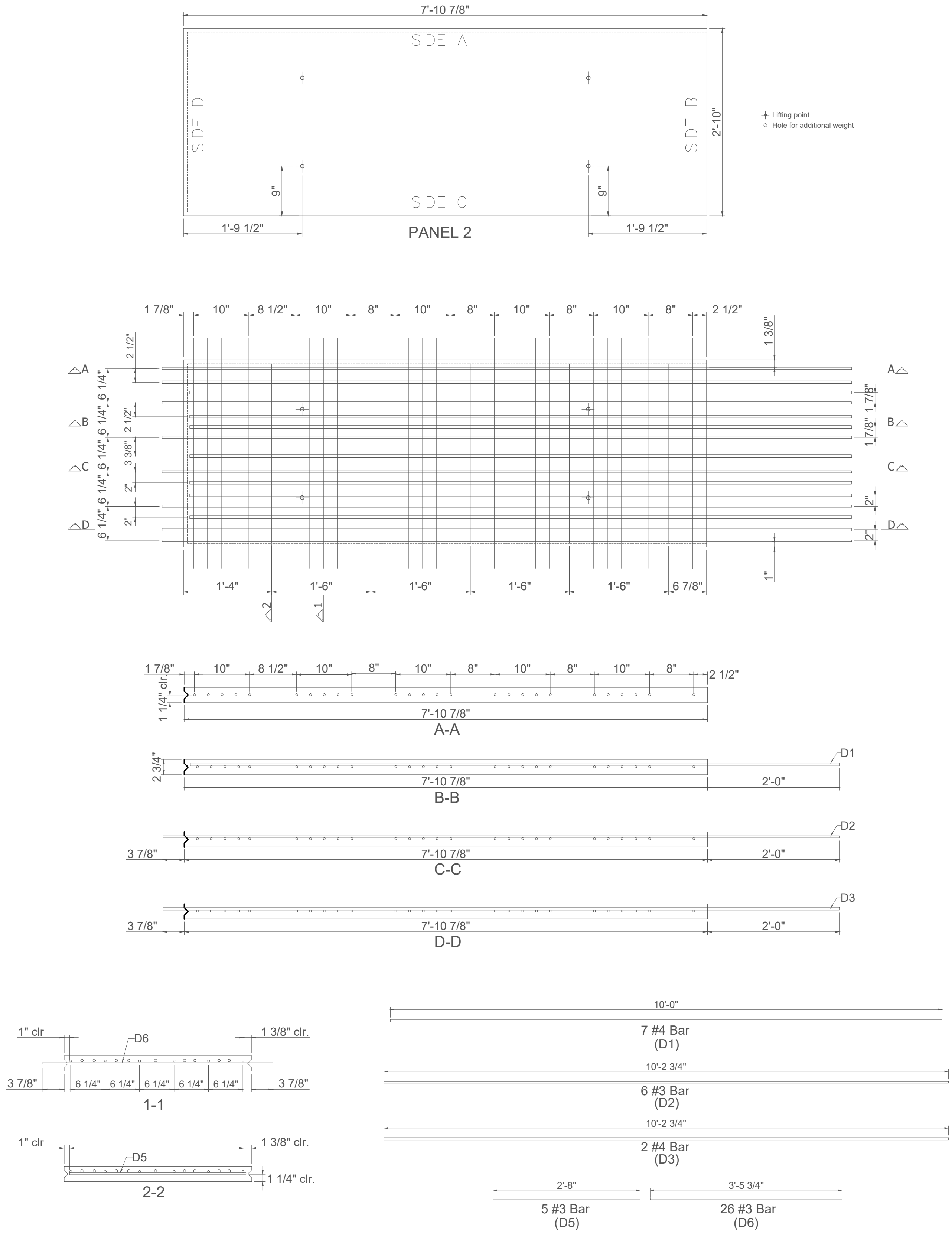

University of Nevada, Reno

Caltrans

Project: ABC Bridge System Project

Contains: Panel 2 (Dimension and Reinforcement)

Designed and Drawn by: José Benjumea

Scale: 1:25

Date: 02/13/2017

Sheet:

01 of 16

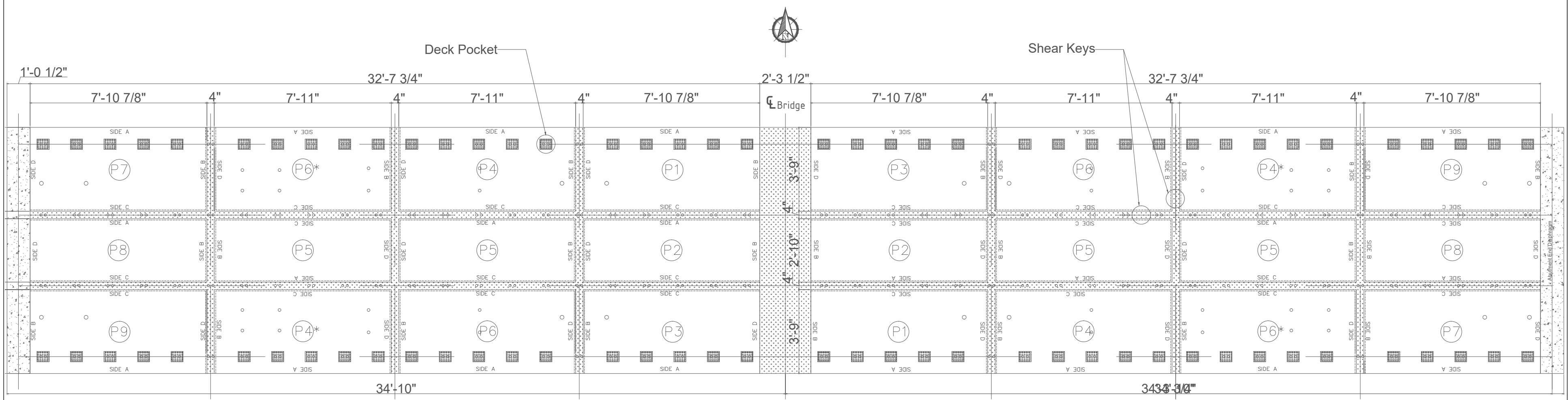

Plan View

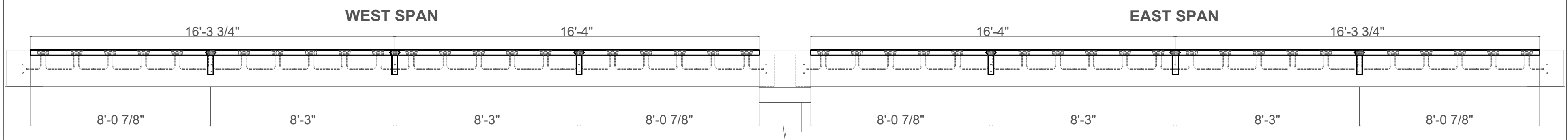

Elevation

Notes
- Concrete: f'c=5000 psi
  3/8"-dia. max. aggr.
- Reinforcement steel is Grade 60

Number of Panels

P1-P3,P5,P7-P9:	2 each type
P4-P6:	4 each type

Panels with a start mark have the same dimensions and reinforcement layout to those panels without the mark. The difference lies in the position and number of the holes required for the additional weight.

University of Nevada, Reno
Caltrans

Project: ABC Bridge System Project
Contains: Longitudinal PC Deck Panels Configuration
Designed and Drawn by: José Benjumea
Scale: 1:80
Date: 02/13/2017
Sheet:
02 of 16

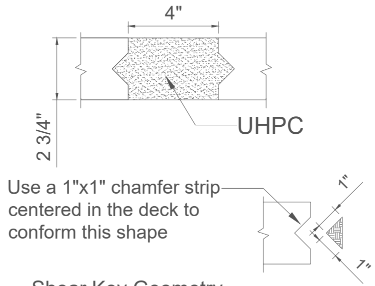

Shear Key Geometry

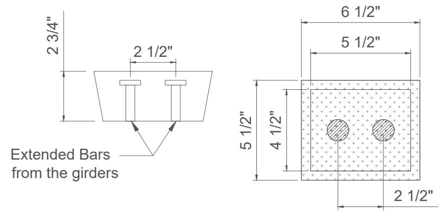

Pocket Dimensions

Recommended Lifting Configuration

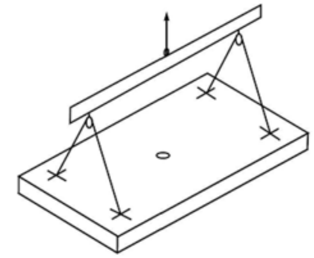

Recommended Insert Coils for Lifting

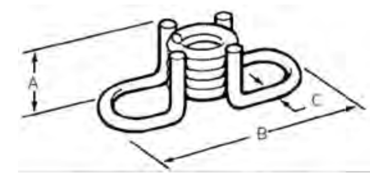

96, F63 Flared Thin Slab Coil Inserts
1/2" bolt x 1-3/4", plain finish or equivalent

Insert should be set back 1/2" back from the surface of the concrete

Maintain at least 3/4" of concrete below the insert

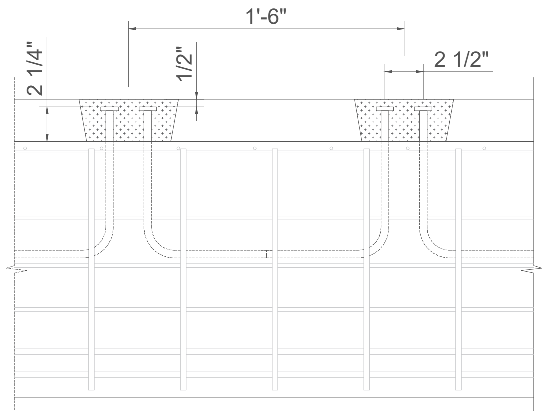

Elevation

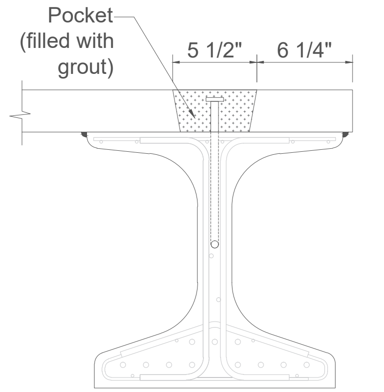

Cross Section (Exterior Girders)

Recommended Bolts for Lifting

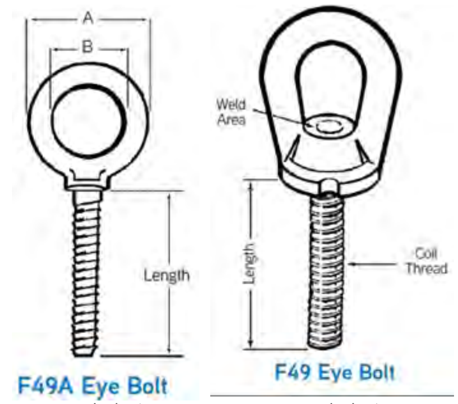

or equivalent

or equivalent

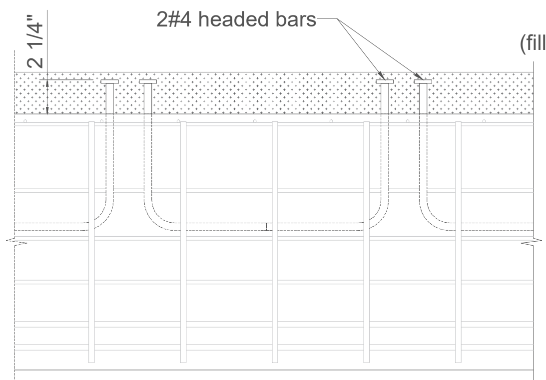

Elevation

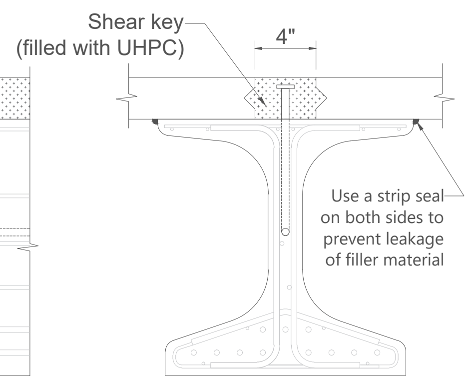

Cross Section (Interior Girders)

University of Nevada, Reno
Caltrans

Project: ABC Bridge System Project
Contains: Shear Keys, Deck Pockets, and Insert Coils for Lifting
Designed and Drawn by: José Benjumea
Scale: Indicated
Date: 02/13/2017
Sheet: 03 of 16

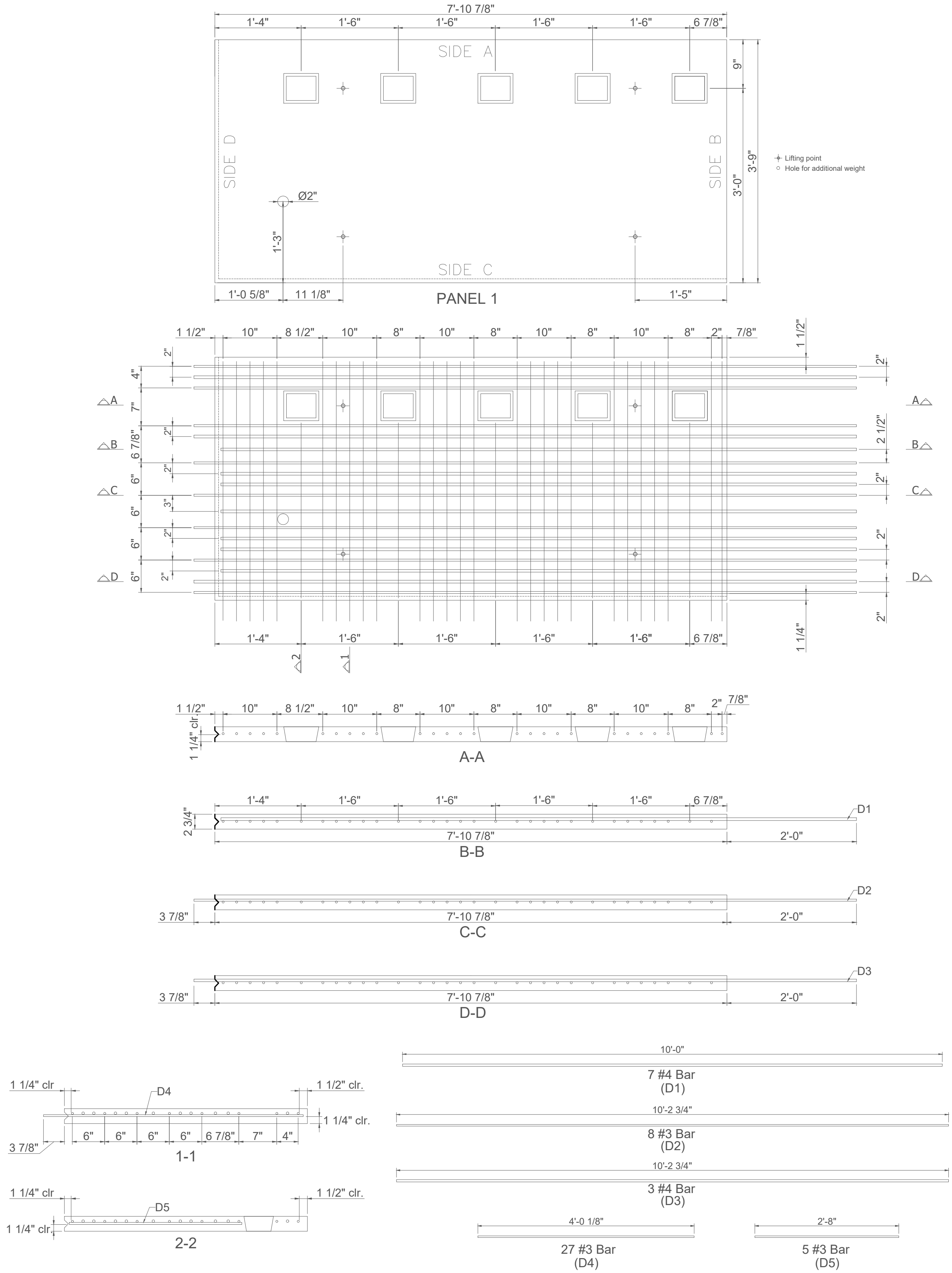

Project: ABC Bridge System Project

Contains: Panel 1 (Dimension and Reinforcement)

Designed and Drawn by: José Benjumea

Scale: 1:25

Date: 02/13/2017

University of Nevada, Reno

Caltrans

Sheet: 04 of 16

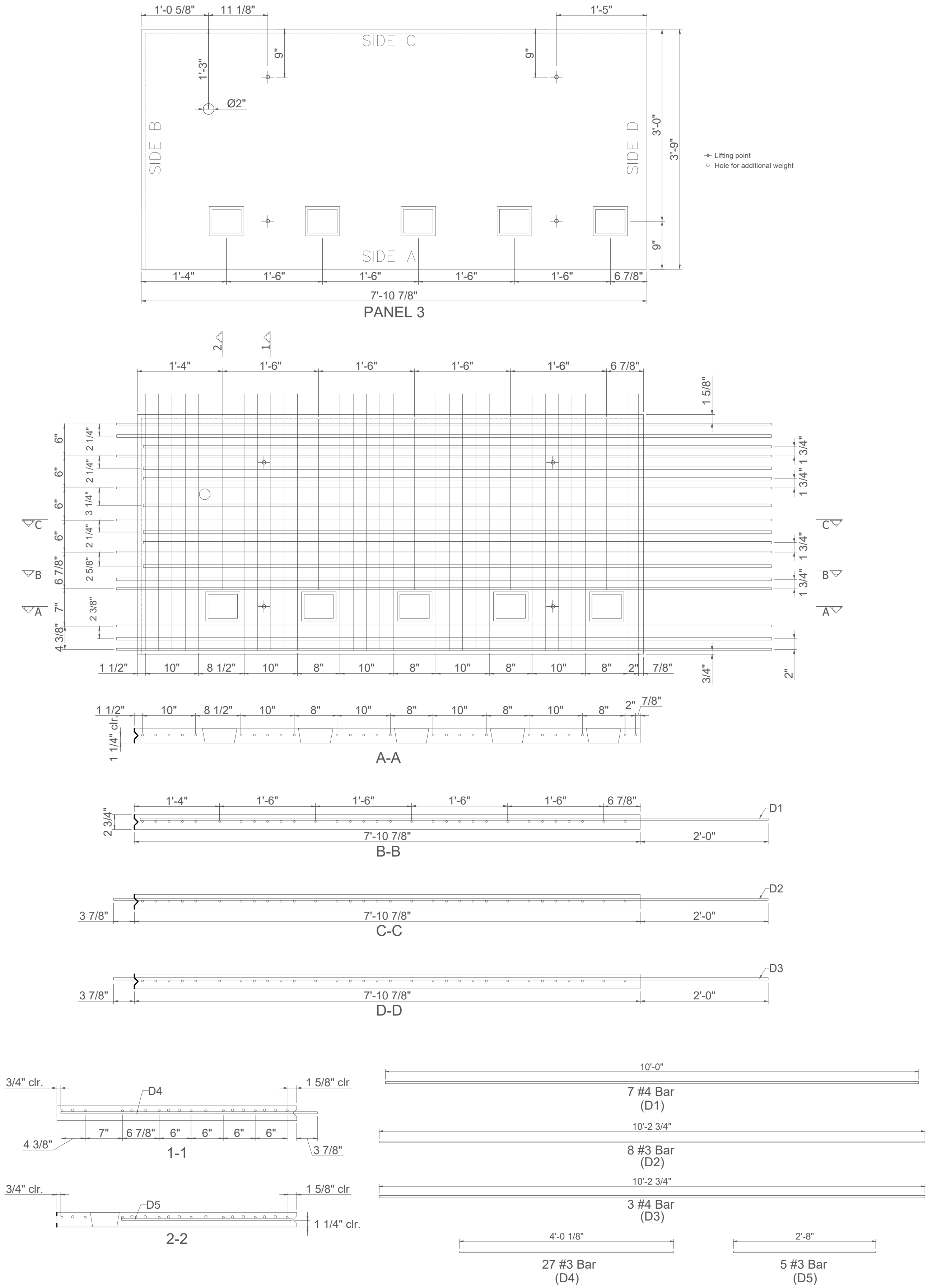

University of Nevada, Reno

Caltrans

Project: ABC Bridge System Project

Contains: Panel 3 (Dimension and Reinforcement)

Designed and Drawn by: José Benjumea

Scale: 1:25

Date: 02/13/2017

Sheet:

05 of 16

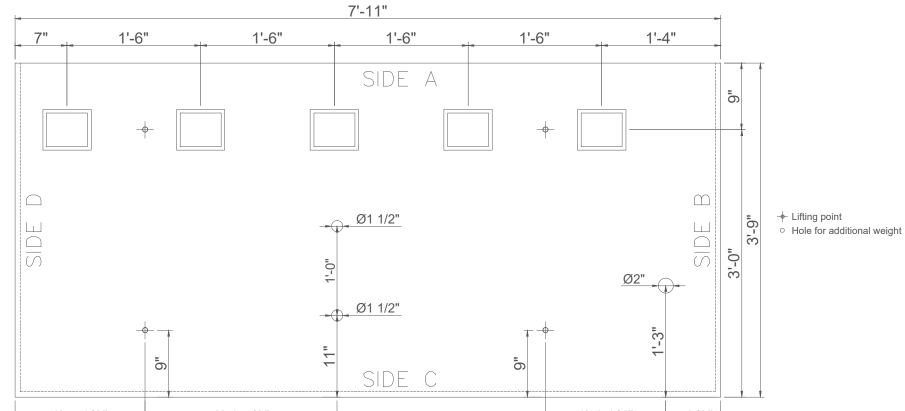

PANEL 4

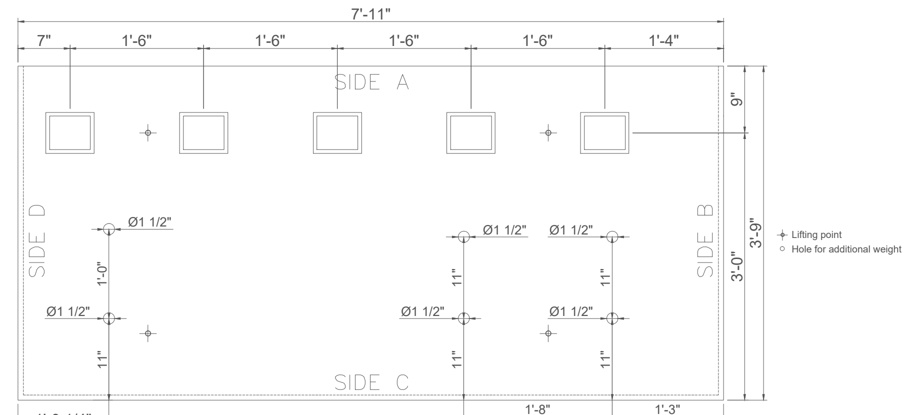

PANEL 4*

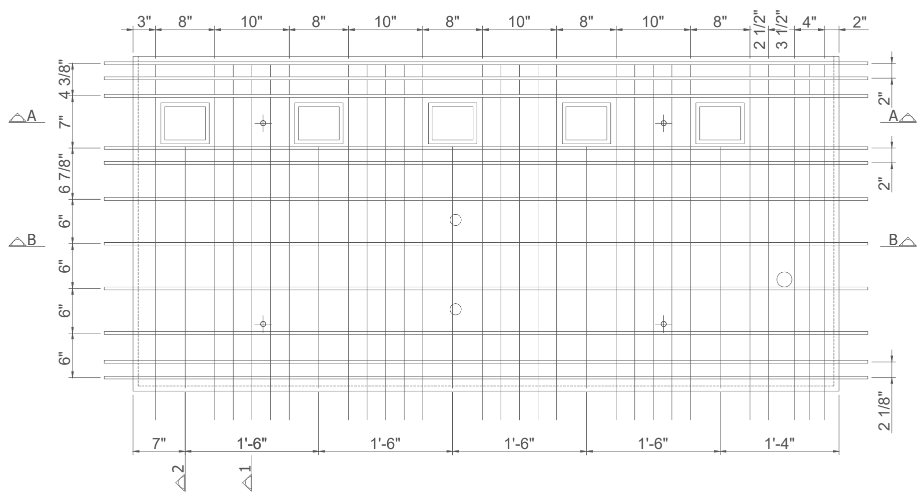

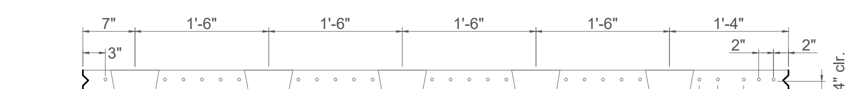

A-A

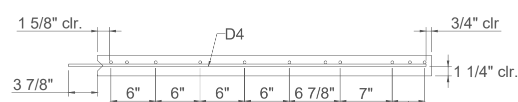

1-1

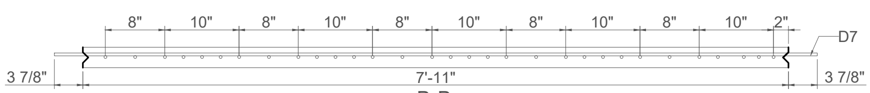

B-B

2-2

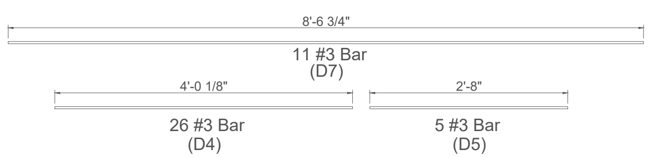

Project: ABC Bridge System Project	
Contains: Panels 4 and 4* (Dimensions and Reinforcement)	Sheet:
Designed and Drawn by: José Benjumea	06 of 16
Scale: 1:25 — Date: 02/13/2017	

University of Nevada, Reno
Caltrans

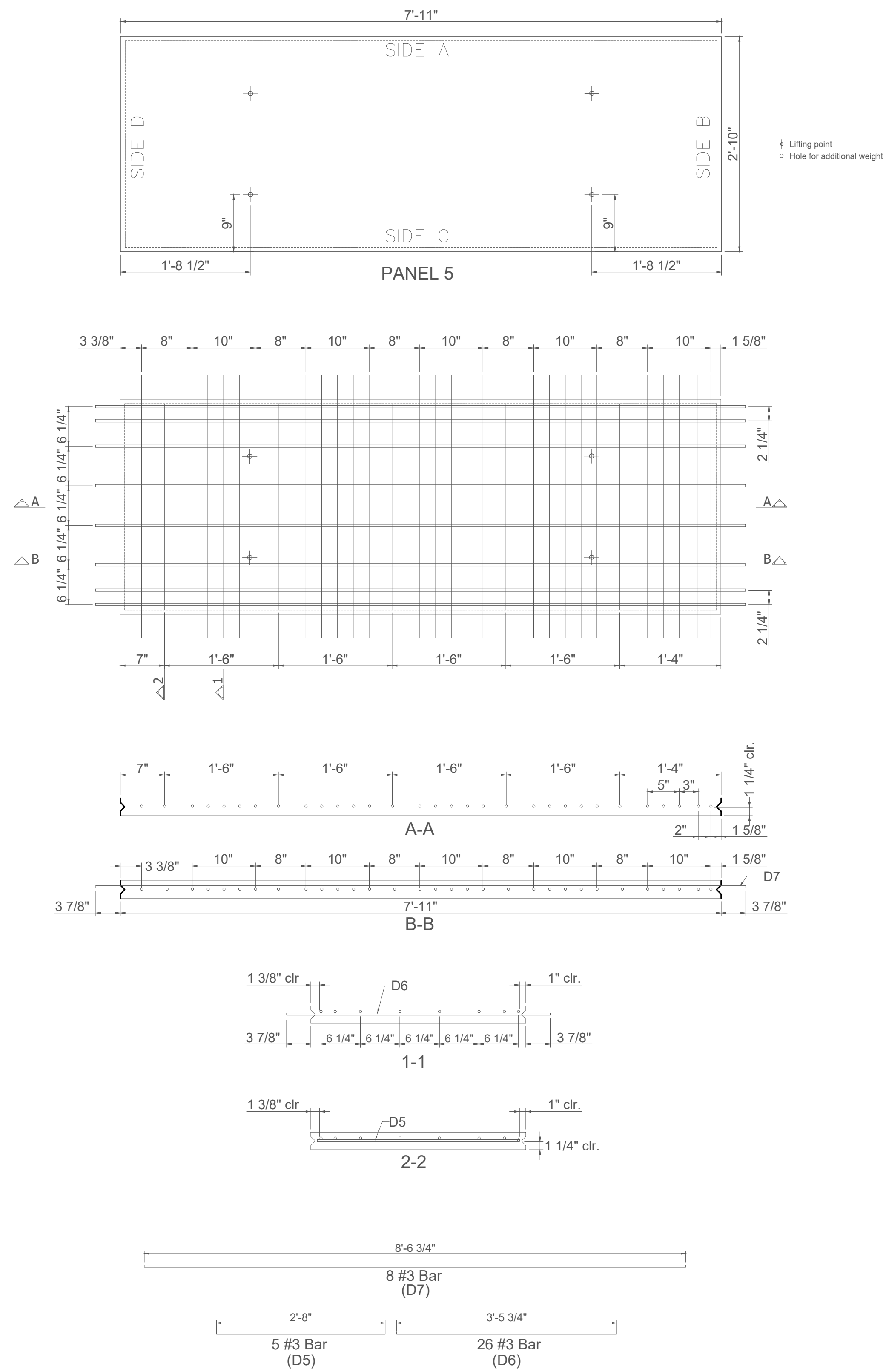

University of Nevada, Reno
Caltrans

Project: ABC Bridge System Project

Contains: Panel 5 (Dimensions and Reinforcement)

Designed and Drawn by: José Benjumea

Scale: 1:25

Date: 02/13/2017

Sheet: 07 of 16

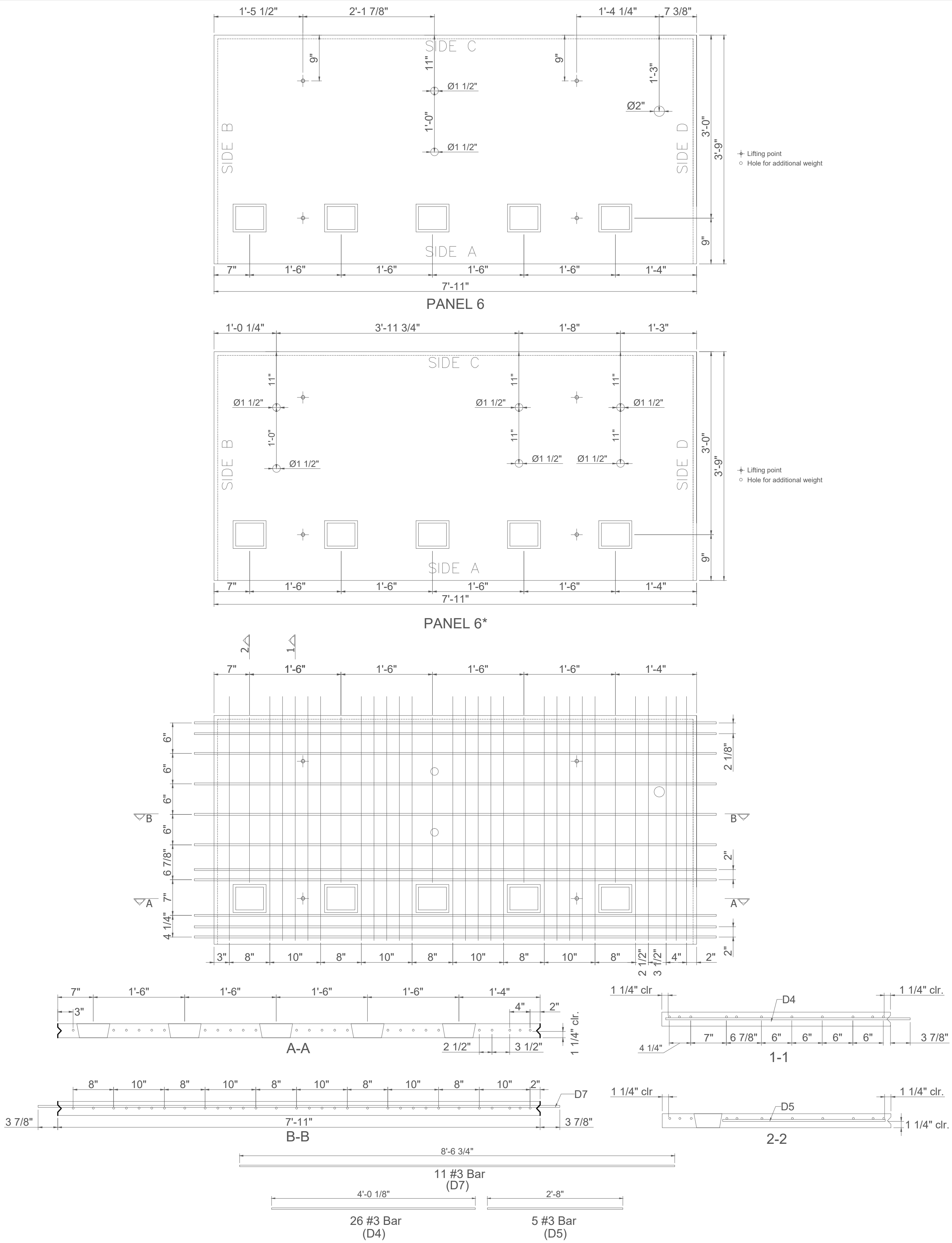

Project: ABC Bridge System Project

Contains: Panels 6 and 6* (Dimensions and Reinforcement)

Designed and Drawn by: José Benjumea

Scale: 1:25

Date: 02/13/2017

Sheet: 08 of 16

University of Nevada, Reno

Caltrans

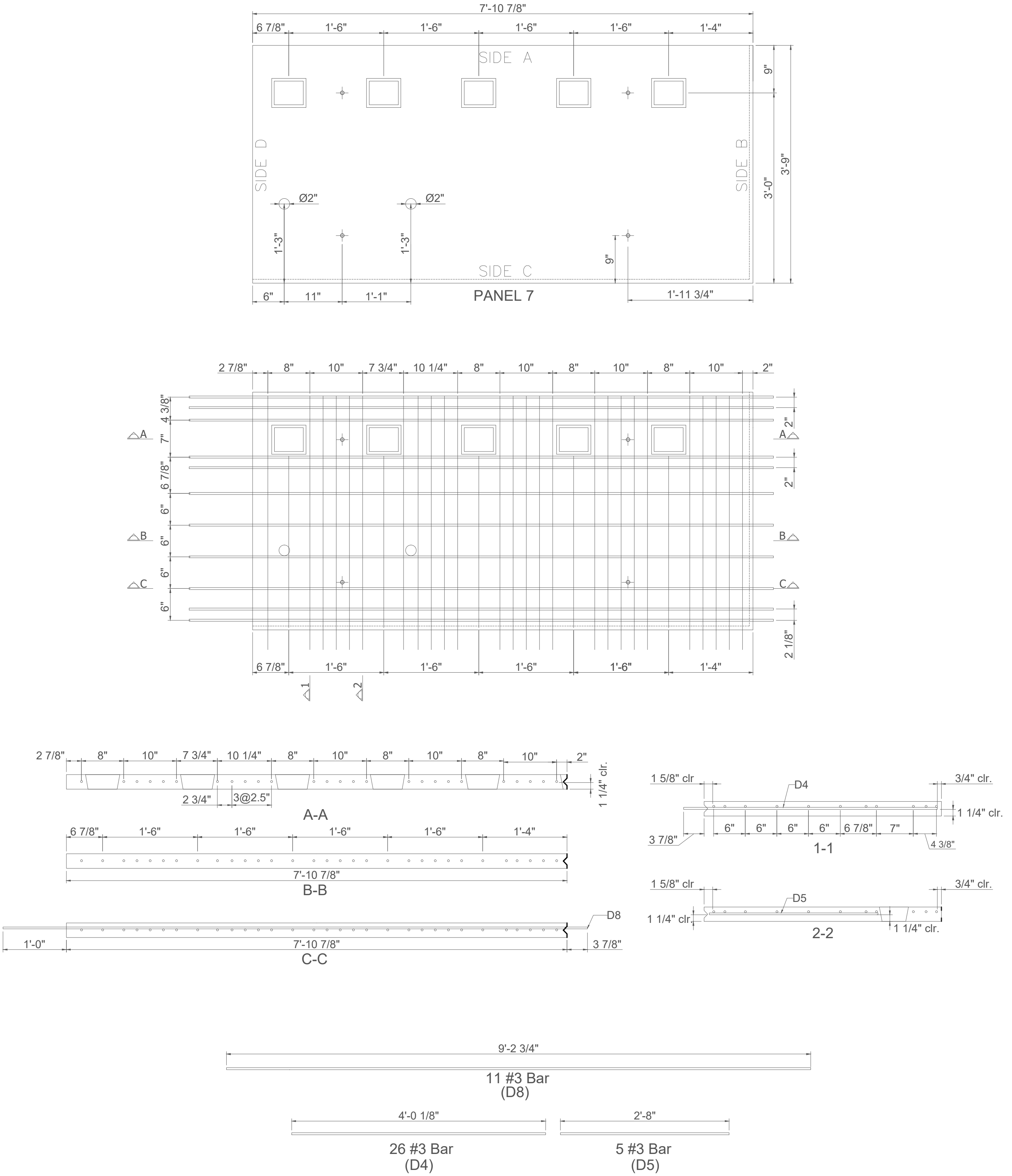

Project: ABC Bridge System Project	
Contains: Panel 7 (Dimensions and Reinforcement)	Sheet:
Designed and Drawn by: José Benjumea	09 of 16
Scale: 1:25	Date: 02/13/2017

University of Nevada, Reno

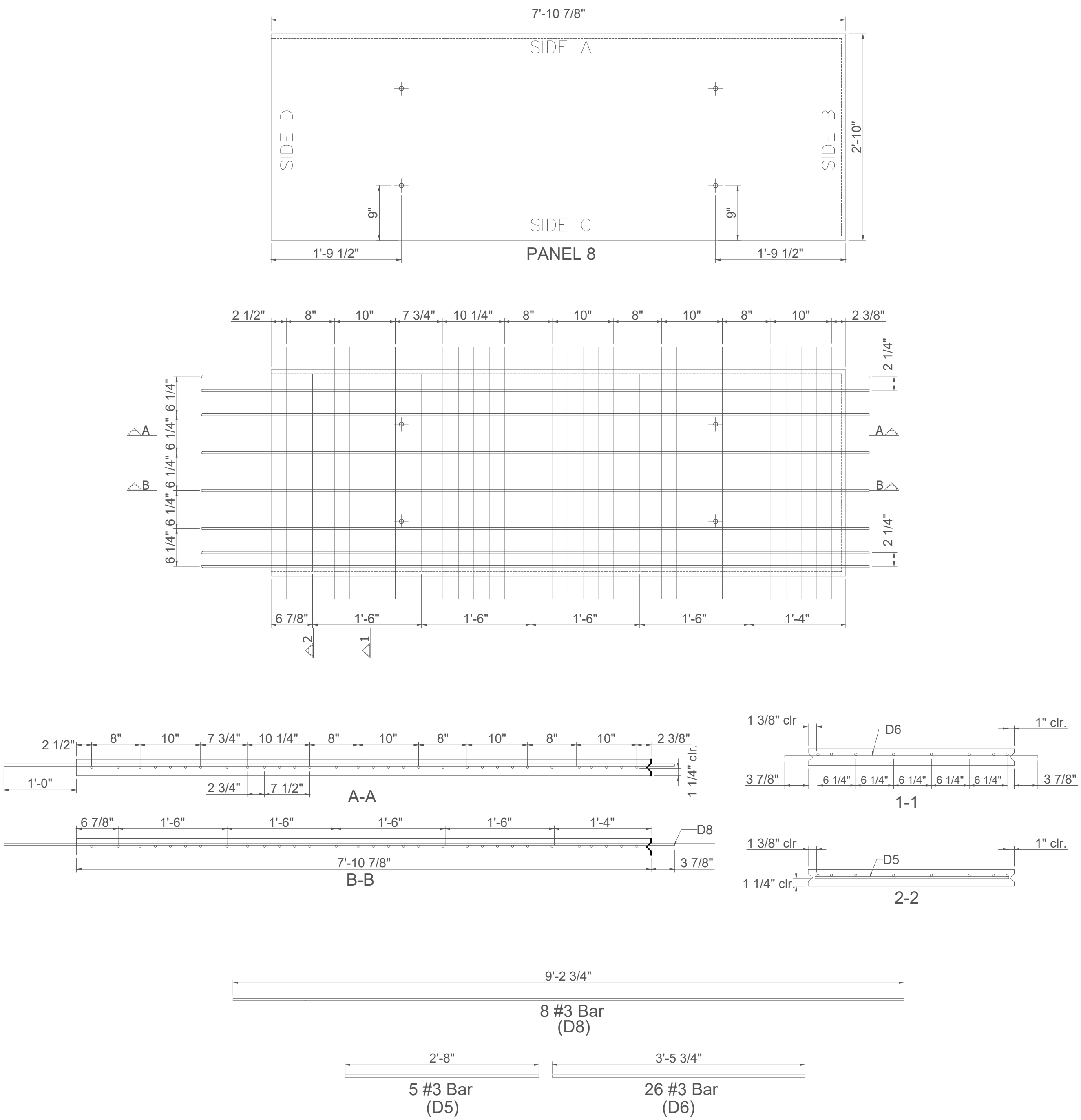

University of Nevada, Reno

Caltrans

Project: ABC Bridge System Project

Contains: Panel 8 (Dimensions and Reinforcement)

Designed and Drawn by: José Benjumea

Scale: 1:25

Date: 02/13/2017

Sheet: 10 of 16

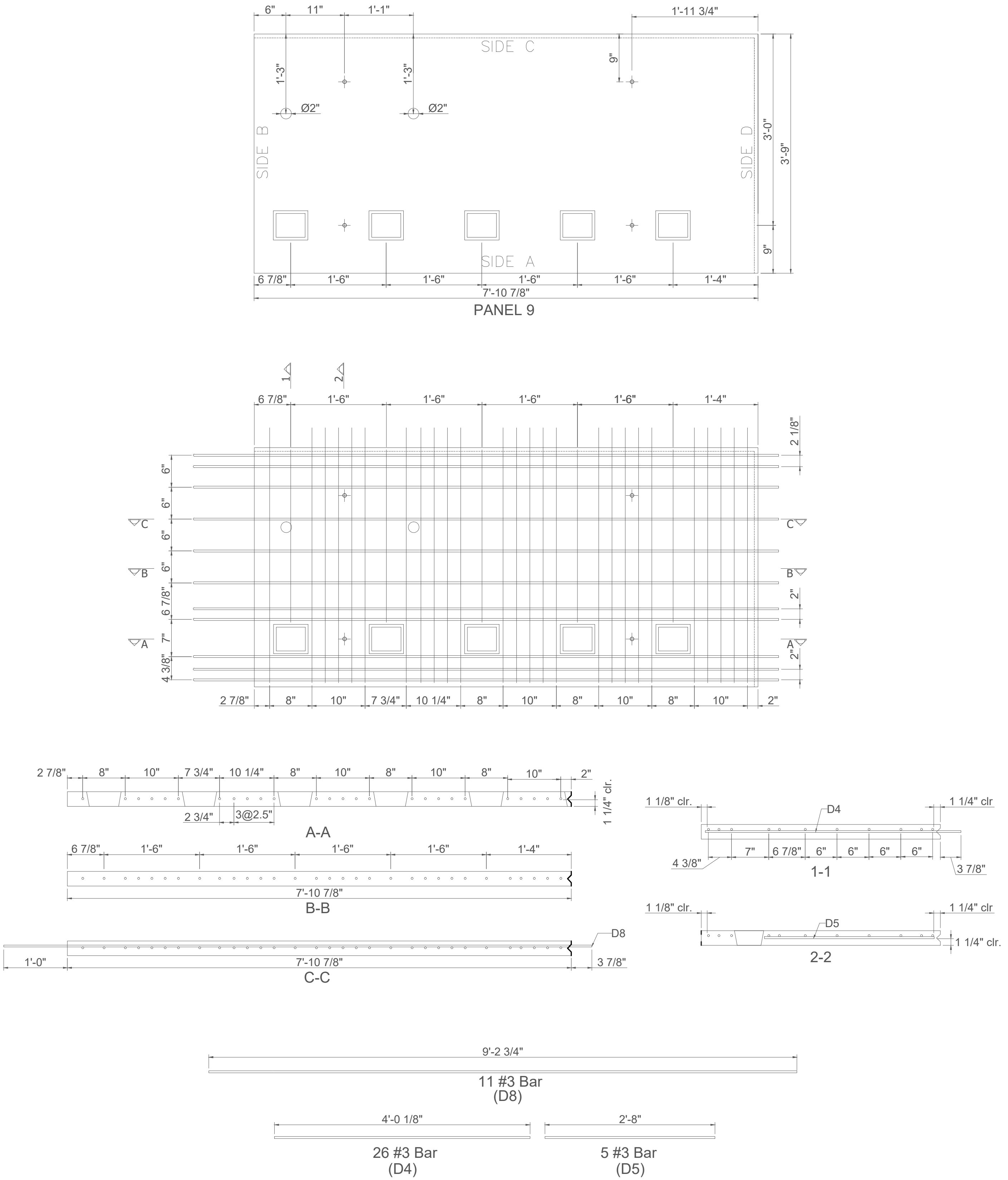

Project: ABC Bridge System Project		
Contains: Panel 9 (Dimensions and Reinforcement)		Sheet:
Designed and Drawn by: José Benjumea		11 of 16
Scale: 1:25	Date: 02/13/2017	

University of Nevada, Reno
Caltrans

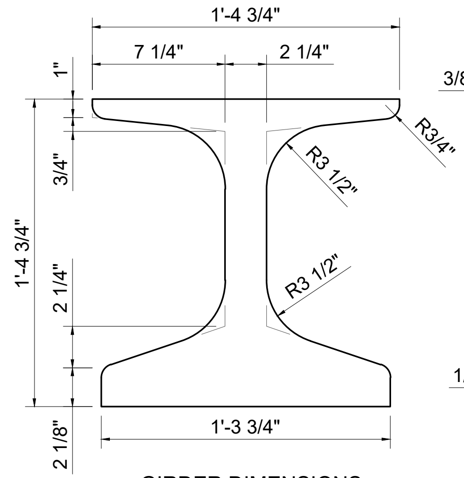

GIRDER DIMENSIONS

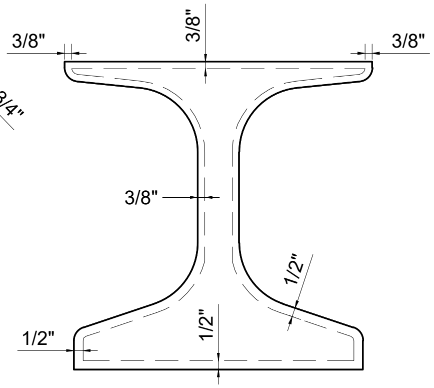

CLEAR COVER

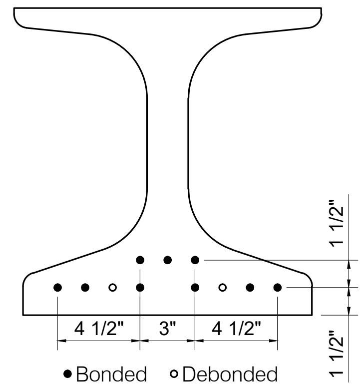

STRAND TEMPLATE &
DEBONDING PATTERN

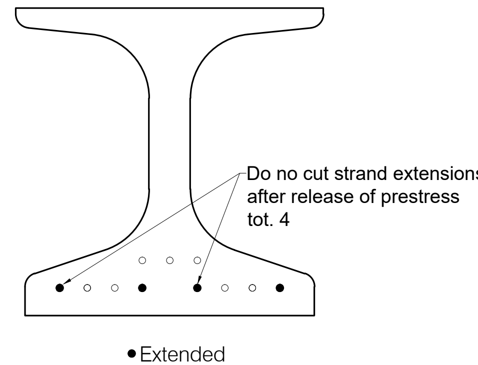

EXTENDED STRANDS AT ONE END

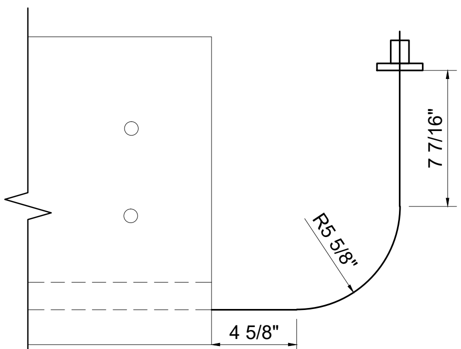

STRAND EXTENSION HOOK DETAIL

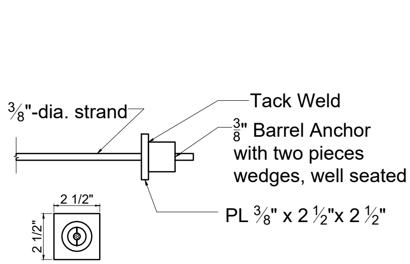

DETAIL A
Strand Chuck Anchorage Detail

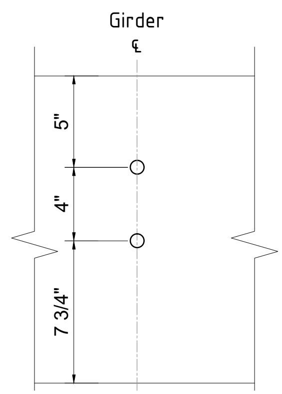

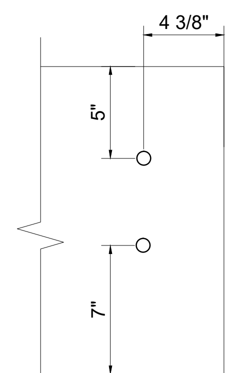

INTERMEDIATE HOLES

END HOLES

Holes are conformed using 3/4" PVC ducts

University of Nevada, Reno — Caltrans

Project: ABC Bridge System Project		
Contains: Girder Section and Strands Template		Sheet:
Designed and Drawn by: José Benjumea		12 of 16
Scale: 1:10	Date: 02/13/2017	

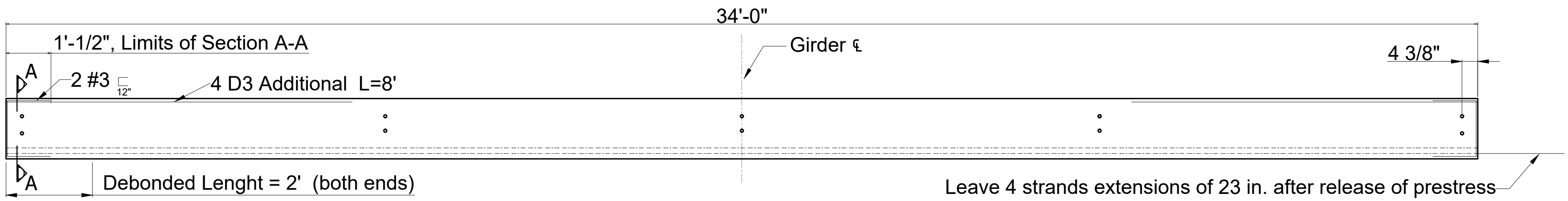

GIRDER ELEVATION

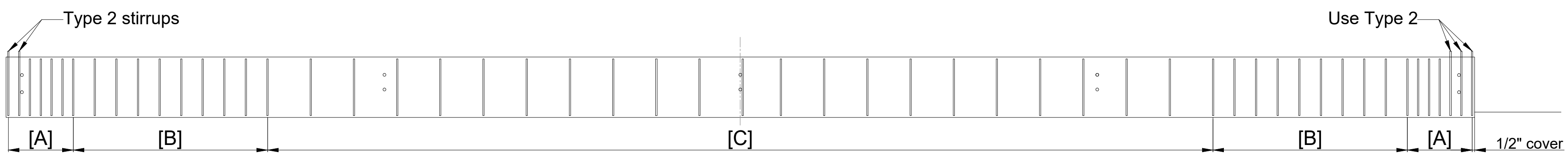

2#3 Stirrups (see Table below)

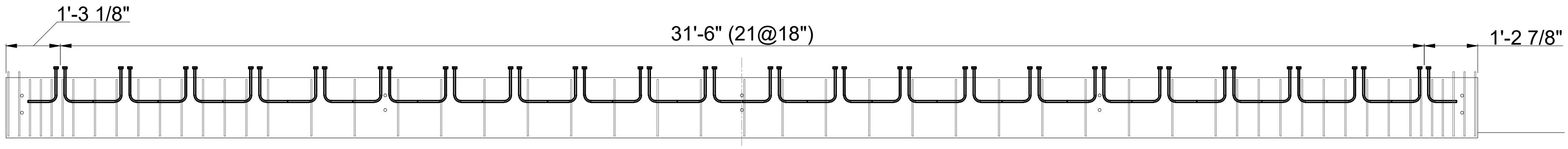

#4 Girder-to-deck Connectors

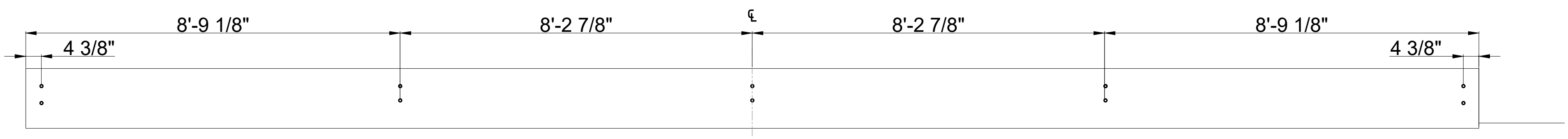

Insert Holes for Intermediate and End Diaphragms

Notes:
1. All prestresses strands are 3/8" diameter and continuously bonded unless otherwise noted.
2. Pjack= 189 kips (17.2 kips/STRAND)
3. After release of prestress, leave 23 in of strand extending from one girder end.
4. Prevent unraveling of extended strands by placing a small pipe around the strands.
5. Prestressing strand shall be 270 ksi low relaxation (ASTM A416).

Concrete Strength

f´ci is 5.5 ksi at time of stressing
f´c is 8.0 ksi at 28 days

Deformed Wire Reinforcement
ASTM A497 (fy=70ksi, fu=80 ksi)

D3: d=0.195 in. A=0.03 in^2
D6: d=0.276 in. A=0.06 in^2

#3 Stirrups Spacing

[A]	L=18"	2#3@3"
[B]	L=54"	2#3@6"
[C]	L=262.625"	2#3@12"

GIRDER PROPERTIES

D:	16.75 in
Area:	107.7 in^2
Inertia:	4088 in^4
yb:	7.214 in
yt:	9.536 in
Sb:	567 in^3
St:	429 in^3

University of Nevada, Reno — Caltrans

Project: ABC Bridge System Project	
Contains: Reinforcement and Girder Elevation	Sheet:
Designed and Drawn by: José Benjumea	13 of 16
Scale: N.A.	Date: 02/13/2017

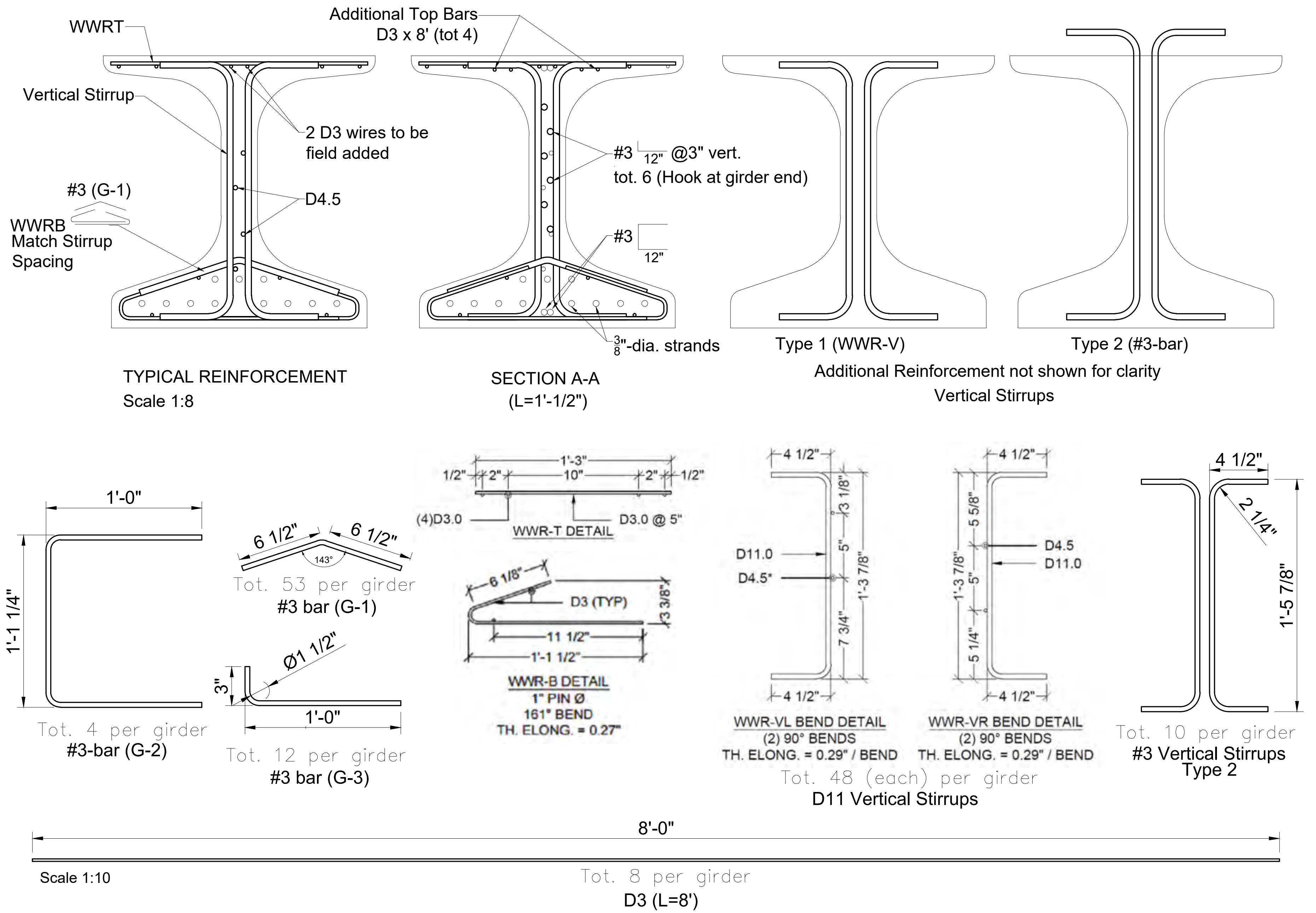

University of Nevada, Reno | Caltrans

Project: ABC Bridge System Project
Contains: Girder Reinforcement Details
Designed and Drawn by: José Benjumea
Scale: Indicated | Date: 02/13/2017

Sheet: 14 of 16

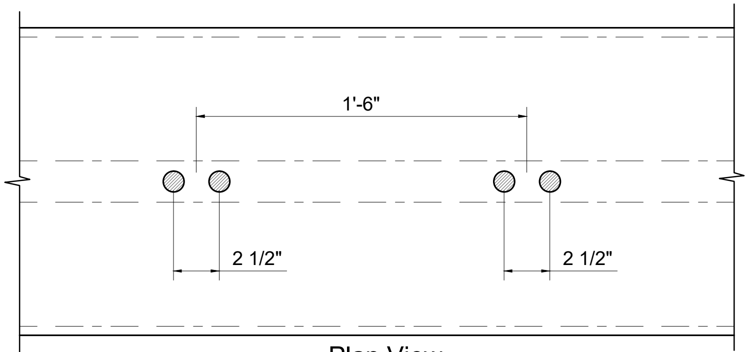

Plan View

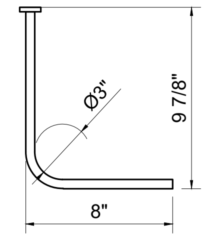

tot. 44 per girder

90-deg. hook #4 headed bars
Use HRC 555 headed bars or equivalent

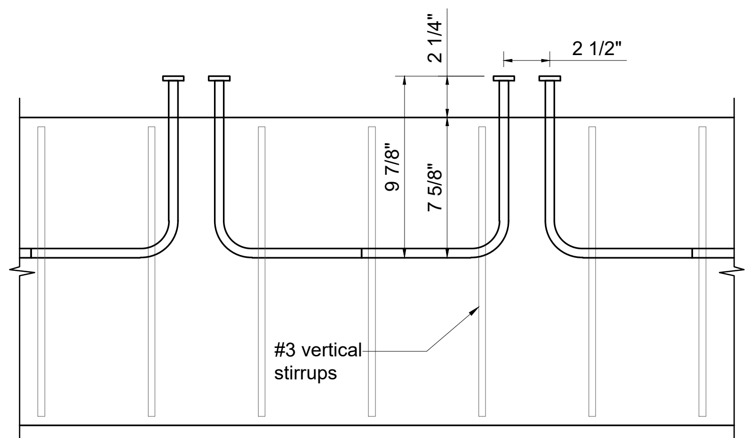

Additional Girder Reinforcement not shown for clarity

Elevation

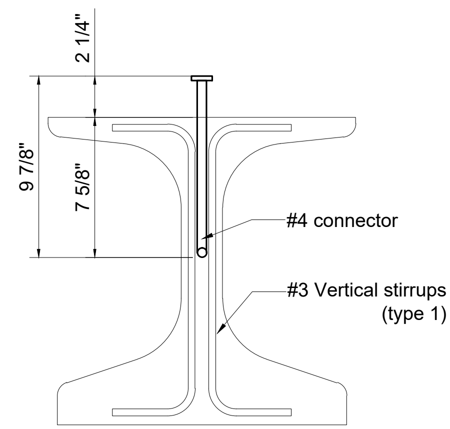

Girder Reinforcement not shown for clarity

Cross Section

Project: ABC Bridge System Project		
Contains: Deck-to-girder Connectors Details		Sheet:
Designed and Drawn by: José Benjumea		15 of 16
Scale: 1:10	Date: 02/13/2017	

University of Nevada, Reno Caltrans

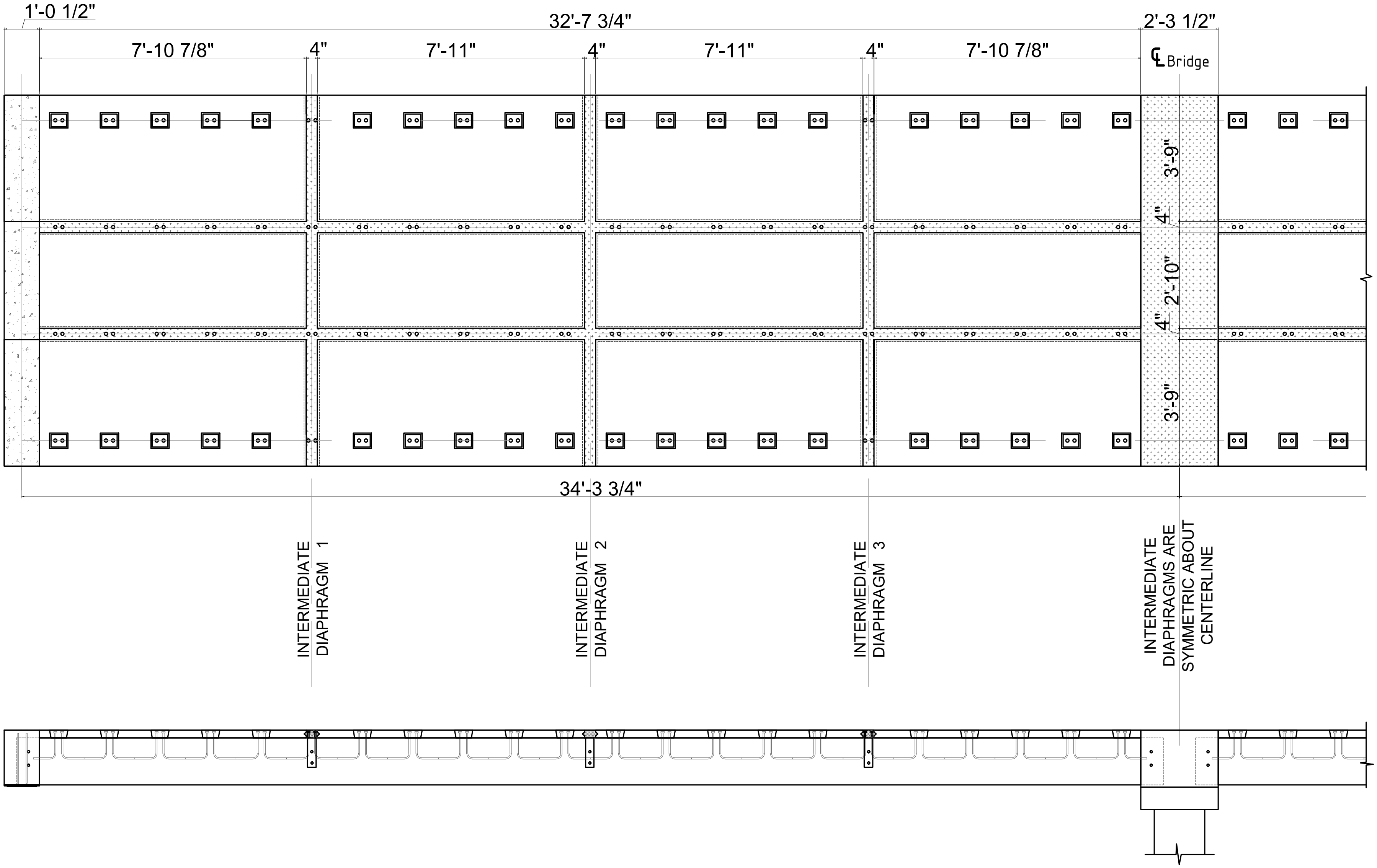

University of Nevada, Reno | Caltrans

Project: ABC Bridge System Project	
Contains: Location of Intermediate Diaphragms per Span	Sheet:
Designed and Drawn by: José Benjumea	16 of 16
Scale: 1:50	Date: 02/13/2017

Cast-in-Place Bent and Diaphragm Drawings

Notes: Includes reinforcement and concrete for CIP portion of bent and diaphragms, and the UHPC for bent and diaphragm topping, and deck joints

University of Nevada, Reno / Caltrans	Project: Calt - ABC Bridge 2	
	Contains: Title Page	Sheet:
	Approved by: Jared Jones	00 of 13
	Scale: Date: 1/29/2018	

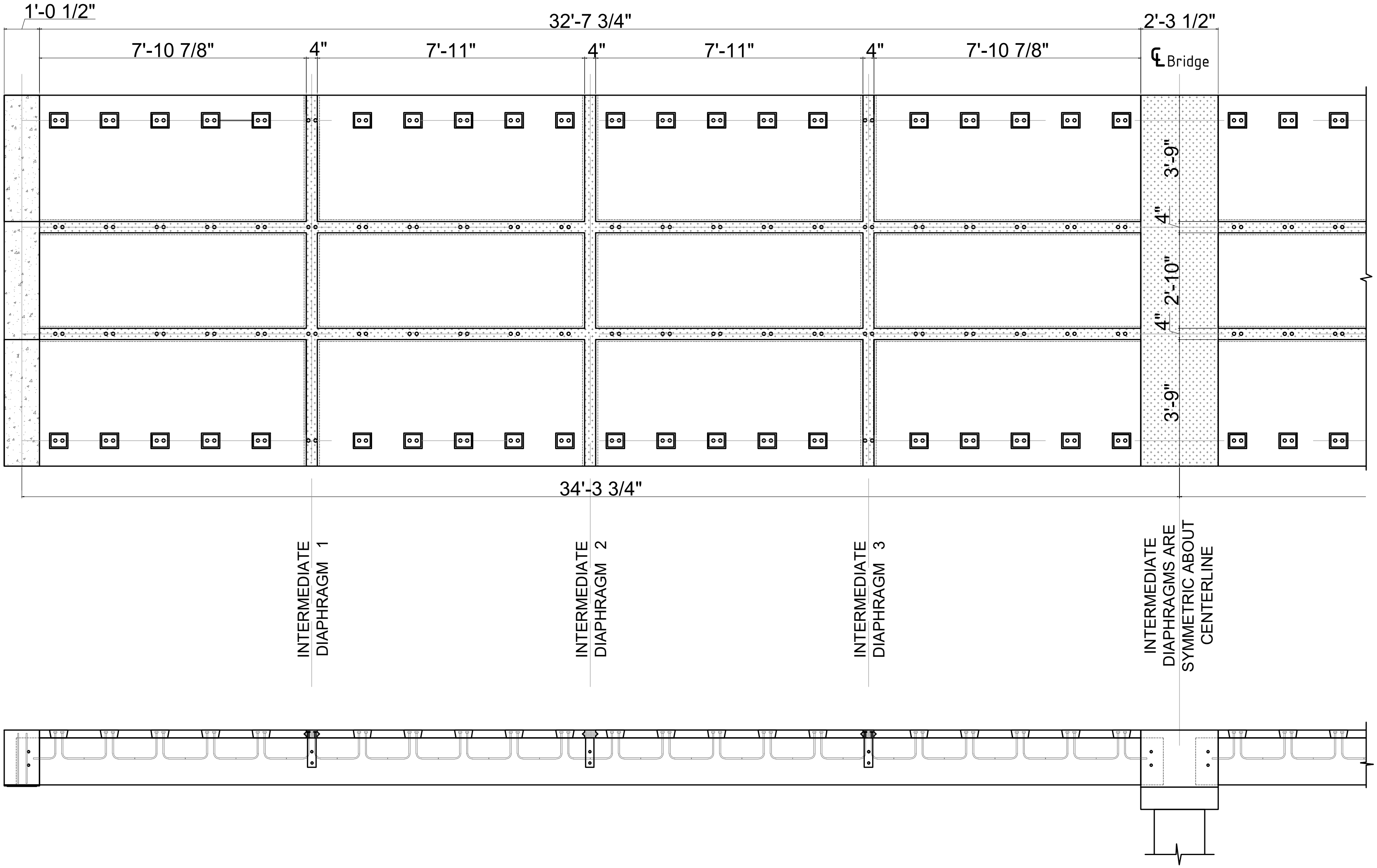

University of Nevada, Reno

Caltrans

Project: ABC Bridge System Project

Contains: Location of Intermediate Diaphragms per Span

Designed and Drawn by: José Benjumea

Scale: 1:50

Date: 02/13/2017

Sheet: 01 of 13

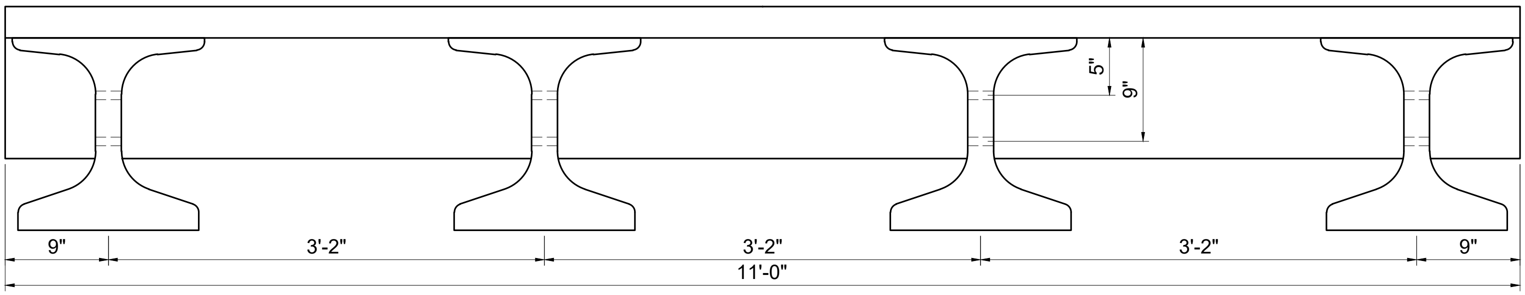

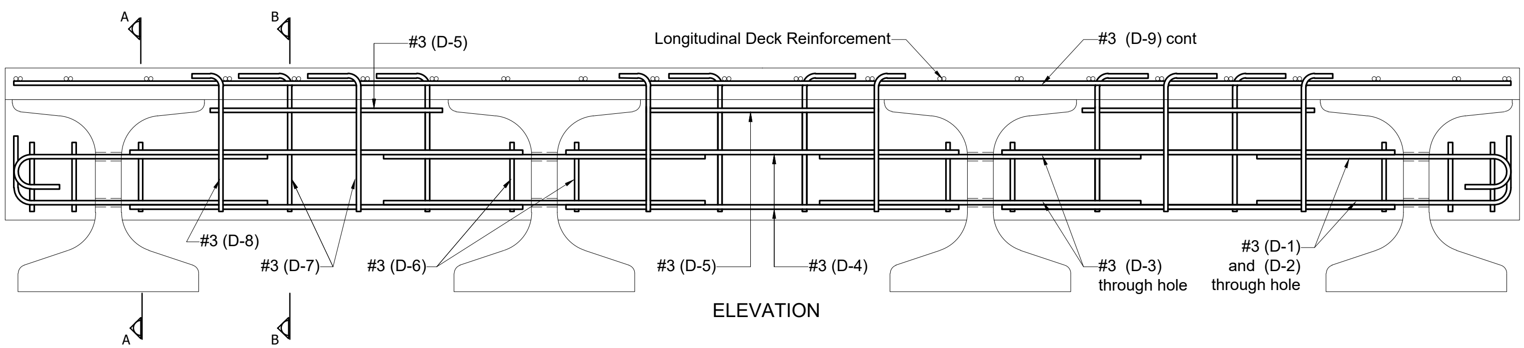

ELEVATION

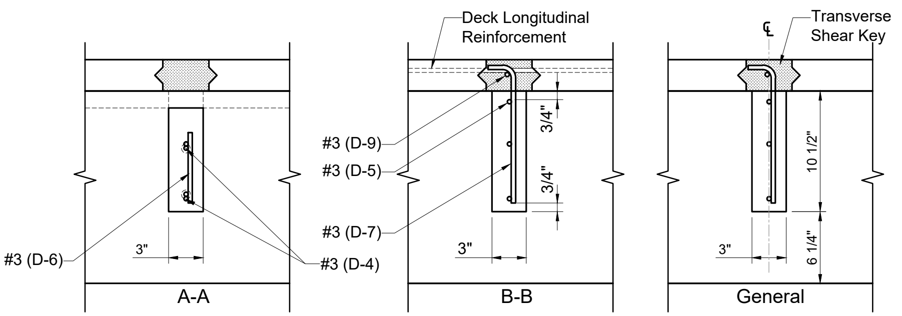

Notes

* Diaphragm is cast in place
* Concrete: f'c=4000 psi
  Recommended SCC
* Reinforcement Steel is Grade 60
* Dowel Bars are grouted in field
* Transverse shear key filled with UHPC

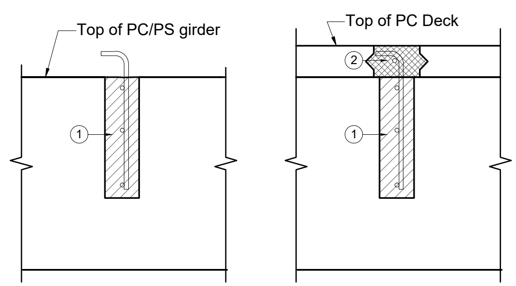

CASTING STAGES
Cast top portion after placement of PC deck panels

University of Nevada, Reno
Caltrans

Project: ABC Bridge System Project	
Contains: Intermediate Diaphragms Dimensions and General Reinforcement	Sheet:
Designed and Drawn by: José Benjumea	02 of 13
Scale: 1:16 / Date: 02/13/2017	

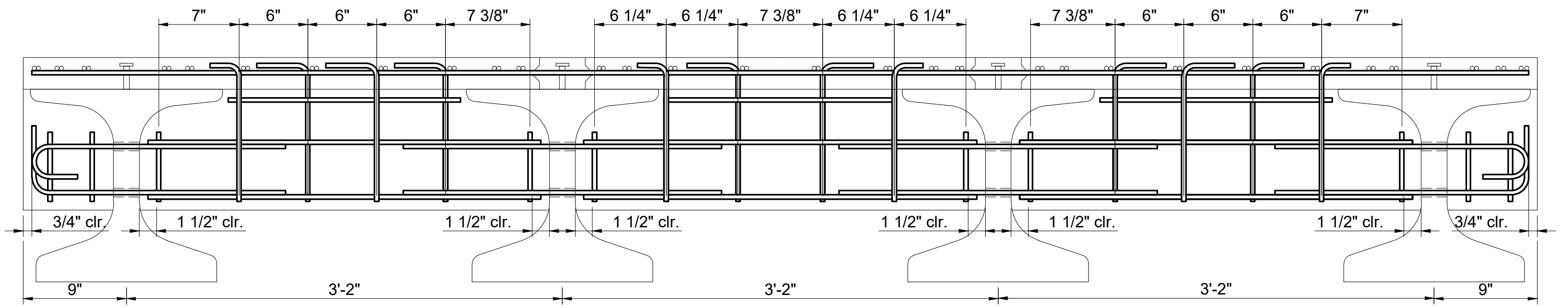

ELEVATION

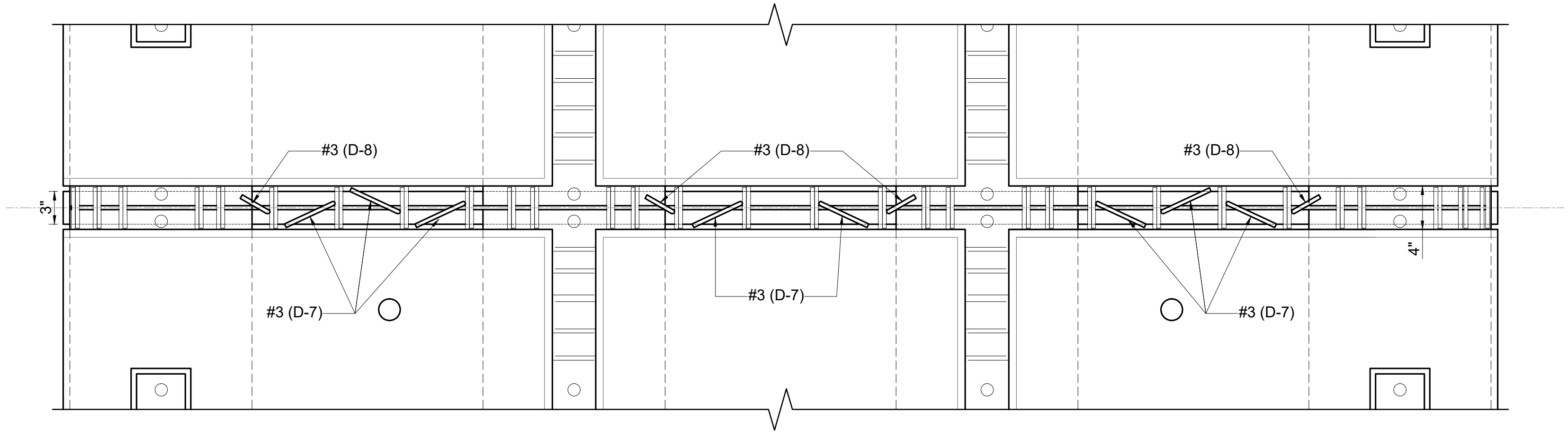

INTERMEDIATE DIAPHRAGM
PLAN VIEW

University of Nevada, Reno / Caltrans	Project: ABC Bridge System Project	
	Contains: Intermediate Diaphragm (Typical Reinforcement)	Sheet:
	Designed and Drawn by: José Benjumea	03 of 13
	Scale: 1:16 / Date: 02/13/2017	

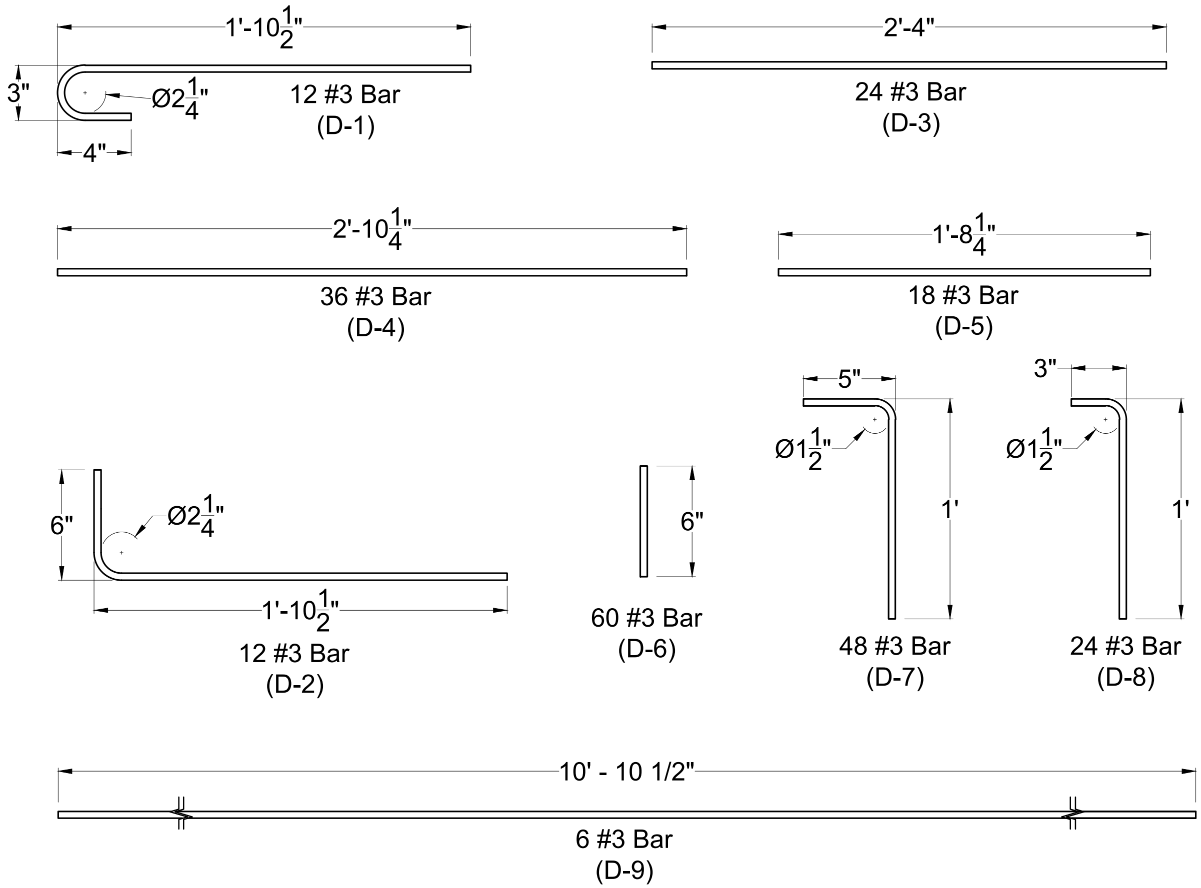

University of Nevada, Reno

Caltrans

Project: ABC Bridge System Project

Contains: Reinforcement Detail (*Quantities for six Intermediate Diaphragms*)

Designed and Drawn by: José Benjumea

Scale: 1:10

Date: 02/13/2017

Sheet: 04 of 13

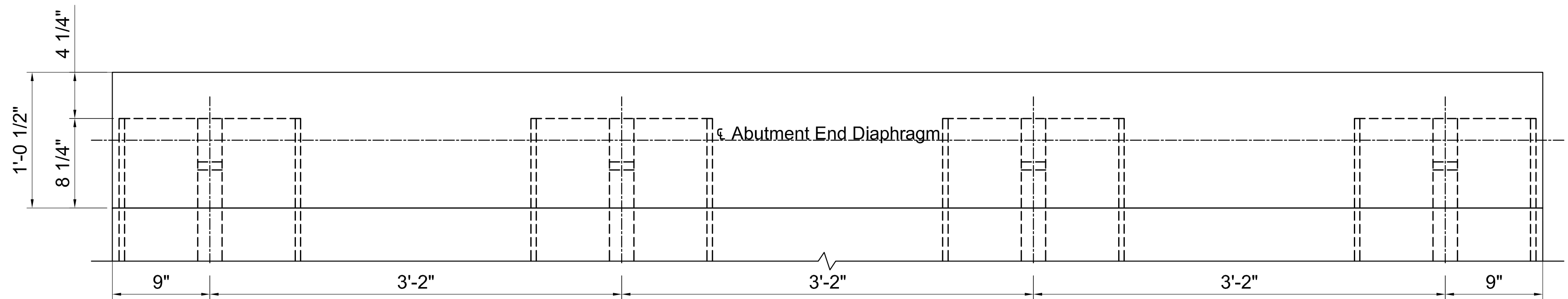

PLAN

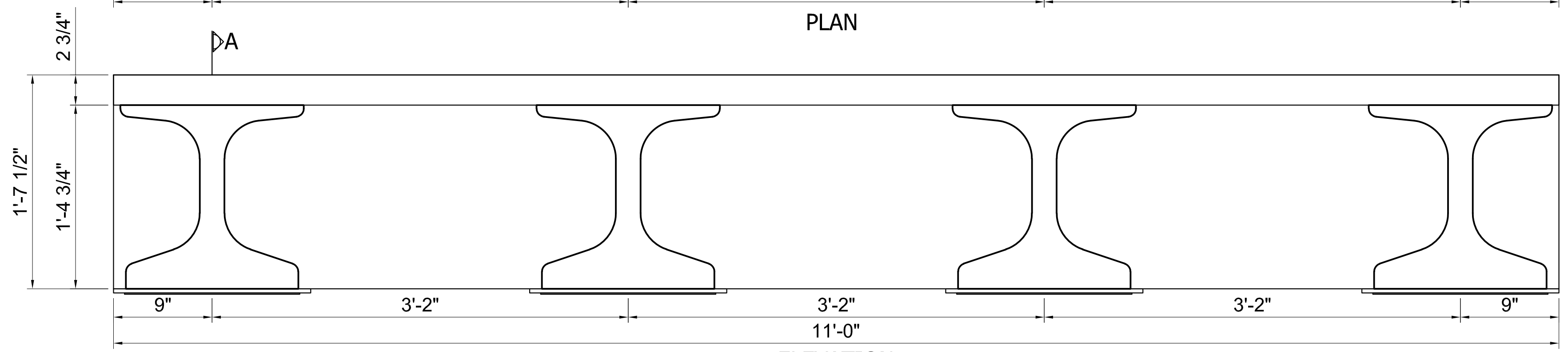

ELEVATION

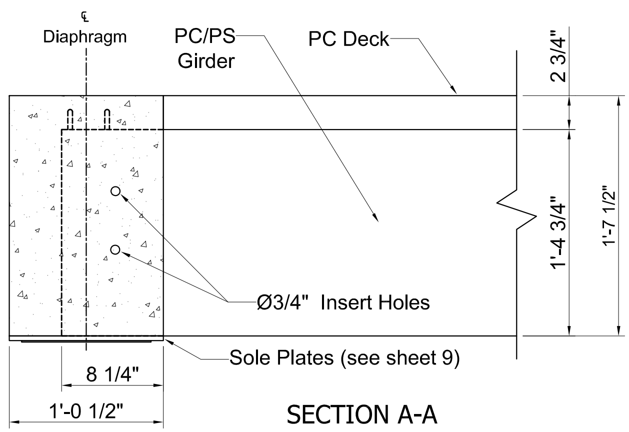

SECTION A-A

Notes
* Abutment E.D. is cast in place
* Concrete: f'c=4000 psi
  3/8"-dia. max. aggr.
* Dowel bars are grouted in field

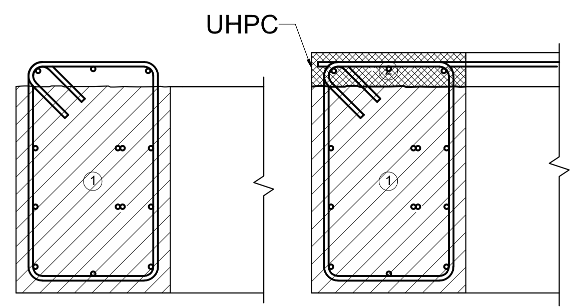

CASTING STAGES
Cast top portion after placement of PC deck panels

University of Nevada, Reno
Caltrans

Project: Calt - ABC Bridge 2	
Contains: Abutment End Diaphragm Dimensions	Sheet:
Approved by: Jared Jones	05 of 13
Scale: 1:16 Date: 01/29/2018	

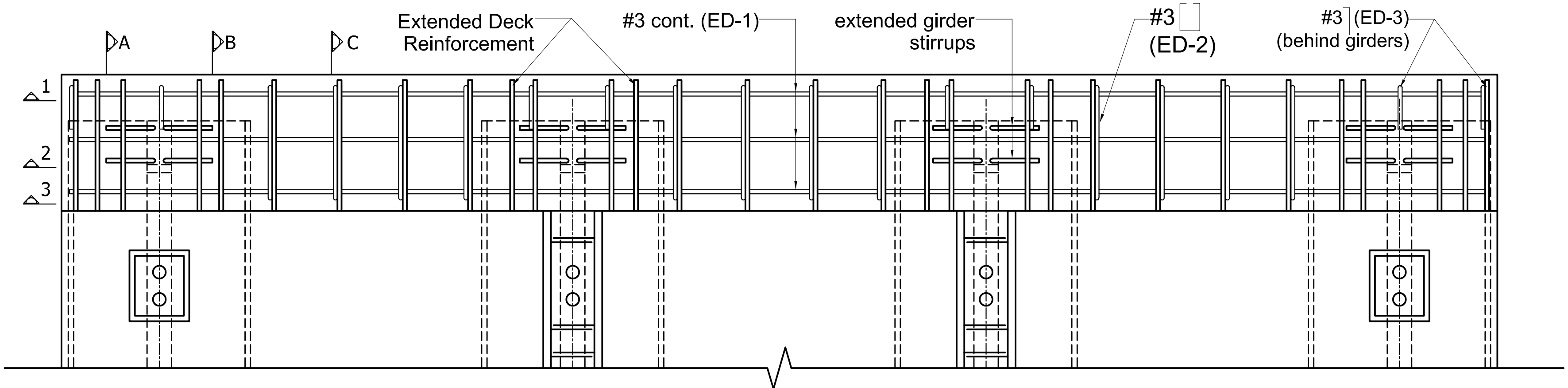

PLAN (Top Layer)

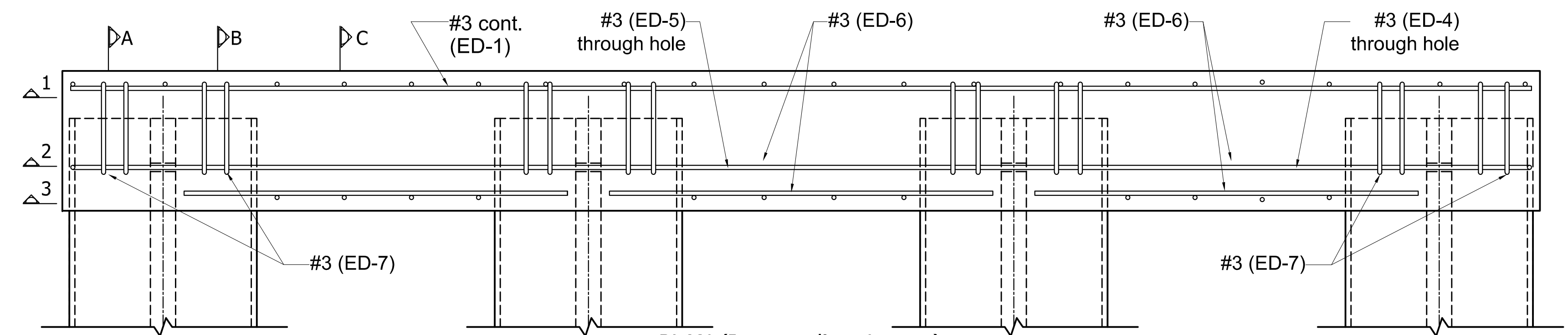

PLAN (Intermediate Layers)

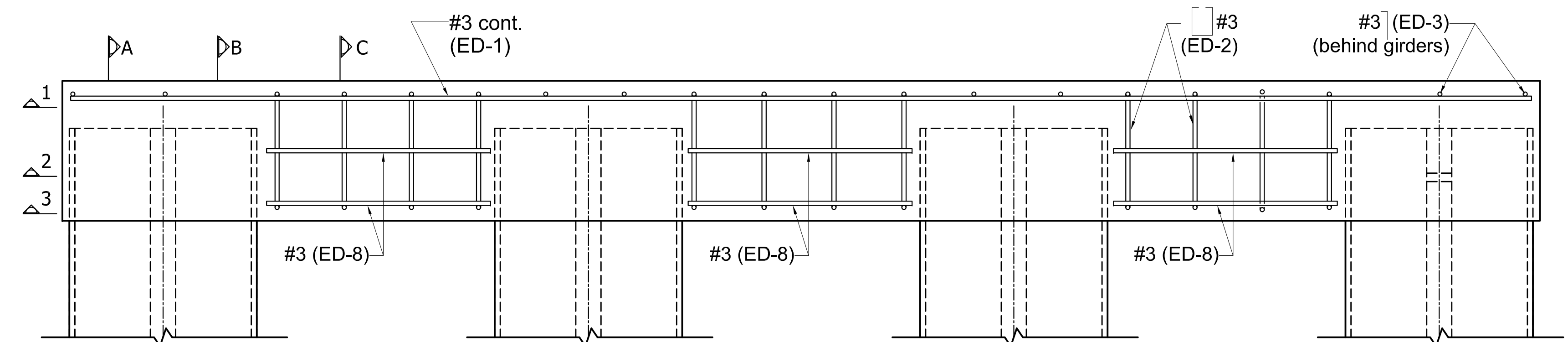

PLAN (Bottom Layer)

University of Nevada, Reno

Caltrans

Project: Calt - ABC Bridge 2	
Contains: Abutment End Diaphragm Reinforcement (1)	Sheet:
Approved by: Jared Jones	06 of 13
Scale: 1:16	Date: 01/29/2018

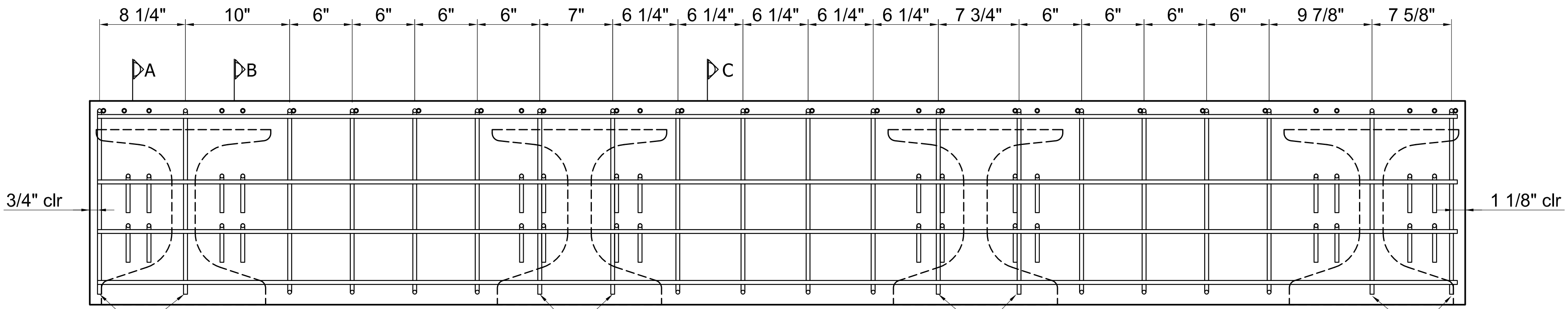

SECTION 1-1

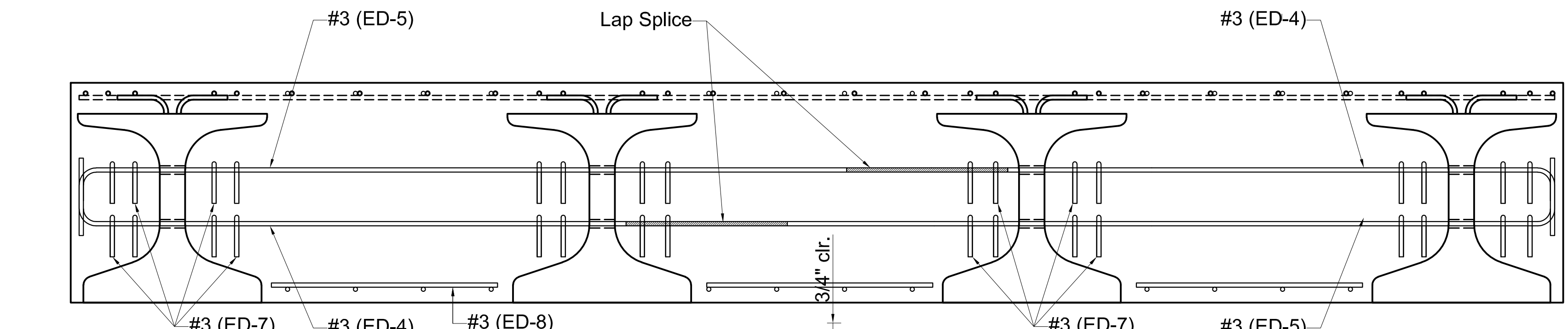

SECTION 2-2

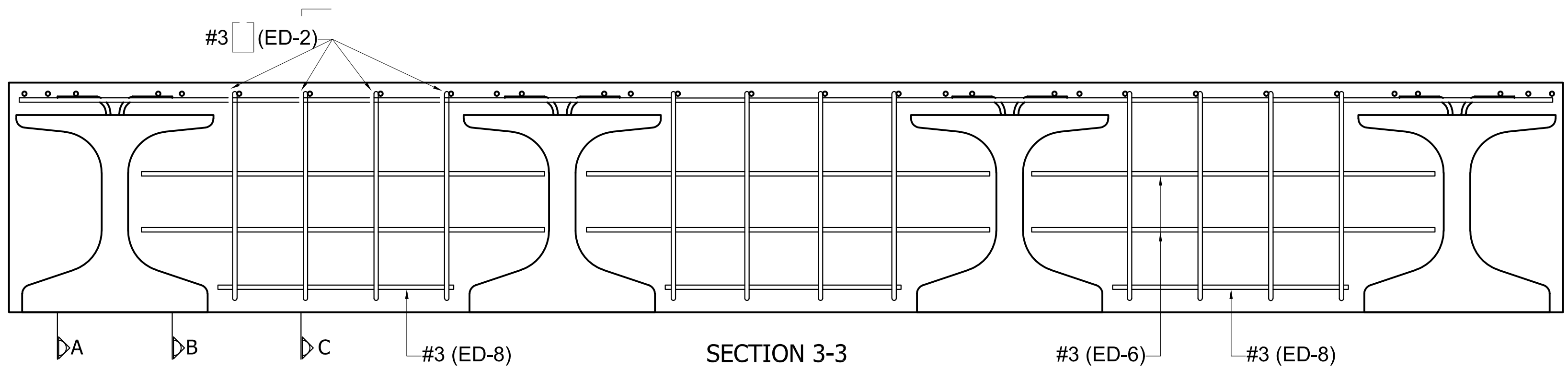

SECTION 3-3

University of Nevada, Reno

Caltrans

Project: Calt - ABC Bridge 2

Contains: Abutment End Diaphragm Reinforcement (2)

Approved by: Jared Jones

Scale: 1:16

Date: 01/29/2018

Sheet: 07 of 13

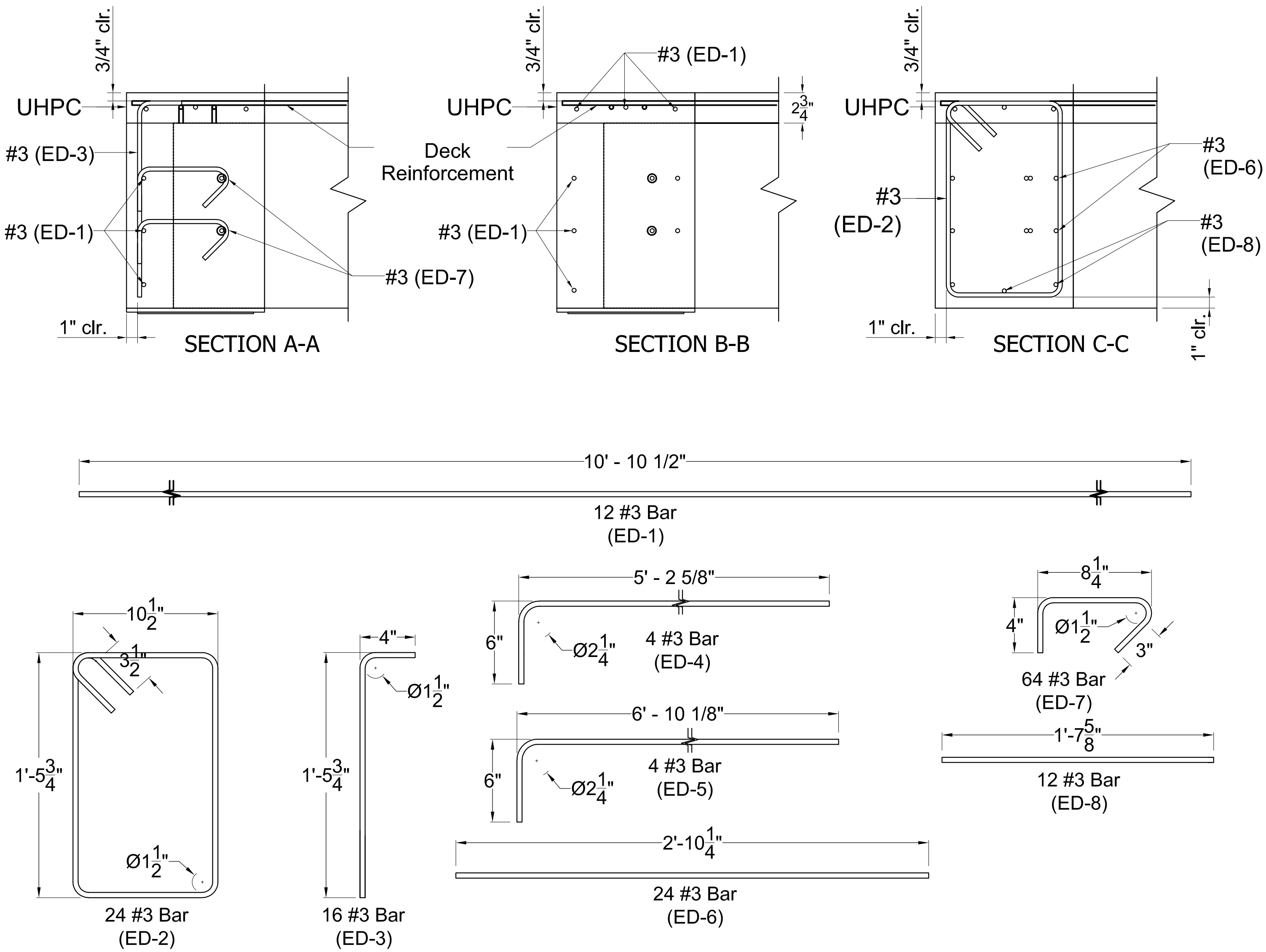

University of Nevada, Reno / Caltrans	Project: Calt - ABC Bridge 2	
	Contains: Abutment End Diaphragm Reinforcement (3)	Sheet:
	Approved by: Jared Jones	08 of 13
	Scale: N.A. — Date: 01/29/2018	

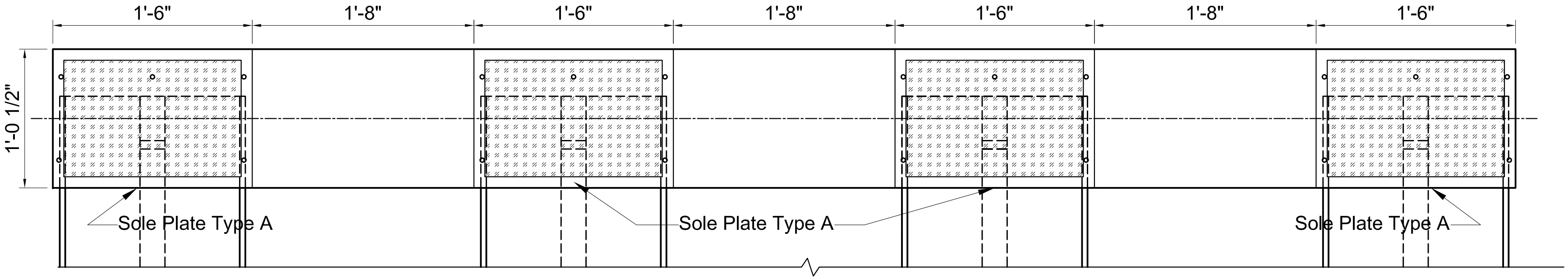

BOTTOM VIEW

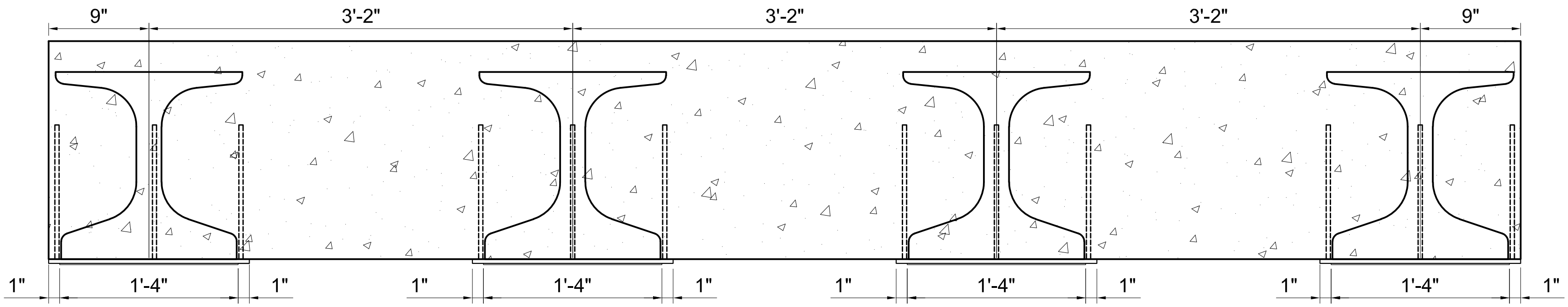

ELEVATION

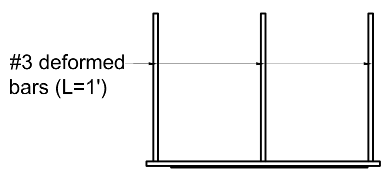

Elevation

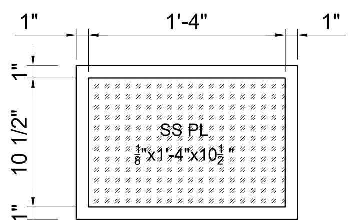

Bottom View

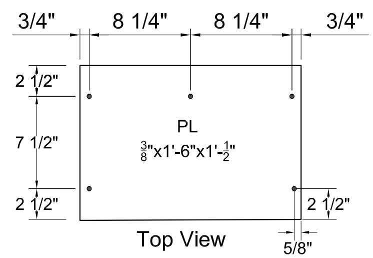

Top View

Type A Sole Plate

Notes

- PL $\frac{3}{8}$"x1'-6"x1'-$\frac{1}{2}$": ASTM A36
- SS PL $\frac{1}{8}$"x1'-4"x10$\frac{1}{2}$": Type 304 Stainless Steel #8 mirror finish ASTM A240 Use stitch TIG to weld the SS plate to the A36 plate in order to control heat distorsion.
- #3 Deformed bars to be installed using a stud gun.

Note: Sole Plates will be provided by engineer

University of Nevada, Reno

Caltrans

Project: Calt - ABC Bridge 2	
Contains: Sole Plates	Sheet:
Approved by: Jared Jones	09 of 13
Scale: 1:16	Date: 01/29/2018

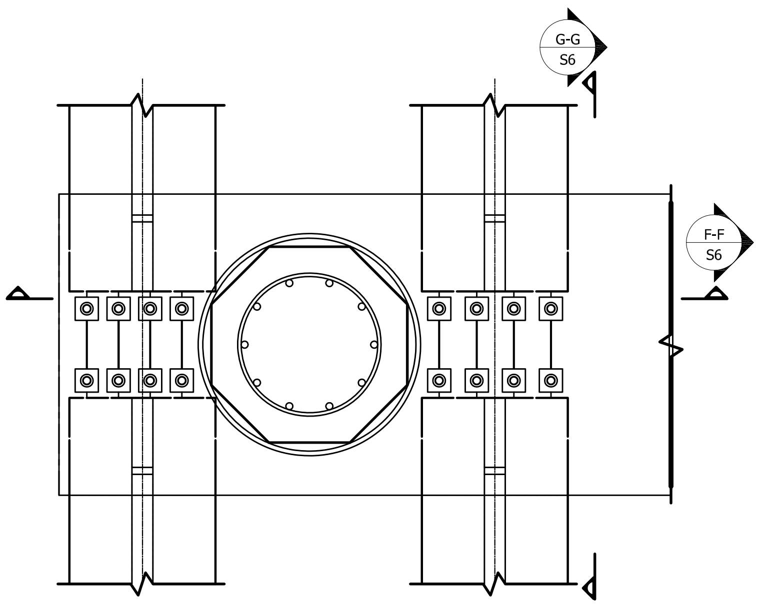

PLAN VIEW - Projected Girder Reinforcement

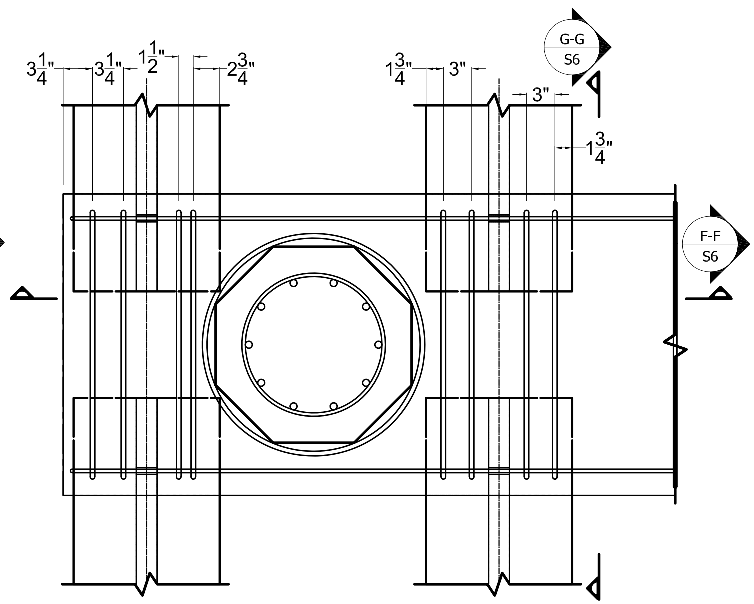

PLAN VIEW - Cap Beam Reinforcement Only

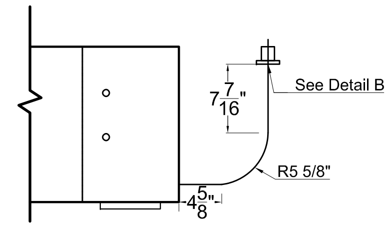

Detail A
Strand Extension Hook Detail

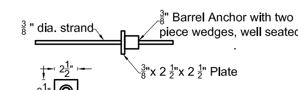

Detail B
Strand Chuck Anchorage Detail

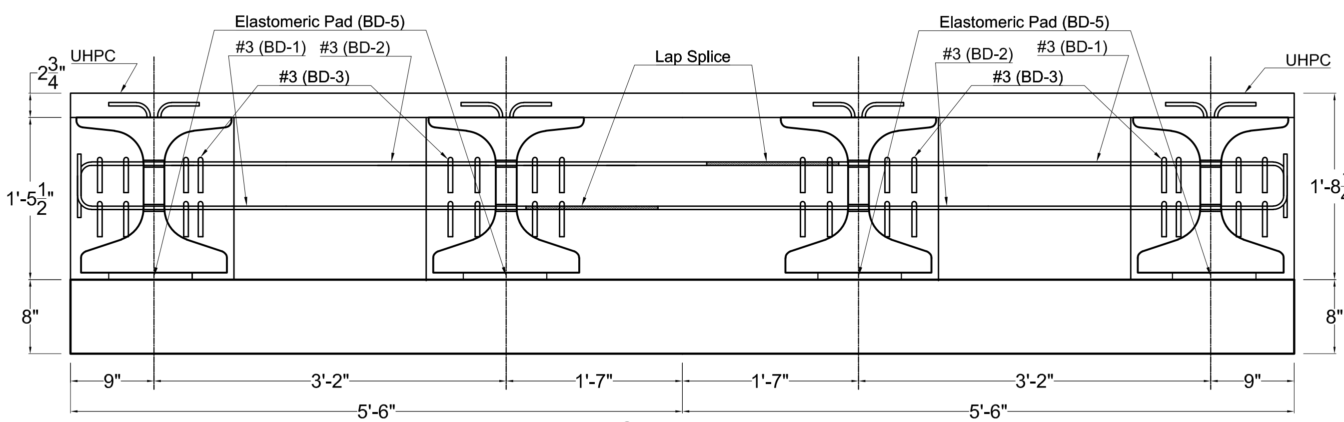

Section F-F
Additional Reinforcement not shown for clarity

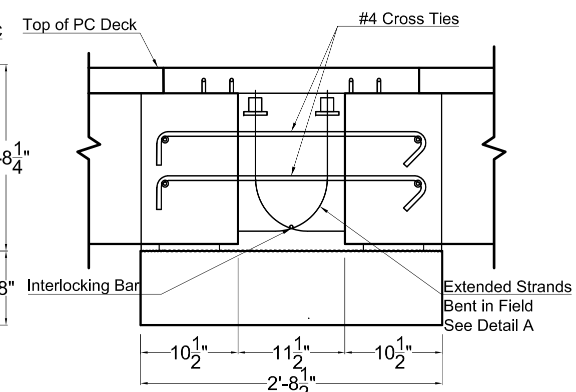

Section G-G
Additional Reinforcement not shown for clarity

University of Nevada, Reno

Caltrans

Project: Calt - ABC Bridge 2	
Contains: Girder Connection Details	Sheet:
Approved by: Jared Jones	10 of 13
Scale: 1/2"=1'-0" Date: 1/29/2018	

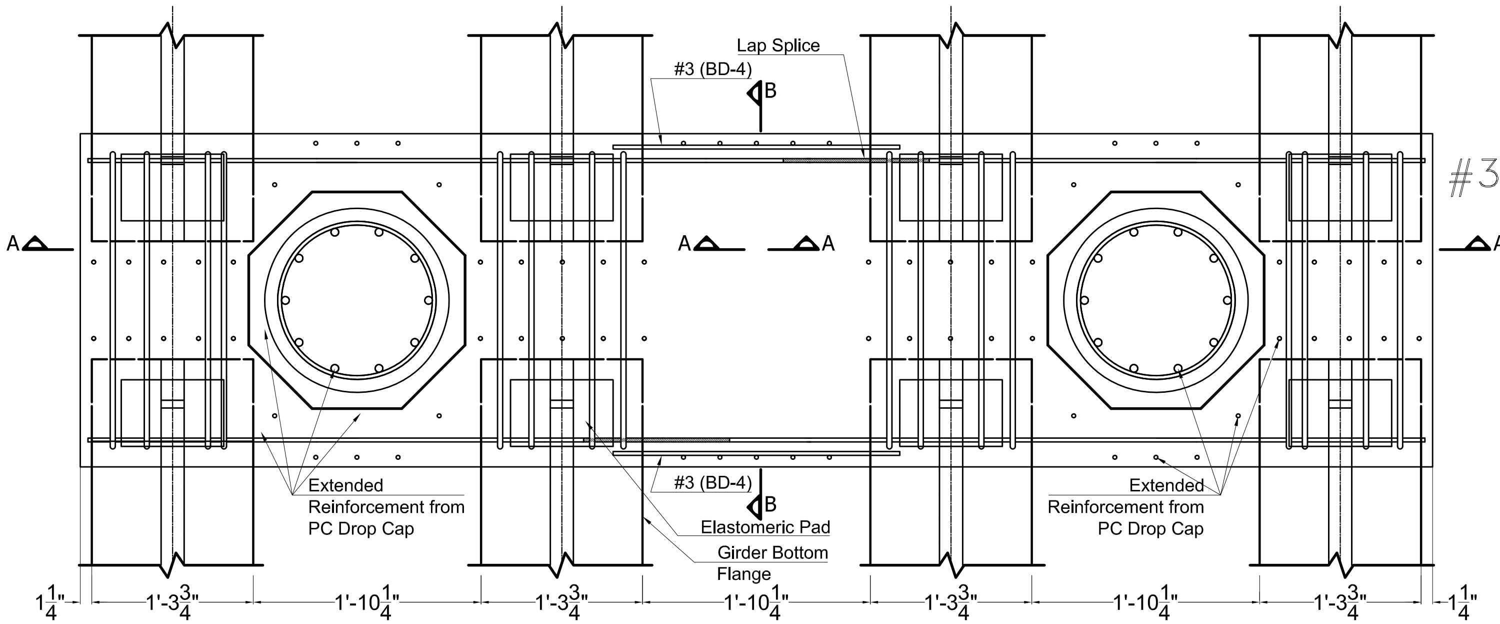

PLAN VIEW

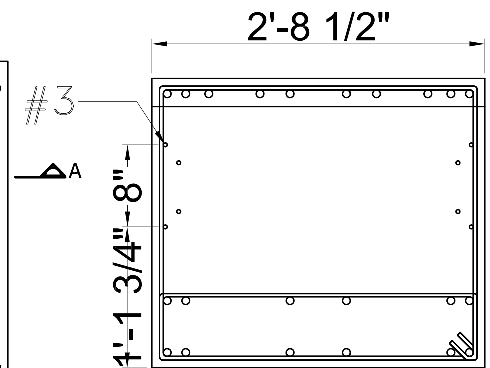

Section B-B

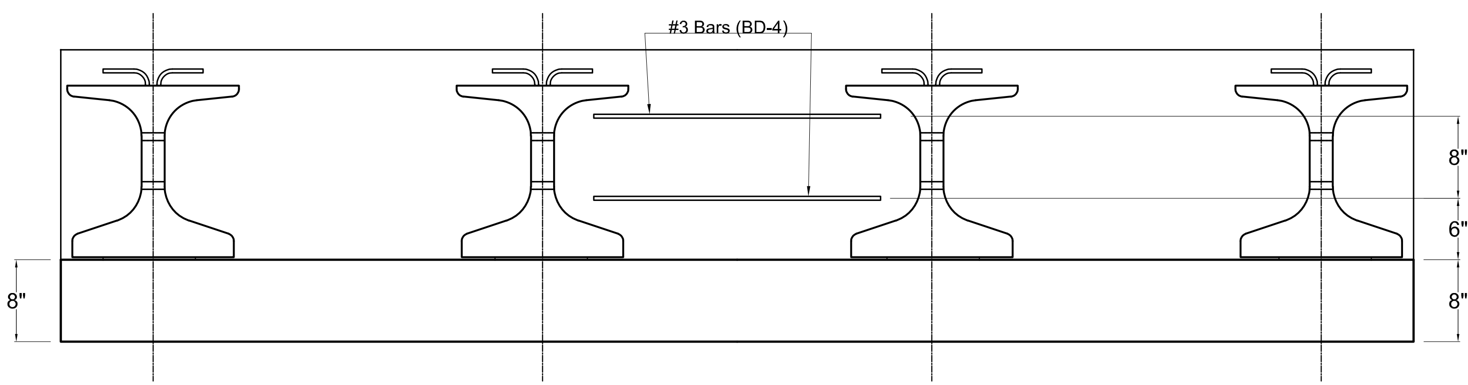

Section A-A

Additional Reinforcement not shown for clarity

University of Nevada, Reno

Caltrans

Project: Calt - ABC Bridge 2

Contains: Temperature and Shrinkage Reinforcement

Approved by: Jared Jones

Scale: 1"=1'-0"

Date: 1/29/2018

Sheet: 11 of 13

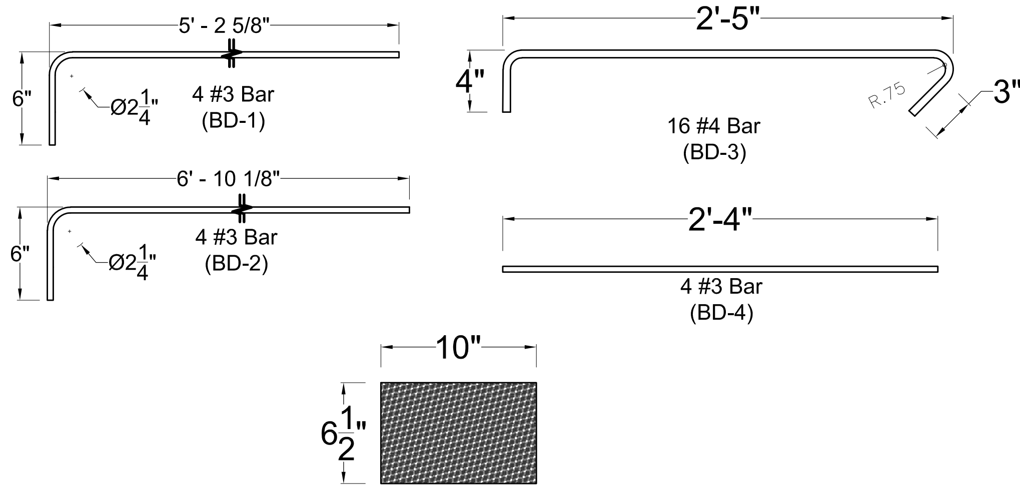

8 Elastomeric Bearing Pads (BD-5)
t=1/4" - Shore 60 A

Note: Elastomeric Pads (BD-5) will be provided by engineer

University of Nevada, Reno
Caltrans

Project: Calt - ABC Bridge 2		
Contains: Girder Connection Reinforcement		Sheet:
Approved by: Jared Jones		12 of 13
Scale: 1"=1'-0"	Date: 1/29/2018	

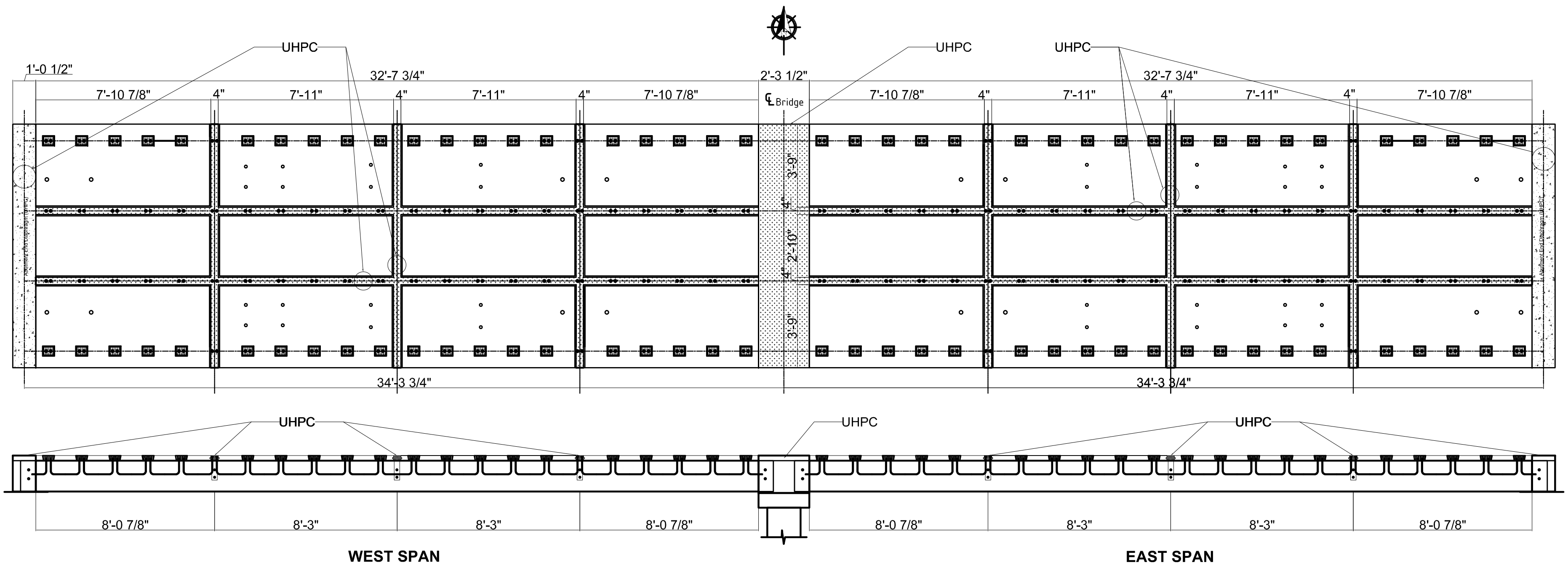

University of Nevada, Reno | Caltrans

Project: Calt - ABC Bridge 2

Contains: Locations of Superstructure UHPC

Approved by: Jared Jones

Scale: 5/16"=1'-0"

Date: 1/29/2018

Sheet: 13 of 13

Appendix B: Design and Detailing Guidelines for Bent Cap Pocket Connections (Tazarv & Saiidi, 2015)

Chapter 4. Design and Detailing Guidelines for Bent Cap Pocket Connections

4.1 Introduction

The AASHTO Guide Specifications (2014) provides a comprehensive design method and thorough detailing for capacity protected members such as cap beams and joints (Sections 8.9 to 8.13). Furthermore, Restrepo et al. (2011) proposed design and construction guidelines in NCHRP 681 for precast cap beams with pockets to facilitate field deployment. This chapter is dedicated to the development of design guidelines for cap beam pocket connections reflecting new detailing and experimental findings reported in recent studies. Both the Guide Specifications and NCHRP 681 were incorporated in the proposed guidelines, which include recommendations (indicated by "R") and commentary (indicated by "C").

4.2 Proposed Guidelines

R1- Cap beams with pocket connections shall be designed in accordance to a legally adopted bridge code.

C1- Bridge components are analyzed and designed according to the AASHTO LRFD (2013) or AASHTO Guide Specifications (2014) regardless of the use of pocket connections since this connection type is emulative of conventional connections. The detailing requirements to accommodate pockets in bent caps are presented in R2 to R10.

R2- The depth of pocket in a cap beam (H_p) (Fig. R-1) shall be at least the greatest of Eq. R-1 through Eq. R-3:

$$H_p \geq 1.25D_c \qquad \text{(R-1)}$$

$$H_p \geq 0.7d_b.f_{ye}/\sqrt{f'_c} \quad [ksi, in.] \qquad \text{(R-2)}$$

$$H_p \geq 24d_b \qquad \text{(R-3)}$$

C2- Experimental studies have shown that full column plastic moment can be transferred to the cap beams when the embedment length of column or column longitudinal reinforcement into the pocket is $1.0D_c$. Eq. R-1 was developed based on these findings including a 1.25 safety factor. Matsumoto et al. (2001) proposed design equation Eq. R-2 for embedment length of column longitudinal bars into the cap beam pockets. The minimum development length of unhooked bars in cap beams according to the Caltrans SDC (2013) is calculated by Eq. R-3.

R3- The depth of bent cap (H_{cap}) shall be allowed to be equal to the pocket depth (H_p) when column longitudinal reinforcement is extended outside the precast column segment and is anchored into the pocket (Alt-3 and 4 in Fig. C-1). For fully precast columns, the depth of bent cap (H_{cap}) shall not be less than $1.25H_p$ as shown in Fig. R-1.

C3- When connecting fully precast columns to cap beams with pocket (Alt-5 in Fig. C-1), the depth of bent cap above the pocket should be sufficiently large to avoid concrete cracking above the pocket during lifting the precast cap beam, and to avoid punching failure above the pocket due to the weight of the precast cap beam. Bent cap depth of $1.25H_p$ can be used as initial design height when columns are either fully or partially precast. Cap beams with a depth of $1.6D_c$ or greater should be designed based on the strut and tie provisions of AASHTO LRFD Bridge Design Specifications and as approved by the Owner.

R4- The width of bent cap with pocket (B_{cap}) shall extend at least 15 *in*. (380 *mm*) on each side of the column when bent cap longitudinal bars are clustered beside the pocket as shown in Fig. R-1. The width of bent cap may only satisfy the clear cover requirements when bent cap longitudinal bars are distributed across the width of the beam (Alt-1 and Alt-3). The gap between the column and the pocket edge shall be no less than 2 *in*. (50 *mm*), but shall not exceed 4 *in*. (100 *mm*) when the column is fully precast. In this case, the bent cap web at the pocket shall be at least 12-*in*. (300-*mm*) wide.

C4- The minimum width of a cap beam according to the AASHTO Guide Specifications (2014) is the column diameter (or side dimension) plus 24 *in*. (610 *mm*) (Article 8.13.4.1.1). This limitation was used as baseline in the present guide with a 6-*in*. (150-*mm*) increase to accommodate pocket. The minimum proposed bent cap width (D_p+2.5 *ft*) provides sufficient space to lump all cap beam longitudinal reinforcement in the web. Nevertheless, this requirement may not be considered when bars are distributed across the width of the cap beam (e.g. Alt. 1 and Alt. 3). The specified gap between the column and the pocket provides sufficient construction tolerance for multi-column bents while ensuring sufficient grout thickness.

R5- The diameter of the opening above the cap beam pocket (D_h) shall be the greater of (a) three times the maximum size of the coarse aggregate of the pocket filler and (b) 4 *in*. (100 *mm*). At least 10% slope shall be provided for the inner edge of the bent cap above pocket as shown in Fig. R-1.

C5- The American Concrete Pumping Association (2011) recommends limiting the maximum size of the coarse aggregate to one-third of the smallest inside diameter of the pump or placing line. A 4-in. (100-mm) opening provides sufficient access to cast concrete and grout from top of the bent cap.

R6- Pockets shall be constructed with helical, lock-seam, corrugated steel pipes conforming to ASTM A760. The pipe thickness (t_p) shall be at least:

$$t_p = A_{sp}.f_{yh}/(S_h.f_{yp}.cos\theta) \geq 0.06\ in.(1.5\ mm) \qquad \text{(R-4)}$$

C6- According to ASTM A760, 31 sizes are allowed for corrugated steel pipes with inner diameter of 4 in. (100 mm) to 144 in. (3600 mm). Furthermore, seven thicknesses are specified from 0.04 in. (1.02 mm) to 0.168 in. (4.27 mm). Table C-1 presents diameter and thickness of steel pipes for practical range of bridge column diameters. Equation R-4, proposed by Restrepo et al. (2011), compensates for the lack of column transverse reinforcement inside the pocket, when column dowels are extended into the pocket, and ensures sufficient confinement by the corrugated steel pipe. Nevertheless, the extension of column hoops or spirals into the pocket is highly recommended as illustrated for Alt-2, Alt-4, and Alt-5 in Fig. C-1. Alt-5 is the easiest alternative to construct and will result in four times faster construction compared to cast-in-place bents. The angle between the horizontal axis of the bent cap and the pipe helical corrugation (θ) is always less than 30-deg for pipes presented in Table C-1 according to the ASTM A760 limitations. Therefore, $\theta = 30°$ may be conservatively used for initial design of the pipe resulting in at most 13% thicker pipes.

R7- The cap beam transverse reinforcement (spiral or hoops) around the pocket (Fig. R-1) shall be placed in the lower half of the bent cap. The transverse reinforcement volumetric ratio shall be the same as that of the column transverse reinforcement.

C7- The required transverse reinforcement around the pocket ensures the integrity of the cap beam in the pocket region. Research has shown that only the transverse reinforcement in the lower half of the pocket is effective in providing confinement (Mehrsoroush and Saiidi, 2014).

R8- Bundling of bent cap longitudinal bars shall be allowed per bridge codes. The bent cap longitudinal bars shall not be discontinuous over the bent length. Bent cap longitudinal bar splices in any form shall not be allowed within $1.0D_c$ from the column center line. Clear cover limitations are not required for inner sides of bent cap sections with pocket.

C8- The AASHTO LRFD (2013) specifies the reinforcement detailing (e.g. spacing and bundling) in Section 5.10. Minimum clear cover is not necessary for the reinforcement inside the pocket because the pocket is filled with concrete or grout.

R9- Pocket shall be filled with either concrete, self-consolidating concrete, or grout when columns are partially precast. For fully precast columns, the pockets shall be filled with non-shrink, high-flow grout.

C9- For partially precast columns in which pockets are almost empty after placing the bent cap (Alt-1 to Alt-4 in Fig. C-1), concrete, self-consolidating concrete (SCC), or grout can be used to fill the pocket. However, a filler with no need for vibration (e.g. SCC) is preferred. Grout should be fluid when fully precast columns are embedded in the pocket (Alt-5 in Fig. C-1) since the gap is small. Aggregate-based grout should not be used for Alt-5 since this type of grout is less workable than non-aggregate grout.

R10- Spacers shall be installed above the fully precast columns to provide a vertical gap. This gap shall be no less than 2 in. (50 mm), but shall not exceed 4 in. (100 mm). These spacers shall not block grout flow into the gap.

C10- The specified gap between the top surface of the fully precast column and the upper part of the cap beam pocket (Alt-5 in Fig, C-1) ensures that the grout will flow through the entire pocket.

4.3 Notation

A_{sp}: Area of one hoop or spiral as transverse reinforcing steel bar (*in.*^{2}*, mm*^{2})
B_{cap}: Bent cap width (*in., mm*)
d_b: Nominal diameter of column longitudinal reinforcing steel bar (*in., mm*)
D_c: Column largest cross sectional dimension (*in., mm*)
D_h: Hole diameter above pocket (*in., mm*)
D_p: Pocket diameter (*in., mm*)
f'_c: Compressive strength of bent cap concrete (*ksi, MPa*)
f_{ye}: Expected yield stress for longitudinal reinforcing steel bar (*ksi, MPa*)
f_{yh}: Nominal yield stress for transverse reinforcing steel bar (*ksi, MPa*)
f_{yp}: Steel pipe yield stress (*ksi, MPa*)
H_{cap}: Depth of cap beam with pocket (*in., mm*)
H_p: Depth of pocket in cap beam (*in., mm*)
S_h: Spacing of transverse hoops or spirals in equivalent CIP joint
t_p: Pipe thickness (*in., mm*)
θ: Angle between the horizontal axis of the bent cap and the pipe helical corrugation or lock seam (*deg*)

Chapter 5. Design Examples for Cap Beam Pocket Connections

5.1 Introduction

A design guideline was presented in the previous chapter to facilitate the application of cap beam pocket connections as a viable ABC connection. This chapter is to demonstrate the guidelines through design of a four-column bent connected to a precast cap beam utilizing pocket connections.

5.2. Reference Cast-in-Place Four-Column Bent

The Federal Highway Administration (FHWA) developed a comprehensive bridge design example (Wassef et al. 2003) to aid designers with the implementation of the 2002 AASHTO LRFD Bridge Design Specifications. The FHWA example included a two-span bridge with a four-column bent and prestressed concrete girders. Figure 5-1 shows the bridge, bent, and column and cap beam detailing. The specified concrete compressive strength was 3.0 *ksi* and the steel bars were Grade 60.

This cast-in-place bent was utilized in the present study to illustrate the pocket cap beam design guidelines and to show the changes that are needed to convert the cast-in-place bent cap of the AASHTO example to a precast bent cap.

5.3 Precast Four-Column Bent

Cap beams in which fully precast columns are inserted into pockets (Alt-5) results in minimal onsite construction time among the five proposed alternatives. However, design of cap beam in Alt-5 is more involved than the design of others because Alt-5 does not require shoring. Accordingly, this alternative was selected in this section to fully demonstrate the guideline. The cap beam detailing of the reference CIP bent was modified herein to accommodate the pockets and to satisfy the Alt-5 minimum requirements.

5.3.1 Cap Beam Dimensions

The total depth of the cap beam (H_{cap}) should be at least 1.25 times the pocket depth (H_p). H_p is the greater of (1), (2), and (3) as:

$$H_p \geq 1.25 D_c = 1.25 \times 42 = 52.5\ in. \quad (1)$$

$$H_p \geq 0.7 d_b . \frac{f_{ye}}{\sqrt{f'_c}} = 0.7 \times 1.0 \times \frac{68}{\sqrt{3.0}} = 27.5 \; in. \qquad (2)$$

$$H_p \geq 24 d_b = 24 \times 1.0 = 24.0 \; in. \qquad (3)$$

Therefore, $H_p = 52.5$ *in*. thus $H_{cap} = 1.25H_p = 65.6$ *in*., or 66 *in*. The minimum width of the cap beam (B_{cap}) for this alternative is the pocket diameter plus 30 *in*. The diameter of a suitable corrugated steel pipe to form the pocket for this column diameter (42-*in*. diameter) is 48-*in*. Thus,

$$B_{cap} \geq 48 + 30 = 78 \; in.$$

The gap between the column and the pocket edge is (48-42)/2=3 *in*., which satisfies the gap requirement.

5.3.2 Bent Cap Depth for Lifting and Punching

The bent cap should remain uncracked during lifting and should be sufficiently strong to resist punching forces when the cap beam bears on the columns. Figure 5-2 shows the precast bent cap moment and punching forces during lifting with the configuration shown. The maximum moment in the pocketed area of the cap beam during lifting due to the cap beam self-weight was 116.5 *kip-ft*, using two lift points as shown in the figure. According to the AASHTO (2013, Article 5.4.2.6), the modulus of rupture for concrete is:

$$f_r = 0.24\sqrt{f'_c} = 0.24\sqrt{3} = 0.41 \; ksi$$

Thus the cracking moment for the pocketed area of the cap beam (an inverted U-shape section) is:

$$M_{cr} = \frac{f_r . I}{y} = \frac{0.41 \times 1064195}{26.55} \times \frac{1}{12} = 1370 \; kip - ft > 116.5 \; kip - ft$$

where I is the inverted U-shape section moment of inertia and y is the distance from the neutral axis to the top edge of the section. The cracking moment at other locations exceeds 1370 *kip-ft* because of the larger sections. The possible cracking should also be checked at the point of the maximum moment. Because the maximum moment of 491.7 *kip-ft* is less than 1370 *kip-ft*, it can be concluded by inspection that the cap beam will not be cracked under self-weight during lifting.

The ACI method (ACI 318-14, Article 22.6.5.2) can be used to estimate the permissible punching shear capacity of the cap beam above the pocket as shown below. Note that the upper part of the cap beam in the pocket area essentially behaves as a slab:

$$V_c = min \begin{cases} \emptyset 4\lambda\sqrt{f'_c} b_o d = 0.75 \times 4 \times 1 \times \sqrt{3000} \times 4 \times 47.5 \times 10.3 \times 10^{-3} = 321 \; kips \\ \emptyset\left(2 + \frac{4}{\beta}\right)\lambda\sqrt{f'_c} b_o d = 0.75\left(2 + \frac{4}{1}\right)\sqrt{3000} \times 4 \times 47.5 \times 10.3 \times 10^{-3} = 482 \; kips \\ \emptyset\left(2 + \frac{\alpha_s d}{b_o}\right)\lambda\sqrt{f'_c} b_o d = 0.75\left(2 + \frac{20 \times 10.3}{4 \times 47.5}\right)\sqrt{3000} \times 4 \times 47.5 \times 10.3 \times 10^{-3} = 248 \; kips \end{cases}$$

where d is the effective cap beam depth above the pocket (13.5-2-0.625-1.128/2=10.3 $in.$) and b_o is the perimeter of the punching shear critical area. The side dimension of the critical section is the side dimension of an equivalent square column (with an area being the same as the circular column area) plus d ($\sqrt{0.25\pi \times 42^2} + 10.3 = 37.22 + 10.3 = 47.5\ in.$). The punching shear force, or column reactions shown in Fig. 5-2, is 75.31 *kips*, which is well below the controlling permissible shear. Overall, the cap beam depth is sufficient to remain uncracked during lifting and to resist the punching forces when it bears on the columns.

5.3.3 Steel Pipe Thickness

The corrugated steel pipe thickness to form the pocket can be estimated using basic properties of the pipe and the adjoining column. According to the AASHTO example, the columns are transversely reinforced with #3 hoops spaced 12 $in.$ on center (Fig. 5-1d). Since the current AASHTO LRFD Bridge Design Specifications (2013) requires higher amount of transverse reinforcement for these columns, new columns reinforced with #5 hoops spaced 12 $in.$ on center (according to the AASHTO LRFD Bridge Design Specifications 2013, Articles 5.8.2.5 and 5.8.2.7) was utilized for further analysis. The pipe has a yield strength (f_{yp}) of 30 *ksi* and a 20° helical corrugation. The required pipe thickness is:

$$t_p = \frac{A_{sp}.f_{yh}}{S_h.f_{yp}.cos\theta} = \frac{0.31 \times 60}{12 \times 30 \times cos20} = 0.054\ in. \qquad use\ 0.06\ in.$$

The pipe thickness is calculated based on the column transverse reinforcement to allow the application of pocket connections for cases in which the column transverse reinforcement is not extended into the pocket (e.g. Alt-1, Alt-3).

5.3.4 Precast Bent Detailing

Figure 5-3 shows the precast cap beam detailing. Since the precast cap beam is larger than the reference cast-in-place cap beam, the bent should be reanalyzed and the design forces for the cap beam and the columns should be updated and the capacity should be checked. Furthermore, the weight of the cap beam with pocket connections is twice that of the original cast-in-place beam, which may cause difficulties in transportation and erection. One solution is to use voided sections between the columns. This is especially favorable since the cap beam longitudinal reinforcement is clustered to accommodate the pockets. Figure 5-3 shows the location of the voids in the cap beam. Another solution is to use different alternatives for this case such as Alt. 3 or Alt. 4, which results is smaller cap beams comparable to the cast-in-place beam.

It was assumed in this example that the reinforcement in the precast cap beam is the same as that of the reference cast-in-place cap beam. A moment-curvature analysis was carried out to evaluate the precast cap beam capacity. Figure 5-4 shows that the precast cap beam yield moment is 50% larger than the column overstrength moment, making the cap beam a capacity protected member. As indicated before, cap beams should be first designed considering all the AASHTO LRFD load combinations. This is followed by seismic performance evaluation using AASHTO Guide Specifications.

LIST OF CCEER PUBLICATIONS

Report No.	Publication
CCEER-84-1	Saiidi, M., and R. Lawver, "User's Manual for LZAK-C64, A Computer Program to Implement the Q-Model on Commodore 64," Civil Engineering Department, Report No. CCEER-84-1, University of Nevada, Reno, January 1984.
CCEER-84-1	Douglas, B., Norris, G., Saiidi, M., Dodd, L., Richardson, J. and Reid, W., "Simple Bridge Models for Earthquakes and Test Data," Civil Engineering Department, Report No. CCEER-84-1 Reprint, University of Nevada, Reno, January 1984.
CCEER-84-2	Douglas, B. and T. Iwasaki, "Proceedings of the First USA-Japan Bridge Engineering Workshop," held at the Public Works Research Institute, Tsukuba, Japan, Civil Engineering Department, Report No. CCEER-84-2, University of Nevada, Reno, April 1984.
CCEER-84-3	Saiidi, M., J. Hart, and B. Douglas, "Inelastic Static and Dynamic Analysis of Short R/C Bridges Subjected to Lateral Loads," Civil Engineering Department, Report No. CCEER-84-3, University of Nevada, Reno, July 1984.
CCEER-84-4	Douglas, B., "A Proposed Plan for a National Bridge Engineering Laboratory," Civil Engineering Department, Report No. CCEER-84-4, University of Nevada, Reno, December 1984.
CCEER-85-1	Norris, G. and P. Abdollaholiaee, "Laterally Loaded Pile Response: Studies with the Strain Wedge Model," Civil Engineering Department, Report No. CCEER-85-1, University of Nevada, Reno, April 1985.
CCEER-86-1	Ghusn, G. and M. Saiidi, "A Simple Hysteretic Element for Biaxial Bending of R/C in NEABS-86," Civil Engineering Department, Report No. CCEER-86-1, University of Nevada, Reno, July 1986.
CCEER-86-2	Saiidi, M., R. Lawver, and J. Hart, "User's Manual of ISADAB and SIBA, Computer Programs for Nonlinear Transverse Analysis of Highway Bridges Subjected to Static and Dynamic Lateral Loads," Civil Engineering Department, Report No. CCEER-86-2, University of Nevada, Reno, September 1986.
CCEER-87-1	Siddharthan, R., "Dynamic Effective Stress Response of Surface and Embedded Footings in Sand," Civil Engineering Department, Report No. CCEER-86-2, University of Nevada, Reno, June 1987.
CCEER-87-2	Norris, G. and R. Sack, "Lateral and Rotational Stiffness of Pile Groups for Seismic Analysis of Highway Bridges," Civil Engineering Department, Report No. CCEER-87-2, University of Nevada, Reno, June 1987.
CCEER-88-1	Orie, J. and M. Saiidi, "A Preliminary Study of One-Way Reinforced Concrete Pier Hinges Subjected to Shear and Flexure," Civil Engineering Department, Report No. CCEER-88-1, University of Nevada, Reno, January 1988.
CCEER-88-2	Orie, D., M. Saiidi, and B. Douglas, "A Micro-CAD System for Seismic Design of Regular Highway Bridges," Civil Engineering Department, Report No. CCEER-88-2, University of Nevada, Reno, June 1988.
CCEER-88-3	Orie, D. and M. Saiidi, "User's Manual for Micro-SARB, a Microcomputer Program for Seismic Analysis of Regular Highway Bridges," Civil Engineering Department, Report No. CCEER-88-3, University of Nevada, Reno, October 1988.

CCEER-89-1 Douglas, B., M. Saiidi, R. Hayes, and G. Holcomb, "A Comprehensive Study of the Loads and Pressures Exerted on Wall Forms by the Placement of Concrete," Civil Engineering Department, Report No. CCEER-89-1, University of Nevada, Reno, February 1989.

CCEER-89-2 Richardson, J. and B. Douglas, "Dynamic Response Analysis of the Dominion Road Bridge Test Data," Civil Engineering Department, Report No. CCEER-89-2, University of Nevada, Reno, March 1989.

CCEER-89-2 Vrontinos, S., M. Saiidi, and B. Douglas, "A Simple Model to Predict the Ultimate Response of R/C Beams with Concrete Overlays," Civil Engineering Department, Report NO. CCEER-89-2, University of Nevada, Reno, June 1989.

CCEER-89-3 Ebrahimpour, A. and P. Jagadish, "Statistical Modeling of Bridge Traffic Loads - A Case Study," Civil Engineering Department, Report No. CCEER-89-3, University of Nevada, Reno, December 1989.

CCEER-89-4 Shields, J. and M. Saiidi, "Direct Field Measurement of Prestress Losses in Box Girder Bridges," Civil Engineering Department, Report No. CCEER-89-4, University of Nevada, Reno, December 1989.

CCEER-90-1 Saiidi, M., E. Maragakis, G. Ghusn, Y. Jiang, and D. Schwartz, "Survey and Evaluation of Nevada's Transportation Infrastructure, Task 7.2 - Highway Bridges, Final Report," Civil Engineering Department, Report No. CCEER 90-1, University of Nevada, Reno, October 1990.

CCEER-90-2 Abdel-Ghaffar, S., E. Maragakis, and M. Saiidi, "Analysis of the Response of Reinforced Concrete Structures During the Whittier Earthquake 1987," Civil Engineering Department, Report No. CCEER 90-2, University of Nevada, Reno, October 1990.

CCEER-91-1 Saiidi, M., E. Hwang, E. Maragakis, and B. Douglas, "Dynamic Testing and the Analysis of the Flamingo Road Interchange," Civil Engineering Department, Report No. CCEER-91-1, University of Nevada, Reno, February 1991.

CCEER-91-2 Norris, G., R. Siddharthan, Z. Zafir, S. Abdel-Ghaffar, and P. Gowda, "Soil-Foundation-Structure Behavior at the Oakland Outer Harbor Wharf," Civil Engineering Department, Report No. CCEER-91-2, University of Nevada, Reno, July 1991.

CCEER-91-3 Norris, G., "Seismic Lateral and Rotational Pile Foundation Stiffnesses at Cypress," Civil Engineering Department, Report No. CCEER-91-3, University of Nevada, Reno, August 1991.

CCEER-91-4 O'Connor, D. and M. Saiidi, "A Study of Protective Overlays for Highway Bridge Decks in Nevada, with Emphasis on Polyester-Styrene Polymer Concrete," Civil Engineering Department, Report No. CCEER-91-4, University of Nevada, Reno, October 1991.

CCEER-91-5 O'Connor, D.N. and M. Saiidi, "Laboratory Studies of Polyester-Styrene Polymer Concrete Engineering Properties," Civil Engineering Department, Report No. CCEER-91-5, University of Nevada, Reno, November 1991.

CCEER-92-1 Straw, D.L. and M. Saiidi, "Scale Model Testing of One-Way Reinforced Concrete Pier Hinges Subject to Combined Axial Force, Shear and Flexure," edited by D.N. O'Connor, Civil Engineering Department, Report No. CCEER-92-1, University of Nevada, Reno, March 1992.

CCEER-92-2 Wehbe, N., M. Saiidi, and F. Gordaninejad, "Basic Behavior of Composite Sections Made of Concrete Slabs and Graphite Epoxy Beams," Civil Engineering Department, Report No. CCEER-92-2, University of Nevada, Reno, August 1992.

CCEER-92-3 Saiidi, M. and E. Hutchens, "A Study of Prestress Changes in A Post-Tensioned Bridge During the First 30 Months," Civil Engineering Department, Report No. CCEER-92-3, University of Nevada, Reno, April 1992.

CCEER-92-4 Saiidi, M., B. Douglas, S. Feng, E. Hwang, and E. Maragakis, “Effects of Axial Force on Frequency of Prestressed Concrete Bridges,” Civil Engineering Department, Report No. CCEER-92-4, University of Nevada, Reno, August 1992.

CCEER-92-5 Siddharthan, R., and Z. Zafir, “Response of Layered Deposits to Traveling Surface Pressure Waves,” Civil Engineering Department, Report No. CCEER-92-5, University of Nevada, Reno, September 1992.

CCEER-92-6 Norris, G., and Z. Zafir, “Liquefaction and Residual Strength of Loose Sands from Drained Triaxial Tests,” Civil Engineering Department, Report No. CCEER-92-6, University of Nevada, Reno, September 1992.

CCEER-92-6-A Norris, G., Siddharthan, R., Zafir, Z. and Madhu, R. “Liquefaction and Residual Strength of Sands from Drained Triaxial Tests,” Civil Engineering Department, Report No. CCEER-92-6-A, University of Nevada, Reno, September 1992.

CCEER-92-7 Douglas, B., “Some Thoughts Regarding the Improvement of the University of Nevada, Reno's National Academic Standing,” Civil Engineering Department, Report No. CCEER-92-7, University of Nevada, Reno, September 1992.

CCEER-92-8 Saiidi, M., E. Maragakis, and S. Feng, “An Evaluation of the Current Caltrans Seismic Restrainer Design Method,” Civil Engineering Department, Report No. CCEER-92-8, University of Nevada, Reno, October 1992.

CCEER-92-9 O'Connor, D., M. Saiidi, and E. Maragakis, “Effect of Hinge Restrainers on the Response of the Madrone Drive Undercrossing During the Loma Prieta Earthquake,” Civil Engineering Department, Report No. CCEER-92-9, University of Nevada, Reno, February 1993.

CCEER-92-10 O'Connor, D., and M. Saiidi, “Laboratory Studies of Polyester Concrete: Compressive Strength at Elevated Temperatures and Following Temperature Cycling, Bond Strength to Portland Cement Concrete, and Modulus of Elasticity,” Civil Engineering Department, Report No. CCEER-92-10, University of Nevada, Reno, February 1993.

CCEER-92-11 Wehbe, N., M. Saiidi, and D. O'Connor, “Economic Impact of Passage of Spent Fuel Traffic on Two Bridges in Northeast Nevada,” Civil Engineering Department, Report No. CCEER-92-11, University of Nevada, Reno, December 1992.

CCEER-93-1 Jiang, Y., and M. Saiidi, “Behavior, Design, and Retrofit of Reinforced Concrete One-way Bridge Column Hinges,” edited by D. O'Connor, Civil Engineering Department, Report No. CCEER-93-1, University of Nevada, Reno, March 1993.

CCEER-93-2 Abdel-Ghaffar, S., E. Maragakis, and M. Saiidi, “Evaluation of the Response of the Aptos Creek Bridge During the 1989 Loma Prieta Earthquake,” Civil Engineering Department, Report No. CCEER-93-2, University of Nevada, Reno, June 1993.

CCEER-93-3 Sanders, D.H., B.M. Douglas, and T.L. Martin, “Seismic Retrofit Prioritization of Nevada Bridges,” Civil Engineering Department, Report No. CCEER-93-3, University of Nevada, Reno, July 1993.

CCEER-93-4 Abdel-Ghaffar, S., E. Maragakis, and M. Saiidi, “Performance of Hinge Restrainers in the Huntington Avenue Overhead During the 1989 Loma Prieta Earthquake,” Civil Engineering Department, Report No. CCEER-93-4, University of Nevada, Reno, June 1993.

CCEER-93-5 Maragakis, E., M. Saiidi, S. Feng, and L. Flournoy, “Effects of Hinge Restrainers on the Response of the San Gregorio Bridge during the Loma Prieta Earthquake,” (in final preparation) Civil Engineering Department, Report No. CCEER-93-5, University of Nevada, Reno.

CCEER-93-6 Saiidi, M., E. Maragakis, S. Abdel-Ghaffar, S. Feng, and D. O'Connor, “Response of Bridge Hinge Restrainers during Earthquakes -Field Performance, Analysis, and Design,” Civil Engineering Department, Report No. CCEER-93-6, University of Nevada, Reno, May 1993.

CCEER-93-7 Wehbe, N., Saiidi, M., Maragakis, E., and Sanders, D., “Adequacy of Three Highway Structures in Southern Nevada for Spent Fuel Transportation,” Civil Engineering Department, Report No. CCEER-93-7, University of Nevada, Reno, August 1993.

CCEER-93-8 Roybal, J., Sanders, D.H., and Maragakis, E., “Vulnerability Assessment of Masonry in the Reno-Carson City Urban Corridor,” Civil Engineering Department, Report No. CCEER-93-8, University of Nevada, Reno, May 1993.

CCEER-93-9 Zafir, Z. and Siddharthan, R., “MOVLOAD: A Program to Determine the Behavior of Nonlinear Horizontally Layered Medium Under Moving Load,” Civil Engineering Department, Report No. CCEER-93-9, University of Nevada, Reno, August 1993.

CCEER-93-10 O'Connor, D.N., Saiidi, M., and Maragakis, E.A., “A Study of Bridge Column Seismic Damage Susceptibility at the Interstate 80/U.S. 395 Interchange in Reno, Nevada,” Civil Engineering Department, Report No. CCEER-93-10, University of Nevada, Reno, October 1993.

CCEER-94-1 Maragakis, E., B. Douglas, and E. Abdelwahed, “Preliminary Dynamic Analysis of a Railroad Bridge,” Report CCEER-94-1, January 1994.

CCEER-94-2 Douglas, B.M., Maragakis, E.A., and Feng, S., “Stiffness Evaluation of Pile Foundation of Cazenovia Creek Overpass,” Civil Engineering Department, Report No. CCEER-94-2, University of Nevada, Reno, March 1994.

CCEER-94-3 Douglas, B.M., Maragakis, E.A., and Feng, S., “Summary of Pretest Analysis of Cazenovia Creek Bridge,” Civil Engineering Department, Report No. CCEER-94-3, University of Nevada, Reno, April 1994.

CCEER-94-4 Norris, G.M., Madhu, R., Valceschini, R., and Ashour, M., “Liquefaction and Residual Strength of Loose Sands from Drained Triaxial Tests,” Report 2, Vol. 1&2, Civil Engineering Department, Report No. CCEER-94-4, University of Nevada, Reno, August 1994.

CCEER-94-5 Saiidi, M., Hutchens, E., and Gardella, D., “Prestress Losses in a Post-Tensioned R/C Box Girder Bridge in Southern Nevada,” Civil Engineering Department, CCEER-94-5, University of Nevada, Reno, August 1994.

CCEER-95-1 Siddharthan, R., El-Gamal, M., and Maragakis, E.A., “Nonlinear Bridge Abutment , Verification, and Design Curves,” Civil Engineering Department, CCEER-95-1, University of Nevada, Reno, January 1995.

CCEER-95-2 Ashour, M. and Norris, G., “Liquefaction and Undrained Response Evaluation of Sands from Drained Formulation,” Civil Engineering Department, Report No. CCEER-95-2, University of Nevada, Reno, February 1995.

CCEER-95-3 Wehbe, N., Saiidi, M., Sanders, D. and Douglas, B., “Ductility of Rectangular Reinforced Concrete Bridge Columns with Moderate Confinement,” Civil Engineering Department, Report No. CCEER-95-3, University of Nevada, Reno, July 1995.

CCEER-95-4 Martin, T.., Saiidi, M. and Sanders, D., “Seismic Retrofit of Column-Pier Cap Connections in Bridges in Northern Nevada,” Civil Engineering Department, Report No. CCEER-95-4, University of Nevada, Reno, August 1995.

CCEER-95-5 Darwish, I., Saiidi, M. and Sanders, D., “Experimental Study of Seismic Susceptibility Column-

Footing Connections in Bridges in Northern Nevada," Civil Engineering Department, Report No. CCEER-95-5, University of Nevada, Reno, September 1995.

CCEER-95-6 Griffin, G., Saiidi, M. and Maragakis, E., "Nonlinear Seismic Response of Isolated Bridges and Effects of Pier Ductility Demand," Civil Engineering Department, Report No. CCEER-95-6, University of Nevada, Reno, November 1995.

CCEER-95-7 Acharya, S.., Saiidi, M. and Sanders, D., "Seismic Retrofit of Bridge Footings and Column-Footing Connections," Civil Engineering Department, Report No. CCEER-95-7, University of Nevada, Reno, November 1995.

CCEER-95-8 Maragakis, E., Douglas, B., and Sandirasegaram, U., "Full-Scale Field Resonance Tests of a Railway Bridge," A Report to the Association of American Railroads, Civil Engineering Department, Report No. CCEER-95-8, University of Nevada, Reno, December 1995.

CCEER-95-9 Douglas, B., Maragakis, E. and Feng, S., "System Identification Studies on Cazenovia Creek Overpass," Report for the National Center for Earthquake Engineering Research, Civil Engineering Department, Report No. CCEER-95-9, University of Nevada, Reno, October 1995.

CCEER-96-1 El-Gamal, M.E. and Siddharthan, R.V., "Programs to Computer Translational Stiffness of Seat-Type Bridge Abutment," Civil Engineering Department, Report No. CCEER-96-1, University of Nevada, Reno, March 1996.

CCEER-96-2 Labia, Y., Saiidi, M. and Douglas, B., "Evaluation and Repair of Full-Scale Prestressed Concrete Box Girders," A Report to the National Science Foundation, Research Grant CMS-9201908, Civil Engineering Department, Report No. CCEER-96-2, University of Nevada, Reno, May 1996.

CCEER-96-3 Darwish, I., Saiidi, M. and Sanders, D., "Seismic Retrofit of R/C Oblong Tapered Bridge Columns with Inadequate Bar Anchorage in Columns and Footings," A Report to the Nevada Department of Transportation, Civil Engineering Department, Report No. CCEER-96-3, University of Nevada, Reno, May 1996.

CCEER-96-4 Ashour, M., Pilling, R., Norris, G. and Perez, H., "The Prediction of Lateral Load Behavior of Single Piles and Pile Groups Using the Strain Wedge Model," A Report to the California Department of Transportation, Civil Engineering Department, Report No. CCEER-96-4, University of Nevada, Reno, June 1996.

CCEER-97-1-A Rimal, P. and Itani, A. "Sensitivity Analysis of Fatigue Evaluations of Steel Bridges," Center for Earthquake Research, Department of Civil Engineering, University of Nevada, Reno, Nevada Report No. CCEER-97-1-A, September, 1997.

CCEER-97-1-B Maragakis, E., Douglas, B., and Sandirasegaram, U. "Full-Scale Field Resonance Tests of a Railway Bridge," A Report to the Association of American Railroads, Civil Engineering Department, University of Nevada, Reno, May, 1996.

CCEER-97-2 Wehbe, N., Saiidi, M., and D. Sanders, "Effect of Confinement and Flares on the Seismic Performance of Reinforced Concrete Bridge Columns," Civil Engineering Department, Report No. CCEER-97-2, University of Nevada, Reno, September 1997.

CCEER-97-3 Darwish, I., M. Saiidi, G. Norris, and E. Maragakis, "Determination of In-Situ Footing Stiffness Using Full-Scale Dynamic Field Testing," A Report to the Nevada Department of Transportation, Structural Design Division, Carson City, Nevada, Report No. CCEER-97-3, University of Nevada, Reno, October 1997.

CCEER-97-4-A Itani, A. "Cyclic Behavior of Richmond-San Rafael Tower Links," Center for Civil Engineering

Earthquake Research, Department of Civil Engineering, University of Nevada, Reno, Nevada, Report No. CCEER-97-4, August 1997.

CCEER-97-4-B Wehbe, N., and M. Saiidi, "User's Manual for RCMC v. 1.2 : A Computer Program for Moment-Curvature Analysis of Confined and Unconfined Reinforced Concrete Sections," Center for Civil Engineering Earthquake Research, Department of Civil Engineering, University of Nevada, Reno, Nevada, Report No. CCEER-97-4, November, 1997.

CCEER-97-5 Isakovic, T., M. Saiidi, and A. Itani, "Influence of new Bridge Configurations on Seismic Performance," Department of Civil Engineering, University of Nevada, Reno, Report No. CCEER-97-5, September, 1997.

CCEER-98-1 Itani, A., Vesco, T. and Dietrich, A., "Cyclic Behavior of "as Built" Laced Members With End Gusset Plates on the San Francisco Bay Bridge," Center for Civil Engineering Earthquake Research, Department of Civil Engineering, University of Nevada, Reno, Nevada Report No. CCEER-98-1, March, 1998.

CCEER-98-2 G. Norris and M. Ashour, "Liquefaction and Undrained Response Evaluation of Sands from Drained Formulation," Center for Civil Engineering Earthquake Research, Department of Civil Engineering, University of Nevada, Reno, Nevada, Report No. CCEER-98-2, May, 1998.

CCEER-98-3 Qingbin, Chen, B. M. Douglas, E. Maragakis, and I. G. Buckle, "Extraction of Nonlinear Hysteretic Properties of Seismically Isolated Bridges from Quick-Release Field Tests," Center for Civil Engineering Earthquake Research, Department of Civil Engineering, University of Nevada, Reno, Nevada, Report No. CCEER-98-3, June, 1998.

CCEER-98-4 Maragakis, E., B. M. Douglas, and C. Qingbin, "Full-Scale Field Capacity Tests of a Railway Bridge," Center for Civil Engineering Earthquake Research, Department of Civil Engineering, University of Nevada, Reno, Nevada, Report No. CCEER-98-4, June, 1998.

CCEER-98-5 Itani, A., Douglas, B., and Woodgate, J., "Cyclic Behavior of Richmond-San Rafael Retrofitted Tower Leg," Center for Civil Engineering Earthquake Research, Department of Civil Engineering, University of Nevada, Reno. Report No. CCEER-98-5, June 1998

CCEER-98-6 Moore, R., Saiidi, M., and Itani, A., "Seismic Behavior of New Bridges with Skew and Curvature," Center for Civil Engineering Earthquake Research, Department of Civil Engineering, University of Nevada, Reno. Report No. CCEER-98-6, October, 1998.

CCEER-98-7 Itani, A and Dietrich, A, "Cyclic Behavior of Double Gusset Plate Connections," Center for Civil Engineering Earthquake Research, Department of Civil Engineering, University of Nevada, Reno, Nevada, Report No. CCEER-98-5, December, 1998.

CCEER-99-1 Caywood, C., M. Saiidi, and D. Sanders, "Seismic Retrofit of Flared Bridge Columns with Steel Jackets," Civil Engineering Department, University of Nevada, Reno, Report No. CCEER-99-1, February 1999.

CCEER-99-2 Mangoba, N., M. Mayberry, and M. Saiidi, "Prestress Loss in Four Box Girder Bridges in Northern Nevada," Civil Engineering Department, University of Nevada, Reno, Report No. CCEER-99-2, March 1999.

CCEER-99-3 Abo-Shadi, N., M. Saiidi, and D. Sanders, "Seismic Response of Bridge Pier Walls in the Weak Direction," Civil Engineering Department, University of Nevada, Reno, Report No. CCEER-99-3, April 1999.

CCEER-99-4 Buzick, A., and M. Saiidi, "Shear Strength and Shear Fatigue Behavior of Full-Scale Prestressed Concrete Box Girders," Civil Engineering Department, University of Nevada, Reno, Report No. CCEER-99-4, April 1999.

CCEER-99-5 Randall, M., M. Saiidi, E. Maragakis and T. Isakovic, "Restrainer Design Procedures For Multi-Span Simply-Supported Bridges," Civil Engineering Department, University of Nevada, Reno, Report No. CCEER-99-5, April 1999.

CCEER-99-6 Wehbe, N. and M. Saiidi, "User's Manual for RCMC v. 1.2, A Computer Program for Moment-Curvature Analysis of Confined and Unconfined Reinforced Concrete Sections," Civil Engineering Department, University of Nevada, Reno, Report No. CCEER-99-6, May 1999.

CCEER-99-7 Burda, J. and A. Itani, "Studies of Seismic Behavior of Steel Base Plates," Civil Engineering Department, University of Nevada, Reno, Report No. CCEER-99-7, May 1999.

CCEER-99-8 Ashour, M. and G. Norris, "Refinement of the Strain Wedge Model Program," Civil Engineering Department, University of Nevada, Reno, Report No. CCEER-99-8, March 1999.

CCEER-99-9 Dietrich, A., and A. Itani, "Cyclic Behavior of Laced and Perforated Steel Members on the San Francisco-Oakland Bay Bridge," Civil Engineering Department, University, Reno, Report No. CCEER-99-9, December 1999.

CCEER 99-10 Itani, A., A. Dietrich, "Cyclic Behavior of Built Up Steel Members and their Connections," Civil Engineering Department, University of Nevada, Reno, Report No. CCEER-99-10, December 1999.

CCEER 99-10-A Itani, A., E. Maragakis and P. He, "Fatigue Behavior of Riveted Open Deck Railroad Bridge Girders," Civil Engineering Department, University of Nevada, Reno, Report No. CCEER-99-10-A, August 1999.

CCEER 99-11 Itani, A., J. Woodgate, "Axial and Rotational Ductility of Built Up Structural Steel Members," Civil Engineering Department, University of Nevada, Reno, Report No. CCEER-99-11, December 1999.

CCEER-99-12 Sgambelluri, M., Sanders, D.H., and Saiidi, M.S., "Behavior of One-Way Reinforced Concrete Bridge Column Hinges in the Weak Direction," Department of Civil Engineering, University of Nevada, Reno, Report No. CCEER-99-12, December 1999.

CCEER-99-13 Laplace, P., Sanders, D.H., Douglas, B, and Saiidi, M, "Shake Table Testing of Flexure Dominated Reinforced Concrete Bridge Columns", Department of Civil Engineering, University of Nevada, Reno, Report No. CCEER-99-13, December 1999.

CCEER-99-14 Ahmad M. Itani, Jose A. Zepeda, and Elizabeth A. Ware "Cyclic Behavior of Steel Moment Frame Connections for the Moscone Center Expansion," Department of Civil Engineering, University of Nevada, Reno, Report No. CCEER-99-14, December 1999.

CCEER 00-1 Ashour, M., and Norris, G. "Undrained Lateral Pile and Pile Group Response in Saturated Sand," Civil Engineering Department, University of Nevada, Reno, Report No. CCEER-00-1, May 1999. January 2000.

CCEER 00-2 Saiidi, M. and Wehbe, N., "A Comparison of Confinement Requirements in Different Codes for Rectangular, Circular, and Double-Spiral RC Bridge Columns," Civil Engineering Department, University of Nevada, Reno, Report No. CCEER-00-2, January 2000.

CCEER 00-3 McElhaney, B., M. Saiidi, and D. Sanders, "Shake Table Testing of Flared Bridge Columns With Steel Jacket Retrofit," Civil Engineering Department, University of Nevada, Reno, Report No. CCEER-00-3, January 2000.

CCEER 00-4 Martinovic, F., M. Saiidi, D. Sanders, and F. Gordaninejad, "Dynamic Testing of Non-Prismatic Reinforced Concrete Bridge Columns Retrofitted with FRP Jackets," Civil Engineering Department, University of Nevada, Reno, Report No. CCEER-00-4, January 2000.

CCEER 00-5 Itani, A., and M. Saiidi, "Seismic Evaluation of Steel Joints for UCLA Center for Health Science Westwood Replacement Hospital," Civil Engineering Department, University of Nevada, Reno, Report No. CCEER-00-5, February 2000.

CCEER 00-6 Will, J. and D. Sanders, "High Performance Concrete Using Nevada Aggregates," Civil Engineering Department, University of Nevada, Reno, Report No. CCEER-00-6, May 2000.

CCEER 00-7 French, C., and M. Saiidi, "A Comparison of Static and Dynamic Performance of Models of Flared Bridge Columns," Civil Engineering Department, University of Nevada, Reno, Report No. CCEER-00-7, October 2000.

CCEER 00-8 Itani, A., H. Sedarat, "Seismic Analysis of the AISI LRFD Design Example of Steel Highway Bridges," Civil Engineering Department, University of Nevada, Reno, Report No. CCEER 00-08, November 2000.

CCEER 00-9 Moore, J., D. Sanders, and M. Saiidi, "Shake Table Testing of 1960's Two Column Bent with Hinges Bases," Civil Engineering Department, University of Nevada, Reno, Report No. CCEER 00-09, December 2000.

CCEER 00-10 Asthana, M., D. Sanders, and M. Saiidi, "One-Way Reinforced Concrete Bridge Column Hinges in the Weak Direction," Civil Engineering Department, University of Nevada, Reno, Report No. CCEER 00-10, April 2001.

CCEER 01-1 Ah Sha, H., D. Sanders, M. Saiidi, "Early Age Shrinkage and Cracking of Nevada Concrete Bridge Decks," Civil Engineering Department, University of Nevada, Reno, Report No. CCEER 01-01, May 2001.

CCEER 01-2 Ashour, M. and G. Norris, "Pile Group program for Full Material Modeling a Progressive Failure," Civil Engineering Department, University of Nevada, Reno, Report No. CCEER 01-02, July 2001.

CCEER 01-3 Itani, A., C. Lanaud, and P. Dusicka, "Non-Linear Finite Element Analysis of Built-Up Shear Links," Civil Engineering Department, University of Nevada, Reno, Report No. CCEER 01-03, July 2001.

CCEER 01-4 Saiidi, M., J. Mortensen, and F. Martinovic, "Analysis and Retrofit of Fixed Flared Columns with Glass Fiber-Reinforced Plastic Jacketing," Civil Engineering Department, University of Nevada, Reno, Report No. CCEER 01-4, August 2001

CCEER 01-5 Not Published

CCEER 01-6 Laplace, P., D. Sanders, and M. Saiidi, "Experimental Study and Analysis of Retrofitted Flexure and Shear Dominated Circular Reinforced Concrete Bridge Columns Subjected to Shake Table Excitation," Civil Engineering Department, University of Nevada, Reno, Report No. CCEER 01-6, June 2001.

CCEER 01-7 Reppi, F., and D. Sanders, "Removal and Replacement of Cast-in-Place, Post-tensioned, Box Girder Bridge," Civil Engineering Department, University of Nevada, Reno, Report No. CCEER 01-7, December 2001.

CCEER 02-1 Pulido, C., M. Saiidi, D. Sanders, and A. Itani, "Seismic Performance and Retrofitting of Reinforced Concrete Bridge Bents," Civil Engineering Department, University of Nevada, Reno, Report No. CCEER 02-1, January 2002.

CCEER 02-2 Yang, Q., M. Saiidi, H. Wang, and A. Itani, "Influence of Ground Motion Incoherency on Earthquake Response of Multi-Support Structures," Civil Engineering Department, University of Nevada, Reno, Report No. CCEER 02-2, May 2002.

CCEER 02-3 M. Saiidi, B. Gopalakrishnan, E. Reinhardt, and R. Siddharthan, "A Preliminary Study of Shake Table Response of A Two-Column Bridge Bent on Flexible Footings," Civil Engineering Department, University of Nevada, Reno, Report No. CCEER 02-03, June 2002.

CCEER 02-4 Not Published

CCEER 02-5 Banghart, A., Sanders, D., Saiidi, M., "Evaluation of Concrete Mixes for Filling the Steel Arches in the Galena Creek Bridge," Civil Engineering Department, University of Nevada, Reno, Report No. CCEER 02-05, June 2002.

CCEER 02-6 Dusicka, P., Itani, A., Buckle, I. G., "Cyclic Behavior of Shear Links and Tower Shaft Assembly of San Francisco – Oakland Bay Bridge Tower," Civil Engineering Department, University of Nevada, Reno, Report No. CCEER 02-06, July 2002.

CCEER 02-7 Mortensen, J., and M. Saiidi, "A Performance-Based Design Method for Confinement in Circular Columns," Civil Engineering Department, University of Nevada, Reno, Report No. CCEER 02-07, November 2002.

CCEER 03-1 Wehbe, N., and M. Saiidi, "User's manual for SPMC v. 1.0 : A Computer Program for Moment-Curvature Analysis of Reinforced Concrete Sections with Interlocking Spirals," Center for Civil Engineering Earthquake Research, Department of Civil Engineering, University of Nevada, Reno, Nevada, Report No. CCEER-03-1, May, 2003.

CCEER 03-2 Wehbe, N., and M. Saiidi, "User's manual for RCMC v. 2.0 : A Computer Program for Moment-Curvature Analysis of Confined and Unconfined Reinforced Concrete Sections," Center for Civil Engineering Earthquake Research, Department of Civil Engineering, University of Nevada, Reno, Nevada, Report No. CCEER-03-2, June, 2003.

CCEER 03-3 Nada, H., D. Sanders, and M. Saiidi, "Seismic Performance of RC Bridge Frames with Architectural-Flared Columns," Civil Engineering Department, University of Nevada, Reno, Report No. CCEER 03-3, January 2003.

CCEER 03-4 Reinhardt, E., M. Saiidi, and R. Siddharthan, "Seismic Performance of a CFRP/ Concrete Bridge Bent on Flexible Footings," Civil Engineering Department, University of Nevada, Reno, Report No. CCEER 03-4, August 2003.

CCEER 03-5 Johnson, N., M. Saiidi, A. Itani, and S. Ladkany, "Seismic Retrofit of Octagonal Columns with Pedestal and One-Way Hinge at the Base," Center for Civil Engineering Earthquake Research, Department of Civil Engineering, University of Nevada, Reno, Nevada, and Report No. CCEER-03-5, August 2003.

CCEER 03-6 Mortensen, C., M. Saiidi, and S. Ladkany, "Creep and Shrinkage Losses in Highly Variable Climates," Center for Civil Engineering Earthquake Research, Department of Civil Engineering, University of Nevada, Reno, Report No. CCEER-03-6, September 2003.

CCEER 03- 7 Ayoub, C., M. Saiidi, and A. Itani, "A Study of Shape-Memory-Alloy-Reinforced Beams and Cubes," Center for Civil Engineering Earthquake Research, Department of Civil Engineering, University of Nevada, Reno, Nevada, Report No. CCEER-03-7, October 2003.

CCEER 03-8 Chandane, S., D. Sanders, and M. Saiidi, "Static and Dynamic Performance of RC Bridge Bents with Architectural-Flared Columns," Center for Civil Engineering Earthquake Research, Department of Civil Engineering, University of Nevada, Reno, Nevada, Report No. CCEER-03-8, November 2003.

CCEER 04-1 Olaegbe, C., and Saiidi, M., "Effect of Loading History on Shake Table Performance of A Two-Column Bent with Infill Wall," Center for Civil Engineering Earthquake Research, Department of Civil Engineering, University of Nevada, Reno, Nevada, Report No. CCEER-04-1, January 2004.

CCEER 04-2 Johnson, R., Maragakis, E., Saiidi, M., and DesRoches, R., "Experimental Evaluation of Seismic Performance of SMA Bridge Restrainers," Center for Civil Engineering Earthquake Research, Department of Civil Engineering, University of Nevada, Reno, Nevada, Report No. CCEER-04-2, February 2004.

CCEER 04-3 Moustafa, K., Sanders, D., and Saiidi, M., "Impact of Aspect Ratio on Two-Column Bent Seismic Performance," Center for Civil Engineering Earthquake Research, Department of Civil Engineering, University of Nevada, Reno, Nevada, Report No. CCEER-04-3, February 2004.

CCEER 04-4 Maragakis, E., Saiidi, M., Sanchez-Camargo, F., and Elfass, S., "Seismic Performance of Bridge Restrainers At In-Span Hinges," Center for Civil Engineering Earthquake Research, Department of Civil Engineering, University of Nevada, Reno, Nevada, Report No. CCEER-04-4, March 2004.

CCEER 04-5 Ashour, M., Norris, G. and Elfass, S., "Analysis of Laterally Loaded Long or Intermediate Drilled Shafts of Small or Large Diameter in Layered Soil," Center for Civil Engineering Earthquake Research, Department of Civil Engineering, University of Nevada, Reno, Nevada, Report No. CCEER-04-5, June 2004.

CCEER 04-6 Correal, J., Saiidi, M. and Sanders, D., "Seismic Performance of RC Bridge Columns Reinforced with Two Interlocking Spirals," Center for Civil Engineering Earthquake Research, Department of Civil Engineering, University of Nevada, Reno, Nevada, Report No. CCEER-04-6, August 2004.

CCEER 04-7 Dusicka, P., Itani, A. and Buckle, I., "Cyclic Response and Low Cycle Fatigue Characteristics of Plate Steels," Center for Civil Engineering Earthquake Research, Department of Civil Engineering, University of Nevada, Reno, Nevada, Report No. CCEER-04-7, November 2004.

CCEER 04-8 Dusicka, P., Itani, A. and Buckle, I., "Built-up Shear Links as Energy Dissipaters for Seismic Protection of Bridges," Center for Civil Engineering Earthquake Research, Department of Civil Engineering, University of Nevada, Reno, Nevada, Report No. CCEER-04-8, November 2004.

CCEER 04-9 Sureshkumar, K., Saiidi, S., Itani, A. and Ladkany, S., "Seismic Retrofit of Two-Column Bents with Diamond Shape Columns," Center for Civil Engineering Earthquake Research, Department of Civil Engineering, University of Nevada, Reno, Nevada, Report No. CCEER-04-9, November 2004.

CCEER 05-1 Wang, H. and Saiidi, S., "A Study of RC Columns with Shape Memory Alloy and Engineered Cementitious Composites," Center for Civil Engineering Earthquake Research, Department of Civil Engineering, University of Nevada, Reno, Nevada, Report No. CCEER-05-1, January 2005.

CCEER 05-2 Johnson, R., Saiidi, S. and Maragakis, E., "A Study of Fiber Reinforced Plastics for Seismic Bridge Restrainers," Center for Civil Engineering Earthquake Research, Department of Civil Engineering, University of Nevada, Reno, Nevada, Report No. CCEER-05-2, January 2005.

CCEER 05-3 Carden, L.P., Itani, A.M., Buckle, I.G, "Seismic Load Path in Steel Girder Bridge Superstructures," Center for Civil Engineering Earthquake Research, Department of Civil Engineering, University of Nevada, Reno, Nevada, Report No. CCEER-05-3, January 2005.

CCEER 05-4 Carden, L.P., Itani, A.M., Buckle, I.G, "Seismic Performance of Steel Girder Bridge Superstructures with Ductile End Cross Frames and Seismic Isolation," Center for Civil Engineering Earthquake Research, Department of Civil Engineering, University of Nevada, Reno, Nevada, Report No. CCEER-05-4, January 2005.

CCEER 05-5 Goodwin, E., Maragakis, M., Itani, A. and Luo, S., "Experimental Evaluation of the Seismic Performance of Hospital Piping Subassemblies," Center for Civil Engineering Earthquake Research, Department of Civil Engineering, University of Nevada, Reno, Nevada, Report No. CCEER-05-5, February 2005.

CCEER 05-6 Zadeh M. S., Saiidi, S, Itani, A. and Ladkany, S., "Seismic Vulnerability Evaluation and Retrofit Design of Las Vegas Downtown Viaduct," Center for Civil Engineering Earthquake Research, Department of Civil Engineering, University of Nevada, Reno, Nevada, Report No. CCEER-05-6, February 2005.

CCEER 05-7 Phan, V., Saiidi, S. and Anderson, J., "Near Fault (Near Field) Ground Motion Effects on Reinforced Concrete Bridge Columns," Center for Civil Engineering Earthquake Research, Department of Civil Engineering, University of Nevada, Reno, Nevada, Report No. CCEER-05-7, August 2005.

CCEER 05-8 Carden, L., Itani, A. and Laplace, P., "Performance of Steel Props at the UNR Fire Science Academy subjected to Repeated Fire," Center for Civil Engineering Earthquake Research, Department of Civil Engineering, University of Nevada, Reno, Nevada, Report No. CCEER-05-8, August 2005.

CCEER 05-9 Yamashita, R. and Sanders, D., "Shake Table Testing and an Analytical Study of Unbonded Prestressed Hollow Concrete Column Constructed with Precast Segments," Center for Civil Engineering Earthquake Research, Department of Civil Engineering, University of Nevada, Reno, Nevada, Report No. CCEER-05-9, August 2005.

CCEER 05-10 Not Published

CCEER 05-11 Carden, L., Itani., A., and Peckan, G., "Recommendations for the Design of Beams and Posts in Bridge Falsework," Center for Civil Engineering Earthquake Research, Department of Civil Engineering, University of Nevada, Reno, Nevada, Report No. CCEER-05-11, October 2005.

CCEER 06-01 Cheng, Z., Saiidi, M., and Sanders, D., "Development of a Seismic Design Method for Reinforced Concrete Two-Way Bridge Column Hinges," Center for Civil Engineering Earthquake Research, Department of Civil Engineering, University of Nevada, Reno, Nevada, Report No. CCEER-06-01, February 2006.

CCEER 06-02 Johnson, N., Saiidi, M., and Sanders, D., "Large-Scale Experimental and Analytical Studies of a Two-Span Reinforced Concrete Bridge System," Center for Civil Engineering Earthquake Research, Department of Civil Engineering, University of Nevada, Reno, Nevada, Report No. CCEER-06-02, March 2006.

CCEER 06-03 Saiidi, M., Ghasemi, H. and Tiras, A., "Seismic Design and Retrofit of Highway Bridges," Proceedings, Second US-Turkey Workshop, Center for Civil Engineering Earthquake Research, Department of Civil Engineering, University of Nevada, Reno, Nevada, Report No. CCEER-06-03, May 2006.

CCEER 07-01 O'Brien, M., Saiidi, M. and Sadrossadat-Zadeh, M., "A Study of Concrete Bridge Columns Using Innovative Materials Subjected to Cyclic Loading," Center for Civil Engineering Earthquake Research, Department of Civil Engineering, University of Nevada, Reno, Nevada, Report No. CCEER-07-01, January 2007.

CCEER 07-02 Sadrossadat-Zadeh, M. and Saiidi, M., "Effect of Strain rate on Stress-Strain Properties and Yield Propagation in Steel Reinforcing Bars," Center for Civil Engineering Earthquake Research, Department of Civil Engineering, University of Nevada, Reno, Nevada, Report No. CCEER-07-02, January 2007.

CCEER 07-03 Sadrossadat-Zadeh, M. and Saiidi, M., "Analytical Study of NEESR-SG 4-Span Bridge Model Using OpenSees," Center for Civil Engineering Earthquake Research, Department of Civil Engineering, University of Nevada, Reno, Nevada, Report No. CCEER-07-03, January 2007.

CCEER 07-04 Nelson, R., Saiidi, M. and Zadeh, S., "Experimental Evaluation of Performance of Conventional Bridge Systems," Center for Civil Engineering Earthquake Research, Department of Civil Engineering, University of Nevada, Reno, Nevada, Report No. CCEER-07-04, October 2007.

CCEER 07-05 Bahen, N. and Sanders, D., "Strut-and-Tie Modeling for Disturbed Regions in Structural Concrete Members with Emphasis on Deep Beams," Center for Civil Engineering Earthquake Research, Department of Civil Engineering, University of Nevada, Reno, Nevada, Report No. CCEER-07-05, December 2007.

CCEER 07-06 Choi, H., Saiidi, M. and Somerville, P., "Effects of Near-Fault Ground Motion and Fault-Rupture on the Seismic Response of Reinforced Concrete Bridges," Center for Civil Engineering Earthquake Research, Department of Civil Engineering, University of Nevada, Reno, Nevada, Report No. CCEER-07-06, December 2007.

CCEER 07-07 Ashour M. and Norris, G., "Report and User Manual on Strain Wedge Model Computer Program for Files and Large Diameter Shafts with LRFD Procedure," Center for Civil Engineering Earthquake Research, Department of Civil Engineering, University of Nevada, Reno, Nevada, Report No. CCEER-07-07, October 2007.

CCEER 08-01 Doyle, K. and Saiidi, M., "Seismic Response of Telescopic Pipe Pin Connections," Center for Civil Engineering Earthquake Research, Department of Civil Engineering, University of Nevada, Reno, Nevada, Report No. CCEER-08-01, February 2008.

CCEER 08-02 Taylor, M. and Sanders, D., "Seismic Time History Analysis and Instrumentation of the Galena Creek Bridge," Center for Civil Engineering Earthquake Research, Department of Civil Engineering, University of Nevada, Reno, Nevada, Report No. CCEER-08-02, April 2008.

CCEER 08-03 Abdel-Mohti, A. and Pekcan, G., "Seismic Response Assessment and Recommendations for the Design of Skewed Post-Tensioned Concrete Box-Girder Highway Bridges," Center for Civil Engineering Earthquake Research, Department of Civil and Environmental Engineering, University of Nevada, Reno, Nevada, Report No. CCEER-08-03, September 2008.

CCEER 08-04 Saiidi, M., Ghasemi, H. and Hook, J., "Long Term Bridge Performance Monitoring, Assessment & Management," Proceedings, FHWA/NSF Workshop on Future Directions," Center for Civil Engineering Earthquake Research, Department of Civil and Environmental Engineering, University of Nevada, Reno, Nevada, Report No. CCEER 08-04, September 2008.

CCEER 09-01 Brown, A., and Saiidi, M., "Investigation of Near-Fault Ground Motion Effects on Substandard Bridge Columns and Bents," Center for Civil Engineering Earthquake Research, Department of Civil and Environmental Engineering, University of Nevada, Reno, Nevada, Report No. CCEER-09-01, July 2009.

CCEER 09-02 Linke, C., Pekcan, G., and Itani, A., "Detailing of Seismically Resilient Special Truss Moment Frames," Center for Civil Engineering Earthquake Research, Department of Civil and

Environmental Engineering, University of Nevada, Reno, Nevada, Report No. CCEER-09-02, August 2009.

CCEER 09-03 Hillis, D., and Saiidi, M., “Design, Construction, and Nonlinear Dynamic Analysis of Three Bridge Bents Used in a Bridge System Test,” Center for Civil Engineering Earthquake Research, Department of Civil and Environmental Engineering, University of Nevada, Reno, Nevada, Report No. CCEER-09-03, August 2009.

CCEER 09-04 Bahrami, H., Itani, A., and Buckle, I., “Guidelines for the Seismic Design of Ductile End Cross Frames in Steel Girder Bridge Superstructures,” Center for Civil Engineering Earthquake Research, Department of Civil and Environmental Engineering, University of Nevada, Reno, Nevada, Report No. CCEER-09-04, September 2so009.

CCEER 10-01 Zaghi, A. E., and Saiidi, M., “Seismic Design of Pipe-Pin Connections in Concrete Bridges,” Center for Civil Engineering Earthquake Research, Department of Civil and Environmental Engineering, University of Nevada, Reno, Nevada, Report No. CCEER-10-01, January 2010.

CCEER 10-02 Pooranampillai, S., Elfass, S., and Norris, G., “Laboratory Study to Assess Load Capacity Increase of Drilled Shafts through Post Grouting,” Center for Civil Engineering Earthquake Research, Department of Civil and Environmental Engineering, University of Nevada, Reno, Nevada, Report No. CCEER-10-02, January 2010.

CCEER 10-03 Itani, A., Grubb, M., and Monzon, E, “Proposed Seismic Provisions and Commentary for Steel Plate Girder Superstructures,” Center for Civil Engineering Earthquake Research, Department of Civil and Environmental Engineering, University of Nevada, Reno, Nevada, Report No. CCEER-10-03, June 2010.

CCEER 10-04 Cruz-Noguez, C., Saiidi, M., “Experimental and Analytical Seismic Studies of a Four-Span Bridge System with Innovative Materials,” Center for Civil Engineering Earthquake Research, Department of Civil and Environmental Engineering, University of Nevada, Reno, Nevada, Report No. CCEER-10-04, September 2010.

CCEER 10-05 Vosooghi, A., Saiidi, M., “Post-Earthquake Evaluation and Emergency Repair of Damaged RC Bridge Columns Using CFRP Materials,” Center for Civil Engineering Earthquake Research, Department of Civil and Environmental Engineering, University of Nevada, Reno, Nevada, Report No. CCEER-10-05, September 2010.

CCEER 10-06 Ayoub, M., Sanders, D., “Testing of Pile Extension Connections to Slab Bridges,” Center for Civil Engineering Earthquake Research, Department of Civil and Environmental Engineering, University of Nevada, Reno, Nevada, Report No. CCEER-10-06, October 2010.

CCEER 10-07 Builes-Mejia, J. C. and Itani, A., “Stability of Bridge Column Rebar Cages during Construction,” Center for Civil Engineering Earthquake Research, Department of Civil and Environmental Engineering, University of Nevada, Reno, Nevada, Report No. CCEER-10-07, November 2010.

CCEER 10-08 Monzon, E.V., “Seismic Performance of Steel Plate Girder Bridges with Integral Abutments,” Center for Civil Engineering Earthquake Research, Department of Civil and Environmental Engineering, University of Nevada, Reno, Nevada, Report No. CCEER-10-08, November 2010.

CCEER 11-01 Motaref, S., Saiidi, M., and Sanders, D., “Seismic Response of Precast Bridge Columns with Energy Dissipating Joints,” Center for Civil Engineering Earthquake Research, Department of Civil and Environmental Engineering, University of Nevada, Reno, Nevada, Report No. CCEER-11-01, May 2011.

CCEER 11-02 Harrison, N. and Sanders, D., "Preliminary Seismic Analysis and Design of Reinforced Concrete Bridge Columns for Curved Bridge Experiments," Center for Civil Engineering Earthquake Research, Department of Civil and Environmental Engineering, University of Nevada, Reno, Nevada, Report No. CCEER-11-02, May 2011.

CCEER 11-03 Vallejera, J. and Sanders, D., "Instrumentation and Monitoring the Galena Creek Bridge," Center for Civil Engineering Earthquake Research, Department of Civil and Environmental Engineering, University of Nevada, Reno, Nevada, Report No. CCEER-11-03, September 2011.

CCEER 11-04 Levi, M., Sanders, D., and Buckle, I., "Seismic Response of Columns in Horizontally Curved Bridges," Center for Civil Engineering Earthquake Research, Department of Civil and Environmental Engineering, University of Nevada, Reno, Nevada, Report No. CCEER-11-04, December 2011.

CCEER 12-01 Saiidi, M., "NSF International Workshop on Bridges of the Future – Wide Spread Implementation of Innovation," Center for Civil Engineering Earthquake Research, Department of Civil and Environmental Engineering, University of Nevada, Reno, Nevada, Report No. CCEER-12-01, January 2012.

CCEER 12-02 Larkin, A.S., Sanders, D., and Saiidi, M., "Unbonded Prestressed Columns for Earthquake Resistance," Center for Civil Engineering Earthquake Research, Department of Civil and Environmental Engineering, University of Nevada, Reno, Nevada, Report No. CCEER-12-02, January 2012.

CCEER 12-03 Arias-Acosta, J. G., Sanders, D., "Seismic Performance of Circular and Interlocking Spirals RC Bridge Columns under Bidirectional Shake Table Loading Part 1," Center for Civil Engineering Earthquake Research, Department of Civil and Environmental Engineering, University of Nevada, Reno, Nevada, Report No. CCEER-12-03, September 2012.

CCEER 12-04 Cukrov, M.E., Sanders, D., "Seismic Performance of Prestressed Pile-To-Bent Cap Connections," Center for Civil Engineering Earthquake Research, Department of Civil and Environmental Engineering, University of Nevada, Reno, Nevada, Report No. CCEER-12-04, September 2012.

CCEER 13-01 Carr, T. and Sanders, D., "Instrumentation and Dynamic Characterization of the Galena Creek Bridge," Center for Civil Engineering Earthquake Research, Department of Civil and Environmental Engineering, University of Nevada, Reno, Nevada, Report No. CCEER-13-01, January 2013.

CCEER 13-02 Vosooghi, A. and Buckle, I., "Evaluation of the Performance of a Conventional Four-Span Bridge During Shake Table Tests," Center for Civil Engineering Earthquake Research, Department of Civil and Environmental Engineering, University of Nevada, Reno, Nevada, Report No. CCEER-13-02, January 2013.

CCEER 13-03 Amirihormozaki, E. and Pekcan, G., "Analytical Fragility Curves for Horizontally Curved Steel Girder Highway Bridges," Center for Civil Engineering Earthquake Research, Department of Civil and Environmental Engineering, University of Nevada, Reno, Nevada, Report No. CCEER-13-03, February 2013.

CCEER 13-04 Almer, K. and Sanders, D., "Longitudinal Seismic Performance of Precast Bridge Girders Integrally Connected to a Cast-in-Place Bentcap," Center for Civil Engineering Earthquake Research, Department of Civil and Environmental Engineering, University of Nevada, Reno, Nevada, Report No. CCEER-13-04, April 2013.

CCEER 13-05 Monzon, E.V., Itani, A.I., and Buckle, I.G., “Seismic Modeling and Analysis of Curved Steel Plate Girder Bridges,” Center for Civil Engineering Earthquake Research, Department of Civil and Environmental Engineering, University of Nevada, Reno, Nevada, Report No. CCEER-13-05, April 2013.

CCEER 13-06 Monzon, E.V., Buckle, I.G., and Itani, A.I., “Seismic Performance of Curved Steel Plate Girder Bridges with Seismic Isolation,” Center for Civil Engineering Earthquake Research, Department of Civil and Environmental Engineering, University of Nevada, Reno, Nevada, Report No. CCEER-13-06, April 2013.

CCEER 13-07 Monzon, E.V., Buckle, I.G., and Itani, A.I., “Seismic Response of Isolated Bridge Superstructure to Incoherent Ground Motions,” Center for Civil Engineering Earthquake Research, Department of Civil and Environmental Engineering, University of Nevada, Reno, Nevada, Report No. CCEER-13-07, April 2013.

CCEER 13-08 Haber, Z.B., Saiidi, M.S., and Sanders, D.H., “Precast Column-Footing Connections for Accelerated Bridge Construction in Seismic Zones,” Center for Civil Engineering Earthquake Research, Department of Civil and Environmental Engineering, University of Nevada, Reno, Nevada, Report No. CCEER-13-08, April 2013.

CCEER 13-09 Ryan, K.L., Coria, C.B., and Dao, N.D., “Large Scale Earthquake Simulation of a Hybrid Lead Rubber Isolation System Designed under Nuclear Seismicity Considerations,” Center for Civil Engineering Earthquake Research, Department of Civil and Environmental Engineering, University of Nevada, Reno, Nevada, Report No. CCEER-13-09, April 2013.

CCEER 13-10 Wibowo, H., Sanford, D.M., Buckle, I.G., and Sanders, D.H., “The Effect of Live Load on the Seismic Response of Bridges,” Center for Civil Engineering Earthquake Research, Department of Civil and Environmental Engineering, University of Nevada, Reno, Nevada, Report No. CCEER-13-10, May 2013.

CCEER 13-11 Sanford, D.M., Wibowo, H., Buckle, I.G., and Sanders, D.H., “Preliminary Experimental Study on the Effect of Live Load on the Seismic Response of Highway Bridges,” Center for Civil Engineering Earthquake Research, Department of Civil and Environmental Engineering, University of Nevada, Reno, Nevada, Report No. CCEER-13-11, May 2013.

CCEER 13-12 Saad, A.S., Sanders, D.H., and Buckle, I.G., “Assessment of Foundation Rocking Behavior in Reducing the Seismic Demand on Horizontally Curved Bridges,” Center for Civil Engineering Earthquake Research, Department of Civil and Environmental Engineering, University of Nevada, Reno, Nevada, Report No. CCEER-13-12, June 2013.

CCEER 13-13 Ardakani, S.M.S. and Saiidi, M.S., “Design of Reinforced Concrete Bridge Columns for Near-Fault Earthquakes,” Center for Civil Engineering Earthquake Research, Department of Civil and Environmental Engineering, University of Nevada, Reno, Nevada, Report No. CCEER-13-13, July 2013.

CCEER 13-14 Wei, C. and Buckle, I., “Seismic Analysis and Response of Highway Bridges with Hybrid Isolation,” Center for Civil Engineering Earthquake Research, Department of Civil and Environmental Engineering, University of Nevada, Reno, Nevada, Report No. CCEER-13-14, August 2013.

CCEER 13-15 Wibowo, H., Buckle, I.G., and Sanders, D.H., “Experimental and Analytical Investigations on the Effects of Live Load on the Seismic Performance of a Highway Bridge,” Center for Civil Engineering Earthquake Research, Department of Civil and Environmental Engineering, University of Nevada, Reno, Nevada, Report No. CCEER-13-15, August 2013.

CCEER 13-16 Itani, A.M., Monzon, E.V., Grubb, M., and Amirihormozaki, E. “Seismic Design and Nonlinear Evaluation of Steel I-Girder Bridges with Ductile End Cross-Frames,” Center for Civil Engineering Earthquake Research, Department of Civil and Environmental Engineering, University of Nevada, Reno, Nevada, Report No. CCEER-13-16, September 2013.

CCEER 13-17 Kavianipour, F. and Saiidi, M.S., “Experimental and Analytical Seismic Studies of a Four-span Bridge System with Composite Piers,” Center for Civil Engineering Earthquake Research, Department of Civil and Environmental Engineering, University of Nevada, Reno, Nevada, Report No. CCEER-13-17, September 2013.

CCEER 13-18 Mohebbi, A., Ryan, K., and Sanders, D., “Seismic Response of a Highway Bridge with Structural Fuses for Seismic Protection of Piers,” Center for Civil Engineering Earthquake Research, Department of Civil and Environmental Engineering, University of Nevada, Reno, Nevada, Report No. CCEER-13-18, December 2013.

CCEER 13-19 Guzman Pujols, Jean C., Ryan, K.L., “Development of Generalized Fragility Functions for Seismic Induced Content Disruption,” Center for Civil Engineering Earthquake Research, Department of Civil and Environmental Engineering, University of Nevada, Reno, Nevada, Report No. CCEER-13-19, December 2013.

CCEER 14-01 Salem, M. M. A., Pekcan, G., and Itani, A., “Seismic Response Control Of Structures Using Semi-Active and Passive Variable Stiffness Devices,” Center for Civil Engineering Earthquake Research, Department of Civil and Environmental Engineering, University of Nevada, Reno, Nevada, Report No. CCEER-14-01, May 2014.

CCEER 14-02 Saini, A. and Saiidi, M., “Performance-Based Probabilistic Damage Control Approach for Seismic Design of Bridge Columns,” Center For Civil Engineering Earthquake Research, Department Of Civil and Environmental Engineering, University of Nevada, Reno, Nevada, Report No. CCEER-14-02, May 2014.

CCEER 14-03 Saini, A. and Saiidi, M., “Post Earthquake Damage Repair of Various Reinforced Concrete Bridge Components,” Center For Civil Engineering Earthquake Research, Department Of Civil and Environmental Engineering, University of Nevada, Reno, Nevada, Report No. CCEER-14-03, May 2014.

CCEER 14-04 Monzon, E.V., Itani, A.M., and Grubb, M.A., “Nonlinear Evaluation of the Proposed Seismic Design Procedure for Steel Bridges with Ductile End Cross Frames,” Center For Civil Engineering Earthquake Research, Department Of Civil and Environmental Engineering, University of Nevada, Reno, Nevada, Report No. CCEER-14-04, July 2014.

CCEER 14-05 Nakashoji, B. and Saiidi, M.S., “Seismic Performance of Square Nickel-Titanium Reinforced ECC Columns with Headed Couplers,” Center For Civil Engineering Earthquake Research, Department Of Civil and Environmental Engineering, University of Nevada, Reno, Nevada, Report No. CCEER-14-05, July 2014.

CCEER 14-06 Tazarv, M. and Saiidi, M.S., “Next Generation of Bridge Columns for Accelerated Bridge Construction in High Seismic Zones,” Center For Civil Engineering Earthquake Research, Department Of Civil and Environmental Engineering, University of Nevada, Reno, Nevada, Report No. CCEER-14-06, August 2014.

CCEER 14-07 Mehrsoroush, A. and Saiidi, M.S., “Experimental and Analytical Seismic Studies of Bridge Piers with Innovative Pipe Pin Column-Footing Connections and Precast Cap Beams,” Center For Civil Engineering Earthquake Research, Department Of Civil and Environmental Engineering, University of Nevada, Reno, Nevada, Report No. CCEER-14-07, December 2014.

CCEER 15-01 Dao, N.D. and Ryan, K.L., “Seismic Response of a Full-scale 5-story Steel Frame Building Isolated by Triple Pendulum Bearings under 3D Excitations,” Center For Civil Engineering

Earthquake Research, Department Of Civil and Environmental Engineering, University of Nevada, Reno, Nevada, Report No. CCEER-15-01, January 2015.

CCEER 15-02 Allen, B.M. and Sanders, D.H., "Post-Tensioning Duct Air Pressure Testing Effects on Web Cracking," Center For Civil Engineering Earthquake Research, Department Of Civil and Environmental Engineering, University of Nevada, Reno, Nevada, Report No. CCEER-15-02, January 2015.

CCEER 15-03 Akl, A. and Saiidi, M.S., "Time-Dependent Deflection of In-Span Hinges in Prestressed Concrete Box Girder Bridges," Center For Civil Engineering Earthquake Research, Department Of Civil and Environmental Engineering, University of Nevada, Reno, Nevada, Report No. CCEER-15-03, May 2015.

CCEER 15-04 Zargar Shotorbani, H. and Ryan, K., "Analytical and Experimental Study of Gap Damper System to Limit Seismic Isolator Displacements in Extreme Earthquakes," Center For Civil Engineering Earthquake Research, Department Of Civil and Environmental Engineering, University of Nevada, Reno, Nevada, Report No. CCEER-15-04, June 2015.

CCEER 15-05 Wieser, J., Maragakis, E.M., and Buckle, I., "Experimental and Analytical Investigation of Seismic Bridge-Abutment Interaction in a Curved Highway Bridge," Center For Civil Engineering Earthquake Research, Department Of Civil and Environmental Engineering, University of Nevada, Reno, Nevada, Report No. CCEER-15-05, July 2015.

CCEER 15-06 Tazarv, M. and Saiidi, M.S., "Design and Construction of Precast Bent Caps with Pocket Connections for High Seismic Regions," Center For Civil Engineering Earthquake Research, Department Of Civil and Environmental Engineering, University of Nevada, Reno, Nevada, Report No. CCEER-15-06, August 2015.

CCEER 15-07 Tazarv, M. and Saiidi, M.S., "Design and Construction of Bridge Columns Incorporating Mechanical Bar Splices in Plastic Hinge Zones," Center For Civil Engineering Earthquake Research, Department Of Civil and Environmental Engineering, University of Nevada, Reno, Nevada, Report No. CCEER-15-07, August 2015.

CCEER 15-08 Sarraf Shirazi, R., Pekcan, G., and Itani, A.M., "Seismic Response and Analytical Fragility Functions for Curved Concrete Box-Girder Bridges," Center For Civil Engineering Earthquake Research, Department Of Civil and Environmental Engineering, University of Nevada, Reno, Nevada, Report No. CCEER-15-08, December 2015.

CCEER 15-09 Coria, C.B., Ryan, K.L., and Dao, N.D., "Response of Lead Rubber Bearings in a Hybrid Isolation System During a Large Scale Shaking Experiment of an Isolated Building," Center For Civil Engineering Earthquake Research, Department Of Civil and Environmental Engineering, University of Nevada, Reno, Nevada, Report No. CCEER-15-09, December 2015.

CCEER 16-01 Mehraein, M and Saiidi, M.S., "Seismic Performance of Bridge Column-Pile-Shaft Pin Connections for Application in Accelerated Bridge Construction," Center For Civil Engineering Earthquake Research, Department Of Civil and Environmental Engineering, University of Nevada, Reno, Nevada, Report No. CCEER-16-01, May 2016.

CCEER 16-02 Varela Fontecha, S. and Saiidi, M.S., "Resilient Earthquake-Resistant Bridges Designed For Disassembly," Center For Civil Engineering Earthquake Research, Department Of Civil and Environmental Engineering, University of Nevada, Reno, Nevada, Report No. CCEER-16-02, May 2016.

CCEER 16-03 Mantawy, I. M, and Sanders, D. H., "Assessment of an Earthquake Resilient Bridge with Pretensioned, Rocking Columns," Center For Civil Engineering Earthquake Research, Department

Of Civil and Environmental Engineering, University of Nevada, Reno, Nevada, Report No. CCEER-16-03, May 2016.

CCEER 16-04 Mohammed, M, Biasi, G., and Sanders, D., "Post-earthquake Assessment of Nevada Bridges using ShakeMap/ShakeCast," Center For Civil Engineering Earthquake Research, Department Of Civil and Environmental Engineering, University of Nevada, Reno, Nevada, Report No. CCEER-16-04, May 2016.

CCEER 16-05 Jones, J, Ryan, K., and Saiidi, M, "Toward Successful Implementation of Prefabricated Deck Panels to Accelerate the Bridge Construction Process," Center For Civil Engineering Earthquake Research, Department Of Civil and Environmental Engineering, University of Nevada, Reno, Nevada, Report No. CCEER-16-05, August 2016.

CCEER 16-06 Mehrsoroush, A. and Saiidi, M., "Probabilistic Seismic Damage Assessment for Sub-standard Bridge Columns," Center For Civil Engineering Earthquake Research, Department Of Civil and Environmental Engineering, University of Nevada, Reno, Nevada, Report No. CCEER-16-06, November 2016.

CCEER 16-07 Nielsen, T., Maree, A., and Sanders, D., "Experimental Investigation into the Long-Term Seismic Performance of Dry Storage Casks," Center For Civil Engineering Earthquake Research, Department Of Civil and Environmental Engineering, University of Nevada, Reno, Nevada, Report No. CCEER-16-07, December 2016.

CCEER 16-08 Wu, S., Buckle, I., and Itani, A., "Effect of Skew on Seismic Performance of Bridges with Seat-Type Abutments," Center For Civil Engineering Earthquake Research, Department Of Civil and Environmental Engineering, University of Nevada, Reno, Nevada, Report No. CCEER-16-08, December 2016.

CCEER 16-09 Mohammed, M., and Sanders, D., "Effect of Earthquake Duration on Reinforced Concrete Bridge Columns," Center For Civil Engineering Earthquake Research, Department Of Civil and Environmental Engineering, University of Nevada, Reno, Nevada, Report No. CCEER-16-09, December 2016.

CCEER 16-10 Guzman Pujols, J., and Ryan, K., "Slab Vibration and Horizontal-Vertical Coupling in the Seismic Response of Irregular Base-Isolated and Conventional Buildings," Center For Civil Engineering Earthquake Research, Department Of Civil and Environmental Engineering, University of Nevada, Reno, Nevada, Report No. CCEER-16-10, December 2016.

CCEER 17-01 White, L., Ryan, K., and Buckle, I., "Thermal Gradients in Southwestern United States and the Effect on Bridge Bearing Loads," Center For Civil Engineering Earthquake Research, Department Of Civil and Environmental Engineering, University of Nevada, Reno, Nevada, Report No. CCEER-17-01, May 2017.

CCEER 17-02 Mohebbi, A., Saiidi, M., and Itani, A., "Development and Seismic Evaluation of Pier Systems w/Pocket Connections, CFRP Tendons, and ECC/UHPC Columns," Center For Civil Engineering Earthquake Research, Department Of Civil and Environmental Engineering, University of Nevada, Reno, Nevada, Report No. CCEER-17-02, May 2017.

CCEER 17-03 Mehrsoroush, A., Saiidi, M., and Ryan, K., "Development of Earthquake-resistant Precast Pier Systems for Accelerated Bridge Construction in Nevada," Center For Civil Engineering Earthquake Research, Department Of Civil and Environmental Engineering, University of Nevada, Reno, Nevada, Report No. CCEER-17-03, June 2017.

CCEER 17-04 Abdollahi, B., Saiidi, M., Siddharthan, R., and Elfass, S., "Shake Table Studies on Soil-Abutment-Structure Interaction in Skewed Bridges," Center For Civil Engineering Earthquake Research, Department Of Civil and Environmental Engineering, University of Nevada, Reno, Nevada, Report No. CCEER-17-04, July 2017.

CCEER 17-05 Shrestha, G., Itani, A., and Saiidi, M., "Seismic Performance of Precast Full-Depth Decks in Accelerated Bridge Construction," Center for Civil Engineering Earthquake Research, Department of Civil and Environmental Engineering, University of Nevada, Reno, Nevada, Report No. CCEER-17-05, September 2017.

CCEER 17-06 Wu, S., Buckle, I., and Ryan, K., "Large-Scale Experimental Verification of an Optically-Based Sensor System for Monitoring Structural Response," Center for Civil Engineering Earthquake Research, Department of Civil and Environmental Engineering, University of Nevada, Reno, Nevada, Report No. CCEER-17-06, October 2017.

CCEER 17-07 Nada, H., and Sanders, D., "Analytical Investigation into Bridge Column Innovations for Mitigating Earthquake Damage," Center For Civil Engineering Earthquake Research, Department Of Civil and Environmental Engineering, University of Nevada, Reno, Nevada, Report No. CCEER-17-07, October 2017.

CCEER 18-01 Maree, A. F., and Sanders, D., "Performance and Design of Anchorage Zones for Post-Tensioned Box Girder Bridges," Center for Civil Engineering Earthquake Research, Department of Civil and Environmental Engineering, University of Nevada, Reno, Nevada, Report No. CCEER-18-01, January 2018.

CCEER 18-02 Mostafa, K., and Sanders, D., "Improving the Long-Term Performance of Bridge Decks using Deck and Crack Sealers," Center for Civil Engineering Earthquake Research, Department of Civil and Environmental Engineering, University of Nevada, Reno, Nevada, Report No. CCEER-18-02, March 2018.

CCEER 18-03 Blount, S., Ryan, K., Henry, R., Lu, Y., and Elwood, K., "Evaluation of lower damage concepts for enhanced repairability of reinforced concrete walls," Center for Civil Engineering Earthquake Research, Department of Civil and Environmental Engineering, University of Nevada, Reno, Nevada, Report No. CCEER-18-03, June 2018.

CCEER 18-04 Mohebbi, A., Jordan, E., and Saiidi, M., "Exploratory Experimental Studies of Spliced Cam Shape Memory Alloy Bars for Seismic Application," Center for Civil Engineering Earthquake Research, Department Of Civil and Environmental Engineering, University of Nevada, Reno, Nevada, Report No. CCEER-18-04, September 2018.

CCEER 19-01 Saint Pierre, E., Elfass, S., Watters, R., Norris, G., and Ashour, M. "Improving Strain Wedge Model Capabilities in Analyzing Laterally Loaded Drilled Shafts in Cemented Soils," Center for Civil Engineering Earthquake Research, Department of Civil and Environmental Engineering, University of Nevada, Reno, Nevada, Report No. CCEER-19-01, March 2019.

CCEER 19-02 Benjumea, J., Saiidi, M., and Itani, A., "Experimental and Analytical Seismic Studies of a Two-Span Bridge System with Precast Concrete Elements and ABC Connections," Center for Civil Engineering Earthquake Research, Department of Civil and Environmental Engineering, University of Nevada, Reno, Nevada, Report No. CCEER-19-02, May 2019.

CCEER 19-03 Subedi, D., Moustafa, M., and Saiidi, M., "Non-Proprietary UHPC for Anchorage of Large Diameter Column Bars in Grouted Ducts," Center for Civil Engineering Earthquake Research, Department of Civil and Environmental Engineering, University of Nevada, Reno, Nevada, Report No. CCEER-19-03, May 2019.

CCEER 19-04 Shoushtari, E, D., Saiidi, M., Itani, A., and Moustafa, M., "Shake Table Studies of a Steel Girder Bridge System with ABC Connections," Center for Civil Engineering Earthquake Research, Department of Civil and Environmental Engineering, University of Nevada, Reno, Nevada, Report No. CCEER-19-04, June 2019.

CCEER 19-05 Wu, S., Miah, M., and McCallen, D., "Four Canonical Steel Moment Frame Buildings and Inter-Code Comparisons of Nonlinear Building Response," Center for Civil Engineering Earthquake Research, Department of Civil and Environmental Engineering, University of Nevada, Reno, Nevada, Report No. CCEER-19-05, September 2019.

CCEER 20-01 Schwartz, T., Saiidi, M., and Moustafa, M., "Simplifying Cast-in-Place Joint Design Using ABC Pocket Connection Details in High Seismic Regions," Center for Civil Engineering Earthquake Research, Department of Civil and Environmental Engineering, University of Nevada, Reno, Nevada, Report No. CCEER-20-01, January 2020.

CCEER 20-02 Shrestha, G., Saiidi, M., and Sanders, D., "Seismic Studies of Spliced Columns and Anchorage of Large Diameter Bars in Grouted Duct," Center for Civil Engineering Earthquake Research, Department of Civil and Environmental Engineering, University of Nevada, Reno, Nevada, Report No. CCEER-20-02, February 2020.

CCEER 20-03 Ozsahin, E. and Pekcan, G., "Torsional Ground Motion Effects on the Seismic Response of Continuous Box-girder Highway Bridges," Center for Civil Engineering Earthquake Research, Department of Civil and Environmental Engineering, University of Nevada, Reno, Nevada, Report No. CCEER-20-03, April 2020.

CCEER 20-04 Wu, S., Eckert, E., Huang, J., and McCallen, D., "Evaluation of the Domain Reduction Method Applied to Broad-Band, Near-Fault Earthquake Ground Motions with Inter-Code Comparisons," Center for Civil Engineering Earthquake Research, Department of Civil and Environmental Engineering, University of Nevada, Reno, Nevada, Report No. CCEER-20-04, June 2020.

CCEER 20-05 Jones, J., Saiidi, M., and Itani, A. "Experimental and Analytical Studies of a Two-Span Bridge System with Precast Elements Incorporating Rebar Hinge and Socket Connections," Center for Civil Engineering Earthquake Research, Department of Civil and Environmental Engineering, University of Nevada, Reno, Nevada, Report No. CCEER-20-05, July 2020.